

S3 | 2017

# Polish Maritime Research

Marine Processes Studies  
and Marine Engineering





# Polish Maritime Research

Special Issue S3 (95) 2017  
Vol. 24

## Marine Processes Studies and Marine Engineering

ADDRESS OF PUBLISHER  
& EDITOR'S OFFICE:

GDAŃSK UNIVERSITY  
OF TECHNOLOGY

Faculty of Ocean Engineering  
& Ship Technology  
G. Narutowicza 11/12  
80-233 Gdańsk, POLAND

tel.: +48 58 347 13 66  
fax: +48 58 341 13 66

EDITORIAL STAFF:

Jacek Rudnicki  
| Editor in Chief  
Rafał Szłapczyński  
| Associate Editor  
Jerzy Świryczuk  
| Associate Editor  
Przemysław Wierzchowski  
| Associate Editor  
Aleksander Kniat  
| Editor for international  
relations

Price:  
single issue: 25 PLN

Prices for abroad  
single issue:  
- in Europe EURO 15  
- overseas USD 20

WEB:  
[pg.edu.pl/pmr](http://pg.edu.pl/pmr)

e-mail: [pmr@post.pl](mailto:pmr@post.pl)

ISSN 1233-2585

## CONTENS

- |    |  |
|----|--|
| 4  | <b>Jie Zhao, Lingyun Bao, Guixuan Wang</b><br><i>NUMERICAL ANALYSIS OF SOIL SETTLEMENT PREDICTION AND ITS APPLICATION IN LARGE-SCALE MARINE RECLAMATION ARTIFICIAL ISLAND PROJECT</i>                        |
| 12 | <b>Pengfei Huang, Yang Liu, Zhixiu Du, Qilong Chen, Jinhai Chen</b><br><i>DESIGN AND IMPLEMENTATION OF LARGE VESSEL NAVIGATION SYSTEM BASED ON BEIDOU CORS</i>   |
| 16 | <b>Liupeng Jiang, Tao Tao, Cheng Zhang, He Jiang, Jiaojiao Wang</b><br><i>SUMMARY OF THE PORT SHORELINE RESOURCE EVALUATION BASED ON TRIANGULAR FUZZY ANALYTIC HIERARCHY PROCESS</i>                         |
| 23 | <b>Tieliu Jiang, Jianguo Jin, Zhanzhou Wang, Lihua Cao, Bo Li</b><br><i>CALCULATING STUDY OF THE TURBINE AT LAST STAGE FLOW FIELD IN THE SMALL VOLUME FLOW CONDITION</i>                                     |
| 28 | <b>He Jiang, Wei Xiong, Yonghui Cao</b><br><i>RISK OF THE MARITIME SUPPLY CHAIN SYSTEM BASED ON INTERPRETATIVE STRUCTURAL MODEL</i>  |
| 34 | <b>He Jiang, Wei Xiong, Yonghui Cao</b><br><i>A CONCEPTUAL MODEL OF EXCELLENT PERFORMANCE MODE OF PORT ENTERPRISE LOGISTICS MANAGEMENT</i>   |
| 41 | <b>Fuyong Liu, Chaohe Chen, Wei Wu</b><br><i>TOWARDS THE BUILDING INFORMATION MODELING-BASED CAPITAL PROJECT LIFECYCLE MANAGEMENT IN THE LUXURY YACHT INDUSTRY</i>   |
| 49 | <b>Ming Liu, Hengxu Liu, Xiongbo Zheng, Hailong Chen, Liquan Wang, Liang Zhang</b><br><i>NONLINEAR PTO EFFECT ON PERFORMANCE OF VERTICAL AXISYMMETRIC WAVE ENERGY CONVERTER USING SEMI-ANALYTICAL METHOD</i> |
| 58 | <b>Lili Wang, Wenwen Xiao, Chengwei Wang</b><br><i>EVOLUTION OF HIERARCHICAL STRUCTURE AND SPATIAL PATTERN OF COASTAL CITIES IN CHINA – BASED ON THE DATA OF DISTRIBUTION OF MARINE-RELATED ENTERPRISES</i>  |
| 65 | <b>Jianjun Li, Ru Bo Zhang, Yu Yang</b><br><i>MULTI-AUV DISTRIBUTED TASK ALLOCATION BASED ON THE DIFFERENTIAL EVOLUTION QUANTUM BEE COLONY OPTIMIZATION ALGORITHM</i>  |
| 72 | <b>Yi Zhang, Xiaodong Zhang, Xueping Chang, Qian Wu</b><br><i>EXPERIMENTAL AND OPTIMIZATION DESIGN OF OFFSHORE DRILLING SEAL</i>   |
| 79 | <b>Lingjie Zhang, Jianbo Sun, Chen Guo</b><br><i>A NOVEL MULTI-OBJECTIVE DISCRETE PARTICLE SWARM OPTIMIZATION WITH ELITIST PERTURBATION FOR RECONFIGURATION OF SHIP POWER SYSTEM</i>                         |

ADDRESS OF PUBLISHER  
& EDITOR'S OFFICE:

GDAŃSK UNIVERSITY  
OF TECHNOLOGY

Faculty of Ocean Engineering  
& Ship Technology  
G. Narutowicza 11/12  
80-233 Gdańsk, POLAND

tel.: +48 58 347 13 66  
fax: +48 58 341 13 66

- 86 **Wenjuan Li, Wei Liu, Xu Xu, Zhijun Gao**  
*THE PORT SERVICE ECOSYSTEM RESEARCH BASED ON THE LOTKA-VOLTERRA MODEL*
- 95 **Yang Shen, Weijian Mi, Zhiwei Zhang**  
*A POSITIONING LOCKHOLES OF CONTAINER CORNER CASTINGS METHOD BASED ON IMAGE RECOGNITION*
- 102 **Yifan Shen, Ning Zhao, Mengjue Xia, Xueqiang Du**  
*A DEEP Q-LEARNING NETWORK FOR SHIP STOWAGE PLANNING PROBLEM*
- 110 **Changsong Yang, Qi Wang**  
*LOW COST INTEGRATED NAVIGATION SYSTEM FOR UNMANNED VESSEL*
- 116 **Xiao Suo, Gui Fu, Chunxue Wang, Qingsong Jia**  
*AN APPLICATION OF 24MODEL TO ANALYSE CAPSIZING OF THE EASTERN STAR FERRY*
- 123 **Cheng Chen, Yigang Wang, Huiming Huang**  
*INVESTIGATIONS OF TOPOGRAPHIC EFFECT ON RADIAL CURRENT IN SOUTH YELLOW SEA*
- 130 **Hongtao Hu, Xiashong Chen, Zhuo Sun**  
*EFFECT OF WATER FLOWS ON SHIP TRAFFIC IN NARROW WATER CHANNELS BASED ON CELLULAR AUTOMATA*
- 136 **Yanbo Che, Jinhuan Zhou, Guojian Liu, Jianmei Xu, Yuancheng Zhao**  
*MODELING AND ANALYSIS OF 12-PULSE INVERTER IN SHIPBOARD OR AIRCRAFT*
- 143 **Hairui Wei, Zhaohan Sheng**  
*DRY PORTS-SEAPORTS SUSTAINABLE LOGISTICS NETWORK OPTIMIZATION: CONSIDERING THE ENVIRONMENT CONSTRAINTS AND THE CONCESSION COOPERATION RELATIONSHIPS*
- 152 **Jian Yang, Jinfu Feng, Yongli Li, An Liu, Junhua Hu, Zongcheng Ma**  
*WATER-EXIT PROCESS MODELING AND ADDED-MASS CALCULATION OF THE SUBMARINE-LAUNCHED MISSILE*
- 165 **Jian Zhang, Yanjun Liu, Jingwen Liu, Tongtong He, Yudong Xie**  
*DYNAMIC CHARACTERISTICS OF MAGNETIC COUPLING IN HORIZONTAL AXIS WAVE ENERGY DEVICE*
- 171 **Renping Zhu**  
*APPLICATION OF COMPUTER IDENTIFICATION AND LOCATION ALGORITHM IN SMALL FAR INFRARED TARGET RECOGNITION OF SHIP UNDER SURGE INTERFERENCE*
- 182 **Jun Tian, Lirong Huang**  
*BIG DATA ANALYSIS AND SIMULATION OF DISTRIBUTED MARINE GREEN ENERGY RESOURCES GRID-CONNECTED SYSTEM*
- 192 **Lei Zheng, Jianbo Hu, Shukui Xu**  
*MARINE SEARCH AND RESCUE OF UAV IN LONG-DISTANCE SECURITY MODELING SIMULATION*
- 200 **Donghua Feng, Yahong Li**  
*RESEARCH ON INTELLIGENT DIAGNOSIS METHOD FOR LARGE-SCALE SHIP ENGINE FAULT IN NON-DETERMINISTIC ENVIRONMENT*
- 207 **Hao Qu, Jufeng Su, Pingming Huang, Xiang Ren**  
*NUMERICAL SIMULATION STUDY ON EXPOSED REINFORCED ANTI-CORROSION LAYER DAMAGE OF THE CROSS-SEA BRIDGE UNDER THE MARINE ENVIRONMENT*
- 213 **Wei Li, Qian Huang**  
*RESEARCH ON INTELLIGENT AVOIDANCE METHOD OF SHIPWRECK BASED ON BIGDATA ANALYSIS*
- 221 **Ganlang Chen**  
*RESEARCH ON BIG DATA ATTRIBUTE SELECTION METHOD IN SUBMARINE OPTICAL FIBER NETWORK FAULT DIAGNOSIS DATABASE*
- 228 **Fangping Yin**  
*A COMPARATIVE STUDY ON THE METHOD OF EXTRACTING EDGE AND CONTOUR INFORMATION OF MULTIFUNCTIONAL DIGITAL SHIP IMAGE*
- 235 **Xuefeng Zhang**  
*IDENTIFICATION ALGORITHM OF UNCERTAIN SONAR SIGNALS IN COMPLEX MARINE ENVIRONMENT*

## Editorial

POLISH MARITIME RESEARCH is a scientific journal of worldwide circulation. The journal appears as a quarterly four times a year. The first issue of it was published in September 1994. Its main aim is to present original, innovative scientific ideas and Research & Development achievements in the field of :

### **Engineering, Computing & Technology, Mechanical Engineering,**

which could find applications in the broad domain of maritime economy. Hence there are published papers which concern methods of the designing, manufacturing and operating processes of such technical objects and devices as : ships, port equipment, ocean engineering units, underwater vehicles and equipment as well as harbour facilities, with accounting for marine environment protection.

The Editors of POLISH MARITIME RESEARCH make also efforts to present problems dealing with education of engineers and scientific and teaching personnel. As a rule, the basic papers are supplemented by information on conferences , important scientific events as well as cooperation in carrying out international scientific research projects.

### Scientific Board

**Chairman : Prof. JERZY GIRTLEK - Gdańsk University of Technology, Poland**

**Vice-chairman : Prof. MIROSLAW L. WYSZYŃSKI - University of Birmingham, United Kingdom**

**Dr POUL ANDERSEN**  
Technical University of Denmark  
Denmark

**Dr MEHMET ATLAR**  
University of Newcastle United  
Kingdom

**Prof. GÖRAN BARK**  
Chalmers University of Technology  
Sweden

**Prof. SERGEY BARSUKOV**  
Army Institute of Odessa Ukraine

**Prof. MUSTAFA BAYHAN**  
Süleyman Demirel University  
Turkey

**Prof. VINCENZO CRUPI**  
University of Messina, Italy

**Prof. MAREK DZIDA**  
Gdańsk University of Technology  
Poland

**Prof. ODD M. FALTINSEN**  
Norwegian University of Science  
and Technology  
Norway

**Prof. PATRICK V. FARRELL**  
University of Wisconsin Madison,  
WI  
USA

**Prof. HASSAN GHASSEMI**  
Amirkabir University of Technology  
Iran

**Prof. STANISŁAW GUCMA**  
Maritime University of Szczecin  
Poland

**Prof. ANTONI ISKRA**  
Poznań University of Technology  
Poland

**Prof. JAN KICIŃSKI**  
Institute of Fluid-Flow Machinery  
of PASci  
Poland

**Prof. ZBIGNIEW KORCZEWSKI**  
Gdańsk University of Technology  
Poland

**Prof. JANUSZ KOZAK**  
Gdańsk University of Technology  
Poland

**Prof. JAN KULCZYK**  
Wrocław University of Technology  
Poland

**Prof. NICOS LADOMMATOS**  
University College London United  
Kingdom

**Prof. JÓZEF LISOWSKI**  
Gdynia Maritime University Poland

**Prof. JERZY MATUSIAK**  
Helsinki University of Technology  
Finland

**Prof. JERZY MERKISZ**  
Poznań University of Technology  
Poland

**Prof. EUGEN NEGRUS**  
University of Bucharest Romania

**Prof. YASUHIKO OHTA**  
Nagoya Institute of Technology  
Japan

**Dr YOSHIO SATO**  
National Traffic Safety and  
Environment Laboratory  
Japan

**Prof. KLAUS SCHIER**  
University of Applied Sciences  
Germany

**Prof. FREDERICK STERN**  
University of Iowa, IA, USA

**Prof. ILCEV DIMOV STOJCE**  
Durban University of Technology  
South Africa

**Prof. JÓZEF SZALA**  
Bydgoszcz University  
of Technology and Agriculture  
Poland

**Prof. WITALIJ SZCZAGIN**  
State Technical University of  
Kaliningrad, Russia

**Prof. BORIS TIKHOMIROV**  
State Marine University of St.  
Petersburg, Russia

**Prof. DRACOS VASSALOS**  
University of Glasgow and  
Strathclyde United Kingdom

# NUMERICAL ANALYSIS OF SOIL SETTLEMENT PREDICTION AND ITS APPLICATION IN LARGE-SCALE MARINE RECLAMATION ARTIFICIAL ISLAND PROJECT

Jie Zhao\*

Lingyun Bao

Guixuan Wang

Civil Engineering Technology Research and Development Center, Dalian University, China

\* corresponding author

## ABSTRACT

*In an artificial island construction project based on the large-scale marine reclamation land, the soil settlement is a key to affect the late safe operation of the whole field. To analyze the factors of the soil settlement in a marine reclamation project, the SEM method in the soil micro-structural analysis method is used to test and study six soil samples such as the representative silt, mucky silty clay, silty clay and clay in the area. The structural characteristics that affect the soil settlement are obtained by observing the SEM charts at different depths. By combining numerical calculation method of Terzaghi's one-dimensional and Biot's two-dimensional consolidation theory, the one-dimensional and two-dimensional creep models are established and the numerical calculation results of two consolidation theories are compared in order to predict the maximum settlement of the soils 100 years after completion. The analysis results indicate that the micro-structural characteristics are the essential factor to affect the settlement in this area. Based on numerical analysis of one-dimensional and two-dimensional settlement, the settlement law and trend obtained by two numerical analysis method is similar. The analysis of this paper can provide reference and guidance to the project related to the marine reclamation land.*

**Keywords:** Microstructure; Consolidation; Creep; Artificial island; Settlement

## INTRODUCTION

With rapid economic development in the coastal areas, the demand for land resources is increasing. To alleviate this problem, the marine land reclamation has gradually become one of the main measures to fully utilize the ocean resources and ensure economic development. The structural distortion, strength change and soil settlement of the soil structure under the comprehensive environment and load become a main focus of the rock engineering field<sup>[1-2]</sup>.

In the 1920s, Terzaghi, a predecessor of soil mechanics, pointed out that the microstructure should be considered when evaluating the geological property of the clay soil and rock work. This started a new research field in the soil

microstructure [3]. The academician Shen Zhujiang pointed out that the structural research of soils is a frontier subject in today's research on soil mechanics and the key issue of the soil mechanics in the 21st century is to develop and establish the soil structure model and corresponding analysis theory [4]. Bai and Smart [5] defined a set of directional indicators, which studied the orientation of clay particles in the process of consolidated-undrained shear according to the analysis of the electron microscope photos. Kong Lingwei and others [6-9] conducted experimental research on soils in different marine areas, analyzed the micromechanism of its special work property from the mineral composition to gap structure, and deepened understanding of the basic property of the ocean soil. The microstructure of sand was studied with

the guide of fractal theory. Based on the analysis of the microstructure of the sandy soil, Moore C.A and Donaldson C.F [10] concluded that the particle shape of sandy soil has fractal characteristics, which indicates that the quantitative study of soil microstructure has entered a new stage.

Domestic and foreign scholars have conducted plentiful research on the soil settlement of the ocean work [11-13]. At Bay Farm Island in San Francisco Bay and Kansai International Airport in Japan, accurate predictions of settlement magnitudes require accurate evaluations of clay compressibility and preconsolidation pressure. Duncan, J developed an improved model of clay compressibility that includes the effects of strain rate [14]. Cheng Xiang and Tongling Zhou [15, 16] studied consolidation settlement of the bank protection structure of the artificial island by using the creep model for numerical simulation, analyzed sensitivity of key parameters, and summarized the response law of the settlement results. Mamoru Mimura [17] studied consolidation settlement of the No .1 runway of the Guangxi International Airport. The actual monitoring values are roughly consistent with the finite numerical calculation results of consolidation settlement after completion. Mesri,G[18] analyzed the soil consolidation settlement of the Guangxi International Airport in Japan. Zhao Jie [19] measured the settlement law by using the dual-frequency GPS and high-precision level gage, based on Terzaghi one-dimensional and Biot two-dimensional consolidation theory.

This paper studies the soil settlement of the large-scale marine reclamation artificial island project based on the above mentioned research work. Terzaghi's one-dimensional and Biot's two-dimensional consolidation theories are used in numerical calculation. The parameters in the engineering report can meet the calculation, whose result is accurate and costing less time. This is a widely used calculation method in actual engineering both domestically and abroad. The SEM method is used for microstructure analysis. With macro numerical calculation and microstructure analysis, the settlement influence law of the whole artificial island is analyzed, so it can provide reference to the design of similar marine reclamation projects.

## BASIC PRINCIPLE

### SCANNING ELECTRON MICROSCOPE (SEM)

Now this method is one of the most popular methods to study the soil microstructure, which features deep visual field, high zoom time and direct research on sample surface. The SEM scans the surface of treated samples with a focused beam of electrons and generates various signals. These signals will change with fluctuation of the surface form of samples. After these signals are detected, zoomed out and processed, they will be transferred to the display system and produce the scanning electronic image of the analyzed area of the samples.

### PRINCIPLE OF ONE-DIMENSIONAL CONSOLIDATION SETTLEMENT ANALYSIS

The foundation consolidation settlement includes instantaneous settlement, main consolidation settlement and secondary consolidation settlement. The main consolidation settlement of the foundation is computed by using e-p curve method based on hierarchical summation method [20]. The calculation equation under the load is described as follows:

$$S_c = \sum_{i=1}^n \frac{e_{0i} - e_{1i}}{1 + e_{0i}} \Delta h_i \quad (1)$$

In this equation,  $S_c$  is the main consolidation settlement,  $m$  and  $n$  are the layer number of the foundation in foundation settlement;  $e_{0i}$  is the stable void ratio at the middle point of  $i$ th layer under action of the self-weight stress when the next-level load is not imposed;  $e_{1i}$  is the stable void ratio at the middle point of  $i$ th layer under action of the self-weight stress and additional stress when the load is imposed;  $\Delta h_i$  is the layer thickness  $m$  in calculation of  $i$ th layer and should be 0.5~1.0m. 0.5m is used in calculation of this work. When the natural stratum boundary occurs in calculation of layer range, it is used as the boundary layer.

### PRINCIPLE OF TWO-DIMENSIONAL CONSOLIDATION SETTLEMENT ANALYSIS

The soft soil consolidation creep model (SSC) is mainly used in the numerical simulation of the two-dimensional consolidation settlement to simulate the foundation consolidation settlement and secondary consolidation settlement in the whole area. The SSC is a 3D creep model extended from the one-dimensional creepage model, which is proposed by Neher&Vermeer [21] based on the standard 24h load consolidation test. The main parameters include natural weight  $\gamma$ , saturated weight  $\gamma_{sat}$ , horizontal permeability  $K_h$ , vertical permeability  $K_v$ , cohesion, internal friction angle  $\varphi$  and dilatancy angle  $\psi$ .

Buisman first proposes the creep equation under the effective stress:

$$\varepsilon = \varepsilon_c - C_B \log \left[ \frac{t_c + t'}{t_c} \right] \quad (2)$$

Later Butterfield proposes a new equation:

$$\varepsilon = \varepsilon_c - C \ln \left[ \frac{\tau_c + t'}{\tau_c} \right] \quad (3)$$

In this equation,  $\varepsilon_c$  is the total strain when the main consolidation is completed;  $t_c$  is the completion time of main consolidation; after  $t_c$  in the equation (2) is replaced with  $\tau_c$

in the equation (3), we can get effective creep time  $t'=t-t_c$ . Based on achievements of other scholars on the creep model,  $\varepsilon_c$  can be described as follows:

$$\varepsilon_c = \varepsilon_c^e + \varepsilon_c^c = -A \ln \left[ \frac{\sigma'}{\sigma_0'} \right] - B \ln \left[ \frac{\sigma_{pc}}{\sigma_{p0}} \right]$$

$$\varepsilon_c = \varepsilon_c^e + \varepsilon_c^c = -A \ln \left[ \frac{\sigma'}{\sigma_0'} \right] - B \ln \left[ \frac{\sigma_{pc}}{\sigma_{p0}} \right] - C \ln \left[ \frac{\tau_c + t'}{\tau_c} \right]$$

In this equation,  $\sigma_0'$  is the initial effective stress prior to loading,  $\sigma'$  is the effective stress of the final load;  $\sigma_{p0}$  and  $\sigma_{pc}$  are the pre-pressing consolidation stress and final consolidation stress prior to loading;  $\sigma_p$  is the pre-pressing consolidation pressure. To compute the derivative for the time and make  $\frac{\tau}{\tau_c} = \left[ \frac{\sigma'}{\sigma_p} \right]^{\frac{B}{C}}$ , the final creep equation is described as follows:

$$\dot{\varepsilon} = \dot{\varepsilon}^e + \dot{\varepsilon}^c = -A \frac{\dot{\sigma}'}{\sigma'} - \frac{C}{\tau} \left[ \frac{\sigma'}{\sigma_p} \right]^{\frac{B}{C}}$$

In the formula,  $A = \frac{C_r}{(1+e_0) \ln 10}$ ;  $B = \frac{C_c C_r}{(1+e_0) \ln 10}$ ;  $C = \frac{C_\alpha}{(1+e_0) \ln 10}$

## WORK OVERVIEW

The total area of the artificial island project based on the marine reclamation land is about 21 km<sup>2</sup> at Linkong Industrial Park, Dalian. This work is 6621.1m long and 3328.3m wide. The stratum is composed of marine facies, marine and land crossing facies and land facies. The coverage layer is 50–80m thick. The settlement layer of marine facies, which includes the silt, mucky silty clay, silty soil and a mixture of silt and sand, is under the fluid plastic and soft plastic state. And in some these areas, there is plenty of fine sand. The settlement layer of marine and land crossing facies, which includes the clay and silty clay, is under the plastic-hard plastic state. The settlement layer of land facies, which includes clay and silty clay, is under the hard plastic state. The bed rock layer mainly consists of strong weathered rock.

## OVERVIEW OF THE MICROSTRUCTURE ANALYSIS METHOD

### SAMPLE PREPARATION METHOD OF SOIL

The vacuum freezing drying method is used to collect the microstructure samples. This method keeps samples dry without deformation and is widely used by foreign and domestic scholars. It is a very effective sampling technology. The vacuum freezing drying method requires sophisticated devices and complicated operation, but it creates small disturbance to soil samples and better reflects the original state of the soil structure.

## SOIL SAMPLE ANALYSIS

The SEM method is used for the microstructure analysis of the soil. SEM of 20kv and 10000 magnification times is used. Representative six soil samples such as silt, mucky silty clay, silty clay under three different depths, and clays are tested and studied at the field (the depth of the soil sample is shown in Table 8). Some SEM photos with different magnification times are used to systematically study the relation between the microstructure features and macro mechanical property of soils in this work. These photos also reflect the essential factors of the microstructure that influence deformation and strength of the soil.

Tab. 1. Depth of soil sample of microstructure analysis

| SN | Name of soil sample | Sample depth   |
|----|---------------------|----------------|
| 1  | silt                | 3.0 m -3.5m    |
| 2  | mucky silty clay    | 9.0 m -9.5m    |
| 3  | silty clay          | 29.1 m -29.3 m |
| 4  | silty clay          | 33.1 m -33.3 m |
| 5  | silty clay          | 47.1 m -47.3 m |
| 6  | clay                | 17.1 m -17.3 m |

## CALCULATION PARAMETERS AND MODELS OF ONE-DIMENSIONAL CONSOLIDATION SETTLEMENT

Based on the engineering investigation report of the rock soil, about 500 geological bores are deployed at the whole field (details are shown in Figure 1). One-dimensional settlement analysis model is established based on the bore column charts in the investigation report. (For the calculation model, refer to the Figure 2.) Based on the plane distribution diagram of the load at the field, the obtained one-dimensional numerical analysis model of the soil can accurately reflect the soil settlement distribution at different positions of the field, so the settlement law of the whole field can be obtained.

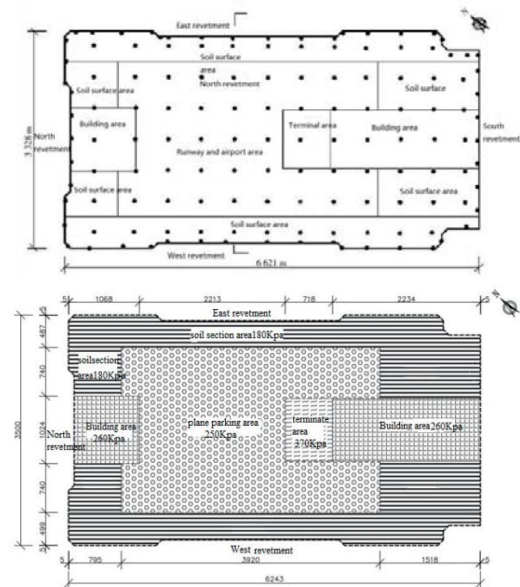


Fig. 1. Plane distribution of the regional and the main layout

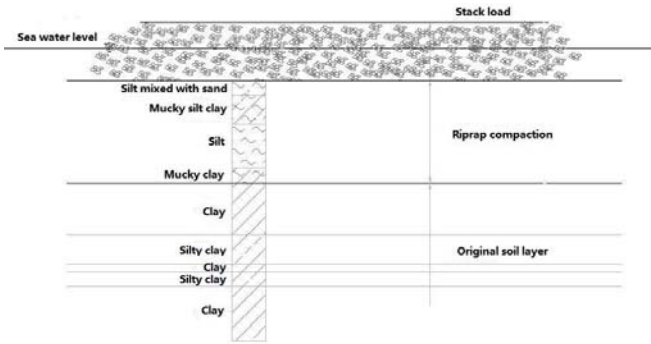


Fig. 2. The calculation model of one-dimensional consolidation settlement

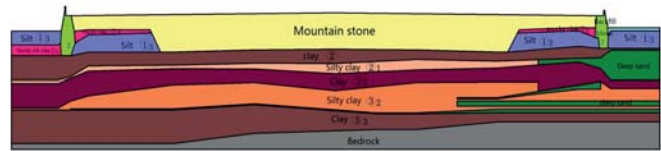


Fig. 3. Structure profile of artificial island

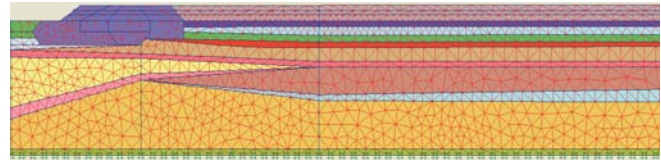


Fig. 4. The settlement analysis model of two-dimensional

When there is not enough data on physical and mechanical property of some bores, the average physical and mechanical parameters of the rock soil in different areas can be used. Table 2 shows the average physical and mechanical property of the soils in the land backfilling area.

Tab. 2. Physical-mechanical property of partial soil in one-dimensional settlement analysis

| Name of soil     | Water content % | Natural density | Vertical consolidation factor | Horizontal consolidation coefficient | Second consolidation coefficient | Compressibility modulus |
|------------------|-----------------|-----------------|-------------------------------|--------------------------------------|----------------------------------|-------------------------|
| Powder soil      | 28.1            | 1910            | 0.01000                       | 10.0000                              | 0.0005                           | 12.10                   |
| Mucky silty Clay | 42.2            | 1760            | 0.00129                       | 0.00169                              | 0.0350                           | 2.900                   |
| Silt             | 63.7            | 1600            | 0.00025                       | 0.00025                              | 0.050                            | 1.510                   |
| Silty clay       | 25.1            | 1960            | 0.00180                       | 0.00238                              | 0.002                            | 6.040                   |
| Clay             | 28.7            | 1910            | 0.00239                       | 0.00175                              | 0.003                            | 6.900                   |

## CALCULATION PARAMETERS AND MODEL OF TWO-DIMENSIONAL CONSOLIDATION SETTLEMENT CALCULATION PARAMETERS

The finite element analysis software PLXIS of the rock engineering specialty is used in calculation. One section of this work is used as the example (Figure 3) in this paper for numerical analysis. The figure shows the structural section of the artificial island. The two-dimensional settlement analysis model is established. The 2-order six-node triangle unit is used in numerical calculation. The maximum length of the model is 80m. Its width is 3500m. 20670 units and 21633 nodes are divided in the finite element model. Figure 4 shows one part of the calculation model. The soils are diversified in the work. This paper lists partial typical calculation parameters of the soils in calculation (Table 3). The SSC model is used for clay soils such as silt, mucky silty clay, clay and silty clay.

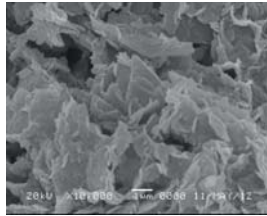
Tab. 3. Soil mechanical parameters of two dimensional settlement analysis

| Soil name                       | Block stone | Strong-weathered rock | Silt    | Clay    | Silty clay |
|---------------------------------|-------------|-----------------------|---------|---------|------------|
| Constitutive model of soil body | M-C         | M-C                   | SSC     | SSC     | SSC        |
| Saturation density              | 2000        | 2050                  | 1660    | 1900    | 1960       |
| void ratio                      |             |                       | 1.64    | 0.91    | 0.78       |
| Cohesion                        | 0.0         | 50.0                  | 13.1    | 38.8    | 41.8       |
| internal friction angle         | 38.0        | 38.0                  | 12.4    | 13.7    | 17.6       |
| Permeability coefficient        | 8.0         | 8.0                   | 0.00025 | 0.00023 | 0.00019    |
| Modified compression index      |             |                       | 0.105   | 0.052   | 0.046      |
| Modified expansion index        |             |                       | 0.021   | 0.0105  | 0.0092     |
| Modified creep index            |             |                       | 0.0042  | 0.0021  | 0.0019     |
| Poisson ratio                   | 0.33        | 0.30                  |         |         |            |
| rigidity                        | 150         | 1000                  |         |         |            |

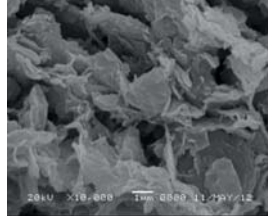
## RESULT ANALYSIS

### MICROSTRUCTURE RESULT ANALYSIS OF SOIL

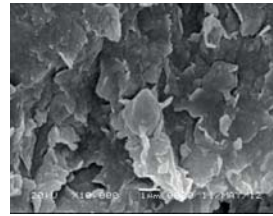
Figure 5 shows the SEM photo of six soil samples with 10000 magnification times under different depths.



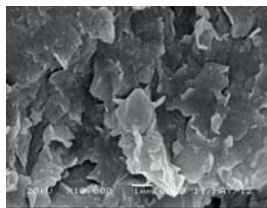
SEM diagram of silt at 3.0-3.5m depth



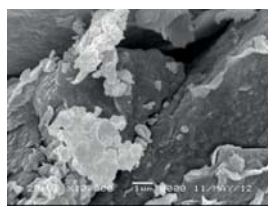
SEM diagram of mucky silty clay at 9.0-9.5m depth



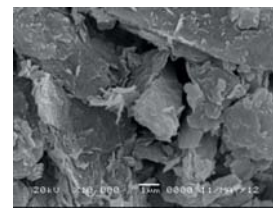
SEM diagram of clay at 17.1-17.3m depth



SEM diagram of silty clay at 29.1-29.3 m depth



SEM diagram of silty clay at 33.1-33.3m depth



SEM diagram of silty clay at 47.1 m -47.3 m depth

Fig. 5. SEM photos of soils at different depths

From the above figure, we can see that:

On the whole, the silt at 3.0-3.5 m depths will be gray and black. From photos of the high-electron microscope, the framework of the soil sample is made of flocculating constituents and the clay connects the flocculating constituent. The sample mainly consists of intergranular pores. It indicates that this silt has low strength and its compressibility, fluidity and sensitivity are relatively high.

The mucky silty clay samples at 9.0-9.5 m depths will be black and there are some ruptures at the middle. From the photos of the high-electron microscope, the framework of the soil sample is flocculating link structure. The sample mainly consists of intergranular pores. This soil sample has low strength, but the strength is higher than that of the silt. Its compressibility, fluidity and sensitivity are relatively low.

The silty clay samples at 17.1-17.3m depths will be light brown. The soil samples are layered and include some sands. After assessment, the soil with sands has greater strength. From the photos of high-electron microscope, the framework of the soil sample is aggregate particles or powder particles and certain gap is distributed between particles.

On the whole, the silty clay samples at 29.1 m -29.3 m depths will be sand yellow. After assessment, this soil sample is much rougher than previous soil samples and has higher hardness. From the photos of the high-electron microscope, the soil sample is cascaded to form the clay "domain".

From the photos of the high-electron microscope, the silty clay at 33.1-33.3m depths is the same as the silty clay sample at

29.1 m -29.3 m and is sand yellow on the whole, but the color is light yellow. After assessment, this soil sample has the top roughness and hardness among all soil samples.

On the whole, the clay at 47.1 m -47.3 m depth is stone gray. From the photos of the high-electron microscope, the framework of this soil sample is the clay sheets formed by the aggregate particles or powder particles. The clay sheets will contact each other in a face-to-face manner and the pore is small, so it belongs to the low-compressibility land facies settlement soil.

### ANALYSIS RESULTS OF ONE-DIMENSIONAL SETTLEMENT

Figure 6 gives the whole settlement distribution after the whole field has operated for 2a, 5a, 10a, 20a, 50a and 100a (refer to the Figure 6). The figure shows that the settlement of the soil section area and building construction area is remarkable and higher than that in other areas. Compared with that, the settlement at the runway and plane parking area is relatively

small. With evolvement of consolidation, the maximal settlement will reach 1.502m in the soil section area after completion for 100a. The maximal settlement will reach 1.752m in the building area, 1.648m in the terminal area, 1.150m in the runway and plane parking area and 0.912m in the bank protection area.

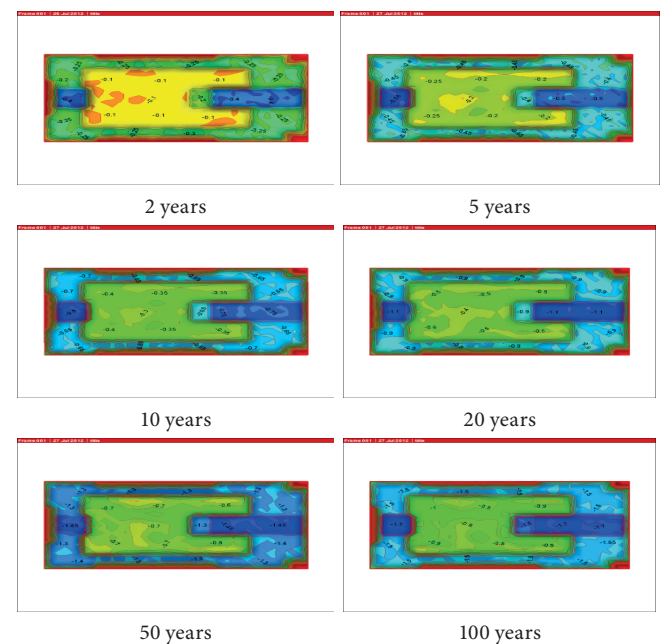


Fig. 6. The map of settlement distribution after work

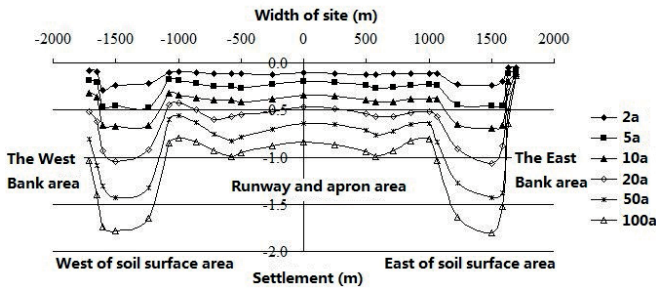


Fig. 7. The map of settlement distribution of section after work.

Figure 7 shows that the settlement differences are significant in different areas at one section. The settlement in the bank protection, runway and plane parking area is relatively small. The settlement is high in terminal areas, building areas and soil section areas. The settlement will increase significantly with time.

### ANALYSIS RESULTS OF TWO-DIMENSIONAL SETTLEMENT

The two-dimensional calculation and analysis results are shown in Table 4 and Figure 8. It indicates the law of the residual settlement in different benchmark periods after completion. The results are described as follows: the maximal settlement is 1.098m in the runway and plane parking area, 0.737m in the bank protection area, 1.517m in the soil section area and 1.098m in the terminal area 100 years after its completion.

Tab. 4. Calculation of residual settlement of sections in different benchmark period

| Section position                   | Settlement of different datum period /m |       |       |       |       |       |
|------------------------------------|---|-------|-------|-------|-------|-------|
|                                    | 2a                                      | 5a    | 10a   | 20a   | 50a   | 100a  |
| Soil section area                  | 0.356                                   | 0.559 | 0.814 | 1.021 | 1.315 | 1.517 |
| Bank protection and wave wall area | 0.074                                   | 0.134 | 0.249 | 0.365 | 0.564 | 0.737 |
| Runway and plane parking area      | 0.185                                   | 0.311 | 0.503 | 0.691 | 0.941 | 1.098 |
| Terminal area                      | 0.201                                   | 0.339 | 0.547 | 0.806 | 1.260 | 1.642 |

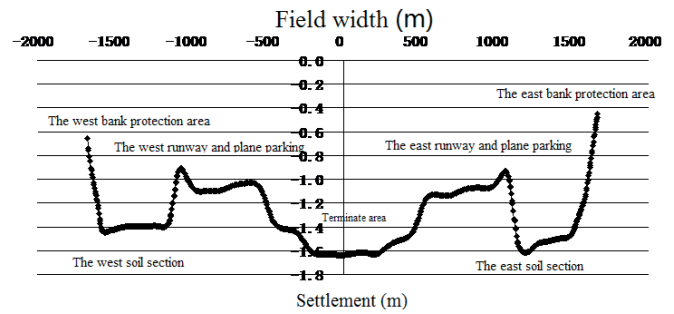
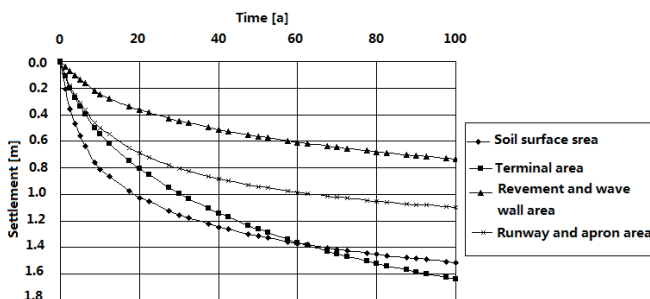


Fig. 8. Trend of cross section settlement after work

### COMPARATIVE ANALYSIS OF ONE-DIMENSIONAL AND TWO-DIMENSIONAL SETTLEMENT VALUES

Based on numerical analysis of one-dimensional and two-dimensional settlement data, the settlement law and trend from two numerical analysis methods are roughly similar. The maximal settlement is about 0.6-0.8m in the bank protection and wave wall area is about 0.6-0.8m. The maximal settlement is about 1.1-1.2m in the runway and plane parking area, the maximal settlement is about 1.4-1.7m in the soil section area. The maximal settlement is about 1.6-1.7m in the terminate area. And the maximal settlement is about 1.8m in the building area 100 years after completion.

### CONCLUSIONS

Based on microstructure analysis on the soil, the gap mainly includes the inter-particle gap and some holes existing in the silt and mucky silty clay, so the soil has high compressibility and low strength. The silty clay has higher compressibility and strength at three different depths. The silt and mucky silty clay has bigger influences on the settlement results and the silty clay has smaller influence on the settlement results in the settlement prediction and analysis at the whole field.

Based on numerical analysis on one-dimensional and two-dimensional settlement, two numerical analysis methods have roughly consistent settlement law and trend. If the complex model is used to calculate the settlement, the parameters are easy to be dispersed in the calculation process, which leads to an increase of computation time and inaccurate result. It is only suitable for academic research. So the sedimentation numerical analysis method of one-dimensional and two-dimensional is more applicable to the engineering practice.

Settlement of the whole field is mainly caused by the soil gap and inter-particle gap. The runway and plane parking are mainly composed of the clay and silty clay. The aggregate or powder particles composing the framework of the soil and particles keeps certain gap among particles, so the settlement is relatively small. The soil section area is covered by silt and mucky silty clay with certain thickness and features low strength and higher compressibility, fluidity and sensitivity, so it leads to bigger settlement. The terminal area and building

area include plentiful deep sands, silt and a small number of mucky silty clay, composing a very loose and soft framework, so the settlement is maximal in these two areas.

The microstructure analysis method for soils can be extensively used in the field of rock soil engineering. It is very significant to combine the macro mechanical shape with microstructural deformation and study their inherent association. Research on this field is insufficient in China, so this field is worthy of further studies.

## REFERENCES

1. K. X. Chen, 2011. Landfill introduction to engineering development trend. *China Water Transport*, 11 (3), 216-217.
2. One-dimensional Numerical Analysis of Consolidated settlement of a Large-scale Land Reclamation Project 2013, 12(6): 10-14.
3. C. S. Tang, B. Shi, B. J. Wang, 2008. Factors affecting analysis of soil microstructure using SEM. 4(4), 560-565.
4. S. Bin, 1996. Review and Prospect of the study on Microstructure of cohesive soil. *Journal of engineering geology*, 4 (1): 39-34.
5. Bai. X, Smart. P, Leng X. 1994. Polarizing microphto metric anlysis. *Geotechnique*, 44 (4): 175-180.
6. J. L. Qi, 1991. Study on the structure of soil and quantitative parameters. Xi'an University of technology, Doctoral dissertation, 1.
7. Z. Q. Hu, 2000. Experimental and numerical analysis of loess structural model and water immersion deformation of loess canal. Xi'an University of technology, Doctoral dissertation, 11.
8. R. L. Hu, 1995. Quantitative model of clay soil microstructure and its engineering geological characteristics. Beijing: Geological publishing house, 3-13.
9. M. J. Jiang, 1996. The analysis of constitutive model of structural clay and the gradual damage of soil mass, Water Conservancy Science Research Institute of Nanjing, Doctoral dissertation. 5.
10. C. A. Moore, C. F. Donaldson, 1995. Quantifying soil microstructure using fractals. *Geotechnique*, 1(45), 105-116.
11. Naohiro Nigorikawa, Yoshiharu Asaka, 2015. Leveling of long-term settlement of Holocene clay ground induced by the 2011 off the Pacific coast of Tohoku earthquake. *Soils and Foundations*, 55 (5), 1318-1325.
12. B. Indraratna, C. Rujikiatkamjorn, A. Balasubramaniam, 2014. Consolidation of Estuarine Marine Clays for Coastal Reclamation Using Vacuum and Surcharge Loading, From Soil Behavior Fundamentals to Innovations in Geotechnical Engineering, 10, 358-369.
13. M. W. Arulrajaha, M. Bob, M. M. Leongc, 2013. DisfaniaPiezometer measurements of prefabricated vertical drain improvement of soft soils under land reclamation fill. *Engineering Geology*, 162, 33-42.
14. J. Duncan, 1993. Limitations of Conventional Analysis of Consolidation Settlement. *Journal of Geotechnical Engineering*. 119: 9(1333), 1333-1359.
15. J. Zhao, T. L. Zhou, G. X. Wang, 2015. Numerical analysis of consolidation settlement and creep deformation of artificial island revetment structure in a large-scale marine reclamation land project. *Maritime research Special issue*, S1 (86), 35-42.
16. J. Zhao, L. Y. Deng, D. Y. Liu, 2015. Offshore channel consolidation settlement analysis of a land reclamation project. *Journal of Liaoning Technical University*, 34 (1), 37-42.
17. M. Mimura, B. G. Jeon, 2011. Numerical assessment for the behavior of the pleistocene marine foundations due to construction of the 1st phase island of Kansai international airport. *Soils and Foundations*, 51(6), 1115-1128.
18. G. Mesri, J. R. Funk, 2015. Settlement of the Kansai International Airport Islands. *Asce-amersoc civil engineer*. 141(2).
19. J. Zhao, L. Y. Deng, D. Y. Liu, 2015. Offshore channel consolidation settlement analysis of a land reclamation project. *Journal of Liaoning Technical University*, 34 (1), 37-42.
20. X. N. Gong. Numerical Methods in Geotechnical Engineering (Beijing: China Architecture and Building Press, 2000).
21. P. A. Vermeer, H. P. Neher A soft soil model that accounts for creep//Beyond 2000 in Computational Geotechnics- 10 Years of PLAXIS International (Netherlands: A Balkema Publishers, 1999).

**CONTACT WITH THE AUTHORS**

**Jie Zhao**

Civil Engineering Technology Research  
and Development Center  
Dalian University  
Dalian 116622  
**CHINA**

# DESIGN AND IMPLEMENTATION OF LARGE VESSEL NAVIGATION SYSTEM BASED ON BEIDOU CORS

Pengfei Huang<sup>1</sup>

Yang Liu<sup>2\*</sup>

Zhixiu Du<sup>3</sup>

Qilong Chen<sup>1</sup>

Jinhai Chen<sup>1</sup>

<sup>1</sup>Navigation College of Jimei University, Xiamen 361021, China

<sup>2</sup>Shandong Jiaotong University, Weihai 264200, China

<sup>3</sup>Fujian Chuanzheng Communications College, Fuzhou 350007, China

\* corresponding author

## ABSTRACT

*The ship's pilot can obtain the ship auxiliary information through the navigation system, when berthing system can display the parameters such as traverse speed and distance of the ship. But most of the system data show that there are insufficient precision. Taking the CORS system to obtain the location information, data Calculation of Berthing System based on Polar Coordinate Algorithm, this paper puts forward a solution to the "dead point" of the berthing and aiding system, which has a certain reference value for the design of the ship berthing assistance system.*

**Keywords:** Berthing; Ship-based; polar Coordinates; CORS

## INTRODUCTION

When the concept of smart ship is put forward, a lot of new equipment has been applied in vessels, especially in modern large vessels. But in some old vessel, the equipment was antiquated, the obtained information from old equipment cannot satisfy informatization. In this view point, ship berthing aids system come into our sight, which can support the pilot.

From the perspective of the location of the berthing aids system, it can be divided into two categories. One is the shore-based navigation device, such as the auxiliary berthing device of using infrared, sonar and radar[1],or using laser technology[2]; The other is ship-based navigation instrument, such as the auxiliary berthing device of using differential positioning[3-5]. Shore-based berthing auxiliary device is short range, it is hard to meet the information support in the

process of the whole large ship berthing. From the perspective of ship-based berthing system. The algorithm design based on the Beidou CORS system finally promote the construction of ship-based berthing information system.

## SHIP-BASED NAVIGATION SYSTEM ALGORITHM

Ship-based navigation device including mainframe, slave and the display terminal. The mainframe and slave can obtain real-time position of vessel with high accuracy from Beidou CORS system. The display terminal real-time calculates ship heading, trend and the relative distance to dock, then combines with ECDIS information to auxiliary ship navigation and berthing. The design principle is shown in Figure 1, with the key lies in the way of solving the vessel's rectangular vertices.

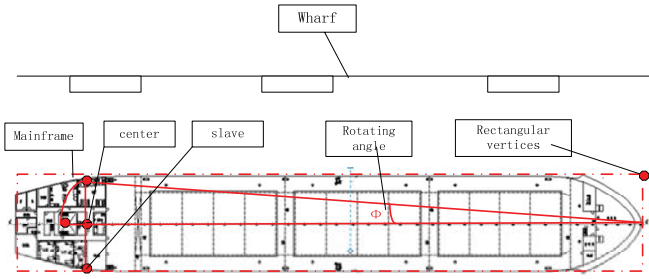


Fig. 1. Ship-Based Navigation system

### CENTER ROTATING COORDINATE ALGORITHM

Three steps are required to complete this algorithm. Specially, the first step is using two sensors location information to determine the center, then combine with length and the width of the ship to solve vertices of the ship type rectangular. Using two consecutive vertexes coordinates and combine with the berth line linear equations to gain transverse speed of that vertex coordinates[6]. The vertex is thought to be the bow or stern. The detailed center position calculation is as follows, and the point P is on behalf of the sensor positions that stand on both sides of the bridge.

$$(O_x, O_y) = \left( \frac{1}{2}(P_{1x} + P_{2x}), \frac{1}{2}(P_{1y} + P_{2y}) \right)$$

The second step is to determine the rotation angle of the bow between default position (true north) and the current location of the bow. According to the above data, we can get any point on the rectangle. The calculations are based on the following equation:

$$(S_x, S_y) = \left[ L * \cos(\theta + \beta) + O_x, L * \cos(\theta + \beta) + O_y \right]$$

Where, S represents the new rectangular vertices (bow), L is the distance from rectangular vertices to the center O. The symbol  $\beta$  means the angle between vectors  $\overline{OA}$  and  $\overline{P_1P_2}$ , and  $\theta$  is the heading of the ship.

The third step is using two continuous S points, and the line of wharf to obtain the distance from S to the wharf, the rate of speed, steering and other information.

It is noteworthy that the location information send out by the sensing device sends is not very accurate, moreover, the result displayed by the system is after three overlay calculation, which also experienced three superposition error. Polar coordinates method can solute t is problem properly.

### POLAR COORDINATES ALGORITHM

Using ship rectangle to establish polar coordinates, as shown in Figure 2:

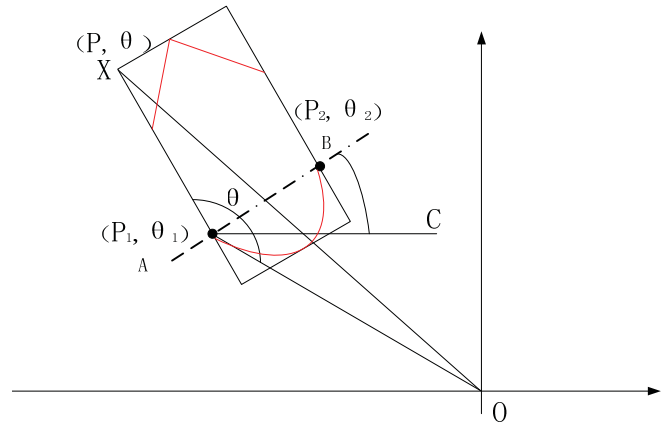


Fig. 2. Ship-Based Polar Coordinates

As shown in Figure 2, point A and point B are the measurement points. For calculation purposes, the rectangle can be regarded as a rectangular trap the ship, in order to eventually get to the animation when berthing, so just need get four rectangular coordinates of the vertices. And an example of X (P,  $\theta$ ) of the polar equation is as follows:

$$p^2 = L^2 + p_1^2 - 2Lp_1 \cos(\angle XAO)$$

P is the length from point X to point O, L is a known quantity from point A to point X. The p1 is a known amount from point A to point O. Therefore, in order to solve point P, we need to solve  $\angle XAO$  firstly.

When the angle between vector  $\overline{AB}$  and X-axis positive is zero, the coordinates of point X is (X1, Y1 +  $\overline{AX}$ ), where X is the abscissa point that accessed from direct.  $\overline{AX}$  is a known quantity from bow to bridge.

When the angel between vector  $\overline{AB}$  and X-axis positive is between 0-90 degrees (counterclockwise),  $\theta_{AB}$  represent the tilt angel of the straight line that passing point A and point B.

$$\begin{cases} \angle XAO = 90^\circ + (180^\circ - \theta_1) + \theta_{AB} \\ \theta_{AB} = \arctan\left(\frac{y_2 - y_1}{x_2 - x_1}\right) \end{cases}$$

Where (x1, y1) and (x2, y2) is converted from points A and B in polar coordinates.

When the angel between vector and X-axis positive is 90 degree, the point X is (x1,  $\overline{AX} + y1$ ).

When the angel between vector  $\overline{AB}$  and X-axis positive is between 90-180 degrees:

$$\begin{cases} \angle XAO = \theta_1 - (90^\circ - \theta_{AB}) \\ \theta_{AB} = \arctan\left(\frac{y_2 - y_1}{x_2 - x_1}\right) \end{cases}$$

When the angel between vector  $\overline{AB}$  and X-axis positive is 180 degrees, the point X is (X1,Y1-L).

When the angel between vector  $\overline{AB}$  and X-axis positive is between 180-270 degrees,  $\angle XAO = \theta_1 - 90^\circ - \theta_{AB}$ .

When the angel between vector  $\overline{AB}$  and X-axis positive is 270 degrees, the point X is (X1-L, Y1).

When the angel between vector  $\overline{AB}$  and X-axis positive is between 270-360 degrees,  $\angle XAO = \theta_1 + \theta_{AB} - 90^\circ$ .

When the angel between vector  $\overline{AB}$  and X-axis positive is 360 degrees, the point X is (X1,Y1-L).

The above situations are the angles between 0-180 degrees. However, if  $\theta_1$  involves angels between 0-90 degree, we need to determine first then summed up as one of the above situations. The other three rectangular similarly available, straight line that passing the quay can be obtained by measuring.

According to the above analysis, we can get the dynamic data of the ship when berthing.

## PERFORMANCE MEASUREMENT

The Experiment is a cargo ship berthing Zhangzhou port. Length and width of the ship is 225 and 32 meters, respectively, with the tonnage as 64,000 tons. Test time interval is 1 hour and 10 minutes. The data recording interval is about 20 minutes before the completion of the ship berthing operation. Owing to output mode of the position sensor device using UDP broadcasts, we prepared two sets of equipment and two sets of display terminals that embedded in the center of the rotating coordinate algorithm and polar algorithm, respectively.

### (1) Center rotating coordinate algorithm experiment

Test data are as follows:

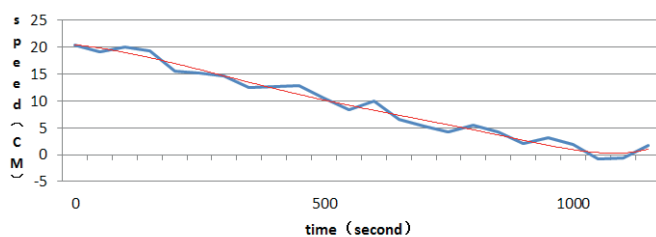


Fig. 3. Data of center rotating coordinate algorithm experiment

### (2) Polar coordinate experiment

Test data are as follows:

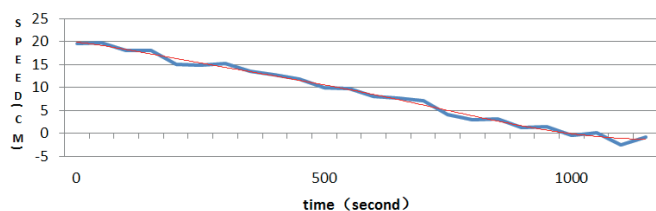


Fig. 4. Data of polar coordinate experiment

The blue line is the recorded testing data, and the red line is 6 degree polynomial fitting curve. By observing the degree of fit between the red line and the blue line, we can determine the extent of the available data.

We take time nodes 500 as segmentation to observe Figure 3, the tested curve and the fitting curve alignment is higher before 500, and emerged many inosculation with weak point after 500. The reason for this is explained as follows: with the passage of time, the ship dock distance become more and more close, subsequently, the seep of ship is slower. In the case when transverse sheep movement becomes slower, the positioning precision of DPGS tends to present alarger leap, leading to a highly inconsistent results between the measured curve and the fitting curve. We take time nodes 500 as segmentation to observe Figure 4, which seems similar to Figure 3. However, compared with these two, it is clearly seen that the data fitting degree is higher than that in Figure 4. Meanwhile, Figure 3 has a higher activity of data. In the center rotating coordinate algorithm, rectangular vertex coordinates are made on the basis of the original coordinate in two. Because the error of original coordinate position by superposition of the secondary, soothe fitting curve and original curve is not in consistent with each other. On the contrary, polar coordinate method can be directly obtained through the final numerical, with a single superposition of error, thus the fitting curve and original curve matches perfectly, which is much better.

Although Figure 4 fits better, in some conditions, the original curve and the curve fitting still have larger difference, the reasons are the presence of "Bad". Here, "Bad" is due to external factors, such as the impact of positioning accuracy, the ionosphere, the distance between RTK terminal and the RTK base station, shelter materials and other factors so that at some extent while positioning error is large, "Bad" error position occurs.

## BAD SOLUTIONS

Occasional "bad" does not mean the point is unavailable, however, we need to pay attention to continuous "Bad". There are two decision for continuous "Bad", the first situation is when the current ship's position indeed changed significantly; the second one is the continuous positioning error caused by external factors. To deal with this situation, the system will retain "Bad" temporary. Only the continuous dates have more than 10 times of "bad", the system is updated to display the real "bad", otherwise the staging point will be completely filtered out. In this way, we can ensure that the displayed speed in the system is more stable, and also ensure the "security".

## BEIDOU CORS SYSTEM USE IN NAVIGATION SYSTEM

Improving data "security" from the source to solve positioning error is feasible, therefore, it is necessary to adopt a positioning system with high precision. At present, the most main GNSS high precision real-time dynamic positioning

technology, CORS technology has many advantages. CORS is widely applied in navigation, berthing system. CORS technology navigation docking device has the following advantages: high positioning accuracy, safe and reliable data, no error accumulation, high work efficiency, CORS automation homework, reduced job requirements, simple operation, strong ability in data processing [7,8].

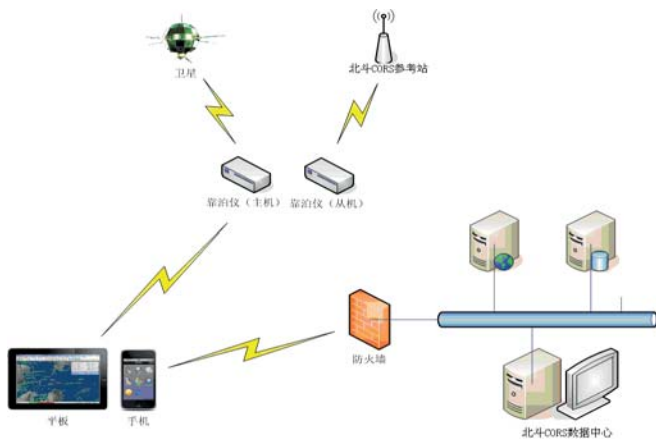


Fig. 5. Beidou CORS ship navigation system framework

## CONCLUSIONS

We obtain real-time cm-level positioning accuracy by using Beidou CORS system and ship berthing dynamic data by polar coordinates to provide powerful information to support the pilot berthing. This paper compared the “center rotating coordinates” and “polar coordinate” method, and analyzed the error source of these two methods. The measured data in this paper is discrete. We use polynomial fitting method to fit the data to determine how jump data, but this might still be insufficient. We will be targeted for research in further. After the test, the system can meet auxiliary information requirements when ship berthing. No matter how to improve the navigation technology, navigation of ships is inseparable from the operation. Human factors play a decisive role in the process of ship’s safe navigation. Ship berthing can’t just rely on a method of positioning or depend on the berthing auxiliary system to determine ship position and berthing speed. We encourage to use all methods of locating to obtain position data in case one method fails while the others are working well.

## REFERENCES

1. ChangsiCai, 2001. Monitoring System Integration for Berthing and Mooring Operation. *Port&waterway Engineering*, 423(1),17-19.
2. Marko Perkovic,Blaz Luin,Tanja Brcko,Maciej Gucma, 2016. Docking System based on Laser Measurements. 5th

Mediterranean Conference on Embedded Computing. 158-163.

3. Hiroyuki Oda, Etsuro Okuyama, Yasushi Kawamori, 2009. New BERTHING Support System Using High Accuracy Different GPS. *Journal of Interactive Media in Education*,44(1), 1-12.
4. .Guojun Peng, Yang Liu, Xingu Zhang, 2012. Design of auxiliary berthing instrument of large ship. *Journal of Traffic and Transportation Engineering*, 12(6),48-53.
5. Guojun Peng, Yongjun Wu, Yang Liu, 2012. Research on Large Ship Berthing Technology Based on DGPS Combination Positioning. *Journal of Geo-information Science*, 14(6),788-793.
6. Yang Liu,2012. Study on ship berthing aids system, JMU. Xiamen.
7. Hongwei Bi,Haibin Bai,Yalong Wei, 2011.The application of CORS in Huaneng Yimin open-pit mine digitalization. *Opencast Mining Technology*,2011(2):63-64.
8. Liming Tang,Chenggang Li, Jianguo Zhang, et al, 2010. Precise monitoring technique for regional surface deformation using GPS/CORS observation , *Bulletin of Surveying and Mapping*, 2010(5): 6-8.

## CONTACT WITH THE AUTHORS

**Yang Liu**

Shandong Jiaotong University  
Weihai 264200  
CHINA

# SUMMARY OF THE PORT SHORELINE RESOURCE EVALUATION BASED ON TRIANGULAR FUZZY ANALYTIC HIERARCHY PROCESS

Liupeng Jiang<sup>1\*</sup>

Tao Tao<sup>2</sup>

Cheng Zhang<sup>1</sup>

He Jiang<sup>1</sup>

Jiaojiao Wang<sup>1</sup>

<sup>1</sup> College of Harbour, Coastal and Offshore Engineering, Hohai University, China

<sup>2</sup> Jiangsu Province Communications Planning and Design Institute Limited Company Co. Ltd.

\* corresponding author

## ABSTRACT

*Port shoreline resources are the basis of port and shipping development, and its assessment method has become one of the hot issues in port research. On the basis of constructing a reasonable index evaluation system, this paper constructs the fuzzy evaluation matrix based on the triangular fuzzy analytic hierarchy process and constructs the fuzzy evaluation matrix by using the fuzzy comprehensive evaluation method, and obtains the maximum membership degree of the port shoreline resources. Compared with the traditional port shoreline Resource evaluation methods, the new one got more advantages in objective and quantitative. Finally, Combined with the Nanjing section of the Yangtze River as a case for verification, the results show that the model can accurately solve the problem of resource evaluation of port shoreline.*

**Keywords:** Port shoreline evaluation; Triangular fuzzy AHP; Fuzzy comprehensive evaluation; Shoreline of Nanjing port

## INTRODUCTION

In recent years, the port has become a gathering point of regional high-quality resources, and become a regional economic growth point. The development and utilization of shoreline resources is closely related to the speed of regional economic development [1, 2]. Therefore, the evaluation of shoreline resources has become an important issue in regional development. It is very important to carry out the evaluation of the rationality of port shoreline resources to the future development of port and port area [3].

On the port shoreline resource evaluation at present, scholars have made a series of results, the current popular methods are mathematical model evaluation and field monitoring. Field monitoring use GPS, GIS, RS and other software as the technical platform, the use of remote sensing image data, the port shoreline resources to monitor the dynamic changes [4, 5], field monitoring methods due to

field monitoring requires a lot of data and equipment, The main shortcomings of the monitoring method are twofold: First, the cost is too expensive, the second is unable to quickly and efficiently form the evaluation conclusion. And the mathematical model evaluation method is convenient and low cost advantage, more conducive to the port shoreline planners and managers to its assessment and decision-making.

## RESEARCH SUMMARY

At present, the main methods of port shoreline resource evaluation are AHP, data envelopment analysis, gray system theory, cellular automata and neural network [6, 10]. The methods are quantitative data Methods. However, some important indicators in the analysis and evaluation of port shoreline resources are qualitative indicators, which cannot be directly quantified, such as the relationship with national policy, the significance of urbanization in the surrounding

areas [11]. Therefore, these methods have difficulties in solving the problem of resource evaluation and analysis of inland riverline with qualitative indicators.

The Analytic Hierarchy Process was first proposed by the scholar Saaty, Analytic Hierarchy Process (AHP) is a measure that is used to measure deterministic and uncertain, tangible and intangible, clear and vague quantitative and qualitative equivalents. Method, because of its practical and effective in dealing with complex decision-making issues, and soon in the world attention and widely used [12, 13]. Triangular Fuzzy Analytic Hierarchy Process (TFAHP) is an improvement to the traditional hierarchical analysis method. Fuzzy theory is used to fuzzify the values of the judgment matrix. When faced with complex and uncertain decisions, the judgment matrix Blurring will yield better results than classical analytic hierarchy process. At present, scholars have applied AHP or fuzzy theory to the evaluation of port shoreline. For example, Ledoux has constructed a systematic evaluation procedure to solve the problem of shoreline resource degradation due to sporadic or unrestricted use of shoreline resources And other issues [14]; Renzo DalCin classifies the southern coast of Marche, Italy, based on the study of the interrelationships between coastal characteristic variables, and establishes models to measure various types of coastal vulnerability and risk [15]; Bagdanavičiute takes the Baltic Sea The southern coast of Lithuania 90 km of the coastline as the object of study, to build a set of coastal vulnerability index system, and the use of hierarchical analysis of the coastline of the vulnerability level [16], Nouri to southern Iran's northern Persian Gulf coastline as the object, through Analysis of its ecological characteristics and tourism development potential[17],

Sha using k cluster analysis method, the classification of China's Fujian coastline, and port development potential assessment[18].

In summary, the current research results are mainly focused on the index system and its quantitative calculation. In the existing research, the index system cannot reflect the dynamic characteristics of the shoreline comprehensively. The weight determination is more subjective and the evaluation method is not rigorous. Therefore, based on the improved triangular fuzzy analytic hierarchy process (AHP), the fuzzy comprehensive evaluation of shoreline is used to overcome the dynamic characteristics and difficult to quantify the characteristics of shoreline evaluation by trigonometric function and fuzzy comprehensive method. It provides the rationality evaluation of port shoreline in the new period new methods to make the evaluation results more consistent with the status quo, to enhance the evaluation results.

### PORT SHORELINE EVALUATION INDEX SYSTEM

Port shoreline comprehensive evaluation, is a kind of typical composite system comprehensive evaluation, which involves the evaluation index and many factors. The evaluation of the use of port shoreline mainly need to consider three aspects: (1) select a reasonable evaluation system of port shoreline; (2) use the trigonometric function to determine the weight of the index system; (3) using the improved fuzzy evaluation to calculate the port shoreline evaluation level. This paper constructs the port shoreline evaluation system as shown in Table 1.

Tab. 1. Port shoreline evaluation index system table

| Target layer                             | criteria layer  |                | indicator layer   |                 |              |
|--|---|----------------|---|-----------------|--------------|
| Port shoreline evaluation index system A | port planning compliance  | B <sub>1</sub> | Operational compliance of the functional properties of the terminal | C <sub>1</sub>  | Qualitative  |
|  |   |                | Coastline level planning compliance                                 | C <sub>2</sub>  | Qualitative  |
|  | usage efficiency  | B <sub>2</sub> | Effective utilization rate of port shoreline                        | C <sub>3</sub>  | Quantitative |
|  |   |                | Unit berth shoreline throughput                                     | C <sub>4</sub>  | Quantitative |
|  | Use benefit   | B <sub>3</sub> | Shoreline public service rate                                       | C <sub>5</sub>  | Quantitative |
|  |   |                | Unit shoreline supply value   | C <sub>6</sub>  | Quantitative |
|  |   |                | Unit shoreline revenue  | C <sub>7</sub>  | Quantitative |
|  |   |                | Unit shoreline employment   | C <sub>8</sub>  | Quantitative |
|  | Area function   | B <sub>4</sub> | And functional zoning compliance                                    | C <sub>9</sub>  | Qualitative  |
|  |   |                | Consistent with the overall urban planning                          | C <sub>10</sub> | Qualitative  |
|  |   |                | Area of the same type of dock capacity ratio                        | C <sub>11</sub> | Quantitative |
|  | Ecological Benefits   | B <sub>5</sub> | Unit throughput comprehensive energy consumption                    | C <sub>12</sub> | Quantitative |
|  |   |                | Unit throughput CO2 emissions                                       | C <sub>13</sub> | Quantitative |
|  | Set the way   | B <sub>6</sub> | Railway transit transport   | C <sub>14</sub> | Qualitative  |
|  |   |                | Road transit transport  | C <sub>15</sub> | Qualitative  |
|  | The match degree of the terminal cargo structure and the local industry | B <sub>7</sub> | Industry agglomeration degree                                       | C <sub>16</sub> | Qualitative  |
|  |   |                | Set distribution level  | C <sub>17</sub> | Qualitative  |
|  | Shoreline layout type   | B <sub>8</sub> | Terminal cluster level  | C <sub>18</sub> | Qualitative  |
|  |   |                | Shoreline contiguous degree   | C <sub>19</sub> | Qualitative  |

## MATERIAL AND METHODS

### METHOD OF WEIGHT DETERMINATION BASED ON TFAHP

**Definition 1:** Set a fuzzy number  $M$  on a real number set  $R = (-\infty, +\infty)$ , and when its membership function  $u_M : R \rightarrow [0, 1]$  satisfies the following formula, it is called a triangular fuzzy number.

$$u_M(x) = \begin{cases} x/(m-1) - I/(m-I), & x \in [I, m] \\ x/(m-u) - u/(m-u), & x \in [m, u] \\ 0, & \text{other} \end{cases} \quad (1)$$

In Equation (1),  $I \leq m \leq u$ ,  $I$  and  $u$  represent the upper and lower bounds of  $M$  support, respectively, and  $m$  is the median of  $M$ , and the triangular fuzzy number  $M$  can be expressed as  $(I, m, u)$ .

**Definition 2:** The algorithm of triangular fuzzy numbers

If  $u_M$  and  $u_N$  denote the membership functions of two triangular fuzzy numbers  $M$  and  $N$  respectively, then the membership function of the triangular fuzzy number  $T = f(M, N)$  is given by:

$$u_T(z) = \sup_{(x,y) \in R^2, z=f(x,y)} \min(u_M(x), u_N(y)) \quad (2)$$

Based on the above formula, the triangular fuzzy number of the algorithm is as follows:

Make  $M_1 = (I_1, m_1, u_1)$ ,  $M_2 = (I_2, m_2, u_2)$  two Triangular fuzzy number, then:

$$M_1 \oplus M_2 = (I_1, m_1, u_1) \oplus (I_2, m_2, u_2) = (I_1 + I_2, m_1 + m_2, u_1 + u_2) \quad (3)$$

$$M_1 \otimes M_2 = (I_1, m_1, u_1) \otimes (I_2, m_2, u_2) = (I_1 + I_2, m_1 + m_2, u_1 + u_2) \quad (4)$$

$$M^{-1} = (I, m, u)^{-1} = \left(\frac{1}{u}, \frac{1}{m}, \frac{1}{I}\right) \quad (5)$$

Tab. 2. Triangular fuzzy number on the basis of the lower bound

| Score self - confidence | $u - I$ | Digital features                          | Score meaning                       |
|-------------------------|---------|---|-------------------------------------|
| High                    | 1       | $(\max(m - 1/2, 1), m, \min(m + 1/2, 9))$ | Experts play scores are not blurred |
| low                     | 2       | $(\max(m - 1, 1), m, \min(m + 1, 9))$     | Experts play scores more vague      |
| normal                  | 3       | $(\max(m - 3/2, 1), m, \min(m + 3/2, 9))$ | Experts play scores very vague      |

The calculation steps of the improved triangular fuzzy hierarchy analysis method are as follows:

**Step 1:** Constructs the triangular fuzzy judgment matrix according to the expert judgment result,  $A = (a_{ij})_{n \times n}$ , where the element  $a_{ij} = (I_{ij}, m_{ij}, u_{ij})$  is a closed interval with  $m_{ij}$  as the median.

For the index between the two pairs of triangular fuzzy values, the average judgment can be used to represent the comprehensive judgment matrix, the formula is:

$$a_{ij} = \frac{1}{T} \otimes (a_{ij}^1 + a_{ij}^2 + \Lambda + a_{ij}^T) \quad (6)$$

In which,  $T = 1, 2, \Lambda, t$  Where  $T$  denotes the number of experts involved in triangular fuzzy judgment.

**Step 2:** Consistency check of the median matrix:

Calculate the maximum eigenvalue  $\lambda_{\max}$  of the median matrix  $M$ , and substitute  $\lambda_{\max}$  into the formula for the consistency check according to the calculation method described earlier.

**Step 3:** Construct the fuzzy evaluation factor matrix  $E$ .

$$E = (e_{ij})_{n \times n} = \begin{bmatrix} 1 & 1 - \frac{u_{12} - I_{12}}{2m_{12}} & \dots & 1 - \frac{u_{1n} - I_{1n}}{2m_{1n}} \\ 1 - \frac{u_{21} - I_{21}}{2m_{21}} & 1 & \dots & 1 - \frac{u_{2n} - I_{2n}}{2m_{2n}} \\ \vdots & \vdots & \ddots & \vdots \\ 1 - \frac{u_{n1} - I_{n1}}{2m_{n1}} & 1 - \frac{u_{n2} - I_{n2}}{2m_{n2}} & \dots & 1 \end{bmatrix} \quad (7)$$

Where  $S_{ij} = (u_{ij} - I_{ij})/2m_{ij}$  is the standard deviation rate, which reflects the fuzzy degree of expert judgment, the greater the  $S_{ij}$  the greater the ambiguity of the evaluation, the less the credibility.

**Step 4:** Calculate the adjustment judgment matrix  $Q$

$$Q = M \times E = \begin{bmatrix} m_{11} & m_{12} & \dots & m_{1n} \\ m_{21} & m_{22} & \dots & m_{2n} \\ \vdots & \vdots & \ddots & \vdots \\ m_{n1} & m_{n2} & \dots & m_{nn} \end{bmatrix} = \begin{bmatrix} 1 & 1 - \frac{u_{12} - I_{12}}{2m_{12}} & \dots & 1 - \frac{u_{1n} - I_{1n}}{2m_{1n}} \\ 1 - \frac{u_{21} - I_{21}}{2m_{21}} & 1 & \dots & 1 - \frac{u_{2n} - I_{2n}}{2m_{2n}} \\ \vdots & \vdots & \ddots & \vdots \\ 1 - \frac{u_{n1} - I_{n1}}{2m_{n1}} & 1 - \frac{u_{n2} - I_{n2}}{2m_{n2}} & \dots & 1 \end{bmatrix} \quad (8)$$

**Step 5:** The adjustment judgment matrix  $Q$  is converted into a judgment matrix  $Q'$  with a diagonal line of 1.

**Step 6:** Use the root method to calculate the weight of the indicators

Calculate the Nth root of all elements of each row:

$$\bar{\omega} = \left( \prod_{j=1}^n a_{ij} \right)^{\frac{1}{n}} \quad i = 1, 2, \Lambda, n \quad (9)$$

Normalize  $\bar{\omega}$ :

$$\bar{\omega}_j = \frac{\bar{\omega}_j}{\sum_{i=1}^n \bar{\omega}_i} \quad i = 1, 2, \Lambda, n \quad (10)$$

Then  $\omega = (\omega_1, \omega_2, \Lambda, \omega_n)^T$  is the approximation of the required weight.

### USING FUZZY COMPREHENSIVE EVALUATION METHOD TO ESTABLISH FUZZY EVALUATION MATRIX

Fuzzy evaluation method, the need to use fuzzy mathematics method to establish a fuzzy evaluation matrix R, the specific evaluation process is as follows:

**Step 1:** Establish a set of evaluation factors

The establishment of the evaluation factor set should be comprehensive, perfect and accurate, and the factors that affect the evaluation object are listed as far as possible, that is,  $U = \{u_1, u_2, \Lambda, u_n\}$ , where  $u_i (i = 1, 2, \Lambda, n)$  is the evaluation factor;  $n$  is the number of individual factors at the same level.

**Step 2:** Determine the level of reviews set

The grade comment set contains all the possible evaluation results in the evaluation object, which can be expressed as:  $V = \{v_1, v_2, \Lambda, v_m\}$ ,  $v_j (j = 1, 2, \Lambda, m)$  is the evaluation grade standard;  $m$  is the number of reviews.

**Step 3:** Determination of membership function

The membership of qualitative indicators in this paper combined with expert experience method, through the questionnaire by the expert scoring to determine the classification criteria, membership function.

**Step 4:** Single factor fuzzy evaluation, the establishment of fuzzy evaluation matrix

Univariate fuzzy evaluation refers to the evaluation of a factor in the process of fuzzy comprehensive evaluation, and to determine the degree of membership of this factor for the evaluation set.

Assuming the  $i$  th evaluation factor  $u_i$ , the evaluation membership degree of the  $j$  th element  $v_j$  is  $r_{ij}$ , where  $0 \leq r_{ij} \leq 1$ . So the fuzzy set can be used to express the evaluation of the  $i$  th element:

$$R_i = (R_{i,1}, R_{i,2}, \Lambda, R_{i,m}) \quad (11)$$

The membership evaluation matrix  $R_{m \times n}$  of the  $n$  factors is finally determined, as shown in the following equation.

$$R = \begin{bmatrix} R_1 \\ R_2 \\ \vdots \\ R_n \end{bmatrix} = \begin{bmatrix} r_{11} & r_{12} & \cdots & r_{1m} \\ r_{21} & r_{22} & \cdots & r_{2m} \\ \vdots & \vdots & \vdots & \vdots \\ r_{n1} & r_{n2} & \cdots & r_{nm} \end{bmatrix} \quad (12)$$

Triangular fuzzy analytic hierarchy process (TFAHP) and fuzzy evaluation method can be used to obtain the comprehensive weight set  $\omega$  and the fuzzy evaluation matrix  $R$ . The final result is the vector product of the first two items, that is, the fuzzy comprehensive evaluation model is obtained as follows.

$$B = \omega^T \cdot R = (\omega_1, \omega_2, \dots, \omega_n) \bullet \begin{bmatrix} r_{11} & r_{12} & \cdots & r_{1m} \\ r_{21} & r_{22} & \cdots & r_{2m} \\ \vdots & \vdots & \vdots & \vdots \\ r_{n1} & r_{n2} & \cdots & r_{nm} \end{bmatrix} = (b_1, b_2, \dots, b_m) \quad (13)$$

According to the principle of maximum membership degree, the fuzzy comprehensive evaluation result vector  $B = (b_i), i = 1, 2, \dots, m$  indicates that the port shoreline use belongs to the comprehensive evaluation level of the port shoreline, so as to determine the  $v_i$  as the finalized evaluation result.

### CASE STUDY

Nanjing is one of the four major cities in the Yangtze River Basin, and is the only city in Jiangsu Province with two coastlines of the Yangtze River. The south bank of Nanjing start from the south bank of the junction of the Soviet Union and the junction of the Cihu mouth, and stops at Ningzhen transfer of the new estuary; north shore from the junction of Jiangsu and Anhui Wujiangkou, stop at the junction of Yizheng Liuhe mouth. This paper chooses the resources of the Nanjing section of the Yangtze River as a case to analyze the correctness of the above model.

Through access to relevant literature, to convene relevant experts and scholars to carry out seminars and to the relevant departments and on-site field research to 2016 as the base year, and ultimately determine the port shoreline index system 11 quantitative indicators of the evaluation level standard. The weight values of the index based on triangular fuzzy analytic hierarchy process are shown in Table 3.

In the determination of qualitative indicators, the evaluation process by inviting a total of 24 experts in the field of 10 qualitative indicators to vote, according to the voting results combined with membership calculation formula to calculate the membership, as shown in Table 4.

Tab. 3. Nanjing port shoreline quantitative indicators grading evaluation criteria table

| index   | unit                                     | GREAT        | GOOD          | NORMAL        | BED       |
|---|--|--------------|---------------|---------------|-----------|
| Effective utilization rate of port shoreline $C_{21}$     | %  | $\geq 60$    | [50–60]       | [40–50]       | $< 40$    |
| Unit berth shoreline throughput $C_{22}$                  | Million tons / m                         | $\geq 0.75$  | [0.6–0.75]    | [0.45–0.6]    | $< 0.45$  |
| Shoreline public service rate $C_{31}$                    | %  | $\geq 80$    | [60–80]       | [40–60]       | $< 40$    |
| Unit shoreline supply value $C_{32}$                      | Million yuan / m                         | $\geq 1300$  | [1000–1300]   | [700–1000]    | $< 700$   |
| Unit shoreline revenue $C_{33}$                           | YUAN/M                                   | $\geq 90000$ | [70000–90000] | [50000–70000] | $< 50000$ |
| Unit shoreline employment $C_{34}$                        | person/km                                | $\geq 180$   | [130–180]     | [80–130]      | $< 80$    |
| Area of the same type of dock capacity ratio $C_{43}$     | 1  | $\geq 1.40$  | [1.20–1.40]   | [1.00–1.20]   | $< 1.00$  |
| Unit throughput comprehensive energy consumption $C_{51}$ | Ton of standard coal / ten thousand tons | $\leq 2.00$  | [2.0–3.0]     | [3.0–4.0]     | $> 4.00$  |
| Unit throughput CO2 emissions $C_{52}$                    | Ton / tonne                              | $\leq 5.00$  | [5.00–7.00]   | [7.00–9.00]   | $> 9.00$  |

Tab. 4. Nanjing coastline qualitative data

| index    | great           |            | good            |            | normal          |            | bad             |            |
|----------|-----------------|------------|-----------------|------------|-----------------|------------|-----------------|------------|
|          | Number of votes | Membership |
| $C_{11}$ | 20              | 0.8333     | 4               | 0.1667     | 0               | 0          | 0               | 0          |
| $C_{12}$ | 22              | 0.9167     | 2               | 0.0833     | 0               | 0          | 0               | 0          |
| $C_{41}$ | 20              | 0.8333     | 3               | 0.1250     | 1               | 0.0417     | 0               | 0          |
| $C_{42}$ | 22              | 0.9167     | 2               | 0.0833     | 0               | 0          | 0               | 0          |
| $C_{61}$ | 19              | 0.7917     | 5               | 0.2083     | 0               | 0          | 0               | 0          |
| $C_{62}$ | 16              | 0.6667     | 6               | 0.2500     | 0               | 0          | 2               | 0.0833     |
| $C_{71}$ | 14              | 0.5833     | 8               | 0.3333     | 1               | 0.0417     | 1               | 0.0417     |
| $C_{72}$ | 23              | 0.9583     | 1               | 0.0417     | 0               | 0          | 0               | 0          |
| $C_{81}$ | 19              | 0.7917     | 4               | 0.1667     | 0               | 0          | 1               | 0.0416     |
| $C_{82}$ | 16              | 0.6667     | 7               | 0.2917     | 1               | 0.0416     | 0               | 0          |

According to the above data analysis results, available in Nanjing port shoreline comprehensive evaluation of the use of “great, good, normal, bad” membership degree  $B = (0.444, 0.276, 0.240, 0.004)$ . The evaluation results meet the principle of normalization, indicating the validity of the evaluation results. According to the principle of maximum membership, because the “good + great” = 0.72 > 0.7, indicating that the year 2016 Nanjing port shoreline use in a better range.

## CONCLUSION

Port shoreline resource use level evaluation is a multi-criteria, multi-attribute problem, the effective evaluation

of the level is a complex work. The results of this paper are as follows: 1) the method of calculating the weight of the index based on the triangular fuzzy analytic hierarchy process has overcome the problem that the decision maker has the deviation of the weight due to the mistake or preference, which provides the basis for the final port shoreline evaluation. 2) The fuzzy comprehensive evaluation model based on triangular fuzzy analytic hierarchy process (AHP) is used to evaluate the coastline of Nanjing port. It is concluded that the use of harbor coastline in Nanjing port is in a good evaluation range. From the calculation process and the results, it can be seen that the method not only can be scientific and rational evaluation of the status quo, and can reflect the level along the coast of the river, indicating that the method is effective.

## ACKNOWLEDGEMENT

In this paper, the research was sponsored by the National Natural Science Fund of China (Project No. 41401120, 51409088) and the Fundamental Research Funds for the Central Universities of China (Project No. 2014B00214).

## REFERENCE

1. A. Artal-Tur, J.M. Gomez-Fuster, J.M. Navarro-Azorin, J.M. Ramos-Parreno, 2016. Estimating the economic impact of a port through regional input-output tables: Case study of the Port of Cartagena (Spain). *MARITIME ECONOMICS & LOGISTICS*, 18(4), 371-390.
2. I. Van Putten, C. Cvitanovic, E.A. Fulton, 2016. A changing marine sector in Australian coastal communities: An analysis of inter and intra sectorial industry connections and employment, *OCEAN & COASTAL MANAGEMENT*, 131, 1-12.
3. M. Acciaro, 2008. The role of ports in the development of Mediterranean islands: the case of Sardinia, *INTERNATIONAL JOURNAL OF TRANSPORT ECONOMICS*, 35(3), 295-323.
4. K. Jayakumar, S. Malarvannan, 2016. Assessment of shoreline changes over the Northern Tamil Nadu Coast, South India using WebGIS techniques, *JOURNAL OF COASTAL CONSERVATION*, 20(6), 477-487.
5. S. Kermani, M. Boutiba, M. Guendouz, M.S. Guettouche, D. Khelfani, 2016. Detection and analysis of shoreline changes using geospatial tools and automatic computation: Case of jijelian sandy coast (East Algeria), *OCEAN & COASTAL MANAGEMENT*, 132, 46-58.
6. Feng. L., Zhu. XD., Sun. X., 2014. Assessing coastal reclamation suitability based on a fuzzy-AHP comprehensive evaluation framework: A case study of Lianyungang, China, *MARINE POLLUTION BULLETIN*, 89(1), 102-111.
7. A. Esmaeili, 2006. Technical efficiency analysis for the Iranian fishery in the Persian Gulf, *ICES JOURNAL OF MARINE SCIENCE*, 63(9), 1759-1764.
8. Lu. X., Fan. HT., 2015. Study on the Risk Assessment Approach of Port Facility Security Based on a Comprehensive Model of Delphi Method, Analytic Hierarchy Process, Grey Theory and Fuzzy Evaluation Method, 3RD INTERNATIONAL CONFERENCE ON TRANSPORTATION INFORMATION AND SAFETY (ICTIS 2015), Wuhan, PEOPLES R CHINA, pp.628-632.
9. A. Akin, S. Berberoglu, M.A. Erdogan, C. Donmez. 2012. Modelling land-use change dynamics in a Mediterranean coastal wetland using CA-Markov Chain analysis, *FRESENIUS ENVIRONMENTAL BULLETIN*, 21(2), 386-396.
10. J. Rocha, J. C. Ferreira, J. Simoes, J. A. Tenedorio, 2007. Modelling Coastal and Land Use Evolution Patterns through Neural Network and Cellular Automata Integration, *JOURNAL OF COASTAL RESEARCH*, 17(3), 827-831,
11. T. L. Saaty, L. T. Tran, 2007. On the invalidity of fuzzifying numerical judgments in the Analytic Hierarchy Process. *Mathematical and Computer Modelling*, 46(7-8), 962-975.
12. Wallenius J., Dyen J S., Fishburn P C., et al. Multiple criteria decision making, multiattribute utility theory: Recent accomplishments and what lied ahead. *Management Science*, 2008, 54(7):1336-1349.
13. Dubois, D. The role of fuzzy sets in decision sciences: Old techniques and new directions. *Fuzzy Sets and Systems*, Vol.184, No.1, pp.3-28, 2011.
14. L. Ledoux., R.K. Tumer., 2002. Valuing ocean and coastal resources: A review of practical Examples and issues for further action, *Ocean & Coastal Management*, 45(9-10), 583-616.
15. R. DalCin, U. Simeoni, 1994. A model for determining the classification, vulnerability and risk in the southern coastal zone of the marehe(Italy), *Journal of Coastal Reseach*, 3,18-29.
16. I. Bagdanaviciute, L. Kelpsaite, T. Soomere, 2015. Multi-criteria evaluation approach to coastal vulnerability index development in micro-tidal low-lying areas, *OCEAN & COASTAL MANAGEMENT*, 104, 124-135.
17. J. Nouri, A. Danehkar, R. Sharifipour, 2008. Evaluation of ecotourism potential in the northern coastline of the Persian Gulf, *ENVIRONMENTAL GEOLOGY*, 55(3), 681-686.
18. Sha, M., Qiu, BH. 2009. Evaluation System and Its Application for Undeveloped Port-shoreline Resources, Proceeding International Conference on Information Management, Innovation and Industrial Engineering, Xi'an, CHINA, pp. 496-501.

**CONTACT WITH THE AUTHORS**

**Liupeng Jiang**

College of Harbour  
Coastal and Offshore Engineering  
Hohai University  
Nanjing 210098  
**CHINA**

## CALCULATING STUDY OF THE TURBINE AT LAST STAGE FLOW FIELD IN THE SMALL VOLUME FLOW CONDITION

Tieliu Jiang\*

Jianguo Jin

Zhazhou Wang

Lihua Cao

Bo Li

School of Energy and Power Engineering, Northeast Electric Power University, China

\* corresponding author

### ABSTRACT

*Based on basic equation and boundary layer theory of pneumodynamics, the thesis conducts numerical modeling and theoretical analysis on the last stage of turbine characteristics at a small volume flow by using FLUENT, gives an emphasized analysis on the position of first occurrence of backflow and its expansion direction and comes up with flow structure of the turbine flow field at last stage in the small volume flow condition. In connection with specific experiments, it puts forward the flow model of backflow occurring in the last stage field and the solution to the model. The flow field at last stage for a 100MW turbine in the small volume flow condition that is calculated by using the model is basically in conformity to the actual result.*

**Keywords:** Turbine; Small volume flow; Flow model; Backflow

### INTRODUCTION

Running experience of and some searches in modern high-power turbine units show that [1] when the turbine is running in the small volume flow condition, its reliability reduces due to high vibrating stress of moveable vanes at last stage and the exhaust part heated. On the other hand, the last stage of a high-power turbine is generally working in the wet steam zone. Backflow carrying water drops behind movable vanes in the small volume flow condition strikes the movable vanes in a high relative speed, resulting in the water erosion at steam outlet side, which has an influence on the service life of movable vanes and safety of turbine units [2-6]. However, many units often have to run in a very low volume flow, such as idle running and primary load stage at startup, units responsible for auxiliary power when line fault, great extraction of stages behind extraction chamber for heating units, units subject to some peak loads. In addition, some

power plants also run under the same condition as the first and second last stage of condensing turbine during increased backpressure heating. In order to ensure high reliability of turbine running and increase its economy, it is of great significance to study on flow characteristics at the last stage in the small volume flow condition [7].

The small volume flow condition is so-called when compared with the design working condition. Small volume flow of turbine means that the condition that the steam flow multiplied by the specific volume is smaller than the specified working condition. In the small volume condition, backflow occurs at root on steam outlet side of movable vanes and eddy forms at the gap between moving and static vanes [8]. Owing to two different flow characteristics, the analysis method widely used in designed working condition is no longer applicable to the small volume flow condition.

As volume flow continuously decreases, steam turbine switches from working condition zone to forced draft zone through transitional condition zone [9]. Where is the

switch point? This is also a question about how much the working scope is. Therefore, it is of theoretical and practical significance to study on flow characteristics of last stage flow path in the small volume flow condition.

Flow study of turbine in the small volume flow condition is under progress, mainly focusing on last stages with methods of test research and numerical modeling. Literature [10-15] numerical modeling shows that the flow field in exhaust cylinder consists of passage eddy, separate eddy, end wall eddy, among which passage eddy is the biggest and the major factor affecting the cylinder loss. Literature [16] measures and studies the wet steam flow at last stage low pressure of 300MW direct air cooling turbine using the developed measuring device; Literature [17, 18] conducts numerical modeling analysis of last stage flow field in wet steam zone. Literature [19-21] simulates eddy flow condition of diffusers with different structures in the exhaust cylinder and in different inlets. Satisfactory results have been resulted from present numerical modeling. Compared with test research at high cost, numerical modeling has a great advantage. Current research result has reached consensus on flow separation of last stage vanes in the small volume flow condition.

When mass flow rate  $G$  flowing through stage reduces or back pressure increases, volume flow  $G_v$  of stage decreases. As volume flow reduces, line flow starts to warp and steam is squeezed to the root in guide vane and towards outer edge in movable vanes. As flow further reduces, this trend is to be intensified. When the volume flow reduces to a certain extent, the flow separation occurs at the root of movable vanes[17]. After flow separation and volume flow decreases more, eddy is formed at outer edge of vane clearance (axial clearance from nozzle outlet edge to movable vane inlet edge). The eddy moves in a peripheral direction in a high speed, which approximates the peripheral speed at the movable vane top in the small flow condition. At this time, the diagonal flow appears in cascade. Volume flow decrease also causes flow redistribution along the vane height direction: flow increases in middle and outer edge parts and decreases in root area. The experiment shows that [7] movable vane root operates in negative degree of reaction under small volume flow direction. Main steam flow only fills outer edge of movable vane passage. Flow at last stages is as follows: main flow to the outlet along vane outer edge, cool and wet steam in vane root condenser side moves from exhaust pipe to flow path. Besides, volume flow decrease and also redistributes of enthalpy drop between guide vane and movable vanes and changes degree of reaction. However, redistribution of both enthalpy drop and flow is caused by fundamental change of flow structures. Things change with a certain rule, so does fluid flow.

## MATERIAL AND METHODS

This mathematical model takes basic formula of streamline curvature method [22] as basic equation to describe this flow condition. The difference is to introduce new boundary conditions according to characteristics in the small volume

flow condition and make it access to definite answers under new condition.

Flow equation sets of S2 flow plane under a cylindrical coordinate system is derived by using two types of flow plane theory[23]:

$$\begin{aligned} C_r \frac{\partial C_r}{\partial r} + C_z \frac{\partial C_r}{\partial z} - \frac{C_u^2}{r} &= -\frac{1}{\rho} \frac{\partial p}{\partial r} \\ C_r \frac{\partial C_z}{\partial r} + C_z \frac{\partial C_z}{\partial z} &= -\frac{1}{\rho} \frac{\partial p}{\partial z} \\ \frac{Di}{Dt} &= \frac{1}{\rho} \frac{Dp}{Dt} + T \frac{Ds}{Dt} \\ \frac{\partial(r\rho C_r)}{r\partial r} + \frac{\partial(\rho C_z)}{\partial z} &= 0 \\ f(p, \rho, T) &= 0 \end{aligned} \quad (1)$$

Motion equation is rewritten as the following form for easier solution:

$$\frac{DC_r}{Dt} - \frac{C_u^2}{r} = -\frac{1}{\rho} \frac{\partial p}{\partial r} \quad (2)$$

$$\frac{DC_z}{Dt} = -\frac{1}{\rho} \frac{\partial p}{\partial z} \quad (3)$$

If the flow is broken into flow in planes  $z$  and  $\theta$  as shown in 3-2, component velocity of steam flow speed  $\vec{c}$  at any point in  $z$  plane is  $C_u$  and that in  $\theta$  plane is  $C_m$ :

$$\vec{C} = i_u C_u + i_m C_m \quad (4)$$

$$i_m C_m = i_r C_r + i_z C_z \quad (5)$$

In which,

$$C_r = C_m \sin \delta \quad (6)$$

$$C_z = C_m \cos \delta \quad (7)$$

$$\frac{1}{r_m} = -\frac{D\delta}{Dm} \quad (8)$$

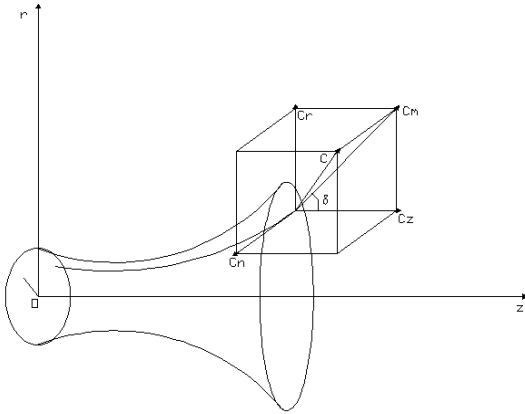


Fig. 1. Flow Velocity Resolution in z Plane and  $\theta$  Plane.

Substitute Equation (6) and Equation (8) into Equation (2), the full radial equilibrium equation is:

$$\frac{1}{\rho} \frac{\partial p}{\partial r} = \frac{C_u^2}{r} + \frac{C_m^2}{r_m} \cos \delta - C_r \frac{\partial C_m}{\partial m} \quad (9)$$

Quasi radial motion equation under absolute coordinate system is derived from Equation (9):

$$\frac{\partial C_m}{\partial y} = \frac{V(r)}{C_m} - U(r) * C_m \quad (10)$$

in which,

$$V(r) = \sin^2 \bar{\alpha} \left[ \frac{\partial H}{\partial y} - T \frac{\partial s}{\partial y} \right]$$

$$U(r) = \sin^2 \bar{\alpha} \left[ \frac{\sin(\delta + \gamma)}{C_m} \frac{\partial C_m}{\partial m} - cty \bar{\alpha} \frac{\partial cty \bar{\alpha}}{\partial y} - \frac{cty^2 \bar{\alpha} \cos \alpha}{r} - \frac{\cos(\delta + \gamma)}{r_m} \right]$$

$$\sin^2 \bar{\beta} = \frac{1}{1 + cty^2 \alpha \cos^2 \delta}$$

Quasi radial motion equation is also derived for relative coordinate system:

$$\frac{\partial C_m}{\partial y} = \frac{V'(r)}{C_m} - U'(r) * C_m \quad (11)$$

in which,

$$V'(r) = \sin^2 \bar{\beta} \left[ \frac{\partial I}{\partial y} - T \frac{\partial s}{\partial y} \right]$$

$$U'(r) = \sin^2 \bar{\beta} \left[ \frac{\sin(\delta + \gamma)}{C_m} \frac{\partial C_m}{\partial m} - \frac{\cos(\delta + \gamma)}{r_m} - cty \bar{\beta} \frac{\partial cty \bar{\beta}}{\partial y} - \frac{cty^2 \bar{\beta} \cos \gamma}{r} - \frac{2wcty \bar{\beta}}{C_m} \right]$$

$$\sin^2 \bar{\beta} = \frac{1}{1 + cty^2 \beta \cos \cos^2 \delta}$$

$$I = i + \frac{\omega^2}{2} - \frac{u^2}{2}$$

State equation:

$$f(p, \rho, T) = 0 \quad (12)$$

Continuity equation in integral form along y:

$$G = \int_{y_h}^{y_t} \rho C_m \cos(\delta + \gamma) 2\pi r dy \quad (13)$$

Energy equation:

$$\frac{D_i}{D_t} = T \frac{Ds}{Dt} \quad (14)$$

Small volume flow condition can be solved as per Equation (10), (11), (12), (13), (14) and corresponding definite conditions.

## RESULTS

Flow field at last stage of 100MW single cylinder turbine is calculated using the mathematical model, incorporating actual measurements. Variable working conditions and actual measurements of cross section at last stage movable vanes outlet are shown in Figure 2 and 3, among which  $\omega_1$  is calculated relative speed;  $\omega_2$  is actual relative speed;  $c_{z1}$  is calculated axial speed;  $c_{z2}$  is actual axial speed;  $\alpha_1$  is calculated absolute eddy angle;  $\alpha_2$  is actual eddy angle. 60MW load in Figure 2 is non-backflow working condition and 40MW in Figure 3 is the working condition for occurred backflow. Compared with tested parameters and calculated values, deviation between calculation value and test value of non-backflow condition is greater.

Main reason for the deviation is that original data used in calculation is from actual measurement and steam outlet angle has a great influence. In actual measurement, steam flow parameters behind movable vanes are the derived speed and outlet angle from pressure value measured with seven-hole spherical probe. A certain deviation will be generated and it relates to flow field condition, precision of measurement system, adaptability and conversion method. For 40MW with backflow (Figure 3), backflow zone height is 0.13m. From test parameters, height of this zone is within 0.12m-0.15m. This indicates that calculated result basically conforms to actual measurement result.

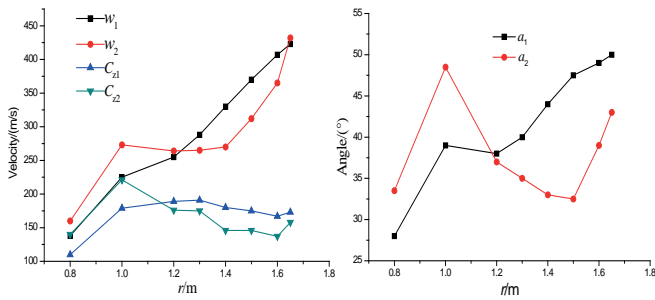


Fig. 2. Contrast between actual measurement and calculation of relative speed, axial speed and absolute eddy at 60MW.

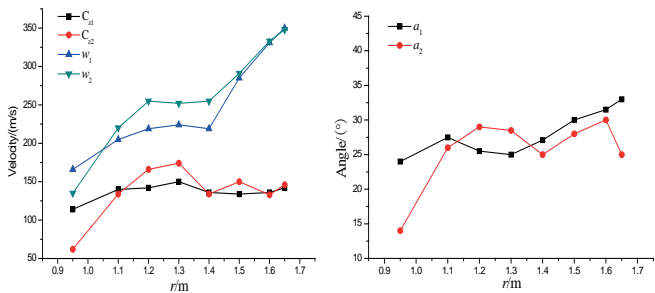


Fig. 3. Contrast between actual measurement and calculation of relative speed, axial speed and absolute eddy at 40MW

## CONCLUSIONS

(1) The reason for backflow at last stage in the small volume flow condition: as volume flow decreases, relatively strong diffusion area forms at last stage movable vanes root and pressure gradient forms at outlet cross section.

(2) Simplified mathematical model of last stage flow field in the small volume flow condition is put forward. It basically conforms to actual condition as approximate calculation and reliable to height calculation of backflow area, but approximates and deficiencies exist in the model itself.

## ACKNOWLEDGEMENTS

This work was supported by Department of Jilin Municipality Natural Science Foundation of China (20160203008SF) and Jilin Municipality Science and Technology Development Program (20161211)

## REFERENCES

1. Z. Q. Cao, 1991. The steam turbine operation mode features. China Water Power Press.
2. J. G. Jin, T. L. Jiang, Y. Li, L. H. Cao, 2011. Large steam turbine rotor blades out of the late-stage research and analysis of the steam side erosion. *Turbine Technology*, 53 (3), 199-201.

3. Q. Liu, 2007. End-stage blade of steam turbine erosion mechanism analysis and Stellite piece replacement study. Shanghai Jiaotong University.
4. G. S. Xie, 2008. Turbine last stage blades Anti-erosion carbon nitride titanium nitride composite coating preparation and basic research. Central South University.
5. W. L. Xu, J. D. Wang, D.R. Chen, F. B. Liu, 2010. Last stage of turbine blade erosion bench design. *Journal of Tsinghua University Natural Sciences*, 50(8), 1201-1204.
6. J. S. Rao, 1998. Application of fracture mechanics in the failure analysis of a last stage steam turbine blade. *Mechanism and Machine Theory*. 33, 599-609.
7. Z. B. Zhang, Y. J. Tian, L. H. Cao, Y. Sun, 2013. Numerical analysis of flow field within the turbine stage small volume flow conditions. *Chemical Machinery*. 40 (1), 94-97.
8. X. S. Cai, T. B. Ning, F. X. Niu, G. C. Wu, Y. Y. Song, Z. T. Sang, Z. L. Xu, C. S. Cen, Y. F. Guo, J. Zhang, G. Li, 2008. Low pressure turbine 300 MW Direct Air Flow Field in the last stage of blast and humidity measurement. *Chinese Society for Electrical Engineering*. 28 (26), 7-13.
9. W. Gerschutz, M. Casey, F. Truckenmuller, 2005. Experimental investigations of rotating flow instabilities in the last stage of a low-pressure model steam turbine during windage. *Proceedings of the Institution of Mechanical Engineers, Part A: Journal of Power and Energy*. 219 (6), 499-510.
10. H. T. Wang, X. C. Zhu, H., D. Yang, W. Zhou, C. H. Du, 2009. Numerical Optimization Design of Turbine Low Pressure Exhaust Hood. *Power Engineering*. 29 (1), 40-45.
11. W. L. Xie, H. T. Wang, X. C. Zhu, 2011. Analysis of the steam turbine low pressure cylinder exhaust diversion baffles affect its performance. *Power Engineering*. 31(5), 347-351.
12. H. T. Wang, X. C. Zhu, Z. H. Du, 2010. Aerodynamic optimization for low pressure turbine exhaust hood using Kriging surrogate model. *International Communications in Heat and Mass Transfer*. 37(8), 998-1003.
13. W. Zhang, Paik, Bu. Geun, Jang, Young Gil, 2007. Particle image velocimetry measurements of the three-dimensional flow in an exhaust hood model of a low-pressure steam turbine. *Journal of Engineering for Gas Turbines and Power*. 129(2), 411-419.
14. V. V. Ris, L. L. Simoyu, 2009. Numerical simulation of flow in a steam-turbine exhaust hood: Comparison results of calculations and data from a full-scale experiment. *Thermal*

Engineering English translation of *Teploenergetika*. 56(4), 277-283.

## CONTACT WITH THE AUTHORS

**Tieliu Jiang**

School of Energy and Power Engineering  
Northeast Electric Power University  
Jinlin 132012  
**CHINA**

15. X. S. Cai, T. B. Ning, F. X. Niu, G. C. Wu, Y. Y. Song, Z. T. Sang, Z. L. Xu, C. S. Cen, Y. F. Guo, J. Zhang, G. Li, 2009. 300MW Direct Air Turbine last stage low pressure wet steam Measurement. *Chinese Society for Electrical Engineering*. 29(2), 1-7.
16. L. Qi, Z. P. Zou, H. Z. Lu, E. L. Yu, D. Q. Tian, L. M. Shi, 2005. Numerical Simulation of Air Cooled Turbine Last Two Stages three-dimensional flow. *Power Engineering*. 25(5), 647-651.
17. L. Qi, N. Zheng, H. G. Cheng, 2005. Numerical Simulation of the last stage turbine unsteady flow. *Journal of Beijing University of Aeronautics and Astronautics*. 31(2), 206-211.
18. J. L. Fu, J. J. Liu, 2008. Influences of inflow condition on non-axisymmetric flows in turbine exhaust hoods, *Journal of Thermal Science*. 17(4), 305-313.
19. J. J. Liu, T. P. Hynes, 2003. The investigation of turbine and exhaust interactions in asymmetric flows-blade-row models applied. Transactions of the ASME. *Journal of Turbomachinery*. 125(1), 121-127.
20. L. J. Huang, 1978. About streamline curvature, Computational Mathematics. Volume 1, Section 1.
21. S. Hao, Q. H. Deng, H. S. Shi, Z. P. Shi, K. Cheng, Z. Y. Peng, 2013. The end of the steam turbine Numerical study of three scheduled regular flow under different volumetric flow. *Journal of Xi'an Jiaotong University*. 47(1), 15-20. (In Chinese)
22. L. J. Huang, 1978, about streamline curvature, Computational Mathematics. Volume 1, Section 1.
23. Y. L. Zhou, 2010. Multiphase flow parameters detection theory and its application. Science and Technology Press.

## RISK OF THE MARITIME SUPPLY CHAIN SYSTEM BASED ON INTERPRETATIVE STRUCTURAL MODEL

He Jiang<sup>1</sup>

Wei Xiong<sup>1</sup>

Yonghui Cao<sup>2,3,4,\*</sup>

<sup>1</sup> School of Management, Zhejiang University, China

<sup>2</sup> School of Economics & Management, Henan Institute of Science and Technology, China

<sup>3</sup> School of E-commerce and Logistics Management, Henan University of Economics and Law, China

<sup>4</sup> China Institute for Reform and Development

\* corresponding author

### ABSTRACT

*Marine transportation is the most important transport mode of in the international trade, but the maritime supply chain is facing with many risks. At present, most of the researches on the risk of the maritime supply chain focus on the risk identification and risk management, and barely carry on the quantitative analysis of the logical structure of each influencing factor. This paper uses the interpretative structure model to analysis the maritime supply chain risk system. On the basis of comprehensive literature analysis and expert opinion, this paper puts forward 16 factors of maritime supply chain risk system. Using the interpretative structure model to construct maritime supply chain risk system, and then optimize the model. The model analyzes the structure of the maritime supply chain risk system and its forming process, and provides a scientific basis for the controlling the maritime supply chain risk, and puts forward some corresponding suggestions for the prevention and control the maritime supply chain risk.*

**Keywords:** Interpretative Structural Mode; Maritime Supply Chain Risk; System Structure

### INTRODUCTION

With the economic globalization, the organization is to survive in a network, rather than as an independent individual to participate in international market competition [1]. Marine transportation is considered to be the world's most important means of transport, and which can promote international trade. About 80% of the world's trade and more than 70% of the value is through the sea transport. The maritime supply chain needs many organizations to participate in the network which is facing many risk from natural and human factors [2]. Because the complexity of network structure, the uncertainty of the external environment, the top management pursuit to lean and other factors, the maritime supply chain becomes

more and more vulnerable to various risks of the invasion. Once a certain risk occurs, it will cause irreversible damage to the maritime supply chain and suffer huge losses, and even lead to the complete disruption of the entire maritime supply chain. The effective maritime supply chain risk management can make the supply chain more flexible, so that the enterprise in the supply chain can avoid or reduce the loss caused by the risk. Therefore, it is very important for each member of the maritime supply chain to analyze the influencing factors of maritime supply chain risk and clarify the internal relationship among the factors.

Many scholars have studied the maritime supply chain risk: Yang attempts to evaluate the impact of risk factors from the container security initiative on the maritime

supply chain in Taiwan, and find out the leading categories of container security initiative risk factors are operational risk, physical risk and financial risk [3]. Lam et al. reveal that geographical location and changes in the constitution of players can have reverberations on the maritime supply chain dynamics that traverse the port [4]. Banomyong discuss the impact of the US container security initiative on maritime supply chains [5]. Barnes et al. suggests that the complexity of interaction between ports, maritime operations and supply chains create vulnerabilities that require analysis that extends beyond the structured requirements of these initiatives and creates significant management challenges [6]. Through the analysis, it is found that most of the research on the risk of the maritime supply chain focuses on the risk identification and risk management. Different scholars put forward different evaluation index system from different aspects. It has not established a perfect risk evaluation index system of maritime supply chain, and has not carry on the quantitative analysis of the logical structure of each influencing factor. Therefore, this paper attempts to use the interpretative structural model to make up for this gap.

The interpretative structural model (ISM) as a system analysis tool, which is characterized by the complex system is decomposed into several sub elements of the system, and find out the relationship between all the factors (including causality, size relationship, upstream and downstream relationships), form figure and structure matrix [7]. By means of the corresponding matrix calculus and transformation, the structure of the fuzzy and complicated system is clarified. At the same time, a hierarchical structure model is constructed to facilitate the analysis of the system.

The risk of maritime supply chain is a complex system formed by many factors. Based on the literature review, this paper establishes a risk assessment index system of the maritime supply chain, and introduces the structural model analysis method to study the risk model of the maritime supply chain, in order to clarify the maritime supply chain risk factors and to identify the key factors. The model analyzes the structure of the maritime supply chain risk system and its forming process, and provides a scientific basis for the controlling the maritime supply chain risk, and puts forward the corresponding countermeasures.

## **ANALYSIS ON THE INFLUENCING FACTORS OF MARITIME SUPPLY CHAIN RISK**

### **THE CONCEPT OF MARITIME SUPPLY CHAIN RISK**

An increasing amount of risk in supply chains is a current logistics trend [8], and according to Singhal et al., disruptions are a critical issue for many companies [9]. More recently, scholars have emphasized the importance of further studying supply chain risks and their management [10, 11]. Supply chain risk management is defined as “the identification of

potential sources of risk and implementation of appropriate strategies through a coordinated approach among supply chain members to reduce supply chain vulnerability” [12]. Similarly, maritime supply chain risk management can be defined as the “process of making and carrying out decisions that will minimize the adverse effects of accidental losses, and is based on risk assessment methods involving operation and communication between all members involved in maritime supply chain activities” [3].

### **THE INFLUENCING FACTORS OF MARITIME SUPPLY CHAIN RISK**

The research on the risk of maritime supply chain is relatively few. Chang et al. (2014) considered that the risk of maritime safety loss may be caused by the container shipping operations [13]. Vilko and Hallikas (2012) think that port workers strike, information system failure, water hidden iceberg, fire is the most important risk of shipping [14]. Gurning and Cahoon (2011) consider the most important maritime risk is port disorder, equipment failure, cleaning problems, container shortage and tariff issues [15]. Richard Oloruntoba studies the complex relationship between ports, shipping and supply chain, and points out a lot of risk from the unreasonable organizational structure and should improve the risk management ability of the maritime supply chain and focus on training managers’ crisis management ability. UNCTAD (2006) argues that many researchers pay too much attention to the environmental and organizational risks, while ignoring the risks associated with the network [16]. The risk will be divided into three categories: 1 – external risk (environmental risk), from the uncertainty of external environment factors, such as earthquake and terrorism; 2– supply chain risk (network related), the risk from outside the organization but limited to the internal supply chain. 3– internal risk comes from internal risk. This classification is supported by other scholars ([17, 18]) Jyri Vilkoa et al(2012) identified 103 factors of maritime supply chain risks based on interviews with senior managers and divided into external and internal risks, then point out that the exogenous risks had a greater impact in terms of time and costs, whereas the endogenous were responsible for more of the quality damage. Exogenous risks accounted for approximately 53% of the time delays, and endogenous risks made up about 49%. Additional costs accompanied 38% of the exogenous risks and 33% of the endogenous.

The paper carries out a special study to analysis the risk factors of maritime supply chain to, we investigate the issue of the 39 managers engaged in maritime operations management. On this basis, we set up a panel of experts and analysis the maritime supply chain risk preliminarily through the literature review and questionnaire survey, then use of Delphy method and reach an agreement finally. The expert group divides the maritime supply chain risk into external risk, cooperation risk, logistics service risk and information risk.

## External Risk

The external risk of the maritime supply chain includes the natural environment risk ( $F_1$ ), macroeconomic risk ( $F_2$ ), social instability factors ( $F_3$ ), policy risk ( $F_4$ ), uncertainty in market demands ( $F_5$ ).

The natural environment risk ( $F_1$ ): mainly refers to the natural disasters (earthquake, tsunami, etc.) and bad weather (typhoon, storm, flood and other factors, etc.). Due to the delivery of maritime supply chain must be achieved through shipping, shipping is affected by natural conditions. Macroeconomic risk ( $F_2$ ) affects the operation of the maritime supply chain indirectly by influencing the economic operation. It mainly includes interest rate change, exchange rate fluctuation, economic crisis, inflation, stock market risk and so on, the impact of the economic crisis on maritime supply chain is the most obvious. Social environment risk ( $F_3$ ) refers to the risk of abnormal changes in the internal and external social environment faced by the maritime supply chain, which mainly including social order risk and war risk. Social order risks such as strikes, pirates, terrorist attacks, demonstrations and so on, which once happen the maritime supply chain will suffer huge losses. Policy risk ( $F_4$ ) mainly includes legal risks and government intervention risks. In order to make the market economy orderly, the state has promulgated and implemented a series of laws and regulations, such as: tax laws and regulations, financial regulations, financial regulations and other laws and regulations, so that the country's legal system is becoming more and more perfect. However, all kinds of laws have a process of gradual improvement, the adjustment of laws and regulations, revision and so on, which is full of uncertain and cause risk. For some special industries and products, the state to macro-control, there will be restrictions. As the cross national and cross regional supply chain, the maritime supply chain also could meet the restriction from government. Uncertainty in market demands ( $F_5$ ): As the maritime supply chain belongs to the pull supply chain, demand driven services and fluctuation of demand will have a direct impact on the operation of the supply chain. Specifically including downstream customer demand reduction or interruption risk (For example, because of the high price of the products or materials, the demand of downstream customers will be reduced), the expansion of the highway and railway, the development of the aviation industry, which all have an important influence on the demand of the maritime supply chain.

## Cooperation Risk

Because the maritime supply chain is facing a lot of uncertainties, the uncertainties will bring some risks to relationship of the partners in supply chain. The cooperation risks include: interest distribution risk ( $F_6$ ), cooperation mechanism ( $F_7$ ), information asymmetry ( $F_8$ ).

Interest distribution risk ( $F_6$ ): The maritime supply chain operation has the advantage of win-win, which is the material premise that different partners or different interest groups

can ally with each other. But if the partners, especially the core partners cannot do justice to the distribute benefits, it will lead to a decline in partnership working enthusiasm, and even mutual constraints of the situation.

Cooperation mechanism ( $F_7$ ): The research of supply chain coordination mechanism can make the node enterprises in maritime supply chain realize the effective integration of internal and external supply chain, which also provides a new opportunity to improve the operational performance and competitive ability in the whole supply chain. Once the cooperation mechanism is unreasonable, it will affect the performance of the whole maritime supply chain.

Information asymmetry ( $F_8$ ): In the field of production and distribution in the maritime supply chain, the rapid and accurate transmission of information plays an important role in the whole process. In the case of information asymmetric, it is difficult to achieve the real optimization of logistics distribution and the whole supply chain, which will affect the performance in the whole supply chain

## Logistics Service Risk

The goal of logistics operation is to deliver the goods at the specified time to the designated location, but also need to ensure the overall balance of the entire supply chain and supply chain operation efficiency. Logistics service risk mainly including personnel operational risk ( $F_9$ ), facility and equipment maintenance ( $F_{10}$ ), the loss or damage of goods ( $F_{11}$ ), delayed in delivery ( $F_{12}$ ).

Personnel operational risk ( $F_9$ ): Personnel operational risk mainly refers to the unskilled staff, Work is not enthusiasm, personnel mobility and so on.

Facility and equipment maintenance ( $F_{10}$ ): Facility and equipment maintenance mainly refers to the maintenance of the infrastructure and equipment, or if there is a failure, there will be a huge loss.

The loss or damage of goods ( $F_{11}$ ): On the ship the cargo loss, the common species are damaged, wet, dirty, rotten, and the number of average weight shortage. Is one of the most common port supply chain risk.

Delayed in delivery ( $F_{12}$ ): If there is time delay in logistics operation, it will reduce the effect of the whole logistics service, and even lead to the failure of the whole logistics project.

## Information Risk

The information transmission between nodes in the supply chain is carried out through information system, the normal operation of the information system can ensure the orderly and efficient operation in the maritime supply chain. The information system risk mainly includes the IT system failure ( $F_{13}$ ), the speed of information transmission ( $F_{14}$ ), the information authenticity ( $F_{15}$ ), the information sharing ( $F_{16}$ ) and so on.

IT system failure ( $F_{13}$ ) mainly refers to the stability of the IT system, once the system is attacked by hackers or the virus,

the entire maritime supply chain information system will be in a state of paralysis, resulting in huge losses. The speed of information transfer ( $F_{14}$ ), information authenticity ( $F_{15}$ ), and information sharing ( $F_{16}$ ) are both directly or indirectly affecting the decision makers, which are crucial to the whole supply chain

## THE CONSTRUCTION OF MARITIME SUPPLY CHAIN RISK MODEL

### 3.1 ESTABLISHMENT OF ADJACENCY MATRIX

The key issue of this paper is the maritime supply chain risk system, first of all, adjacency matrix is established. The adjacency matrix describes the direct relationship between the factors of supply chain risk system. In accordance with the requirements of the interpretative structural model, the adjacency matrix of system for n factors  $S(F_1, F_2 \dots F_n)$  is defined as following.

$$A=[a_{ij}] = \begin{cases} 1, & \text{if } A \text{ has a direct impact on } B \\ 0, & \text{else} \end{cases}$$

In order to ensure the adjacency matrix is reliable, on the basis of consulting the opinions of 5 experts, this paper constructs the adjacency matrix A as shown in Table 1.

Tab. 1. The adjacency matrix of risk factors of maritime supply chain

|                 | F <sub>1</sub> | F <sub>2</sub> | F <sub>3</sub> | F <sub>4</sub> | F <sub>5</sub> | F <sub>6</sub> | F <sub>7</sub> | F <sub>8</sub> | F <sub>9</sub> | F <sub>10</sub> | F <sub>11</sub> | F <sub>12</sub> | F <sub>13</sub> | F <sub>14</sub> | F <sub>15</sub> | F <sub>16</sub> | F <sub>17</sub> |
|-----------------|----------------|----------------|----------------|----------------|----------------|----------------|----------------|----------------|----------------|-----------------|-----------------|-----------------|-----------------|-----------------|-----------------|-----------------|-----------------|
| F <sub>1</sub>  | 0              | 0              | 0              | 0              | 0              | 0              | 0              | 0              | 0              | 1               | 1               | 1               | 0               | 0               | 0               | 0               | 1               |
| F <sub>2</sub>  | 0              | 0              | 0              | 1              | 1              | 0              | 0              | 0              | 0              | 0               | 0               | 0               | 0               | 0               | 0               | 0               | 1               |
| F <sub>3</sub>  | 0              | 0              | 0              | 0              | 0              | 0              | 0              | 0              | 0              | 0               | 1               | 1               | 0               | 1               | 0               | 0               | 1               |
| F <sub>4</sub>  | 0              | 0              | 0              | 0              | 0              | 0              | 0              | 0              | 0              | 0               | 0               | 0               | 0               | 0               | 0               | 0               | 1               |
| F <sub>5</sub>  | 0              | 0              | 0              | 0              | 0              | 0              | 1              | 1              | 0              | 0               | 0               | 0               | 0               | 0               | 0               | 0               | 1               |
| F <sub>6</sub>  | 0              | 0              | 0              | 0              | 0              | 0              | 1              | 0              | 0              | 0               | 0               | 0               | 0               | 0               | 0               | 0               | 1               |
| F <sub>7</sub>  | 0              | 0              | 0              | 0              | 0              | 1              | 1              | 0              | 0              | 0               | 0               | 0               | 0               | 0               | 1               | 0               | 1               |
| F <sub>8</sub>  | 0              | 0              | 0              | 0              | 0              | 0              | 0              | 0              | 0              | 0               | 1               | 1               | 0               | 0               | 0               | 0               | 1               |
| F <sub>9</sub>  | 0              | 0              | 0              | 0              | 0              | 0              | 0              | 0              | 0              | 0               | 1               | 1               | 0               | 0               | 0               | 0               | 1               |
| F <sub>10</sub> | 0              | 0              | 0              | 0              | 0              | 0              | 0              | 0              | 0              | 0               | 0               | 1               | 0               | 0               | 0               | 0               | 1               |
| F <sub>11</sub> | 0              | 0              | 0              | 0              | 0              | 0              | 0              | 0              | 0              | 0               | 0               | 0               | 0               | 0               | 0               | 0               | 1               |
| F <sub>12</sub> | 0              | 0              | 0              | 0              | 0              | 0              | 0              | 0              | 0              | 0               | 0               | 0               | 0               | 0               | 0               | 0               | 1               |
| F <sub>13</sub> | 0              | 0              | 0              | 0              | 0              | 0              | 0              | 0              | 0              | 0               | 1               | 1               | 0               | 1               | 1               | 0               | 1               |
| F <sub>14</sub> | 0              | 0              | 0              | 0              | 0              | 0              | 0              | 1              | 0              | 0               | 0               | 1               | 0               | 0               | 0               | 1               | 1               |
| F <sub>15</sub> | 0              | 0              | 0              | 0              | 0              | 0              | 0              | 1              | 0              | 0               | 0               | 1               | 0               | 0               | 0               | 1               | 1               |
| F <sub>16</sub> | 0              | 0              | 0              | 0              | 0              | 0              | 1              | 1              | 0              | 0               | 0               | 0               | 0               | 0               | 0               | 0               | 1               |
| F <sub>17</sub> | 0              | 0              | 0              | 0              | 0              | 0              | 0              | 0              | 0              | 0               | 0               | 0               | 0               | 0               | 0               | 0               | 0               |

### ESTABLISHMENT OF REACHABILITY MATRIX

Based on the adjacency matrix A of risk factors of maritime supply chain, we can obtain matrix (A+E). The power operation of the matrix (A+E), based on Boolean algebra is established, until  $(A + E)^i \Rightarrow (A + E)^{i+1}$ . The reachability matrix M can be obtained by calculation. It indicates whether there is a link from one factor of the supply chain risk to another factor, that is, whether or not. Based on the reachability matrix, the reachable set of the factors affecting the maritime supply chain risk is calculated:  $P(S_i)$ , linear set:  $Q(S_i)$  and common set:  $P(S_i) \cap Q(S_i)$ , As shown in Table 3. When  $P(S_i) \cap Q(S_i) = P(S_i)$ , get the highest rank factor, which will draw from the table,

With the same method to get the next level of elements, so has been done, you can level by level to divide the elements according to the grade, and as a basis for the rearrangement of the reachable matrix, as shown in table 2.

Tab. 2. The relationship of influence factors of maritime supply chain risk system

| number | factors  | P(S)   | Q(S)   | P(S) ∩ Q(S)  |
|--------|--|--|--|--|
| 1      | natural environment risk (F <sub>1</sub> )               | F <sub>1</sub> ,F <sub>10</sub> ,F <sub>11</sub> ,F <sub>12</sub> ,F <sub>17</sub>   | F <sub>1</sub>   | F <sub>1</sub>   |
| 2      | macroeconomic risk (F <sub>2</sub> )                     | F <sub>2</sub> ,F <sub>3</sub> ,F <sub>4</sub> ,F <sub>5</sub> ,F <sub>6</sub> ,F <sub>7</sub> ,F <sub>8</sub> ,F <sub>9</sub> ,F <sub>10</sub> ,F <sub>11</sub> ,F <sub>12</sub> ,F <sub>17</sub> | F <sub>2</sub>   | F <sub>2</sub>   |
| 3      | social instability factors (F <sub>3</sub> )             | F <sub>3</sub> ,F <sub>4</sub> ,F <sub>5</sub> ,F <sub>6</sub> ,F <sub>7</sub> ,F <sub>8</sub> ,F <sub>9</sub> ,F <sub>10</sub> ,F <sub>11</sub> ,F <sub>12</sub> ,F <sub>17</sub>                 | F <sub>3</sub>   | F <sub>3</sub>   |
| 4      | policy risk (F <sub>4</sub> )                            | F <sub>4</sub> ,F <sub>11</sub>  | F <sub>4</sub>   | F <sub>4</sub>   |
| 5      | uncertainty in market demands (F <sub>5</sub> )          | F <sub>5</sub> ,F <sub>6</sub> ,F <sub>7</sub> ,F <sub>8</sub> ,F <sub>9</sub> ,F <sub>10</sub> ,F <sub>11</sub> ,F <sub>12</sub> ,F <sub>17</sub>   | F <sub>5</sub> ,F <sub>7</sub>   | F <sub>5</sub>   |
| 6      | interest distribution risk (F <sub>6</sub> )             | F <sub>6</sub> ,F <sub>7</sub> ,F <sub>8</sub> ,F <sub>9</sub> ,F <sub>10</sub> ,F <sub>11</sub> ,F <sub>12</sub> ,F <sub>17</sub>   | F <sub>6</sub> ,F <sub>7</sub> ,F <sub>8</sub> ,F <sub>9</sub> ,F <sub>10</sub> ,F <sub>11</sub> ,F <sub>12</sub> ,F <sub>17</sub> | F <sub>6</sub> ,F <sub>7</sub> ,F <sub>8</sub> ,F <sub>9</sub> ,F <sub>10</sub> ,F <sub>11</sub> ,F <sub>12</sub> ,F <sub>17</sub> |
| 7      | cooperation mechanism (F <sub>7</sub> )                  | F <sub>7</sub> ,F <sub>8</sub> ,F <sub>9</sub> ,F <sub>10</sub> ,F <sub>11</sub> ,F <sub>12</sub> ,F <sub>17</sub>   | F <sub>7</sub> ,F <sub>8</sub> ,F <sub>9</sub> ,F <sub>10</sub> ,F <sub>11</sub> ,F <sub>12</sub> ,F <sub>17</sub>                 | F <sub>7</sub> ,F <sub>8</sub> ,F <sub>9</sub> ,F <sub>10</sub> ,F <sub>11</sub> ,F <sub>12</sub> ,F <sub>17</sub>                 |
| 8      | information asymmetry (F <sub>8</sub> )                  | F <sub>8</sub> ,F <sub>9</sub> ,F <sub>10</sub> ,F <sub>11</sub> ,F <sub>12</sub> ,F <sub>17</sub>   | F <sub>8</sub> ,F <sub>9</sub> ,F <sub>10</sub> ,F <sub>11</sub> ,F <sub>12</sub> ,F <sub>17</sub>                                 | F <sub>8</sub> ,F <sub>9</sub> ,F <sub>10</sub> ,F <sub>11</sub> ,F <sub>12</sub> ,F <sub>17</sub>                                 |
| 9      | personnel operational risk (F <sub>9</sub> )             | F <sub>9</sub> ,F <sub>10</sub> ,F <sub>11</sub> ,F <sub>12</sub> ,F <sub>17</sub>   | F <sub>9</sub>   | F <sub>9</sub>   |
| 10     | facility and equipment maintenance (F <sub>10</sub> )    | F <sub>10</sub> ,F <sub>11</sub> ,F <sub>12</sub> ,F <sub>17</sub>   | F <sub>10</sub>  | F <sub>10</sub>  |
| 11     | the loss or damage of goods (F <sub>11</sub> )           | F <sub>11</sub> ,F <sub>12</sub> ,F <sub>17</sub>  | F <sub>11</sub> ,F <sub>12</sub> ,F <sub>17</sub>  | F <sub>11</sub> ,F <sub>12</sub> ,F <sub>17</sub>  |
| 12     | delayed in delivery (F <sub>12</sub> )                   | F <sub>12</sub> ,F <sub>17</sub>   | F <sub>12</sub>  | F <sub>12</sub>  |
| 13     | IT system failure (F <sub>13</sub> )                     | F <sub>13</sub> ,F <sub>14</sub> ,F <sub>15</sub> ,F <sub>16</sub> ,F <sub>17</sub>  | F <sub>13</sub>  | F <sub>13</sub>  |
| 14     | the speed of information transmission (F <sub>14</sub> ) | F <sub>14</sub> ,F <sub>15</sub> ,F <sub>16</sub> ,F <sub>17</sub>   | F <sub>14</sub> ,F <sub>15</sub> ,F <sub>16</sub>  | F <sub>14</sub>  |
| 15     | the information authenticity (F <sub>15</sub> )          | F <sub>15</sub> ,F <sub>16</sub> ,F <sub>17</sub>  | F <sub>15</sub> ,F <sub>16</sub> ,F <sub>17</sub>  | F <sub>15</sub> ,F <sub>16</sub> ,F <sub>17</sub>  |
| 16     | the information sharing (F <sub>16</sub> )               | F <sub>16</sub> ,F <sub>17</sub>   | F <sub>16</sub> ,F <sub>17</sub>   | F <sub>16</sub> ,F <sub>17</sub>   |
| 17     | maritime supply chain risk(F <sub>17</sub> )             | F <sub>17</sub>  | F <sub>17</sub>  | F <sub>17</sub>  |

Further, according to the level of the maritime supply chain risk system, the hierarchy of the supply chain risk system is drawn, which is shown in Figure 1.

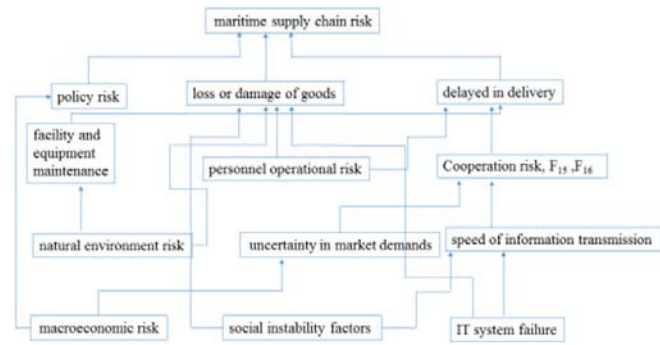


Fig. 1. Hierarchical structure of risk system of maritime supply chain

## MODEL ANALYSIS

The maritime supply chain risk is directly affected by policy factors, the loss or damage of goods, delayed in delivery, which is in the second layer. Obviously, there is conducive to all countries to establish international trade agreements, such as the establishment of the FTA tariff reduction, the reduction of trade barriers, as well as assure the quality and quantity of goods, timely and accurate delivery, these measures can achieve the direct reduction of maritime supply chain risk. As can be seen from the figure, the damage caused by natural disasters caused by the destruction of facilities and equipment, and thus the destruction of the goods in the supply chain and lead to delays in delivery, so the natural disasters has a direct effect on the maritime supply chain risk. The macroeconomic factors will directly effect on the formulation of relevant policies, but also through the uncertainty of market demands, the risk of cooperation, which leads to delayed in delivery. The factors of social instability will directly cause the loss and destruction of goods in the maritime supply chain, which is also possible to cause the delay in delivery through

the information transmission. Now shipping information is transmitted through the Internet, therefore, if the IT system failure, which will cause the maritime supply chain is in a state of collapse, cannot run normally, also causing loss / damage of goods and delay in delivery.

Through the ISM method to analyze the structural relationship model of the risk factors of the maritime supply chain, we can clearly describe the complex relationship among the factors into a multi-level hierarchical structure model. Based on this model, we can distinguish the relationship between risk factors. The factors that affect the risk of maritime supply chain are classified: the surface layer factors, the middle layer factors and the underlying factors. Which is conducive to understanding the formation and development mechanism of maritime supply chain risk. Fundamentally speaking, the risk of maritime supply chain is mainly from natural disasters, macroeconomic risk, social instability factors and fault information system. It can be seen, to ensure sustained and effective operation of maritime supply chain, which cannot do without cooperation, the efforts of all sectors of society.

In this paper, the author puts forward the following suggestions for the prevention and control of maritime supply chain risk:

(1) We should establish the accurate natural disaster forecasting system, do a good job in the prediction of natural disasters. And we need to set up a perfect maritime rescue system, once the natural disasters happen, we can rescue rapidly, and so that the loss will be reduced to a minimum

(2) We should stabilize the world economic environment, stabilize interest rates / exchange rates, lower tariffs and cut trade barriers.

(3) We should maintain social peace, to establish a good social order, at the same time do a good job security measures.

(4) Strengthen the development of IT technology, it needs to establish a stable information system to achieve the organization and integration of information between the enterprise and the maritime enterprise supply chain node enterprises

## CONCLUSION

The risk of maritime supply chain is a complex system composed of a number of key factors, which play a different role in the process of maritime supply chain risk formation. This paper constructs the maritime supply chain risk model using ISM method, the model shows that the factors directly affect the supply chain risk is policy factors, the loss or damage of goods, delayed in delivery. The root causes of risk are natural disasters, macroeconomic factors, social instability and IT system failures.

Empirical research is an important method of management research, but it is still in the stage of theoretical model. Based on literature review, expert consultation and exploratory factor analysis, this paper presents a theoretical model for empirical research. The maritime supply chain risk system

based on ISM method is more reliable, which can effectively avoid the failure of empirical research.

In short, with the economic globalization, the maritime supply chain plays an increasingly important role in international trade. In recent years, the uncertainties of international economic and political are increasing, and correctly grasp the logical structure of the risk factors faced by the port supply chain, which is valuable for the decision-makers in the prevention and control of the supply chain risk. The conclusion of this paper can provide theoretical support for the construction of maritime supply chain risk system, which has practical value, and has important reference value for further research.

## ACKNOWLEDGEMENTS

This work is financially supported by science and technology innovation talent support program of Henan province higher education (HUMANITIES AND SOCIAL SCIENCES), 2017-cxrc-04; Ministry of education humanities and Social Science Fund(15YJC630006); Henan social science program of Henan Province in 2016(2016BJJ017); Key research projects of Humanities and social sciences of Henan Provincial Department of education in 2016(2016-zd-046); 2014 Henan provincial government decision-making research tender topic(2014154); Key research projects of Humanities and social sciences of Henan Provincial Department of education in 2014(2014-zd-011); General research project of Humanities and social sciences of Henan Provincial Department of education in 2016(2016-gh-122); General research project of Humanities and social sciences of Henan Provincial Department of education in 2017(2017-ZZJH-163) Henan Institute of Science and Technology major research projects(2015); The major project of National Social Science Fund (12&ZD206). Thanks for the help.

## REFERENCES

1. H., Carvalho, A. P. Barroso, V. H. Machado, S. Azevedo, & Cruz-Machado, 2012. Supply chain redesign for resilience using simulation. *Computers & Industrial Engineering*, 62(1), 329-341.
2. J. Lam, J. Dai, 2015. Developing supply chain security design of logistics service providers: an analytical network process-quality function deployment approach. *Int. J. Phys. Distrib. Logistics Manage.* 45 (No. 7), 674–690.
3. Y. C Yang, 2011. Risk management of Taiwan's maritime supply chain security. *Safety science*, 49(3): 382-393.
4. J. S. L. Lam, 2011. Patterns of maritime supply chains: slot capacity analysis. *Journal of Transport Geography*, 19(2): 366-374.

## CONTACT WITH THE AUTHORS

**Yonghui Cao**

China Institute for Reform and Development  
Haikou 570311  
**CHINA**

5. R. Banomyong\*, 2005, The impact of port and trade security initiatives on maritime supply-chain management. *Maritime Policy & Management*, 32(1): 3-13.
6. P. Barnes, R. Oloruntoba, Assurance of security in maritime supply chains: Conceptual issues of vulnerability and crisis management. *Journal of International Management*, 11(4): 519-540.
7. A. Mandal, S. G. Deshmukh, 1994. Vendor selection using interpretive structural modeling (ISM). *International Journal of Operations & Production Management*, 14(6): 52-59.
8. T. Minahan, 2005. The Supply Risk Benchmark Report. Aberdeen Group, Boston.
9. V. Singhal, K. Hendricks, R. Zhang, 2009. The effect of operational slack diversification, and vertical relatedness on the stock market reaction to supply chain disruptions. *J. Oper. Manag.* 27 (3), 233–246.
10. F. Wiengarten, P. Humphreys, C. Gimenez, R. McIvor, 2016. Risk, risk management practices, and the success of supply chain integration. *Int. J. Prod.Econ.* 171 (3), 361–370.
11. J. S. L .Lam, 2015. Designing a sustainable maritime supply chain: a hybrid QFD-ANP approach. *Transp. Res. Part E* 78, 70–81.
12. M. Christopher, H. Peck, C. Rutherford, U. Juttner, 2003. Supply chain resilience. Cranfield Centre for Logistics & Supply Chain Management, November, appendix, 1.
13. C. H. Chang, J. J. Xu, D. P. Song, 2014. An analysis of safety and security risks in container shipping operations: a case study of Taiwan. *Saf. Sci.* 63 (3), 168–178
14. J. P. P. Vilko, J. M. Hallikas, 2012. Risk assessment in multimodal supply chains. *Int. J. Prod. Econ.* 140, 586–595.
15. S. Gurning, S. Cahoon, 2011. Analysis of multi-mitigation scenarios on maritime disruptions. *Marit. Pol. Manage.* 38 (3), 251–268.
16. UNCTAD, 2006. Maritime Security: Elements of an Analytical Framework for Compliance Measurement and Risk Assessment. *Reported by UNCTAD*, 1-10.
17. U. Juttner, H. Peck, M. Christopher, 2003. Supply chain risk management: outlining an agenda for future research. *Int. J. Logist.: Res. Appl.* 6 (4), 197–210.
18. J. S. L .Lam, 2015. Designing a sustainable maritime supply chain: a hybrid QFD-ANP approach. *Transp. Res. Part E* 78, 70–81.

# A CONCEPTUAL MODEL OF EXCELLENT PERFORMANCE MODE OF PORT ENTERPRISE LOGISTICS MANAGEMENT

He Jiang<sup>1</sup>

Wei Xiong<sup>1</sup>

Yonghui Cao<sup>2,3,4,\*</sup>

<sup>1</sup> School of Management, Zhejiang University, China

<sup>2</sup> School of Economics & Management, Henan Institute of Science and Technology, China

<sup>3</sup> School of E-commerce and Logistics Management, Henan University of Economics and Law, China

<sup>4</sup> China Institute for Reform and Development

\* corresponding author

## ABSTRACT

*Port as one of the key hubs of international logistics, which has become the main part and the base of global logistics management. The port enterprises, plays an important role in the global supply chain. However, due to the lack of understanding in port supply chain management, coordination between the port enterprises, the integration of business process is not perfect, the lack of information sharing between various organizations, ports enterprises usually failed to fully play its positive role. Based on this, the paper makes the port enterprises as the research object, and introduces the excellent performance mode into the port enterprises. In order to study the port enterprises how to carry out effective quality management, and formation the coordination and integration of upstream and downstream of enterprises, so as to realize the competitive advantage in port logistics.*

**Keywords:** Port Enterprises; Performance Excellence Model; Logistics Management

## INTRODUCTION

As one of the key hubs of international logistics and transportation, the port plays an important role in the global maritime supply chain, and it has become the main link and operating base in the global logistics. As an important node of the global maritime supply chain, port enterprises meet the needs of customers better which has become the main target to enhance the competitiveness, in order to achieve this goal, port enterprises must make the high value-added maximize, to achieve the requirement of low cost and high quality, only through this way, the port enterprise can improve customer satisfaction, and create more profit[1-4]. However, due to the lack of understanding in port supply chain management,

coordination between the port enterprises, the integration of business process is not perfect, the lack of information sharing between various organizations, ports enterprises usually failed to fully play its positive role[5-8]. Applying the theory of supply chain management to the practice of port management and research on port supply chain management further, which has become a strategic weapon for port enterprises to obtain international competitiveness in the knowledge economy and the background of globalization[10].

The supply chain management research mainly focus on manufacturing enterprises, nearly 10 years the researchers begin to study the port supply chain management, but empirical articles is very few. Even in the port supply chain management, different scholars have different ideas[11-13]. Robinson (2002)

## **CONSTRUCT THE EXCELLENT PERFORMANCE MANAGEMENT MODEL FOR PORT ENTERPRISE**

### **PRINCIPLE IN MODEL BUILDING**

In the process of constructing the excellent logistics system of port enterprises, we put forward the principle: “leadership support, focusing on the customers, implementing the comprehensive system, emphasis on application effectiveness, realizing the information support, emphasizing the continuous improvement”. The “leadership support” principle requires that the development of excellent performance model should be from the perspective of core competence in the leadership and strategic level, guide the organizations form systematic thinking in customer service, resource management, process management, system management and self enhancement effectively , so as to form a unified organizational goals and visionary leadership. “Focus on customers” principle requires excellent performance management mode is not empty talk, not only to optimize the internal procedure as the foothold, and should take the core competitiveness as the direction, to win customers trust and support, mining customer demand deeply, manage the customer value and customer satisfaction. The principle of “implementing the comprehensive system” requires of the excellent performance management system should promote systematically, and achieves leadership, strategy, customers and markets, resources, processes, measurement analysis and improvement and overall improvement of business results. However, which should identify the foothold, and strive to achieve the overall promotion through a single point of breakthrough, should not blindly comprehensive system. The principle of “focus on the application effect of” ask the excellent performance management to improve the management efficiency as the goal, the effect is obvious before and after the application; and combine the modern logistics management work with the excellent performance management model together, promote customer service, organizational learning, agile supply chain, innovation management, process optimization and other results. “Information support” ask should not meet the requirements of performance excellence management only by documents, should solidify into the information system, and apply into the daily work, to form “curing, quantization, optimization” effect. The principle of “emphasis on continuous improvement” requires the formation of an organizational culture of self-diagnosis, self-improvement and self-promotion through excellent performance management.

### **MODEL BUILDING**

On the basis of core values and concepts, according to the performance management standards, the paper sets up: leadership vision; customer orientation in the pursuit of excellence; organization and members of the organization learning; respect for employees and partners; sensitivity; focus

who researches on port supply chain management pointed out that due to the increase of port freight volume, shipping and land transportation enterprises seek economies of scale, and hope that there will be obvious rationalization and functional integration of Port Logistics[14]. Carbone and Martino (2003) analysis the characteristics of port service supply chain in the perspective of how to integrated the structure of supply chain management, and point that the higher the integration is, the whole supply chain can be more competitiveness[15]. Panayides and Song (2008) propose the terminal supply chain integration model which is an empirical structural model, and including “information and communication systems”, “value-added services”, “multimodal systems and operations”, “supply chain integration practices” and other measurement variables[16]. Rodrigue and Notteboom(2009) argue that the port enterprise is facing the increasingly complex international trade patterns, the global terminal operators and the requirements of transportation companies and other strategic behaviors, which require to integrate the inland transport and port logistics system[17].

In addition, the excellence performance model is a management framework to enhance the enterprises competitiveness, since its birth, the world has caused a boom in learning. In essence, the excellence performance model comes from the quality management practice. In the past 30 years, many scholars have tried to define the connotation and operational definition of quality management practice. Feigenbaum, Deming, Juran et al according to their own practical experience and management philosophy, outline the conceptual framework and the core elements of quality management practice including senior leadership support, employee participation and process management etc. Saraph et al. take the quality management practice as a complete concept to build on the basis of the experience of the great masters in quality first, point out that quality management practice is a kind of management measures and plans for improving quality, reducing cost and improving production efficiency. The development of the theory of quality management practice, which promote the enthusiasm of enterprises to implement quality work. Today, the theory of total quality management is becoming more and more popular, enterprises pay more and more attention to the development of strategic quality.

Based on the above analysis, introducing excellent performance mode into port logistics enterprise, which will become a new research idea to improve the performance of the port logistics enterprises, so as to enhance the competitiveness of the port logistics enterprises[18-19]. However, through the literature review, the relevant research is very few, and the logistics system as an important part of the port enterprise operation, it is urgent to study it deeply[20-21]. Based on this, this paper takes the port enterprises as the research object, studies how to carry out supply chain management effectively in the port enterprises, and forms the coordination and integration of upstream and downstream, so as to realize the competitive advantage of port enterprises

the future; management innovation; management based on fact; social responsibility; focus on results and innovation value; system view. So, the paper bases on the process of Method - Expansion - Learning - Integration - Results, and make seven criteria for the development in enterprise management maturity: leadership, strategy, resources, customer and market, process management, measurement, analysis and improvement and business results. The “leadership” holds the organization direction, and pay close attention to the “business results”, so “leadership”, “strategy”, “customer and market” which constitutes a “leading role” triangle; “resources”, “process management”, “business results” constitute a triangle of “resources, process and the result”. The “measurement”, “analysis and improvement” are the basis for organization operating, which is the chain to link the two triangles, and turn the PDCA wheel of improvement and innovation.

Excellent performance management model focus on the application process and the practice needs in modern logistics construction, port enterprise excellent performance management model is shown in Figure 1.

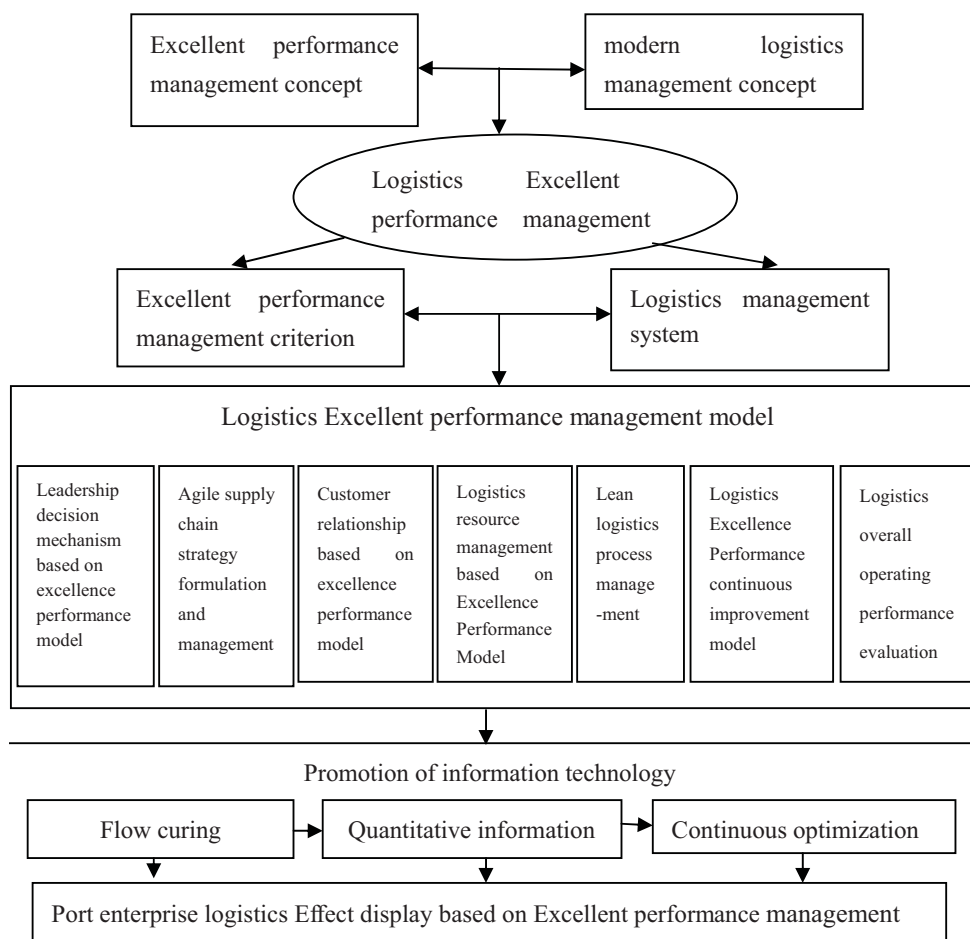


Fig. 1. Port enterprise logistics system excellent performance model

## Leadership

Based on the excellent performance management criteria, aiming at the construction and management of modern logistics in port enterprises, which make the enterprise leaders to form a new understanding in the core business of modern logistics, to establish an efficient organizational leadership for the purpose of building modern logistics construction and form the core competitiveness. Through the introduction of the leadership promoting project, build the leader decision consultant mechanism, and form distinctive leadership in the port logistics management

## Strategy

From the strategy, the excellent performance management should aim at the construction of modern logistics system in port enterprises. According to the requirements of excellence performance management criteria, forming the specific strategic objectives and strategic deployment, to build the integration of upstream and downstream of the agile supply chain, and to form the strategic decision-making mechanism accords with modern logistics.

## Customer and market

At the customer and market level, the port enterprises should be in accordance with the requirements of excellence performance management, to build a excellence service brand system, according to customer driven principle, optimize the internal operation and management mechanism, using customer expectations, customer demand, customer value, customer complaints, customer satisfaction and so on to establish the quantitative evaluation index and evaluation method of customer satisfaction in logistics distribution, and realize the customer relationship management information. By providing customers with standardized and differentiated services, build the service system in the excellence performance model,

and provide customers with effective value-added services, and constantly achieve market control

**Resources**

In terms of resources, mainly from human resources, financial management, logistics infrastructure, logistics information system, logistics engineering technology and so on, Based on the goal and strategy of modern logistics construction, in accordance with the requirements of excellence performance criteria, to build logistics training system, form excellent logistics management platform, improve the financial cost accounting control system and investment management mechanism. Optimize the logistics infrastructure construction, equipment investment and management, through the logistics information system curing management process, using Internet and other logistics engineering technology to improve logistics efficiency and so as to form an excellent management model

**Process management**

In process management aspect, the key point is the operation management in logistics center, internal process management, marketing docking, coordination between upstream and downstream of the enterprise. And then, it takes process reengineering as a breakthrough, to form process management mechanism of background service.

The introduction of a total production management concept, which can form lean logistics management model by using the internet of things technology to solidify the excellent model for process management. Finally build a comprehensive perception, interoperability, intelligent processing of the whole logistics process management model.

**Measurement, analysis and improvement**

Focusing on the key performance indicators (KPI) of logistics center as a breakthrough, the port enterprise establish performance management and performance analysis mechanism to achieve the management system in logistics center and post performance. Under the guidance of the excellent performance criteria, it will form the self-evaluation and diagnosis management mechanism of logistics center and form a more mature logistics center PDCA management model.

Through the introduction of information technology to achieve excellence performance standards for measurement, analysis and improvement of management requirements, it will automatic achieve the acquisition of KPI data, analysis of the operation data, the excellent management effect of the intelligent decision diagnosis. On the basis of the above, the excellent performance criteria improve management level.

**Business results**

Using the excellent performance management model to guide the development of logistics cost center to profit center, which form customer service performance, product and service performance, resource performance, financial

performance, process performance and other aspects performance and evaluation mechanism.

**THE PLANNING OF EXCELLENCE PERFORMANCE MODEL IN PORT ENTERPRISE**

The excellence performance model cannot be accomplished overnight in port enterprise, which need to be carried out in a planned way. In this paper, the author puts forward the short-term and long-term proposal, so that the port enterprises can be used as reference in the process of constructing the excellent logistics system

**THE SHORT-TERM CONSTRUCTION CONTENT IN PORT ENTERPRISE**

In the short-term, the construction content is shown in Figure 2.

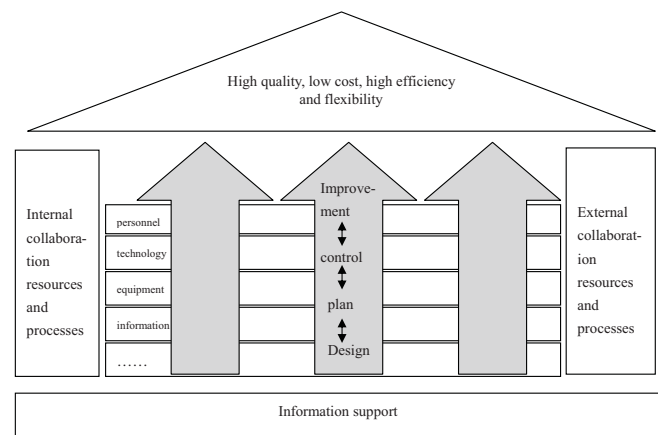


Fig. 2. The framework of excellence performance model in short-term construction

First, the lean management is the direction of the port enterprises, to sort out the internal logistics activities. That is, the port enterprise card the logistics management involves the “technology, equipment, personnel, information,” and other resources and processes activities, to complete the initial accumulation of the best practices in the logistics operation, and combined with the actual situation to the form the mechanism of “design, plan, control, improvement”.

Second, combing with the company’s internal and external resources and processes, the port enterprise form a special improvement program in the direction of excellent performance.

Third, the port enterprise realize information support of excellent performance management. Based on the present logistics information technology, the enterprise should integrate and enhance the application further, and to support the modern logistics operation management of port enterprises

## THE LONG-TERM CONSTRUCTION CONTENT IN PORT ENTERPRISE

In the long-term, the construction content is shown in Figure 3.

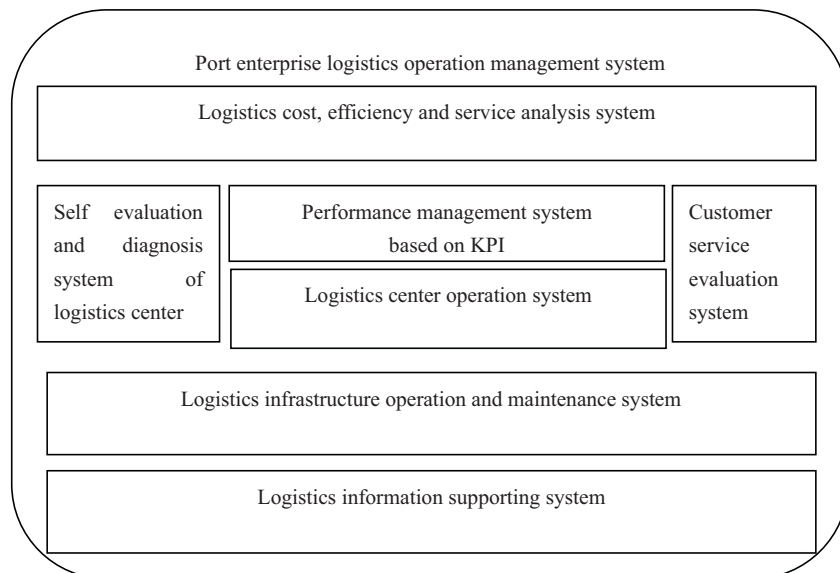


Fig. 3. The framework of excellence performance model in long-term construction

The short-term construction content corresponds to figure 3 in the “logistics center operation system”, “logistics infrastructure operation and maintenance system” and part of the “support system of Logistics information”. In the long term, which will be divided into four steps:

First, based on the current port enterprise logistics center evaluation rules, we should build and improve the performance management system based on KPI, then take comprehensive evaluation and measurement of logistics business operation, and implement in department and post.

Second, it will establish logistics center self-evaluation system, and the object of self-evaluation needs to cover the entire logistics center staff, in addition to cross evaluation, up and down evaluation each other. It will establish logistics center diagnosis system, which carry out a full range of diagnosis in responsibility orientation, process design, feedback mechanism, trace retention, examination results, etc. and implement improvement effectively.

Third, we will improve customer communication channels, and do an effective customer satisfaction survey to establish an objective customer service evaluation system which verify the quality and effectiveness of logistics operations from the perspective of the customer.

Fourth, it will build a comprehensive logistics cost, efficiency and service analysis system, which is the highest point of total operation management and the engine of macro guidance and strategic decision making. Through the analysis of the mechanism, we can find out the existing problems, explore the potential value, analyze the trend of the operation, and provide the scientific development plan for all employees

In addition, in the long-term construction, logistics information support system should be updated and improved

## CONCLUSION

To sum up, the “excellent performance management model” provides a set of evaluation criteria for management maturity of port enterprises, and the port enterprise can accept the concept and method which integrated the modern quality management. Through review its own logistics system, the port enterprise could find the performance gap between itself and the evaluation criteria, and then guide the enterprise logistics system to improve the management of the system, and then guide the enterprise logistics system to improve the management system. At the same time, through the introduction of the excellence performance model, the port enterprise needs to build a lean logistics value chain based on requirement driven in the business level, and take to measurement, analysis and improvement

in the management level, and form the agile supply chain, customer and market centric strategy, and gradually improve the efficiency of logistics management, improve customer service level, to achieve excellent performance goal.

In this paper, the research provides a framework for the effective implementation of logistics management in Port Enterprises. Compared with the previous research results, it pays more attention to the synergy and excellence of the implementation, which provides a new perspective for the study of port enterprise logistics management. Because the excellent performance management model is still in the initial research in port logistics management, this paper just makes a framework for discussion. Future research can be further studied by data empirical research.

## ACKNOWLEDGEMENTS

This work is financially supported by science and technology innovation talent support program of Henan province higher education (HUMANITIES AND SOCIAL SCIENCES), 2017-cxrc-04; Ministry of education humanities and Social Science Fund(15YJC630006); Henan social science program of Henan Province in 2016(2016BJJ017); Key research projects of Humanities and social sciences of Henan Provincial Department of education in 2016(2016-zd-046); 2014 Henan provincial government decision-making research tender topic(2014154); Key research projects of Humanities and social sciences of Henan Provincial Department of education in 2014(2014-zd-011); General research project of Humanities and social sciences of Henan Provincial Department of education in 2016(2016-gh-122); General research project of Humanities and social sciences of Henan

Provincial Department of education in 2017(2017-ZZJH-163); Henan Institute of Science and Technology major research projects(2015); The major project of National Social Science Fund (12&ZD206). Thanks for the help.

## REFERENCE

1. R. Cimpeanu, M. T. Devine, & C. O'Brien, 2017. A simulation model for the management and expansion of extended port terminal operations. *Transportation Research Part E: Logistics and Transportation Review*, 98, 105-131.
2. D. S. H. Moon, J. K. Woo, 2014. The impact of port operations on efficient ship operation from both economic and environmental perspectives. *Maritime Policy & Management*, 41(5), 444-461.
3. H. Davarzani, B. Fahimnia, M. Bell, & J. Sarkis, 2016. Greening ports and maritime logistics: A review. *Transportation Research Part D: Transport and Environment*, 48, 473-487.
4. N. Akbari, C. A. Irawan, D. F. Jones, & D. Menachof, 2017. A multi-criteria port suitability assessment for developments in the offshore wind industry. *Renewable Energy*, 102, 118-133.
5. S. H. Min, H. D. Choi, E. Y. Yun, D. W. Kang, & Y. S. Kim, 2015. A Study on the Operation of Ship Supply Common Logistics in Utilizing the Busan Port International Ship Supply Center. *Journal of Navigation and Port Research*, 39(6), 553-559.
6. G. B. B. Vieira, F. J. Kliemann Neto, & F. G. Amaral, 2014. Governance, governance models and port performance: A systematic review. *Transport Reviews*, 34(5), 645-662.
7. J. J. Liu, Z. Wang, D. Q. Yao, & X. Yue, 2016. Transaction cost analysis of supply chain logistics services: firm-based versus port-focal. *Journal of the Operational Research Society*, 67(2), 176-186.
8. W. U. Jianni, 2013. Research on Index System of Port Logistics Industry Cluster Competitiveness Based on Entropy Weight Method. *Science and Technology Management Research*, 6, 45-49.
9. T. Li, , L. Liang, 2016. Study on the Coupling Relationship between the Modern Port Logistics and Port-Vicinity Industry Agglomeration A Case Study of Dalian Port. *International Journal of u-and e-Service, Science and Technology*, 9(10), 131-142.
10. J. Havenga, Z. Simpson, L. Goedhals-Gerber, 2017. International trade logistics costs in South Africa: Informing the port reform agenda. *Research in Transportation Business & Management*, 22, 263-275.
11. F. Caselli, M. Reyes, M. Beale, Y. Akakura, & K. Ono, 2016. Methodology and procedure of business impact analysis for improving port logistics business continuity management. *IDRiM Journal*, 6(1), 1-29.
12. L. M. Ascencio, R. G. González-Ramírez, L. A. Bearzotti, N. R. Smith, & J. F. Camacho-Vallejo, 2014. A collaborative supply chain management system for a maritime port logistics chain. *Journal of applied research and technology*, 12(3), 444-458.
13. J. Wang, B. Zhu, Y. Wang, & L. Huang, 2016. Mining organizational behaviors in collaborative logistics chain: An empirical study in a port. In *Logistics, Informatics and Service Sciences (LISS), 2016 International Conference on* . IEEE, 1-5
14. R. Robinson, 2002. Ports as elements in value-driven chain systems: The new paradigm. *Maritime Policy and Management*, 29(3): 241-255.
15. V. Carbone, M. De Martino, 2003. The changing role of ports in supply chain management: an empirical analysis. *Maritime Policy and Management*, 30(4): 305-320.
16. P. M. Panayides, D.W. Song, 2008. Evaluating the integration of seaport container terminals in supply chains, *International Journal of Physical Distribution & Logistics Management*, 38(7): 562-584.
17. J.P. Rodrigue, T. Notteboom, 2009. The terminalization of supply chains: reassessing the role of terminals in port/hinterland logistical relationships. *Maritime Policy & Management*, 36(2): 165-183.
18. H. Chen, Y. Chen, 2016. The Performance Appraisal of Port Logistics Informationization. In *International Conference on Internet and Distributed Computing Systems*. Springer International Publishing., 9,413-420
19. M. Doods, F. Parola, 2016. Port Management Studies. *The Asian Journal of Shipping and Logistics*, 32(1), 001-002.
20. C. Expósito-Izquiero, E. Lalla-Ruiz, T. Lamata, B. Melián-Batista, & J. M. Moreno-Vega, 2016. Fuzzy optimization models for seaside port logistics: berthing and quay crane scheduling. In *Computational Intelligence*. Springer International Publishing, 323-343.
21. R. A. Sutrisnowati, H. Bae, M. Song, 2015. Bayesian network construction from event log for lateness analysis in port logistics. *Computers & Industrial Engineering*, 89, 53-66.

**CONTACT WITH THE AUTHOR**

**Yonghui Cao**

China Institute for Reform and Development  
Haikou 570311  
**CHINA**

# TOWARDS THE BUILDING INFORMATION MODELING-BASED CAPITAL PROJECT LIFECYCLE MANAGEMENT IN THE LUXURY YACHT INDUSTRY

Fuyong Liu<sup>1</sup>

Chaohe Chen<sup>2\*</sup>

Wei Wu<sup>3</sup>

<sup>1</sup> Department of Naval Architecture and Ocean Engineering, South China University of Technology, China

<sup>2</sup> Department of Naval Architecture and Ocean Engineering, South China University of Technology, China

<sup>3</sup> Department of Construction Management, California State University at Fresno, USA

\* corresponding author

## ABSTRACT

*It will be a new approach that BIM's capital project lifecycle management (CPLM) applied to the yacht industry. This paper explored the feasibility of applying the principles and rationales of BIM for capital project lifecycle management in luxury yacht design, engineering, fabrication, construction and operation. The paper examined the premises and backbone technology of BIM. It then evaluated leading naval engineering and shipbuilding software applications and their development trends from the functional lens of BIM. To systematically investigate a BIM-based approach for capital project lifecycle management (CPLM) in the luxury yacht industry, the paper proposed and outlined an implementation framework. A case study and a student competition use case were discussed to delineate the core constituents and processes of the proposed framework. The case of BIM was reviewed. Through the domestic custom luxury yacht design and prototyping student competition, the application of this framework in educational research is demonstrated and the initial quantitative assessment of the framework is carried out. Conclusions: a BIM-based CPLM implementation framework can help the luxury yacht industry capitalize on the global transformation to an information-centric and data-driven new business paradigm in shipbuilding with integrated design, manufacturing and production.*

**Keywords:** Building Information Modeling; Luxury Yacht; Communication; Interoperability; Capital; Project Lifecycle Management; Framework

## INTRODUCTION

BIM is developed on the basis of 3D digital design technology, and is usually defined as the digital representation of the physical and functional characteristics of projects [1]. As such, BIM serves as the integrative reservoir of multidisciplinary project data and supports business decision-making through the project's lifecycle [2]. Similar to building facilities, luxury yacht projects were usually delivered in a highly heterogeneous environment that involves broad participation of stakeholders and needs to accommodate a range of key design, engineering, fabrication, construction and operation factors such as cost, time, material, constructability, aesthetic value, performance, and sustainability, to name a few [3]. Recent trends in luxury

yacht market also suggest increased client engagement in luxury yacht project lifecycle for informed decision-making and pursuit for greater customization and superior project performance. Market reports [4,5] have shown strong evidence of BIM's business value in enhancing design communication, increasing constructability, streamlining fabrication and installation, and improving overall project outcomes. This paper envisions BIM as a disruptive technology applied in luxury yacht industry. It reviewed the technological premises of BIM and discussed how BIM can shift the paradigm of luxury yacht lifecycle management to embrace a collaborative, integrative and data-intensive project delivery process. The paper proposed and outlined a BIM-based implementation framework for luxury yacht lifecycle management, delineated

its core constituents and working mechanism, and conducted preliminary qualitative and quantitative evaluation of the proposed framework.

## MATERIAL AND METHODS

### PREMISES & BACKBONE TECHNOLOGY OF BIM

#### Parametric modeling

Designing a luxury yacht design is usually a lengthy, tedious and repetitive process. At the early stage, designers will usually spend months on conceptualization and weighing different options to seek for the optimal design representation that meets the client's expectation. Piles of design sketches are hand-drafted and a tremendous amount of geometric and non-geometric data are generated amid the design evolution. BIM can greatly relieve designers from this labor-intensive workflow and improve design productivity with parametric modeling. Parametric modeling is the foundation to object-based modeling technology such as BIM [6]. It empowers designers with the capacity to update design parameters, compare design options and visualize the differences simultaneously. Changes in one place will be automatically populated across all affected design, which significantly reduces the work load and eliminates inconsistency among design documents.



Fig. 1. Revit architecture shaded view of the Enchanted Castle [7]



Fig. 2. Documentation generation: BIM vs CAD [7]

BIM software solutions today (e.g. Autodesk Revit, Intergraph Smart 3D) foster intelligent 3D modeling beyond

simple geometric forms and shapes. Best practices in BIM implementation have demonstrated the ease of prototyping for designs with non-typical complexities and magnitudes. A superior example can be found in the Shanghai Disney Resort project. As shown in Fig. 1, the Enchanted Storybook Castle married traditional architectural detailing with modern building technology. It presented an extremely complex, dynamic yet harmonious design that meet all the programmatic, operational, accessibility, seismic, fire, mechanical, and technological requirements. Unprecedented 3D visualization accomplished in the BIM software environment streamlined the communication between designers of 142 disciplines and the client to reach consensus [7]. An exceptional advantage of BIM-based design workflow is the automated documentation generation. Parametric modeling allows customized view representation of the design in literally any standardized or non-standardized manner. Typical building plans, including plan, elevation, section and detail views, can then be produced and updated momentarily. As shown in Fig. 2, by switching to a BIM-based solution, many time-consuming steps could be eliminated from the traditional clean-up process. Instead of manually adjusting each 2D drawing, drawings were organically produced from the model(s) and modifications would be populated automatically and consistently across all affected sheets. Building standards and specifications can also be integrated within the model environment for further plan proofing and code compliance checking before bid documents are generated.

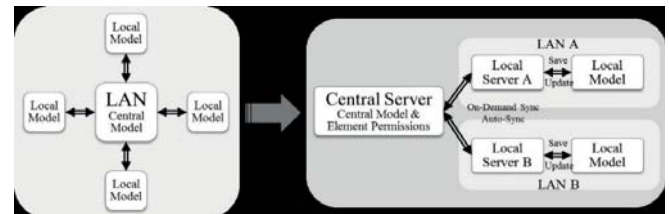


Fig. 3. Server-based file sharing and collaboration [8]

#### Concurrent collaborative design and construction coordination

Similar to the AEC industry, there is fragmentation-induced loss of productivity in luxury yacht industry, where projects are typically delivered with highly multidisciplinary, large and complex project teams. BIM provides an opportunity to offer a common information and communication platform and facilitate a truly collaborative working environment [9]. Before the BIM server technology is based on file sharing, to make the work fully synchronized, different teams must be between the model file editing. Full size model synchronization takes considerable time and bandwidth and thus becomes a serious performance and productivity bottleneck to the overall workflow, especially when Wide Area Network (WAN) instead of Local Area Network (LAN) collaboration is desired [8]. Recent advancement in cloud computing and BIM server

technology offers a much better option to allow component-based real-time design collaboration and synchronization. Fig. 3 describe the transition to a shared infrastructure. It is expected that future development of collaborative design and construction coordination platform for luxury yacht industry will most likely take the cloud-based BIM server approach.

### **Information exchange and interoperability standards**

The luxury yacht project lifecycle features large-volume and frequent information generation, exchanging, and updating/reconciliation. The complex engineering and business processes also necessitate the information interdependence among project team members. Highly varied project information with different sizes (e.g. small or large), complexities (structured or unstructured), formats (e.g. text, numeric or graphic) and priorities (low or high) also demand specially tailored, carefully classified exchange protocols. Classification of information exchange protocols not only saves resources, but can also improve quality and efficiency in information exchange process [10]. With a comprehensive underlying database, BIM can readily serve as a common reservoir for capital project lifecycle information. During the design process, designers and domain experts will all contribute to the model authoring. Then quite often, project information will be shared and passed along between team members in various business processes and critical project tasks such as energy simulation and structural analysis. During construction, ad-hoc information generated from day-to-day operation and installation can be quickly fed back to BIM via reality modeling technology such as 3D laser scanning to check against design model information to ensure compliance with performance and quality requirements.

Transferability of BIM-based technology to shipbuilding industry As a new frontier of research, several studies have been conducted to investigate how BIM-enabled technology and best practices could be transferred to the shipbuilding industry. Through structured interviews and literature review on BIM uses in comparison with 3D CAD applications in the shipbuilding industry, four BIM best practices including visualization, clash detection, quantity takeoff and scheduling/4D simulation were identified as highly transferrable [11-13]. Unlike the other three best practices that might find their counterparts in the shipbuilding industry, scheduling/4D simulation was regarded as a unique innovation in the AEC industry by integrating 3D design data with construction schedule data to foster smooth transition of project delivery between the design phase and construction phase. Recent research suggested that data sharing across design sectors and simulation of the construction process to predict time and cost are the key factors for concurrent engineering and integrated lifecycle management in shipbuilding industry [14-16]. Based upon these observations, it is safe to conclude that a BIM-based integrative design and construction approach for shipbuilding project delivery and lifecycle management is not only feasible but highly desirable.

## **STATE-OF-THE-ART SOFTWARE SOLUTIONS IN LUXURY YACHT INDUSTRY**

Currently, major software vendors in the marine and shipbuilding industry are undergoing significant transformation to embrace intelligent 3D modeling technology and integrated collaborative design, fabrication and production process, which is comparable to the adoption and implementation trajectory of BIM in the AEC industry. The following paragraphs review several leading marine engineering and shipbuilding software applications in the market, and identify the trends and opportunities towards the BIM-based lifecycle management for the luxury yacht industry.

### **NUPAS-CADMATIC/CADMATIC Marine Design**

Now CADMATIC Marine Design, provides a complete solution for the entire ship and offshore building process with advanced modeling and database technologies that ensures consistent design and production phases. It aims to enable highly efficient global distribution of projects and supports both online and offline sharing of 3D models seamlessly across stakeholders, which achieves full lifecycle management of vessels from early design to operation and decommissioning. Marketed as a highly integrated multidisciplinary solution, CADMATIC Marine Design covers shell, structural, piping and outfitting disciplines. Noticeably, CADMATIC Marine Design is a database-centric intelligent client server system that configures 3D ship models, documents, and component libraries in the primary and replica databases hosted by the database server system. Allegedly, always ensure the integrity of the project data and security, in the CADMATIC distributed design system to obtain the greatest advantage. Thus, in a globally distributed project, it is expected that the data will be updated through the interval set between the remote design sites via an online network such as the Internet, or through a file in an e-mail attachment. Designers can be assured that automated replication systems are responsible for data synchronization, ensuring that design time is not wasted due to incorrect information [17].

### **Intergraph Smart 3D/Intergraph SmartMarine Enterprise**

Intergraph Smart 3D uses an engineering approach that utilizes real-time parallel design, rules, relationships, and automation [18]. Intergraph Smart 3D provides a range of functions needed to design marine facilities. It is a data-centric, large-scale complex project with centralized visibility and control based on powerful rules and relationships, custom automation capabilities, and integration. Known as the world's first and only next-generation 3D design solution. The SmartMarine Enterprise, which is comparable to sophisticated BIM applications, provides a full range of design, fabrication, assembly, and lifecycle management capabilities within a single integrated environment [19].

## TECHNOLOGY TRENDS AND OPPORTUNITIES FOR BIM-BASED LUXURY YACHT CPLM

Review of the above leading marine and shipbuilding software solutions has helped identify the technology readiness for a paradigm shift in the luxury yacht industry to embrace more collaborative, information-centric and data-intensive business processes. It also seemed to be fairly obvious that Intergraph's SmartMarine 3D resemble advanced BIM applications such as the Autodesk Revit to a great degree. Based upon these observations and evaluations, the paper argues that a luxury yacht is not just a regular product and the scope and complexity of managing a luxury yacht project delivery seem to be more comparable to the capital projects management instead of conventional product management [20]. Therefore, a Capital Project Lifecycle Management (CPLM) approach is proposed by this research instead of the conventional Product Lifecycle Management (PLM).

### BIM-based CPLM for luxury yacht industry: implementation framework

Due to the lack of empirical evidence and established best practices to sufficiently justify the feasibility and validity of the BIM-based CPLM, a generic implementation framework that delineates its rationale and embedded business processes will be of common interest to stakeholders in the luxury yacht industry. The core constituents and processes of the framework are illustrated in Fig. 4, which consists of several interdependent functional layers that channel the project information through the full lifecycle of luxury yacht projects. Reconciling the characteristics of both the AEC and luxury yacht industries, the proposed framework depicts an information-centric lifecycle management approach that organically internalize five functional layers including: the CRM layer, the ERP layer, the Product Information layer, the Process Information layer, and the Network Server Platform layer. Development of this framework embraces and reflects an important principle in technology intervention to product development business process such as BIM's adoption and implementation and market transformation in the AEC industry, which is known as the "people, process and product" (3Ps) rule [21]. Specifically, the CRM layer manages the client relationship and solicits project requirements. The ERP layer manages internal technical and design resources for standardized workflow. Product and Process Information layer represent the information evolution and information stewardship supporting critical business decisions through the design, fabrication, construction and operation of a luxury yacht project. Last but not least, the Network Server Platform layer constitutes the technological infrastructure of the framework, and defines the business protocols for information exchange and sharing among stakeholders and key players in different layers.

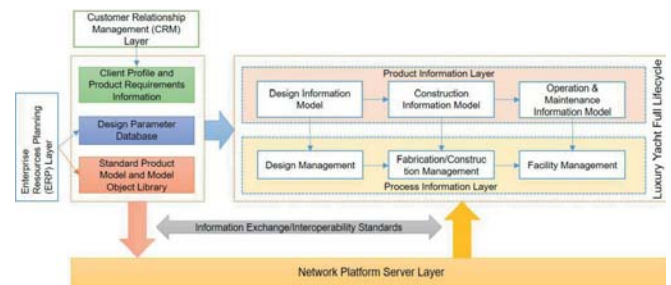


Fig. 4. Proposed implementation framework for full lifecycle luxury yacht design

### BIM-based CPLM implementation framework: case study

As a new concept, there is a lack of empirical evidence and documented literature validating the feasibility of utilizing BIM for capital project lifecycle management in the marine and shipbuilding industry. Other than a few anecdotal claims on promises and business benefits of BIM use in marine and shipbuilding industry, [22] presented an interesting case study of BIM use in new aircraft carrier pier and bulkhead rehabilitation design. Although not about BIM implementation directly involved in the aircraft carrier design and construction, it showcased the decision making and performance of a BIM-facilitated workflow in its waterfront structure design and construction, which provided valuable reference.

**Project background:** In April 2009, Naval Facilities Engineering Command (NAVFAC) Mid-Atlantic, Norfolk, Virginia, awarded a contract to Moffatt & Nichol (M&N)-led MN3M joint venture to design a replacement for Ship Repair Pier 5 at Norfolk Naval Shipyard. The design involved the demolition of two 1,000-foot-long piers (Pier 4 and Pier 5) and five additional buildings to accommodate a new 1,225-foot-long, 230-foot-wide pier (Pier 5) supported by more than 1,200 of 36-inch precast, pre-stressed concrete cylinder piles. A primary design goal set by the Navy was to achieve low maintenance needs for the piers' 75-year service life.

**Rationale of decision to use BIM:** When the design began in 2009, BIM was becoming a standard in vertical structure design, but had hardly been used for piers and other waterfront structures. Traditionally construction documents for waterfront projects relied on 2D drawings with independent manually-created section, plan, and detail views. Bill of materials used for estimation purposes were obtained through traditional quantity takeoff methods, which required an extensive amount of review and coordination between disciplines to identify and mediate element conflicts throughout the construction documents. In this project, which could be very labor intensive using traditional design methods. The Moffatt & Nichol (M&N)-led MN3M joint venture decided to utilize BIM to improve coordination among design disciplines, identify potential construction conflicts, reduce errors in design, help visualize the end product, and provide the Navy with a model to be used for asset management.

**Design outcomes and transition to construction:** MN3M delivered the final design in February 2010, less than a year after contract award and \$10 million under the Navy's initial estimates for construction. In addition to the design, Moffatt & Nichol also provides design, planning, analysis, tender and other contract documents, pre-project management and post-project construction services. A comprehensive Autodesk Revit 3D model of the pier and wharf was part of the design deliverables. With the Revit model being produced at 35% design completion, information exchange and real time collaboration among the MN3M team members were significantly enhanced to allow dynamic detection of conflicts between disciplines and unprecedented visualization of the end design by the Navy. The Revit model was also expected to be used by the Navy as part of their asset management program with great accountability of elements, spaces, equipment and systems in the facility.

**BIM-based CPLM implementation framework: use case in academia**

The BIM-based CPLM framework also find its applicability in educational contexts. In 2015 and 2016, students from the South China University of Technology competed in the 3<sup>rd</sup> and 4<sup>th</sup> Sunbird (sponsor) National Student Competition on Luxury Yacht Design. The theme of this competition was to design a 100-foot luxury yacht to meet not only technical innovation and functional requirements, but also to integrate client-centered aesthetics, sustainability, cost efficiency and marketability criteria. The deliverables included design drawings, specifications and a physical mockup. This comprehensive competition necessitated interdisciplinary teamwork, collaborative design and construction (mockup) efforts, which offered a great scenario to simulate the BIM-based CPLM implementation framework. A total of fifteen students with diverse backgrounds in fine arts, naval architecture and ocean engineering, industrial engineering and computer science participated in the two competitions.

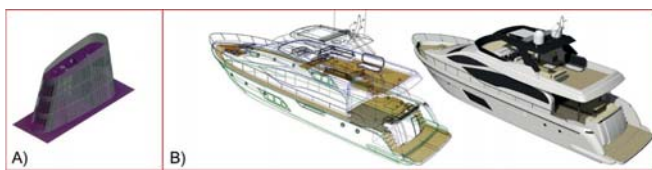


Fig. 5. A) Cabin surface by Smart 3D and B) complex hull surface model by Rhinoceros

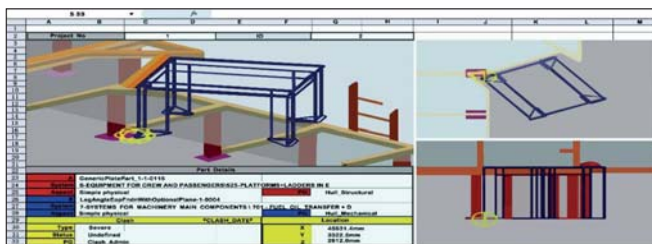


Fig. 6. Material report and clash detection in the hybrid model

Both 3D CAD applications (i.e. AutoCAD and Rhinoceros) and BIM-based solution (i.e. Intergraph Smart 3D) were used to streamline the conceptual design, detail design, construction documentation and mockup construction. Students complimented Smart 3D for its advanced data-centric, rule-driven solution for streamlining the yacht design processes while preserving design data and making it more usable/reusable for documentation generation and constructability review purposes. It is a highly integrative software solution to design and build a luxury yacht. Nevertheless, the disadvantage of Smart 3D is its weakness in complex surface engineering and modeling, for which students relied on Rhinoceros, as shown in Fig. 5. Smart 3D is a mixed model of CAD format that shares engineering data between multiple design teams with SmartPlant Enterprise. Students then utilized the hybrid model to run clash detection for constructability review, and leveraged the rich design data to perform quantity takeoff and generate the Bill of Materials (BOM) for fabrication, procurement and construction purposes (see Fig. 6). Design drawings and specifications were also automated (Fig. 7).

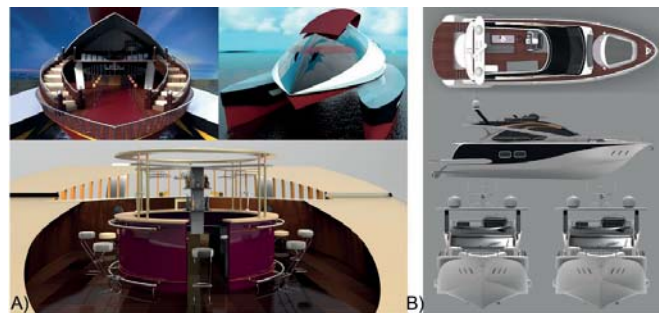


Fig. 7. A) 2015 design renderings and B) 2016 design renderings

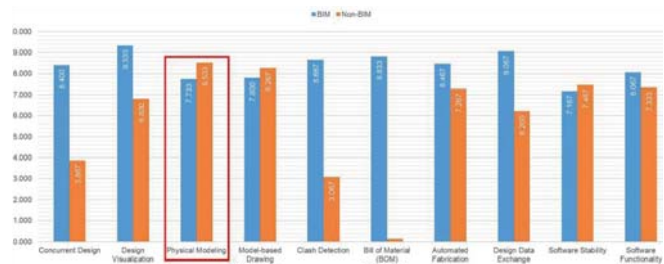


Fig. 8. Preliminary quantitative evaluation of BIM vs. non-BIM ingredients against ten performance criteria

In the competition debriefing meetings, students reflected that a BIM-facilitated approach could speed up the overall delivery of the project. However, at the conceptual design stage, there was no obvious advantage due to the fact that 3D CAD-based solutions were playing more essential roles in geometry design and surface modeling. It was into the detailed design and forward they started to gain significant improvement in efficiency and effectiveness in terms of generating design deliverables and bill of materials, performing clash detection and planning for mockup construction. They also indicated that applications of enterprise resources planning, fabrication

and construction management systems could greatly improve cost control and reduce overall construction costs. To gain more insights of students' perception towards a BIM-integrated CPLM framework versus traditional luxury yacht project delivery, the 15 students from two competition teams were invited to participate in a short survey that evaluated the BIM-ingredients against the non-BIM ingredients during the competitions, considering that students used both. A set of ten criteria were utilized as assessment measures with a 10-point scale (higher scores indicated more positive perceptions). The results were summarized in Table 1. A two-tailed two-sample unequal-variance student t-test was conducted to calculate if there was a statistically significant difference between students' evaluation on BIM and non-BIM ingredients by each measure. Apparently, except for "Model-based Drawing Generation" and "Software Stability", students' perception towards BIM and non-BIM ingredients differed significantly by the rest of the eight measures. Noticeably, BIM was considered to outperform non-BIM ingredients in seven measures except for "Physical Modeling", which was related to complex surface modeling and was discussed in previous paragraphs (Fig. 8). Therefore, this preliminary quantitative evaluation via an educational use case confirmed that a BIM-based CPLM approach could potentially benefit the luxury yacht industry from various perspectives.

## DISCUSSION

A BIM-facilitated CPLM has the advantage to not only facilitate smooth project delivery via enhanced communication and collaboration among team members, but also leverage consistent project information for decision making throughout the project lifecycle. This is accomplished through a highly integrative common data environment where all project parties can contribute, extract, update, exchange and manage project information with pre-defined business rules and interoperability protocols. With BIM, the project team of the Norfolk Naval Shipyard project was able to eliminate the intrinsic fragmentation in conventional workflow, and proactively involve the owner/operator, designer and contractor establish common project goals and performance requirements. Communication channels enabled by BIM and business intelligence achieved through synthesis of comprehensive multidisciplinary project dallowed the project team to reduce design error, improve constructability, cut project duration and save overall project costs.

## CONCLUSIONS

Information-driven modeling and advanced information technology are transforming business paradigms across different industry sectors, and best practices in one industry may also shed light on the other. This paper investigated opportunities of introducing more collaborative and integrative project delivery and lifecycle management in

the luxury yacht industry, based upon principles and best practices of BIM applied in the AEC industry. Literature review suggested strong resemblance of the IT infrastructure and project delivery between the two industries, and capacities of state-of-the-art software applications also demonstrated the readiness for the luxury yacht industry to embrace new business paradigms and BIM-based capital project lifecycle management. An implementation framework was thus proposed to delineate the rationale, constituents and business processes of the BIM-based CPLM. The implementation framework followed the "people, process and product" principle in adopting disruptive technology innovations. The framework was modularized with multiple functional layers that the ultimate goal was to channel both the product and process information of luxury yacht through its full lifecycle. Due to the lack of empirical evidence and best practices, the paper relied on a case study and an educational use case to preliminarily evaluate its feasibility and validity with considerable limitations and possible bias. Nevertheless, the case study and the educational use case consistently confirmed positive perceptions of both professionals and college students towards the BIM-based CPLM in future shipbuilding industry.

As global-distributed design and engineering workflow becoming standard practices, both the AEC industry and shipbuilding industry are facing challenges as well as opportunities in conducting business with data-driven, information-centric decision making. Developing the BIM-based CPLM seems to help enterprises improve business agility and gain competitive advantage in a global market. Future research on BIM-based CPLM can proceed with both macro and micro perspectives, including further development of the implementation framework with comprehensive business process mapping; the common project data environment and data sharing & exchange protocols; data analytics and big data analytics in sensor-deployed, automated luxury yacht project lifecycle management, to name a few.

## ACKNOWLEDGEMENTS

This paper is supported by the National Natural Science Foundation of China (Grant No.51039006). First of all, I would like to extend my sincere gratitude to my supervisor, Chaohe Chen, for his instructive advice and useful suggestions on my thesis. I am deeply grateful to Dr. Wu for his help in translation studies. I am also deeply grateful of their help in the completion of this thesis. Special thanks should go to the students who have put considerable time and effort into their comments on the questionnaire survey.

Tab.1. Preliminary quantitative evaluation of BIM vs. non-BIM ingredients in luxury yacht project delivery based upon a survey on student competitions.

| N=15          | concurrent design |      | visualization |      | physical modeling |      | model-based drawing |      | clash detection |      | bill of material |      | automated fabrication |      | design data exchange |      | software stability |      | software functionality |      |
|---------------|-------------------|------|---------------|------|-------------------|------|---------------------|------|-----------------|------|------------------|------|-----------------------|------|----------------------|------|--------------------|------|------------------------|------|
|               | BIM               | no   | BIM           | no   | BIM               | no   | BIM                 | no   | BIM             | no   | BIM              | no   | BIM                   | no   | BIM                  | no   | BIM                | no   | BIM                    | no   |
| 1             | 8                 | 4    | 9             | 7    | 8                 | 8    | 8                   | 7    | 8               | 3    | 7                | 0    | 9                     | 7    | 9                    | 6    | 7                  | 7    | 8                      | 7    |
| 2             | 9                 | 4    | 8             | 5    | 9                 | 9    | 8                   | 7    | 8               | 3    | 9                | 2    | 9                     | 8    | 9                    | 7    | 7                  | 8    | 8                      | 7    |
| 3             | 9                 | 4    | 8             | 7    | 9                 | 8    | 8                   | 8    | 8               | 3    | 9                | 0    | 8                     | 7    | 9                    | 6    | 8                  | 7    | 8                      | 8    |
| 4             | 8                 | 5    | 8             | 7    | 8                 | 6    | 9                   | 8    | 8               | 3    | 9                | 0    | 8                     | 8    | 9                    | 6    | 7                  | 8    | 9                      | 7    |
| 5             | 8                 | 4    | 10            | 6    | 7                 | 9    | 8                   | 8    | 9               | 2    | 9                | 0    | 7                     | 6    | 8                    | 6    | 7                  | 7    | 8                      | 8    |
| 6             | 8                 | 5    | 10            | 8    | 7                 | 9    | 7                   | 9    | 9               | 2    | 9                | 0    | 9                     | 6    | 8                    | 6    | 7                  | 7    | 9                      | 7    |
| 7             | 10                | 4    | 10            | 7    | 8                 | 9    | 8                   | 9    | 9               | 3    | 7                | 0    | 9                     | 7    | 8                    | 6    | 8                  | 8    | 8                      | 8    |
| 8             | 8                 | 6    | 9             | 6    | 7                 | 9    | 7                   | 8    | 8               | 5    | 9                | 0    | 9                     | 7    | 9                    | 5    | 7                  | 7    | 8                      | 7    |
| 9             | 7                 | 4    | 10            | 7    | 7                 | 9    | 8                   | 9    | 9               | 3    | 9                | 0    | 9                     | 8    | 10                   | 7    | 7                  | 7    | 8                      | 8    |
| 10            | 9                 | 3    | 10            | 6    | 7                 | 9    | 8                   | 9    | 8               | 5    | 10               | 0    | 8                     | 7    | 10                   | 6    | 7                  | 7    | 8                      | 7    |
| 11            | 8                 | 4    | 10            | 7    | 8                 | 9    | 7                   | 9    | 10              | 2    | 10               | 0    | 8                     | 8    | 10                   | 6    | 7                  | 7    | 8                      | 7    |
| 12            | 9                 | 2    | 10            | 7    | 8                 | 8    | 8                   | 8    | 10              | 3    | 10               | 0    | 8                     | 7    | 9                    | 6    | 7                  | 8    | 8                      | 7    |
| 13            | 9                 | 1    | 10            | 7    | 8                 | 8    | 8                   | 7    | 10              | 1    | 9                | 0    | 9                     | 9    | 10                   | 7    | 7                  | 8    | 8                      | 7    |
| 14            | 8                 | 4    | 9             | 8    | 8                 | 9    | 8                   | 9    | 8               | 5    | 7                | 0    | 9                     | 7    | 9                    | 6    | 7                  | 8    | 8                      | 7    |
| 15            | 8                 | 4    | 9             | 7    | 7                 | 9    | 7                   | 9    | 8               | 3    | 9                | 0    | 8                     | 7    | 9                    | 7    | 7                  | 8    | 8                      | 8    |
| Mean          | 8.40              | 3.87 | 9.33          | 6.80 | 7.73              | 8.53 | 7.80                | 8.27 | 8.67            | 3.07 | 8.83             | 0.13 | 8.47                  | 7.27 | 9.07                 | 6.20 | 7.17               | 7.47 | 8.07                   | 7.33 |
| median        | 8                 | 4    | 10            | 7    | 8                 | 9    | 8                   | 8    | 8               | 3    | 9                | 0    | 9                     | 7    | 9                    | 6    | 7                  | 7    | 8                      | 7    |
| variance      | 0.54              | 1.41 | 0.67          | 0.60 | 0.47              | 0.70 | 0.31                | 0.64 | 0.67            | 1.35 | 1.06             | 0.27 | 0.41                  | 0.64 | 0.50                 | 0.31 | 0.13               | 0.27 | 0.21                   | 0.24 |
| SD            | 0.74              | 1.19 | 0.82          | 0.78 | 0.70              | 0.83 | 0.56                | 0.80 | 0.82            | 1.16 | 1.03             | 0.52 | 0.64                  | 0.80 | 0.70                 | 0.56 | 0.36               | 0.52 | 0.46                   | 0.49 |
| t-Test        | <b>0.000</b>      |      | <b>0.000</b>  |      | <b>0.008</b>      |      | <b>0.076</b>        |      | <b>0.000</b>    |      | <b>0.000</b>     |      | <b>0.000</b>          |      | <b>0.000</b>         |      | <b>0.077</b>       |      | <b>0.000</b>           |      |
| Statistically | <b>Yes</b>        |      | <b>Yes</b>    |      | <b>Yes</b>        |      | <b>No</b>           |      | <b>Yes</b>      |      | <b>Yes</b>       |      | <b>Yes</b>            |      | <b>Yes</b>           |      | <b>No</b>          |      | <b>Yes</b>             |      |

## REFERENCES

- NIBS. 2007. Unite States National Building Information Modeling Standard, Version 1 – Part 1: Overview, Principles, and Methodologies Washington, DC.
- J. Yang, X. Zhang, 2009. Building Information Integration Model and Supporting Technology Standard. *Construction Technology*, 38(10), 109-112.
- W. Wu, R. R. A. Issa, 2010. Feasibility of integrating building information modeling and LEED certification process. In: International Conference on Computing in Civil and Building Engineering. Nottingham. pp. 161.
- McGraw-Hill Construction, 2009. The Business Value of BIM: Getting Building Information Modeling to the Bottom Line. M.-H. Construction, Bedford, MA.
- McGraw-Hill Construction. 2012. The Business Value of BIM in North America: Multi-Year Trend Analysis and User Ratings (2007–2012). M.-H. Construction, Bedford, MA.
- C. Eastman, P. Teicholz, R. Sacks, K. Liston, 2011. BIM Handbook: A Guide to Building Information Modeling for Owners, Managers, Designers, Engineers and Contractors (2nd ed.). NJ: John Wiley and Sons, Hoboken.
- AIA, 2014. AIA TAP BIM Awards - 2014 Professionals' Choice BIM Award. <http://bimforum.org/wp-content/uploads/2014/04/9ab-2014-Professionals-Choice-BIM-Award-MASTER-FINAL-PPT-04172014.pdf>.
- W. Wu, R. R. A. Issa, 2012. Leveraging Cloud-BIM for LEED Automation. *Journal of Information Technology in Construction*, 17, 367-384.
- B. Becerik-Gerber, K. Ku, F. Jazizadeh, 2012. BIM-Enabled Virtual and Collaborative Construction Engineering and Management. *Journal of Professional Issues in Engineering Education and Practice*, 138(3), pp. 234-245.
- W. Zhong, T. Jiang, 2014. Collaborative Construction based on BIM Standard. *Journal of Information Technology in Civil Engineering and Architecture*, 6(5), pp. 95-101.
- L. Ran, 2015. Transferring best practices enabled by Building information modeling (BIM) in Architecture, Engineering and Construction (AEC) to shipbuilding industry: An explorative study. (Industry Engineering and Management Master), Aalto University, Espoo, Finland. [https://aalto.fi/bitstream/handle/123456789/17703/master\\_Ran\\_Luming\\_2015.pdf?sequence=1](https://aalto.fi/bitstream/handle/123456789/17703/master_Ran_Luming_2015.pdf?sequence=1).
- L. Ran, V. Singh, 2016a. Building information modelling-enabled best practices in AEC and takeaways for Finnish

shipbuilding industry. *International Journal of Product Lifecycle Management*, 9(3), pp. 238.

13. L. Ran, V. Singh, 2016b. Comparing BIM in Construction with 3D Modeling in Shipbuilding Industries: Is the Grass Greener on the Other Side? In A. Bouras, B. Eynard, S. Foufou, & K.-D. Thoben (Eds.), *Product Lifecycle Management in the Era of Internet of Things* (pp. 193-202): Springer International Publishing.
14. M. Braglia, D. Castellano, M. Frosolini, 2014. Computer-aided activity planning (CAAP) in large-scale projects with an application in the yachting industry. *Computers in Industry*, 65(4), pp. 733-745.
15. K. Hiekata, M. Grau, 2014. Case Studies for Concurrent Engineering Concept in Shipbuilding Industry. In J. Cha, S.-Y. Chou, J. Stjepandić, R. Curran, & W. Xu (Eds.), *Moving Integrated Product Development to Service Clouds in the Global Economy* (Vol. 1, pp. 102-111): IOS Press Inc.
16. W. Tann, H.-J. Shaw, R. Bronsart, 2005. Integrating the Collaborative Environment in Shipbuilding: An Implementation Strategy. *Journal of Ship Production*, 21(1), pp. 37-45.
17. CADMATIC, 2016. CADMATIC Marine Design. <http://www.nupas-cadmatic.com/company/overview.html>.
18. Intergraph, 2016a. Intergraph Smart 3D. <http://ppm.intergraph.com/products/3d-product-family/intergraph-smart-3d>.
19. Intergraph, 2016b. SmartMarine Enterprise: Improving the Complete Marine Life Cycle. <http://viewer.zmags.com/publication/f19dd27d#/f19dd27d/1>.
20. Intergraph, 2009. Capital Project Life Cycle Management (cPLM) vs. Product Life Cycle Management (PLM) for the Shipbuilding, Marine, and Offshore Industries. <http://www.intergraph.com/assets/pdf/IntergraphcPLMvsPLMwhitepaper.pdf>.
21. N. Gu, K. London, 2010. Understanding and facilitating BIM adoption in the AEC industry. *Automation in Construction*, 19(8), pp. 988-999.
22. J. E. Gaul, M. N. Rieger, 2016. BIM Use in New Aircraft Carrier Pier and Bulkhead Rehabilitation Design. <http://www.aecbytes.com/feature/2016/BIM-PierBulkheadDesign.html>.

## CONTACT WITH THE AUTHORS

**Wei Wu**

Department of Construction Management  
California State University at Fresno  
Fresno, CA  
USA

# NONLINEAR PTO EFFECT ON PERFORMANCE OF VERTICAL AXISYMMETRIC WAVE ENERGY CONVERTER USING SEMI-ANALYTICAL METHOD

Ming Liu<sup>1</sup>

Hengxu Liu<sup>2\*</sup>

Xiongbao Zheng<sup>3</sup>

Hailong Chen<sup>2</sup>

Liquan Wang<sup>1</sup>

Liang Zhang<sup>2</sup>

<sup>1</sup> College of Mechanical and Electrical Engineering, Harbin Engineering University, China

<sup>2</sup> College of Shipbuilding Engineering, Harbin Engineering University, China

<sup>3</sup> College of Science, Harbin Engineering University, China

\* corresponding author

## ABSTRACT

*The wave energy, as a clean and non-pollution renewable energy sources, has become a hot research topic at home and abroad and is likely to become a new industry in the future. In this article, to effectively extract and maximize the energy from ocean waves, a vertical axisymmetric wave energy converter (WEC) was presented according to investigating of the advantages and disadvantages of the current WEC. The linear and quadratic equations in frequency-domain for the reactive controlled single-point converter property under regular waves condition are proposed for an efficient power take-off (PTO). A method of damping coefficients, theoretical added mass and exciting force are calculated with the analytical method which is in use of the series expansion of eigen functions. The loads of optimal reactive and resistive, the amplitudes of corresponding oscillation, and the width ratios of energy capture are determined approximately and discussed in numerical results.*

**Keywords:** Wave energy converter (WEC); power take-off (PTO); capture width ratios; analytical method; eigen function

## INTRODUCTION

With the oil and other fossil energy depletion and climate changing resulting from the greenhouse gas emission, low carbon, energy conservation and sustainable use, the renewable energy sources development and utilization are the most attractive themes of the world's energy development. Ocean energy is stored in the water in the inexhaustible renewable energy, including wave energy, tidal energy, tidal energy, thermal energy, salt and so on. The wave energy, which contains the kinetic energy and potential energy due to ocean surface wave can be considered to be of high value in the form of ocean energy and likely to become a new industry in the

future. Using of the periodic wave motion characteristics, WEC converts the wave energy into mechanical energy or hydraulic energy, and then transforms it into the available energy. Many devices of WEC have been created and motivated a wide variety of investigations. We especially pay close attention to a representative type of WECs, called oscillating buoy, which has small dimensions comparing with the incoming wave length. At present, research on the oscillating buoy WEC is still mainly concentrated in Europe and other countries.

The most common buoy oscillating WEC is the use of its heave motion. Early work can be traced to 1984 in Japan Tanaka<sup>[1]</sup> (1984) developed a G-IT WEC which includes

a wedge floating buoy and sliding rail of breakwater. This is a typical WEC which is mainly based on heaving motion. The size of oscillating buoy at the waterline surface is 1.8(m) × 1.2(m) and oscillating buoy slide along the breakwater under wave action. Sea trial was carried out in Tokyo Bay and in order to deal with the continuous wave of output energy, the use of the hydraulic cylinder type of pneumatic accumulator to deal with the purpose of achieving stable energy. The corresponding period, Budal *et al.*<sup>[2]</sup> (1982) developed a kind of oscillating buoy WEC based on the principle of float, called Norwegian Buoy (Fig.1). The device is made of upright post which is connected to the bottom of the sea and spherical oscillating buoy which absorb wave energy through heaving motion along the upright post. In 1983, the device model with the diameter of 1(m) spherical oscillating buoy was carried out by sea trial in the Trondheim fjord. The device comprises a power output device, a wind impeller is installed in the inner of the device, and the power output can be adjusted effectively. Early research provides technical basis for further research and many kinds of heaving WEC generation have been developed in recent years. Representative work is that Prado<sup>[3]</sup> (2008) in Holland developed a kind of WEC called Archimedes Wave Swing (Fig.2). The supporter of device is fixed in the seabed. The floating buoy and the supporter are connected by a linear motor. Floating buoy generate electricity through its heaving motion in wave peak and valley. After theoretical calculation, a comprehensive sea trial test was carried out in 2001 and 2002. The sea trial test is very not ideal well since the device is submerged in the water and not very well seal installation. In 2004, they improved the installation program, using a new sealing method on the power output device and finally the sea tries to succeed. Soon later, Elwood *et al.*<sup>[4]</sup> (2009) research a L-10 WEC (Fig.3). The WEC is consisting of a deep draft cylinder and an annular floating buoy. Deep draft cylinder connected with seabed by tension type mooring and annular floating buoy on the wave slide along a track in cylinder. This design limits the movement of other degrees of freedom in addition to the vertical swing. They developed a prototype of the 10kW power plant, the middle cylindrical draft 6.7(m), float outer radius 3.5(m) and sea trials conducted in the Gulf of Oregon, Newport.



Fig. 1. Norwegian Buoy



Fig. 2. Archimedes Wave Swing

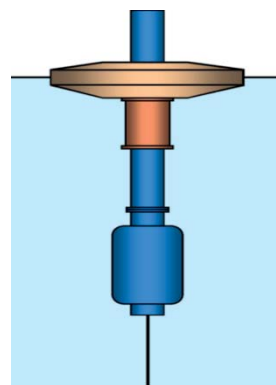


Fig 3. L-10

Another common buoy oscillating WEC is the use of its surging motion. It is well known that the wave force decreases with the increase of water depth. For this kind of WEC, the force along a shaft of a moving absorbing is usually converted to a moment of force. If that, surging motion converted to the pitching motion. So we usually called this type of WEC as flap WEC. According to the different installation position of the hinge shaft, flap WEC can be divided into two kinds of buoyant flap and suspension flap. Countries around the world have a lot of investment for the concept design and experimental research and practical applications of flap WEC and a number of typical flap WEC have been developed in recent years. Following are some brief introduction to the design and application of these classics. Cameron *et al.*<sup>[5]</sup> (2010) presented a flap WEC which consist of buoyancy flap, hydraulic cylinder, high pressure pipe and power station, called Oyster (Fig.4). The force pushes the buoyancy flap moving. The hydraulic cylinder, which is connected between the swing plate and the base, is compressed to convey the high pressure water to the shore through the submarine pipeline. A hydraulic motor is installed in the power station on the shore and high pressure water drive hydraulic motor and the hydraulic motor drives the generator to generate electricity. Currently Oyster has developed two generations of products. Different with flap WEC above, Finland AW-Energy company<sup>[6]</sup> (2010) developed a kind of flap WEC for generating electricity by using wave motion at sea floor,

called WaveRoller near shore ocean wave generator (Fig.5). It is installed on a platform at the bottom of the sea. Under the impetus of the waves, the blade of the WaveRoller generating set generates energy by swinging back and forth. After the hydraulic system is collected, the hydraulic motor and the generator are converted to electric energy by the shore. In 2003, WaveRoller generator for the first time at the Gulf of Finland small prototype pilot test. Soon Flocard and Finnigan<sup>[7]</sup> (2009) developed a flap WEC named BioWAVE (Fig.6). The base of the BioWAVE is fixed to the seabed and the flap buoy is hinged connect with the base. The flap buoy swings with the motion of the waves and in order to cope with the wave direction, the flap buoy can rotate around the vertical axis of the center of the base.

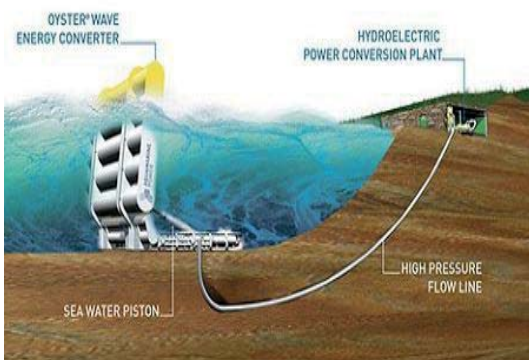


Fig. 4. Oyster

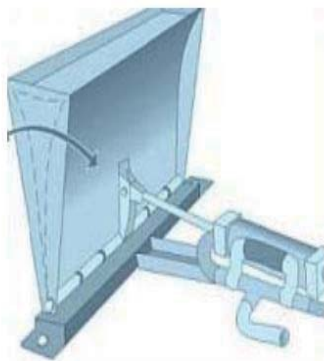


Fig. 5. WaveRoller

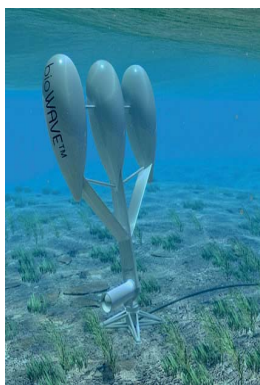


Fig. 6. BioWave

With several typical buoy oscillating WEC presented, scientists around the world began to research the theory of the concept model of buoy oscillating WEC, especially for its hydrodynamic characteristics and capture width ratios. For example, Mavrakos *et al.*<sup>[8]</sup> (2009) introduced into the traditional conical or cylindrical absorbers several creative structures, such as exterior torus, two piston-like arranged internal floater, and bottom-mounted vertical and horizontal skirts. And they analyzed the floaters geometries' effects of the wave energy converters, which is tightly moored, vertical and axisymmetric. These absorbers were comparatively evaluated in his research. Nazari *et al.*<sup>[9]</sup> (2013) analyzed and designed a point absorber of wave energy convertor for the wave condition of Assaluyeh coastal on Persian Gulf. In this analysis, he got the optimum wave power production by changing the shape of flat buoy to conical cylindrical to adjust the damping and natural frequency. Soulard<sup>[10]</sup> (2009) conducted the research works to create models and optimize the geometric of a two-body oscillating system, in which, a floating body forces against a submerged body through a linear power takeoff system and force reacting principle can be used. Goggins *et al.*<sup>[11]</sup> (2014) further developed this model by changing the geometry of floating oscillating absorber, optimized its hydrodynamic performance, and studied an unstrained WEC system. The offshore engineering groups, such as Chakrabarti *et al.*<sup>[12]</sup> (1983), Eatock Taylor *et al.*<sup>[13]</sup> (1983); Ran and Kim<sup>[14]</sup> (1995), studied vertical cylinders pivoted at the sea floor to articulated tower platform. Very recently, Caska and Finnigan<sup>[15]</sup> (2008) studied methods of hydrodynamic analysis for the application of a damped vertically oriented cylinder pivoted near the sea floor in the middle depth. Soon after, Stansby *et al.*<sup>[16]</sup> (2015) developed a wave energy absorber with a damped vertical bottom-pivoted cylinder and studied its motion response and corresponding power conversion capability.

The theory of the effect of the linear PTO comprising a linear spring and a linear damper was first presented by Evans<sup>[17]</sup> (1976) by a single freedom oscillating body under the regular waves. The linear PTO theory appeared subsequently in many other articles, and extended to multiple degree of freedom, such as Falnes (2002). Eriksson *et al.*<sup>[18]</sup> (2005) investigated the coupling response of the floating buoy and the linear generator under the frequency domain. Fitzgerald *et al.*<sup>[19]</sup> (2008) investigated the heave, surge and pitch motions of a moored WEC driven by regular waves, and also including results for the unmoored system with a linear PTO system. Price *et al.*<sup>[20]</sup> (2009) studied the WECs capture width detailedly, and discussed its influences of the linear PTO control.

Very recently, another important aspect of this research is turning to the quadratic PTO, such as Sheng and Lewis (2016). The problem becomes more complicated and much less research work have been done. The aim of this paper is to research quadratic PTO according to some claims have been made that quadratic PTO is better than the linear PTO due to quadratic PTO can convert more power than those of linear PTO. Thus in this work, the equation of linear and quadratic

PTO damping were carried out under the assumption of the linear hydrodynamics of a vertical axisymmetric WEC in regular waves. A method of damping coefficients, theoretical added mass and exciting force are calculated on the analytical method which is based on the series expansion of eigen functions. Numerical results concerning for optimizing resistive and damping PTO are presented to maximize wave energy.

## MATHEMATICAL MODEL

The Sketch of the vertical axisymmetric WEC and the fluid divisions are shown in Fig.7. We defined a cylindrical coordinial system  $(r,\theta,z)$ , with the origin point  $o$  locating at the absorber center and in the plane of the mean free surface, and the axis  $oz$  being vertically upwards. The wetted surface of absorber is supposed to be consist of a cylindrical surface and a curved surface with vertical axisymmetry. The fluid domain due to the device can be divided into several sub-domain in order to obtain hydrodynamic coefficients.

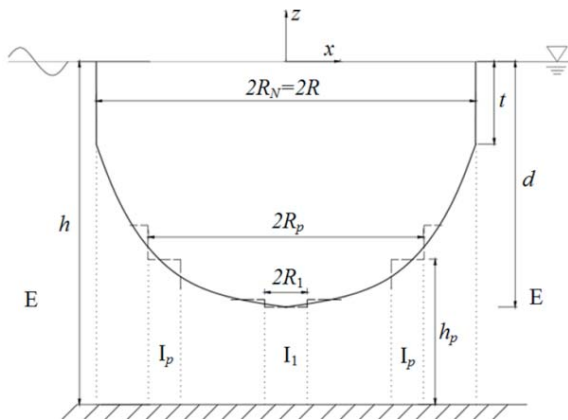


Fig. 7. The sketch of the device and the subdomain division

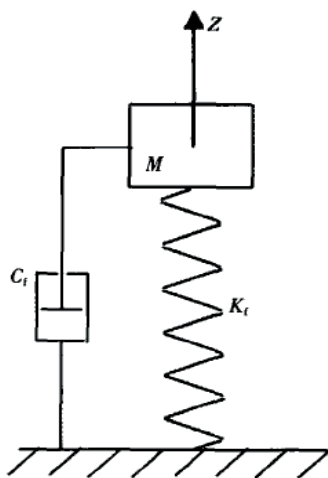


Fig. 8. Schematic diagram of wave energy conversion

## WAVE ENERGY CONVERSION

The schematic diagram of wave energy conversion is shown in Fig.8. When a PTO is applied to connect the buoy and the fixed reference system such as seabed, the motion of the buoy can drive the PTO to convert the mechanical power into useful energy. Straightforward application of Newton's second law, the equation of motion in regular waves for the system is

$$M\ddot{X} = F_d + F_r + F_s + F_m \quad (1)$$

where  $M$  is the buoy mass;  $X$  is the displacement; the symbol  $F_d$ ,  $F_r$ ,  $F_s$  and  $F_m$  denote the wave excitation force, radiation force, hydrostatic restoring force and PTO force, respectively. Under the assumption of linear wave theory, the radiation and hydrostatic restoring force can be written as

$$\begin{aligned} F_r &= \mu\ddot{X} + \lambda\dot{X} \\ F_s &= bX \end{aligned} \quad (2)$$

Where  $\mu$  stands for added mass;  $\lambda$  stands for damping coefficient;  $b$  is hydrostatic recovery coefficient. The PTO force can be separated two parts

$$F_m = F_m^k + F_m^c \quad (3)$$

And

$$\begin{aligned} F_m^k &= kX \\ F_m^c &= cf(\dot{X}) \end{aligned} \quad (4)$$

in which  $k$  is the stiffness coefficient of PTO;  $c$  is the damping coefficients of the PTO. For a linear PTO, the function of motion velocity in the pure damper is

$$f(\dot{X}) = \dot{X} \quad (5)$$

For a quadratic PTO, the function of motion velocity in the pure damper is

$$f(\dot{X}) = \dot{X}|\dot{X}| \quad (6)$$

Once the equation of motion is solved, the power conversion is simply calculated as

$$P = |F_m^c \dot{X}| \quad (7)$$

the corresponding average power is given by

$$\bar{P} = \frac{1}{T} \int_0^T P dt \quad (8)$$

Where  $T$  is the time interval for calculating the average power.

## HYDRODYNAMIC ANALYSIS

Hydrodynamic analysis of wave energy conversion is studied using a semi-analytical method is based upon eigenfunction matching. For the linear wave theory, it is convenient to decompose the spatial velocity potential  $\Phi$  as the following part

$$\Phi = \Phi_0 + \Phi_7 + \sum_{j=1}^6 \Phi_j \quad (9)$$

where  $\Phi_0$ ,  $\Phi_j$  stand for incident wave and diffraction velocity potential respectively.  $\Phi_j$  ( $j=1\dots6$ ) stand for radiated velocity potential for different motion modes. According to the potential flow theory, the aforementioned velocity potential should satisfied the following boundary condition,

Laplace boundary condition:

$$\nabla^2 \Phi_j = 0 \quad (j=1,2\dots7) \quad (\text{in fluid domain}) \quad (10)$$

Freesurface boundary condition:

$$-f^2 \Phi_j + \partial_z \Phi_j = 0 \quad (j=1,2\dots7) \quad (z=0) \quad (11)$$

Bottom boundary condition:

$$\partial_z \Phi_j = 0 \quad (j=1,2\dots7) \quad (z=-h) \quad (12)$$

Hull boundary condition:

$$\partial_n \Phi_j = V_n \quad (j=1,2\dots6), \quad \partial_n \Phi_7 = -\partial_n \Phi_0 \quad (13)$$

Radiation boundary condition:

$$\lim_{r \rightarrow \infty} \sqrt{r} (\partial_r \Phi_j - ik_0 \Phi_j) = 0 \quad (j=1,2\dots7) \quad (14)$$

in which  $f^2 = \omega^2/g$ , and  $\omega$  is the wave frequency,  $g$  is the acceleration due to gravity. The wave number  $k_0$  can be defined by the dispersion equation  $k_0 \tanh k_0 h = f^2$ , which is obtained by meeting the boundary condition. The  $V_n$  is the cylinder's velocity in the direction normal to the hull. The incident wave velocity potential in cylindrical coordinates  $(r, \theta, z)$  can be given as

$$\Phi_0 = -\frac{Ag}{\omega} \sum_{\ell=0}^{\infty} \varphi_0^\ell \cos \ell \theta \quad (15)$$

With

$$\varphi_0^\ell = \varepsilon_\ell Z_0(z) J_\ell(k_0 r) \quad (16)$$

where  $J_\ell(\cdot)$  is the first category Bessel function with the order  $\ell$  and the expression for known function  $Z_0(z)$  and coefficients

$\varepsilon_\ell$  are given in the **Appendix A**. In the same way of incoming wave, diffraction velocity potential  $\Phi_7$  can be expressed as

$$\Phi_7 = -\frac{Ag}{\omega} \sum_{\ell=0}^{\infty} \varphi_7^\ell \cos \ell \theta \quad (17)$$

The potential of the radiation velocity, which is caused by the forced vertical axisymmetric body motion can be expressed as

$$\Phi_1 = \varphi_1^1 \cos \theta \quad (18)$$

in surge direction;

$$\Phi_3 = \varphi_3^0 \quad (19)$$

in heave direction;

$$\Phi_5 = \varphi_5^1 \cos \theta \quad (20)$$

in pitch direction.

To develop the velocity potentials of diffraction and radiation, the fluid domain can be developed into outer cylindrical sub-domain named as E and inner cylindrical sub-domains named as  $I_p$  ( $1 \leq p \leq N$ ) as shown in Fig. 1. Velocity potential in domain E is

$$\varphi_j^{\ell,E} = \alpha_j^{\ell,E,0} Z_0(z) \frac{\mathbf{H}_\ell(k_0 r)}{\mathbf{H}_\ell(k_0 R)} + \sum_{n=1}^{\infty} \alpha_j^{\ell,E,n} Z_n(z) \frac{\mathbf{K}_\ell(k_n r)}{\mathbf{K}_\ell(k_n R)} + \Omega_j^{\ell,E}(r, z) \quad (21)$$

Where the  $\mathbf{H}_\ell(\cdot)$  and  $\mathbf{K}_\ell(\cdot)$  are the first category Hankel function and the modified second category Bessel function with the order  $\ell$  separately. The wave number  $k_n$  is defined by dispersion equation  $k_n \tanh k_n h = f^2$  for ( $n \geq 1$ ). Velocity potential in domain  $I_1$  is

$$\varphi_j^{\ell,I_1} = \alpha_j^{\ell,I_1,0} r^\ell + \sum_{n=1}^{\infty} \alpha_j^{\ell,I_1,n} \mathbf{I}_\ell(\lambda_n r) \cos \lambda_n(z+h) + \Omega_j^{\ell,I_1}(r, z) \quad (22)$$

In which,  $\mathbf{I}_\ell(\cdot)$  is the second category Bessel function with the order  $\ell$ . Velocity potential in domain  $I_p$  ( $2 \leq p \leq N$ ) is

$$\begin{aligned} \varphi_j^{\ell,I_p} = & \alpha_j^{\ell,I_p,0} Q^{\ell,0}(r) + \sum_{n=1}^{\infty} \alpha_j^{\ell,I_p,n} Q^{\ell,n}(r) \cos \lambda_n(z+h) + \\ & + \tilde{\alpha}_j^{\ell,I_p,0} \tilde{Q}^{\ell,0}(r) + \sum_{n=1}^{\infty} \tilde{\alpha}_j^{\ell,I_p,n} \tilde{Q}^{\ell,n}(r) \cos \lambda_n(z+h) + \Omega_j^{\ell,I_p}(r, z) \end{aligned} \quad (23)$$

In the velocity potentials' eigenfunction expansion, expressions for known function  $Q(\cdot)$ ,  $Z(\cdot)$  and  $\Omega(\cdot)$  are listed in the **Appendix A** to make it easy for readers. The unknown coefficients  $\alpha$  could be determined by Garrett's method<sup>[21-26]</sup>, according to matching the potential and its normal derivative on the surface of concatenate boundaries, which is shared by the subdomains.

Once velocity potentials in six degree of freedom are known, hydrodynamic coefficients and diffraction wave forces of the absorber can be calculated by the integration of the pressure on the hull. In this research, single heave direction have been considered due to application in wave energy conversion. Thus, diffraction wave force  $f_d$  is expressed by

$$f_d = i2\pi\rho g R_p \sum_{p=1}^N \int_{R_{p-1}}^{R_p} \phi_{7,0}^{I_p}(r, h_p - h) r dr \quad (24)$$

Hydrodynamic coefficients  $\mu$  and  $\lambda$  is expressed by

$$\mu + i\lambda/\omega = -2\rho\pi R_p \sum_{p=1}^N \int_{R_{p-1}}^{R_p} \phi_{3,0}^{I_p}(r, h_p - h) r dr \quad (25)$$

## NUMERICAL RESULTS AND DISCUSSION

The wave energy convergence ability of oscillating body WEC is usually determined by physical parameter of PTO damping coefficients. In this section, the case of a inverted cone with angle  $\alpha=90^\circ$  and high  $t=10\text{m}$  is considered as a kind of vertical axisymmetric WEC. Linear as well as quadratic damping coefficients of PTO  $c$  have been examined based upon the optimized stiffness coefficient of PTO  $k$  according to resonance system.

$$k = \omega^2(m + \mu) - b \quad (26)$$

Power due to the linear PTO effect is depicted in Fig.9 for period  $T=5, 8, 10$  and  $12\text{s}$ , respectively. As shown in Fig.9, the power for higher periods is larger than that for lower periods. For different period  $T$ , there is a peak with varying linear damping coefficients of PTO  $c$ . In fact the peak position is

$$c = \lambda \quad (27)$$

It is not a surprise, due to it is the optimized damping coefficients of PTO  $c$  in order to satisfy the function  $\partial_c P=0$ .

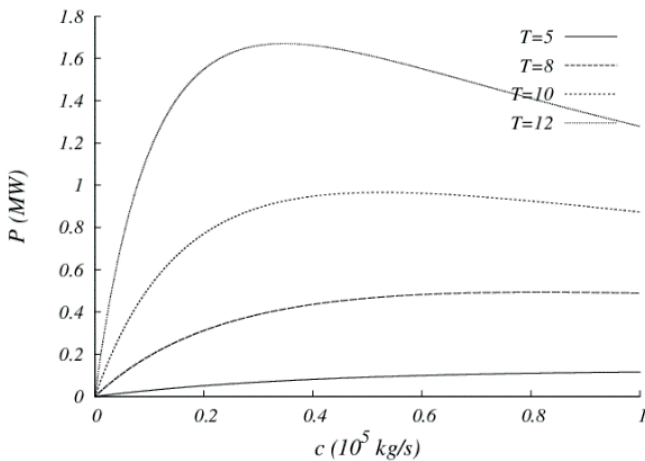


Fig.9. Power due to the linear PTO effect

Power due to the quadratic PTO effect depicted in Fig.10 for period  $T=5, 8, 10$  and  $12\text{s}$ , respectively.

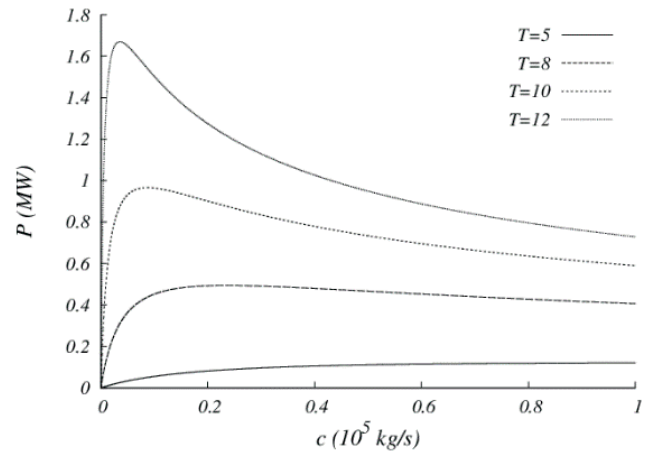


Fig.10. Power due to the quadratic PTO effect

Similar with power due to the linear PTO effect, the power for higher period is more than that for lower period and for different period  $T$ , there is a peak with varying linear damping coefficients of PTO  $c$ . However, the peak position is not as the linear PTO effect nearly the same with different period  $T$  and smaller than that for linear PTO effect. Fig.11 and Fig.12 shows the comparative results for power due to the linear and quadratic PTO effect at the higher period  $T=12$  and the lower period  $T=5$ . Several important features can be observed in the Figs.

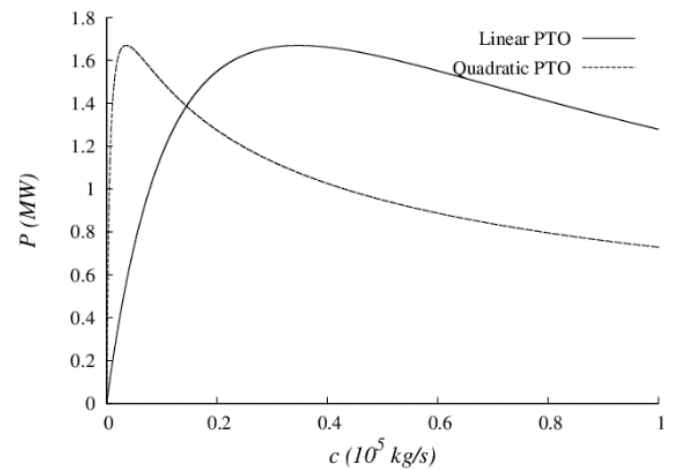


Fig.11 Power due to the linear and quadratic PTO effect at  $T=12$

First, at the higher period  $T=12$ , it can be seen that the maximum power  $P \approx 1.6\text{MW}$  is nearly the same but the peak position for quadratic PTO  $c \approx 0.08(10^5 \text{ kg/s})$  is smaller than that for linear PTO  $c \approx 0.25(10^5 \text{ kg/s})$ , in other words, quadratic PTO effect can reach the peak before the linear PTO effect.

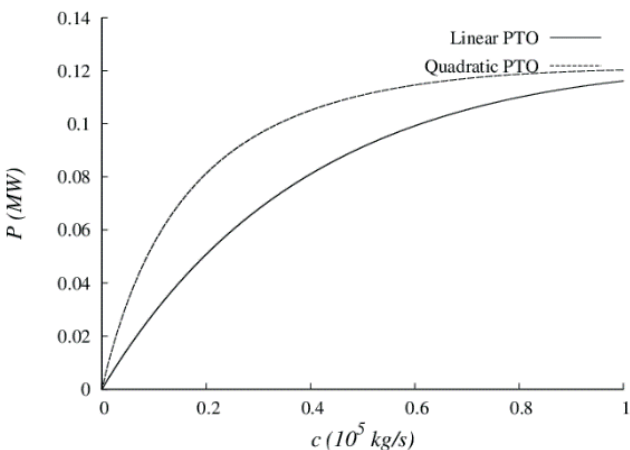


Fig.12. Power due to the linear and quadratic PTO effect at  $T=5$

Second, also at higher period, there is a critical position  $c \approx 0.18(10^5 \text{ kg/s})$ . At that position, power due to quadratic PTO is equal to power due to linear PTO. Before the critical position, the power due to quadratic PTO is higher, on the contrary, the power due to linear PTO is higher. Third, at the lower period  $T=5$ , power due to the quadratic PTO is always higher than power due to the linear PTO.

## CONCLUSIONS

In this investigation, the linear and quadratic PTO effect have been applied in converting wave power into useful energy on the analytical method which is based on the series expansion of eigenfunctions. From the investigation, the following conclusions can be drawn:

(1). For linear PTO effect, the optimized linear damping coefficients of PTO  $c$  is obtained by the formulae and confirmed by the numerical results.

(2). For quadratic PTO effect, the optimized quadratic damping coefficients of PTO  $c$  is found by the numerical results.

(3). The comparisons have been made between the linear and quadratic PTO effect. At higher period, power due to quadratic PTO effect can reach the peak before the linear PTO effect. At the lower period, power due to the quadratic PTO is always higher than the linear PTO.

## ACKNOWLEDGEMENT

This research is financially supported by the National Natural Science Foundation of China (No.51509048 and No.51679044).

## APPENDIX A

The expression for known function  $Z_0(z)$  and  $Z_n(z)$  are given

$$Z_0(z) = \cosh k_0 h \cosh k_0 (z+h) (2k_0 h + \sinh 2k_0 h)$$

$$Z_n(z) = \cos k_n h \cos k_n (z+h) (2k_n h + \sin 2k_n h)$$

The coefficients  $\varepsilon_\ell$  in velocity potential of incident wave are given

$$\varepsilon_\ell = \begin{cases} 1/Z_0(z) & (\ell=0) \\ 2i^\ell/Z_0(z) & (\ell \geq 1) \end{cases}$$

The known function  $P(\cdot)$ ,  $Q(\cdot)$  and  $\Omega(\cdot)$  in diffraction and radiation potential are given

$$P_0^\ell(r) = \begin{cases} \ln(r/R_1)/\ln(R_2/R_1) & (\ell=0) \\ [r/R_1]^\ell - (R_1/r)^\ell / [(R_2/R_1)^\ell - (R_1/R_2)^\ell] & (\ell \geq 1) \end{cases}$$

$$\tilde{P}_0^\ell(r) = \begin{cases} \ln(R_2/r)/\ln(R_2/R_1) & (\ell=0) \\ [R_2/r]^\ell - (r/R_2)^\ell / [(R_2/R_1)^\ell - (R_1/R_2)^\ell] & (\ell \geq 1) \end{cases}$$

$$Q_n^\ell(r) = \mathbf{K}_1^{n\ell} \mathbf{I}_\ell(\lambda_n r) - \mathbf{I}_1^{n\ell} \mathbf{K}_\ell(\lambda_n r)$$

$$\tilde{Q}_n^\ell(r) = \mathbf{I}_2^{n\ell} \mathbf{K}_\ell(\lambda_n r) - \mathbf{K}_2^{n\ell} \mathbf{I}_\ell(\lambda_n r)$$

In which  $\lambda_n = n\pi/(h-d)$  and the constants are

$$\{\mathbf{K}_1^{n\ell}, \mathbf{I}_1^{n\ell}, \mathbf{K}_2^{n\ell}, \mathbf{I}_2^{n\ell}\} = \frac{\mathbf{K}_\ell(\lambda_n R_1) \mathbf{I}_\ell(\lambda_n R_1) \mathbf{K}_\ell(\lambda_n R_2) \mathbf{I}_\ell(\lambda_n R_2)}{\mathbf{K}_\ell(\lambda_n R_1) \mathbf{I}_\ell(\lambda_n R_2) - \mathbf{K}_\ell(\lambda_n R_2) \mathbf{I}_\ell(\lambda_n R_1)}$$

$$\Omega_{7,\ell}^I(r, z) = \phi_{0,\ell}$$

$$\Omega_{7,\ell}^{II(1,2), III(1,2), IV, V, VI}(r, z) = 0$$

$$\Omega_{3,\ell}^{I, IV}(r, z) = 0$$

$$\Omega_{3,\ell}^{II(1,2), V}(r, z) = (z\omega^2 + g)/\omega^2$$

$$\Omega_{3,\ell}^{III(1,2), VI}(r, z) = [2(z+h)^2 - r^2]/4(h-d)$$

## REFERNCE

1. Tanaka H. Sea Trial of a Heaving Body Wave Power Absorber. *Transactions of the Japan Society of Mechanical Engineers B*, 1984, 50:2325-2333.
2. Budal K, Falnes J, Iversen LC, Lillebekken PM, Oltedal G, Hals. The Norwegian wave-power buoy project . In: Berge H, editor. *Proceedings of 2nd International Symposium on Wave Energy Utilization*, Trondheim, Norway; 1982, p.323-344.
3. Prado M. Archimedes wave swing (AWS) . In: Cruz J, editor. *Ocean Wave Energy*. Berlin: Springer, 2008. p. 297–304.
4. Elwood D, Schacher A, Rhinefrank K, Prudell J, Yim S, Amon E. Numerical modelling and ocean testing of a direct-drive wave energy device utilizing a permanent magnet linear generator for power take-off . In: *Proceedings of 28th International Conference on Ocean Offshore Arctic Engineering*, ASME, Honolulu, Hawaii, 2009, No.OMAE2009-79146.
5. L. Cameron, R. Doherty. *Design of the Next Generation of the Oyster Wave Energy Converter*. 3th International Conference on Ocean Energy, Bilbao, 2010: 1-12.
6. *Harnessing the Blue Energy [R/OL]*. (2010-06) [2012-07-06]. <http://www.aw-energy.com/concept.html>.
7. F. Flocard, T.D. Finnigan. Experiment investigation of power capture from pitching point absorbers. *Proceedings of the 8th European Wave and Tidal Energy Conference*, Uppsala, Sweden, 2009: 400-409.
8. Mavrakos SA, Katsaounis GM, Apostolidis MS (2009) Effects of floaters' geometry on the performance characteristics of tightly moored wave energy converters. In *Proceedings of the 28th International Conference on Ocean Offshore Arctic Engineering*, ASME, Honolulu, Hawaii, Paper No. OMAE 2009-80133.
9. Mehdi Nazari, Hassan Ghassemi, Mahmoud Ghiasi, Mesbah Sayehbani (2013) Design of the point absorber wave energy converter for Assaluyeh Port. *Iranica Journal of Energy & Environment*, 4(2):130-135.
10. Thomas Soulard, Marco Alves, António Sarmiento (2009) Force reacting principle applied to a heave point absorber wave energy converter. In: *The Nineteenth International Offshore and Polar Engineering Conference*, Osaka, Japan, 21-26 June.
11. Jamie Goggins, William Finnegan (2014) Shape optimization of floating wave energy converters for a specified wave energy spectrum. *Renewable Energy*, 71:208-220.
12. Chakrabarti S K, Cotter D C, Libby A R. Hydrodynamic coefficients of a harmonically oscillated tower. *Applied Ocean Research*, 1983, 5(4):226-233.
13. Taylor R E, Drake K R, Duncan P E. The dynamics of a flexible articulated column in waves. *Engineering Structures*, 1983, 5(3):181-198.
14. Ran Z, Kim M H. Responses of Articulated Loading Platform in Irregular Waves. *Journal of Waterway Port Coastal & Ocean Engineering*, 1995, 121(6):283-293.
15. Caska A J, Finnigan T D. Hydrodynamic characteristics of a cylindrical bottom-pivoted wave energy absorber. *Ocean Engineering*, 2008, 35(1):6-16.
16. Stansby P, Moreno E C, Stallard T, et al. Three-float broadband resonant line absorber with surge for wave energy conversion. *Renewable Energy*, 2015, 78:132-140.
17. Evans, D. V. (1976). A theory for wave-power absorption by oscillating bodies. *Journal of Fluid Mechanics*, 77(1), 1-25. (Journal)
18. Falnes, J. (2002). *Linear interaction including wave-energy extraction. Ocean waves and oscillating system*. Cambridge University press. (Textbook)
19. Wanan Sheng and Anthony Lewis (2016). Power Takeoff Optimization for Maximizing Energy Conversion of Wave-Activated Bodies. *IEEE Journal of Oceanic Engineering*, 1-12. (Journal)
20. Price, A. A. E., Dent, C. J., and Wallace, A. R. (2009). On the capture width of wave energy converters. *Applied Ocean Research*, 31(4), 251-259. (Journal)
21. Fitzgerald, J., & Bergdahl, L. (2008). Including moorings in the assessment of a generic offshore wave energy converter: a frequency domain approach. *Marine Structures*, 21(1), 23-46. (Journal)
22. Liu Haibin, Liu zhenling. (2010). "Recycling Utilization Patterns of Coal Mining Waste in China." *Resources, Reservation and recycling*(12): 1331-1340.
23. Eriksson, M., Isberg, J., and Leijon, M. (2005). Hydrodynamic modelling of a direct drive wave energy converter. *International Journal of Engineering Science*, 43(s 17–18), 1377-1387. (Journal)
24. Sheng, W., & Lewis, A. (2016). Power takeoff optimization for maximizing energy conversion of wave-activated bodies. *IEEE Journal of Oceanic Engineering*, 1-12. (Journal)
25. Cui, H. R., Liu, F. X., Armentani E., (2016). Analysis and assessment of the value of carbon assets based on

monte-carlo simulation. Journal of Mechanical Engineering Research and Developments 39 (2): 555-564.

26. Garrett CJR (1971) Waves forces on a circular dock. Journal of Fluid Mechanics, 46:129-39.

#### **CONTACT WITH THE AUTHORS**

**Hengxu Liu**

College of Shipbuilding Engineering  
Harbin Engineering University  
Harbin 150001  
**China**

# EVOLUTION OF HIERARCHICAL STRUCTURE AND SPATIAL PATTERN OF COASTAL CITIES IN CHINA – BASED ON THE DATA OF DISTRIBUTION OF MARINE-RELATED ENTERPRISES

Lili Wang<sup>1</sup>

Wenwen Xiao<sup>2\*</sup>

Chengwei Wang<sup>2</sup>

<sup>1</sup> Business School, Shandong Jianzhu University, China

<sup>2</sup> School of Management, Shandong University, China

\* corresponding author

## ABSTRACT

*In this paper, a comprehensive research of the evolution of the hierarchical structure and spatial pattern of coastal cities in China was conducted based on the data of distribution of the headquarters and subsidiaries of marine-related enterprises in 1995, 2005 and 2015 using the city network research method proposed by Taylor. The results of the empirical research showed: China's coastal city network had an obvious hierarchical characteristics of "national coastal city-regional coastal city-sub-regional coastal city-local coastal city", in the 20 years of development process, the hierarchies of coastal cities in China showed a hierarchical progressive evolution; in past 20 years, the spatial pattern and network structure of coastal cities in China tended to be complete, and the city network was more uniform, forming a "three tiers and three urban agglomerations" network structure; the strength of connection among the cities was obviously strengthened, and the efficiency of urban spatial connection was improved overall.*

**Keywords:** Hierarchical structure; Spatial pattern; City network

## INTRODUCTION

At the beginning of this century, the United Nations proposed "The 21st century is the century of ocean", believing that the ocean is the main field of international competition of the 21st century[1]. Later, China introduced the Outline of the National Planning for Development of Ocean Economy in 2003 and the "Twelfth Five-Year Plan" for National Marine Economic Development in 2012, regarding the marine economy as a new economic growth point[2]. Meanwhile, taking the coastal city carrying the marine economic activities as the regional development priority, China formulated the Development Plan for the Blue Economic Zone in Shandong Peninsula, Development Plan for the Blue Economic Experimental Zone in Fujian Strait and other national strategies to promote the development of coastal

cities. In recent years, the coastal cities in China have achieved rapid development with the help of excellent geographical environment[3-5], policy support[6-8], market factors[9, 10] and FDI[11, 12], and complex and diverse changes have taken place in urban spatial pattern, gradually forming an urban system of perfect structure and reasonable hierarchy.

The rapid development of coastal cities in China continuously drives relevant academic research, and issues such as economic disparities of coastal cities[13-15] and economic structures of coastal cities[16-18] have become research hotspots, and certain research achievements have been made on mutual actions between coastal cities and tourism[19-21], population[22, 23] and so on. However, there have been few literatures on the development of coastal cities based on marine economy, this may because few statistics on marine economy lead to difficulty in quantitative measuring

as marine economy is a new economic form. Therefore, to study the influence of China's marine economic development on coastal cities, this paper studied the hierarchical structure and spatial pattern of coastal cities in China using the micro-main body of marine economic activities-marine-related enterprise. Studying China's coastal city network based on the distribution of marine-related enterprises has its rationality. From the perspective of the dynamic mechanism of the formation of city network, enterprise is one of the important driving forces of the formation of city network[24], besides, Taylor pointed out that infrastructures in a city, such as road, airport and railway, do not constitute a real city network, which in fact is formed by connecting enterprises' strategies[25]; under the condition of market economy, the marine-related enterprise is the micro-main body of marine economic activities, and the connection among marine-related enterprises in different cities influences and even decides the connection among cities and spatial pattern. From the perspective of spatial position, the business activities of marine-related enterprises have distinctive geographical characteristics, thus its spatial distribution and hierarchy can reflect the hierarchical structure of the city to a certain extent.

Based on this, a comprehensive research of the evolution of the hierarchical structure and spatial pattern of coastal cities in China was conducted based on the data of distribution of the headquarters and subsidiaries of marine-related enterprises. With coastal cities in 1995, 2005 and 2015 being taken as the research object, firstly, China's coastal city networks in different years were respectively constructed using the city network research method proposed by Taylor; secondly, the relative network connection rates of coastal cities were calculated, based on which the urban hierarchies were classified and the evolution was analyzed; thirdly, the evolution of the spatial pattern of coastal cities was analyzed; finally, pertinent policies and suggestions were put forward on the basis of empirical analysis.

marine-related enterprises meeting the standards in 1995, 2005 and 2015 were determined, for example, a total of 64 marine-related enterprises meeting the standards in 2015 were selected, including 11 marine fisheries, 2 offshore oil and gas industries, 4 sea salt industries, 5 marine chemical industries, 14 marine communications and transportation industries, 17 marine equipment manufacture industries, 4 marine biopharmaceutics industries and 7 coastal tourism industries.

After the marine-related enterprises meeting the standards in 1995, 2005 and 2015 were determined, the city where the marine-related enterprise was located was assigned with different score in light of the importance of marine-related enterprise, of which, the city where the headquarter of marine-related enterprise was located was assigned with 3 scores, and the city where the subsidiary of marine-related enterprise was located was assigned with 2 scores, and the city where the office of marine-related enterprise was located was assigned with 1 score, if the city had no branch of marine-related enterprise, it was assigned with 0 score. Considering that some cities were assigned with lower scores in the scoring of coastal cities in China by using the above method, thus, the cities assigned with 3 scores or above were selected in this paper<sup>1</sup>.

As can be seen from Table 1, the 17 cities in 1995 selected included two categories, the first category was city with the high administrative rank, such as capital, municipality and capital city of coastal province, the second category was developed coastal city. The 11 new cities in 2005 were mostly coastal cities, where marine-related enterprises gradually emerged and formed connections among cities thanks to their geographical advantage of being by the sea. The 13 new cities in 2015 first included inland cities, such as Jinan and Taizhou, presenting sea-land connection development.

Tab. 1. Major coastal cities in China in 1995, 2005 and 2015.

|                    |         |             |         |          |         |           |           |           |           |
|--------------------|---------|-------------|---------|----------|---------|-----------|-----------|-----------|-----------|
| Cities in 1995     | Dalian  | Beijing     | Tianjin | Qingdao  | Yantai  | Nanjing   | Nantong   | Suzhou    | Shanghai  |
|                    | Xiamen  | Ningbo      | Fuzhou  | Hangzhou | Zhuhai  | Shenzhen  | Guangzhou | Shantou   |           |
| New cities in 2005 | Dandong | Weihai      | Rizhao  | Dongying | Wuxi    | Wenzhou   | Zhoushan  | Foshan    | Zhanjiang |
|                    | Huludao | Lianyungang |         |          |         |           |           |           |           |
| New cities in 2015 | Yingkou | Weifang     | Ji'nan  | Binzhou  | Taizhou | Zhenjiang | Xuzhou    | Changzhou |           |
|                    | Ningde  | Zhongshan   | Huizhou | Maoming  | Suqian  |           |           |           |           |

## DATA AND RESEARCH METHODS

### RESEARCH OBJECTS AND DATA PROCESSING

The marine-related enterprise to be selected in this paper must meet two standards, the first standard was that it must have a standard enterprise website containing information about the location and scale of its subsidiaries or offices; the second standard was that it must have subsidiary or office in at least two coastal cities. By querying the websites of all marine-related enterprises, China Marine Statistical Yearbook, statistical yearbooks and statistical bulletins of relevant provinces or cities, relevant bulletins released by the State Oceanic Administration and so on, the

### RESEARCH METHODS

In this paper, first, the value matrix for the distribution of marine-related enterprise in coastal city was constructed using the GaWC network method[25], then, the connection matrix about coastal cities was obtained, based on which China's coastal city network was constructed. According to the information about the distribution of marine-related enterprises, the city where the headquarter of marine-related enterprise was located was assigned with 3 scores, and the

<sup>1</sup> A few cities, such as Beijing, Jinan and Nanjing, are not cities by the sea, but they have high administrative ranks and marine-related enterprise headquarters. To reflect the relationship among coastal cities more comprehensively and objectively, these cities were classified as coastal cities in this paper.

city where the subsidiary of marine-related enterprise was located was assigned with 2 scores, and the city where the office of marine-related enterprise was located was assigned with 1 score, and the value matrix  $V$  between coastal city and marine-related enterprise was constructed:

$$V = \begin{pmatrix} V_{11} & V_{12} & \cdots & V_{1n} & \cdots & V_{1r} \\ V_{21} & V_{22} & \cdots & V_{2n} & \cdots & V_{2r} \\ \vdots & \vdots & \ddots & \vdots & \ddots & \vdots \\ V_{m1} & V_{m2} & \cdots & V_{mn} & \cdots & V_{mr} \\ \vdots & \vdots & \ddots & \vdots & \ddots & \vdots \\ V_{s1} & V_{s2} & \cdots & V_{sn} & \cdots & V_{sr} \end{pmatrix} \quad V_{mn} = \begin{cases} 3 & \text{city } m \text{ has the headquarter} \\ 2 & \text{city } m \text{ has the subsidiary} \\ 1 & \text{city } m \text{ has the office} \\ 0 & \text{otherwise} \end{cases} \quad (1)$$

The aggregated score of marine-related enterprises in city  $m$  was  $V_m = \sum_{n=1} V_{mn}$ , the cities assigned with 3 scores or above were selected. As the city is the carrier of the enterprise, and the connection among enterprises in two cities constitutes the connection among the cities, so the degree of connection between two cities is the accumulated connection among marine-related enterprises shared by the two cities. The connection value generated from marine-related enterprise  $n$  between city  $\alpha$  and city  $\beta$  was defined as  $R_{\alpha\beta,n} = V_{\alpha n} \times V_{\beta n}$ , and the total connection value between city  $\alpha$  and city  $\beta$  was defined as  $R_{\alpha\beta} = \sum V_{\alpha n} \times V_{\beta n}$ . Based on this, the incidence matrix  $R_{s \times s}$  among  $s$  cities was constructed, and the city network was obtained using ArcGIS software. The total connection value of city network was defined as  $T = \sum_{\alpha=1} \sum_{\beta=1} R_{\alpha\beta}$ , and the connection value between city  $\alpha$  and all the other cities was defined as  $T_\alpha = \sum_{\beta=1} R_{\alpha\beta}$ , and the network connection rate of city  $\alpha$  was defined as  $t_\alpha = \frac{T_\alpha}{T}$ , and the relative network connection rate  $pt_\alpha = \frac{T_\alpha}{T}$  was obtained with city  $\gamma$  with the highest network connection rate as the benchmark.

## CALCULATED RESULTS AND ANALYSIS

### EVOLUTION OF THE HIERARCHICAL STRUCTURE OF COASTAL CITIES IN CHINA

The relative network connection rates<sup>2</sup> of coastal cities in China in 1995, 2005 and 2015 were calculated based on the relative network connection rate, and the results are shown in Table 2.

The relative network connection rate of city node can reflect the status and influence of the city in the network, the more

Tab. 2. Network connection rates of coastal cities in China in different years.

| City      | 1995 | 2005 | 2015 | City     | 1995 | 2005 | 2015 | City        | 2005 | 2015 | City      | 2015 |
|-----------|------|------|------|----------|------|------|------|-------------|------|------|-----------|------|
| Shanghai  | 1    | 1    | 1    | Fuzhou   | 0.24 | 0.24 | 0.24 | Lianyungang | 0.21 | 0.29 | Jinan     | 0.09 |
| Beijing   | 0.62 | 0.67 | 0.74 | Hangzhou | 0.36 | 0.46 | 0.40 | Dandong     | 0.02 | 0.02 | Binzhou   | 0.03 |
| Tianjin   | 0.60 | 0.61 | 0.69 | Suzhou   | 0.38 | 0.48 | 0.50 | Huludao     | 0.02 | 0.02 | Taizhou   | 0.21 |
| Shenzhen  | 0.53 | 0.53 | 0.76 | Ningbo   | 0.31 | 0.41 | 0.39 | Weihai      | 0.39 | 0.37 | Zhenjiang | 0.04 |
| Qingdao   | 0.43 | 0.53 | 0.73 | Yantai   | 0.17 | 0.47 | 0.42 | Rizhao      | 0.09 | 0.19 | Xuzhou    | 0.04 |
| Dalian    | 0.40 | 0.43 | 0.63 | Zhuhai   | 0.18 | 0.18 | 0.18 | Dongying    | 0.05 | 0.16 | Changzhou | 0.02 |
| Nanjing   | 0.39 | 0.29 | 0.39 | Shantou  | 0.04 | 0.12 | 0.05 | Zhanjiang   | 0.09 | 0.17 | Suqian    | 0.03 |
| Guangzhou | 0.46 | 0.46 | 0.57 | Wenzhou  | —    | 0.17 | 0.17 | Wuxi        | 0.11 | 0.11 | Ningde    | 0.05 |
| Xiamen    | 0.41 | 0.51 | 0.52 | Zhoushan | —    | 0.25 | 0.25 | Yingkou     | —    | 0.01 | Zhongshan | 0.09 |
| Nantong   | 0.29 | 0.35 | 0.31 | Foshan   | —    | 0.04 | 0.06 | Weifang     | —    | 0.11 | Huizhou   | 0.06 |
|           |      |      |      |          |      |      |      |             |      |      | Maoming   | 0.05 |

<sup>2</sup> The number of coastal cities in 1995, 2005 and 2015 selected in this paper were 17, 28 and 41 respectively, thus some cities lacked relative network connection rate of 1995 or 2005.

important the city, the higher the relative network connection rate[26]. The cities were clustered using the K-Cluster module of SPSS, and the cities with similar relative network connection rates were classified as a group, thus the coastal cities in China were divided into national coastal city, regional coastal city, sub-regional coastal city and local coastal city according to their importance in the network. Taking 2015 for example, Figure 1 was made.

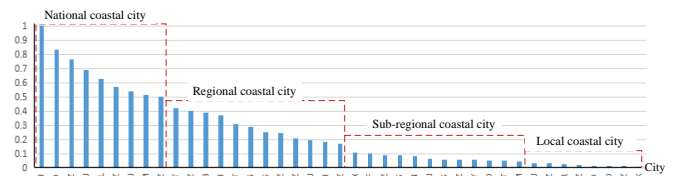


Fig. 1. Ordering and classification of relative network connection rates of coastal city nodes in China in 2015.

As can be seen from Figure 1, the higher the relative network connection rate of a city, the greater the role and influence of the city in China's marine economic development. By clustering, 41 coastal cities in 2015 were divided into 4 groups: the first group was national coastal city, including 9 cities of Shanghai, Qingdao, Shenzhen, Tianjin, Dalian, Guangzhou, Beijing, Xiamen and Suzhou, these cities were the hubs of connection among coastal city networks, and had great influence and competitiveness; the second group was regional coastal city, including 12 cities of Yantai, Hangzhou, Ningbo, Weihai, Nantong, Lianyungang, Zhoushan, Fuzhou, Taizhou, Nanjing, Zhuhai and Wenzhou, these cities were the priorities of regional connection, and had strong radiation depth and breadth for the other coastal cities; the third group was sub-regional coastal city, including 12 cities of Wuxi, Weifang, Rizhao, Zhongshan, Jinan, Zhanjiang, Foshan, Huizhou, Dongying, Ningde, Shantou and Maoming, these cities enjoyed rapid marine economic development, with increasing strength; the fourth group was local coastal city, including 8 cities of Zhenjiang, Xuzhou, Suqian, Binzhou, Dandong, Huludao, Changzhou and Yingkou, these cities were new cities of developing the marine economy.

According to the cluster analysis of coastal cities in 1995, 2005 and 2015, the hierarchical structures of coastal cities in

China were obtained. To directly reflect the characteristics and evolution of the hierarchical structures of coastal cities in China from 1995 to 2005 and to 2015, Table 3 and Figure 2 were made.

Tab. 3. Hierarchical structure of coastal cities in China in different years

| Year | City hierarchy              | City name   |
|------|-----------------------------|---|
| 1995 | National Coastal Cities     | Shanghai, Beijing, Tianjin, Shenzhen  |
|      | Regional coastal cities     | Qingdao, Dalian, Nanjing, Guangzhou, Xiamen   |
|      | Sub-regional coastal cities | Nantong, Fuzhou, Hangzhou, Suzhou, Ningbo   |
|      | Local coastal cities        | Yantai, Zhuhai, Shantou   |
| 2005 | National Coastal Cities     | Shanghai, Beijing, Tianjin, Qingdao, Shenzhen, Xiamen   |
|      | Regional coastal cities     | Dalian, Yantai, Suzhou, Ningbo, Fuzhou, Nanjing   |
|      | Sub-regional coastal cities | Hangzhou, Nantong, Wenzhou, Zhoushan, Foshan, Zhuhai  |
|      | Local coastal cities        | Dandong, Huludao, Weihai, Rizhao, Dongying, Lianyungang, Wuxi, Zhanjiang, Shantou                           |
| 2015 | National Coastal Cities     | Shanghai, Beijing, Tianjin, Qingdao, Shenzhen, Xiamen, Dalian, Suzhou, Guangzhou                            |
|      | Regional coastal cities     | Yantai, Hangzhou, Ningbo, Weihai, Nantong, Lianyungang, Zhoushan, Fuzhou, Taizhou, Nanjing, Zhuhai, Wenzhou |
|      | Sub-regional coastal cities | Wuxi, Weifang, Rizhao, Zhongshan, Ji'nan, Zhanjiang, Foshan, Huizhou, Dongying, Ningde, Shantou, Maoming    |
|      | Local coastal cities        | Zhenjiang, Xuzhou, Suqian, Binzhou, Dandong, Huludao, Changzhou, Yingkou                                    |

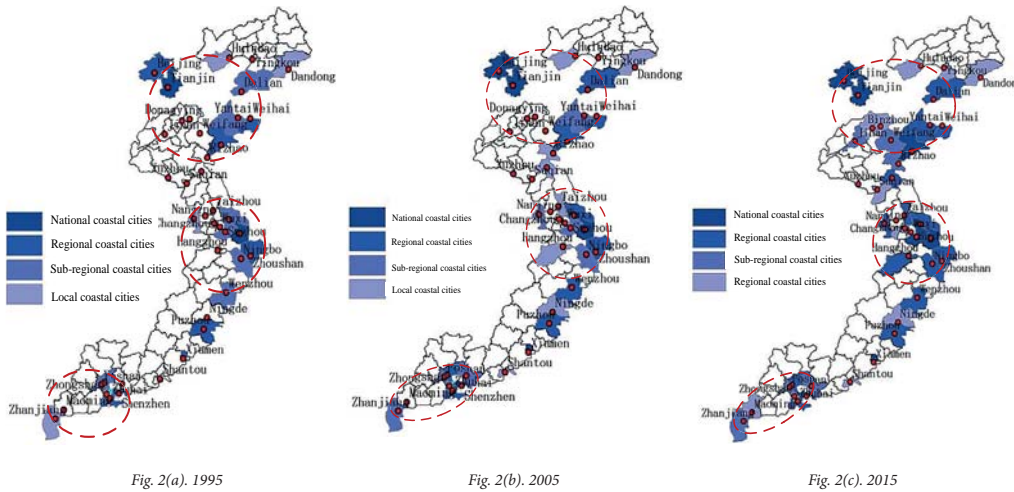


Fig. 2. Hierarchical structures of coastal cities in China in different years

As can be seen from Table 3 and Figure 2, the coastal cities in China and their hierarchical structure had the following characteristics: (1) The hierarchical structure of coastal cities in China had a significant positive correlation with the urban administrative rank and the level of urban economic development. In the hierarchical structure of coastal cities in China, all the national coastal cities in China were municipalities or sub-provincial cities, especially capital Beijing, a city not by the sea, unexpectedly had many headquarters of marine-related enterprises, so it had an important influence on other coastal cities. The reason may be that these cities had higher administrative ranks and easier access to political, economic and social resources, so the marine-related enterprises were first established in these cities to expand the market radius and develop the marine economy by making use of the influence of these cities. (2) The hierarchical structures of coastal cities in China were closely related to geographical location. The marine economy had obvious geographical characteristics, the closer to the sea of a city, the more abundant marine resources the city had, the faster the marine economic development, and the

higher hierarchy of the city in the hierarchies of coastal cities. (3) The coastal city agglomerations in China can be divided into three major urban agglomerations overall, including the Circum-Bohai Sea Urban Agglomeration, Yangtze River Delta

Urban Agglomeration and Pearl River Delta Urban Agglomeration, where the phenomenon of coastal city agglomeration was obvious.

The evolution of the hierarchical structure of coastal cities in China from 1995 to 2005 and to 2015 included:

(1) The hierarchies of coastal cities in China presented a hierarchical progressive evolution. Driven by marine policy, China's marine economy developed rapidly, and the marine-related enterprises expanded rapidly relying on urban impact, and the coastal cities developed to a higher hierarchy, and the hierarchies of coastal cities in China showed a progressive rise process, in particular, the hierarchies of cities such as Yantai, Weihai, Lianyungang, Fuzhou, Foshan, Zhuhai and Zhanjiang rose obviously.

From 1995 to 2005 and to 2015, the hierarchies of coastal cities in China presented a hierarchical progressive evolution, and the new cities of all hierarchies in 2005 and 2015 were mostly developed from the cities of lower hierarchies, for example, Zhuhai, just a local coastal city in 1995, rose to a sub-regional coastal city in 2005, and a regional coastal city in 2015. (2) The coastal city agglomerations in China formed a "three tiers and three urban agglomerations" network structure, the "three tiers" were Beijing, Shanghai and Shenzhen, and the "three urban agglomerations" were the Circum-Bohai Sea Urban Agglomeration, Yangtze River Delta Urban Agglomeration and Pearl River Delta Urban Agglomeration. From 1995 to 2005 and to 2015, in the 20 years of China's marine economic development, new coastal cities mainly emerged centering around the core cities of Beijing, Shanghai and Shenzhen, and the Circum-Bohai Sea Urban Agglomeration with Beijing as the center, Yangtze River Delta Urban Agglomeration with Shanghai as the center and Pearl River Delta Urban Agglomeration with Shenzhen as the center expanded continuously and their scales expanded gradually.

## EVOLUTION OF THE SPATIAL PATTERN OF COASTAL CITIES IN CHINA

To analyze the association between the spatial patterns and coastal cities, the city network model was constructed using ArcGIS software according to the incidence matrix among coastal cities in China in 1995, 2005 and 2015, as shown in Figure 3.

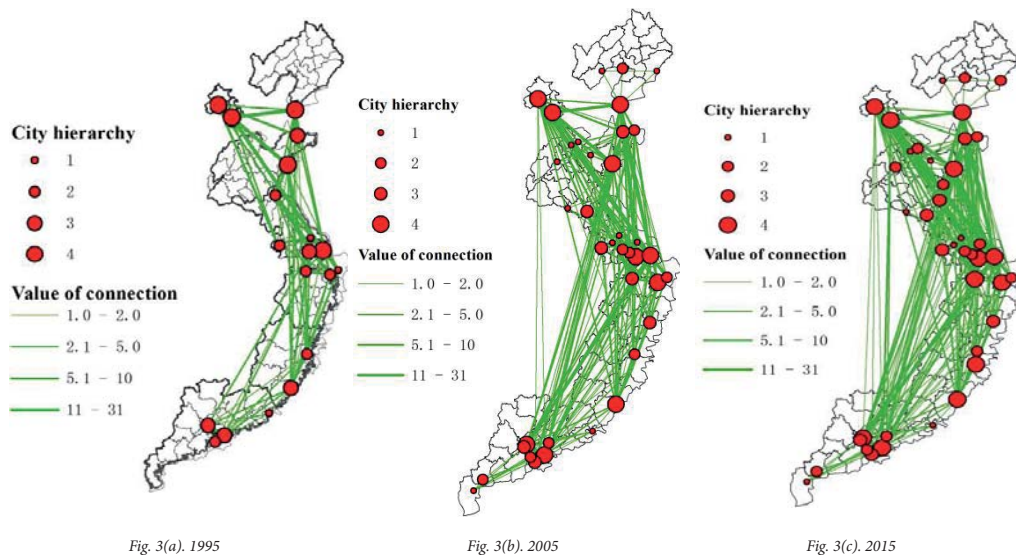


Fig. 3. Spatial patterns of coastal cities in China in different years

As can be intuitively seen from Figure 3, from 1995 to 2005 and to 2015, the strength of connection among coastal cities in China was gradually strengthened, and the density of city network gradually increased, and the urban spatial structure was becoming complete day by day. In 1995, the spatial pattern of coastal cities in China were not yet complete, and the strength of connection among coastal cities in China was weak. In 2005, the strength of connection among coastal cities in China was further strengthened, and the value of connection among some coastal cities was above 10, and the total value of connection among coastal city networks increased to 1,189, and the connection among coastal cities was closer, however, the strength of connection between new coastal cities and other cities was still low. In 2015, the spatial structure and network structure tended to be complete, the city network was more uniform, and the strength of connection among coastal cities in China was significantly strengthened, and the efficiency of urban spatial connection was improved overall.

## CONCLUSIONS

In this paper, a comprehensive research of the evolution of the hierarchical structure and spatial pattern of coastal cities in China was conducted based on the data of distributions of the headquarters and subsidiaries of marine-related enterprises in 1995, 2005 and 2015 using the city network research method proposed by Taylor. According to the empirical research,

the following conclusions were drawn: (1) China's coastal city network had an obvious hierarchical characteristics of "national coastal city-regional coastal city-sub-regional coastal city-local coastal city", in the 20 years of development process, the hierarchies of coastal cities in China showed a hierarchical progressive evolution. The high-hierarchy coastal cities were mostly municipalities or sub-provincial cities or seaside cities near the sea, these cities and their association

constituted the basic framework of the spatial patterns of coastal cities in China. (2) In the 20 years of development process, the strength of connection among coastal cities in China was gradually strengthened, and the density of city network increased gradually, and the urban spatial structure was becoming complete day by day. The coastal city agglomerations in China formed a "three tiers and three urban agglomerations" network structure, the "three tiers" were Beijing, Shanghai and

Shenzhen, and the "three urban agglomerations" were the Circum-Bohai Sea Urban Agglomeration, Yangtze River Delta Urban Agglomeration and Pearl River Delta Urban Agglomeration. (3) The structures of the three major coastal urban agglomerations became more complete, but there were differences in their internal and external spatial patterns. In the 20 years of development process, the association between the three major urban agglomerations and internal cities was strengthened, and the association among the three major urban agglomerations and external cities also became close gradually, and the connection among the cities became more direct and efficient. The Circum-Bohai Sea Urban Agglomeration had prominent internal connection while the Yangtze River Delta Urban Agglomeration had prominent external connection. Combined with the empirical analysis, this paper put forward the following policy recommendations.

In view of the obvious hierarchical structures of coastal cities in China, a long-term, overall planning based on China's overall marine economic development should be developed. Firstly, the government should attach importance to the construction of high-hierarchy coastal cities, cultivate and build the core coastal cities with competitive strength and influence, if the core coastal cities can not play their roles, the whole city network will be in a state of paralysis; secondly, form the urban agglomerations promoting China's marine economic development relying on the radiation and diffusion effects of high-hierarchy coastal cities to play the spatial polarization effect, so as to connect secondary development cities and promote China's marine economic

development; finally, give full play to the supporting roles of low-hierarchy coastal cities, avoid duplication of similar projects and industrial isomorphism, help them find their own positions in the industry, play their own advantages, and actively create a suitable external investment environment to strive to become a new coastal city with development potential.

## ACKNOWLEDGMENTS

This research was financially supported by the National Natural Science Foundation of China (No. 71371108) and National Social Science Foundation of China(Key Program) (No. 16AZD009).

## REFERENCES

1. L.Wang, W. Xiao, 2016. Analysis of China's Marine Industry Linkage and Sea-Land Industry Linkage Development Based on Input-Output Model. *Economic Geography*, 1, 113-119.
2. W.Xiao, B. Zhao, L.Wang, 2016. Marine Industrial Cluster Structure and its Coupling Relationship with Urban Development:A Case of Shandong Province. *Polish Maritime Research*,23, 115-122.
3. S.Démurger, J.D. Sachs, W.T. Woo, et al., 2002. Geography, economic policy, and regional development in China. *Asian Economic Papers*, 1,146-197.
4. S.Bao, G.H. Chang, J.D. Sachs, et al., 2002. Geographic factors and China's regional development under market reforms, 1978-1998. *China Economic Review*, 13(1),89-111.
5. T. Kim, G. Knaap, 2001. The spatial dispersion of economic activities and development trends in China: 1952-1985. *The Annals of Regional Science*, 35(1), 39-57.
6. J. Zhang, D. Jiang, 2014. Study on differences of regional financing policy-from the perspective of national planning area in coastal area. *Reform of Economic System*, 5,48-52.
7. B. Zhao, W. Xiao, and R. Tong et al., 2015. Blue economic connotation in industrial network perspective and its correlation structure effect-A case study of Shandong Province. *China Soft Science*, 8, 135-147.
8. Y. Liu, M. Liu, 2011. Investment of preferential policies and regional development disparity in open economy. *World Economy Studies*, 6, 3-9+87.
9. Q.Wei, A.Wang, J. Wang, 2014. The rise of China's coastal areas: power of market. *Economic research journal*, 8,170-183.
10. Q.Wang, H.Chen, 2016. Ratio of marketization to labour income: based on the empirical evidence of China's provincial panel data. *China Soft Science*, 9,156-167.
11. X. Jing, 2011. Comparison and evaluation of the use of FDI by Chinese open coastal cities. *Social Sciences in Guangdong*,3,27-33.
12. Z. Wang, S. Yang, 2011. Comparative research on mechanism of influence of FDI on the economic growth of three metropolis regions in China's eastern coast. *Comparative Economic & Social Systems*, 6,112-119.
13. L. Zhao, Z. Zhao, 2014. Dynamical evolution of spatial differences in economy of China's coastal areas. *World Regional Studies*, 1,45-54.
14. W. Qin, Y. Zhang, S. Li, 2014. Spatial-temporal evolution of development of tourism in China's eastern coastal cities. *Geographical Research*, 10,1956-1965.
15. Z. Qin, P. Zhang, G. Wang, 2012. A study on the evolution and optimization of spatial structure of Liaoning Coastal Economic Zone. *Economic Geography*, 10, 36-41.
16. M. Yan, X. Ma, C. Lou, 2016. Comparative study of the division of labor and its complementarity in the coastal megalopolis of China. *Economic Geography*, 1,69-74+88.
17. Z. Qin, P. Zhang, 2011. Evolution of spatial structure of the coastal urban belt in Liaoning. *Progress in Geography*, 4,491-497.
18. F. Fan, C. Sun, 2010. Differences in the urbanization level and its change of location in the Bohai Sea Economic Circle. *Urban Studies*, 12,30-35.
19. R.Li, D.Wu, H.Yin et al., 2014. Comprehensive measuring and temporal-spatial characteristics of the development efficiency of urban tourism of the four major coastal urban agglomerations in eastern China since 2000. *Geographical Research*, 5,961-977.
20. J. Liu, J. Zhao, Y. Du, 2013. Study on the relationship between tourism development and regional economic growth in coastal cities-based on spatial dynamic panel data model. *Inquiry Into Economic Issues*, 7,172-180.
21. J. Bi, H. Jiang, 2016. Research on development of the urban tourism in Liaoning coastal economic zone under the "The Belt and Road" strategy background. *Estate and Science Tribune*, 1,30-31.
22. Y. Zhang, Z. Ren, 2012. Population change and its spatial distribution patterns of coastal cities based on GIS. *Areal Research and Development*, 4,152-156.

23. Y. Fu, Y. Chen, Z. Zhang, 2014. Temporal and spatial variation of population density of coastal cities during 1985-2010 in China. *Tropical Geography*, 5,635-642.
24. L.Ye, X. J. Duan, 2016. City network structure of the Yangtze River Delta region based on logistics enterprise network. *Progress in Geography*, 5,622-631.
25. P. J. Taylor, 2001. Specification of the world city network. *Geographical analysis*, 33(2), 181-194.
26. J. Yin, F. Zhen, C. Wang, 2011. China's city network pattern: an empirical analysis based on financial enterprises layout. *Economic Geography*, 5,754 -759.

## CONTACT WITH THE AUTHORS

**Wenwen Xiao**

School of Management  
Shandong University  
Jinan 250100  
**CHINA**

# MULTI-AUV DISTRIBUTED TASK ALLOCATION BASED ON THE DIFFERENTIAL EVOLUTION QUANTUM BEE COLONY OPTIMIZATION ALGORITHM

Jianjun Li<sup>1,2\*</sup>

Ru Bo Zhang<sup>1,3</sup>

Yu Yang<sup>2</sup>

<sup>1</sup> College of Computer Science and Technology, Harbin Engineering University, China

<sup>2</sup> School of Computer and Information Engineering, Harbin University of Commerce, China

<sup>3</sup> College of Electromechanical & Information Engineering, Dalian Nationalities University, China

\* corresponding author

## ABSTRACT

*The multi-autonomous underwater vehicle (AUV) distributed task allocation model of a contract net, which introduces an equilibrium coefficient, has been established to solve the multi-AUV distributed task allocation problem. A differential evolution quantum artificial bee colony (DEQABC) optimization algorithm is proposed to solve the multi-AUV optimal task allocation scheme. The algorithm is based on the quantum artificial bee colony algorithm, and it takes advantage of the characteristics of the differential evolution algorithm. This algorithm can remember the individual optimal solution in the population evolution and internal information sharing in groups and obtain the optimal solution through competition and cooperation among individuals in a population. Finally, a simulation experiment was performed to evaluate the distributed task allocation performance of the differential evolution quantum bee colony optimization algorithm. The simulation results demonstrate that the DEQABC algorithm converges faster than the QABC and ABC algorithms in terms of both iterations and running time. The DEQABC algorithm can effectively improve AUV distributed multi-tasking performance.*

**Keywords:** Differential evolution quantum artificial bee colony algorithm; Multi-AUV; Contract net; Task allocation

## INTRODUCTION

Currently, research on underwater vehicle AUVs focuses on two dimensions: task allocation modeling and algorithm optimization. In recent years, to avoid the multi-robot centralized solution of the large calculation load of the central node, poor system robustness and other defects, scientific researchers worldwide have devised independent coordination and control technology for multi underwater vehicle AUVs according to the group behavior, which appears in biological group interaction mechanisms and reaction mechanisms. This effort provides a new method to solve the problem of distributed task allocation [1-3]. Distributed task allocation offers many advantages, such as strong

autonomous system scalability, calculation simplicity, and the lack of a defined coordination control center. It has no prominent hierarchical system feature. This method uses the bottom-up data-driven form, which distinguishes it from the traditional up-down task-planning model. It represents a new direction in the research field of multi underwater robot AUV task allocation.

With the rapid development of swarm intelligence algorithms, many researchers have simulated insect foraging behavior and have introduced a response threshold model to assign tasks; other experts have introduced the ant colony algorithm to solve the large-scale task allocation problem based on the time series [4-6]. Some experts have also designed a task model and proposed an improved discrete

particle swarm optimization algorithm to solve the problem [7,8]. These methods provide a new way to solve the problem of allocating tasks among multiple robots. The present paper explores AUV mission planning theory for multi-AUV task allocation, particularly to study distributed AUV dynamic task allocation, which uses the differential evolution quantum colony optimization algorithm in the bionic task allocation method.

## MATERIAL AND METHODS

### QUANTUM ARTIFICIAL BEE COLONY OPTIMIZATION ALGORITHM

The bee colony optimization algorithm is a type of meta-heuristic optimization method to imitate the behavior of natural bees. Ferrante et al. [9] proposed a self-organization model, which was applied to task partitioning. Grozinger [10] proposed a self-organizing model, which showed the communication in the bee colony through many methods, including “swing dance” and odor. This self-organization model can complete different tasks in different social classes. Karaboga and Bastruk. proposed a meta-heuristic bee colony algorithm to solve the maximum-weight problem [11, 12]. Tsai et al. [13] introduced an algorithm that imitated honeybees using the method of neighborhood search and random search for combinatorial optimization and function optimization. Karaboga et al. [14] successfully applied the colony algorithm to the problem of function extremum optimization and systematically introduced the artificial bee colony (ABC) model. Civicioglu and Besdok [15] analyzed a conceptual comparison of the Cuckoo search, particle swarm optimization, differential evolution and artificial bee colony algorithms. Loubière et al. [16] proposed a sensitivity analysis method for driving the artificial bee colony algorithm’s search process, a new approach to random selection in neighborhood search. Karaboga and Akay [17] and Ozturk et al. [18] proposed an improved clustering criterion artificial bee colony algorithm.

In the quantum space, the particle state  $i\hbar \frac{\lambda}{\lambda t} \varphi(X, t) = H\varphi(X, t)$  is represented by wave function  $\varphi(X, t)$ , where H is the Hamiltonian operator and h is Planck’s constant. If the particle undergoes a one-dimensional potential well movement at the center point of Q, the position determined by the stochastic equation is  $x=Q \pm \frac{h^2}{2m\gamma} \ln(1/u)$ , which m is mass of the particle,  $u$  is the random number distributed on the interval (0, 1) uniformity [19].

Thus, we can obtain a formula of the quantum artificial bee colony algorithm:

$$X_{i,j}(t+1) = Q_{i,j}(t) \pm \lambda |X_{i,j}(t) - X_{i \neq j,j}(t)| \ln(1/u_{i,j}(t)) \quad (1)$$

In the formula,  $i$  is the bee number,  $j$  is the dimension,  $X_{i,j}$  is the bee optimization position, and  $\lambda$  is a constant. In addition,

$$Q_{i,j}(t) = \alpha_j(t) \times Q_{i,j}(t-1) + (1 - \alpha_j) \times G_j(t) \quad (2)$$

In the formula,  $\alpha_j$  is the random number distributed on the interval (0, 1) uniformity,  $Q_{i,j}(t)$  is the best current position of an individual bee, and  $G_j(t)$  is the best estimate of the current position of all bees.

The best estimate of the position of the  $i$ -th bee is

$$Q_i(t) = \begin{cases} X_i(t) & f[X_i(t)] < f[Q_i(t-1)] \\ Q_i(t-1) & f[X_i(t)] \geq f[Q_i(t-1)] \end{cases} \quad (3)$$

The best estimate of the global position is determined by  $g = \arg \min_{1 \leq i \leq m} \{f[Q_i(t)]\}$  and  $G(t) = Q_g(t)$ .

### OPTIMIZATION ALGORITHM OF DIFFERENTIAL EVOLUTION OF QUANTUM COLONY

The differential evolution algorithm incorporates the individual optimal solution in the group evolution and shares the internal information groups  $X(0) = \{x_1^0, x_2^0, \dots, x_{NP}^0\}$ , through the cooperation and competition among individuals within the group to achieve the optimal solution. Assume that population size is  $NP$ , when the population evolves to the  $m$  generation, the population is  $X(m)$ , and the dimension of the solution space is  $K$ . In the initial population, the individual solution of  $I$  is  $x_i^0 = [x_{i,1}^0, x_{i,2}^0, \dots, x_{i,k}^0]$ . The individual components are as follows:

$$x_{i,j}^0 = x_{j,\min} + rand(x_{j,\max} - x_{j,\min}) \quad (4)$$

where  $x_{j,\max}$  is the upper bound of the solution space and  $x_{j,\min}$  is the lower bound of the solution space. The differential evolution algorithm has three types of operation: mutation, crossover and selection [20-22].

The use of fewer colony algorithm parameter settings make the algorithm easier to obtain and allows effective solution of complex optimization problems but also risks falling into a local optimum. Differential evolution quantum approaches must incorporate many operations, such as variation, crossover and selection. The optimal solution is obtained by iterating. Many problems can arise during the optimization process, such as slower convergence speed and premature solution. Akay B et al. proposed a differential evolution algorithm with a search strategy for an artificial bee colony [23]. The differential evolution quantum artificial bee colony (DEQABC) algorithm incorporates the artificial bee colony search strategy into the iteration process, which can allow it to escape a local optimum and avoid the premature phenomenon [24,25].

$$v_{ij} = x_{ij} + \alpha(x_{ij} - x_{kj}), i \neq k \quad (5)$$

Because of the lack of development of the formula, Ozturk C et al. proposed a novel binary version of the artificial bee colony algorithm based on genetic operators (GB-ABC) such as crossover and swap to solve binary optimization problems [26].

$$v_{ij} = x_{ij} + \alpha(x_{ij} - x_{kj}) + \beta(x_j^{Global} - x_{ij}), i \neq k \quad (6)$$

Therefore, the differential evolution optimization algorithm improves the convergence speed and avoids the prematurity phenomenon. The specific steps are as follows:

- (1) Initialize: F shrinkage factor, CR cross factor, maxCycle maximum iterations.
  - (2) Initial population: Randomly generate M solutions  $X_i$ , ( $i = 1, 2, \dots, M$ ).
  - (3) Execute the program:
- While the stop conditions are not satisfied, do  
 For i=1 to M, do  
 Do mutation, crossover and selection for  $X_i$ .  
 For k=1 to K, do  
 Use formulas (1) and (2) to search the candidate solutions near  $Z_i$ .  
 If  $f(Z_i) < f(X_i)$   
 $X_i = Z_i$   
 End if  
 End for  
 End for  
 End while

## RESULTS

### MULTI-AUV DISTRIBUTED TASK ALLOCATION OF THE CONTRACT NET WITH THE INTRODUCED BALANCE COEFFICIENT

To enable multiple AUVs to quickly complete the task and achieve global optimization, first, the task is distributed to the entire AUV team with the smallest cost using the contract net to ensure the global optimization of task implementation. Then, the balance coefficient is used to make the entire AUV team distribute and achieve the tasks in the shortest time.

The balanced coefficient  $B_{eq}^R$  is introduced in the contract net distributed robot task allocation. Each robot uses its cost function to count the workload: the workload is the cost of robot R in the entire process of the work. Each robot broadcasts its workload to the entire team and calculate its  $B_{eq}^R$ . The formula of the balance coefficient for robot R is as follows:

$$B_{eq}^R = \frac{wa(R) - \overline{wa}}{wa} \quad (7)$$

where  $\overline{wa}$  is the average workload of all robots in the team.  
 $B_{eq}^R < 0$ : robot R has a lighter workload than the other robots;  
 $B_{eq}^R > 0$ : robot R has a heavier workload than the other robots;  
 $B_{eq}^R > B_{eq}^{R1}$ : robot R has a heavier workload than robot R1.

In the contract net, the robot can take the task at the minimum cost, and the workload to be obtained should not be excessive. Thus, the task can be estimated from the balance coefficient  $B_{eq}^R$ . The formula of the task is estimated by robot R as follows:

$$rt^R(T_i) = rt^R(T_i) - B_{eq}^R \times |rt^R(T_i)| \quad (8)$$

The task can be estimated using the balance coefficient  $B_{eq}^R$  of robot R. The following effects can be obtained:

- (1) A robot with a larger workload cannot easily obtain new tasks, and its tasks are more likely to be reassigned because its task utility is low.
- (2) A robot with a smaller workload easily obtains new tasks and does not easily give up its task because its task utility is high.

### CONTRACT NET TASK ALLOCATION MODEL BASED ON DIFFERENTIAL EVOLUTION QUANTUM BEE COLONY ALGORITHM

The managers are denoted by  $AUV_\alpha$  in the distributed contract net. They are responsible for managing the task, and the other  $AUV_i$  are responsible for bidding the task. The task allocation process includes four steps: task bidding, bid, bid winning and task execution based on the contract net. The contract net task allocation model based on the differential evolution quantum bee colony algorithm is as follows:

Assume that there are  $N_V$  AUVs,  $Task = \{Task_1, Task_2, \dots, Task_{N_M}\}$ , the number of task targets is  $N_M$ ,  $V = \{V_1, V_2, \dots, V_{N_V}\}$ , the number of AUVs is  $N_V$ ,  $Menace = \{Menace_1, Menace_2, \dots, Menace_{N_Q}\}$ , and the number of threat sources is  $N_Q$ . The AUVs, task targets, and threat sources can include many types. If the same type of task is performed by different AUVs, the implementation effect is different. Assuming that the task set assigned to  $AUV_i$  is  $T_i = \{Task_i^1, Task_i^2, \dots, Task_i^{n_i}\}$ , the multi-AUV distributed task allocation problem can be translated as follows: Assign the existing tasks to multiple AUVs in the shortest possible time, i.e.,  $\bigcup_{i=1}^{N_V} T_i = Task$ ; each AUV has only one task, i.e.,  $\forall i, j \in \{1, \dots, N_V\}$ ,  $i \neq j$  and  $T_i \cap T_j = \emptyset$ . If the maximum number of tasks executed by the multi-AUV system is less than the number of tasks that should be allocated, the assignment can be optimized to improve the overall efficiency of the multi-AUV task allocation system according to the following objectives.

Objective one: To maximize the overall effectiveness  $\sum_{i=1}^{N_V} \theta_i(T_i)$  of the AUV after finishing the task,  $\theta_i(T_i)$  is the performance after the task set  $T_i$  is completed by  $V_i$ .

Objective two: To minimize the required time  $\max_{i \in V} Time_i(T_i)$  of the task to be completed by the AUV,  $Time_i(T_i)$  is the time at which the task set  $T_i$  is finished by  $V_i$ .

Objective three: To balance the task load of each AUV,  $\sum_{i=1}^{N_v} |Tload_i(T_i) - Tload|$  is minimized, where  $Tload_i(T_i)$  is the task load of  $V_i$ ,  $Tload$  is the average task load for each AUV.

## DISCUSSION

### EXPERIMENTAL PARAMETER ASSIGNMENT

To evaluate the performance of the distributed task allocation model based on the differential evolution quantum bee colony algorithm, the study included the corresponding simulation experiment. The conditions of the simulation experiment are as follows:

A set of thirty task items to be assigned is selected. The thirty tasks can be divided into three categories:  $T_1$ ,  $T_2$ , and  $T_3$ .  $AUV_1$ ,  $AUV_2$ , and  $AUV_3$  are involved in the bidding of the AUVs and all tasks of the bid. The bid value of the completed task, trust and initial ability are shown in Table 1. The influence factors of the AUV load, ability and trust degree are 0.3, 0.4 and 0.2, respectively, in the bidding strategies of the contract net task allocation based on the differential evolution quantum bee colony algorithm.

Tab. 1. Initial value of the completed task, trust and ability.

| T1            |              |         | T2            |              |         | T3            |              |         |
|---------------|--------------|---------|---------------|--------------|---------|---------------|--------------|---------|
| Bidding value | Trust degree | Ability | Bidding value | Trust degree | Ability | Bidding value | Trust degree | Ability |
| 3             | 0.6          | 0.8     | 2             | 0.5          | 0.6     | 2             | 0.8          | 0.7     |
| 4             | 0.8          | 0.6     | 2             | 0.9          | 0.8     | 3             | 0.9          | 0.6     |
| 5             | 0.9          | 0.7     | 3             | 0.7          | 0.7     | 4             | 0.6          | 0.8     |

The simulation experiment has 2 objectives. When the bidding and tendering stage are identical, the first objective is to test and compare the contract net model based on the differential evolution quantum bee colony algorithm and the contract net traditional model. The second objective is to compare the performance in four aspects: efficiency of task allocation, average AUV load, number of bid AUV allocated tasks, and proportion relation of the corresponding type of task ability.

### EXPERIMENTAL VERIFICATION

After the experiment, the simulation results are as follows. Figure 1 shows the average load of  $AUV_1$ ,  $AUV_2$  and  $AUV_3$  in the contract net traditional model AUV. Figure 2 shows the reduced proportion (%) when  $AUV_1$ ,  $AUV_2$  and  $AUV_3$  execute tasks in the contract net traditional model.

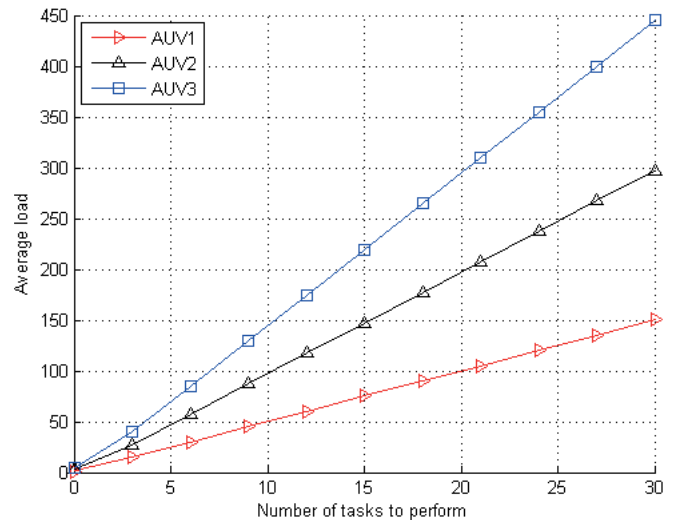


Fig. 1. Average Load of AUV1, AUV2 and AUV3 in the Contract Net Traditional Model AUV.

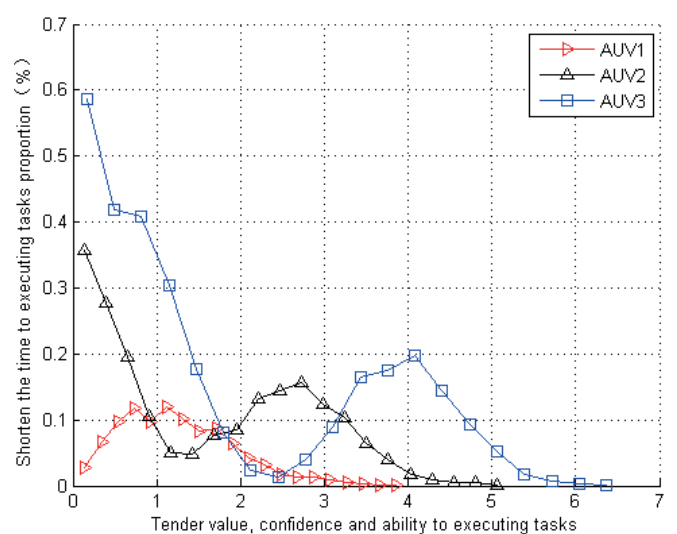


Fig. 2. Reduced Proportion (%) of AUV1, AUV2 and AUV3 when they Executed Tasks in the Traditional Contract Net Model.

Figure 3 shows the average load of the AUVs in the contract net model based on the differential evolution quantum bee colony algorithm. Figure 4 shows the reduced proportion (%) of execution time in the contract net model with the introduced balance coefficient based on the differential evolution quantum bee colony algorithm.

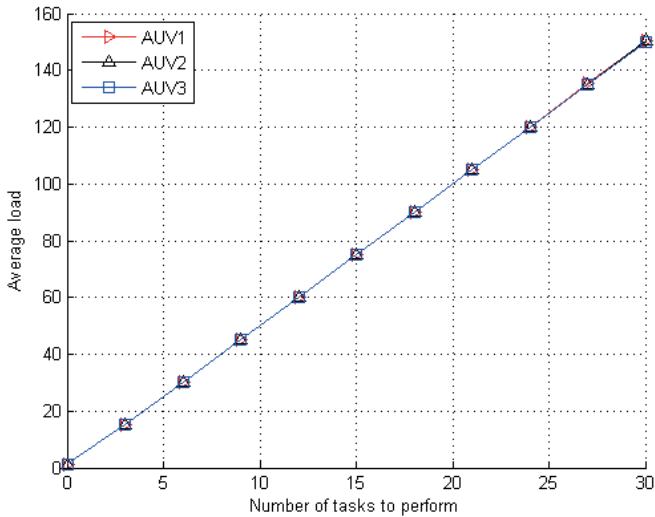


Fig. 3. Average Load of AUV1, AUV2 and AUV3 in the Contract Net Improved Model AUV.

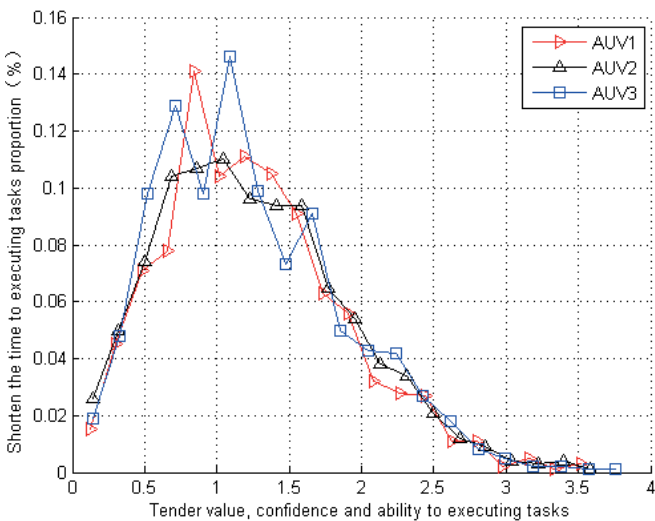


Fig. 4. Reduced Proportion (%) of AUV1, AUV2 and AUV3 Tasks in the Contract Net Improved Model.

Comparing the front and back images, we observe that the traditional contract net does not consider the load balance of the bidding AUV, which causes a large load difference for the bidding AUV. The improved contract net model satisfies the requirement of load balance because the proportions of load and task execution time of three bidding AUVs are basically equivalent.

Figure 5 shows that the comparison of the executive entirety effectiveness of multiple AUVs in the distributed task allocation experiment in the traditional contract net

model and the contract net model with the introduced balance coefficient based on the differential evolution quantum bee colony algorithm.

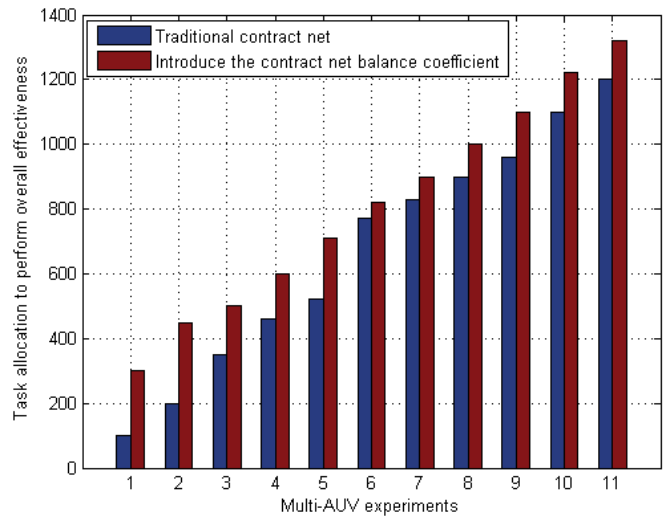


Fig. 5. Comparison of the Executive Entirety Effectiveness of the Multi-AUV Distributed Task Allocation.

Figure 6 shows the comparison of the convergence performance of the ABC, QABC, and DEQABC algorithms in the process of multi-AUV distributed task allocation.

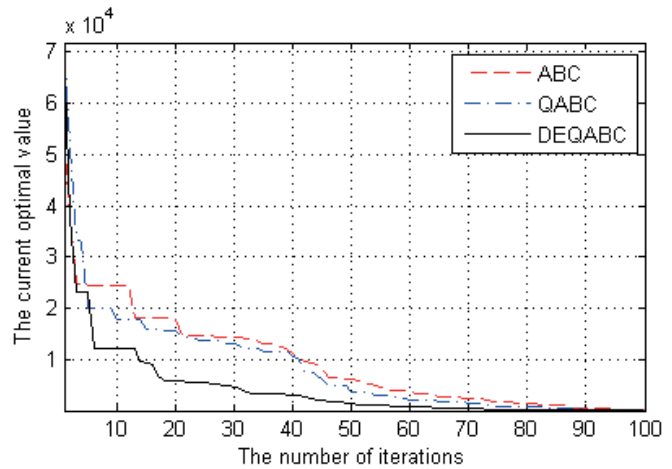


Fig. 6. Comparison of the Convergence Performance of the ABC, QABC, and DEQABC Algorithms.

Figure 7 and Figure 8 show the comparison of the number of iterations and running time when the ABC, QABC, and DEQABC algorithms are used to solve 10 task allocation cases to obtain the optimal solution.

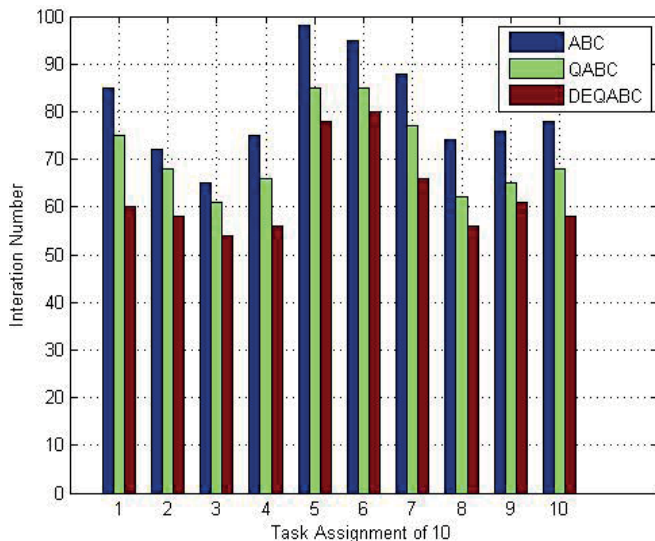


Fig. 7. Comparison of the Number of Iterations for the ABC, QABC, and DEQABC Algorithms.

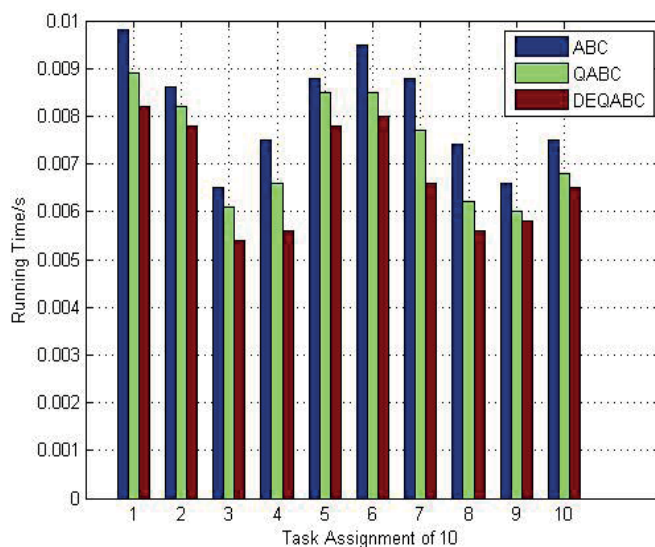


Fig. 8. Comparison of the Running Time for the ABC, QABC, and DEQABC Algorithms.

## CONCLUSIONS

In this paper, we propose a distributed task allocation model based on the differential evolution quantum bee colony algorithm to allow more rapid task allocation for a greater number of AUVs and achieve global optimization in the multi-AUV distributed task allocation. The balance coefficient is introduced to distribute the robot task allocation of the traditional contract net. The unbalanced load and other defects are improved in the multi-AUV distributed task allocation of the traditional contract net. The differential evolution quantum bee colony algorithm is applied to the process of multi-AUV dynamic distributed task allocation.

The simulation experiment verifies that the quantum bee colony based on differential evolution can avoid falling into local optima; shorten the convergence time; reduce the number of iterations; enhance the global, dynamic and adaptive capability of the bee colony algorithm; and effectively improve the overall performance of distributed task allocation for multiple AUVs.

## ACKNOWLEDGMENT

This work was supported in part by the National Natural Science Foundation of China (60975071,61100005), Ministry of Education, Scientific Research Project (13YJA790123).

## REFERENCES

1. B He, L Ying, S Zhang, X Feng, R Nian, 2015. Autonomous navigation based on unscent ed-FastSL AM using particle swarm optimization for autonomous underwater vehicles. *Measurement*, 71(1), 89-101.
2. Y Shen, H Zhang, B He, T Yan, 2015. Autonomous Navigation Based on SEIF with Consistency Constraint for C-Ranger AUV. *Mathematical Problems in Engineering*, 3(1), 231-243.
3. Daqi Zhu, Huan Huang, and Simon X. Yang, 2013. Dynamic Task Assignment and Path Planning of Multi-AUV System Based on an Improved Self-Organizing Map and Velocity Synthesis Method in Three-Dimensional Underwater Workspace. *IEEE Transactions on Cybernetics*, 43(2), 504-514.
4. DF Yuan, L Cong-Ying, 2013. Application of Improved Ant Colony Algorithm for Quadratic Assignment Problems. *Computer and Modernization*, 3(1), 9-11.
5. Parag C. Pendharkar, 2015. An ant colony optimization heuristic for constrained task allocation problem. *Journal of Computational Science*, 7(1), 37-47.
6. Celal Özkale, Alpaslan Fırlalı, 2013. Evaluation of the multiobjective ant colony algorithm performances on biobjective quadratic assignment problems. *Applied Mathematical Modelling*, 37(1), 7822-7838.
7. Zahra Beheshti, Siti Mariyam Shamsuddin, 2015. Non-parametric particle swarm optimization for global optimization. *Applied Soft Computing*, 28(2), 345-359.
8. AI Awad, NA El-Hefnawy, HM Abdel\_Kader, 2015. Enhanced Particle Swarm Optimization for Task Scheduling in Cloud Computing Environments. *Procedia Computer Science*, 35(1), 920-929.
9. Eliseo Ferrante, Ali Emre Turgut, Edgar Duéñez-Guzmán, Marco Dorigo, Tom Wenseleers, 2015. Evolution

- of Self-Organized Task Specialization in Robot Swarms. *Computational Biology*, 10(3), 1371-1392.
10. Christina M. Grozinger, Jessica Richards, Heather R. Mattila, 2014. From molecules to societies: mechanisms regulating swarming behavior in honey bees. *Apidologie*, 45(3), 327-346.
  11. D Karaboga, Basturk, 2007. A powerful and efficient algorithm for numerical function optimization: artificial bee colony (ABC) algorithm. *Journal of Global Optimization*, 39(3), 459-471.
  12. R Akbari, A Mohammadi, K Ziarati, 2010. A novel bee swarm optimization algorithm for numerical function optimization. *Communications in Nonlinear Science and Numerica Simulat*, 15(5), 3142-3155.
  13. Hsing-Chih Tsai, 2014. Integrating the artificial bee colony and bees algorithm to face constrained optimization problems. *Information Sciences*, 258(2), 80-93.
  14. Dervis Karaboga, Beyza Gorkemli, Celal Ozturk, Nurhan Karaboga, 2014. A comprehensive survey: artificial bee colony (ABC) algorithm and applications. *Artificial Intelligence Review*, 42(1), 21-57.
  15. Pinar Civicioglu, Erkan Besdok, 2013. A conceptual comparison of the Cuckoo-search, particle swarm optimization, differential evolution and artificial bee colony algorithms. *Artificial Intelligence Review*, 39(2), 315-346.
  16. Peio Loubière, Astrid Jourdana, Patrick Siarry, Achid Chelouaha, 2016. A sensitivity analysis method for driving the Artificial Bee Colony algorithm's search process. *Applied Soft Computing*, 41(1), 515-531.
  17. D Karaboga, B Akay, 2009. A survey: algorithms simulating bee swarm intelligence. *Artificial Intelligence Review*, 31(1), 61-85.
  18. Celal Ozturk, Emrah Hancer, Dervis Karaboga, 2015. Improved clustering criterion for image clustering with artificial bee colony algorithm. *Pattern Analysis and Applications*, 18(3), 587-599.
  19. J Sun, W Fang, X Wu, 2014. Quantum-Behaved Particle Swarm Optimization: Analysis of Individual Particle Behavior and Parameter Selection. *Evolutionary Computation*, 20(3), 349-393.
  20. Miha Mlakar, Dejan Petelin, Tea Tušar, Bogdan Filipič, 2015. GP-DEMO: Differential evolution for multiobjective optimization based on Gaussian process models. *European Journal of Operational Research*, 243(2), 347-361.
  21. A. C. Biju, T. Aruldoss Albert Victoire, and Kumaresan Mohanasundaram, 2015. An Improved Differential Evolution Solution for Software Project Scheduling Problem. *Scientific World Journal*, 2(1), 1-9.
  22. Sk. Minhazul Islam, Swagatam Das, 2012. An Adaptive Differential Evolution Algorithm With Novel Mutation and Crossover Strategies for Global Numerical Optimization. *IEEE Transactions on Systems, Man, and Cybernetics, Part B (Cybernetics)*, 42(2), 482-500.
  23. Bahriye Akay, Dervis Karaboga, 2012. Artificial bee colony has a differential evolution algorithm search strategy. *Journal of Intelligent Manufacturing*, 23(4), 1001-1014.
  24. A Bouaziz, A Draa, S Chikhi, 2013. A Quantum-inspired Artificial Bee Colony algorithm for numerical optimization. In: *International Symposium on Programming & Systems*. Algiers Algeria. pp. 81-88.
  25. X li, M yin, 2014. Parameter estimation for chaotic systems by hybrid differential evolution algorithm and artificial bee colony algorithm. *Nonlinear Dynamics*, 77(1), 61-71.
  26. D Karaboga, B Gorkemli, C Ozturk, N Karaboga, 2014. A comprehensive survey: artificial bee colony (ABC) algorithm and applications. *Artificial Intelligence Review*, 42(1), 21-57

## CONTACT WITH THE AUTHORS

**Jianjun Li**

College of Computer Science and Technology  
Harbin Engineering University  
Harbin 150001  
**CHINA**

School of Computer and Information Engineering  
Harbin University of Commerce  
Harbin 150028  
**CHINA**

## EXPERIMENTAL AND OPTIMIZATION DESIGN OF OFFSHORE DRILLING SEAL

Yi Zhang\*

Xiaodong Zhang

Xueping Chang

Qian Wu

School of Mechatronic Engineering, Southwest Petroleum University, Chengdu 610500, China

\* corresponding author

### ABSTRACT

*Three-cone bit is the key equipment in the exploration of the oil in offshore drilling and exploration, the bearing system and the seal system are the critical components for the bit. Especially in the offshore drilling environment, the seal design need to be carefully considered. A multi-objective optimization design including orthogonal design method and F-test with finite element analysis for a three-cone bit seal is proposed. Firstly, the calculation method of optimization targets are given, including the minimization of maximum contact pressure and leakage rate analyzed by ANSYS and MATLAB respectively, to maximize seal life and reliability. Then, an orthogonal experiment approach is used to investigate the effects of the eleven parameters on the seal performance, and the influence degrees of the seal factors on the optimization targets have been confirmed by F-test, and the reasonable factors can be determined by the trend of the targets. Finally, in order to validate the analysis results, a new seal was designed and tested on a seal tester compared to the previous seal. In this test, the seal maximum interface temperature that reflects the position of maximum contact pressure can be obtained by using three high precision thermocouples. Both the experiment results and the numerical analyses proved that the maximum contact pressure and leakage rate of the improved seal have been reduced compared to the previous.*

**Keywords:** Offshore drilling; Design Optimization; Seals; Finite Element Analysis; MATLAB

### INTRODUCTION

Three-cone bit is the key equipment in the exploration of the oil and natural gas field resources in offshore drilling and exploration. Harsh marine environment brings many problems to drilling, one of the most significant questions which must be answered by the drilling engineers is whether the reliability of three-cone bit can be guaranteed [1]. However, statistics indicated that the main reason for the bit failure is the early seal failure [2].

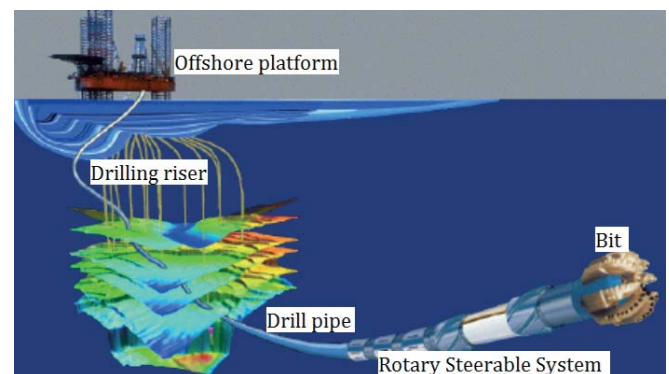


Fig. 1. Schematic diagram of offshore drilling system

Compared to a common seal, the bit seal has more complicated structure, and the high temperature and high pressure of well bottom-hole will lead to the lubricant leakage increases. The statistics identified that the main reason of the bit failure is the early seal failure [3]. The seal fail will lead to the lubricant leakage and fatigue wear caused by the contact pressure of the seal interface [4]. The structure of the SEMS2 is shown in Figure 2: the stator, O-ring, and the rubber support ring are stationary while the rotor rotates together with the shaft. The rubber support ring and the O-ring can supply seal pressure for the seal interface.

In the most recent years, several descriptive studies have been carried out to examine the seal structure and failure reason. Joseph L [5] pointed out that the life of the cone bit bearing is determined by the seal and bearing, and forecasted the life of the lubrication system. Shunhe Xiong [6] produced an axisymmetric numerical model of mechanical seal for down-hole tools, and discussed the relationship between the environmental pressure and the lubricant film. Based on the hypothesis that the drilling fluid has the same fluid properties, a transient seal model and a dynamic tracking model is developed. Considering the seal interface pressure distribution, the second generation SEMS2 has been and improved by Baker Hughes in 2003 [7].

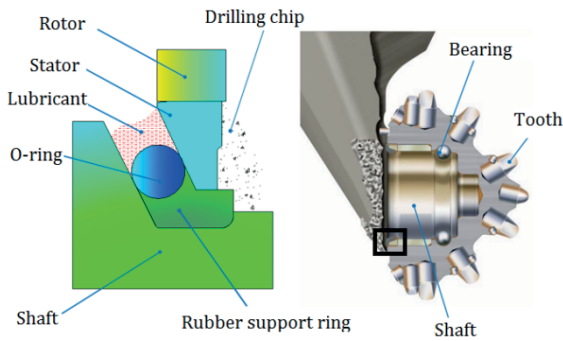


Fig. 2. Seal installation position on the cone bit

As to the bit seal, the sealing force produced by elastomer is non-linear, which further aggravates the research difficulty. Although numerical analysis makes great contributions to the down-hole seal, there still exists some problems for this new seal design. Its seal properties vary with the amount of rubber non-linear behavior, down-hole pressure and seal design parameters. However, very few factors have been considered for the structure optimum design of the cone bit seal nowadays. For the seal optimum design, the artificial neural network [8, 9], Taguchi method [10] and finite element analysis [11] have been recognized as strong tools. However, due to the structure and special environment of the bit seal, the numerical analysis of multiple objectives remains complex.

In this paper, in order to increase the computational efficiency, the inverse method is employed to approximate the pressure distribution of lubricant film by FEM simulation. Furthermore, an orthogonal experiment with orthogonal array and F-test are used to determine the importance of the

seal parameters on the optimum targets. Then the optimal values can be determined by the trend of the average values of maximum contact pressure and leakage rate, and the parameters are verified through numerical analyses and experimental studies.

## MATERIAL AND METHODS

### MATERIAL PARAMETERS

The material of the head seal and cone insert is hard metal alloy YG8, the backup ring and the head energizer are made of HNBR rubber with a hardness of about 80 IRHD, a material that ensures high temperature resistance together with high compatibility for lubricants, and this material also exhibits highly nonlinear elastic. In this paper, the Mooney–Rivlin model belongs to a type of constitutive models to describe rubber is selected to describe the mechanical properties of rubber with less than 150% deformation. The function of strain potential energy can be expressed as [12]:

$$W = C_1(I_1 - 3) + C_2(I_2 - 3) \quad (1)$$

Where  $C_1, C_2$  are Mooney–Rivlin coefficient,  $I_1, I_2$  are the first and second order invariable strain values. The relationship of stress, strain potential energy, and strain can be expressed as:

$$\sigma = \partial W / \partial \epsilon \quad (2)$$

As to the incompressible materials, shear modulus  $G$  and rubber material parameters can be written as:

$$G = 2(C_1 + C_2) \quad (3)$$

The performance parameters  $C_1$  and  $C_2$  can be obtained by uniaxial compression tests, furthermore, the constitutive model parameters of rubber material can be fitted by means of the least square method. According to the fitting results, the constants  $C_1, C_2$  are 1.856 and 0.046 respectively.

### CALCULATION METHOD OF OPTIMIZATION TARGETS

#### SEAL CONTACT PRESSURE

The interface between the stator and the rotor isolates the lubricant from the drilling fluid, and lubricant pressure is higher than drilling fluid by means of the piston balance system, which can prevent the drilling fluid from flowing into the bearings. According to the experimental data, the environmental pressure difference between the lubricant and drilling fluid ranges from 0.3MPa to 0.7MPa [3]. The seal interface contact pressure in downhole condition can be calculated by finite element simulation. The seal assembly

process is first simulated, wherein the shaft is fixed and the axial compressive displacement of stator is 3 mm (Figure 3a). Secondly, the lubricant pressure 30.5 MPa and drilling fluid pressure 30 MPa are exerted on the inside and outside of the seal, respectively, shown in Figure 3b. The result of the contact pressure are depicted in Figure 3c, which shows the outer contact pressure of the interface is smaller than that of the inner at the high pressure environment, and the contact distribution can result in the inner position to be worn easily in the drilling process. Hence, the maximum contact pressure  $P$  should be an optimization objective.

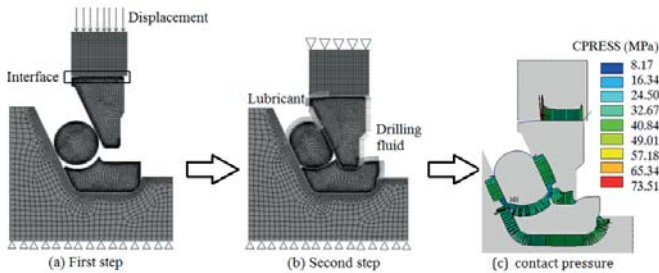


Fig. 3. The steps of the finite element analysis.

#### SEAL LEAKAGE RATE

The leakage rate is an important index to evaluate the seal life, which can be computed by solving Reynolds equation. Due to the low rotational speed, the inverse method is used to analyze the film thickness of the seal interface to simplify the numerical computation. Due to the axisymmetry of seal geometry and load, the seal surface deformation and flow field of the seal interface can be assumed to be axisymmetric. Based on these hypothesis, the lubrication equation can be expressed as [13]:

$$\frac{1}{r} \frac{\partial}{\partial r} \left( \frac{\phi_r r h^3}{12\mu} \frac{\partial P}{\partial r} \right) = 0 \quad (4)$$

The boundary conditions are:  $P=P_1$ , at  $r=r_0$  (lubricant-side);  $P=P_2$ , at  $r=r_1$  (drilling fluid-side). Where  $\mu$  represents the dynamic viscosity of the lubricant;  $P_1$ ,  $P_2$ ,  $h$ ,  $r_0$ , and  $r_1$  are the lubricant pressure, drilling fluid pressure, film thickness, inner radius of the seal, and the outer radius of the seal, respectively. The leakage rate  $Q$  can be calculated from Equation (5):

$$Q = \int_0^{2\pi} \frac{\rho \phi_r r h^3}{12\mu} \frac{\partial p}{\partial r} d\theta \quad (5)$$

The contact pressure gradient distribution of the seal interface can be obtained by finite element simulation. Combined with the Equation (4), the film distribution of the seal interface can be calculated. Based on the film distribution, the seal leakage at the minimum film thickness can be obtained according to the Equation (5).

#### MULTI-PARAMETER OPTIMIZATION DESIGN

It is obvious that the environmental pressure difference and seal geometric parameters have great influences on the contact pressure and leakage rate. In order to optimize the structural parameters of the seal, the orthogonal design tests and F-tests are used to evaluate the impact degrees on the seal performance.

The seal parameters include environmental pressure difference  $\Delta p$  and ten geometric parameters. The geometric parameters are shown in Figure 4.

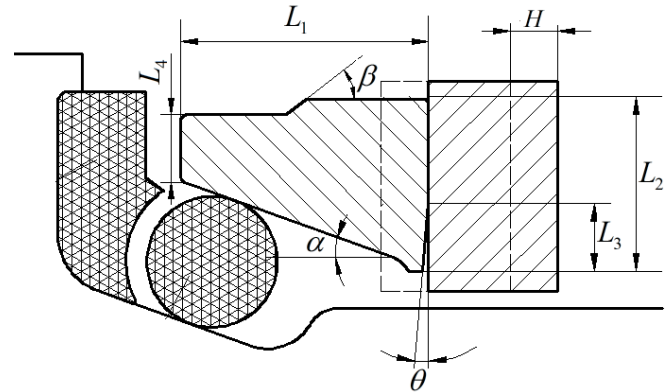


Fig. 4. Parameters of the bearing seal.

The orthogonal design can improve experimental efficiency and has been widely used in industry. In this trial, the factors are labeled as A–M, and each factor has three levels, and the range of each factor has been determined by design experience. The orthogonal design can be conducted by  $L_{27}(3^{11})$  Orthogonal Array [14–15]. The levels and factors are given in Table 1.

Tab. 1. Levels and factors of seal parameters

| Factors                                      | Parameters | Unit | Levels |     |     |
|--|------------|------|--------|-----|-----|
| Axial length of the stator(A)                | L1         | mm   | 4      | 5   | 6   |
| Width of the sealing interface(B)            | L2         | mm   | 5      | 5.5 | 6   |
| Length of the wedge angle (C)                | L3         | mm   | 1      | 2   | 3   |
| Inside angle of the stator (D)               | $\alpha$   | deg  | 30     | 25  | 20  |
| Outside angle of the stator(E)               | $\beta$    | deg  | 30     | 45  | 60  |
| Wedge angle of the stator (F)                | $\theta$   | deg  | 2      | 5   | 8   |
| Bottom width of the stator (G)               | L4         | mm   | 2      | 2.5 | 3   |
| Hardness of the energizer(I)                 | HA         | HIRD | 70     | 80  | 90  |
| Hardness of the rubber support ring (J)      | HB         | HIRD | 70     | 80  | 90  |
| Axial displacement of the rotor(K)           | H          | mm   | 1.4    | 1.6 | 1.8 |
| Difference of the environmental pressure (M) | $\Delta P$ | MPa  | 0.3    | 0.5 | 0.7 |

## RESULTS

### MAXIMUM CONTACT PRESSURE AND LEAKAGE RATE

According to the fluid numerical model, the contact pressure gradient distribution can be analyzed by ANSYS. Coupled with the film thickness, the leakage rate  $Q$  can be computed by MATLAB. In this paper, the environmental temperature  $T=50^\circ$ , and the shaft rotating speed  $n=200$  r/min. Based on the orthogonal design tests, the maximum contact pressure and the leakage rate are presented in Figure 5. It can be seen that the maximum contact pressure for the 27 trials range from 54.68 MPa to 122.1 MPa; the numbers relatively small are 2, 3, 13, and 14. Meanwhile, the number 2, 3, 13, and 26 trails have relatively larger leakage rate.

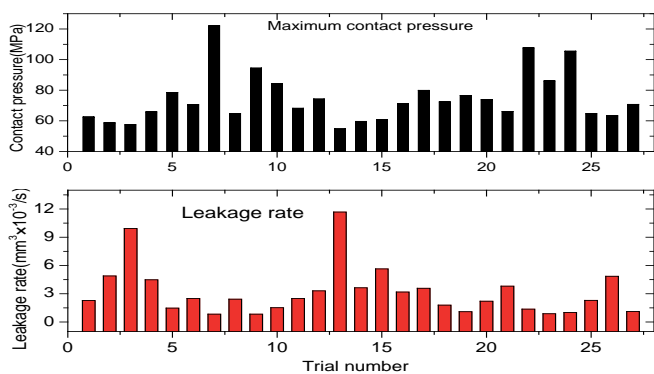


Fig. 5. Maximum contact pressure and leakage rate.

### IMPACT FACTORS

According to the results of orthogonal design tests, the variance of the factors can be calculated [16]:

$$S = \frac{1}{a} \sum_{i=1}^b K_i^2 - \frac{1}{n} \left( \sum_{k=1}^n x_k \right)^2 \quad (6)$$

Where,

$$K_i = \sum_{j=1}^a x_j \quad (7)$$

$n$ ,  $a$ , and  $b$  stands for the total number of trials, number of trials for each level, and levels for each factor,  $x_j$  is the calculations of the trial  $j$  at level  $i$  ( $i=1, 2, \dots, b; j=1, 2, \dots, a$ ). The variances of the maximum contact pressure  $P$  and leakage rate  $Q$  can be seen in Table 2.

Tab. 2. Results of variance analysis of the factors

| Variances | Factors |       |       |       |      |       |        |       |       |      |        |
|-----------|---------|-------|-------|-------|------|-------|--------|-------|-------|------|--------|
|           | A       | B     | C     | D     | E    | F     | G      | I     | J     | K    | M      |
| Q         | 186.55  | 93.40 | 36.88 | 586.5 | 6.99 | 13.64 | 141.92 | 21.53 | 96.20 | 5.35 | 545.62 |
| P         | 27.53   | 17.96 | 4.26  | 17.96 | 5.94 | 1.59  | 5.01   | 35.71 | 22.46 | 124  | 2.21   |

### F-TEST

Based on the orthogonal design and analysis of variance, the influence degree of the factors on the optimization objectives can be confirmed by F-test [17]. The F values of the maximum contact pressure and leakage rate can be calculated by Equation (8):

$$F = \frac{S_i/f_i}{S_E/f_E} \quad (8)$$

Where  $f_i$  and  $f_E$  are respectively the degrees of freedom of the factor  $i$  ( $i=A, B, \dots, M$ ) and of the error;  $S_i$  and  $S_E$  are the sum of squares of factor  $i$  and error respectively. The F-test values can be expressed as the ratio of the variance of the factor  $i$  to the variance of the error. In this paper, according to the orthogonal design tests,  $n=27$ ,  $a=3$ , and the trial number of each factor is 9, so the degrees of freedom  $f_i=2, f_E=8$ .

The criteria of F values can be found from F distribution table. If  $\Phi=0.1$ , the confidence level is 90%. For the factors, the larger the F values is, the greater the impact on the optimization objective is. If  $F_i > F_{0.001}(2,8)$ , the factor  $i$  is highly significant, marked as "\*\*\*\*\*". If  $F_{0.001}(2,8) > F_i > F_{0.005}(2,8)$ . The factor  $i$  marked as "\*\*\*\*". With the F value increasing from 0.005 to 0.05, the impact on the maximum contact pressure and leakage rate reduces gradually. If  $F_{0.05}(2,8) > F_i$ , the influence of the factors can be neglected.

According to the criteria, the F values of  $P$  and  $Q$  for the eleven factors are shown in Table 3. It can be seen that the F values of factors C, E, and F are lower than  $F_{0.05}(2,8)$ , which means that these factors have little or no effect on  $P$  and  $Q$ , and the other eight factors need to be further discussed.

Tab. 3. Evaluation results of the factors

| Factors | F values |       |      |       |      |      |       |       |       |       |       |
|---------|----------|-------|------|-------|------|------|-------|-------|-------|-------|-------|
|         | A        | B     | C    | D     | E    | F    | G     | I     | J     | K     | M     |
| P       | 9.84     | 6.42  | 1.52 | 6.42  | 2.12 | 0.57 | 1.79  | 12.77 | 8.03  | 44.66 | 0.79  |
| Q       | 24.49    | 12.26 | 4.84 | 77.02 | 0.92 | 1.79 | 18.63 | 2.83  | 12.63 | 0.70  | 71.64 |

## DISCUSSION

### OPTIMAL VALUES OF THE OTHER FACTORS

As described above, the influence of the factors C, E, and F can be ignored. For the other eight factors, each factor has nine calculation results on the maximum contact pressure  $P$  by the orthogonal array, and so does the leakage rate  $Q$ . The average values of  $P$  and  $Q$  for the same level can be defined as  $K-Q$  and  $K-P$ , then the optimal values can be determined by the trend of the curve of  $K-Q$  and  $K-P$ . Figure 6 presents the trends of  $K-P$  and  $K-Q$  against the levels for the factors. It can be seen that the factors G and J have great effect on the  $K-P$ , and the factors B and D have highly effect on the  $K-Q$ .

In order to extend the seal life, the average values of  $P$  and  $Q$  need to be reduced as much as possible. According to the trend of  $K-P$  and  $K-Q$ , the level 1, level 1, level 1, and level 3 are chosen as the optimal values for the factors  $G$ ,  $J$ ,  $B$ , and  $D$ .

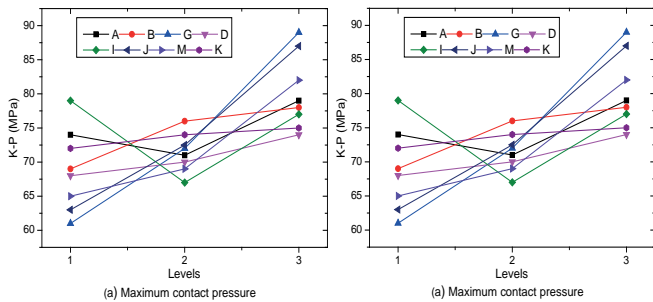


Fig. 6. Average values of the maximum contact pressure and leakage rate.

For the factors  $A$ ,  $I$ ,  $K$ , and  $M$ , Figure 6 shows that the factors  $I$  and  $M$  have greater impact on the  $K-P$  than the  $K-Q$ , so the  $K-P$  should be mainly considered, and the minimum average values for the  $I$  and  $M$  are level 2 and level 1 respectively, shown in Figure 6(a). By the same reason, the factors  $A$  and  $K$  have greater impact on the  $K-Q$  than the  $K-P$ , according to Figure 6(b), the level 2, level 2 are considered as the reasonable levels for the seal.

### COMPARISON OF SEAL PERFORMANCE

The optimal levels of the seal factors have been obtained through the orthogonal design and F-test, and the comparison of the improved and previous seal is shown in Figure 7. It can be seen that the width of the sealing interface and inner angle of the stator is 4.0mm and 20° versus 5.5 mm and 25° of the previous seal.

Figure 8 shows the contact pressure distributions of improved and previous seal interface. It can be seen that the highest contact pressure is decreased from 73.51MPa to 56.80 MPa, and the middle interface contact pressure distributions are more uniform, which will offer good lubrication environment for the seal. Figure 8 also shows the improved seal increased the outer contact pressure to 55.24MPa versus 48.428MPa for the previous seal, which means that the improved seal can prevent penetration of abrasive particles at the seal outer edge.

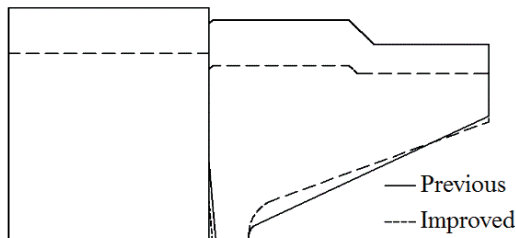


Fig. 7. Seal structure: improved versus the previous.

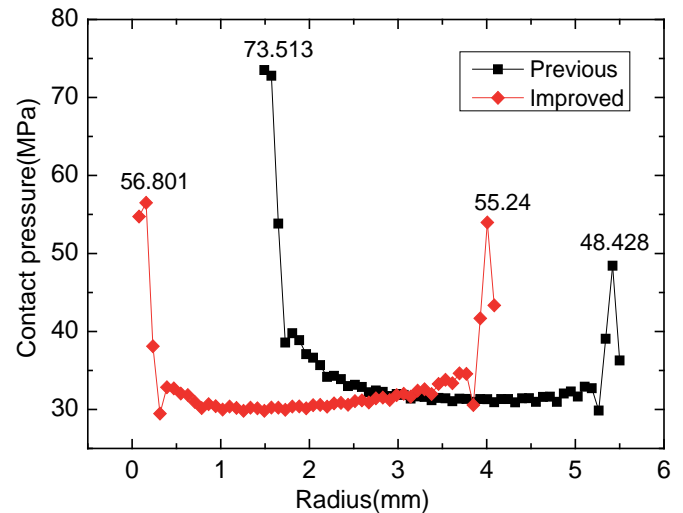


Fig. 8. Comparison of seal contact pressure

### SEALING PERFORMANCE TEST

It is difficult to obtain seal contact pressure through experiments. However, the higher contact pressure is the more the friction heat is, so the contact pressure distribution is consistent with temperature distribution, and the interface temperature for the rotor can be measured by three thermocouples at different radius. The seal sample is shown in Fig.8, and the head seal and cone insert are made of stainless steel, after low temperature plasma carburizing, the surface hardness, wear resistance and fatigue capability of stainless steels are largely increased. The schematic of the mechanical seal test rig is shown in Figure 10. The two sides of the cylinder are the lubricant and the water, and an spring in the cylinder can ensure that the lubricant pressure is 0.5 MPa higher than that of the water pressure, the seal leakage can be calculated through the piston area and the piston displacement which can be measured by the displacement sensor.



Fig. 9. Thermocouples installation of the rotor

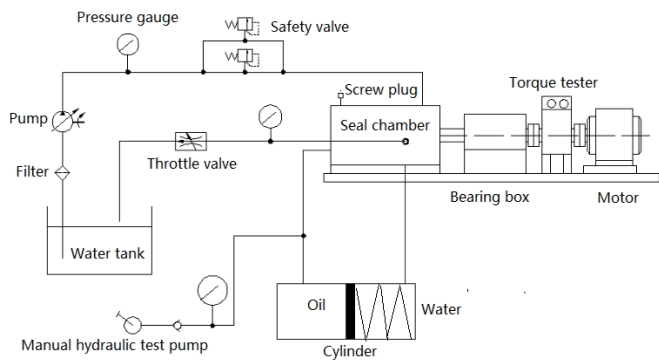


Fig. 10. Schematic of the mechanical seal test rig.

In seal testing, the water pressure is 3MPa. Figure 11 shows that the surface temperature and seal leakage rate rise increases as the seal speed increases. It can be seen that the improved seal temperature is lower than the previous, and both of the trend of the seal leakage rate and the surface temperature are almost the same. When the seal speed reaches 160r/min, the improved seal reduces the temperature to 73° and leakage rate to 2.65 mm<sup>3</sup>/s versus 76.5° and 3.01 mm<sup>3</sup>/s for the previous seal.

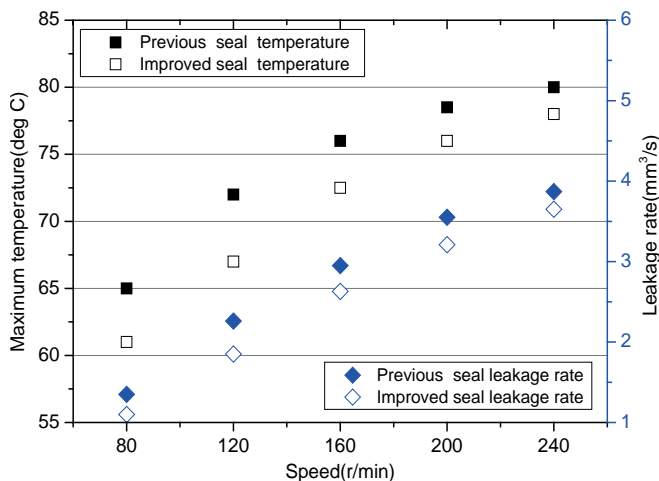


Fig. 11. Comparison of the sealing performance of the test

## CONCLUSIONS

This paper has studied the structural optimum design of offshore drilling seal using the numerical simulation and orthogonal design method to extend the sealing life. The contact pressure distribution is obtained by finite element analysis and the pressure gradient distribution is found, then the leakage rate has been computed by MATLAB. The seal parameters are improved after multi-parameter optimization. The numerical analyses and the experiment validate that the maximum contact pressure and leakage rate of the improved seal have been reduced compared to the previous.

(1) On the basis of the fluid mechanics and the numerical method, a new optimization design method of SEMS2 seal has been put forward under the offshore drilling environment.

(2) How to select seal characteristic parameters for decreasing the contact pressure and leakage rate has been analyzed. The result shows that the width of the seal interface, inside angle of the stator, length of the wedge angle, and the bottom width of the stator are important factors and play an important role in the design of the bit seal.

(3) The numerical analyses and experiment validate that the maximum contact pressure and leakage rate for the improved seal have been reduced compared to the previous, thus the optimization method for the bit seal proves to be correct.

(4) Furthermore, the ideal single seal is proposed to have the following characteristics: a more uniform contact pressure distributions to reduce wear and to prolong seal life, and a larger contact pressure on the outer edge to prevent the abrasive particles from coming through.

## ACKNOWLEDGEMENTS

This work supported by Research Program supported by the Education Department of Sichuan Province (No.16ZA0062) and the Project of Science and Technology Department of Sichuan Province of China (2014JY0229).

## REFERENCES

- Hugo M. Ayala, Douglas P. Hart. 1998. "Wear of elastomeric seal in abrasive slurries." *Wear* 220: 9-21.
- Z Huang, Q Li, Y Zhou, S Jing, et al. 2013. "Experimental research on the surface strengthening technology of roller cone bit bearing based on the failure analysis." *Eng Fail Anal* 29:12-26.
- Y Zhou, Z Huang, L Tan, et al. 2014. "Cone bit bearing seal failure analysis based on the finite element analysis." *Eng Fail Anal* 45: 292-299.
- Joseph L, Kelly Jr. 1990. "Forecasting the Life of Rock Bit Journal Bearings." *SPE* 17565. doi:10.2118/17565-PA.
- Shunhe Xiong, Richard F. Salant. 2000. "A Numerical Model of a Rock Bit Bearing Seal." *Tribology Transactions*. 43 (3): 542-548.
- Tariq A, Mahmoud AH, Tamer W, et al. 2005. "New slim hole technology maximizes productivity in Middle East horizontal drilling programs." *SPE* 92376. doi:10.2118/1105-0058-JPT.
- Karen Bybee. 2006. "Step Change in Performance: Upgraded Bit Technology Improves Drilling Economics." *SPE* 103074. doi:10.2118/1206-0078-JPT.

8. SP Asok, K Sankaranarayanan, T Sundararajan, K Rajesh, GS Ganeshan. 2007. "Neural network and CFD-based optimisation of square cavity and curved cavity static labyrinth seals." *Tribology International* 40(7): 1204-1216.
9. X Ni, Z Zhou, X Wen, L Li. 2011. "The use of Taguchi method to optimize the laser welding of sealing neuro-stimulator." *Optics & Lasers in Engineering* 49(3): 297-304.
10. CT Li, SJ Wu, WL Yu .2014. "Parameter design on the multi-objectives of PEM fuel cell stack using an adaptive neuro-fuzzy inference system and genetic algorithms." *International Journal of Hydrogen Energy* 39(9): 4502-4515.
11. Ping C.Sui, Seth Anderle. 2011. "Optimization of contact pressure profile for performance improvement of a rotary elastomeric seal operating in abrasive drilling environment." *Wear* 271:2466-2470.
12. Beomkeun K, Seong BL, Jayone L, et al. 2012. "A comparison among Neo-Hookean model, Mooney-Rivlin model, and Ogden Model for chloroprene rubber." *Int J Precis Eng Manuf* 13(5):759-764.
13. T Schmidt, M Andre, G Poll. 2010. "A transient 2D-finite-element approach for the simulation of mixed lubrication effects of reciprocating hydraulic rod seals." *Tribology International* 43(10):1775-1785.
14. C Watanabe, A Nagamatsu, C Griffy-Brown. 2003. "Behavior of technology in reducing prices of innovative goods—an analysis of the governing factors of variance of PV module prices." *Technovation* 23(5): 423-436.
15. Xiaohong Jia, Fei Guo, Le Huang, Richard F Salant. 2013. "Parameter analysis of the radial lip seal by orthogonal array method." *Tribology Int* 64:96-102.
16. H.Zhao, G.C.Barber, Q.Zou. 2002. "A study of flank wear in orthogonal cutting with internal cooling." *Wear* 253:957-962.
17. W.H. Yang, Y.S. Tang. 1998. "Design optimization of cutting parameters for turning operations based on the Taguchi method." *J. Mater. Process. Technol* 84:122-129.

## CONTACT WITH THE AUTHORS

**Yi Zhang**

School of Mechatronic Engineering  
Southwest Petroleum University  
Chengdu 610500  
**CHINA**

# A NOVEL MULTI-OBJECTIVE DISCRETE PARTICLE SWARM OPTIMIZATION WITH ELITIST PERTURBATION FOR RECONFIGURATION OF SHIP POWER SYSTEM

Lingjie Zhang<sup>\*</sup>

Jianbo Sun<sup>1</sup>

Chen Guo<sup>2</sup>

<sup>1</sup> Marine Engineering College, Dalian Maritime University, China

<sup>2</sup> Information Science and Technology College, Dalian Maritime University, China

\* corresponding author

## ABSTRACT

*A novel multi-objective discrete particle swarm optimization with elitist perturbation strategy (EPSMODPSO) is proposed and applied to solve the reconfiguration problem of shipboard power system (SPS). The new algorithm uses the velocity to decide each particle to move one step toward positive or negative direction to update the position. An elitist perturbation strategy is proposed to improve the local search ability of the algorithm. Reconfiguration model of SPS is established with multiple objectives, and an inherent homogeneity index is adopted as the auxiliary estimating index. Test results of examples show that the proposed EPSMODPSO performs excellent in terms of diversity and convergence of the obtained Pareto optimal front. It is competent to solve network reconfiguration of shipboard power system and other multi-objective discrete optimization problems.*

**Keywords:** Shipboard power system, Reconfiguration, Multi-objective, Discrete PSO, Elitist perturbation

## INTRODUCTION

Reconfiguration of an electrical network in ship power system (SPS) refers to the ability of ship power system to redirect power by closing or opening the breakers related to the loads in the event of a component failure, fault or generator loss, its main task is to maximize the survivability, security and reliability of ships[1]. The generation capacity and ship scale keep enlarging in space with the application of high power density integrated generating system, DC medium voltage transmission, zonal distribution system, power conversion device, and the high power electric propulsion system, which makes it more and more difficult to reconfigure the SPS effectively[2].

Reconfiguration of SPS is a typical discrete, nonlinear, NP complete combinatorial optimization problem with multiple objectives and multiple constraints[3]. The traditional methods based on how to reduce the network loss of the

land power system do not work well on the ship[4]. Hence, additional objectives, such as load balance, transmission, and stability margins have been considered when dealing with the reconfiguration of SPS. While in solving this kind of multi-objective reconfiguration problems, the main approach adopted in traditional methods is: firstly, converting the multi-objective optimization problems (MOP) to the single objective optimization problems (SOPs) through a certain weight vector which reflects the priority between the objectives, then, utilizing the computational intelligence algorithms to optimize the SOPs[5]. Up to now, lots of single objective optimization algorithms (SOAs) are proposed and applied to reconfigure the SPS, including genetic algorithms, particle swarm optimization (PSO), differential evolution, ant colony optimization, hybrid approach and some other heuristic algorithms[6-12].

However, the reconfiguration solutions obtained by the SOAs could not always satisfy the requirements under

the uncertain circumstances. On one hand, due to the different nature of each objective, it is difficult to make quantitative analysis when converting the MOPs to SOPs. On the other hand, the distribution of the coefficients in the weight vector between the objectives relies mainly on subjective experience and lack theoretical support[13]. Since the MOPs always contain conflicting objectives, there is no single optimal solution but a set of Pareto optimal solutions as a result[14]. Fortunately, multi-objective optimization algorithms(MOAs) based on Pareto dominance are proposed by researchers to solve the MOPs. Among them, the multi-objective particle swarm optimization(MOPSO), which has a fast convergence speed and simple structure, seems to be one of the most potential method[15]. The challenge remained in MOPSO is how to effectively and efficiently achieve a better balance between convergence and diversity of the swarm[16]. More research works need to be done to handle the multi-objective reconfiguration problem of SPS.

Based on the above analysis, this paper presents a novel multi-objective discrete particle swarm optimization with elitist perturbation strategy(EPSMODPSO) to solve the multi-objective reconfiguration problem of SPS. While in establishing the mathematical model of SPS, the power system homogeneity index is adopted as an auxiliary evaluation of the obtained Pareto optimal solutions. To achieve the conversion between the multiple discrete states(0,1,2), the particle's velocity value is utilized as the probability to determine the particle to move one step in the positive or negative direction. An elitist perturbation strategy(EPS), in which several dimensions are selected to be perturbed, is also proposed to help the algorithm to improve its local searching ability and jumping out ability. In the external archive updating process, the crowding distance of the obtained Pareto optimal solutions in objective space are calculated to keep the archive a good diversity.

## RECONFIGURATION MATHEMATICAL MODEL OF SPS

### RELATED WORK

Generally, a multi-objective optimization problem can be described as follow:

$$\min F(x) = [f_1(x), f_2(x), \dots, f_m(x)] \quad (1)$$

where  $x=(x_1, x_2, \dots, x_m)$  is a n-dimensional vector bounded in the decision space  $\Omega$ ,  $m$  is the number of objective functions and the mapping function  $F: \Omega \rightarrow R^m$  defines  $m$  objective functions bounded in the objective space  $R^m$ . The objectives may contradict each other, thus the best trade-offs among the objectives can be defined in terms of Pareto optimality.

**Definition 1.** (Pareto dominance): a decision vector  $x$  is said to dominate another decision vector  $y$  (noted as  $x \succ y$ ) if and only if  $\{\forall i \in \{1, 2, \dots, m\}: f_i(x) \leq f_i(y)\} \wedge \{\exists i \in \{1, 2, \dots, m\}: f_i(x) < f_i(y)\}$ .

**Definition 2.** (Pareto optimal): a solution  $x$  is said to be Pareto optimal if and only if  $\neg \exists y \in \Omega: y \succ x$ .

**Definition 3.** (Pareto optimal set, PS): The set of PS is defined as:  $PS = \{x \in \Omega \mid \neg \exists y \in \Omega: y \succ x\}$ .

**Definition 4.** (Pareto front, PF): The PF is defined as:  $PF = \{F(x) \mid x \in PS\}$ .

### THE RECONFIGURATION FORMULATION

Modern SPS usually consists of several generators and lots of loads, and interconnected by buses and breakers into a ring or network structure. The critical loads are supplied with two power circuit: the normal circuit and the standby circuit. Some critical are directly connected to the main buses to guarantee the power supply priority.

#### Objective 1: minimize the load loss of SPS

SPS requires the maximum restoration of loads with a certain priority after network reconfiguration, the loads are divided into 3 grades by priority. The objective function to minimize the load loss is defined as follow:

$$\min f_1 = \lambda_1 \sum_{i=1}^{N_1} (1-x_i) L_{g1i} + \lambda_2 \sum_{j=1}^{N_2} (1-x_j) L_{g2j} + \lambda_3 \sum_{k=1}^{N_3} (1-x_k) L_{g3k} \quad (2)$$

Where  $f_1$  is the total loss of loads;  $N_1$ ,  $N_2$  and  $N_3$  are the total numbers of each grade loads, the toward number of loads is  $N_L = N_1 + N_2 + N_3$ ;  $L_{g1i}$ ,  $L_{g2j}$  and  $L_{g3k}$  are the 3 grade loads;  $\lambda_1$ ,  $\lambda_2$  and  $\lambda_3$  are the weight coefficients which indicate the priority of each grade loads;  $x_i$ ,  $x_j$  and  $x_k$  are the Boolean power state of the loads.

#### Objective 2: minimize the switching operation cost

The switching operation cost(SOC) is an important index to measure the rapidity of the fault recovery solutions, and SPS requires the total operation times of switches as fewer as possible. The objective function to minimize the SOC is described as follow:

$$\min f_2 = \theta_1 S_1 + \theta_2 S_2 \quad (3)$$

Where  $\theta_1$  and  $\theta_2$  are the weight coefficients of automatic switches and manual switches;  $S_1$  and  $S_2$  are the total numbers of each kind of switches.

It is necessary to mention that, the switching of the generator is determined by the energy management system according to the actual situation of the ship, and it takes a long time to put the generator into work. While in the emergency conditions, all the generators are required to be operated in parallel to protect the power supply. Hence, the switching operation of the generators will not be considered in this study.

## CONSTRAINTS

### Constraint 1: switching constraint

For the loads can be restored, there is only one closure between the normal power supply path and the alternative path. Then, the constraint is defined as:

$$z_{i\alpha} + z_{i\beta} = 1 \quad (4)$$

Where  $i = 1, 2, \dots, \Omega$ ,  $\Omega$  is the number of transfer switches;  $z_{i\alpha}$  and  $z_{i\beta}$  are the Boolean state of the normal switch and the alternative switch.

### Constraint 2: branch capacity constraint.

The load of each branch cannot exceed its permission capacity.

$$y_i S_{C_i} \leq C_i \quad (5)$$

Where  $i = 1, 2, \dots, N_f$  is the index number of the branches,  $N_f$  is the number of the branches;  $S_{C_i}$  is the needed capacity of branch  $i$  after reconfiguration;  $y_i$  is the Boolean state of each branch;  $C_i$  is the rated capacity.

## THE AUXILIARY EVALUATION INDEX

Since the optimization result of MOP is a set of Pareto optimal solutions, an auxiliary evaluation index of the obtained Pareto solutions is needed to help the decision makers to choose the appropriate solutions. The power system homogeneity is an effective approach to evaluate the ability of the power system to deal with all kinds of uncertain factors[17]. The larger the index value, the better the reliability and economy of the system. Assume that the load rate of the power line as  $L = [L_1, L_2, \dots, L_{NL}]$ , and the load rate  $L_i$  of branch  $i$  is defined as :

$$L_i = P_i / P_{i,\max} \quad (6)$$

Where  $P_i$  is the working power of breach  $i$ , and  $P_{i,\max}$  are the maximum capacity.

Then the power system state homogeneity  $H$  is defined as:

$$H = 1 - std(L) \quad (7)$$

Where  $std$  is the standard deviation function.

## EPSMODPSO

The basic MOPSO algorithm has a simple structure and a fast convergence speed, it is easy to realize through

programming. However, due to the sensitivity to the initial value and the weak local search ability, the diversity of the population is poor and it is easy to fall into local extremum when dealing with complex MOPs. Therefore, this paper improves the algorithm, and proposes a novel multi-objective discrete particle swarm optimization with elitist perturbation strategy (EPSMODPSO).

## MODPSO

Traditional PSO uses the personal best ( $pBest$ ) along with the global best ( $gBest$ ) or local best ( $lBest$ ) to guide the member particles search in the decision space. However, global PSO may be unable to locate the Pareto front because there is no single optimal solution could be selected as  $gBest$  or  $lBest$  which optimizing all objective functions simultaneously. Thus, we utilize the local best ( $lBest$ ) to guide the member particles. The  $lBest$  is randomly selected from the external archive in each iteration, it is a effective approach to keep the swarm a good diversity. The iteration function is described as follow:

$$v_{id}(t+1) = \omega v_{id}(t) + c_1 r_1 (pBest_{id} - x_{id}(t)) + c_2 r_2 (lBest_{id} - x_{id}(t)) \quad (8)$$

$$x_{id}(t+1) = x_{id}(t) + sign(v_{id}(t+1)) \quad if \quad rand < sigm(v_{id}(t+1)) \quad (9)$$

Where  $i = 1, 2, \dots, S$ ,  $S$  is the number of particles;  $d = 1, 2, \dots, D$ ,  $D$  is the maximum dimension of the decision space;  $\omega$ ,  $c_1$  and  $c_2$  are the coefficients;  $r_1$  and  $r_2$  are two random numbers within  $[0, 1]$ ;  $v$  and  $x$  are the velocity vector and position vector;  $sigm(v) = abs(2 / (1 + exp(-vt / T_{\max}))) - 1$ ,  $abs()$  is the absolute value function;  $t$  is iteration steps;  $sign()$  is the sign function.

## ELITIST PERTURBATION STRATEGY

The elitist particles are employed to guide the group members approaching to the Pareto optimal front. When the objective functions are complex, there may be many local optimal solutions in the solution space. These solutions are easy to lead the population to fall into the local traps, and make the algorithm enter the stagnation condition. What's more, when the optimal area of the MOP is relatively smooth, it is difficult for the population to improve the search accuracy without additional search strategy. Based on the above situation, an elitist perturbation strategy is proposed to increase the local search ability of the population.

Since the elitist particles are already the optimal solutions obtained by the current population, the current population can no longer provide more effective search information for the elitist particles. Firstly, generate a random integer  $c$ , let  $E = \{E_1, E_2, \dots, E_c\}$ , where  $E_1, E_2, \dots, E_c$  are randomly selected from  $[1, 2, \dots, D]$ . Then, for each selected dimension of one elitist particle, perturb as follow:

$$lBest_{E_k}^{esp} = lBest_{E_k} + (\max(X_{E_k}) - \min(X_{E_k})) \cdot N(\mu, \sigma^2) \quad (10)$$

Where  $k = 1, 2, \dots, c$ ;  $N(\mu, \sigma^2)$  is a random number of normal distribution with a mean value  $\mu = 0$ , standard deviation  $\sigma$  is calculated as :

$$\sigma = R_{\max} - (R_{\max} - R_{\min}) \cdot t / T_{\max} \quad (11)$$

Where  $t$  is the current iteration step,  $T_{\max}$  is the maximum step;  $R_{\max} = 1$  and  $R_{\min} = 0.1$  are the maximum and minimum disturbance limit.

The random integer number  $c$  is generate as follow:

$$c = \text{ceil}(\text{Rand} \cdot (1 + 3 \cdot t / T_{\max})) \quad (12)$$

Where  $\text{ceil}()$  is a ceiling function, and  $\text{Rand}$  is a random number within  $[0, 1]$ .

### ARCHIVE UPDATE

While in updating the external archive, the Pareto dominance relationship between the obtained optimal solutions and the archive solutions are checked firstly, then the non-dominanced solutions will be save into the archive. Since the number of the Pareto optimal solutions of a MOP could be very large, which will rapidly increase the computational time, it is necessary to limit the size of the archive. When the number of the obtained Pareto optimal solutions exceed the limit size, the European distance in objective space between the solutions will be calculated, and the most crowding solutions will be deleted until the number of the optimal solutions meets the requirement.

### THE COMPLETE FRAMEWORK

As shown in Figure 1 is the complete framework of the proposed EPSMODPSO. In EPSMODPSO, a population is generated and initialized at first, then, the algorithm goes into the iterative process. When the iteration of the algorithm ends, output the optimal solutions in the archive.

| EPSMODPSO |   |
|-----------|---|
| 1:        | Randomly generate a swarm with N particles ;  |
| 2:        | Initial the position $x = \{x_1, x_2, \dots, x_N\}$ , and the velocity $v = \{v_1, v_2, \dots, v_N\}$ ; |
| 3:        | Calculate the objective function $F(x)$ with equation 2~5 ;   |
| 4:        | Initial the archive with position vector $x$ ;  |
| 5:        | <b>For</b> $t=1$ to $T_{\max}$  |
| 6:        | <b>For</b> $i = 1$ to $N$   |
| 7:        | $lBest_i$ = randomly select an elitist solution from the archive ;                                      |
| 8:        | Update $v_i$ and $x_i$ with equation 8,9 ;  |
| 9:        | Calculate objective function $F(x_i)$ with equation 2~5 ;   |
| 10:       | Perform the EPS strategy on $lBest_i$ with equation 10~12 ;   |
| 11:       | <b>End for</b> ;  |
| 12:       | Update the archive with all the generated positions ;   |
| 13:       | <b>End for</b>  |
| 14:       | Output the archive solutions;   |
| 15:       | Calculate the auxiliary index $H$ of obtained solutions with equation 6,7 ;                             |

Fig. 1. The complete framework of EPSMODPSO

## RECONFIGURATION OF SPS BASED ON EPSMODPSO

Considering a classical model of SPS as shown in Figure 2, and the related topological parameters are present in Table1. The generators are connected through the main buses, parts of critical loads with high priority are directly powered by the main buses, and the remaining loads are powered through the regional buses. In figure 2, symbol G represents the generators, LC is the connecting line between the main buses. The critical loads are powered with two supply lines, the solid lines represent the normal power supply lines, and the dotted lines represent the alternative lines. “•” is the endpoint of a device or a breach, “↓” represents the load L, “□” represents the circuit breaker CB. ABT is the automatic breaker transfer, and MBT is the manual breaker transfer.

The reconfiguration of SPS is a discrete switching problem with multiple objectives, while in the use of EPSMODPSO to solve this problem, it is necessary to discrete the variables of the switches in the SPS model. According to the characteristics of SPS, in this paper, the encoding states of 0,1,2 are utilized for the transfer switches, 0,1 coding for the other switches. 0 represents the loss of power or unloading, 1 represents the loads are powered by the normal lines, 2 represents the loads are powered by the alternative lines. Each dimension of a particle represents a switch, the number of dimensions depends on the total number of switches.

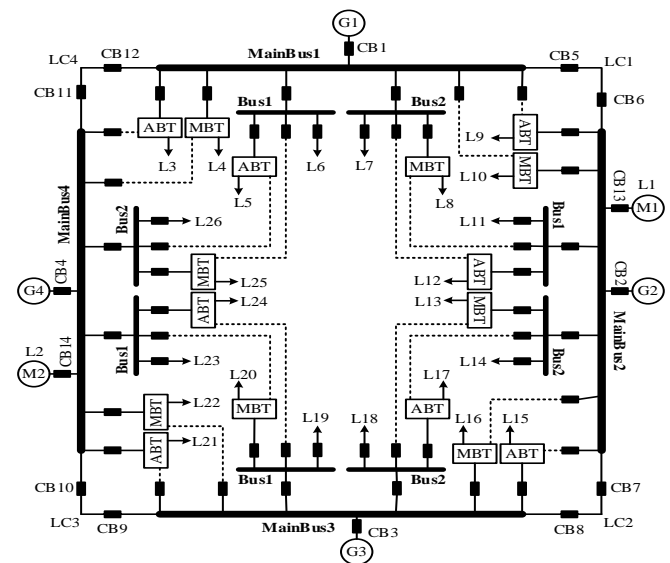


Fig. 2. A classical shipboard power system

Tab. 1. Parameters of elements

| Number         | Rated power | Priority | Number          | Rated power | Priority |
|----------------|-------------|----------|-----------------|-------------|----------|
| L <sub>1</sub> | 5.0         | 2        | L <sub>18</sub> | 0.022       | 3        |
| L <sub>2</sub> | 5.0         | 2        | L <sub>19</sub> | 0.075       | 3        |
| L <sub>3</sub> | 0.168       | 1        | L <sub>20</sub> | 0.086       | 2        |
| L <sub>4</sub> | 0.208       | 2        | L <sub>21</sub> | 0.135       | 1        |
| L <sub>5</sub> | 0.067       | 1        | L <sub>22</sub> | 0.217       | 2        |
| L <sub>6</sub> | 0.061       | 3        | L <sub>23</sub> | 0.027       | 3        |
| L <sub>7</sub> | 0.052       | 3        | L <sub>24</sub> | 0.069       | 1        |

| Number          | Rated power | Priority | Number          | Rated power | Priority |
|-----------------|-------------|----------|-----------------|-------------|----------|
| L <sub>8</sub>  | 0.063       | 2        | L <sub>25</sub> | 0.023       | 2        |
| L <sub>9</sub>  | 0.163       | 1        | L <sub>26</sub> | 0.031       | 3        |
| L <sub>10</sub> | 0.163       | 2        | G <sub>1</sub>  | 1           | -        |
| L <sub>11</sub> | 0.062       | 3        | G <sub>2</sub>  | 6           | -        |
| L <sub>12</sub> | 0.030       | 1        | G <sub>3</sub>  | 1           | -        |
| L <sub>13</sub> | 0.081       | 2        | G <sub>4</sub>  | 6           | -        |
| L <sub>14</sub> | 0.021       | 3        | LC <sub>1</sub> | 3           | -        |
| L <sub>15</sub> | 0.123       | 1        | LC <sub>2</sub> | 3           | -        |
| L <sub>16</sub> | 0.225       | 2        | LC <sub>3</sub> | 3           | -        |
| L <sub>17</sub> | 0.077       | 1        | LC <sub>4</sub> | 3           | -        |

## SIMULATION STUDIES

The settings of the controlling parameters for EPSMODPSO are summarized as : the particle number  $N = 200$  , the maximum iteration  $T_{max} = 100$  , the weight coefficient  $\omega$  linearly decrease from 0.9 to 0.4 with the iterative steps, coefficients  $c_1 = c_2 = 2$ . The priority weight coefficients of the loads  $\lambda_1 = 1000$  ,  $\lambda_2 = 5$  ,  $\lambda_3 = 1000$ . The weight coefficients of the switches  $\theta_1$  and  $\theta_2$  are all set as 1 in this test. The initial operation state of SPS is : generator G1,G3,G4 are paralyzed through the main buses, generator G2 is out of service. The MainBus2 are powered through the connecting switches CB7 and CB9. The connecting switches CB2,CB5 and CB13 are broke off, and the other switches are all closed. All the loads are powered through the normal breach lines.

### FAULT EXAMPLE 1

Fault description: contacting line LL3 occurs a short-circuit fault, switch CB9, CB10 and CB3 are broke off for protection, generator G3 quits operation, the loads of MainBus2 and MainBus3 lose the power.

Tab. 2. Reconfiguration results of fault example 1

| No. | Reconfiguration solutions  | $f_1$  | $f_2$ | H(%)  |
|-----|--|--------|-------|-------|
| 1   | G1,G4 run in parallel; close switch CB5, MainBus2 is restored via the interconnection switches; unload L2                    | 50     | 2     | 86.20 |
| 2   | G1,G4 run in parallel; close switch CB5, MainBus2 is restored via the interconnection switches; unload L4,L7                 | 26.092 | 3     | 88.67 |
| 3   | G1,G4 run in parallel; close switch CB5, MainBus2 is restored via the interconnection switches; unload L6,L10,L23            | 25.903 | 4     | 92.19 |
| 4   | G1,G4 run in parallel; close switch CB5, MainBus2 is restored via the interconnection switches; unload L6,L7,L11,L19         | 25.250 | 5     | 90.82 |
| 5   | G1,G4 run in parallel; close switch CB5, MainBus2 is restored via the interconnection switches; unload L6,L7,L11,L14,L18,L26 | 25.249 | 7     | 90.99 |

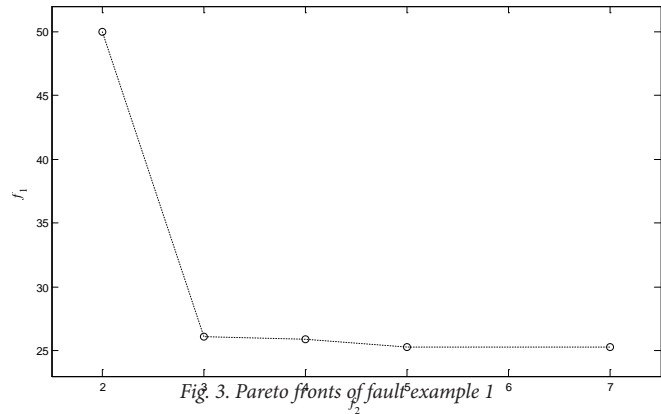


Fig. 3. Pareto fronts of fault example 1

The reconfiguration results of Fault Example 1 using EPSMODPSO are presented in Table 2, and the Pareto optimal front in Figure 3. Analyzing on the Fault Example 1, it can be seen that, the loads of MainBus2 and MainBus3 can only be restored by closing the switch CB5. However, in this situation, the capacity of the running generators is  $G1+G4=7$ , while the total loads are 7.249. Therefore, in the reconfiguration solution 1, after the closure of CB5, the load L2 is also cut off to ensure the power supply for the SPS. Solution 1 holds the least operation costs of function  $f_2$  , but the largest load loss of function  $f_1$  . Solution 5 holds the least loads loss of function  $f_1$  , but the operation cost is the largest in all the solutions at the same time, because it need to cut off 6 loads of grade 3 in priority, including L6,L7and the others. Solution 2~4 are the trade-offs, while solution 3 holds the highest auxiliary index value  $H$ , which indicates that the load ratio of the connecting lines is more well-distributed.

### FAULT EXAMPLE 2

Fault description: MainBus2 occurs a short-circuit fault, the connecting switch CB7 is broke off for protection, MainBus2 loses the power.

Tab. 3. Reconfiguration results of fault example 2

| No. | Reconfiguration solutions  | $f_1$  | $f_2$ | H(%)  |
|-----|--|--------|-------|-------|
| 1   | Transfer L9 to the standby power lines; Unload L10,L11,L12,L13,L14 | 56.303 | 1     | 95.90 |
| 2   | Transfer L9,L12to the standby power lines; Unload L10,L11,L13,L14  | 26.303 | 2     | 95.19 |
| 3   | Transfer L9,L10,L12 to the standby power lines; Unload L11,L13,L14 | 25.488 | 3     | 95.56 |
| 4   | Transfer L9,L10,L12,L13 to the standby power lines; Unload L11,L14 | 25.083 | 4     | 96.99 |

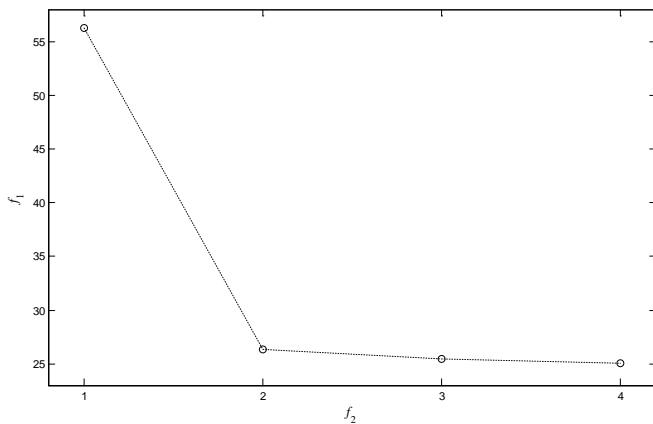


Fig. 4. Pareto fronts of fault example 2

Solve the multi-objective fault reconfiguration problem using EPSMODPSO, the obtained Pareto optimal solutions are presented in Table 3, and the Pareto optimal front is shown in Figure 4. Through Fault Example 2, it is clear to see that, there is no way to restore the MainBus2, thus, the loads of MainBus2 have to transfer to the alternative power lines. Therefore, in solution 1, the largest load L9 with grade 1 in priority is transferred to its standby power line. Solution 1 holds the least operation cost of all the solutions. In solution 4, 4 loads including L9, L10 and the others are transferred to the standby power lines, and the L11, L14 are cut off because there is no alternative line to restore. Solution 4 holds the least loss of loads, but the largest operation cost and auxiliary index value  $H$  at the same time. Solution 2 and 3 are two trade-offs.

## DISCUSSION

From the test results it can be seen that the proposed EPSMODPSO is very excellent in terms of searching accuracy, diversity and convergence, which makes the EPSMODPSO possible to satisfy the demands of MOPs. The EPS strategy adopted to increase the local search ability and jumping out ability of the swarm is very helpful. In the discrete decision space, the traditional perturbation strategies which select only one dimension are not always effective to help the algorithms to jumping out the local traps. Taking two dimensional discrete decision space as an example, assume that "01" is the current discrete binary state, while the global optimal state is "10". If state "00" and "11" are not accepted as a Pareto optimal state, then, the single dimensional perturbation can never transfer from state "01" to state "10" within one step. Therefore, the proposed EPS employed an inter  $c$  to select several dimensions to perform the perturbation operation at the same time, which could increase the possibility to jump out the local traps. To achieve the conversion between the multiple discrete states (0,1,2), the particle's velocity value is utilized as the probability to determine the particle to move one step in the positive or negative direction. This strategy simplified the coding of the discrete variables, and help the algorithm to realize the encode of switches with multiple state (0,1,2).

The test results indicate that the proposed EPSMODPSO is competent to solve the reconfiguration problem of SPS and obtain a Pareto optimal front with good diversity. It is necessary to mention that, since the EPSMODPSO exhibited superior performance in the experimental results reported in the previous subsections, our future study will further enhance the performance of EPSMODPSO, and extend it for tackling MOPs with more objectives. Moreover, the future research direction can also be pursued on the present study to investigate the performance improvement with parallel computation technology.

## CONCLUSION

This paper presents a novel multi-objective discrete particle swarm optimization with elitist perturbation strategy (EPSMODPSO) to solve the multi-objective reconfiguration problem of SPS. To achieve the conversion between the multiple discrete states (0,1,2) of the switches, the particle's velocity value is utilized as the probability to determine the particle to move one step in the positive or negative direction. The proposed elitist perturbation strategy (EPS) in which several dimensions are selected to be perturbed, has been proved to be able to improve the local searching ability and jumping out ability of the particle swarm. While in establishing the mathematical model of SPS, the power system state homogeneity is adopted as an auxiliary evaluation of the obtained Pareto optimal solutions to help the decision makers choose the appropriate solutions. In the external archive updating process, the crowding distance of the obtained Pareto optimal solutions in objective space are calculated to keep the archive a good diversity. Test results of examples show that the proposed EPSMODPSO performs excellent in terms of reliability, efficiency and convergence. It is competent to solve network reconfiguration of shipboard power system and other multi-objective discrete optimization problems.

## ACKNOWLEDGMENTS

The authors express their sincere thanks to the associate editor and the reviewers for their significant contributions to the improvement of the final paper. The research was supported by National Natural Science Foundation of China (61374114).

## REFERENCES

1. Z. Wang, L. Xia, Y. J. Wang, 2014. Multiagent and particle swarm optimization for ship integrated power system network reconfiguration. *Mathematical Problems in Engineering*, 2014(3):1-7.
2. S. Bose, S. Pal, B. Natarajan, et al, 2012. Analysis of optimal reconfiguration of shipboard power systems. *IEEE Transactions on Power Systems*, 27(1):189-197.

3. Sanjoy Das, Sayak Bose, Siddharth Pal, et al, 2012. Dynamic reconfiguration of shipboard power systems using reinforcement learning. *IEEE Transactions on Power Systems*, 27(1):189-197.
4. T. Zhao, Y. Zhang, Z.Q.Zhang, 2015. Power system reconstruction based on hierarchical and partitioned restoration. *Automation of Electric Power Systems*, 39(14):30-67.
5. H. Li, Q. Zhang, 2009. Multiobjective Optimization Problems With Complicated Pareto Sets, MOEA/D and NSGA-II, *IEEE Trans. Evol. Comput.* 13 (2) 284-302.
6. X. H. Wang, J. J. Li, J. M. Xiao, 2007. Network reconfiguration of the shipboard power system based on gradient discretization method of particle swarm optimization. *Transactions of China Electrotechnical Society*, 22(12):140-145.
7. J. Huang, X. F. Zhang, Z. H. Ye, 2011. Method of restoration for integrated ship power system based on multi-agent systems. *Proceedings of the CSEE*, 31(13):71-78.
8. L. J. Yang, J. C. Liu, Z. G. Lu, et al, 2012. Fault restoration of multi-objective distribution system based on multi-Agent evolutionary algorithm. *Power System Protection and Control*, 40(4):54-58.
9. X. X. Yang, X. F. Zhang, Y. Zhang, 2003. The study of network reconfiguration of the shipboard power system based on heuristic genetic algorithm. *Proceedings of the CSEE*, 23(10):42-46.
10. D. Das, 2006. A fuzzy multiobjective approach for network reconfiguration of distribution systems. *IEEE Transactions on Power Delivery*, 21(1):202-209.
11. Y. J. Jiang, J. G. Jiang, S. T. Qiao, 2011. Intelligent Service Restoration of Shipboard Power Network Using Nature Multiobjective Evolutionary Algorithm. *Proceedings of the CSEE*, 31(31):118-124.
12. Z. H. Zhang, N. L. Tai, 2011. Intelligent approach for service restoration of distribution system with distributed generations. *Power System Protection and Control*, 39(14):79-85.
13. J. Huang, X. F. Zhang, Y. Chen, et al, 2010. Multiobjective optimal model of service restoration for integrated ship power system and its application. *Transactions of China Electrotechnical Society*, 25(3):130-137.
14. Y. J. Wang, Y. P. Yang, 2009. Particle swarm optimization with preference order ranking for multi-objective optimization. *Information Sciences*, 179(12):1944-1959.
15. Q. Z. Lin, J. Q. Li, Z. H. Du, et al, 2015. A novel multi-objective particle swarm optimization with multiple search strategies. *European Journal of Operational Research*, 247(3):732-744.
16. J. L. Wang, L. Xia, Z. G. Wu, 2012. Multiobjective optimal network reconfiguration of shipboard power system based on non-dominated sorting genetic algorithm-II. *Power System Technology*, 36(11):58-64.
17. W. Q. Sun, C. M. Wang, Y. Zhang, et al, 2014. Analysis and Evaluation on Power System Operation Homogeneity. *Transactions of China Electrotechnical Society*, 29(4):173-180.
18. M. Nelson, PE. Jordan, 2015. Automatic reconfiguration of a ship's power system using graph theory principles. *IEEE Transactions on industry applications*, 51(3):2651-2656.
19. D. Q. Bi, F. Zhang, X. G. Zeng, et al, 2015. Research on fault restoration of shipboard DC zone distribution systems. *Power System Protection and Control*, 43(19)60-65.

#### CONTACT WITH THE AUTHORS

**Lingjie Zhang**

Marine Engineering College  
Dalian Maritime University  
Dalian 116026  
**CHINA**

## THE PORT SERVICE ECOSYSTEM RESEARCH BASED ON THE LOTKA-VOLTERRA MODEL

Wenjuan Li<sup>1</sup>

Wei Liu<sup>1</sup>

Xu Xu<sup>2</sup>

Zhijun Gao<sup>1</sup>

<sup>1</sup> College of Transport and Communications, Shanghai Maritime University, China

<sup>2</sup> Business School, Shanghai Dian Ji University, China

### ABSTRACT

*Under the new normal of China's economy, the competition among the port enterprises is not only the competition of the core competence of the port, the port industry chain or the port supply chain, but also the competition of the port service ecosystem. In this paper, the concept and characteristics of the port service ecosystem is discussed, a hierarchical model of the port service ecosystem is constructed. As an extended logistic model, Lotka-Volterra model is applied to study the competitive co-evolution and mutually beneficial co-evolution of enterprises in the port service ecosystem. This paper simulates the co-evolution of enterprises in the port service ecosystem by using MATLAB programming. The simulation results show that the breadth of the niche of the enterprises is changing with the change of the competition coefficient and the coefficient of mutual benefit in the port service ecosystem. Based on that, some proposals are put forward to ensure the healthy and orderly development of the port service ecosystem.*

**Keywords:** the port service ecosystem, the niche breadth, competitive co-evolution, mutually beneficial co-evolution

### INTRODUCTION

Since the implementation of reform and opening up in the late 1970s in China, the ports have developed rapidly and the overall capacity tends to equilibrium of supply and demand, but there are structural, regional overcapacity tendencies [1] [2]. Most of the ports along the coast have common economic hinterlands and the vicious competition in the price is growing [3]. The lack of cooperation and over-competition between ports hinders the sustainable development of ports. In addition, the infrastructure in some of China's ports, especially the inland ports, cannot meet the needs of large-scale and diversified goods, and the problem of low degree of information in China's ports also affects the communication among different departments and results in lower efficiency and customer satisfaction.

The establishment of the port service ecosystem can effectively promote the connection between ports and the relevant enterprises, and also can contribute to information exchange and knowledge sharing. The competition of the port enterprises will be the competition of the ecosystem which regards the port enterprise as a core. It's an important goal of "the Belt and Road Initiatives" project to promote the development of align national and regional economic and trade. Ports are important nodes of the 21st-Century Maritime Silk Road. That will create a favourable political and economic environment for the construction of the port service ecosystem, and ports will usher in new development opportunities [4].

The term "ecosystem" was first used in a publication by British ecologist Arthur Tansley. He later refined the term, describing it as the whole system, including not only the

organism-complex, but also the whole complex of physical factors forming what we call the environment. After that, the concept of ecosystem was introduced into business research. As a famous American strategic management scientist, Moor put forward the concept of “business ecosystem” in Harvard Business Review [5]. He explained the new competition among enterprises, the symbiosis and the way of sustainable development of enterprises and environment. Moore pointed out that the enterprise ecosystem is an economic community based on interaction between organization and individual in his book “The Death of Competition” [6].

Zhao et al. discussed the basic structure of the enterprise ecosystem, analyzed the characteristics and the evolution of the enterprise ecosystem, and used the logistic model to describe the process of the evolution of the enterprise ecosystem [7]. Meanwhile, the study put forward the strategy of enterprise ecosystem evolution in according with the above. The model of tourism industry ecosystem was constructed from five aspects: material and energy source, Producers, consumers, decomposers and ecological environment [8]. Zhao summarized the concept of port strategic synergy, systematically studied the horizontal strategic cooperation and vertical strategic coordination, and then put forward the strategic integration of alliance of ports in Zhejiang province in China [9].

In 2016, China Merchants Port proposed to build a comprehensive port service ecosystem, the Shanghai Port Group also proposed to build a smart port service ecosystem in China. However, there are few literatures on the study of port service ecosystem. This paper will study the concept of port service ecosystem, hierarchical model and co-evolution of the port service ecosystem.

## CONNOTATION AND CHARACTERISTICS OF THE PORT SERVICE ECOSYSTEM

### THE CONCEPT OF THE PORT SERVICE ECOSYSTEM

Combined the concept of business ecosystem with enterprise ecosystem, port service ecosystem can be defined. In order to ensure its sustainable development, port enterprises integrate the upstream and downstream port industry chain and connect the various port elements. Port service ecosystem is a sort of economic association that is formed by ports and related organizations. Its members include port enterprises, shipping companies, freight forwarding companies, shippers, market intermediaries, etc., to a certain extent, also include competitors. These members form value chains, and the interweaving of different chains forms a network of values. Material, energy and information flow through the value network among members [10]. The members of port service ecosystem make rational use of resources and improve the work efficiency and the ability to work together, so that the port service ecosystem is in a relatively stable dynamic

equilibrium in a certain period of time and provides quality services to customers.

### THE COMPOSITION OF THE PORT SERVICE ECOSYSTEM

In ecology, the ecosystem is divided into four levels as individual, population, community and ecosystem. Enterprise ecosystem, in analogy to natural ecosystem, consists of a variety of biological members including biological and non-biological components which are mutually dependent. The main biological members of port service ecosystem are port enterprises and populations formed by homogeneous enterprises  $\sum a_i$  (other ports within the region), customers  $\sum b_i$  (shippers, shipping companies, etc.), port service providers  $\sum c_i$  (carriers, stevedoring firms, warehousing enterprises, logistics service providers, port equipment maintenance, etc.), market intermediaries  $\sum d_i$  (freight forwarders, customer agents, shipping agents, shipping exchanges, port and shipping trading sites and platforms, etc.), financial institutions  $\sum e_i$  and investors  $\sum f_i$  and so on [11] [12]. In the external environment of enterprise ecosystem, there are a variety of non-biological factors, including political ecological factors  $\sum A_i$ , economic ecological factors  $\sum B_i$ , social ecological factors  $\sum C_i$ , natural ecological factors  $\sum D_i$ , etc. There are two types of relationship between populations. One is vertical relationship and the other is horizontal relationship. Port service providers, customers, port market intermediaries, etc. are vertical relations, while competitors, government departments, research institutions, other stakeholders, and other related industries or departments are horizontal relations [13].

The function of the port service ecosystem can be expressed as:

The port service ecosystem = F (biological components, non-biological components)

$$= F(\sum a_i, \sum b_i, \sum c_i, \sum d_i, \sum e_i, \sum f_i, \dots, \sum A_i, \sum B_i, \sum C_i, \sum D_i, \dots).$$

In addition, the port service ecosystem also includes the relevant institutions which set standards and relevant government departments (maritime, customs, border inspection, etc.), association representing the consumers (ship-owners' associations, shippers' associations) and suppliers' associations (logistics associations, etc.) and so on.

### THE HIERARCHICAL MODEL AND BUSINESS AREA OF THE PORT SERVICE ECOSYSTEM

If natural ecological system centered on plants and animals, and the port service ecosystem centred on port enterprises. From the aspect of the tightness and importance of biological members, the port service ecosystem can be divided into three levels as the core ecosystem, the expansion ecosystem and the complete port service ecosystem. The core of the port service ecosystem includes port enterprises, port service suppliers and port service customers. The expansion layer includes the suppliers of port service suppliers, customers of port service customers, and related industries. The simplified hierarchical model of the port service ecosystem is shown in Fig. 1.

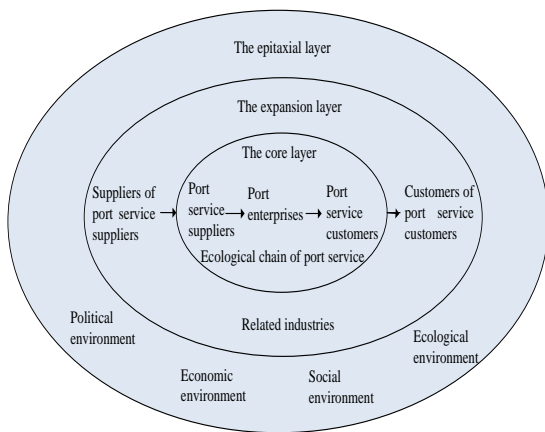


Fig. 1. The hierarchical model of the port service ecosystem

The main business of port enterprises is terminal operation and management. In recent years with the needs of development, the business of port enterprises extends to modern logistics, trade, consulting, information, insurance, finance, tourism and leisure, and others. The business domain of the port service ecosystem is shown in Fig.2 [14].

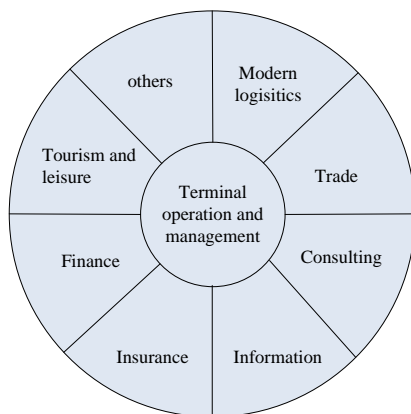


Fig. 2. The business domain of the port service ecosystem

## CHARACTERISTICS OF THE PORT SERVICE ECOSYSTEM

The existence of a series of interactions among members is not only one of the main characteristics of the biological ecosystem, but also the basic condition for the survival of species. Most of the interactions in the ecosystem are indirect, and the impact of specific interactions may be far greater than the impact on both sides of the interaction. In the interactive route, the core species is usually the node that is necessary for interaction. Port enterprises are the core species of port ecology, and the interaction of port enterprises with other members of the ecosystem (including both direct and indirect interaction) is an important feature of the port service ecosystem.

Similar to the biological ecosystem, the business ecosystem also has a large number of loosely connected participants. Each

participant gets their own required living resources from the other participants. Co-evolution is a kind of objective existence in the port service ecosystem, which is another important feature of the port service ecosystem. It is impractical for the port enterprises to develop alone if port enterprises have to develop. Port enterprises need to understand and grasp the relationship between the relevant enterprises and departments correctly and comprehensively, cooperate with other logistics service suppliers scientifically and reasonably, and ensure that these enterprises make a supplementary contribution, which thereby can enhance their own competitiveness and create more value for customers.

Another feature of the port service ecosystem is openness. Previously, the internal and external boundaries of enterprises are clear, but now the boundaries of enterprise and industries in the port service ecosystem become blurred and openness becomes more obvious. Therefore who can meet customer needs and create value for customers can be allowed in the port service ecosystem, otherwise they will be refused by the port service ecosystem.

## THE CONNOTATION OF CO-EVOLUTION OF PORT SERVICE ECOSYSTEM

### CONCEPT OF THE PORT SERVICE ECOSYSTEM SYNERGY

As a system theory, synergy has the characteristics of universality. The port service ecosystem is a port-based ecosystem, so synergy is applicable to study on the port service ecosystem. Port strategic synergy includes port horizontal strategic synergy and port vertical strategic synergy. Port horizontal strategic synergy refers to the regional port alliance of two or more port enterprises that are complementary to each other and prevent vicious competition to improve regional port competitiveness in the same area, which is mainly arterial and branch port alliance and hub port alliance. Port vertical strategic synergy refers that the port enterprises, upstream and downstream enterprises and the relevant units or departments form a port supply chain with the feature of rationalization of business and risk-sharing. Port service ecosystem synergy not only refers to the port strategy synergy, but also includes the synergy between elements of the enterprise (member) within the port service ecosystem, between the enterprise (member) and the enterprise (member), and between the enterprise (member) and the environment.

### THE NECESSITY OF STUDYING CO-EVOLUTION OF PORT SERVICE ECOSYSTEM

Port enterprise operation environment is constantly changing, and growing problems are becoming increasingly complex. Since challenges, uncertainties, risks, and crisis exist side by side, it is very necessary and beneficial to do

a systematic analysis of the development of port enterprises from the perspective of biological co-evolution. Co-evolution is an important feature of biological evolution, which emphasizes the collaboration between different populations to improve the efficiency of population use of environmental resources and improve the viability of the population. The coordinated development between enterprises constitutes the basic conditions for the survival and development of enterprises, and the evolution of an enterprise depends not only on the firm itself, but also on the evolution of other members of the ecosystem. In complex and volatile business environment, it is blind to only care about the business development of their own business. Therefore, the port enterprises need to pay close attention to the changes in other port enterprises, port service suppliers, port service customers (shipping companies, land transport companies, shippers and so on), port industry, political environment, economic environment, social environment, and natural environment of port business, and also need to make the appropriate adjustments according to these changes, to improve the adaptability to external markets [15]. Thus, it is necessary to study the co-evolution of the port service ecosystem.

## THE CONNOTATION OF CO-EVOLUTION OF THE PORT SERVICE ECOSYSTEM

The co-evolution of the port service ecosystem includes the co-evolution within the enterprises (members) of the port service ecosystem, the co-evolution between the enterprises (members), and the co-evolution between the enterprises (members) and the external environment. The co-evolution between enterprises is discussed in this paper, which includes independent evolution, competitive co-evolution, amensalism co-evolution, commensalism co-evolution, mutually beneficial co-evolution and so on. Amensalism co-evolution can be viewed as a special case of competitive co-evolution and partial cooperative co-evolution can be viewed as a special case of mutually beneficial co-evolution (as shown in 5.1.2), thus the competitive co-evolution model and the mutually beneficial co-evolution model is focus on in this paper.

## CONSTRUCTION AND SIMULATION OF COOPERATIVE EVOLUTION MODEL OF THE PORT SERVICE ECOSYSTEM

In ecological research, Lotka-Volterra model can be applied to the co-evolution among organisms, and can also be used to study the relationship among biological population group [16] [17]. In this part, this model is used to analyze the cooperative evolution mechanism between different populations of the port service ecosystem.

The ecological niche can be used to describe the cooperative evolution among enterprises and enterprises, enterprises and resources. The ecological niche refers to the

space and time position and function of each individual or population in population or community. The niche size of an enterprise is the width of the niche or niche breadth, which is the sum of all kinds of resources that can be utilized by the enterprise. If the niche breadth of the enterprise is larger, the competitiveness of the enterprise will be stronger. Niche overlap is the phenomenon that two or more enterprises of the same ecological niche share or compete for common resources. Due to the limited resources, when a number of enterprises coexist in the port ecological niche and if their niche overlaps, there will be competition for resources.

## CO-EVOLUTIONARY MODELLING

Modelling assumption:

(1) Assuming that the external environment of the port service ecosystem is unchanged, that is, without considering the impact of the external environment on the co-evolution between enterprises.

(2) Assuming that all kinds of resource elements in the port service ecosystem are constant, restricted by ecological factors  $E_i$ .

(3) Assuming that there are only two enterprises in the port service ecosystem, for enterprise 1 and enterprise 2. When enterprise 1 and enterprise 2 survive alone, following the law of Logistic.

### 1. Competitive co-evolution

$N_1, N_2$  indicate the niche breadth of enterprise 1 and enterprise 2 respectively.  $t$  represents time variable.  $r_1, r_2$  indicate that the maximum growth rate of the niche of two companies living alone respectively.  $\alpha_1$  indicates that competition coefficient of enterprise 1 to enterprise 2, that is, inhibitory effect of enterprise 2 on 1,  $0 < \alpha_1 < 1$ .  $\alpha_2$  indicates that competition coefficient of enterprise 2 to enterprise 1, that is, inhibitory effect of enterprise 1 on 2,  $0 < \alpha_2 < 1$ .  $K_1, K_2$  indicate the maximum environmental capacity or environmental load of two enterprises respectively. Competitive co-evolutionary model is established as shown in equation (1):

$$\begin{cases} \frac{dN_1}{dt} = r_1 N_1 \left(1 - \frac{N_1}{K_1} - \frac{\alpha_1 N_2}{K_1}\right) \\ \frac{dN_2}{dt} = r_2 N_2 \left(1 - \frac{N_2}{K_2} - \frac{\alpha_2 N_1}{K_2}\right) \end{cases} \quad (1)$$

In the formula (1),  $\frac{N_1}{K_1}$  is the resource space of the enterprise 1,  $\frac{\alpha_1 N_2}{K_1}$  is the resource space of enterprise 2 seizing 1.  $1 - \frac{N_1}{K_1} - \frac{\alpha_1 N_2}{K_1}$  is the residual resource space that can be used by enterprises.  $\alpha_1, \alpha_2$  reflect the degree of niche overlap. The more the value, the higher degree of niche overlaps of the two companies, the little the value, the lower degree of niche overlaps. When the values of  $\alpha_1$  and  $\alpha_2$  are infinitely close to 1, the niche of the two enterprises tends to be completely overlap. When the values of  $\alpha_1$  and  $\alpha_2$  are infinitely close to 0, the niche of the two enterprises is close to complete separation. In

the formula (1), if  $\alpha_1 = 0$  and  $0 < \alpha_2 < 1$ , or  $0 < \alpha_1 < 1$  and  $\alpha_2 = 0$ , the model is an amensalism co-evolution model.

## 2. Mutual benefit co-evolution model

Enterprises are not only competitive, but also certainly cooperation with each other in the port service ecosystems. In the process of providing transportation service, logistics service or supply chain service to customers, the mutual beneficial cooperation between the firms in the port service ecosystem is indispensable. Mutually beneficial cooperation is the basis of win-win or multi-win between enterprises and also the embodiment of the overall efficiency of the port service ecosystem. Mutual benefit co-evolution model can solve the problem of how to cooperate effectively and realize the co-evolution between enterprises.

$\beta_1$  represents the niche mutual benefit coefficient of enterprise 1 to enterprise 2,  $0 < \beta_1 < 1$ ,  $\beta_2$  represents the niche mutual benefit coefficient of enterprise 2 to enterprise 1,  $0 < \beta_2 < 1$ ,  $K_1, K_2$  indicate the maximum environmental capacity or environmental load of two enterprises respectively. Using mathematical model to establish mutually beneficial co-evolution model as shown in equation (2):

$$\begin{cases} \frac{dN_1}{dt} = r_1 N_1 \left(1 - \frac{N_1}{K_1} + \frac{\beta_1 N_2}{K_2}\right) \\ \frac{dN_2}{dt} = r_2 N_2 \left(1 - \frac{N_2}{K_2} + \frac{\beta_2 N_1}{K_1}\right) \end{cases} \quad (2)$$

There is a mutually beneficial relationship among enterprises, which create synergistic effects in the port service ecosystem. In the formula (2),  $\frac{\beta_1 N_2}{K_2}$  is the resource space that the enterprise 2 brings to the  $K_1$  enterprise 1 through mutually beneficial relationship.  $1 - \frac{N_1}{K_1} + \frac{\beta_1 N_2}{K_2}$  represents the remaining resource space that  $K_1$  enterprise 1 can use. In the equation (2), when  $\beta_1 = 0$  and  $0 < \beta_2 < 1$ , or  $0 < \beta_1 < 1$  and  $\beta_2 = 0$ , then the model is a commensalism co-evolution model.

## SIMULATION AND RESULTS ANALYSIS

### 1. Competitive co-evolutionary simulation

Based on the MATLAB software, four cases are simulated as follows.

When  $K_1 = K_2 = 100, r_1 = r_2 = 1, \alpha_1 = 0.1, \beta_2 = 0.4$ , the niche breadth of enterprise 1 and enterprise 2 is shown in Figure 3. When  $K_1 = K_2 = 100, r_1 = r_2 = 1, \alpha_1 = 0.3, \alpha_2 = 0.9$ , the niche of enterprise 1 and enterprise 2 is shown in Fig4. When  $K_1 = K_2 = 100, r_1 = r_2 = 1, \alpha_1 = 0.5, \alpha_2 = 0.9$ , the niche of enterprise 1 and enterprise 2 is shown in Figure 5. When  $K_1 = K_2 = 100, r_1 = r_2 = 1, \alpha_1 = 0, \alpha_2 = 0.5$ , the niche of enterprise 1 and enterprise 2 is shown in Fig. 6.

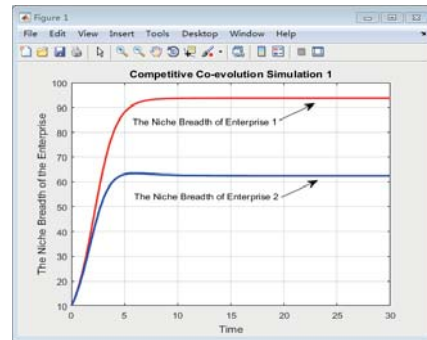


Fig. 3. Competitive Co-evolution Simulation 1

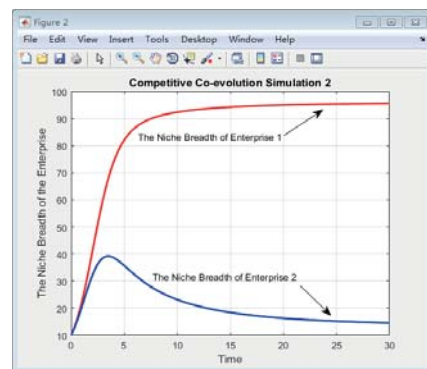


Fig. 4. Competitive Co-evolution Simulation

As can be seen from Fig.3 to Fig.6, when  $K_1 = K_2, r_1 = r_2, \alpha_1 < \alpha_2$ , then  $0 < N_2 < N_1 < 100$ ; As can be seen from Fig.3 and Fig.4, When  $K_1, K_2, r_1, r_2$  do not change,  $\alpha_1, \alpha_2$  increase at the same time, then  $N_1, N_2$  both decreases; As can be seen from Fig.4 and Fig.5, When  $K_1, K_2, r_1, r_2, \alpha_2$  do not change,  $\alpha_1$  increases, then  $N_1$  decreases and  $N_2$  increases; As can be seen from Fig.5 and Fig.6, When  $K_1, K_2, r_1, r_2$  do not change,  $\alpha_1, \alpha_2$  decrease at the same time, then  $N_1, N_2$  both increase, and while  $\alpha_1 = 0, N_1$  approaches to 100. In other words, it can be seen from the figures that if the competition coefficient is bigger, the niche breadth decrease more quickly in the port service ecosystem. The smaller the competition coefficient, the slower the niches breadth reduces. The competition coefficient is proportional to the reduction of the overall niche of the ecosystem, which reflects the synergies between the enterprises because of the competitive relationship.

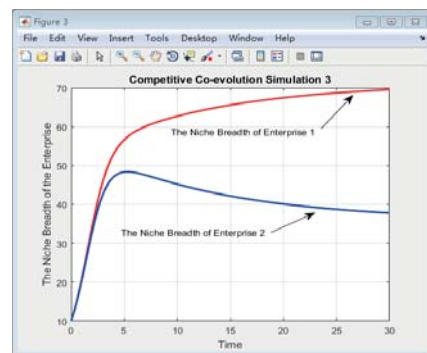


Fig. 5. Competitive Co-evolution Simulation 3

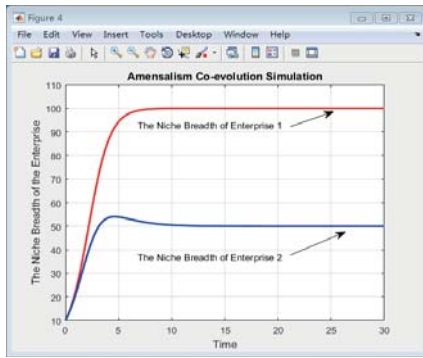


Fig. 6. Amensalism Co-evolution Simulation

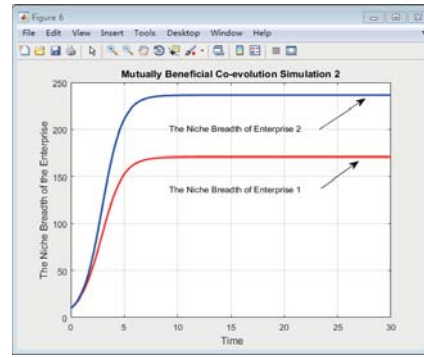


Fig. 8. Mutually Beneficial Co-evolution Simulation 2

## 2. Mutual benefit co-evolutionary simulation

When  $K_1 = K_2 = 100$ ,  $r_1 = r_2 = 1$ ,  $\beta_1 = 0.3$ ,  $\beta_2 = 0.4$ , the niche breadth of enterprise 1 and enterprise 2 is shown in Fig.7. When  $K_1 = K_2 = 100$ ,  $r_1 = r_2 = 1$ ,  $\beta_1 = 0.3$ ,  $\beta_2 = 0.8$ , the niche breadth of enterprise 1 and enterprise 2 is shown in Figure 8. When  $K_1 = K_2 = 100$ ,  $r_1 = r_2 = 1$ ,  $\beta_1 = 0.7$ ,  $\beta_2 = 0.8$ , the niche breadth of enterprise 1 and enterprise 2 is shown in Fig. 9. When  $K_1 = K_2 = 100$ ,  $r_1 = r_2 = 1$ ,  $\beta_1 = 0$ ,  $\beta_2 = 0.5$ , the niche breadth of enterprise 1 and enterprise 2 is shown in Fig. 10.

As can be seen from Fig. 7 to Fig. 10, when  $K_1 = K_2$ ,  $r_1 = r_2$ ,  $\beta_1 < \beta_2$ , then  $100 < N_1 < N_2$ ; As can be seen from Fig. 7 and Fig.8, When  $K_1, K_2, r_1, r_2, \beta_1$  do not change,  $\beta_2$  increases, then  $N_1, N_2$  both increase and  $N_1$  increases faster than  $N_2$ ; As can be seen from Fig.7 and Fig. 9, When  $K_1, K_2, r_1, r_2$  do not change,  $\beta_1$  and  $\beta_2$  both increase, then  $N_1$  and  $N_2$  both increase; As can be seen from Fig. 9 and Fig. 10, When  $K_1, K_2, r_1, r_2$  do not change,  $\beta_1$  and  $\beta_2$  both decrease, then  $N_1, N_2$  both decreases and while  $\beta_1 = 0$ ,  $N_1$  approaches to 100. The four figures illustrate that while the mutual benefit coefficient is bigger, the larger the niche scale of the port service ecosystem, and the smaller the coefficient of mutual benefit, the smaller the niche scale of the whole ecosystem. The coefficient of mutual benefit is proportional to the growth of the overall niche of the ecosystem, which reflects the synergy between enterprises because of the mutually beneficial relationships.

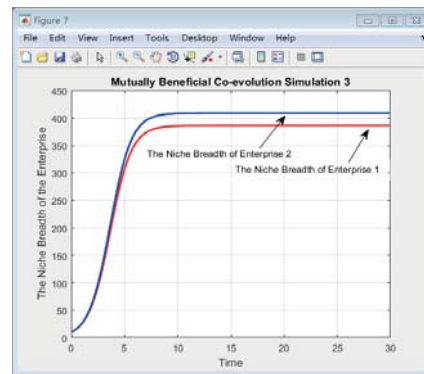


Fig. 9. Mutually Beneficial Co-evolution Simulation

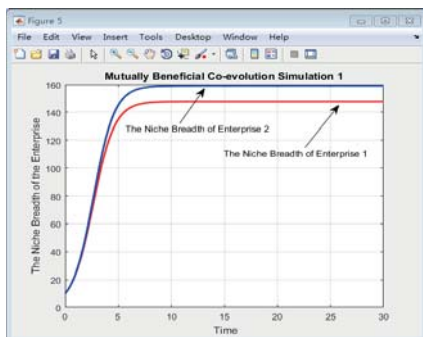


Fig. 7. Mutually Beneficial Co-evolution Simulation 1

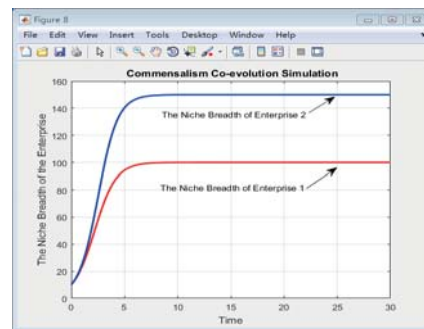


Fig. 10 Commensalism Co-evolution Simulation

With the rapid development of global economy, the increase of uncertainty and the intensification of competition, it is difficult for the enterprises in the port service ecosystem to cope with the fierce competition and meet the needs of users on its own. If the enterprise niche overlaps, it will inevitably increase the use of resources competition. If there is a trend of niche separation, the resource competition between each other can be reduced. In order to obtain the maximum interests of the whole ecosystem, the port service ecosystem enterprises should try to reduce the formation of niche overlap, niche complementary and cooperation, and ultimately achieve the development from the pursuit of their own interests to maximize the pursuit of win-win or even win-win cooperation in the direction of cooperation, and co-evolution.

## EXTENSION OF COMPETITIVE CO-EVOLUTION MODEL

### 1. Extension of competitive co-evolution model

It is assumed that there are only two enterprises in the ecosystem. But in practice, there are a large number of enterprises. The model (1) is extended to construct a co-evolution model for a number of competitive enterprises in the ecosystem, such as formula (3).

$$\frac{dN_i}{dt} = r_i N_i \left( 1 - \frac{N_i}{K_i} - \sum_{j=1}^n \frac{\alpha_{ij} N_j}{K_i} \right), \quad i \neq j \quad (3)$$

$N_i$  and  $N_j$  represent the niche width of enterprise  $i$  and enterprise  $j$ , respectively.  $r_i$  indicates the maximum growth rate of the niche width when the enterprise  $i$  is alone.  $K_i$  indicates the environmental capacity of the niche of enterprise  $i$ .  $\alpha_{ij}$  indicates the competition coefficient that the niche of enterprise  $i$  competes with enterprise  $j$ .

### 2. Extension of the mutually beneficial co-evolutionary model

$K_j$  indicates the environmental capacity of the niche of enterprise  $j$ . There are a number of enterprises with mutually beneficial relations in the port service ecosystem. The model (2) is extended to construct a co-evolutionary model which is suitable for the port service ecosystem, such as formula (4).

$$\frac{dN_i}{dt} = r_i N_i \left( 1 - \frac{N_i}{K_i} + \sum_{j=1}^n \frac{\beta_{ij} N_j}{K_j} \right) \quad (4)$$

### 3. Extension of competitive-mutually beneficial co-evolutionary model

In fact, enterprises are no longer just a competitive relationship or a mutually beneficial relationship, but a competitive relationship and a mutually beneficial at the same time in the port service ecosystem. By integrating the competitive co-evolution and the mutually beneficial co evolutionary model, we can get the co-evolution model, such as (5). The symbolic meaning of the model is the same as before.

$$\frac{dN_i}{dt} = r_i N_i \left( 1 - \frac{N_i}{K_i} - \sum_{j=1}^n \frac{\alpha_{ij} N_j}{K_i} + \sum_{j=1}^n \frac{\beta_{ij} N_j}{K_j} \right), \quad i \neq j \quad (5)$$

According to the formula (5), the synergistic effect is determined by the parameters of  $\alpha_{ij}$ ,  $\beta_{ij}$ ,  $K_i$ ,  $K_j$ . That is to say the synergistic effect is determined by the competition coefficient, the coefficient of mutual benefit, and the limiting capacity of the enterprise niche. Suppose  $\gamma_{ij} = \frac{\beta_{ij}}{K_j} - \frac{\alpha_{ij}}{K_i}$ , When  $\gamma_{ij} > 0$  is used, the niche breadth of the mutual benefit relationship between the enterprises is growth than that of the niche overlap caused by the competition, which makes the overall synergy of the port service ecosystem increase.

When  $\gamma_{ij} = 0$ , mutual benefit influence and competition influence cancels each other and the whole ecological effect of port service ecosystem is unchanged. When  $\gamma_{ij} < 0$ , the impact of competition is greater than the benefits brought by the cooperation of mutual benefit. Because of the overlap, the overall size of niche width of the Port enterprise ecosystem decreases. Under the pressure of competition, the enterprises in the port service ecosystem constantly tap resources, enhance their competitiveness and expand their niche.

The model (5) is of great significance for the accurate representation of the cooperative evolution behaviour of firms in the port service ecosystem. Meanwhile, there is a competition and mutually beneficial cooperation between enterprises in the port service ecosystem. In order to survive and develop, enterprises have to improve their competitiveness, improve the utilization of resources, and expand their niche breadth.

## ADVICE FOR THE DEVELOPMENT OF THE PORT SERVICE ECOSYSTEM

### ESTABLISHMENT OF THE PORT SERVICE ECOSYSTEM

In order to set up a port service ecosystem with itself as the core, large-scale port enterprises can select vertical or horizontal strategy. They can choose right companies as their logistics service provider to form an industry cluster combining core enterprises with affiliated ones. In addition, the port enterprises can establish a long-term cooperation, strengthen the contact and communication with relevant companies, departments in business and technology to build an ecological chain of port service. Under the new normal of China's economy, port enterprises can cooperate with each other by forming strategic alliances or partnerships, and upgrading production efficiency, utilization rate and service quality to adapt to periodic and regional surplus in port capacity. In a whole, the foundation of port service ecosystem will be well improved.

### THE ROLE AS THE KEYSTONE

The roles acted by members in the port service ecosystem can be designated into four types, which are keystone, dominator, hub landlord and niche [18]. In accordance with their different roles, they boast distinct influence on the port service ecosystem, varying their opportunities to benefit from the ecosystem. The keystone enterprise has significant impact on the stability, variety and productivity of the ecosystem. The port enterprise is the keystone species of the port ecosystem, which should exploit their key status in the ecosystem to create value and share merits with others, then make a proper balance between value creation and value occupation to achieve synergy effect [19, 20]. The port enterprise should not take too much value from the ecosystem, otherwise it

will be transformed into hub landlord, which is bad for the health of the port service ecosystem and not conducive to synergy evolution.

## K-STRATEGY

In order to ensure the sustainable development of ecosystem and maintain the species variety, the port service ecosystem needs to keep in continuous contacting with the exterior aiming at the exchange of materials, information and energy. New companies are encouraged to be absorbed into not only the ecosystem even into the ecological chain. However, the number of the companies involved is not the more the better owing to the environmental limitation. Consequently, it will do harm to the progress of the ecosystem if it outweighs the limitation. Ecological strategies are formed in the process of environmental adaptation and biological evolution. During the competition, those who choose R-strategy spend most energy on reproduction while those who choose K-Strategy prefer to improve their living rate. Instead of relying on the expansion of production scale only or implementing low-cost tactic, the enterprises in the ecosystem should improve their service, develop core technologies and exploit their creativity, transforming from the quantity essence to the quality one to hold their status and benefits.

## A PLATFORM FOR INTERACTION

With the development of the Internet and large data, the global economy into the "Internet +" era, in which the accuracy of information, timeliness and sharing requirements have never been so high, so it's pretty imminent to build an information sharing platform in the port service ecosystem [21]. The open platform not only facilitates the exchange and interaction among the members of the ecosystem, maintains the relative stability of the ecosystem, but also facilitates the co-evolution of the members of the ecosystem and the external environment. What's more, its establishment is beneficial to attract more enterprises to join the ecosystem, bring new dynamics to the ecosystem.

## CONCLUSION

This paper constructs competitive co-evolution and mutual beneficial co-evolution models of the port service ecosystem. The models are solved, and the results are analyzed. On the basis of these, the competition and cooperation co-evolution model of port service ecosystem is constructed. How cooperative effect of the port service ecosystem is determined by the capacity of the resources and the coefficient of competition and mutual benefit. The co-evolutionary models are of great significance for the accurate representation of the co-evolution of the port service ecosystem.

Under the new normal of China's economy, the market features and operational environment of China's ports have changed a lot. The members should take measures to reduce the

competition coefficient and increase the coefficient of mutual benefit. When the number of the enterprises in the port service ecosystem exceeds 2, synergy effect is only expressed in the model rather than the simulation, which need to be studied. Apart from that, actual examples aren't associated with the theory, which also should be studied further.

## ACKNOWLEDGEMENTS

The authors are thankful to the National Natural Science Foundation, the Ministry of Education of China, and Shanghai Maritime University Graduate Student Innovation Fund for providing support for this research (Grant#71272219; 11YJA630067; 2013ycx057, respectively).

## REFERENCES

1. Wei Liu, Wenjuan Li, and Xu Xu, The Analysis of the PPP Financing Model Application in Ports of China. *Journal of Coastal Research*. 2015, 73(spl): 4–8, DOI: 10.2112/SI73-002.1
2. Shanqing Zhu, Jianxin Chen. Review of coastal ports infrastructure in 2015. *China Ports*, 2016, (5): 9-11. DOI:10.3969/j.issn.1006-124X.2016.05.004
3. Xin Shi, Huan Li. Developing the port hinterland: Different perspectives and their application to Shenzhen Port, China. *Research in Transportation Business & Management*, 2016. 6. DOI: 10.1016/j.rtbm.2016.05.004
4. Guohua Zhang. The Road of Ports transformation and upgrading under the strategy of "the Belt and Road". *China National Conditions and Strength*. 2015, (3): 17-19. DOI: 10.3969/j.issn.1004-2008.2015.03.006
5. Moore, J. F. Predators and prey: the new ecology of competition. *Harvard Business Review*. 1993, 71(3), 75-83.
6. Moore, J. F. *The Death of Competition: Leader and Strategy in the Age of Business Eco-systems*. New York: Harper Business Press, 1996.
7. Shukuan Zhao, Taoqun Hao and Jinjin Li. Analysis of enterprise ecosystem evolution based on logistic model. *Industrial Technology Economics*, 2008, 27(10), 70-72. DOI:10.3969/j.issn.1004-910X.2008.10.021.
8. Yong Ma and Chan Zhou. Construction and Management Innovation of Tourism Industry Ecosystem. *Journal of Wuhan University*, 2014, (4): 5-9. DOI: 10.3969/j.issn.1009-2277.2014.04.001.
9. Na Zhao. *Port Strategic Coordination*. Zhejiang University Press, 2012.

10. Cebrian J. Energy flows in ecosystems. *Science*, 2015, 349: 1053-1054. DOI:10.1126/science.aad0684
11. Bin Hu. The Dynamic Evolution and Operation of Enterprise Ecosystems. Hohai University, 2006.
12. Flint D J, Lusch R F, Vargo S L. The supply chain management of shopper marketing as viewed through a service ecosystem lens. *International Journal of Physical Distribution & Logistics Management*, 2014, 44(1/2): 23-38. DOI: 10.1108/IJPDLM-12-2012-0350.
13. Chen, Jihong, et al. Operational Efficiency Evaluation of Iron Ore Logistics at the Ports of Bohai Bay in China: Based on the PCA-DEA Model. *Mathematical Problems in Engineering*. 2016(1), 1-13. DOI: 10.1155/2016/9604819
14. Zou, De Ling, M. Xu, and C. J. Zheng. "The Evaluation and Analysis on Port Service Development — As Ningbo and Shanghai Port for Example." *Advanced Materials Research*, 2013, 712-715: 2986-2990. DOI:10.4028/www.scientific.net/AMR.712-715.2986.
15. Ye Caihong, Dong Xinping, Zhuang Peijun. Study on Resources Integration Mechanism Model in Collaborative Development of Harbor Clusters. *Logistics technology*. 2016, (6): 81-85. DOI:10.3969/j.issn.1005-152X.2016.06.018
16. Wei Wang. Based on Lotka-Volterra Model of Chengdu Multi-Airport System. *Logistics Engineering and Management*. 2015, 0(9): 177-179. DOI:10.3969/j.issn.1674-4993.2015.09.069.
17. Ruifrok J L, Janzen T, Kuijper D P, et al. Cyclical succession in grazed ecosystems: the importance of interactions between different-sized herbivores and different-sized predators. *Theoretical Population Biology*, 2015, in press: 31-39. DOI: 10.1016/j.tpb.2015.02.001
18. Iansiti M and Levien R. The Keystone Advantage: What the New Dynamics of Business Ecosystems Mean for Strategy, Innovation, and Sustainability. *Future Survey*, 2004, 20(2): 88-90. DOI: 10.5465/AMP.2006.20591015
19. Zhijun Gao, shan liu .Study on Value Creating in Service Ecosystem Based on Service Dominated Logic. *Service Science and Management*. 2017,6 : 83-97. DOI: 10.12677/SSEM.2017.62012
20. Shiyuan Zheng, R.R. Negenborn. Price negotiation between supplier and buyer under uncertainty with fixed demand and elastic demand. *International Journal of Production Economics*. 2015-06-01. DOI: 10.1016/j.ijpe.2015.05.024.
21. Waller M A, Fawcett S E. Data Science, Predictive Analytics, and Big Data: A Revolution That Will Transform Supply

Chain Design and Management. *Journal of Business Logistics*, 2013, 34(2): 77–84. DOI: 10.1111/jbl.12010.

#### CONTACT WITH THE AUTHORS

**Wenjuan Li**  
**Wei Liu**  
**Zhijun Gao**

College of Transport and Communications  
 Shanghai Maritime University  
 NO.1550 Haigang Ave  
 Shanghai 201306  
**CHINA**

**Xu Xu**  
 Business School ,Shanghai  
 Dian Ji University  
 NO.1350 Ganlan Road,  
 Shanghai 201306  
**CHINA**

# A POSITIONING LOCKHOLES OF CONTAINER CORNER CASTINGS METHOD BASED ON IMAGE RECOGNITION

Yang Shen<sup>1,2\*</sup>

Weijian Mi<sup>3</sup>

Zhiwei Zhang<sup>4</sup>

<sup>1</sup>Institute of Logistics Science & Engineering, Shanghai Maritime University, Shanghai 201306, China

<sup>2</sup>Higher Technical College, Shanghai Maritime University, China

<sup>3</sup>Container Supply Chain Tech. Engineering Research Center, Shanghai Maritime University, China

<sup>4</sup>Shanghai Weiguo Port Equipment Company Limited

\* corresponding author

## ABSTRACT

*This article proposes a method of locating and recognizing lockholes in shipping container corner castings. This method converts the original image of the containers captured by a camera into the HSV (Hue, Saturation, Value) color space. To reduce the influence of the surface color of the containers and lights from the environment on the locating and recognizing algorithm, most noisy points of the image are filtered by binarization and a morphology opening operation to make the features of the containers clearer in the image. Thus, the container body can be separated from the total image. Then, the position and size of the corner castings are defined through calculation based on the international standard of the shipping container size. Lastly, by using this method, we can locate the corner casting in the image by using the General Hough Transform fitting algorithm onto ellipses.*

**Keywords:** Lockholes of container corner; HSV; Lockholes positioning; Hough transformation

## INTRODUCTION

In recent years, with rapid developments in export and import trading and the shipping market, major container terminals in the world are facing the challenge of rapid growth in container throughput capacity. To cope with the rising freight volume, the need for larger container vessels and operation machines is becoming more evident [1-2]. However, the need to maximize container ship stowage capacity and minimize the time for handling a ship in port result in significant pressure on increasing cargo handling efficiency. Thus, automation container terminals have become key projects all over the world.

Following this trend, large-scale machinery in automation ports is more automated and intelligent [3-5]. Earlier, the self-direction function of automated terminal crane equipment was usually possessed by the encoder, which may not be

as flexible or efficient as the directing method of machine vision. Nowadays, more researchers are using various ways to automate terminal crane equipment in their projects. The machine vision system has been one of the most popular ways to actualize automation in recent years [6-8].

The terminal machine vision system was originally applied to recognize case numbers on shipping containers [9]. Later automated recognition systems tracked and located large targets such as containers and container trucks. However, it is still difficult to recognize or posit on tiny but important features of container targets. For example, an automated recognition system cannot identify small accessories of containers such as the precise lockhole position on a container corner casting. It is also difficult to judge if the lock is attached to the container.

Hence, this article researches the identification of lockholes of containers based on a machine vision system. The purpose

of this paper is to quickly locate containers and specifically positing the lockholes of containers picture by the algorithm. After determining the specific positions of the lockholes, the container checking system will be able to calculate the positions of other key accessories and check their situations automatically.

Mi Chao et al. presented a rapid automated vision system for container corner casting recognition by using histograms of oriented gradients (HOG) descriptors [10]. Chen Mo et al. proposed a method to extract the container code characters (CCCs) when all 11 CCCs appear in an image and when some CCCs are missing. This method can estimate the positions of missing characters [11].

Kumano, S et al. used a character recognition scheme based on a dynamic design method to recognize different character string layouts in container marks or numbers [12]. This scheme can filter various container colors. Abbate Stefano presented a nonconventional approach in which each container was equipped with nodes that used wireless communication to detect neighbor containers, and to send proximity information to a base station [13]. The positions of containers can be determined by the base station.

Wu and Wei et al. proposed a segmentation-based approach to recognize characters in single-character blocks, and a hidden Markov model (HMM)-based method for multi-character blocks [14].

## IMAGE PREPROCESSING

At container terminals, camera locations may influence the angles in which photos are taken. This may cause slopes, zooms, and deformations of the targets, as shown in Figure 1. This kind of deformation will later influence processing images directly.

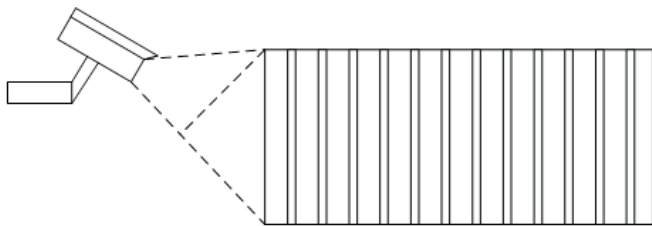


Fig. 1. Camera installation position for image recognition

In order to correct these deformations, the original image of a container will be sized by geometric transformation. During our image processing, the original image will be adjusted by linear and nonlinear transformations including affine transformations of zoom, rotation, and translation, and perspective transformations that may correct twist distortions [15] [16]. As formula 1 indicates, the perspective transformation will be conducted using a  $3 \times 3$  matrix. The result of the perspective transformation will also depend on this matrix.

$$[wx, wy, w] = [u, v, 1] \begin{bmatrix} a_{11} & a_{12} & a_{13} \\ a_{21} & a_{22} & a_{23} \\ a_{31} & a_{32} & a_{33} \end{bmatrix} \quad (1)$$

In the expression,  $u, v$  are the coordinates of the container's original image, and  $x, y$  are the coordinates after transformation.

The transformation matrix  $\begin{bmatrix} a_{11} & a_{12} & a_{13} \\ a_{21} & a_{22} & a_{23} \\ a_{31} & a_{32} & a_{33} \end{bmatrix}$  contains three sections: linear transformation section  $\begin{bmatrix} a_{11} & a_{12} \\ a_{21} & a_{22} \end{bmatrix}$  translation transformation section  $[a_{31} \ a_{32}]$ , and perspective transformation section  $[a_{13} \ a_{23}]^T$ .

In order to eliminate image distortion, the distortion parameter of the perspective transformation will be demarcated manually before recognizing the lockholes of the corner casting. Thus, we gain the best visual result of the original container image taken by cameras through the above transformations.

Figure 2 compares the images of a container before and after the perspective transformation.



Fig. 2. Comparison between source image and perspective transformed image

In the practical loading and unloading operation process at ports, the brightness of the container body in the original image is almost the same as the background, but the container colors may differ because of various shipping companies and the different type of cargo inside. Hence, to eliminate the influence of different container surface colors on the recognition algorithm, we convert the image from the original RGB color space into the HSV color space [17]. Our computers locate the container body in the HSV color space faster by using our algorithm, and then find the corner castings in the image.

The following formula 2 processes the original image from the RGB color space into the HSV color space.

$$H = \begin{cases} \frac{G-B}{Max-Min} * 60^\circ, (R = Max) \\ \left(2 + \frac{B-R}{Max-Min}\right) * 60^\circ, (G = Max) \\ \left(4 + \frac{R-G}{Max-Min}\right) * 60^\circ, (B = Max) \end{cases} \quad (2)$$

$$S = \frac{Max - Min}{Max}$$

$$V = Max$$

In the expression, the R, G, and B components are normalized into the range of [0,1]. In addition, *Max* is the highest number among these three components, and is the smallest number. In the result, H is the hue angle degree, which is between 0°–360°. S and V represent the saturation level and brightness, respectively, which are between 0–1. Figure 3 shows the container image after being converted into the HSV color space.

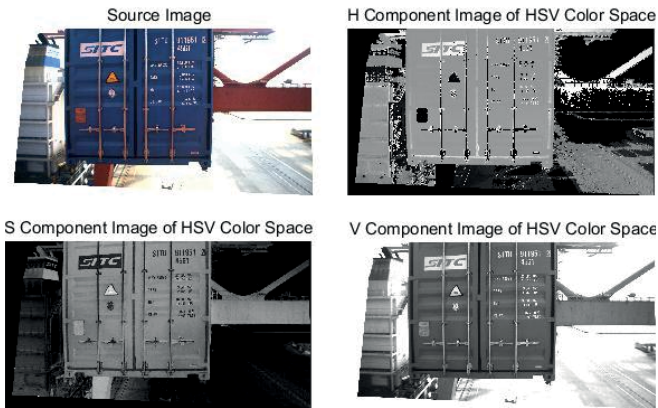


Fig. 3. HSV color space of container image

After changing into the HSV color space, we use the S channel image to process other transformations because the H channel may be affected by the container’s surface color. In addition, the V channel may be affected by environmental lighting. In order to separate the container body from the background in the image, the S channel image is by binarization. Each pixel has only one S value in the S channel, which equals a grayscale image. Here, grayscale is a color value between 0–255. In this experiment, we use formula 3 for the binary S channel image, in which  $f(x, y)$  represents the grayscale value, and  $s$  is the threshold value of binarization. Here, we take  $s$  as 120.

$$f(x, y) = \begin{cases} 0, & f(x, y) < s \\ 255, & f(x, y) > s \end{cases} \quad (3)$$

After binarization, many interfering points from the background environment still remain in the image, but these points can be filtered through a morphology opening operation.



Fig. 4. Binarization and opening operation of S component image

In Figure 4, the features of the container are clearer after being denoised by binarization in the S channel and the morphology opening operation [18].

## LOCATING CONTAINERS IN IMAGE

After binarization and filtering, the algorithm is able to precisely locate the container body in the binarization image using projective histograms.

The calculation steps are as follows:

1. We projected the binarization image in the vertical and horizontal directions [19]. The projected curve is shown in Figure 5.

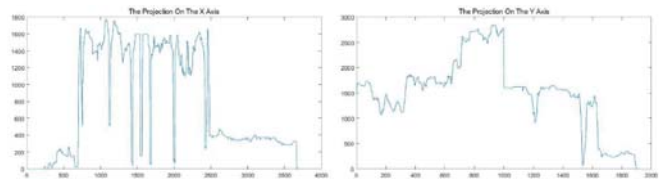


Fig. 5. Projection on X and Y axes

2. As formula 4 indicates, first we choose the proper threshold based on the value of the peak area. Then, we use a binary threshold on these two projection curves. In other words, we choose a specific threshold value. Then, any point that is bigger than this threshold value will be represented as 1, and any other smaller value will be represented as 0. The result of the threshold operation is shown in Figure 6.

$$f(x) = \begin{cases} 1, & \text{if } f(x) > t \\ 0, & \text{otherwise} \end{cases} \quad (4)$$

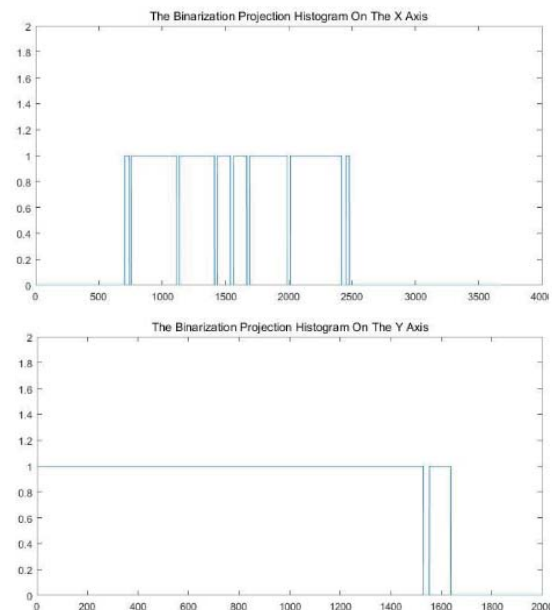


Fig. 6. Binarization projection histogram

3. We obtain the four limitation coordinates Xmin, Xmax, Ymin and Ymax of the container by calculating the location coordinates of the first rise edge and the last fall edge.

4. As shown in Figure 7, according to the square shape confirmed by the four limitation coordinates, the container shape can be cut out in the S channel image.



Fig. 7. Cut out container target

## LOCKHOLE RECOGNITION

In order to eliminate the influence of various marks on the container surface on the recognition algorithm, and to improve the calculating speed, the corner casting shape is separated from the total image. ISO 6346 regulates the size of corner castings. The height of a corner casting is assumed to be  $h$ , and the width-height ratio of a standard corner casting is  $\lambda$ . Thus, the width of the corner castings is  $\lambda h$ . The alignment and segmentation of two downside corner castings is expressed in formula 5 to adjust the error.

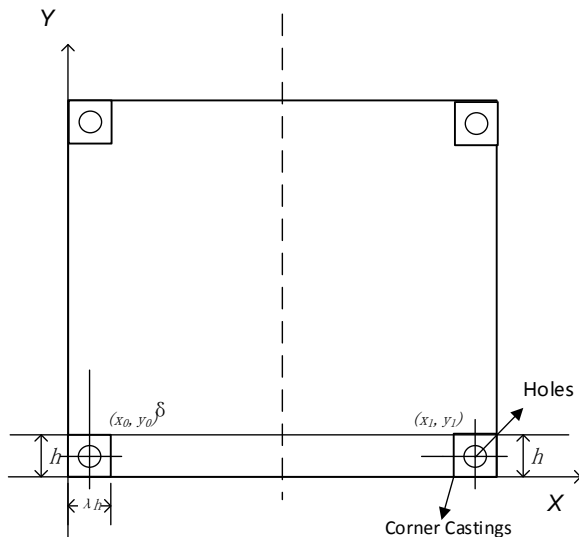


Fig. 8. Size of container corner castings.

$$\begin{cases} x_0 = \lambda(h + \delta) \\ y_0 = h + \delta \\ x_1 = W - \lambda(h + \delta) \\ y_1 = H - (h + \delta) \end{cases} \quad (5)$$

In the above expression, are the coordinates of the lower left and right corner castings.  $\lambda$  is the width-height ratio,

as mentioned earlier in this paper. In ISO 6346, the corner casting size is defined as 178 (l)  $\times$  162 (w)  $\times$  118 (h). Thus,  $\lambda=1.37$ .  $W$  and  $H$  are, respectively, the width and height of the container's segmented image, and  $\delta$  is the error parameter that can be set according to the practical situation.

Based on the sizes that we determined above, the corner casting figure can be separated from the container image. The isolated corner casting image will be grayscaled and then binarized, and will also be processed by a Canny edge detector. Last, the edge features of the corner casting will be extracted [20]. Afterward, the outline pixels will be analyzed so that connected pixel points will be determined as one outline. In doing so, the corner casting shape will be presented as outline curves.

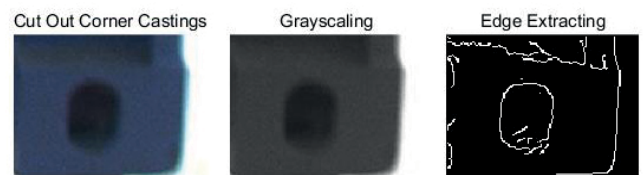


Fig. 9. Corner casting image processing

A Hough transformation can be applied in detecting circles based on the principles of the algorithm. This is called the General Hough Transform. There is one additional parameter radius  $R$  in the circle standard expression. To recognize a round shape by the algorithm, the parameter plane will be developed into a three-dimensional space  $x - y - R$ . Every pixel point in the picture corresponds to a circle in a parameter space with a different radius value. In the end, the entire figure in the parameter space will be presented as a circular cone. Furthermore, the General Hough Transform can be applied to ellipses as well as variants of circles. The following are parameter expressions of ellipse shapes:

$$\begin{cases} x = \alpha \cos T \cos \theta - \beta \sin T \sin \theta + p \\ y = \alpha \cos T \sin \theta + \beta \sin T \cos \theta + q \end{cases} \quad (6)$$

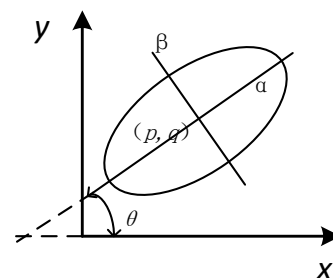


Fig. 10. Ellipse free parameter representation.

As shown in Figure 10, each ellipse has a total of five free parameters, including the center coordinates, major and minor axis radius, and the fleet angle degree. Under usual circumstances, to solve these five free parameters, we need at least five boundary coordinates. During the recognition process for container lockholes, the algorithm will detect

elliptical shapes on a closed outline in order. Hence, the center point, major and minor axis radius, and fleet angle of the lockhole shape will be determined by the program. The ellipses of lockholes will be redrawn according to the parameter set. The final detecting result is shown in Figure 11.

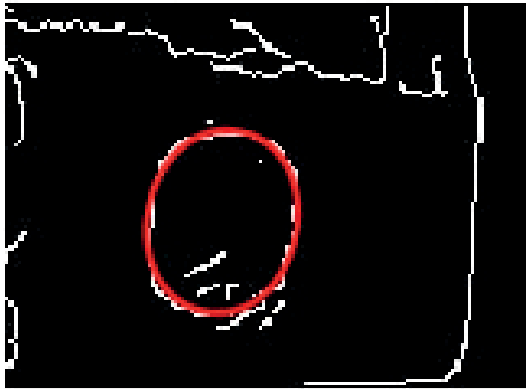


Fig. 11. Hole of container corner recognition results

## EXPERIMENTAL RESULTS AND ANALYSIS

The experiment of this article was completed in Taicang Port, Jiangsu Province, China. Four sets of samples were collected and divided by two sizes of containers and different lighting situations: 20-foot container in daylight, 40-foot container in daylight, 20-foot container at night, and 40-foot container at night. Our researchers picked 250 samples from each set to test the adaptability of our algorithm in an entire-day situation. The results are listed in the following Table.

Tab. 1. Experimental results.

| Lightness | Container Size | Samples Quantity | Effective samples quantity | Correct Amount | Recognition rate | Detecting time (ms) |
|-----------|----------------|------------------|----------------------------|----------------|------------------|---------------------|
| Daytime   | 20             | 250              | 486                        | 466            | 95.9%            | 300                 |
|           | 40             | 250              | 473                        | 458            | 96.8%            |                     |
| Nighttime | 20             | 250              | 461                        | 432            | 93.7%            |                     |
|           | 40             | 250              | 465                        | 433            | 93.1%            |                     |

In practical application, the two upper lockholes are usually covered by the hangers from port machines. Thus, only the two lower lockholes will be recognized by the algorithm. Because the timing of taking pictures is hard to control, the effective sample quantity cannot reach the ideal sample quantity. Table 1 reveals the actual number of lockholes that we obtained.

An analysis of this result indicates that the algorithm effectively recognizes lockholes in daylight. The recognition rate can be over 95%, especially in sufficient light conditions. Meantime, the recognition rate for nighttime arrives 93% which is lower than daytime rate because the light sources in the port at nighttime are fill lights pointed in various directions. These complicated lighting conditions cause different degrees of shadow on the lockholes and around the area. This impacts the locating and recognizing function.

In this experiment, we set different parameter thresholds in the detecting stage for different sizes of containers. According to the results Table, the difference between the 20-foot and 40-foot containers is smaller in the daytime. At night, the lockholes on 20-foot containers are smaller and are more susceptible to lightness. Thus, the recognition rate for a 20-foot container at night is below the rate of the 40-foot container.

With regard to the effectivity of this algorithm, the average recognition time is approximately 300 ms, which satisfies the needs of real-time performance in automatic ports.

## CONCLUSION

Machinery vision technology is important when actualizing automatic container ports, and is gaining attention from other researchers. This article studies the recognition of container lockholes using practical experience. It also introduces the current research direction and situation in automatic container ports. We explain the basic process of lockhole recognition in detail, including image preprocessing, isolating the container body image, and locating lockholes. Then, we show the specific operation steps. Using an entire-day practical test and various parameter calibrations, this system qualifies for practical application and performs well, as proven by experimental results.

## ACKNOWLEDGEMENT

This research was supported by the National Natural Science Foundation of China (No.61540045), the Science and Technology Commission of Shanghai Municipality (No.15YF1404900, No.14170501500), Ministry of Education of the PR China (No.20133121110005), Shanghai Municipal Education Commission (No. 14ZZ140), Shanghai Maritime University (No.2014ycx040).

## REFERENCES

1. Lam Jasmine Siu Lee, Song Dong-Wook, "Seaport network performance measurement in the context of global freight supply chains", Polish Maritime Research, Vol. 20, SI. 1, pp. 47-54 (2013)
2. Gamal Abd El-Nasser A. Said, El-Sayed M. El-Horbaty, "An intelligent optimization approach for storage space allocation at seaports: A case study", 2015 IEEE Seventh International Conference on Intelligent Computing and Information Systems (ICICIS), pp. 66-72 (2015)
3. Song Su, "Ship emissions inventory, social cost and eco-efficiency in Shanghai Yangshan port", ATMOSPHERIC ENVIRONMENT, Vol. 82, pp. 288-297 (2014)
4. Mi Chao, Huang Youfang, Liu Haiwei, Shen Yang, Mi Weijian. "Study on Target Detection & Recognition Using

- Laser 3D Vision System for Automatic Ship Loader,” *Sensor & Transducers*, Vol. 158, No.11, pp. 436-442 (2013)
5. Yun Xie, Qifan Bao, Zhenqiang Yao, Zhongxiong Ge, Zhengchun Du, “First automatic empty container yard with no operator in China”, *Technology and Innovation Conference, 2006. ITIC 2006. International*, pp. 1509-1513 (2006)
  6. Mi Chao, Shen Yang, Mi Weijian, Huang Youfang, “Ship Identification Algorithm Based on 3D Point Cloud for Automated Ship Loaders”, *Journal of Coastal Research*, SI.73, pp.28-34 (2015)
  7. Mi Chao, Zhang Zhiwei, He Xin, Huang Youfang, Mi Weijian, “Two-stage classification approach for human detection in camera video in bulk ports”, *POLISH MARITIME RESEARCH*, Vol. 22, pp. 163-170 (2015)
  8. Mi Chao, He Xin, Liu Haiwei, Huang Youfang, Mi Weijian, “Research on a Fast Human-Detection Algorithm for Unmanned Surveillance Area in Bulk Ports”, *MATHEMATICAL PROBLEMS IN ENGINEERING* (2015)
  9. M. Goccia, M. Bruzzo, C. Scagliola, S. Dellepiane, “Recognition of container code characters through gray-level feature extraction and gradient-based classifier optimization”, *Document Analysis and Recognition*, pp. 973-977 (2003)
  10. Mi Chao, Zhang Zhiwei, Huang Youfang, Shen Yang, “A Fast Automated Vision System for Container Corner Casting Recognition”, *Journal of Marine Science and Technology - Taiwan*, Vol.24, No.1, pp.54-60 (2016)
  11. Chen Mo, Wu Wei, Yang Xiaomin, He Xiaohai, “Hidden-Markov-Model-Based Segmentation Confidence Applied to Container Code Character Extraction”, *IEEE TRANSACTIONS ON INTELLIGENT TRANSPORTATION SYSTEMS*, Vol. 12, No. 4, pp. 1147-1156 (2011)
  12. Kumano S., Miyamoto K., Tamagawa M., et al., “Development of a container identification mark recognition system”, *ELECTRONICS AND COMMUNICATIONS IN JAPAN PART II-ELECTRONICS*, Vol. 87, No. 12, pp. 38-50 (2004)
  13. Abbate, Stefano, Avvenuti, Marco, Corsini, Paolo, et al., “An Integer Linear Programming Approach for Radio-Based Localization of Shipping Containers in the Presence of Incomplete Proximity Information”, *IEEE TRANSACTIONS ON INTELLIGENT TRANSPORTATION SYSTEMS*, Vol. 13, No. 3, pp. 1404-1419 (2012)
  14. Wu Wei, Liu Zheng, Chen Mo, “A New Framework for Container Code Recognition by Using Segmentation-Based and HMM-Based Approaches”, *INTERNATIONAL JOURNAL OF PATTERN RECOGNITION AND ARTIFICIAL INTELLIGENCE*, Vol. 29, No. 1, 2015
  15. Yamashita Yukihiro, Wakahara Toru, “Affine-transformation and 2D-projection invariant k-NN classification of handwritten characters via a new matching measure”, *PATTERN RECOGNITION*, Vol. 52, pp. 459-470 (2016)
  16. Alzati Alberto, Carlos Sierra Jose, “Special birational transformations of projective spaces”, *ADVANCES IN MATHEMATICS*, Vol. 289, pp. 567-602 (2016)
  17. Silva A. S., Severgnini F. M. Q., Oliveira M. L., et al., “Object Tracking by Color and Active Contour Models Segmentation”, *IEEE LATIN AMERICA TRANSACTIONS*, Vol. 14, No. 3, pp. 1488-1493 (2016)
  18. Pezeshk Aria, Tutwiler Richard L., “Automatic Feature Extraction and Text Recognition From Scanned Topographic Maps”, *IEEE TRANSACTIONS ON GEOSCIENCE AND REMOTE SENSING*, Vol. 49, No. 12, pp. 5047-5063 (2011)
  19. Kim H., Johnson JT., “Radar images of rough surface scattering: Comparison of numerical and analytical models”, *IEEE TRANSACTIONS ON ANTENNAS AND PROPAGATION*, Vol. 50, No. 2, pp. 94-100 (2002)
  20. Yasmin Jaseema, Sathik Mohamed, “An Improved Iterative Segmentation Algorithm using Canny Edge Detector for Skin Lesion Border Detection”, *INTERNATIONAL ARAB JOURNAL OF INFORMATION TECHNOLOGY*, Vol. 12, No. 4, pp. 325-332 (2015)
  21. Lu Tingting, Hu Weiduo, Liu Chang, “Effective ellipse detector with polygonal curve and likelihood ratio test”, *IET COMPUTER VISION*, Vol. 9, No. 6, pp. 914-925 (2016)
  22. Fornaciari Michele, Prati Andrea, Cucchiara Rita, “A fast and effective ellipse detector for embedded vision applications”, *PATTERN RECOGNITION*, Vol. 47, No. 11, pp. 3693-3708 (2014)

## CONTACT WITH THE AUTHORS

**Yang Shen**

Institute of Logistics Science & Engineering  
Shanghai Maritime University  
Shanghai 201306  
**CHINA**

Higher Technical College  
Shanghai Maritime University  
Shanghai 201306  
**CHINA**

# A DEEP Q-LEARNING NETWORK FOR SHIP STOWAGE PLANNING PROBLEM

Yifan Shen<sup>1</sup>  
Ning Zhao<sup>2\*</sup>  
Mengjue Xia<sup>1</sup>  
Xueqiang Du<sup>2</sup>

<sup>1</sup> Scientific Research Academy, Shanghai Maritime University, China

<sup>2</sup> Logistics Engineering College, Shanghai Maritime University, China

\* corresponding author

## ABSTRACT

*Ship stowage plan is the management connection of quae crane scheduling and yard crane scheduling. The quality of ship stowage plan affects the productivity greatly. Previous studies mainly focuses on solving stowage planning problem with online searching algorithm, efficiency of which is significantly affected by case size. In this study, a Deep Q-Learning Network (DQN) is proposed to solve ship stowage planning problem. With DQN, massive calculation and training is done in pre-training stage, while in application stage stowage plan can be made in seconds. To formulate network input, decision factors are analyzed to compose feature vector of stowage plan. States subject to constraints, available action and reward function of Q-value are designed. With these information and design, an 8-layer DQN is formulated with an evaluation function of mean square error is composed to learn stowage planning. At the end of this study, several production cases are solved with proposed DQN to validate the effectiveness and generalization ability. Result shows a good availability of DQN to solve ship stowage planning problem.*

**Keywords:** Deep Q-Leaning Network (DQN); Container terminal; Ship stowage plan; Markov decision process; Value function approximation; Generalization

## INTRODUCTION

In Recent years more and more researchers devoted themselves to the study of marine science, port logistics and so on [1-3], cause ocean is one of the important resources for human beings. Especially in ports, researchers have made great contributions to container terminal equipment [4-7] and planning [8-10] intelligence. In container terminals, stowage plan is one of the most important and time consuming planning phase. In present time, stowage planning is mainly made by hand with computer assistance. Such manual planning management mode relies heavily on experience of planners, which costs labor and time. With automation currency in container terminal, the manual planning hinders management automation process. At the same time, container ships has been larger and larger in recent

time, which increases planning labor and time consumption. Under such circumstances, stowage planning automation or intelligent stowage planning has been a critical technology to be broke through in container terminal management to optimize both cost and efficiency.

Previous studies of container ship stowage planning focus on stowage planning model and algorithms to solve this problem.

In terms of stowage planning model, Master Bay Plan and In-Bay Plan have been the mainstream. Among Master Bay Plan, Todd D S and Sen P [11] propose a Master Bay Plan model minimizing reshuffling, with trimming moment, heeling moment, ship stability and position as constraints. A GA is designed to solve this problem. Zhao N and Mi W J [12] made a multi-objective mixed integer programming model with ship stability factors and operation factors as constraints to optimize reshuffles and yard crane efficiency.

The proposed MIP model can only solve small scale problems with traditional planning solver. Moura A and Oliveira J et al [13] proposed a MIP model optimizing total transportation cost with shipping line in consideration. Amone In-Bay Plan, Avriel M and Penn M [14] proposed a MIP model minimizing reshuffles. Proposed algorithm can solve small scale problems. J.J.Shields [15] made a comparison between model solving outputs and actual loading outputs to validate proposed model. Imai et al [16-18] proposed multi-objective MIP model minimizing reshuffles. Numerical experiments reveals more binary variables and binary constraints would significantly increase complexity and significantly lower solving efficiency. Haghani and Kaisar et al [19] proposed a MIP model with turnaround time and ship parameters as constraints.

In terms of stowage planning algorithm, most researches prefer intelligent optimization algorithms. Álvarez et al [20] proposed a tabu-search algorithm with multiple initial solutions to solve the problem optimizing moving distance of stackers, shuffles and container weight distribution in ship. Numerical experiments show that proposed tabu-search algorithm can solve cases with more than 100 containers in short time while MIP solvers cannot solve cases with more than 40 containers. Kim et al [21-24] proposed beam-search algorithm to solve stowage planning problem. Y.Lee et al [25] decomposes stowage planning problem into smaller scale sub-problems using hierarchy theory to solve stowage planning problem. An Ant Colony Optimization-Tabu Search hybrid algorithm is proposed, and numerical experiment shows superiority of proposed hybrid algorithm over original independent algorithms.

These analyses shows that stowage planning studies at the moment concentrate on composing a MIP model and design a heuristic algorithm to solve the model. Such method performs well in small scale cases while has limitations such as poor performance in large scale cases and weak ability of generalization. Thus in this paper a deep reinforcement learning algorithm is proposed to solve stowage planning problem. Intelligent agent of stowage planning is trained to solve stowage planning problem efficiently and maintain better generalization.

## CONTAINER SHIP STOWAGE PLANNING PROBLEM

### DECISION FACTORS

In stowage planning process, several factors needs to be considered to ensure seaworthiness of container ship and improve operation efficiency.

#### 1. Ship slot location and sequence relationship factor

To ensure efficiency during ship loading process, ship slots has relative loading sequence relationship such as slot 8401 can only be loaded when the slot right under slot 8401 which is 8201, and relative sea side slots should better be loaded

before land side slots. This sequence relationship between slot locations varies between Deck Stowage Plan and Hold Stowage Plan. Deck has more constraints to ensure ship stability and operation safety.

#### 2. Ship slot weight limit factor

Before In-Bay Planning, Master Bay Plan has preplanned allocation to suggest a weight limit for each ship slot to guarantee ship stability and securing capacity. Thus each slot has a weight range constraint.

#### 3. Heavy-over-light limit factor

Theoretically, heavy containers should be loaded under light containers to ensure ship stability. While in actual planning, heavy containers are allowed to load over light containers if these containers weighs close. Thus, a heavy-over-light limit factor is applied to formulate this constraint.

### OPTIMIZATION OBJECTIVES

#### 1. Staircase shape sequencing in deck stowage planning

In terms of loading sequence, containers should better be loaded in stair shape, which means avoid insert a container between containers to improve loading operation efficiency and safety.

#### 2. Minimizing reshuffles

When a container needs to be loaded before containers over itself in container yard, reshuffle is needed. Reshuffles caused by stowage plan should be minimized during planning to improve loading efficiency.

#### 3. Minimizing yard crane shifts

When containers with adjacent planned loading sequence locates in different yard bays or even in different yard blocks, yard crane needs to shift from one bay to another to load these two containers. Unreasonable plan causes yard crane to shift back and forth to pick containers, which affects loading efficiency. Thus, yard crane shifts should be minimized to improve loading efficiency.

## DEEP REINFORCEMENT LEARNING ALGORITHM FOR STOWAGE PLANNING PROBLEM

### MARKOV DECISION PROCESS

L. S. Shapley first proposes Markov Decision Processes (MDP) in stochastic games research. R.Bellman then proposes dynamic programming method to solve general sequential problem. R.A.Howard and D.Blackwell proposed general theoretical framework and effective method for MDP. A MDP is a 5-tuple  $(s, a, r, T, \pi)$ , where

$s_i$  is a finite set of states,

$a_i$  is a finite set of actions available from state  $s_i$ ,

$r_t$  is immediate reward (or expected immediate reward),  
 $T$  is the transit function from state  $s_t$  to  $s_{t+1}$ ,  
 $\pi$  is the strategy or policy

The problem of MDP is to find a policy  $\pi$  that specifies actions that the decision maker will choose when in state  $s_t$ .

## MDP FOR STOWAGE PROBLEM

MDP for stowage planning problem is formulated according to basis of MDP. Fig. 2 shows a example of stowage planning MDP.

|    |    |    |
|----|----|----|
| M4 | M5 | M6 |
| M1 | M2 | M3 |

Fig. 1. Slot Scheme.

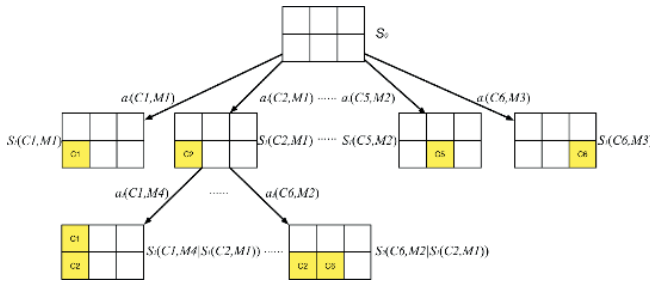


Fig. 2. MDP for Stowage Planning Problem

### 1. Stowage State

In stowage planning,  $t$  is stowage sequence,  $t=0$  is the initial state when no container is loaded,  $t=1$  is the next state when the first container is loaded,  $t=2$  is the state when the second container is loaded, and so on. In Fig. 2,  $S_0$  is the initial state when the whole bay is empty,  $S_1$  is the next state when the first container C1 is stowed, and then  $S_2$ . As is shown, when in  $S_0$ , there are several available actions, which is to stow which container in which available slot.  $S_1(C2, M1)$  means stow C2 into M1 slot in state  $S_1$ ,  $S_2(C6, M2 | S_1(C2, M1))$  means two containers are stowed, first stow C2 into M1 slot and then stow C6 into M2 in state  $S_2$ .

### 2. Stowage Action

In stowage planning, an action is to mate a container with a slot, which means stow this container in this slot. In different state, available actions are different. In Fig. 2, when in  $S_0$ , if stowage constraints are ignored, there are 36 available actions or mate of containers to slots.

### 3. Stowage Reward

In reinforcement learning, reward represents the environment. In stowage planning learning, reward mainly expresses objectives and constraints. Since the result of a stowage plan is evaluated by availability, reshuffling, yard crane shifting, and these evaluations have different scales of importance, the stowage reward is as follow.

$$r_1 = \begin{cases} -500, & \text{if stowage plan is available} \\ 500, & \text{if stowage plan is not available} \\ 0, & \text{else} \end{cases} \quad (1)$$

$$r_2 = -10 * \phi(5) \quad (2)$$

$$r_3 = -30 * \phi(9) \quad (3)$$

Formula (1) is the reward of availability, (2) is the reward of reshuffling, (3) is the reward of yard crane shifting.

## 4. Stowage Planning Evaluation Function and Action Evaluation Function

$$v^\pi(s) = \sum_{s'} T(s'|s, a) [r_{t+1}(s'|s, a) + \lambda v^\pi(s_{t+1}) | s_t = s] \quad (4)$$

$$Q^\pi(s, a) = \sum_{s'} T(s'|s, a) [r_{t+1}(s'|s, a) + \lambda v(s_{t+1})] \quad (5)$$

$$V^*(s) = \max_a \sum_{s'} T(s'|s, a) [R(s'|s, a) + \lambda V^*(s')] \quad (6)$$

$$Q^*(s, a) = \sum_{s'} T(s'|s, a) [R(s'|s, a) + \lambda V^*(s')] \quad (7)$$

$\pi$  is the stowage strategy or policy,

$\lambda$  is the discount factor, which represents the influence of next stowage move to this move,

$T(s'|s, a)$  is the probability of taking action  $a$  to get state  $s'$  in state  $s$ ,

$R(s'|s, a)$  is the reward of taking action  $a$  to get state  $s'$  in state  $s$ ,

$v(s)$  is expected reward of taking various actions in state  $s$ , or expected reward of stowing other containers after state  $s$ ,

$Q(s, a)$  is the total reward of taking action  $a$  in state  $s$ ,

$V^*(s)$  is the maximum reward in state  $s$ ,

$Q^*(s, a)$  is the maximum reward of taking action  $a$  in state  $s$ .

## STOWAGE PLANNING FEATURES

The dimensions of different ship bays are usually different in stowage planning, and reinforcement learning needs a training set with same dimensions. Thus, stowage features are introduced to approximate different stowage states. In this research, 9 features are selected as the feature vector of a stowage state,  $\Phi = \{\phi(1), \phi(2), \dots, \phi(8), \phi(9)\}$

$$\phi_i(1) = W_i / W_{\max} \quad (8)$$

$$\phi_i(2) = T_i / T_{\max} \quad (9)$$

$$\phi_i(3) = \begin{cases} (W_j - W_i) / W_{\max}, & \text{if } T_i > 1 \\ (W_{\max} - W_i) / W_{\max}, & \text{if } T_i = 1 \end{cases} \quad (10)$$

$$\phi_i(4) = P_i - S_i \quad (11)$$

$$\phi_i(5) = F_i / F_{\max} \quad (12)$$

$$\phi_i(6) = X_i - X_j / X_{\max} \quad (13)$$

$$\phi_i(7) = X_i - X_k / X_{\max} \quad (14)$$

$$\phi_i(8) = (G_i - G_j) + (G_i - G_k) / 2G_{\max} \quad (15)$$

$$\phi_i(9) = \begin{cases} 1, & \text{if this container is located in} \\ & \text{the same yard bay with the} \\ & \text{previous one} \\ 0, & \text{else} \end{cases} \quad (16)$$

(8) Represents the normalized weight of selected container.

(9) Represents the normalized tier number of selected slot.

(10) Represents the normalized weight gap between selected container and the container located right under it on the ship.

(11) Represents the potential of selected match of container and slot (or action), which means number of remaining lighter container minus available ship slots above selected slot, or expression of influence of selected action to later stowage planning.

(12) Represents normalized reshuffles caused by this action.

(13) Represents normalized sequential gap between selected container with containers located left of selected.

(14) Represents normalized sequential gap between selected containers with containers located right under selected container.

(15) Represents normalized sum of sequential gap between selected container with containers located left of selected and sequential gap between selected containers with containers located right under selected container.

(16) Represents whether this container locates in the same yard bay with the previous one.

## DEEP REINFORCEMENT LEARNING ALGORITHM FOR STOWAGE PLANNING PROBLEM

Figure 3 shows the framework of reinforcement learning or Q-Learning for stowage plan. In the initial state of learning, the intelligent agent is like a naïve planner, every action the planner take will have a reward to update  $Q(s, a)$ , and the agent will decide next action for next state depending on updated  $Q(s, a)$ , this is the iteration of reinforcement learning. Actually, the agent learns from iterations of attempts and

rewards to maximize the final reward and make the policy better.

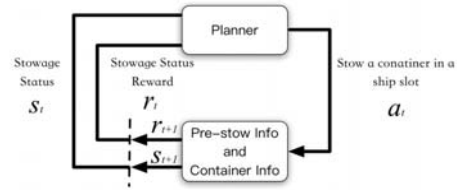


Fig. 3. Framework of Reinforcement Learning

The difference between Deep Q-Learning and Q-Learning is that the look up table is replaced by deep neuron network to update  $Q(s, a)$ , which enables effectiveness in super large state space scale. And the deep neuron network can be trained with minimizing lost function  $L_i(w_i)$  which updates in each iteration.

$$L_i(w_i) = E[(r + \underbrace{\gamma \max_{a'} Q(s', a'; w_i)}_{\text{Target}}) - Q(s, a; w_i)]^2 \quad (17)$$

$s'$  is the next state, and  $a'$  is the next action. The partial in the  $w_i$  direction is in (18).

$$\nabla_{w_i} L_i(w_i) = E_{s, a, r, s'}[(r + \gamma \max_{a'} Q(s', a'; w_i) - Q(s, a; w_i)) \nabla_{w_i} Q(s, a; w_i)] \quad (18)$$

Stochastic Gradient Descent is used to optimize the lost function, and the weight updates after every iteration, which is quite similar to traditional Q-Learning algorithm.

In order to approximate reward for new states that never appeared before, a evaluation function approximation function is introduced to improve generalization ability. Unlike supervised learning, reinforcement learning doesn't have known tags for training, tags are obtained through iterations. While a state and an action is updated, the change of weight for this match can affect other matches, which causes ineffectiveness of previous state and action matches, and then it causes longer training time or even failure of training. Thus, an experience replay method is introduced to prevent ineffectiveness.

Experience replay stores the experience of time  $t$  as  $(\phi_t, a_t, r_t, \phi_{t+1})$  in experience history queue  $D$ , and then  $D$  is stochastically sampled as  $(\phi_j, a_j, r_j, \phi_{j+1})$  to do mini-batch to update the weight. This ensures every history points are considered when updating a new data point. Experience replay stores all previous states and action in a sequence to minimize objective function when Q-Function updates.

$$L_i(w_i) = E_{(s, a, r, s') \sim U(D)}[(r + \gamma \max_b Q(s', b; w_i) - Q(s, a; w_i)]^2 \quad (19)$$

$D$  represents a sequence of previous states and actions,  $U(D)$  is a uniform distribution among experience sequence  $D$ . Experience replay based upon uniform distribution lowered data dependency to improve learning robustness.

The deep network for the stowage planning problem is designed as follows.

### 1. Input layer and output layer

For stowage planning problem, the input layer is a matrix of feature vector of stowage samples, the output layer is the approximate Q-value. Thus, the number of nodes in input layer is 9, the number of nodes in output layer is 1.

### 2. Number of hidden layers

Generally, more hidden layer makes higher precision of approximation, while more hidden layer costs more training and greater probability of over-fitting. In this case, 9 hidden layer is accepted.

### 3. Number of nodes in hidden layers

To avoid over-fitting and maintain better generalization ability, the number of nodes in hidden layer should be minimized when the precision is assured. Number of nodes in hidden layer is related to number of nodes in input layer, number of nodes in output layer, complexity of learning problem, transition function and sample data. Too few nodes causes poor training performance, and too many nodes causes less system error but may cause over-fitting.

### 4. Activation function

There are three widely used activation functions,  $TanH$ ,  $Sigmoid$  and  $Relu$  (Rectified Linear Units).  $Relu$  has better training performance especially in attenuation of gradient and network sparsely. Thus,  $Relu$  is used as the activation function of this research.

$$Relu : f(x) = \max(0, x) \quad (20)$$

The designed deep neuron network for stowage planning problem is shown in Figure 4.

According to deep network design, DQN training algorithm is designed, pseudo code for DQN Algorithm for Stowage Planning is shown in Table 1, and flowchart in Figure 5.

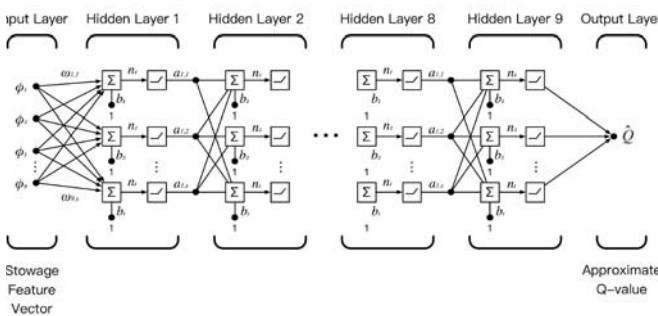


Figure 4. Deep Neuron Network for Stowage Planning Problem

Tab. 1. DQN Algorithm for Stowage Planning

| DQN Training Algorithm for Stowage Planning   |  |
|---|--|
| Initialize experience history queue $D$ with length $N$   |  |
| Initialize $Q(s, a; w)$ with random weight $w_0$  |  |
| For each stowage episode loop:  |  |
| Initialize observation sequence $s_1 = \{x_1\}$ and feature sequence $\phi_1 = \phi(s_1)$                                   |  |
| For each step in an episode loop:   |  |
| Select an action to perform in state $s$ with $\epsilon(\text{softmax}) - \text{greedy}$                                    |  |
| Update reward and extract feature $\phi_t = \phi(s_t)$  |  |
| Save experience tuple $(\phi_t, a_t, r_t, \phi_{t+1})$ into experience history queue $D$                                    |  |
| Collect samples $(\phi_j, a_j, r_j, \phi_{j+1})$ with size of random sampling mini-batch                                    |  |
| Transform sample $(\phi_j, a_j, r_j, \phi_{j+1})$ into training tuple $(x_k, y_k)$  |  |
| $x_k = \phi_j, y_k = r + \lambda \max_{a'} Q_i(\phi_{j+1}, a', w_{i-1})$  |  |
| Update network weights of training set $\{(x_k, y_k)\}_m$ according to $\nabla_w L_i(w_i)$ with stochastic gradient descent |  |
| Loop until end of states $S$  |  |
| Loop until end of episodes  |  |

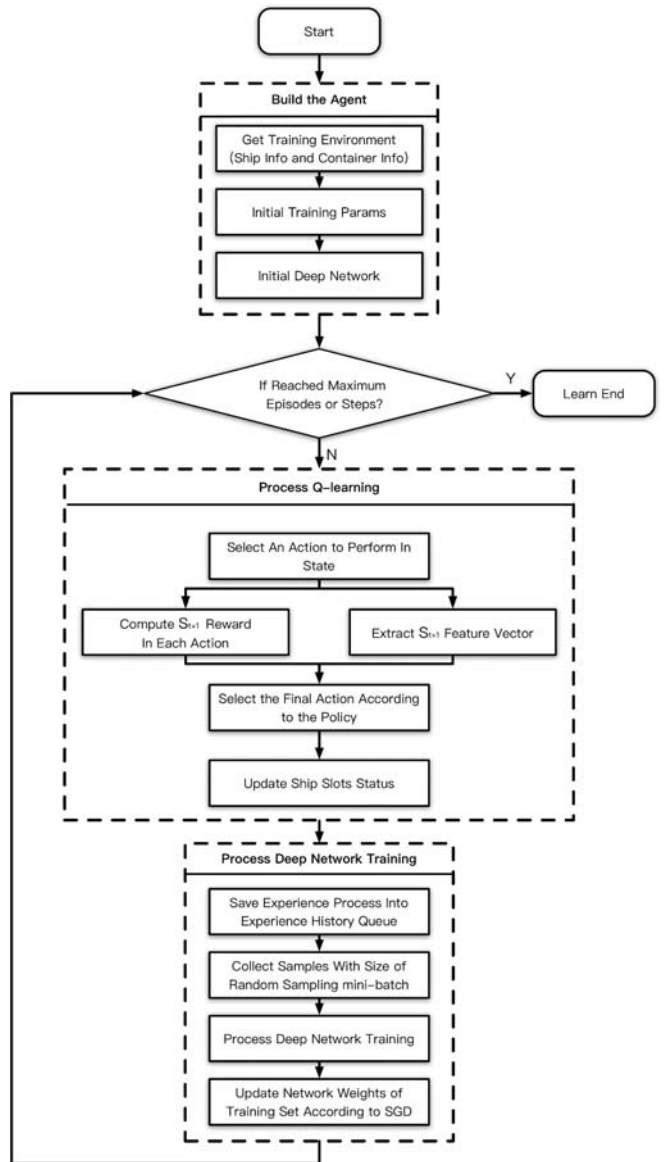


Fig. 5. Flowchart for DQN Algorithm for Stowage Planning

# STOWAGE CASE STUDY OF DQN STOWAGE PLANNING

## CASE DESCRIPTION

In this case, production data of Ningbo Port is used to verify proposed method. Selected ship bay has 19 slots, 19 corresponding containers locate in 4 yard bays in 2 blocks. Ship bay is shown in Figure 6, this bay has 4 tiers and 5 rows, each weight box is a slot to be stowed. Container distribution in yard is shown in Figure 7. Number inside each box in Figure 7 is the weight of each container.

Parameter setup for stowage planning is shown in Table 2 and parameter setup for DQN learning algorithm is in Table 3. Random exploration rate  $\epsilon$  indicates that in the initial state of iterations, the random exploration rate equals to 1 to improve exploration. After each 1% of total iterations, the exploration rate decrease by a step of 0.09 to reach 0.1 when iterations finish. With this descending, the agent can focus on optimized solution gradually to converge while keeping a moderate ability of exploration.

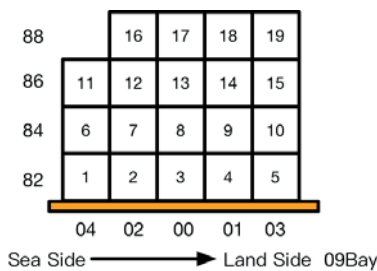


Fig. 6. Ship Bay Layout

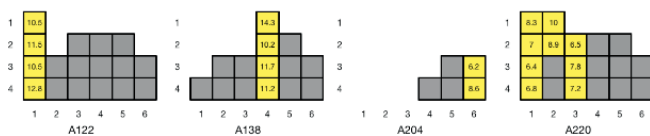


Fig. 7. Container Distribution

Tab. 2. Parameter setup for stowage planning

| Heavy-over-light limit factor $\delta$ | Reshuffle weight $w_1$ | Yard crane shift weight $w_2$ |
|--|------------------------|-------------------------------|
| 0.5 t                                  | 3                      | 1                             |

Tab. 3. Parameter Setup for DQN Learning Algorithm

| Learning ratio $\alpha$                 | Discount factor $\lambda$ | Random exploration rate $\epsilon$ |
|---|---------------------------|------------------------------------|
| $1 \times 10^{-4}$                      | 0.3                       | 1 to 0.1 with step of -0.09        |
| Random exploration rate update internal | Experience replay depth   | Number of nodes in hidden layers   |
| 1%                                      | 5000                      | 128                                |

## STOWAGE RESULT ANALYSIS

The proposed DQN is trained with production data for 200000 iterations, which costs 2 hours and 46 mins. The trained DQN can finish the test case in 0.069 seconds, and the stowage result of the test case is as in Figure 8.

The upper left figure shows the weight distribution of stowage, the upper right figure shows the sequence of stowage. The boxes are filled with different colors to distinguish its original yard bay. In this stowage plan, 1 reshuffle and 3 shifts are needed to finish loading of this ship bay, of which 3 shifts are necessary (because there are 4 yard bays in total). The reshuffle of container with sequence 18 is unnecessary, but it is still a good solution. With all that, the effectiveness of DQN trained with production data is validated.

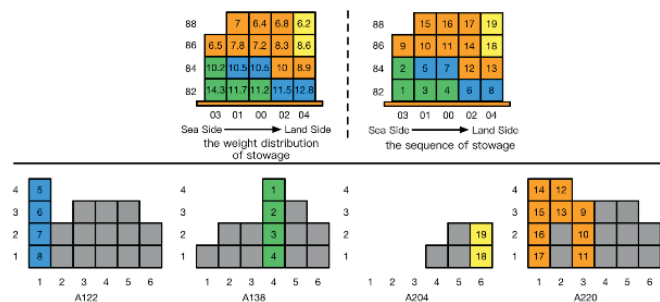


Fig. 8. Stowage result of test case

## GENERALIZATION ABILITY ANALYSIS

### 1. Generalization of Data with Same Size

To verify the generalization of same size data, another stowage case with 19 containers is introduced. This case (case. 2) comes from a different ship of same port. Stowage result has 1 reshuffle and 4 shifts, 4 shifts of witch are all necessary. With comparison with port planners' stowage results, the stowage plan of DQN shows a good performance. Manual plan costs 121 seconds on average, while DQN can complete the calculation in 0.073s. This case study shows a good result in terms of generalization of same size data.

### 2 Generalization of Data with Different Size

To verify the generalization of different size data, a stowage case with 40 containers is introduced. This case (case. 3) has a big difference with the previous one both in case size and container distribution. Result of DQN of this case shows some heavy-over-light containers, while the weight gaps are all in the heavy-over-light limit. The result has 12 reshuffles and 11 shifts, 4 shifts are unnecessary. For the complexity of this case, port planners show varieties in their plans, with an average of 10.2 reshuffles and 9.6 shifts. Port planners takes 237s to make the plan while DQN costs 0.131s. Thus, DQN shows comparable ability in this case with human competitors with much better time consumption. This case study shows a good result in terms of generalization of different size data.

## ROBUSTNESS ANALYSIS

In stowage planning DQN learning, robustness of algorithm refers to whether the training algorithm can get good DQN with various stowage planning cases.

In generalization analysis part, DQN trained with case. 1 is used to plan case. 2 and case. 3. To verify the robustness of proposed algorithm, case. 2 and case. 3 are used as training set to get new DQNs. Planning results of different DQNs are shown below.

Tab. 4. Training parameters and time consumption

| Training Set | No. of Containers | Iterations | Training time |
|--------------|-------------------|------------|---------------|
| Case. 1      | 19                | 150000     | 2 h 46 min    |
| Case. 2      | 19                | 150000     | 2 h 53 min    |
| Case. 3      | 28                | 150000     | 4 h 21 min    |

Table 4 shows that these three training has same iteration setup, and with same case size, the training time is quite similar.

Tab. 5. Comparison of DQNs' planning results

| Training Set  | Case. 1 |         |         | Case. 2 |         |         | Case. 3 |         |         |
|---------------|---------|---------|---------|---------|---------|---------|---------|---------|---------|
|               | Case. 1 | Case. 2 | Case. 3 | Case. 1 | Case. 2 | Case. 3 | Case. 1 | Case. 2 | Case. 3 |
| Reshuffles    | 1       | 1       | 12      | 2       | 1       | 12      | 1       | 1       | 10      |
| Shifts        | 3       | 4       | 11      | 3       | 4       | 12      | 3       | 5       | 11      |
| Training Time | 0.069   | 0.073   | 0.131   | 0.071   | 0.081   | 0.142   | 0.068   | 0.073   | 0.137   |

As in Table 5, different test cases shows good result with different trained DQNs, and the efficiency of different DQNs are quite similar, which means influence of different training cases and test cases are negligible. Thus, the proposed algorithm has good stability and robustness.

## CONCLUSIONS

In this study, a DQN and a learning method for this DQN is proposed to solve ship stowage planning problem, innovations are as follows.

1. Introduces deep learning algorithm to solve planning problem. With DQN, massive calculation and training is done in pre-training stage, while in application the planning problem can be solved in seconds

2. Objectives and constraints of ship stowage planning problem are transformed to feature vectors to extract stowage policies with deep learning algorithm automatically. Policies from data tends to have less bias than designed heuristics in previous studies.

3. Experience replay is introduced in DQN to enforce generalization and robustness of proposed algorithm.

4. Provided reference to solving planning problem in container terminals such as yard storage planning and equipment scheduling.

## ACKNOWLEDGEMENTS

This research was supported by the National Natural Science Foundation of China (No.61540045), the Science and Technology Commission of Shanghai Municipality (No.15YF1404900, No.14170501500), Ministry of Education of the PR China (No.20133121110005), Shanghai Municipal Education Commission (No. 14ZZ140), Shanghai Maritime University (No.2014ycx040).

## REFERENCES

1. M. Omar, S. S. Supadi. 2012. Integrated models for shipping a vendor's final production batch to a single buyer under linearly decreasing demand for consignment policy. *Sains Malaysiana* 41.3: 367-370.
2. C. Mi, Z. W. Zhang, Y. F. Huang, Y. Shen, 2013. A fast automated vision system for container corner casting recognition. *Journal of Marine Science and Technology-Taiwan*, 24(1): 54-60. DOI: 10.6119/JMST-016-0125-8
3. X. P. Rui, X. T. Yu, J. Lu, et al. 2016. An algorithm for generation of DEMs from contour lines considering geomorphic features. *Earth Sciences Research Journal*, 20(2): G1-G9, 20(2):G1-G9.
4. Y. Shen, 2016. An Anti-Collision Method of Slip Barrel for Automatic Ship Loading in Bulk Terminal. *Polish Maritime Research*, 23(s1).
5. C. Mi, Y. Shen, W. J. Mi, Y. F. Huang, 2015. Ship Identification Algorithm Based on 3D Point Cloud for Automated Ship Loaders. *Journal of Coastal Research*, 2015(SI.73): 28-34. DOI: 10.2112/SI73-006.
6. C. Mi, Z. W. Zhang, X. He, Y. F. Huang, W. J. Mi, 2015. Two-stage classification approach for human detection in camera video in bulk ports, *Polish Maritime Research*, 22(SI.1):163-170. DOI: 10.1515/pomr-2015-0049
7. C. Mi, H. W. Liu, Y. F. Huang, W. J. Mi, Y. Shen, 2016. Fatigue alarm systems for port machine operators. *Asia Life Sciences*, 25(1): 31-41.
8. Yifan S, Ning Z, Weijian M. 2016. Group-Bay Stowage Planning Problem for Container Ship. *Polish Maritime Research*, 23(s1).
9. Mengjue X., Ning Z, Weijian M. 2016. Storage Allocation in Automated Container Terminals: the Upper Level. *Polish Maritime Research*, 23(s1).
10. C. Mi, X. He, H. W. Liu, Y. F. Huang, W. J. Mi, 2014. Research on a Fast Human-Detection Algorithm for Unmanned Surveillance Area in Bulk Ports. *Mathematical Problems in Engineering*. DOI: 10.1155/2014/386764

11. D. S. Todd, P. Sen, 1997. A Multiple Criteria Genetic Algorithm for Containership Loading International Conference on Genetic Algorithms, East Lansing, Mi, Usa, July. DBLP, 674-681.
12. N. Zhao, W. J. Mi, 2008. Robust approach in stowage planning at container terminals. *IEEE proceeding of the 4th International Conference on Intelligent Logistic System*, 191-204.
13. A. Moura, J. Oliveira, C. Pimentel, 2013. A Mathematical Model for the Container Stowage and Ship Routing Problem. *Journal of Mathematical Modelling and Algorithms in Operations Research*, 12(3): 217-231.
14. M. Avriel, M. Penn, 1993. Exact and approximate solutions of the container ship stowage problem. *Computers & Industrial Engineering*, 25(1-4):271-274.
15. J. J. Shields, 1984. Containership Stowage: A Computer-Aided Preplanning System. *Marine Technology*, 21(4): 370-383.
16. A. Imai, T. Miki, 1989. A heuristic algorithm with expected utility for an optimal sequence of loading containers into a containerized ship. *Journal of Japan Institute of Navigation*, 80: 117-124 (in Japanese).
17. A. Imai, E. Nishimura, K. Sasaki, S. Papadimitriou, 2001. Solution comparisons of algorithms for the containership loading problem. Proceedings of the International Conference on Shipping: Technology and Environment, available on CD-ROM.
18. A. Imai, E. Nishimura, K. Sasaki, S. Papadimitriou, 2001. Solution comparisons of algorithms for the containership loading problem. Proceedings of the International Conference on Shipping: Technology and Environment, available on CD-ROM.
19. A. Haghani, E. I. Kaiser, 2001. A model for designing container loading plans for containerships. In: 80th Transportation Research Board Annual Meeting, Washington, DC, USA.
20. J. F. Álvarez, 2006. A heuristic for Vessel planning in a reach stacker terminal. *Journal of Maritime Research Jmr*, 3(1): págs. 3-16.
21. K. H. Kim, 1994. Analysis of rehandles of transfer crane in a container yard. *APORS-Conference*, 3: 357-365.
22. K. H. Kim. 1997. Evaluation of the number of rehandles in container yards. *Computers & Industrial Engineering*, 32: 701-711.
23. K. H. Kim, Y. M. Park, K. R. Ryu, 2000. Deriving decision rules to locate export containers in container yards. *European Journal of Operational Research*, 124: 89-101.
24. K. H. Kim, J. S. Kang, K. R. Ryu, 2000. A beam search algorithm for the load sequencing of outbound containers in port container terminals. *OR Spectrum*, 26: 93-116.
25. Y. Lee, J. Kang, K. R. Ryu, K. H. Kim, 2005. Optimization of Container Load Sequencing by a Hybrid of Ant Colony Optimization and Tabu Search, *Natural Computation Lecture Notes in Computer Science*, 3611, 1259-1268.

## CONTACT WITH THE AUTHORS

**Ning Zhao**

Logistics Engineering College  
Shanghai Maritime University  
Shanghai201306  
**CHINA**

## LOW COST INTEGRATED NAVIGATION SYSTEM FOR UNMANNED VESSEL

Changsong Yang<sup>1\*</sup>

Qi Wang<sup>2</sup>

<sup>1</sup> School of Information & Control, Nanjing University of Information Science & Technology, China

<sup>2</sup> School of Computer & Software, Nanjing University of Information Science & Technology, China

\* corresponding author

### ABSTRACT

*Large errors of low-cost MEMS inertial measurement unit (MIMU) lead to huge navigation errors, even wrong navigation information. An integrated navigation system for unmanned vessel is proposed. It consists of a low-cost MIMU and Doppler velocity sonar (DVS). This paper presents an integrated navigation method, to improve the performance of navigation system. The integrated navigation system is tested using simulation and semi-physical simulation experiments, whose results show that attitude, velocity and position accuracy has improved awfully, giving exactly accurate navigation results. By means of the combination of low-cost MIMU and DVS, the proposed system is able to overcome fast drift problems of the low cost IMU.*

**Keywords:** Low cost; MEMS; Inertial navigation; Integrated navigation

### INTRODUCTION

Unmanned vessel (UV) is an effective tool in ocean exploitation. The recent upsurge of interest in ocean exploitation necessitates the development of small and lightweight UVs[1]-[5]. Precision navigation is one of the key technologies and of great importance for UVs and UV-based ocean surveying and exploitation. This paper focuses on mini-sized unmanned vessels, which have a limited weight, size and cost, making low cost navigation system the best, and most of time, the only choice.

This paper presents a navigation system scheme for UVs. Low cost Micro-Electro-Mechanical Systems (MEMS) based inertial measurement unit (IMU) is used, to determine the position, velocity and attitude of the UV, in which the IMU is fixed - this is so called inertial navigation system (INS). The operation of inertial navigation systems depends upon the laws of classical mechanics as formulated by Isaac Newton.

It is the process whereby the measurements provided by gyroscopes and accelerometers are used to determine the position, velocity and attitude of the vehicle in which they are installed. Inertial navigation system is entirely self-contained within the vehicle, in the sense that they are not dependent on the transmission of signals from the vehicle or reception from an external source. So it is widely used. But inaccuracies arise because of initial alignment errors, imperfections in the performance of the inertial instruments and limitations in the computational process. For high-precision IMU, the position error will increase slowly; so INS still give high-precision navigation information in not a long time. Yet for low cost MIMU, large errors (as shown in Table I) lead to huge navigation errors, even wrong navigation information even in a minute. It cannot be used in isolation. So we combined INS and doppler velocity sonar (DVS) to an integrated navigation system, to improve the accuracy of the inertial navigation system[6]-[9].



## THE INTEGRATED NAVIGATION SYSTEM DESIGN

The integrated navigation system scheme is shown in Figure 2. INS and DVS are combined to a Kalman filter, to estimate and correct IMU biases and inertial navigation system errors, in order to overcome fast drift problems of the low-cost INS, then improve navigation accuracy[11] [12].

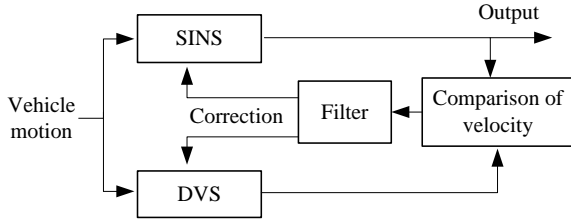


Fig. 2 Integrated navigation system schematic for unmanned vessel

## INTEGRATED NAVIGATION SYSTEM FILTER DESIGN

### System equation

Equation (5) is the Kalman filter system equation.

### Measurement equation

The inertial navigation system output velocities are compared with DVS velocity measurements. The velocities difference of INS/DVS are used as Kalman filter measurements, to estimate and correct INS errors.

The inertial navigation system output velocities and DVS velocity measurements are as Equ. (6) and (7) respectively:

$$\begin{cases} v_{IE} = v_E + \delta v_E \\ v_{IN} = v_N + \delta v_N \end{cases} \quad (6)$$

$$\begin{cases} v_{DE} = v_E + \delta v_{DE} \\ v_{DN} = v_N + \delta v_{DN} \end{cases} \quad (7)$$

where  $\delta v_{DE}$ ,  $\delta v_{DN}$  represent the errors in the DVS velocity measurements.

The differences between the DVS measurements and INS measurements are referred to as the filter measurements and are as follows:

$$\begin{aligned} \mathbf{Z}_v &= \begin{bmatrix} v_{IE} - v_{DE} \\ v_{IN} - v_{DN} \end{bmatrix} = \begin{bmatrix} \delta v_E - \delta v_{DE} + w_1 \\ \delta v_N - \delta v_{DN} + w_2 \end{bmatrix} \\ &= \begin{bmatrix} 1 & 0 \\ 0 & 1 \end{bmatrix} \begin{bmatrix} \mathbf{X}_I \\ \mathbf{X}_D \end{bmatrix} + \begin{bmatrix} w_1 \\ w_2 \end{bmatrix} \\ &\triangleq \mathbf{H}_v \begin{bmatrix} \mathbf{X}_I \\ \mathbf{X}_D \end{bmatrix} + \mathbf{V}_v \end{aligned} \quad (8)$$

where  $\mathbf{H}_v = \begin{bmatrix} 1 & 0 \\ 0 & 1 \end{bmatrix} \mathbf{O}_{2 \times 10}$ ,  $\mathbf{V}_v = \begin{bmatrix} w_1 \\ w_2 \end{bmatrix}$  is assumed to be a zero mean, Gaussian white-noise process.

In order to allow a discrete Kalman filter to be constructed, it is necessary to express the system error equation (5), the measurement equation (8) in discrete form as follows:

$$\mathbf{X}_k = \boldsymbol{\varphi}_{k,k-1} \mathbf{X}_{k-1} + \boldsymbol{\Gamma}_{k-1} \mathbf{W}_{k-1} \quad (9)$$

$$\mathbf{Z}_k = \mathbf{H}_k \mathbf{X}_k + \mathbf{V}_k \quad (10)$$

### Kalman filter process

Equations (9) and (10) are the system and measurement equations needed to construct a Kalman filter. The equations for the Kalman filter take the following form for the integrated navigation system for unmanned vessel considered here.

#### 1) Filter prediction step

The covariance matrix is predicted forward in time using the expression:

$$\mathbf{P}_{k/k-1} = \boldsymbol{\varphi}_{k,k-1} \mathbf{P}_{k-1} \boldsymbol{\varphi}_{k,k-1}^T + \boldsymbol{\Gamma}_{k-1} \mathbf{Q}_{k-1} \boldsymbol{\Gamma}_{k-1}^T \quad (11)$$

and the state prediction equation:

$$\mathbf{X}_{k/k-1} = \boldsymbol{\varphi}_{k,k-1} \hat{\mathbf{X}}_{k-1} \quad (12)$$

#### 2) Filter update

The estimates of the errors in the inertial navigation system states are derived using:

$$\hat{\mathbf{X}}_k = \mathbf{X}_{k/k-1} + \mathbf{K}_k (\mathbf{Z}_k - \mathbf{H}_k \mathbf{X}_{k/k-1}) \quad (13)$$

and the covariance matrix is updated according to:

$$\mathbf{P}_k = (\mathbf{I} - \mathbf{K}_k \mathbf{H}_k) \mathbf{P}_{k/k-1} \quad (14)$$

where

$$\mathbf{K}_k = \mathbf{P}_{k/k-1} \mathbf{H}_k^T (\mathbf{H}_k \mathbf{P}_{k/k-1} \mathbf{H}_k^T + \mathbf{R}_k)^{-1} \quad (15)$$

## RESULTS

### SIMULATION RESULTS

According to sample data from the MIMU we used, the following errors sources are included.

Gyroscope white noise = 40°/h, gyroscope bias = 360°/h, accelerometer bias = 2mg, accelerometer white noise = 2mg.

Body motion: constant velocity=15m/s, initial latitude = 32°, longitude=118°. Sine angular motion: initial yaw=45deg,

pitch=9deg, roll=12deg, and frequency: yaw=1/6, pitch=1/8, roll=1/10.

The simulated INS errors are shown in Figure 3.

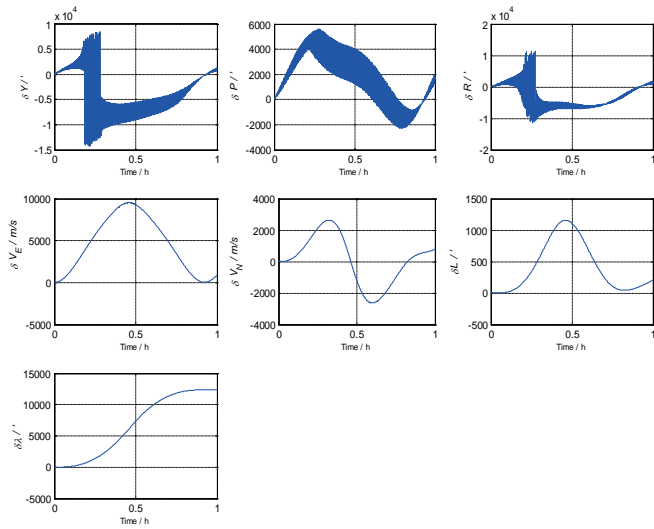


Fig. 3. Simulated INS errors

$\delta Y$ ,  $\delta P$ ,  $\delta R$ ,  $\delta VE$ ,  $\delta VN$ ,  $\delta L$  and  $\delta \lambda$  are yaw error, pitch error, roll error, east velocity error, north velocity error, latitude error, longitude error respectively.

Figure 3 shows huge navigation errors; this caused by the large errors from gyroscopes and accelerometers. The INS navigation results are worthless.

So we combined INS and DVS to the above integrated navigation system, then the simulated navigational accuracy is shown in Figure 4.

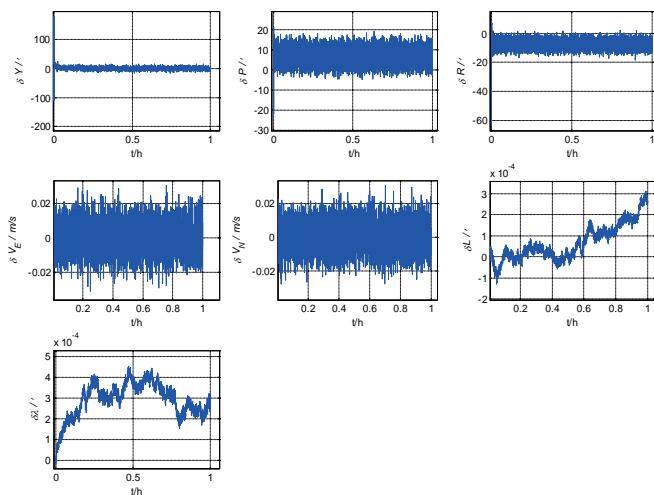


Fig. 4 Integrated navigation system errors

DVS velocity noise is 0.01m/s. Figure 4 shows that the integrated navigation system improves navigational accuracy awfully, giving exactly accurate navigation results.

## SEMI-PHYSICAL SIMULATION RESULTS

For further testing the integrated navigation system, semi-physical simulation was carried out. A low cost MIMU was used in this test. The MIMU was placed on a table under static conditions. About 5-10 minutes data are collected. The sample data are shown in Figure 5.

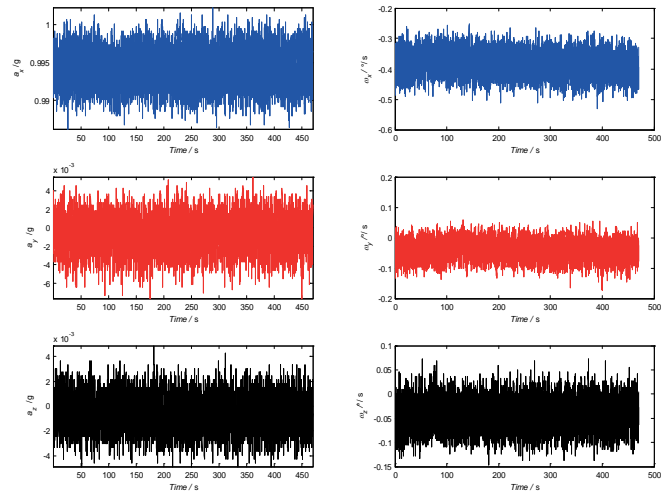


Fig. 5 MIMU Sample data under static conditions

$a_x$ ,  $a_y$ ,  $a_z$ ,  $\omega_x$ ,  $\omega_y$ ,  $\omega_z$  are x-axis, y-axis and z-axis specific forces and angular rates respectively.

Figure 5 shows that the gyroscopes and accelerometers have notable null bias errors.

Using these data, we have gotten INS results shown in Figure 6. The navigational errors are quite notable. So it's not worth a straw if working by itself. Then we have gotten INS results after IMU errors compensation, shown in Figure 7.

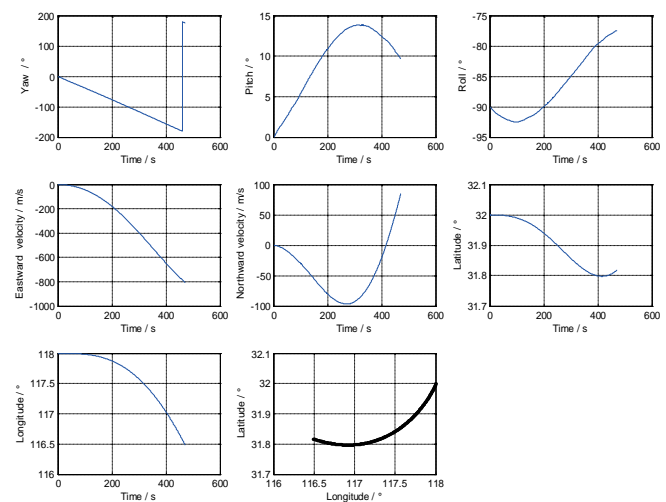


Fig. 6 INS navigational results – no IMU errors compensation

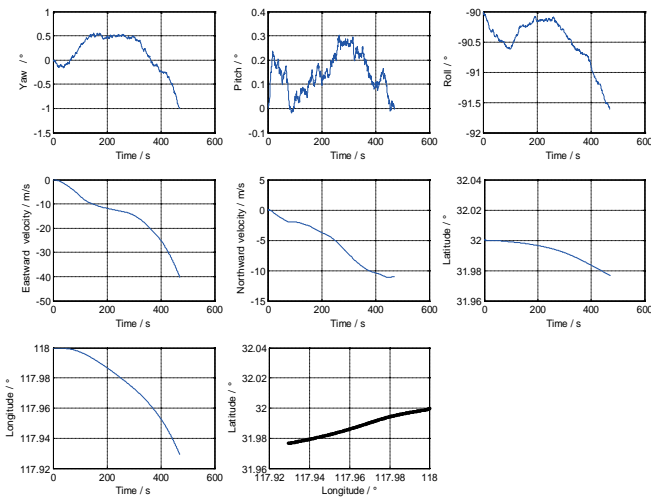


Fig. 7. INS results – after IMU errors compensation

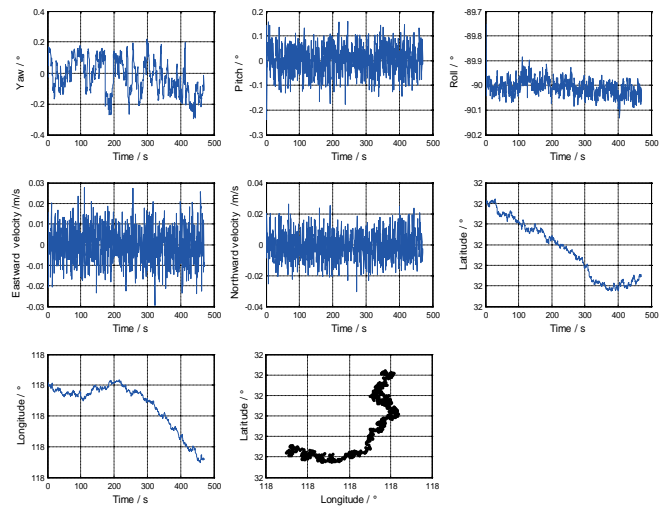


Fig. 9 Integrated navigation results - after IMU errors compensation

The navigational accuracy is improved greatly. Yet there are still large errors, esp. for velocity and position.

The MIMU sample data are used to the above integrated navigation system, then the navigational results are shown in Figure 8 and Figure 9.

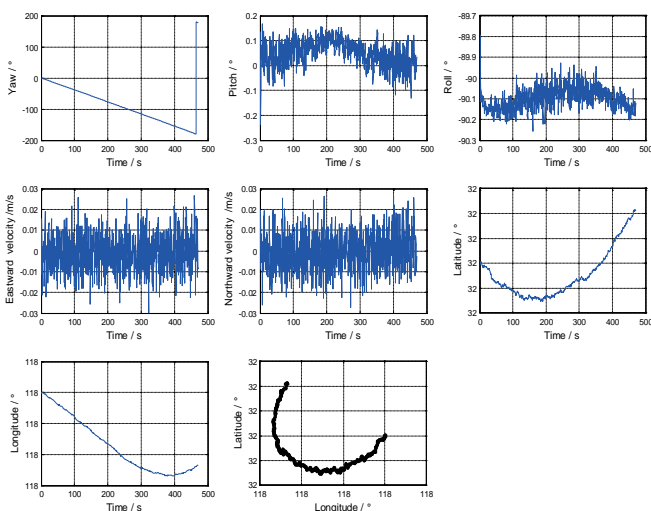


Fig. 8. Integrated navigation results – no IMU errors compensation.

Figure 9 shows that the results are much accurate. Yaw error is less than 0.3 deg; pitch and roll errors are less than 0.2deg; by Matlab data statistics tools, we can see the maximum position error is 0.65m. The integrated navigation system designed above improved navigational accuracy awfully, giving exactly accurate navigation results.

## CONCLUSIONS

In this work, an unmanned vessel navigation system based on a low cost MEMS inertial measurement unit and a doppler velocity sonar has been presented. By fusing measurements from both sensor sources with a Kalman filter model, the problem that large errors of low cost MIMU will lead to huge navigation errors has been overcome. Simulation and semi-physical simulation results have demonstrated that the accuracy of the inertial navigation system has improved greatly.

## ACKNOWLEDGEMENTS

This work was supported by project NSFC (No. 61302189) and NSFJ (No. BK20160955).

## REFERENCES

1. J. M. Daly, M. J. Tribou and S. L. Waslander, 2012. A nonlinear path following controller for an underactuated unmanned surface vessel. In: 2012 IEEE/RSJ International Conference on Intelligent Robots and Systems. Vilamoura. pp. 82-87.
2. M. H. Ghani, L. R. Hole, Ilker Fer, et al., 2014. The SailBuoy remotely-controlled unmanned vessel: Measurements of near surface temperature, salinity and oxygen concentration in the Northern Gulf of Mexico. *Methods in Oceanography*, (10), 104-121.
3. P. W. Pritchett, 2015. Ghost Vessels: Why the Law Should Embrace Unmanned Vessel Technology. *Tulane Maritime Law Journal*, 40(1), 197.
4. Y. Man, M. Lundh, T. Porathe, et al., 2015. From desk to field - Human factor issues in remote monitoring and

controlling of autonomous unmanned vessels. *Procedia Manufacturing*, (3), 2674-2681.

5. J. M. Larrazabal, M. S. Peñas, 2016. Intelligent rudder control of an unmanned surface vessel. *Expert Systems with Applications*, (55), 106–117.
6. L. Zhang, Z. Xiong, J. Lai, et al., 2016. Optical flow-aided navigation for UAV: A novel information fusion of integrated MEMS navigation system. *Optik*, (127), 447-451.
7. M. Morgado, P. Oliveira, and C. Silvestre, 2010. Design and experimental evaluation of an integrated USBL/INS system for AUVs. In: IEEE International Conference on Robotics and Automation, Alaska, pp.4264-4269.
8. Y. Geng, R. Martins, J. Sousa, 2010. Accuracy Analysis of DVL/IMU/Magnetometer Integrated Navigation System using Different IMUs in AUV. In: IEEE International Conference on Control and Automation, Xiamen, pp. 516-521.
9. C. Eling, L. Klingbeil and H. Kuhlmann, 2015. Real-Time Single-Frequency GPS/MEMS-IMU Attitude Determination of Lightweight UAVs. *Sensors*, (15): 26212-26235.
10. Y. Qin, 2006. Inertial navigation. Science Press, Beijing, 355-361.
11. M. S. Grewal, A. P. Andrews, and C. G. Bartone, 2013. Global navigation satellite systems, inertial navigation, and integration, Third edition. John Wiley & Sons, Inc., Hoboken, New Jersey.
12. V. Awale, H. B. Hablani, 2015. Fusion of Redundant Aided-inertial Sensors with Decentralised Kalman Filter for Autonomous Underwater Vehicle Navigation. *Defence Science Journal*, 65(6), 425-430.

## CONTACT WITH THE AUTHOR

**Changsong Yang**

School of Information & Control  
Nanjing University of Information Science & Technology  
Nanjing, 210044  
**CHINA**

## AN APPLICATION OF 24MODEL TO ANALYSE CAPSIZING OF THE EASTERN STAR FERRY

Xiao Suo<sup>1,2\*</sup>

Gui Fu<sup>1,2</sup>

Chunxue Wang<sup>3</sup>

Qingsong Jia<sup>1,2</sup>

<sup>1</sup> School of Resources & Safety Engineering, China University of Mining and Technology (Beijing), China

<sup>2</sup> State Key Laboratory of Coal Resources and Safe Mining, China University of Mining and Technology (Beijing), China

<sup>3</sup> School of Safety & Environmental Engineering, Capital University of Economics & Business, China

\* corresponding author

### ABSTRACT

*In the present study, the Eastern Star ferry accident was analyzed via 24Model. 24Model, as an accident causation model based on system thinking, holds that all causations of the accident are hazards and all hazards in the system need to be identified and comprehensively controlled in accident prevention. The result showed that five factors were the main causes of the accident. First, the direct causes: bad weather, the bad condition of the hull and the unsafe acts of the captain. Second, the indirect cause: the lack of safety awareness and safety knowledge of both the captain and the company's senior management. Third, there were loopholes in safety management system, including the training, supervision and execution of the company. Forth, the root cause: the company didn't establish a good safety culture. Last, the external causes: the severe market pressure, excessive regulatory authorities with puzzled relations and responsibilities—seriously hindered effective supervision. In order to prevent this kind of accident and to secure shipping system, the shipping companies and the relevant regulatory units should draw lessons from the five factors mentioned above, and take measures to identify and control those hazards.*

**Keywords:** Eastern Star ferry accident; 24Model; Systematic accident causation model; Accident analysis; Hazards

### INTRODUCTION

The capsizing of the Eastern Star ferry is the worst ship disasters in China in recent 60 years. The shipwreck caused 442 deaths (only 12 were rescued out of 454 people). The purposes of analysing the accident are to discover the causation, and to provide possible scheme for the prevention of such incidents. As a complex production system[1] the operating status is directly related to the safety of numerous passengers on board. In marine accident research, Özkan Uğurluet et al. employed the fault tree analysis to analyse the collision and grounding in oil tanker[2]. Also, Marine Accident Investigation Branch made a detailed study into bridge watchkeeping safety based

on 65 collisions, near collisions, groundings and contacts, and offered specific recommendations[3]. Additionally, Jintta Ylitalo established marine accident frequency models to analyse the accident frequency in the Gulf of Finland[4]/c. System thinking [5, 6], which is helpful to the analysis of the systemic characteristics of emergence and components interaction, is an important theoretical guide to solve the limitation of classical analytical methods based on reduction theory. In order to draw lessons from this serious accident, the present study applied the systematic accident causation model and 24Model to conduct a comprehensive analysis of such faulty shipping system. The human, technical, organizational, and social factors[7] that caused the accident have been

analyzed, and the experiences of preventing such accidents and the corresponding countermeasures were proposed. The case studies mainly based on accident analysis report[8].

The remaining of the paper is organized as follows: In Section 2, we elaborated the process of accident and introduced 24Model. In Section 3, we conducted a case study based on 24Model. In Section 4, we discussed the results of the analysis. Finally, we conclude this work in Section 5.

## MATERIAL AND METHODS

### PROCESS OF THE ACCIDENT

13 o'clock on May 28<sup>th</sup>, 2015, Eastern Star ferry started its voyage from Wumadu Port in Nanjing, Jiangsu Province. The ship planned to arrive at its destination in Chongqing at 6:30, June 7<sup>th</sup>. The accident occurred at about 21:32 on June 1<sup>st</sup> – the detailed description is as follows:

- 21:03. Eastern Star ferry sailed to the “Buoy of Tianziyihao” (one of the middle reaches of the Yangtze River, mileage of about 297.5 km). Its speed was about 14 km/h. At this time, there was lightning, and then it began to rain.
- 21:18. Eastern Star ferry sailed to “No.3 Red Buoy of Damazhou” (Middle reach of the Yangtze River, mileage of 301.0 km). It encountered a squall line weather system, with the south wind turning to the northwest wind, and rainstorm began to increase.
- 21:19. The captain heard the rainstorm getting stronger, and he rushed into the cab. At this moment, the chief officer on duty was commanding driving behind the radar; helmsman was in the steering, and sailor was standing by the bell to give assistance. The captain took over the command after acquiring the basic situation from chief officer.
- 21:21. Rainstorm continued to increase: the instantaneous maximum wind speed was 24.6 m/s and visibility declined significantly. The captain ordered the chief officer to slow down to 12.0 km/h, rudder left slightly to the right bank and implement anchor.
- 21:22. Eastern Star ferry was at the speed of 7.5 km/h.
- 21:23. Eastern Star ferry gradually dropped to 2.2 km/h. Subsequently, the speed gradually decreased to 0 km/h.
- 21:24. Due to the strong wind, the ship gradually fell backwards to its right rear with the speed of 4.0 km/h. Subsequently, the retreat speed was at 5.6 km/h. The captain noticed the ship was falling backwards, and he ordered the chief officer to increase the engine speed.
- 21:26. The speed of retreat reduced to 5.0 km/h. At this point this water area was in downburst which caused a sudden strengthening of the wind, instantaneous maximum wind speed was at 32 to 38 m/s.
- 21:29. The retreat speed was slowed down to 4.0 km/h.

21:30. In the strong rainstorm, the ship is out of control with a deflection and the wind angle increased, the speed increased to 6 km/h at that point. Subsequently, the ship suddenly tilted to the right and water began to infuse.

21:31. The ship’s main engine stopped, and the ship stated to tilt to the right heel quickly.

About 21:32. Eastern Star ferry capsized with AIS and GPS signals disappeared.

### INTRODUCTION OF 24MODEL

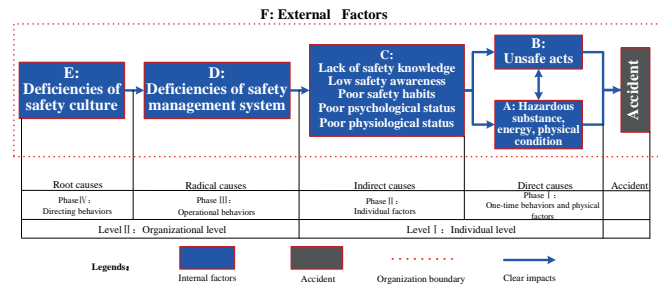


Fig. 1. 24Model[9-11].

24Model[9-11] as shown in Figure 1 is proposed and refined by the author’s research team. 24model is put forward based on the Heinrich’s[12], Reason’s[1] accident causation model and the systematic thinking. The model redefines the individual and organizational dimensions and redefines the concept of hazards.

Safety is the emergence of the system from the viewpoint of system thinking[13]. Systematic accident causation model calls for dynamic and hierarchical characteristics. The hierarchical characteristics of 24Model are reflected in the two levels and four phases. Specifically, the two levels are individual level and organizational level; four phases are one-time behavior (acts), physical factors, safety management system and safety culture. In addition, the executors of unsafe acts in 24Model does not take the individual level into account—namely all the staff of the organization’s unsafe acts are included. The organizational integrated behavior only contains the safety culture (philosophy, attitudes) and safety management system (files). The 24model redefines the individual and organizational behavior to make it easy to do statistical analysis of unsafe behavior of individuals and organization distinctly which reflecting the scale invariance[14]. Dynamic characteristic of 24Model is manifested on sustaining hazard identification and accident statistics continuously with the system changing. It can support the organization’s daily safety management and continuous improvement and achieve the goal of accidents prevention through a hazards identification table and highly structured accident statistics formed based on the 24Model.



Fig. 2. Relationship of accidents and hazards

24model holds that the hazards are equivalent to the causations of the accident. From a systematic point of view, the system is a group of interconnected entities, which means that the accident is the consequence of the system migrating to the high risk status integrally. So that the failures and adverse interactions of all components in system are the causes of the accident, hazards contain human factors, physical factors, organization, organizational external factors.

As shown in Figure 2, an accident is incited by subset hazards of universe regarding all the hazards in the system as universe. This definition is consistent with the practice operating as well, such as ISO 45001 DIS[15] requiring taking the human factors, physical factors, organizational factors, organizational and external factors into fully consideration when hazards identification.

## RESULTS

### A Hazardous substance, energy and physical condition

A1 The squall line weather system.

The squall line system appeared “above the waters where Eastern Star” navigated accompanied by a downburst, tornadoes, other short-term local heavy rainfall as well as severe convective weather at the time of accident and therefore the ferry capsized suffering strong storms.

A2 The accident occurred between 9:00 p.m. and 10:00 p.m., when all the passengers were asleep or prepare to sleep. Therefore, it was difficult for them to escape.

A3 There was no side channel of the passengers’ rooms that above the main deck.

A4 There were no weathertight covers or unfixed bunks on the cabin door and other related facilities.

A5 Wind pressure stability criterion was small.

A6 The ship veered rapidly leading the wind angle increasing.

A7 GPS signal were lost when the ship capsized but no one caught it in time.

### B Unsafe acts

B1 The captain failed to make a decision in time to drop anchor in the bad weather. It was too late to drop anchor when the ship had been hit by the downburst and capsized.

However, due to timely anchoring, the ships near the Eastern Star ferry were safe.

B2 The captain and the crew failed to notice the receding of Eastern Star in time.

B3 In an emergency, the captain and chief officers failed to send out distress signal. Nor did they alarm the whole ship to arrange abandonment and evacuation of the ship.

B4 The management of the company let the designer dismantle the side channel when they remodeled the ship in 1997.

B5 The management of the company didn’t notice that the cabin door, and other related facilities lacked the weathertight covers, and the bunks were unfixed.

B6 The management of the company cut the ship maintenance cost.

B7 Having been remodeled for three times, the stability criteria got smaller and smaller, although the value of it was still greater than 1. But the hull stability was getting worse; the specific changes of K value see Table 1. The ship remodeled in 1997. The ship remodeled in 2008. The company illegally hired the engineers who didn’t acquire professional operating qualifications to transform the round bottom’s ballast tank and water tank without submitting for approval in 2015.

Tab. 1. Changes of the stability criterion

| Years                                 | 1994  | 1997 | 2008  | 2015  |
|---------------------------------------|-------|------|-------|-------|
| Ship stability (weather) criteria (K) | 1.355 | 1.09 | 1.018 | 1.014 |

B8 The company safety supervision departments do not set up full-time vessels GPS monitoring personnel.

### C Individual factors

C1 The captain and the chief officer lacked the safety knowledge of recognizing the seriousness of bad weather.

C2 Low safety consciousness led the captain and crew’s failing to remain vigilant in a dangerous environment and find the receding of Eastern Star in time.

C3 Senior management of the company lacked the safety knowledge.

C31 Failed to realize risk posed by reduction of stability criteria after the transformation and inconvenience of escaping in emergency.

C32 Failed to realize the impact of weathertight and fixed bunks for the stability of the ship.

C33 Failed to realize the importance of GPS regulation.

C4 Poor safety habits of the senior management resulted in the long-term neglect of the ship’s safety check and the assessment and training to the staff.

### D Deficiencies of safety management system

D1 Chongqing Eastern Shipping Corporation did not develop the emergency treatment documents.

D2 Chongqing Eastern Shipping Corporation had loopholes in the crew’s training system for ships, navigation and emergency knowledge. Besides, the company implemented assessment fraud which violates the “People’s Republic

of China River Traffic Safety Management Regulations”, Chapter II, Article IX.

D3 Chongqing Eastern Shipping Corporation did not establish a strict GPS regulatory system in management system.

**E Deficiencies of safety culture**

The table of Safety culture of the 32 elements See literature[16] for details.

- E1 Lack of Safety Importance.
- E4 Lack of Safety and Management Integration.
- E6 Lack of Primary Responsibility for Workplace Safety.
- E7 Lack of Safety Investment.
- E8 Lack of Role of Safety Regulations.
- E10 Lack of Safety Responsibility of Mangers.
- E13 Lack of Demand of Safety Training.
- E15 Lack of Role of Management System.
- E32 Lack of Emergency Capability.

**F External factors**

F1 Market pressure made the senior management of the company cut the ship maintenance cost (Table 2 shows the Chongqing Eastern Shipping Corporation’s financial status which depicts the company’s poor profitability, higher debt in 2013 and 2014) and asked the trip must be completed original schedule on time.

Tab. 2. Chongqing Eastern Shipping Corporation’s financial status[17]

|                         | 2013          | 2014          |                    | 2013           | 2014           |
|-------------------------|---------------|---------------|--------------------|----------------|----------------|
| General assets          | 7,220 Million | 8,975 Million | Total equities     | -9,626 Million | -9,493 Million |
| Gross revenue           | 2,758 Million | 3,315 Million | Total profit       | -395 Million   | 133 Million    |
| Prime operating revenue | 2,519 Million | 3,128 Million | Net margin         | -395 Million   | 133 Million    |
| Total tax               | 29 Million    | 184 Million   | Total indebtedness | 16,846 Million | 18,468 Million |

Unit: Chinese yuan

F2 Numerous management agencies with complex relationships and cross-functions.

The units that have supervisory responsibility for Chongqing Eastern Shipping Corporation include vertical supervision units of the Yangtze River Navigation Affairs Administration (Table 3) and the local government of Chongqing (Table 4).

Tab. 3. Ministry of Communications regulatory level (Vertical management)

| 1   | 2                 | 3             | 4           |
|---|-------------------|---------------|-------------|
| Yangtze River Navigation Affairs Administration | Yangtze River MSA | Chongqing MSA | Wanzhou MSA |
|   |                   | Yueyang MSA   | --          |

Yangtze River Navigation Affairs Administration had a poor supervision on Chongqing MSA and Wanzhou MSA. Wanzhou MSA as frontline law enforcement unit was not strict

with the company’s safety management system check. Neither did they find that the responsible person of the company’s top management in charge of safety management did not have the corresponding qualifications nor they find the loopholes of GPS monitoring system, training and assessment, unfixed bunks, weather tight and so on. The control center of Yangtze River MSA ignored the affair of the control center of Yueyang MSA failed to perform duties seriously. Yueyang MSA did not constantly monitor the ship’s status. When Eastern Star lost contact, they did not take measures to verify the status of the ship timely.

Table 4. Chongqing regulatory authorities level (Local government subordinate departments)

| 1                              | 2                                  | 3   | 4   |
|--------------------------------|------------------------------------|---|---|
| Chongqing municipal government | Chongqing transportation committee | Chongqing Navigational Affairs Administration | Wanzhou District Navigational Affairs Administration;<br>Wanzhou shipping administration;<br>Wanzhou Ship inspection Bureau |
|                                |                                    | Chongqing shipping administration             |   |
|                                |                                    | Chongqing Ship Inspection Bureau              |   |
|                                | Wanzhou municipal government       | Wanzhou transportation committee              |   |
|                                | Chongqing SASAC                    | Wanzhou SASAC                                 |   |

Wanzhou District Navigational Affairs Administration, as frontline law enforcement unit of local government, lacked strict inspection on Chongqing Eastern Shipping Corporation. The problems of illegal adjustment of ballast tanks and poor equipment in cabins were ignored and water transport permit was issued without careful inspection. SASAC of Wanzhou District was in charge of the Chongqing Eastern Shipping Corporation, but it did not carry out strict safety supervision and inspection of the company and did not find the fraud in training and assessment or the unhealthy management regime of the company.

F3 The imperfection of information sharing between China Meteorological Administration and maritime sector caused the maritime sector did not issue bad weather warnings to the Eastern Star.

**DISCUSSION**

The accident process is divided into two parts which are the capsizing and evacuating adversely. The specific path of the accident is shown in Figure 3 From the path of the accident can be seen that hazardous substance, energy and physical condition, unsafe acts, Individual factors, deficiencies of safety management system, deficiencies of safety culture and external factors interact and lead to mishap eventually.

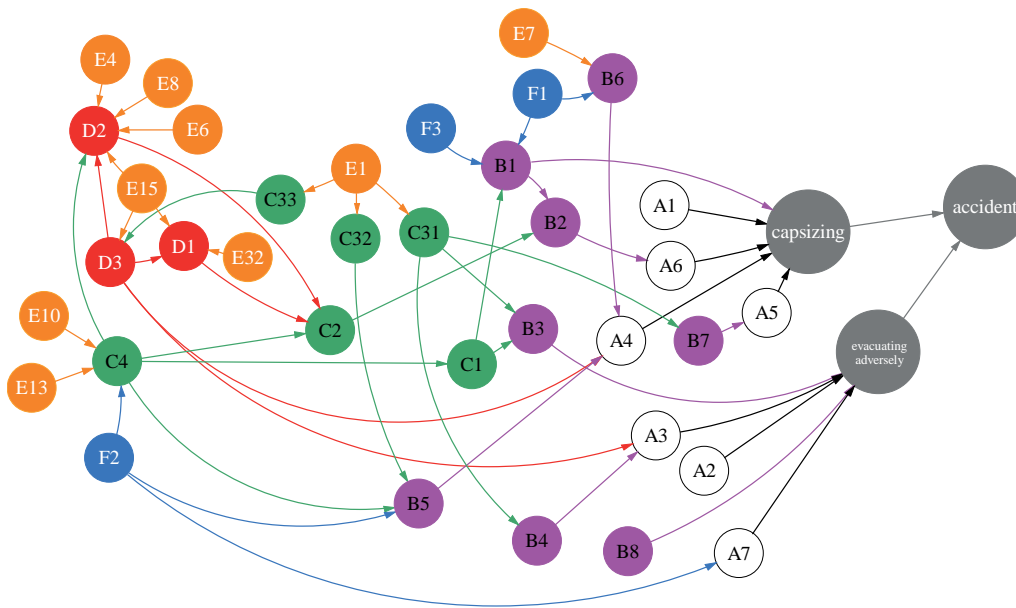


Fig. 3. The path of the Eastern Star ferry Accident

From the individual level of 24Model the direct cause of this inland waterways shipwreck was the ship met the squall line weather system which is a strong convective cloud formed by many monolithic thunderstorms and arranged side by side. What's more, the ferry was attacked by downburst (a strong sinking air flow in the local thunderstorm, after reaching the ground will produce a linear wind, the closer to the ground the faster wind speed it is, the maximum ground wind up to 15) at the same time. The hull stability was greatly challenged by the sudden strong convective weather. In addition, the hull was in a poor condition after the three times transformation (No side channel and stability significantly reduced). However, the captain yielded to market pressure and continued sailing in the bad weather, finally leading to capsizing.

To analyze the deeper causes from the organizational level of 24Model, the corporation, as the main body of the responsibility, should ensure the provision of transport services and guarantee the safety of passengers at the same time. However, Chongqing Eastern Shipping Corporation, the Eastern Star belongs to, has laid the groundwork for the accident through day-to-day management and operation. Furthermore, the three times' reconstruction made the stability criteria getting smaller and smaller and the side channel was cancelled as well. In the meantime, there were no weathertight covers on the cabin door and other related facilities, and the bunks were unfixed. Additionally, the wrong operations of the captain and chief officer in emergency and sailing at night lead to the difficulty in escaping after capsizing. All these unsafe conditions have not been properly handled due to the unsound safety system and safety culture. The ship transportation organization should balance profits and safety and promote safety culture around deficiencies of safety culture mentioned earlier.

From the perspective of external organization factors, market pressure made the company in a poor business condition which led to catch up on travel schedule in a hurry and cut maintenance costs, so that the captain choose to continue sailing in such bad weather conditions.

The causes above are all belongs to subject responsibilities of the Chongqing Eastern Shipping Corporation. In external factors, oversight of Supervision department and insufficient early warning capabilities of

China Meteorological Administration made contribution to the accident as well. Regulatory departments are divided into vertical departments of MSA and various departments of the local government, but still mismanagement. The functions of numerous regulatory authorities repeated in a way, may shift responsibility onto others. Due to this circumstance, it is recommended to simplify the shipping regulatory authorities, clear regulatory responsibilities and implement the implementation, so that the effective supervision of business enterprises.

It can be concluded that the mishap is the result of the overall deviation of the entire passenger transport system including hazards of human factors, physical factors, organizational factors and external factors. These hazards interact in the system and eventually led to overturning of the ship. The direct cause of the accident was the rarely bad weather and the unsafe acts of the captain. The countermeasure to the direct cause of the accident is to implement anchoring. Deep-seated causes were the safety management system of Chongqing Eastern Shipping Corporation confusion, deficiencies of safety culture, poor business conditions and regulatory supervision. The countermeasures to such causes above are: enterprises should establish a sound safety culture, and then develop a comprehensive safety management system. Moreover, the senior management and ship personnel need to implement the established rules of the system effectively to eliminate unsafe physical condition and unsafe acts. For the regulatory authorities, it's necessary to make clear the regulatory responsibilities and take effective supervision. To prevent accident, it is necessary to know well the path of accidents, and to improve the system comprehensively. If only implement rectification on one or several hazards, accidents cannot be prevented. For example, a sound safety management system and safety culture are established within the company, however, the flaws of the senior management implementation will generate the unsafe physical condition and unsafe acts of the ship personnel. Once the opportunity

is ripe, unsafe physical condition and unsafe acts will lead to the occurrence of the accident. In the case of preventing such accidents, it cannot be narrowed down to only identify and improve certain or several hazards. As elaborated in accident causation model based on system thinking 24Model, accident prevention should deploy the overall identification and control from viewpoint of the system level to achieve a good integration of system safety and functional achievement.

Additionally, it is also advisable for the customers and passengers to choose cruise companies with a good business operating status rather than a bad one, and to choose the ships with higher stability. Also, passengers should learn and remember how to use the escape facility in advance.

## CONCLUSIONS

In the present study, a comprehensive analysis of the capsizing of the Eastern Star ferry was carried out via 24Model. Conclusions are as follows.

1. All the hazards that led to the accident have been analyzed and path of each hazard interaction has been mapped based on 24Model. The hazards contain all the components and the components interaction of the system. An accident is incited by subset hazards of universe, regarding all the hazards in the system as universe. For the daily safety management of shipping organizations, it is necessary to apply comprehensive hazards identification and control from the perspective of system so as to maintain the shipping system functions smooth and safe.

2. From the individual level of 24Model, the direct causes of the accident were the rarely bad weather and the unsafe decision-making of the captain. The countermeasure to prevent such direct causes is to anchor the ship.

3. From the organizational level of 24Model to analyze, the deep causes of the accident were the deficiencies of the management system and safety culture, the company's poor financial status and the misconduct of the regulatory authorities. The countermeasures to prevent such deep causes are forcing the enterprise to establish a sound safety culture, developing a comprehensive safety management system and implementing the effectively, and eliminating unsafe physical condition and unsafe acts. For regulators, it is necessary to simplify the organization structure, to confirm regulatory responsibility and implement effectively.

4. It is recommended that passengers should choose a cruise company with good financial condition when taking a cruise trip and understand the basic safety of the vessel before departure.

## ACKNOWLEDGEMENTS

The authors gratefully acknowledge the funding support from Natural Science Foundation of China Project (No. 51534008).

## REFERENCES

1. J. Reason, 1990. Human error. Cambridge university press, New York.
2. Ö. Uğurlu, E. Köse, U. Yıldırım, et al., 2015. Marine accident analysis for collision and grounding in oil tanker using FTA method. *Maritime Policy & Management*, 42(2), 163-185.
3. M.A.I. Branch, , House C., and Place C., 2004. Bridge watchkeeping safety study. Department for Transportation, Marine Accident Investigation Branch, Southampton.
4. [4] J. Ylitalo, 2010. Modelling marine accident frequency. Aalto University, Helsinki.
5. P. Checkland, 1981. Systems thinking, systems practice. John Wiley & Sons, New York.
6. X. Qian, J. Yu, and R. Dai, 1993. A New Discipline of Science-The Study of Open Complex Giant System and Its Methodology. *Journal of Systems Engineering & Electronics*, 4(2), 2-12.
7. Z.H. Qureshi, 2007. A review of accident modelling approaches for complex socio-technical systems. In: Proceedings of the twelfth Australian workshop on Safety critical systems and software and safety-related programmable systems. Adelaide. pp. 47-59.
8. State Council of the PRC investigation team of "Eastern Star" ferry capsized accident, 2015. The investigation report of Eastern Star ferry capsized accident. [http://www.chinasafety.gov.cn/newpage/Contents/Channel\\_21356/2015/1230/262992/content\\_262992.htm](http://www.chinasafety.gov.cn/newpage/Contents/Channel_21356/2015/1230/262992/content_262992.htm).
9. G. Fu, Lu B., and X. Chen, 2015. Behavior Based Model for Organizational Safety Management. *China Safety Science Journal*, 15(9), 21-27.
10. G. Fu, W. Yin, J. Dong, et al., 2013. Behavior-based accident causation: the "2-4" model and its safety implications in coal mine. *Journal of China Coal Society*, 38(7), 1123-1129.
11. G. Fu, Y. Fan, R. Tong, et al., 2016. A Universal Methodology for the Causation Analysis of Accidents(4th Edition). *Journal of Accident Prevention*, 2(1), 7-12.
12. H.W. Heinrich, D.C. Petersen, and N.R. Roos, 1980. Industrial accident prevention: A safety management approach. 5th ed. McGraw-Hill Companies, New York.
13. N. Leveson, 2011. Engineering a safer world: Systems thinking applied to safety. MIT press, Cambridge.

14. E. Hollnagel, 2012. FRAM, the functional resonance analysis method: modelling complex socio-technical systems. Ashgate Publishing, Ltd, Farnham.
15. International Organization for Standardization, 2016. ISO/DIS 45001:2016(E) Occupational health and safety management systems.
16. G. Fu, Y. Dong, S. Zhang, et al., 2013. Further Discussions on Definition of Safety Culture and Its Assessment Indicators. *China Safety Science Journal*, 23(4), 140-145.
17. National Enterprise credit information publicity system. 2017. [http://www.chinasafety.gov.cn/newpage/Contents/Channel\\_21356/2015/1230/262992/content\\_262992.htm](http://www.chinasafety.gov.cn/newpage/Contents/Channel_21356/2015/1230/262992/content_262992.htm).

## CONTACT WITH THE AUTHORS

**Xiao Suo**

School of Resources & Safety Engineering  
China University of Mining and Technology (Beijing)  
Beijing 100083

**CHINA**

State Key Laboratory of Coal Resources and Safe Mining  
China University of Mining and Technology (Beijing)  
Beijing 100083

**CHINA**

# INVESTIGATIONS OF TOPOGRAPHIC EFFECT ON RADIAL CURRENT IN SOUTH YELLOW SEA

Cheng Chen<sup>1,\*</sup>

Yigang Wang<sup>2</sup>

Huiming Huang<sup>2</sup>

<sup>1</sup> College of Civil Engineering, Fuzhou University, Fuzhou 350116, China

<sup>2</sup> College of Harbor, Coastal and Offshore Engineering, Hohai University, Nanjing 210098, China

\* corresponding author

## ABSTRACT

*Large scaled projects are conducted in South Yellow Sea in recent years. Topographic effect and tidal current are key issues to the coastal engineering and the ocean engineering. In this study, field surveys were conducted to investigate the tidal level, current velocity, and current direction in South Yellow Sea. A numerical model was developed to simulate the radial current field based on the field data. To investigate the mechanism of the radial current field, the actual topography and a smoothed topography were applied in the numerical model, respectively. Results show that, the current field appears radial because of the tidal system rather than the submarine topography. Local topography centralized the radiation centre and shifted the high-velocity zones. The actual topographic effect is proposed, and results show that local topography increases the flood tide velocity and decreases the ebb tide velocity. Lagrangian residual currents are calculated to illustrate possible sediment sources and transport routes.*

**Keywords:** Field survey; Numerical model; Topography; Radial current; Lagrangian residual current

## INTRODUCTION

The sand ridges are formed due to the interactions of tidal currents and sediments [1], and further shaped by waves [2]. The coast of Eastern China includes more than 10 large sand ridges [3], which will be reclaimed before 2020 [4]. However, there is a radial current field in the coast of Eastern China, which makes reclamation project need to be investigated.

To have a better understanding of this current field, some numerical works have been done by researchers. Xia et al. [5] simulated the M2 tide in the Yellow Sea, using 20 km computational grids to smoothed the detailed topography. The results showed that the radial tidal currents still exist in this study area even using such coarse computational grids. Zhu et al. [6] established a 2-D tidal current model using finer computational grids (10 km) with an approximately

rectangular coastline. It was also found that the radial current field was not generated by marine topography. Further considering tidal currents, waves and storm surges in the numerical simulation, Zhang et al. [7] explained how the radial sand ridge topography had been forming and evolving, i.e. tidal current-induced formation, storm-induced change, tidal current-induced recovery. The radial current field has existed for thousands of years [8, 9], providing sufficient time to generate the sand ridge topography. Zhang et al. [8] conducted numerical experiments on the propagation of M2 tidal wave in ancient coast conditions and generated the similar tidal wave system as present. Zhu [9] established a 2-D numerical model for tidal current research in Bohai Sea, Yellow Sea and East China Sea to simulate the tidal current in 7000a B.P. and 3800a B.P.. The results showed that a standing tidal wave system existed solitarily at both 7000a B.P. and

3800a B.P., respectively. Besides, the radial tidal current field has been in Jiangsu coastal area since maximum marine transgression in the last glacial age, i.e. there is no obvious change with the coastline variation. The local tidal currents are also influenced by the sand ridge topography. Chen et al. [10] showed that, the sand ridges are migrating southward due to the large-scaled hydrodynamic effect, and the current velocity tends to increase in the waterways between sand ridges. Xing et al.'s [11] numerical model indicated the erosion occurred in deep channels and the accretion occurred in shallow ridges. The previous discussions on the variation of sand ridge suggest that the sand ridge is the results of the radial current system over thousands of years.

In this study, a series of large-scaled field surveys were conducted and the data were used to validate the 2-D large-scaled hydrodynamic model in this study. This study was supportive to the previous findings on radial current fields. The current fields were simulated using gradually changing (smoothed) topography and actual (sand ridge) topography, respectively. Actual Topographic effect (ATE) is proposed as the difference between flow with and without sand ridge, to investigate the topographic effect on current field. The results from this numerical model proposed possible hydrodynamic explanations of the sediment sources and sediment transport routes.

## MATERIAL AND METHODS

### FIELD DATA COLLECTION

In this field survey, 14 stations were distributed in the study area (shown in Figure 1). Eight stations conducted surveys during both the spring tide and neap tide; another six stations conducted surveys during the spring tide.

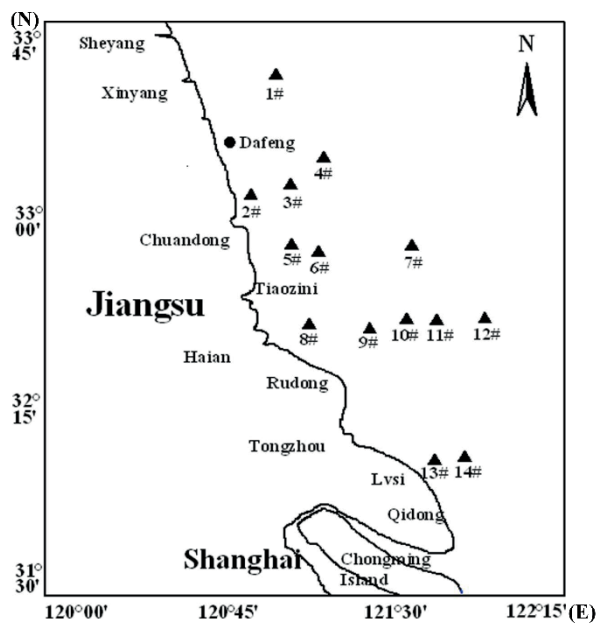


Fig. 1. Locations of the survey stations

Table 1 shows the detailed information for each survey station. The time-histories of tidal levels, current velocities and current directions were recorded in this field study. In addition, a long-term survey was conducted at Dafeng Port to record the time-history of tidal levels for 12 months. The stations cover most part of the South Yellow sea.

Tab. 1. Information of the survey stations

| Stations | Latitude/(°N) | Longitude/(°E) | Survey period           | Approximate position     |
|----------|---------------|----------------|-------------------------|--------------------------|
| 1#       | 33.66         | 120.97         | Spring tide             | Outer Xinyang Port       |
| 2#       | 33.17         | 120.86         | Spring tide & Neap tide | North of Chuandong Port  |
| 3#       | 33.18         | 120.91         | Spring tide             | North of Chuandong Port  |
| 4#       | 33.33         | 121.23         | Spring tide & Neap tide | Outer Wang Port          |
| 5#       | 32.97         | 120.97         | Spring tide & Neap tide | South of Chuandong Port  |
| 6#       | 32.90         | 121.05         | Spring tide             | South of Chuandong Port  |
| 7#       | 32.95         | 121.54         | Spring tide & Neap tide | East of Chuandong Port   |
| 8#       | 32.58         | 121.15         | Spring tide & Neap tide | Outer Xiaoyangkou Port   |
| 9#       | 32.55         | 121.33         | Spring tide             | Outer Xiaoyangkou Port   |
| 10#      | 32.66         | 121.50         | Spring tide & Neap tide | East of Xiaoyangkou Port |
| 11#      | 32.66         | 121.62         | Spring tide             | East of Xiaoyangkou Port |
| 12#      | 32.66         | 121.75         | Spring tide             | East of Xiaoyangkou Port |
| 13#      | 32.08         | 121.74         | Spring tide & Neap tide | Outer Lvsu Port          |
| 14#      | 32.09         | 121.81         | Spring tide & Neap tide | Outer Lvsu Port          |
| Dafeng   | 33.28         | 120.80         | 12 months               | Dafeng Port              |

The short-term survey for each individual station started at its local low tide. The initial recording times for all stations were different. This is because in this study area, local tidal wave phases at different stations were not exactly the same. In general, the recording lasted for approximately 27 hours, covering the one tidal cycle. To capture the current variations, samples were taken in 30 minute intervals during the maximum flood and the ebb period. During the rest of the time, samples were taken in 60 minute intervals. Table 2 shows the detailed recording periods for each survey station.

Tab. 2. Recording periods for each station

| Sub-area                | Spring tide                        |                 |                 | Neap tide            |                 |                 |
|-------------------------|------------------------------------|-----------------|-----------------|----------------------|-----------------|-----------------|
|                         | Survey Station                     | Start Time      | End Time        | Survey Station       | Start Time      | End Time        |
| Xingyang Port           | 1#                                 | 17:00<br>Jan. 3 | 19:00<br>Jan. 4 |                      |                 |                 |
| Wang Port               | 4#                                 | 18:00<br>Jan. 3 | 19:00<br>Jan. 4 | 4#                   | 5:00<br>Jan. 11 | 7:00<br>Jan. 12 |
| Chuandong Port          | 2#, 3#, 5#, 6#                     | 17:00<br>Jan. 3 | 13:00<br>Jan. 4 | 2#, 5#               | 5:00<br>Jan. 11 | 7:00<br>Jan. 12 |
| Outer Chuandong Port    | 7#                                 | 17:00<br>Jan. 3 | 19:00<br>Jan. 4 | 7#                   | 5:00<br>Jan. 11 | 7:00<br>Jan. 12 |
| Xiaoyangkou & Lvsi Port | 8#, 9#, 10#, 11#,<br>12#, 13#, 14# | 17:00<br>Jan. 3 | 21:00<br>Jan. 4 | 8#, 10#,<br>13#, 14# | 5:00<br>Jan. 11 | 7:00<br>Jan. 12 |

Roundtrip measurements were applied in the field surveys to increase the accuracy of the data. If the water is deeper than 5 m, six-point sampling method was adopted along the vertical profile. If the water is shallower than 5 m, three-point sampling method was adopted instead. In the two-dimensional numerical model, the current velocities were validated by the field data of mean velocities calculated from the vertical profile. The major devices and instruments for the survey are listed in Table 3.

Tab. 3. Main devices for field surveys

| Instruments              | Type  | Application                 |
|--------------------------|---|-----------------------------|
| GPS Receivers            | Trimble 4700  | Positioning System          |
| Beacon Receivers         | Trimble DSM212  | Hydrological Measurement    |
| Hand-held GPS            | Garmin 12xlc  | Investigation System        |
| Navigation Software      | HYPACK(V8.1a)   | Navigation Data Acquisition |
| Flow Velocity Instrument | ZSX-III Series  | Current Data Collection     |
| Others                   | Current Meter, Anemometer, Hydrographic Winch, Fish Lead, Laptop, Electric Generator, Wireless interphone, etc. |                             |

## NUMERICAL MODEL

In this study, a numerical model MIKE21 was used and validated based on field data. DHI's Software contains a modelling system for estuaries, coastal waters and seas. Therefore, a two-dimensional model was built within the commercial MIKE 21 FM package to simulate tidal hydrodynamics in the study area. The main governing equations are the continuity equation and the incompressible Reynolds-averaged Navier-Stokes (RANS) equations. The N-S equations are used based on the static pressure hypothesis and Boussinesq hypothesis. The vertical current acceleration is ignored compared to the gravity acceleration, and the turbulence stress is with respect to the time averaged velocity gradient. The basic equations to describe tidal hydrodynamics can be written as:

$$\frac{\partial h}{\partial t} + \frac{\partial h\bar{u}}{\partial x} + \frac{\partial h\bar{v}}{\partial y} = hS \quad (1)$$

$$\begin{aligned} \frac{\partial h\bar{u}}{\partial t} + \frac{\partial h\bar{u}^2}{\partial x} + \frac{\partial h\bar{u}\bar{v}}{\partial y} = f\bar{v}h - gh \frac{\partial \eta}{\partial x} - \frac{h}{\rho_0} \frac{\partial P_a}{\partial x} - \frac{gh^2}{2\rho_0} \frac{\partial \rho}{\partial x} + \\ \frac{\tau_{sx}}{\rho_0} - \frac{\tau_{bx}}{\rho_0} - \frac{1}{\rho_0} \left( \frac{\partial S_{xx}}{\partial x} + \frac{\partial S_{xy}}{\partial y} \right) + \\ \frac{\partial}{\partial x} (hT_{xx}) + \frac{\partial}{\partial y} (hT_{xy}) + hu_s S \end{aligned} \quad (2)$$

$$\begin{aligned} \frac{\partial h\bar{v}}{\partial t} + \frac{\partial h\bar{u}\bar{v}}{\partial x} + \frac{\partial h\bar{v}^2}{\partial y} = -f\bar{u}h - gh \frac{\partial \eta}{\partial y} - \frac{h}{\rho_0} \frac{\partial P_a}{\partial y} - \frac{gh^2}{2\rho_0} \frac{\partial \rho}{\partial y} + \\ \frac{\tau_{sy}}{\rho_0} - \frac{\tau_{by}}{\rho_0} - \frac{1}{\rho_0} \left( \frac{\partial S_{yx}}{\partial x} + \frac{\partial S_{yy}}{\partial y} \right) + \\ \frac{\partial}{\partial x} (hT_{xy}) + \frac{\partial}{\partial y} (hT_{yy}) + hv_s S \end{aligned} \quad (3)$$

where  $x$  and  $y$  are horizontal Cartesian coordinates;  $\eta$  is the surface elevation;  $t$  is time;  $h$  is the total water depth;  $\bar{u}$  and  $\bar{v}$  are depth-averaged velocity components in  $x$  and  $y$  directions, respectively;  $P_a$  is the local atmospheric pressure;  $\rho_0$  is the reference of water density;  $\rho$  is the density of water;  $f$  is the Coriolis parameter;  $S_{xx}$ ,  $S_{xy}$ ,  $S_{yx}$ ,  $S_{xz}$ ,  $S_{yy}$  are components of radiation stress tensor;  $T_{xx}$ ,  $T_{xy}$ ,  $T_{yx}$  are the lateral stress including viscous friction, turbulent friction, and differential advection;  $(\tau_{sx}, \tau_{sy})$  and  $(\tau_{bx}, \tau_{by})$  are the components of wind stress and bottom stress, respectively;  $S$  is magnitude of point source discharge.

The model domain was established in a large-scaled area to provide a relatively accurate tidal wave system. The model boundaries were from 23°N northwards to the Asian continent coastline, and 128.5°E westwards to the Asian continent coastline (shown in Figure 2). The simulation time was from 8:00 30/12/2006 to 8:00 12/01/2007, which covered the spring tide period (from 17:00 03/01/2007 to 19:00 04/01/2007) and neap tide period (from 5:00 11/01/2007 to 7:00 12/01/2007). The study area was self-nested in the large-scaled model, which was from 31.8°N northwards to 34.2°N, and 122.8°E westwards to the Asian continent coastline. The actual (sand ridge) topography data and gradually changing (smoothed) topography data were used in the model, respectively. Therefore, two sets of corresponded current fields were simulated using the same hydrodynamic model setup except for the topography.

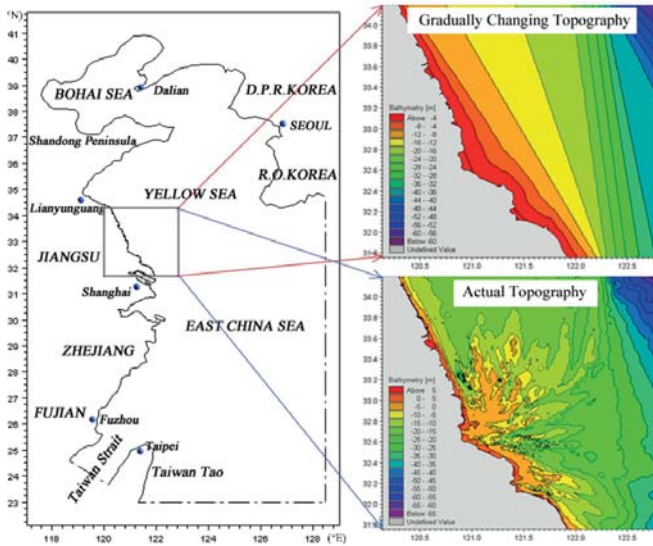


Fig. 2. Numerical model domain and topography in study area

The overview of the computational grids is shown in Figure 3. The unstructured grids were applied in the numerical model, and the grid sizes were changable. The coarser computational grids (larger than 10 km) were applied in the large-scaled model to reduce the computation work, while finer computational grids (less than 1 km) were applied in the self-nested area to provide relatively accurate modelling results.

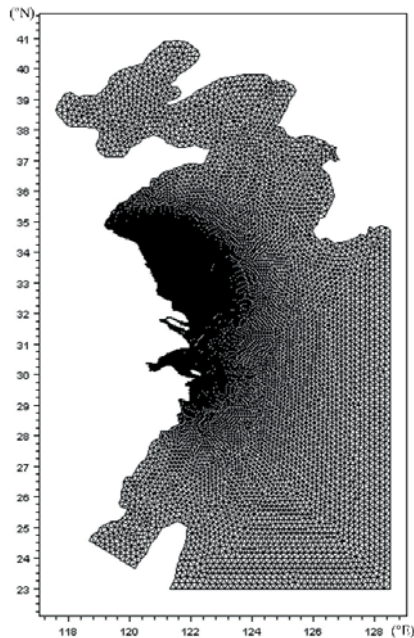


Fig. 3. Overview of the computational grids

The field data (including time-histories of tidal levels, current velocities and current directions) were collected to validate this numerical model. Figure 4 shows the time-history of the tidal levels for Dafeng Port as an example. The horizontal axis is the time (in hour). The initial time (0) stands

for 17:00 03/01/2007, which is the beginning of the spring tide. Results of the tidal level indicate that the agreement between the measured value and simulated value is good.

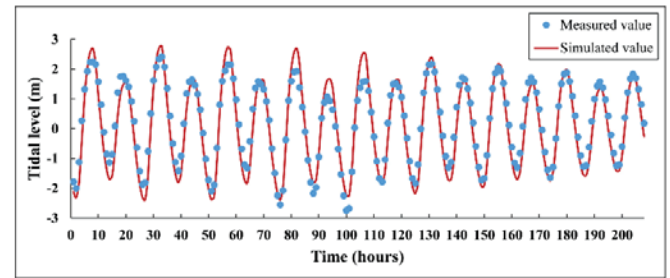


Fig. 4. Time-history of tidal level for Dafeng Port

Figure 5 shows the time-history of current velocities and directions for Lvsj Port (13# in Figure 1) as an example. The initial time (0) for Figure 5(a) and Figure 5(b) stands for 17:00 03/01/2007 (the beginning of the spring tide); the initial time for Figure 5(c) and Figure 5(d) stands for 05:00 11/01/2007 (the beginning of the neap tide). Good agreements were observed between the measured values and simulated values. Therefore, this hydrodynamic model was applied to study the current field, and two parallel experimental results from actual topography and gradually changing topography were compared and discussed. Results of the currents indicate that good agreement was observed between measured value and simulated value, and the numerical model has reliable results in current fields.

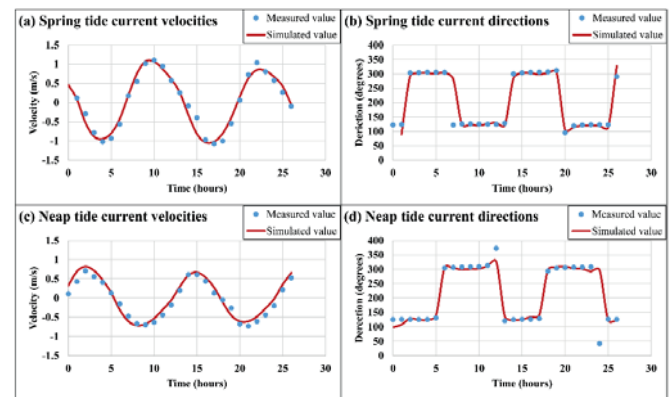


Fig. 5. Time-histories of current velocities and directions in for Lvsj Port (13# in Figure 1)

## RESULTS AND DISCUSSIONS

### CURRENT FIELDS AND MAXIMUM VELOCITIES

Figure 6(a) and Figure 6(b) present the radial current field on two topographies during flood period, and Figure 6(c) and Figure 6(d) are the ones during ebb period. The horizontal axis is the longitude (in °E), and the vertical axis is the latitude (in °N). The results indicated the radial

current field was not generated by the actual (sand ridge) topography since it also existed on the gradually changing (smoothed) topography. Numerical model results also showed the moving progress of the tidal wave. It was observed that there are two tidal waves in this study area, i.e. a progressive tidal wave propagating from the southeast towards the Yellow Sea, and a counter-clockwise rotary tidal wave reflected by the Shangdong Peninsula. These two tidal waves converged as a dual-tide system and generated a unique radial current field.

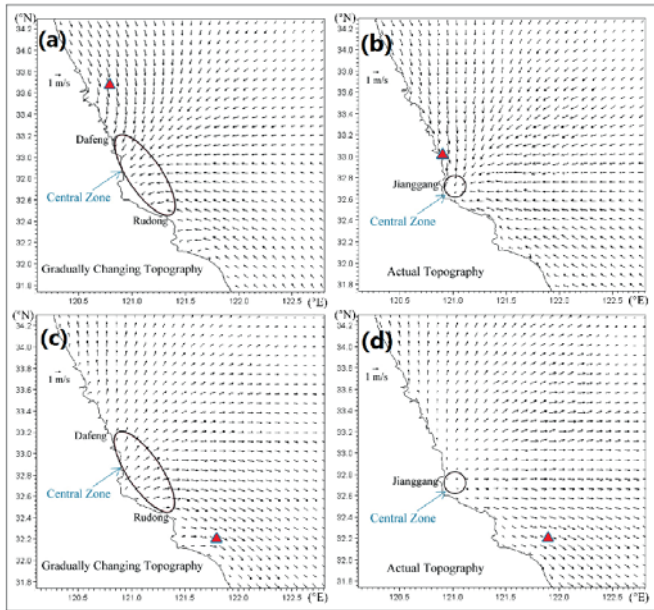


Fig. 6. Radial current field in study area. (a) gradually changing topography during flood tide period; (b) actual topography during flood tide period; (c) gradually changing topography during ebb tide period; (d) actual topography during ebb tide period

However, the actual (sand ridge) topography still demonstrated some effects on current field: 1) it narrowed the centre zone of the radial current field; 2) it increased the maximum flood velocity from 1.75 m/s to 2.19 m/s, and decreased the maximum ebb velocity from 1.66 m/s to 1.61 m/s; 3) it shifted the strongest flood point for approximately 73 km, from (120°49'27"E, 33°40'19"N) to (120°53'54"E, 33°0'45"N), and shifted the strongest ebb point for approximately 11 km, from (121°47'23"E, 32°10'47"N) to (121°54'31"E, 32°10'14"N).

#### ACTUAL TOPOGRAPHIC EFFECT (ATE)

The ATE is proposed herein to better investigate the actual (sand ridge) topographic effect on current field. VTE is expressed as follows:

$$\vec{A}_{ij} = (u_{aij} - u_{gij}, v_{aij} - v_{gij}) \quad (4)$$

where  $\vec{A}_{ij}$  is a vector indicating the actual topographic effect at position  $(i, j)$ ;  $u_{aij}$  is the horizontal component of actual topography current velocity at position  $(i, j)$ ;  $u_{gij}$  is the horizontal component of gradually changing topography

current velocity at position  $((i, j))$ ;  $v_{aij}$  is the vertical component of actual topography current velocity at position  $((i, j))$ ;  $v_{gij}$  is the vertical component of gradually changing topography current velocity at position  $((i, j))$ . Figure 7 shows the unit ATE in the study area. The horizontal axis is the longitude (in °E), and the vertical axis is the latitude (in °N). During the flood period, most vectors point to the central zone, which means the actual (sand ridge) topography centralized the radial currents. As a result, sediments transported to the central zone due to the actual topography. During the ebb tide, most vectors point to the coast line, which means the sediments transported to the coastal area due to the actual topography. So it can be concluded that, the actual topography stimulated the sediment transport to the central zone and the coastal area, providing sediments for reclamation projects.

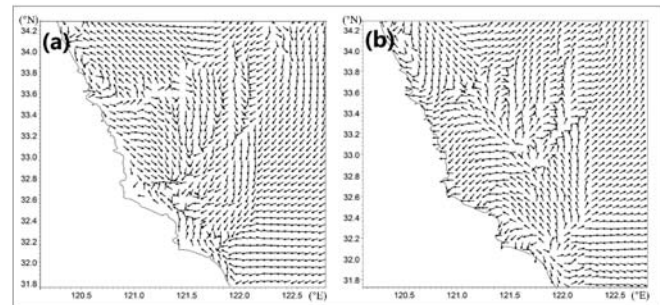


Fig. 7. Unit ATE in study area. (a) flood tide period; (b) ebb tide period

#### LAGRANGE RESIDUAL CURRENT

For the large-scaled circulation currents, the residual current is defined as the ratio of the water particle drift to the time period accordingly [12-14]. The process of the long-term mass transport depends on Lagrangian residual currents [15]. Therefore, the Lagrangian residual currents can be roughly analysed to present the sediment sources and transport routes (shown in Figure 8). The horizontal axis is the longitude (in °E), and the vertical axis is the latitude (in °N).

Figure 8(a) shows the Lagrangian residual currents are relatively simple on gradually changing topography. The residual currents near the coastline appear to be stronger than others. The residual current A travelled from the ancient Yellow River estuary towards south with the velocities of 0.12-0.16 m/s; the residual current B travelled from Yangtze River estuary towards north with the velocities of 0.1-0.18 m/s. Residual currents A and B converged in the central area and transformed into a circular residual current C with the velocities of 0.05-0.18 m/s. These results indicate that: 1) before the sand ridges were generated, the sediments were carried by residual currents; 2) the original source of the sediment could be either the ancient Yellow River estuary or Yangtze River estuary. This hydrodynamic finding is consistent with the environmental magnetism results [16] and the sediment composition results [17]. Once the sand ridges had been formed, the Lagrangian residual current varied (shown in

Figure 8(b)). The actual (sand ridge) topography weakened the external residual currents. As a result, the study area became a quasi-closed system without abundant sediment supply from outside. While in the sand ridges area several circular residual currents were generated with the velocities of 0.08-0.17 m/s. These residual currents transported and redistributed the sediments in this quasi-closed system.

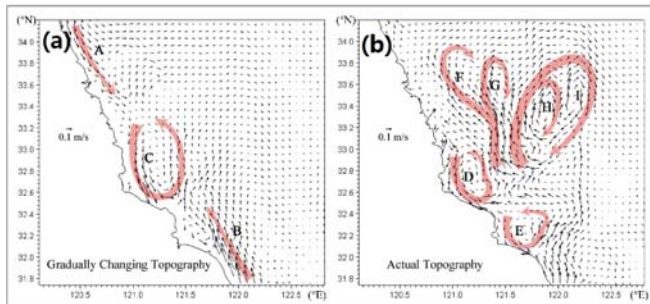


Fig. 8. Lagrangian residual currents in study area. (a) on gradually changing topography, the sediment transported to the study area; (b) on actual topography, no more sediment transported to the study area, so it is a quasi-closed system.

## CONCLUSIONS

In this study, field surveys were conducted to investigate the time-histories of tidal levels, current velocities and current directions in South Yellow Sea, China. Based on field data, a large-scaled numerical model was developed to simulate the radial current fields. Two parallel experiments were conducted on the actual topography and the gradually changing topography, respectively. The conclusions are drawn as follows:

- (1) A unique radial current field is generated by dual-tide system rather than actual (sand ridge) topography.
- (2) The actual (sand ridge) topography narrows the central zone of the radial current field, increases the flood velocities and decreases the ebb velocities.
- (3) Actual topographic effect is proposed in this study. Results show that actual topography stimulates the sediments to be transported to the central zone and the coastal area.
- (4) The observations of the Lagrangian residual currents show the sediments originally travel from the ancient Yellow River estuary or Yangtze River estuary. The actual (sand ridge) topography makes study area become a quasi-closed system.

## ACKNOWLEDGEMENTS

The authors gratefully acknowledge the support of Fuzhou University scientific start-up expenses (No. 0050-510479), the National Key Technologies R&D Program of P. R. China (No. 2012BAB03B01), the Jiangsu Natural Science Foundation for the Youth (No. BK2012411), and the Cultivation and Innovation Project for Postgraduate in Jiangsu (No. CXZZ13\_0258).

## REFERENCES

1. Z. Liu, S. Berne, H. Yu, A. Trentesaux, K. Uehara, P. Yin, J. P. Liu, C. Li, G. Hu, 2007. Internal architecture and mobility of tidal sand ridges in the east china sea. *Continental Shelf Research*, 27 (13), 1820-1834.
2. K. R. Dyer, D. A. Huntley, 1999. The origin, classification and modelling of sand banks and ridges. *Continental Shelf Research*, 19 (10), 1285-1330.
3. C. Chen, Y. G. Wang, H. M. Huang, C. G. Yuan, 2013. Advancement in impacts of tidal dynamics on radial sand ridges. *Port & Waterway Engineering*, 8, 17-24. (in Chinese)
4. Y. G. Wang, C. Chen, H. M. Huang, 2012. Beach reclamation related issues of tiaozini in jiangsu. *Zhejiang Hydrotechnics*, 1, 4-7. (in Chinese)
5. Z. W. Xia, Z. J. Wang, H. M. Huang, 1984. Numerical model of the m2 constituent in the huanghai sea. *J Oceanogr Hungai Bohai Seas*, 2 (1), 1-7. (in Chinese)
6. Y. R. Zhu, R. F. Chang, 1997. Explanation of the origin of radial sand ridges in the southern yellow sea with numerical simulation results of tidal currents. *Journal of Ocean University of Qingdao*, 27 (2), 218-224. (in Chinese)
7. C. Zhang, D. Zhang, Z. Wang, 1999. Tidal current-induced formation—storm-induced change—tidal current-induced recovery. *Science in China Series D: Earth Sciences*, 42 (1), 1-12.
8. D. Zhang, J. Zhang, 1996. M2 tidal wave in the yellow sea radiate shoal region. *Journal of Hohai University*, 24, 35-40. (in Chinese)
9. Y. Zhu, 1998. Numerical simulation of paleo-tidal current field in the subei littoral plain area and its verification. *Marine Science Bulletin-Tianjin*, 17, 7-13. (in Chinese)
10. K. Chen, P. Lu, Y. Wang, G. Yu, 2010. Hydrodynamic mechanism of evolvement trends in radial sandbank of south yellow sea, china. *Advances in Water Science*, 21 (2), 123-129. (in Chinese)
11. F. Xing, Y. P. Wang, H. V. Wang, 2012. Tidal hydrodynamics and fine-grained sediment transport on the radial sand ridge sys-tem in the southern yellow sea. *Marine Geology*, 291, 192-210.
12. M. S. Longuet-Higgins, 1969. On the transport of mass by time-varying ocean currents. *Deep Sea Research and Oceanographic Abstracts (Elsevier)*, 16 (5), 431-447.
13. J. Zimmerman, 1979. On the euler-lagrange transformation and the stokes drift in the presence of oscillatory and

residual currents. Deep Sea Research Part A Oceanographic Research Papers, 26 (5), 505-520.

14. R. T. Cheng, V. Casulli, 1982. On lagrangian residual currents with applications in south san francisco bay, california. Water Resources Research, 18 (6), 1652-1662.
15. S. Feng, R. T. Cheng, X. Pangen, 1986. On tide-induced lagrangian residual current and residual transport: 1. Lagrangian residual current. Water Resources Research, 22 (12), 1623-1634.
16. C. Li, J. Zhang, S. Yang, D. Fan, 1999. Characteristic and paleoenvironmental evolution of subaerial tidal sand body in subei coastal plain. Science in China Series D: Earth Sciences, 42 (1), 52-60.
17. Y. Wang, Y. Zhang, X. Zou, D. Zhu, D. Piper, 2012. The sand ridge field of the south yellow sea: Origin by river-sea interaction Marine Geology, 291, 132-146.

## CONTACT WITH THE AUTHOR

**Cheng Chen**

College of Civil Engineering  
Fuzhou University  
Fuzhou 350116

**CHINA**

# EFFECT OF WATER FLOWS ON SHIP TRAFFIC IN NARROW WATER CHANNELS BASED ON CELLULAR AUTOMATA

Hongtao Hu<sup>1\*</sup>

Xiazhong Chen<sup>2</sup>

Zhuo Sun<sup>3</sup>

<sup>1</sup> Logistics Engineering College, Shanghai Maritime University, Shanghai 201306, China

<sup>2</sup> Institute of Logistics Science & Engineering, Shanghai Maritime University, Shanghai 201306, China

<sup>3</sup> Transportation Management College, Dalian Maritime University, Dalian 116026, China

\* corresponding author

## ABSTRACT

*In narrow water channels, ship traffic may be affected by water flows and ship interactions. Studying their effects can help maritime authorities to establish appropriate management strategies. In this study, a two-lane cellular automata model is proposed. Further, the behavior of ship traffic is analyzed by setting different water flow velocities and considering ship interactions. Numerical experiment results show that the ship traffic density-flux relation is significantly different from the results obtained by classical models. Furthermore, due to ship interactions, the ship lane-change rate is influenced by the water flow to a certain degree.*

**Keywords:** Narrow channel, Cellular automata, Simulation, Ship interaction

## INTRODUCTION

A narrow channel often refers to navigable water restricted by its lane width, and to some extent, sailing in narrow channel restricts the ship maneuvers [1]. Due to some features of narrow channels, such as the narrow width, changeable water depth, large density of ships etc., ship collisions often occur in narrow channels, which seriously holds back the development of marine transportation [2, 3]. Therefore, it is important to investigate the characteristics of ship traffic in narrow channels.

General vehicle traffic models are based on basic kinetics models, which cannot simulate dynamic traffic features. However, Cellular Automata (CA) can be used to study phenomena where many individuals interact with each other. The CA can reproduce the time and satisfies the dynamic system needs for evolution in a discrete form [4].

In the 1980s, the CA technology entered people's field of vision. The NaSch model and BML model proposed by Nagel and Schreckberg are classical traffic flow models based on the CA [5]. The NaSch model is a classical single-lane model, After improvement, this classical model can reproduce many major features of traffic flows [6]. However, the NaSch model does not allow overtaking, which is a limitation. Accordingly, many single-track multiple lanes models considering overtaking [7-9] and many lane-change rules [10-12] were proposed. Nowadays, the CA is widely used in studying of road traffic flows. Tieqiao Tang et al. [13] develop a macro traffic flow model with consideration of varying road conditions. Xiaobo Qu et al. [14] develop an improved multi-value cellular automata model for heterogeneous bicycle traffic flow taking the higher maximum speed of electric bicycles into consideration, greatly enhances the realism of the bicycle traffic model.

In marine traffic flows, Xiaobo Qu et al. [15] propose a cellular automata model based simulation approach for the Singapore Strait, and a two-lane cellular automata model is proposed by Zhuo Sun et al. [16] to investigate the traffic flow patterns in narrow water channels. There are two main differences between water traffic and road traffic. First, both water flow direction and velocity can accelerate or hold back ships. In ship traffic flows, the actual speed of ships equals the composition of the hydrostatic speed and water velocity. The hydrostatic speed changes frequently in a range. Through superposition, the range of the actual speed of ships also changes, and the lower bound of this range depends on the water velocity. The second important difference is due to ship interactions [17]. When two ships sail in parallel in close lanes, the water accelerates between the two ships, since the water pressure decreases, and the water slows down on the external side of the ship where the water pressure is relatively high. As a result, a difference in pressure is produced between the portside and starboard, so that the two ships are pushed towards each other.

## MODEL

A ship interaction cellular automation model (SICA) based on the NaSch model is proposed. The new lane-change update rule for the period from  $t$  to  $t+1$  is introduced as follows.

**Rule1** Acceleration:

$$v_n^{t+1} = \min(v_n^t + a_n, v_{\max}) \quad (1)$$

where  $v_n^t$  and  $v_n^{t+1}$  represent the speed of ship  $n$  at moment  $t$  and  $t+1$ , respectively,  $a_n$  is the acceleration of ship  $n$ , and  $v_{\max}$  is the maximum speed of the ship. Rule1 describes the feature that the driver wants to maneuver the ship at the maximum speed.

**Rule2** Deceleration to avoid ship collisions:

$$v_n^{t+1} = \min(v_n^t, d_n^t) \quad (2)$$

where  $d_n^t = x_{n+1}^t - x_n^t - l_{n+1}$ ,  $x_n^t$  and  $x_{n+1}^t$  represent the position of ship  $n$  and the front ship  $n+1$  at moment  $t$ , respectively, and  $l_{n+1}$  is the length of the front ship  $n+1$ . Accordingly,  $d_n^t$  means the distance between the front ship and the rear ship. Rule2 describes the action of the driver to avoid a collision between the two ships.

**Rule3** Deceleration due to a ship interaction:

$$v_n^{t+1} = \max\left(\min(v_n^t - a_n, d_n^t), v_{\min}\right) \quad (3)$$

Considering a ship interaction, the rule says: if overtaking happens in two lanes, the ship having a lower speed needs to slow down, and, while avoiding the collision with the front ship, it should also keep the speed over the minimum speed  $v_{\min}$ .

**Rule4** Lane changing:

$$L_n^{t+1} = \begin{cases} \text{other lane} & \text{if } d_n^t < \min(v_{\max}, v_n^t + 1) \text{ and } d_{n,oa}^t > d_n^t \text{ and } d_{n,ob}^t > d_{safe} \\ \text{not change} & \text{otherwise} \end{cases} \quad (4)$$

where  $L_n^{t+1}$  denotes the lane ship  $n$  stays in at moment  $t+1$ ,  $d_{n,oa}^t$  and  $d_{n,ob}^t$  represent the distance between ship  $n$  and the front or rear ship in adjacent lanes, and  $d_{safe}$  denotes the safe distance. Taking the example of ship A in the right lane in Fig.1, at moment  $t$ , the horizontal distance  $d_{n,oa}^t$  is larger than the distance  $d_n^t$ . And in the left lane, the horizontal distance  $d_{n,ob}^t$  is larger than the safe distance  $d_{safe}$ . At moment  $t+1$ , ship A changes the lane from right to left. However, if one of the above conditions cannot be satisfied, ship A cannot change the lane.

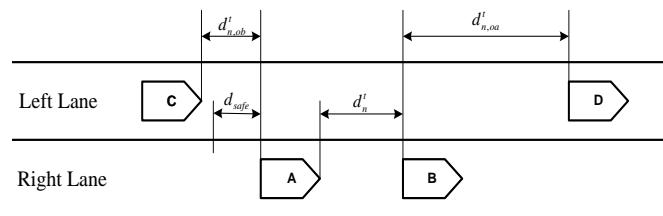


Fig.1. The description of the formula (4) parameter

**Rule5** Randomization with possibility  $p$ :

$$v_n^{t+1} = \max(v_n^t - 1, v_{\min}) \quad (5)$$

Due to many uncertainties, such as poor conditions for sailing, different mentalities of drivers, and so on, ships may slow down.

**Rule6** Updated positions:

$$x_n^{t+1} = x_n^t + v_n^t + v_{n,flow}^t \quad (6)$$

where  $v_{n,flow}^t$  denotes the water velocity in the lane of ship A at moment  $t$ . The sailing distance per unit time is not only related to the speed of the ship but also to the water velocity in the lane.

## NUMERICAL EXPERIMENT

The simulation is based on the open source software MicroCity (<http://microcity.github.io>). A two-dimensional  $1000 \times 140$  simulation space is built, where the square's

length is defined as 30 meters. The value 120 of ordinate is the position of the left lane, and the value 80 of ordinate is the position of the right lane. The important parameters used in the simulation are shown in Table 1.

We assume that the water flows in the two lanes are the same and unchangeable during the simulation. When the water velocity is positive, this means that the water flows are downstream; when the water velocity is negative, this means that the water flows are upstream; when the water velocity is zero, this means that the water is static.

Tab. 1. Important parameters used in the simulation

| The name of the simulation parameter | Parameter value |
|--------------------------------------|-----------------|
| Cell Size                            | 30              |
| Lane Length (cells)                  | 1000            |
| Ship Length (cells)                  | 4               |
| Slow Ship Speed (cells/unit time)    | 3               |
| Fast Ship Speed (cells/unit time)    | 5               |
| Ship Minimum Speed (cells/unit time) | 0               |
| Slow Ships / All Ships               | 0.5             |
| Safe Space (cells)                   | 4               |
| Ship Acceleration (cells/unit time)  | 1               |
| Deceleration Probability             | 0.3             |
| Left Lane Speed                      | 0               |
| Right Lane Speed                     | 0               |

## FUNDAMENTAL DIAGRAMS

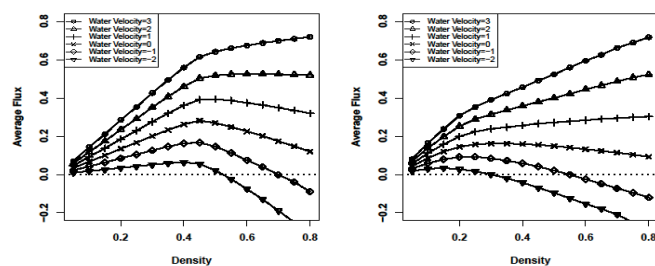


Fig. 2. The density-average flux diagram: (a) the NO-SICA model; (b) the SICA model

Fig. 2(a) shows that without ship interactions, with a small density, the average flux in all lanes shows a linear increase with an increase in the density. When the density increases constantly, the lanes start to be crowded. To avoid collisions, ships have to slow down. Additionally, random slowing down also plays an important role in the increase in the density, so the average speed of ships in all lanes is also lowered. As a result, the slope is changed at 0.45 in Fig. 2(a).

By comparing 2(a) and 2(b), with ship interactions and a medium density, the average flux is lower than without ship interactions. The curve of the density-average flux becomes smooth, and the “Peak Phenomenon” is not evident. The reason is that with ship interactions, an overtaken ship needs to slow down to reduce the time of the ship interaction, so that the speeds in all lanes are influenced, resulting in the offset of the average flux brought by the density.

The effect of water flows is further considered. From Fig. 2(b), a conclusion can be drawn: regardless of whether upstream or downstream, the “Peak Phenomenon” is

undermined by an increase in the water velocity, and further, the “Peak Phenomenon” disappears when downstream, with ship interactions, where this situation is even more evident.

Regarding why an increase in the water velocity undermines the “Peak Phenomenon”, we consider the downstream case with ship interactions as an example. If the density of the lanes is significantly large, ships slow down to avoid collisions. At the same time, randomization also can hold back ships significantly with a high density. Without the consideration of the water velocity, the average flux of the lanes should decline sharply. However, it hardly changes, because the water velocity of the downstream is high. So, compared to a high water velocity, the influence of the speed of ships on the average flux of the lanes is small. When the water velocity is close to or larger than the speed of ships, the influence from random slowing down can be ignored, and the average flux of the lanes depends on the water velocity. According to the formula of the average flux, Average flux = (Density × Composite speed of ships considering water velocity) / Average ship length, the density-average flux curve is infinitely close to a linear one with an increase in the water velocity.

This result is meaningful for ships sailing in narrow channels. With ship interactions, the experimental results show that if the upstream velocity is high, the value of the average flux can even be negative even if the density is small, which means that the upstream is so strong that ships go backward instead of going forward. Furthermore, narrow channels have many features, such as the narrow width, changeable water depth and flux, curved vessel lanes, low speed of ships, and so on. Additionally, ships often change directions to overtake other ships, so the load on the propeller changes drastically. Therefore, facing terrible sailing conditions, such as a high upstream velocity or dead wind, all crews have to pay more attention to the changes in various parameters related to the power, and corresponding actions should be taken to avoid ship’s reversing.

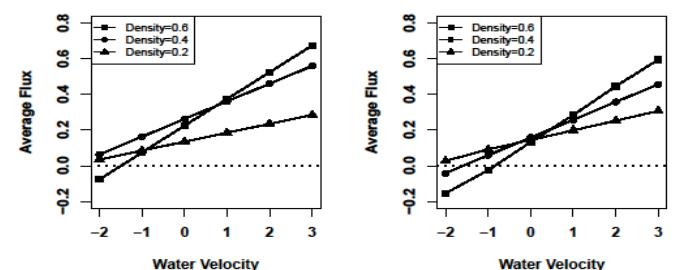


Fig. 3. The water velocity diagram: (a) the NO-SICA model; (b) the SICA model

In Fig. 3, regardless of whether with ship interactions or without them, the slope of the water velocity-average flux curve is the same for the same density values. This means that when the water velocity increases by one unit, the average flux increases by the same quantity. The reason is that the water velocity is an external environment. But with different densities, the effect of the water velocity on the average flux is different. The higher the density, the more clear the effect on the average flux. According to the formula of the average flux,

Average flux = (Density  $\times$  Composite speed of ship considering water velocity) / Average ship length, when the water speed and average ship length are unchanged, the density becomes the only changeable parameter. So, the higher the density, the larger the average flux.

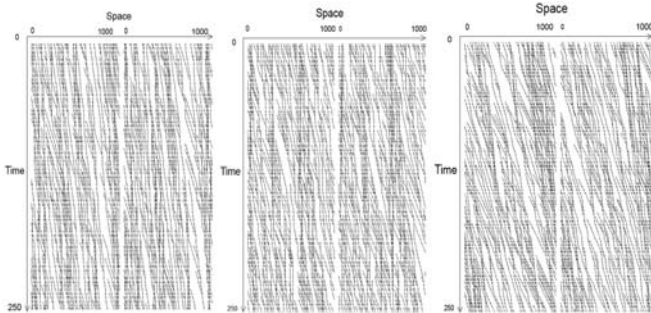


Fig.4. The time-space diagram for the SICA model:  
(a) water velocity=-1; (b) water velocity=0; (c) water velocity=1

Fig.4 shows the time-space diagram with ship interactions under different water velocity conditions, where the density is equal to 0.6. Lanes are symmetric, so the diagrams for the right lane and left lane have similar features. Comparing the three diagrams for the water velocity equal to -1, 0 and 1, we can notice that the downstream water makes ships faster, and with the water velocity -1, the motion of ships is viscous. Fig.4(a) also shows that the upstream makes lanes more crowded, and it is hard for ships to move under these conditions.

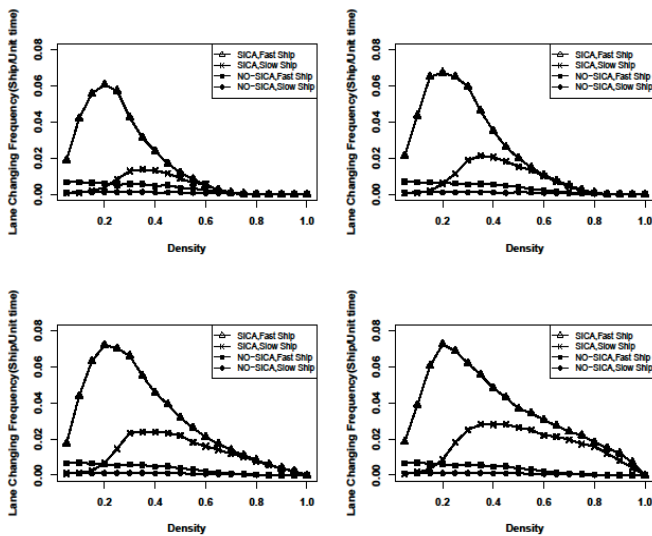


Fig.5. The density-lane-change frequency diagram:  
(a) water velocity=-1; (b) water velocity=0; (c) water velocity=1;  
(d) water velocity=2

## LANE-CHANGE FREQUENCY

According to Fig.5, without ship interactions, the lane-change frequency of slow ships is almost zero, because slow ships' speed is the lowest in all lanes. Accordingly, overtaking

of front ships rarely occurs. On the contrary, fast ships choose to change lanes if the density is small and the distance is safe. However, with a high density, both lanes are crowded, and the distance is not enough for ships to change lanes, so all ships can only sail in the same lane keeping the safe distance. In this situation, the lane-change frequency is close to zero.

With ship interactions, the density-lane-change frequency diagram shows a great difference. For both fast ships and slow ships, their lane-change frequency increases dramatically. The reason is that ship interactions slow down ships frequently, and to avoid collisions, the rear ship has to change lanes frequently to pass the entire channel quickly.

Furthermore, Fig.5 also shows that with ship interactions, an increase in the downstream velocity can hold back the decrease of the lane-change frequency. To clearly observe the influence of different water velocities on the lane-change frequency, Fig.6 shows the relationship between the water speed and lane-change frequency with ship interactions.

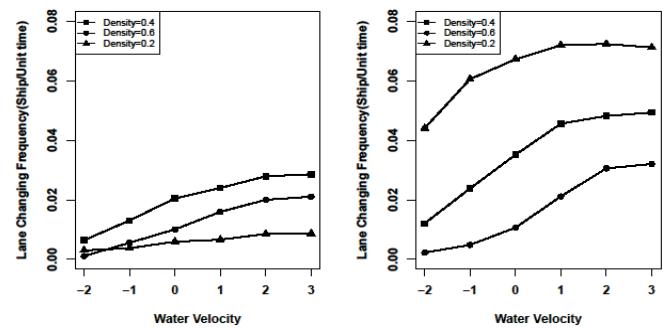


Fig.6. The water velocity-lane-change frequency diagram: (a) slow ships;  
(b) fast ships

Fig.6 shows that ships are held back when sailing in the upstream case. So, the lane-change frequency is the lowest under this circumstance. When downstream, the rear ship can find many chances to overtake the front ship, so the lane-change frequency is increased. However, with an increase in the water velocity, the lane-change frequency stays at a certain value. The reason is that even with an increase in the water velocity, the relative speeds of ships are unchanged, and the relative distances between ships are also not related to the water velocity. So, an increase in the water velocity does not clearly affect the lane-change frequency.

Furthermore, Fig.6 also shows that the lane-change frequency of a fast ship is influenced more by the water velocity than that of a slow ship, because the slow ship is restricted by its maximum sailing speed. Therefore, rarely can the front ship be overtaken by a slow ship.

## CONCLUSIONS

This article studies the effect of water flows on vessel traffic flows in narrow channels. Based on the one-lane NaSch model, and considering the water velocity, a ship interaction cellular automation model is built. Using simulation, ships having different velocities in two lanes are compared. Considering the

density, as well as ship interactions, the influence of different water velocities on the average flux and the lane-change frequency is studied. After the analysis of a large amount of experimental data from many simulation experiments, the results show that in both downstream and upstream cases, an increase in the water velocity makes the “Peak Phenomenon” undermined and even disappeared in the density-average flux curve, especially with ship interactions. Furthermore, using independent analysis of fast ships and slow ships, the results show that, for both fast ships and slow ships, an increase in the water velocity can render the lane-change frequency stable and unchangeable gradually. However, the lane-change frequency of fast ships is influenced by the water velocity more clearly than that of slow ships.

Many factors are considered in this article, and each factor is analyzed and compared accompanied by the corresponding explanation. Therefore, meaningful references can be provided to vessel traffic in narrow channels in real applications. However, vessel traffic is much more complicated in real life situations, and further research can be done based on this article to make the model more suitable for real life situations, providing greater contributions to the shipping industry.

#### ACKNOWLEDGMENTS

This research is supported by the National Natural Science Foundation of China [grant number 71201099]. Innovation Program of Shanghai Municipal Education Commission [No. 14YZ111], Shanghai Young Eastern Scholar Programme [QD2015041], Shanghai Pu Jiang Program (No. 13PJC066).

#### REFERENCES

1. Dam K T, Tanimoto K, Fatimah E. Investigation of ship waves in a narrow channel. *Journal of Marine Science & Technology*, 2008, 13(3):223-230.
2. Lee C K, Moon S B, Jeong T G. The investigation of ship maneuvering with hydrodynamic effects between ships in curved narrow channel. *International Journal of Naval Architecture & Ocean Engineering*, 2016, 8(1):102-109.
3. Gao X, Makino H, Furusho M. Analysis of ship drifting in a narrow channel using Automatic Identification System (AIS) data. *Wmu Journal of Maritime Affairs*, 2016:1-13.
4. Lárraga M E, Alvarez-Icaza L. Cellular automata model for traffic flow with safe driving conditions. *Chinese Physica A*, 2014, 23(5):216-226.
5. Nagel K, Schreckenberg M. Cellular automaton model for freeway traffic. *J Phys I (Paris) 2:2221. Journal De Physique I*, 1992, 2(12).
6. Feng H, Bao X, Zhou J, et al. Cellular automata model on AIS-based for variable two-way waterway. *Journal of Industrial Engineering & Management*, 2015, 8(3):págs. 674-692.
7. Chowdhury D, Wolf D E, Schreckenberg M. Particle hopping models for two-lane traffic with two kinds of vehicles: Effects of lane-changing rules. *Physica A Statistical Mechanics & Its Applications*, 1997, 235(3-4):417-439.
8. Wagner P, Kai N, Wolf D E. Realistic multi-lane traffic rules for cellular automata. *Physica A Statistical Mechanics & Its Applications*, 1997, 234(3-4):687-698.
9. Deutsch J C, Santhosh-Kumar C R, Rickert M, et al. Two lane traffic simulations using cellular automata. *Physica A Statistical Mechanics & Its Applications*, 1995, 231(4):534-550.
10. Knospe W, Santen L, Schadschneider A, et al. Disorder effects in cellular automata for two-lane traffic. *Physica A Statistical Mechanics & Its Applications*, 1999, volume 265(3):614-633.
11. Qu X, Meng Q. Development and applications of a simulation model for vessels in the Singapore Straits. *Expert Systems with Applications*, 2012, 39(9):8430-8438.
12. Zhao H T, Nie C, Li J R, et al. A two-lane cellular automaton traffic flow model with the influence of driver, vehicle and road. *International Journal of Modern Physics C*, 2015, 27(02):1650018-.
13. Tang T Q, Lou C, Wu Y H, et al. A macro model for traffic flow on road networks with varying road conditions. *Journal of Advanced Transportation*, 2014, 48(4):304-317.
14. Qu X, Meng Q. Simulation Model for Ship Movements in Singapore Strait and Its Applications[C]// *Transportation Research Board 90th Annual Meeting*. 2011.
15. Jin S, Qu X, Xu C, et al. An improved multi-value cellular automata model for heterogeneous bicycle traffic flow. *Physics Letters A*, 2015, 379(39):2409-2416.
16. Sun Z, Chen Z, Hu H, et al. Ship interaction in narrow water channels: A two-lane cellular automata approach. *Physica A Statistical Mechanics & Its Applications*, 2015, 431:46-51.
17. Yuan Z M, He S, Kellett P, et al. Ship-to-Ship Interaction During Overtaking Operation in Shallow Water. *Journal of Ship Research*, 2015, 59(3):1-16.

**CONTACT WITH THE AUTHORS**

**Hongtao Hu**

Logistics Engineering College  
Shanghai Maritime University  
Shanghai 201306  
**CHINA**

## MODELING AND ANALYSIS OF 12-PULSE INVERTER IN SHIPBOARD OR AIRCRAFT

Yanbo Che\*

Jinhuan Zhou

Guojian Liu

Jianmei Xu

Yuancheng Zhao

Key Laboratory of Smart Grid of Ministry of Education, Tianjin University, China

\* corresponding author

### ABSTRACT

*With the development of DC distribution system within the isolated power system of a ship or an aircraft, more constant frequency loads will be supplied by inverters connected to DC main bus. In the operating mode conversion process of an isolated power system, inverters will inevitably suffer from serious disturbance and affect the stability of the system. Therefore, it is important to establish a model of the inverter that reflects its dynamic characteristics and based on which to conduct the stability analysis. This paper proposes a 12-pulse inverter model based on the generalized state space averaging (GSSA) method. This model can overcome the limitations of 12-pulse inverter state space averaging (SSA) model in transient analysis with good accuracy and fast analysis ability effectively. Three kinds of models for a 12-pulse aircraft inverter are built in MATLAB, namely GSSA model, SSA model and detail device model. The simulation results show the high accuracy of GSSA model in stability analysis. This study provides an effective analytical tool for stability analysis of 12-pulse inverter and also provides a reference for inverter modeling research of isolated power system such as in aircraft or ship.*

**Keywords:**

### INTRODUCTION

With the concern of energy crisis and environment pollution, the application of electricity expands to various domains for its efficiency, cleanness and high quality energy [1]. The power supply in vehicles such as ship, aircraft and spacecraft is gradually replaced by electricity [2-4]. Isolated power system is characterized with localized power production and consumption, avoiding long distance transmission of electricity and supporting the costume-made according to the user demand. These characteristics make isolated power system well suited to new forms of power demand. Isolated power system such as ship, aircraft and spacecraft requires a multitude of power electronic converters during the process

of power storage, transmission and consumption[5,6]. But the space is so limited that the proportion of power electronic device in isolated power systems is much larger than that in traditional interconnected electric power system.

Stimulated by the advantages of lightweight and energy saving, new vehicle isolated power system mostly adopts a distribution system based on DC main bus [7, 8]. The original AC loads in the AC power distribution system will be supplied by inverters connected to the DC main bus, which increase loads of inverters greatly. The stability of inverters will directly affect the safe and stable operation of the isolated power system [9-12].

So far, stability analysis of inverter largely depends on detailed device model and mathematical analytic model.

A power system model is employed in [13] to simulate the transient process of shipboard power system. The hardware in the loop simulation verification of the multiple inverters in aircraft power systems is performed in [14]. The device model is complicated in modeling, as it describes the thorough dynamic process of the system. On the other hand, it can't reveal the relationship between system parameters and system stability, which can't be used in system design and optimization. The mathematical analytic model is used to seek the analytic expression of the characteristics of the inverter by theoretical analysis, which can represent the steady-state and dynamic mathematical characteristics of the system. The most representative one is the state space averaging method. Being one of the most representative approaches, state space averaging method was applied to establish small-signal models of inverter for single-phase and three-phase [15, 16]. It was also used to build the state space averaging model of electromechanical actuators and rotating rectifier [17, 18]. However, in the derivation the state variables are assumed to have small change within the switching cycle and the dynamic characteristics of inverter are ignored, the state space averaging method cannot meet the fast response and dynamic analysis of large disturbance.

In 1991, Professor Seth R. Sanders and his students proposed the generalized state space averaging (GSSA) model, which is a tradeoff between the detailed device model and the simplified state space model [19]. Considering the invariant components of the state space model, GSSA also takes into account of the higher order components, which can be used not only for small disturbance analysis, but also for large disturbance analysis.

Taking into account of the electrical characteristics of the DC power distribution system, this paper applies the generalized state space method to build a 12-pulse inverter model in MATLAB/Simulink. The stability analysis is carried out based on the model, and the validity of the model by simulation results.

## GENERALIZED STATE SPACE AVERAGING METHOD

Generalized state space averaging method employs the Fourier series with time-dependent coefficients. The signals are divided into invariants and high-order variables, and the order of precision is chosen according to actual needs. A waveform  $x(t)$  over the interval  $[t-T, T]$  can be approximated with a Fourier series representation of the form

$$x(t) = \sum_{k=-n}^n \langle x \rangle_k (t) e^{jk\omega t} \quad (1)$$

Where  $\omega = 2\pi / t$  is the fundamental angular frequency. When there is just invariant,  $k = 0$ , it is state space average. The higher orders take into consideration, the higher accuracy the results obtained. When  $n$  is infinite, the deviation between

generalized state space operation and the actual error is zero, but the computation is large at this time. Hence,  $n$  depends on the required degree of accuracy.  $\langle x \rangle_k$  is  $k$ -th Fourier coefficients defined as

$$\langle x \rangle_k (t) = \frac{1}{T} \int_{t-T}^t x(t) e^{-jk\omega t} dt \quad (2)$$

So a signal in (1) can be calculated and given by

$$x(t) = \langle x \rangle_0 + 2 \sum_{k=1}^{\infty} \left\{ \text{Re} \langle x \rangle_k \cos(k\omega t) - \text{Im} \langle x \rangle_k \sin(k\omega t) \right\} \quad (3)$$

Three basic characteristics of Fourier transform are normally required, which are expressed by

$$\langle x(t) + y(t) \rangle_k = \langle x \rangle_k (t) + \langle y \rangle_k (t) \quad (4)$$

$$\langle x(t) y(t) \rangle_k = \sum_{i=-\infty}^{\infty} \langle x(t) \rangle_{k-i} \langle y(t) \rangle_i \quad (5)$$

$$\frac{d}{dt} \langle x(t) \rangle_k = \left\langle \frac{dx(t)}{dt} \right\rangle_k - jk\omega \langle x(t) \rangle_k \quad (6)$$

## MODELING AND ANALYSIS OF INVERTER

### THE INVERTER CIRCUIT IN POWER ELECTRONIC

A circuit of SPWM-controlled 12-pulse voltage source inverter in isolated power system is shown in Figure 1.

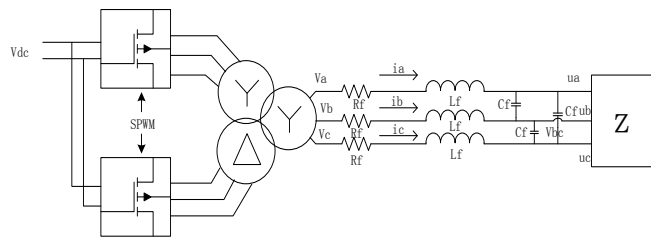


Fig. 1. 12-pulse voltage source inverter

The DC main bus voltage is shown by  $V_{dc}$ , which is 270V. Two three-phase inverters bridges, which connected through the Y-Δ/Y in parallel, are controlled by PWM. The transformer link was utilized to increase the voltage adjustment range. Since the neutral points of the AC load side and the DC main bus are not connected, line voltage measurement and analysis were adopted when building the generalized state space averaging model.

## MODELING OF THE INVERTER CIRCUIT

The switching function  $s$  is defined as that  $s=1$  means a switch is on,  $s=0$  means off. The switch functions in a SPWM-controlled inverter,  $s_{ui}$  and  $s_{di}$ ,  $i \in \{a, b, c\}$ , represent the states of up and down bridge arms in phase  $i$ , which satisfying  $s_{ui} + s_{di} = 1$ . The switching function is periodic, and can be replaced by Fourier series

$$s_1(t) = \sum_{n=1, \text{ odd}}^{\infty} A_n \sin(n \omega t) \quad (7)$$

where  $A_n$  represents the coefficient of order  $n$ . The AC line voltage in the secondary side of the transformer can be expressed

$$v_{ab} = v_{ab1} + v_{ab2} \quad (8)$$

where  $v_{ab1}$  was generated by the first inverter bridge, and

$$v_{ab1}(\omega t) = v_{a1}(\omega t) - v_{b1}(\omega t) = \frac{m\sqrt{3}V_{dc}}{2n} \sum_{n=1, \text{ odd}}^{\infty} A_n \sin[n(\omega t + \varphi + \frac{\pi}{6})] \quad (9)$$

where  $m$  is SPWM modulation ratio,  $n$  is the transformer ratio,  $A_n$  is  $n$ -th Fourier coefficient,  $\varphi$  is the initial phase angle. From symmetrical relationship we can obtain

$$\begin{cases} v_{bc1} = v_{ab1}(\omega t - 2\pi/3) \\ v_{ca} = v_{ab1}(\omega t + 2\pi/3) \\ v_{ab2} = v_{ab1}(\omega t + \pi/6) \\ v_{bc2} = v_{ab1}(\omega t - \pi/2) \\ v_{ca2} = v_{ab1}(\omega t + 5\pi/6) \end{cases} \quad (10)$$

where  $v_{ab2}$ ,  $v_{bc2}$  and  $v_{ca2}$  are secondary side voltages of the transformer generated by the second inverter bridge.

Denote virtual line currents as  $i_{ab}$ ,  $i_{bc}$  and  $i_{ca}$ . The three-phase loads are symmetrical, and their phase voltages or line currents are equal in amplitude with phase shift of  $120^\circ$ . According to the vector relation we can obtain

$$i_{ab} = \frac{1}{3}(i_a - i_b); i_{bc} = \frac{1}{3}(i_b - i_c); i_{ca} = \frac{1}{3}(i_c - i_a) \quad (11)$$

Suppose that the symmetrical loads are delta-connected with impedance  $Z_L$ , and AC side output currents and load voltages are selected as state variables, then

$$\begin{bmatrix} v_{ab} \\ v_{bc} \\ v_{ca} \end{bmatrix} = \begin{bmatrix} v_a - v_b \\ v_b - v_c \\ v_c - v_a \end{bmatrix} = \begin{bmatrix} L_f \frac{di_a}{dt} - L_f \frac{di_b}{dt} \\ L_f \frac{di_b}{dt} - L_f \frac{di_c}{dt} \\ L_f \frac{di_c}{dt} - L_f \frac{di_a}{dt} \end{bmatrix} + R_f \begin{bmatrix} i_a - i_b \\ i_b - i_c \\ i_c - i_a \end{bmatrix} + \begin{bmatrix} u_{ab} \\ u_{bc} \\ u_{ca} \end{bmatrix} \quad (12)$$

$$\begin{bmatrix} i_{ab} \\ i_{bc} \\ i_{ca} \end{bmatrix} = C_f \frac{d}{dt} \begin{bmatrix} u_{ab} \\ u_{bc} \\ u_{ca} \end{bmatrix} + \frac{1}{Z_L} \begin{bmatrix} u_{ab} \\ u_{bc} \\ u_{ca} \end{bmatrix} \quad (13)$$

where  $R_f$ ,  $L_f$  and  $C_f$  are resistance, inductance and capacitance of low pass filter in Fig.1, respectively.

The state equation of inverter currents is constructed as

$$\frac{d}{dt} \begin{bmatrix} i_{ab} \\ i_{bc} \\ i_{ca} \end{bmatrix} = -\frac{R_f}{L_f} \begin{bmatrix} i_{ab} \\ i_{bc} \\ i_{ca} \end{bmatrix} - \frac{1}{3L_f} \begin{bmatrix} u_{ab} \\ u_{bc} \\ u_{ca} \end{bmatrix} + \frac{\sqrt{3}mV_{dc}}{6nL_f} \begin{bmatrix} \sin(\omega t + \varphi + \frac{\pi}{6}) + \sin(\omega t + \varphi + \frac{\pi}{3}) \\ \sin(\omega t + \varphi + \frac{5\pi}{6}) + \sin(\omega t + \varphi + \pi) \\ \sin(\omega t + \varphi - \frac{\pi}{2}) + \sin(\omega t + \varphi - \frac{\pi}{3}) \end{bmatrix} \quad (14)$$

$$\begin{bmatrix} i_{ab} \\ i_{bc} \\ i_{ca} \end{bmatrix} = C_f \frac{d}{dt} \begin{bmatrix} u_{ab} \\ u_{bc} \\ u_{ca} \end{bmatrix} + \frac{1}{Z_L} \begin{bmatrix} u_{ab} \\ u_{bc} \\ u_{ca} \end{bmatrix} \quad (15)$$

## GENERALIZED STATE SPACE AVERAGING MODELING

Since the DC main bus bar contains few harmonic components, only the DC component is considered in the calculation. Combining with the generalized state space algorithms, the first order of the state variables is substituted into equation (12) and (14). The generalized state space variables are chosen as that,  $x_1, x_2, \dots, x_6$  are DC components,  $x_7, x_9, \dots, x_{17}$  and  $x_8, x_{10}, \dots, x_{18}$  are the real part and the imaginary parts of the fundamental component respectively, then the load-side voltages and AC currents can be expressed by

$$\begin{cases} \langle u_{ab} \rangle_0 = x_1, \langle u_{bc} \rangle_0 = x_2, \langle u_{ca} \rangle_0 = x_3; \\ \langle i_{ab} \rangle_0 = x_4, \langle i_{bc} \rangle_0 = x_5, \langle i_{ca} \rangle_0 = x_6; \\ \langle u_{ab} \rangle_1 = x_7 + jx_8, \langle u_{bc} \rangle_1 = x_9 + jx_{10}, \\ \langle u_{ca} \rangle_1 = x_{11} + jx_{12}; \\ \langle i_{ab} \rangle_1 = x_{13} + jx_{14}, \langle i_{bc} \rangle_1 = x_{15} + jx_{16}, \\ \langle i_{ca} \rangle_1 = x_{17} + jx_{18}; \end{cases} \quad (16)$$

Taking  $ZL=R$  and combining with the generalized state space algorithms, the final GSSA model is deduced as

$$\begin{bmatrix} \dot{x}_1 \\ \dot{x}_2 \\ \dot{x}_3 \\ \dot{x}_4 \\ \dot{x}_5 \\ \dot{x}_6 \end{bmatrix} = \begin{bmatrix} -\frac{1}{RC} & 0 & 0 & \frac{1}{C} & 0 & 0 \\ 0 & -\frac{1}{RC} & 0 & 0 & \frac{1}{C} & 0 \\ 0 & 0 & -\frac{1}{RC} & 0 & 0 & \frac{1}{C} \\ -\frac{1}{3L} & 0 & 0 & -\frac{R_f}{L_f} & 0 & 0 \\ 0 & -\frac{1}{3L} & 0 & 0 & -\frac{R_f}{L_f} & 0 \\ 0 & 0 & -\frac{1}{3L} & 0 & 0 & -\frac{R_f}{L_f} \end{bmatrix} \begin{bmatrix} x_1 \\ x_2 \\ x_3 \\ x_4 \\ x_5 \\ x_6 \end{bmatrix} \quad (17)$$

$$\begin{bmatrix} \dot{x}_7 \\ \dot{x}_8 \\ \dot{x}_9 \\ \dot{x}_{10} \\ \dot{x}_{11} \\ \dot{x}_{12} \\ \dot{x}_{13} \\ \dot{x}_{14} \\ \dot{x}_{15} \\ \dot{x}_{16} \\ \dot{x}_{17} \\ \dot{x}_{18} \end{bmatrix} = \begin{bmatrix} \frac{1}{RC} & \omega & 0 & 0 & 0 & 0 & \frac{1}{C} & 0 & 0 & 0 & 0 & 0 & 0 & 0 & 0 & 0 & 0 \\ -\omega & -\frac{1}{RC} & 0 & 0 & 0 & 0 & 0 & \frac{1}{C} & 0 & 0 & 0 & 0 & 0 & 0 & 0 & 0 & 0 \\ 0 & 0 & -\frac{1}{RC} & \omega & 0 & 0 & 0 & 0 & \frac{1}{C} & 0 & 0 & 0 & 0 & 0 & 0 & 0 & 0 \\ 0 & 0 & -\omega & -\frac{1}{RC} & 0 & 0 & 0 & 0 & 0 & \frac{1}{C} & 0 & 0 & 0 & 0 & 0 & 0 & 0 \\ 0 & 0 & 0 & 0 & -\frac{1}{RC} & \omega & 0 & 0 & 0 & 0 & \frac{1}{C} & 0 & 0 & 0 & 0 & 0 & 0 \\ 0 & 0 & 0 & 0 & 0 & -\frac{1}{RC} & 0 & 0 & 0 & 0 & 0 & \frac{1}{C} & 0 & 0 & 0 & 0 & 0 \\ -\frac{1}{3L} & 0 & 0 & 0 & 0 & 0 & -\frac{R_f}{L_f} & \omega & 0 & 0 & 0 & 0 & 0 & 0 & 0 & 0 & 0 \\ 0 & -\frac{1}{3L} & 0 & 0 & 0 & 0 & -\omega & -\frac{R_f}{L_f} & 0 & 0 & 0 & 0 & 0 & 0 & 0 & 0 & 0 \\ 0 & 0 & -\frac{1}{3L} & 0 & 0 & 0 & 0 & -\omega & -\frac{R_f}{L_f} & \omega & 0 & 0 & 0 & 0 & 0 & 0 & 0 \\ 0 & 0 & 0 & -\frac{1}{3L} & 0 & 0 & 0 & 0 & -\omega & -\frac{R_f}{L_f} & 0 & 0 & 0 & 0 & 0 & 0 & 0 \\ 0 & 0 & 0 & 0 & -\frac{1}{3L} & 0 & 0 & 0 & 0 & 0 & -\frac{R_f}{L_f} & \omega & 0 & 0 & 0 & 0 & 0 \\ 0 & 0 & 0 & 0 & 0 & -\frac{1}{3L} & 0 & 0 & 0 & 0 & 0 & -\frac{R_f}{L_f} & \omega & 0 & 0 & 0 & 0 \\ 0 & 0 & 0 & 0 & 0 & 0 & -\frac{1}{3L} & 0 & 0 & 0 & 0 & 0 & -\frac{R_f}{L_f} & \omega & 0 & 0 & 0 \end{bmatrix} \begin{bmatrix} x_7 \\ x_8 \\ x_9 \\ x_{10} \\ x_{11} \\ x_{12} \\ x_{13} \\ x_{14} \\ x_{15} \\ x_{16} \\ x_{17} \\ x_{18} \end{bmatrix} + \begin{bmatrix} 0 \\ 0 \\ 0 \\ 0 \\ 0 \\ 0 \\ 0 \\ 0 \\ 0 \\ 0 \\ 0 \\ 0 \end{bmatrix} \quad (18)$$

$$\begin{bmatrix} 0 \\ 0 \\ 0 \\ 0 \\ 0 \\ 0 \\ \frac{\sqrt{3}mV_{dc}}{12nR_f} \sin(\varphi + \frac{\pi}{6}) + \sin(\varphi + \frac{\pi}{3}) \\ -\cos(\varphi + \frac{\pi}{6}) - \cos(\varphi + \frac{\pi}{3}) \\ \sin(\varphi - \frac{\pi}{2}) + \sin(\varphi - \frac{\pi}{3}) \\ -\cos(\varphi - \frac{\pi}{2}) - \cos(\varphi - \frac{\pi}{3}) \\ \sin(\varphi + \frac{5\pi}{6}) + \sin(\varphi + \pi) \\ -\cos(\varphi + \frac{5\pi}{6}) - \cos(\varphi + \pi) \end{bmatrix}$$

The load voltages and virtual line currents of inverter circuit can be expressed by generalized state variables as

$$\begin{cases} u_{ab} = x_1 + 2x_7 \cos \omega t - 2x_8 \sin \omega t \\ u_{bc} = x_2 + 2x_9 \cos \omega t - 2x_{10} \sin \omega t \\ u_{ca} = x_3 + 2x_{11} \cos \omega t - 2x_{12} \sin \omega t \\ i_{ab} = x_4 + 2x_{13} \cos \omega t - 2x_{14} \sin \omega t \\ i_{bc} = x_5 + 2x_{15} \cos \omega t - 2x_{16} \sin \omega t \\ i_{ca} = x_6 + 2x_{17} \cos \omega t - 2x_{18} \sin \omega t \end{cases} \quad (19)$$

## EXPERIMENTAL RESULTS

The circuit in Fig.1 is simulated to analyze the load line voltage  $V_{ab}$  and the virtual line current  $I_{ab}$ . Detail device model, SSA model and GSSA model are built in MATLAB/Simulink and their simulation results are compared and analyzed.

Parameters of 12-pulse inverter circuit are listed in the follow Table 1. SPWM is adopted in order to control the on-off states of the switches in inverters, and the equivalent resistance of three-phase symmetrical loads is  $80\Omega$ .

Tab. 1. The parameters of inverter circuit

| Description                | Symbol    | Value | Unit     |
|----------------------------|-----------|-------|----------|
| Main bus voltage           | $V_{dc}$  | 270   | V        |
| Amplitude modulation ratio | $m$       | 0.8   | —        |
| Fundamental frequency      | $f$       | 400   | Hz       |
| Switching frequency        | $f_s$     | 10800 | Hz       |
| Initial phase angle        | $\varphi$ | 0     | Rad/s    |
| Filtering resistor         | $R_f$     | 0.1   | $\Omega$ |
| Filtering inductor         | $L_f$     | 4.3   | mH       |
| Filtering capacitor        | $C_f$     | 3.2   | $\mu F$  |
| Transformer ratio          | $n$       | 2     | —        |

Figure 2 (a) shows the block diagram of the detail device simulation of the 12-pulse inverter, and (b) is the GSSA model. The GSSA model reduces to SSA model when the state variables only contain zero-order part.

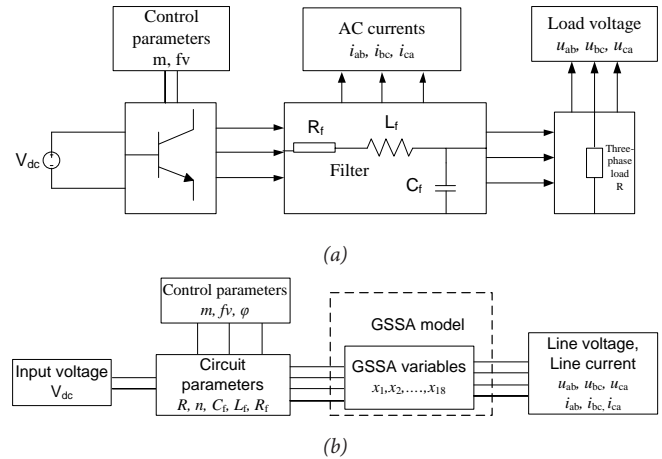


Fig. 2. Diagrams of the 12-pulse inverter  
(a) simulation diagram of the detail device model  
(b) simulation diagram of generalized state space averaging

Waveforms for SPWM signal and the transformer secondary voltage are shown in Figure 3.

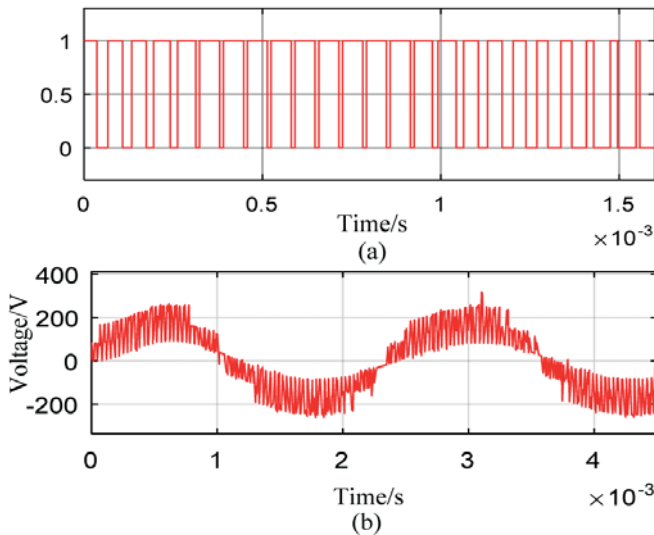


Fig. 3. SPWM modulation results  
 a) PWM signal output  
 (b) Transformer secondary voltage

Generated by the 12-pulse inverter and through the transformer, the secondary voltage waveform before low-pass filter contains a large number of high-order harmonics. Only when the parameters of the inverter circuit are appropriately set can the load gets qualified voltage.

When the power system switches its operating condition, the 12-pulse inverter is subject to large disturbance. Assuming that the inverter loads suddenly altered when the isolate power system changes its operation condition at 10ms, the load changes from 80Ω to 40Ω. The large signal disturbance will occur and affect the inverter.

The waveforms for the output line voltage  $V_{ab}$  and the virtual current  $I_{ab}$  are shown in Figure 4 and Figure 5. The results represent waveforms of detail device model, GSSA and SSA respectively.

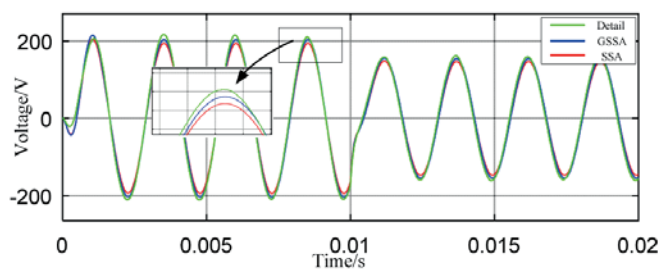


Fig. 4. Waveform of  $V_{ab}$  voltage at load port

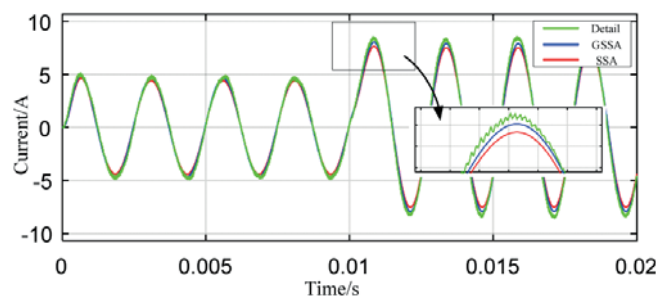


Fig. 5. Waveform of  $I_{ab}$  at AC side

By comparing with the detail device simulation, the deviation of SSA model is about 6% when large signal disturbance occurred, and that of GSSA model is only about 3%. The accuracy of GSSA model is upgraded nearly doubled. Therefore, the results of GSSA model can better reflect the dynamic response process.

In addition, the voltage  $V_{ab}$  and the current  $I_{ab}$  of three models are analyzed with fast Fourier transform. The fundamental frequency is 400Hz. Contents of harmonics under 5th order are shown in Table 2 and Table 3.

Tab. 2. Comparison of current harmonic analysis of three models (unit:%)

| Harmonic frequency | 0    | 400  | 800  | 1200 | 1600 | 2000 | Total harmonic |
|--------------------|------|------|------|------|------|------|----------------|
| Switch             | 3.58 | 100  | 9.99 | 6.21 | 3.20 | 1.93 | 12.53          |
| GSSA               | 3.26 | 95.8 | 9.01 | 5.68 | 2.93 | 1.77 | 12.04          |
| SSA                | 2.55 | 87.7 | 7.15 | 4.33 | 2.14 | 1.55 | 9.25           |

Tab. 3. Comparison of voltage harmonic analysis of three models (unit:%)

| Harmonic frequency | 0 DC | 400  | 800   | 1200  | 1600 | 2000 | Total harmonic |
|--------------------|------|------|-------|-------|------|------|----------------|
| Switch             | 3.88 | 100  | 18.39 | 11.96 | 8.63 | 6.79 | 27.67          |
| GSSA               | 3.22 | 93.6 | 17.24 | 9.25  | 6.63 | 5.67 | 22.20          |
| SSA                | 2.59 | 85.2 | 10.73 | 8.23  | 5.25 | 4.05 | 16.17          |

Figure 6 shows the comparison between the harmonic values of  $V_{ab}$  and  $I_{ab}$  when the inverter suffers large disturbance.

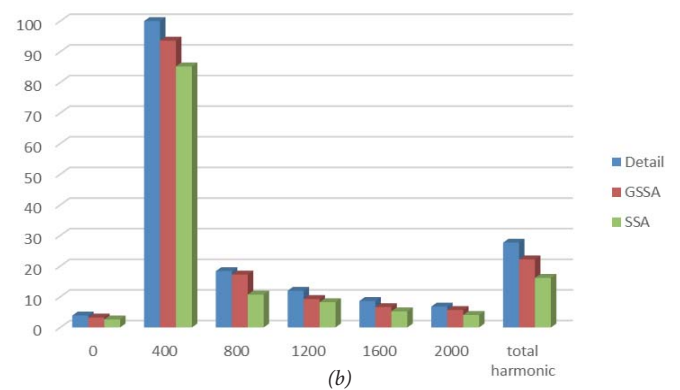
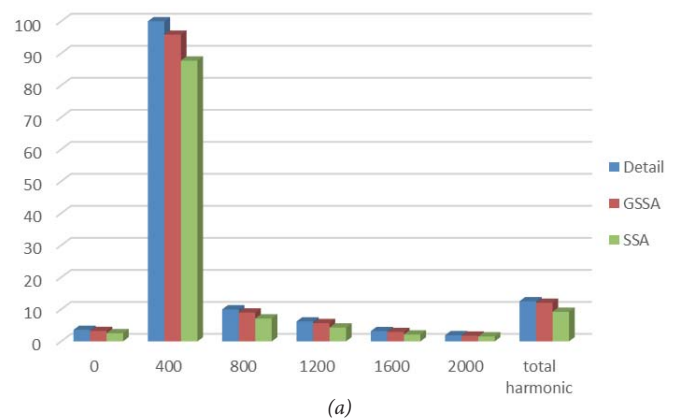


Fig. 6. The comparison of models  
 (a) current harmonic analysis of three models  
 (b) voltage harmonic analysis of three models

In consideration of high-order variables, the generalized state space model can analyze the harmonic content accurately when the power system encounters large disturbance. Compared with the SSA model, this model has a great improvement on the first-order harmonic analysis and increases the accuracy of the analysis of high-order harmonic content.

Simulation speeds for the three models are shown in Table 4.

Tab. 4. Experimental simulation speed

| model                             | Simulation t(s) |
|-----------------------------------|-----------------|
| Detail device model               | 60              |
| State space averaging             | 10              |
| Generalized state space averaging | 13              |

Compared with the state space averaging model, the generalized state space averaging model spends more than 30% time, but its analysis accuracy has been greatly improved, can well meet the analysis requirements of 12-pulse inverter in the accuracy of stability analysis.

## CONCLUSION

Based on the GSSA approach, a model of 12-pulse inverter commonly used in isolated power systems is built in the MATLAB simulation environment. The following conclusions can be drawn from the theoretical and experimental analysis:

(a) Compared with the state space modeling approach, GSSA modeling considers high order components. The higher the order is, the smaller the error will be. The error will have a tendency to zero when the order tends to infinity. Selection of order is determined by the required accuracy and simulation speed.

(b) The GSSA model containing high order components can reflect the actual dynamic characteristics of the inverter, and can improve the accuracy of harmonic analysis of the 12-pulse inverter under large disturbances like operation mode conversion. Having a perfect utilitarian value, this model can meet the requirements of isolated power system analysis including not only small disturbance stability but also large disturbance variation under working conditions switching.

Therefore, the GSSA model offers good feasibility and accuracy in analysis, can provide a basic model for the analysis of large-disturbance dynamic characteristics of 12-pulse inverter circuit. In addition, this model can also be applied to the analysis of other isolated power systems.

## ACKNOWLEDGMENTS

This research was financially supported by National Natural Science Foundation of China (Grant No. U1533126).

## REFERENCES

1. L. J. Chen, S. W. Mei, X. U. Yin, et al, 2011. A new pattern of future power grids: Isolated power system. *Journal of Electric Power Science & Technology*.
2. Y. Khersonsky, N. Hingorani, K. L. PetersSon, 2009. IEEE Electric Ship Technologies Initiative. *IEEE Industry Applications Magazine*, 17(1), 65-73.
3. M. Hirst, A. Mcloughlin, P. J. Norman, et al, 2011. Demonstrating the more electric engine: a step towards the power optimised aircraft. *Iet Electric Power Applications*, 5(1), 3-13.
4. L. T. Lam, R. Louey, 2006. Development of ultra-battery for hybrid-electric vehicle applications. *Journal of Power Sources*, 158(2), 1140-1148.
5. L. Prisse, D. Ferer, H. Foch, et al, 2009. New power centre and power electronics sharing in aircraft. European Conference on Power Electronics and Applications. IEEE. pp. 1-9.
6. K. P. Logan, 2007. Intelligent diagnostic requirements of future all-electric ship integrated power system. *IEEE Transactions on Industry Applications*, 43(1), 139-149.
7. K. Satpathi, A. Ukil, N. Thukral, et al, 2016. Modelling of DC Shipboard Power System. IEEE International Conference on Power Electronics, drives and Energy Systems. IEEE.
8. Y. Wang, C. Xiang, S. Hu, 2014. Design and control strategy for a new hybrid energy storage system. Applied Power Electronics Conference and Exposition. IEEE. 3401-3405.
9. D. Izquierdo, R. Azcona, F. J. L. Del Cerro, et al, 2010. Electrical power distribution system (HV270DC) for application in more electric aircraft. Applied Power Electronics Conference and Exposition (APEC). Palm Springs: IEEE. 1300-1305.
10. C. R. Avery, S. G. Burrow, P. H. Mellor, 2007. Electrical generation and distribution for the more electric aircraft. Universities Power Engineering Conference (UPEC) 2007. Brighton: IEEE. 1007-1012.
11. H. Zhang, F. Mollet, C. Saudemont, et al, 2010. Experimental validation of energy storage system management strategies for a local dc distribution system of more electric aircraft. *Industrial Electronics*, 57(12), 3905-3916.
12. T. Wu, S. V. Bozhko, G. M. Asher, 2010. High speed modeling approach of aircraft Electrical power systems under both normal and abnormal scenarios. International Symposium Industrial Electronics (ISIE). Bari: IEEE. 870-877.

13. 15 Real-Time Distributed Coordination of Power Electronic Converters in a DC Shipboard Distribution System
14. S. R. Mathew, P. V. R. Sai Kiran, M. Anand, 2014. Design and implementation of a three level diode clamped inverter for more electric aircraft applications using hardware in the loop simulator. 2014 International conference on Advances in Electronics, Computers and Computers Communications (ICAIECC). Bangalore: IEEE. 1-6.
15. S. Ahmed, Z. Shen, P. Mattavelli, et al, 2011. Small-signal model of a Voltage Source Inverter (VSI) Considering the Dead-Time Effect and Space Vector Modulation Types. The 26th annual Applied Power Electronics Conference and Exposition. Fort worth: IEEE. 685-690.
16. D. Y. Hyun, C. S. Lim, R. Y. Kim, et al, 2013. Averaged modeling and control of a single-phase grid-connected two-stage inverter for battery application. Industrial Electronic Society. Vienna: IEEE. 489-494.
17. T. Wu, S. Bozhko, G. M. Asher, et al, 2008. Fast reduced functional models of electromechanical actuators for more-electric aircraft power system study. Bellevue WA: SAE Technical Paper.
18. T. Wu, S. V. Bozhko, G. Asher, et al, 2009. A Fast Dynamic Phasor Model of Autotransformer Rectifier Unit for More Electric Aircraft. Industrial Electronics 35th Annual Conference of IEEE. Porto: IEEE. 2531-2536.
19. S. R. Sanders, J. M. Noworolski, X. Z. Liu, et al, 1991. Generalized averaging method for power conversion circuits. *Power Electronics IEEE Transactions on*, 6(2), 251-259.

## CONTACT WITH THE AUTHORS

**Yanbo Che**

Key Laboratory of Smart Grid of Ministry of Education,  
Tianjin University  
Tianjin 300072  
**CHINA**

# DRY PORTS-SEAPORTS SUSTAINABLE LOGISTICS NETWORK OPTIMIZATION: CONSIDERING THE ENVIRONMENT CONSTRAINTS AND THE CONCESSION COOPERATION RELATIONSHIPS

Hairui Wei<sup>1</sup>

Zhaohan Sheng<sup>2</sup>

<sup>1</sup> Logistics Research Center, Shanghai Maritime University, Shanghai 201306, China.

<sup>2</sup> School of Management & Engineering, Nanjing University, Nanjing 210093, China.

\* corresponding author

## ABSTRACT

*In China dry ports enter into a rapid development period now, however for many Chinese dry ports, the operation faces difficulties duo to inefficient logistics networks and cooperation relationship between dry ports and seaports. Focusing on the concession cooperation mechanism of seaports and dry ports, and the environmental constraints (carbon emissions and congestion cost), a bi-objective location-allocation MILP model for the sustainable hinterland-dry ports-seaports logistics network optimization is formulated, aiming at the system logistics costs and carbon emissions to be minimized. Moreover, for the cooperation mechanism of seaports to dry ports, a parameter called cooperation cost concession coefficient is proposed for the optimization model, and a new evaluation method based on the ordered weighted averaging (OWA) operator is used to evaluate it. Then a location-allocation decision-making framework for the hinterland-dry port-seaport logistics network is proposed. The innovative aspect of the model is that it can propose a effective and environment friendly dry ports location strategic and also give insights into the connective cooperation relationships, and cargo flows of the network. A case study involving configuration of dry ports in Henan Province is conducted, and the model is successfully applied.*

**Keywords:** Dry port; Port logistics; Logistics network; Location-allocation; Sustainable; Relationships evaluation

## INTRODUCTION

Dry port (also known as inland port) refers to a kind of modern logistics center with customs declaration, inspection and quarantine, and other port services functions except ships loading and unloading [1]. As the growing competition of seaport for the hinterland resources and the needs of inland areas to develop open economics, dry ports in China enter into a rapid development period now. They have played a certain role in the economic development of hinterlands and the competitiveness ascension of some seaports [2]. However,

many problems also exist during the development of dry ports [3], and most dry ports in China now are in a difficult operation state, which makes the research of the effective dry ports logistics network become very necessary.

Dry ports aim at moving the road transport onto the rail networks to reduce traffic congestion of the terminal cities, pollution emissions, and logistics cost [5]. So a efficient dry port relays on the coordinated development of various transportation modes, meanwhile contributes to the integration of various transportation modes [4]. In this sense, the environmental benefits of the dry ports should not be ignored.

In addition, due to the strong position of the harbors and the distinct feature of the government behavior in China, the development of Chinese dry port often relies on the support of local government and the cooperative seaports. So, in order to design an efficient sustainable dry ports-seaports network, decision makers must synthetically consider environmental constraints and cooperation mechanism among seaports and dry ports.

However, there are few researches on the dry ports-seaports logistics networks from this perspective. Roso et al. pointed out that the location of dry ports became an import issue of research due to dry ports playing a key role in connecting seaports to hinterland[5]. Heaver et al., Notteboom and Robinson proposed different spatial configuration of dry ports from the functional relationship between ports and dry ports[6-8]. Mansour identified and analyzed a number of inland port sites in the five counties surrounding Los Angeles using a location-allocation methodology[9]. Feng proposed a location-allocation NLP model for dry pots locati-seaports network, considering the probability of through the dry ports to seaports or not[10]. Ambrosino studied the location of the location of mid-range dry ports focused on the intermodal transportation networks[11]. Samir evaluated the dry ports location problems with Multi-Criteria Decision Analysis, DELPHI Methodology and so on[12][13].

This paper studies the location of dry port and the hinterland-dry port-seaport logistics network optimization, taking into the cost concession partnership between the dry ports and seaports, and the environmental factors at the same time. The contribution of this paper lies in: firstly, focusing on the cost concession partnership mechanism of seaports and candidate dry ports, we proposed a new method based on OWA operator to evaluate the cost concession partnership between them, which laid the foundation for network location-allocation optimization; secondly, we also considered the environment factors and proposed a bi-objective location-allocation MILP model for the dry ports-seaports logistics network, which extend the interests attention from the shippers to the comprehensive benefit of the logistics network system.

## MATERIAL AND METHODS

### THE EVALUATION OF THE COST CONCESSION PARTNERSHIP AMONG SEAPORTS AND DRY PORTS

In china, compared with dry ports, seaports have the absolute dominant position. Dry port often relies on the efficient and beneficial relationship with one or some seaports to attract cargoes, reduce logistics cost and obtain preliminary development opportunities. And according the more and more competition in the port hinterland resources, the seaports are also willing to offer a discount to dry ports for more supply of goods. For the same seaport, the concession relationship for different dry ports are different based on the

comprehensive evaluation of some basic factors, such as the cargo demand, traffic connectivity, the emphasis of the local government and so on. And the same factor between different seaports and dry ports may has different influence on the concession relationships. According to this feature, a new method based on OWA operator is proposed to figure out the cost concession coefficient for each seaport-dry port pair.

The ordered weighted averaging operator was first proposed by Yager [18], which is used to aggregate and evaluate information in multi-criteria or multi-expert decision-making problem. Suppose a function  $F(U)$  is a real number set, and  $U = (u_1, u_2, \dots, u_n)$ . Given  $n$  weights  $W = \{w_j\}_1^n$  with the domain of discourse  $[0,1]$  and  $\sum_{j=1}^n w_j = 1$  associated with function  $F(U)$ . Let  $u_{\sigma(j)}$  be the  $j$ th highest element of  $\{u_1, u_2, \dots, u_n\}$ .  $F(U)$  is an OWA operator, if

$$F(u_1, u_2, \dots, u_n) = \sum_{j=1}^n w_j u_{\sigma(j)} \quad (1)$$

It's worth noting that weight  $w_j$  is corresponding to a certain position sequence, rather than element  $u_i$  [17]. As we know in the above, the same factor for different seaport-dry port pairs has defferent effect degrees, so for the same factor the evaluation weight may different for the different seaport-dry port pairs, which means the weights and evaluation factors has no corresponding relation. Therefore, OWA operator is an effective method to evaluate the cooperation relationship coefficient.

Suppose that the exporting cargo volume of the candidate dry port city and its surrounding cities ( $u_1$ ), traffic connectivity between seaports and candidate dry ports ( $u_2$ ), the emphasis and support of the local government ( $u_3$ ), and the importance of the dry port to the network layout strategy of the seaport ( $u_4$ ). The evaluation steps are as follows:

Step 1: Set weights  $W = \{w_n\}_1^N$  by the expert evaluation method and the experts are from the seaport management and operation practice. Here  $N = 4$ .

Step 2: Determine the evaluation matrix  $P = [p_{kn}]_{KN}$ . Set candidate dry port vector  $X = \{x_k\}_1^K$ , where  $K$  is the total number of candidate dry ports. For seaport  $j$ , Let  $p_{kn}$  is the evaluation value of factor  $u_n$  for dry port  $x_k$  and seaport  $j$ . If  $u_i$  is a quantitative factor,  $p_{kn}$  is obtained by its real value, otherwise if  $u_i$  is a qualitative factor,  $p_{kn}$  is chosen from the domain of discourse  $\{1, 2, 3, 4, \text{ and } 5\}$ . Then the evaluation matrix  $P = [p_{kn}]_{KN}$  can be obtained.

Step 3: Normalize evaluation matrix  $P = [p_{kn}]_{KN}$ , obtain the normalized evaluation matrix  $R = [r_{kn}]_{KN}$ . If the greater the  $p_{kn}$  value, the greater of the influence on dry port  $x_k$  and seaport  $j$ , then the  $p_{kn}$  is with the benefit-type attribute normalized by Equation (2), otherwise  $p_{kn}$  is with cost-type attributes normalized by Equation (3).

$$r_{kn} = \frac{p_{kn}}{\sum_k p_{kn}} \quad k \in K \quad (2)$$

Step 4: Aggregate the evaluation matrix  $R = [r_{kn}]_{KN}$ . Let matrix  $R' = [r_{\sigma(kn)}]_{KN}$  be obtained from the ranking components of each row vector in  $R = [r_{kn}]_{KN}$  from bigger to smaller, and let  $a_{kj}$  be the comprehensively-evaluated value of the dry port  $x_k$  and seaport  $j$ , then

$$a_{kj} = (r_{\sigma(k1)}, r_{\sigma(k2)}, \dots, r_{\sigma(kN)})W \quad (4)$$

Step 5: Compute cost discount coefficient  $s_{kj}$ .  $s_{kj}$  is the cost discount coefficient of seaport  $j$  to dry port  $x_k$ . For seaport  $j$ , suppose  $a_{\max j}$  is the largest one of  $(a_{1j}, a_{2j}, \dots, a_{kj})$ , and the maximum cost discount coefficient for seaport  $j$  to each candidate dry port is  $\lambda$ , then

$$s_{kj} = \frac{\lambda(1 - a_{kj})}{1 - a_{\max j}} \quad (5)$$

Step 6: Repeat steps 2-4 for each seaport, Suppose the number of seaports is  $J$ , then obtain the cooperation cost concession coefficient matrix  $S = [s_{kj}]_{KJ}$ .

## THE BI-OBJECTIVE LOCATION-ALLOCATION MODEL FOR DRY PORTS-SEAPORTS NETWORK OPTIMIZATION

### Problem Definition and Model Formulation

The hinterland-dry port-seaport logistics network studied in this paper is shown in Figure 1, where the cargoes transportation by road between hinterland and dry port, the cargoes transportation by rail between dry port and seaports, or the cargoes directly transport from hinterland to seaport by road with higher environmental cost.

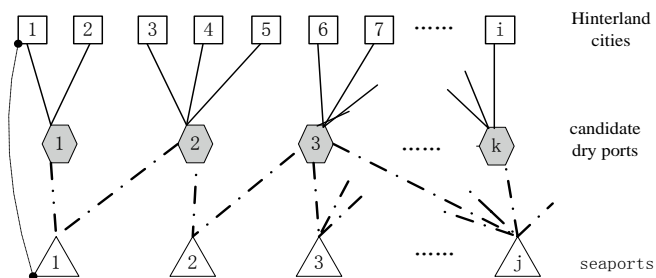


Fig. 1. The Structure of the hinterland-dry port-seaport logistics network

Based on the cooperation cost concession partnership from the Section 2.1, and taking into account the logistics transportation cost, terminal city congestion cost and emissions pollution, a bi-objective MILP location-allocation model for the hinterland-dry port-seaport logistics network optimization is established in this section. The logistics

costs and carbon emissions are our objective functions to be minimized.

$$M \inf_1 = \sum_i \sum_k q_{ik} c_{ik} l_{ik} + \sum_k \sum_j s_{kj} q_{kj} c_{kj} l_{kj} + \sum_i \sum_j l_{ioj} q_{ioj} (c_{ioj} + c_d) + \sum_k b_k x_k + \sum_k \sum_j b_{kj} y_{kj} \quad (6)$$

$$M \inf_2 = \sum_i \sum_k q_{ik} K_{road} + \sum_k \sum_j q_{kj} l_{kj} K_{rail} + \sum_i \sum_j l_{ioj} q_{ioj} K_{road} \quad (7)$$

$$\sum_i q_{ik} = \sum_j q_{kj} \quad (8)$$

$$\sum_i q_{ik} \leq m_k x_k \quad (9)$$

$$\sum_j q_{kj} \leq m_k x_k \quad (10)$$

$$q_{kj} \leq M y_{kj} \quad (11)$$

$$\sum_k q_{ik} + \sum_j q_{ioj} = q_i \quad (12)$$

$$q_{ik}, q_{kj}, q_{ioj} \geq 0 \quad (13)$$

$$x_k \in \{0, 1\} \quad (14)$$

$$y_{kj} \in \{0, 1\} \quad (15)$$

Where, the subscripts  $i, j, k$  denote hinterland cities, seaports, and dry port candidate sites, respectively.  $l, q, c$  respectively denote the distance, the cargoes volume, and the unit transportation cost, and their subscripts  $ik, kj, ioj$  denote from the hinterland city  $i$  to the candidate dry port  $k$ , from the candidate dry port  $k$  to the seaport  $j$ , from the hinterland city  $i$  to the seaport  $j$  respectively.  $b_k$  denotes the built cost per year of the candidate dry port  $k$ .  $b_{kj}$  denotes the cooperation relationship maintenance cost per year of  $k$  seaport  $j$  and the candidate dry port  $k$  (such as traffic aisle maintenance, customs clearance and inspection operations costs).  $K_{road}$  and  $K_{rail}$  denote the road and rail carbon emissions coefficients respectively. Note that  $c_d$  denotes the congestion cost coefficients of road transport, which and emissions pollution are the two factors considered in the environment Constraints. Constraints (8) specify the relationships of the input and output cargo volume of dry port  $k$ . Constraints (9) and (10) specify the capacity of the candidate dry port  $k$ . Supposed the railway capacity can meet the transportation demand expressed in Constraints (11),  $M$  is a very large constant. Constraints (12) expresses all the original cargo transportation demand can be met. Constraints (14) and (15) specify feasible values of the decision variables.

### Meeting logistics cost and carbon emissions objectives

According the characters of the multi-objective programming, the objectives trade-off strategy in this paper is presented in Equation (16) [18]. The strategy comprises two steps. The first step minimizes  $f_1$  and the minimum is denoted by  $f_1^*$ ; then minimizes  $f_2$ , where  $\varepsilon$  is a relaxation coefficient for  $f_1$ . The advantages of this objectives trade-off strategy is that it doesn't need a unified dimension for the two different objective function logistics cost and pollution discharge, and at the same time decision makers can according to themselves compromise degree will of the increasing the logistics cost to decrease the environmental emissions to determine the coefficient of relaxation of the cost target function, and obtain satisfactory solution of multi-objective programming.

$$\min_{x \in X, f_1 \leq (1+\varepsilon)f_1^*} f_2, \text{ where } f_1^* = \min_{x \in X} f_1 \quad (16)$$

### The hinterland-dry port-seaport logistics network location-allocation framework

As a summary of the above methods for the evaluation of the cost concession partnership among seaports and dry ports and the modeling of the bi-objective MILP location-allocation model for the network optimization, we propose the hinterland-dry port-seaport logistics network location-allocation decision-making framework (see Figure 2).

From the framework we can see the decision-makers should determine the candidate dry ports firstly, collect all basic data of the hinterland cities, candidate dry ports and seaports, and then negotiate with all possible cooperative seaports to obtain the cost concession from seaports to dry ports, and finally based on the bi-objective MILP location-allocation model locate dry ports among the alternatives and allocate hinterland cargo resource to dry ports and cooperative seaports.

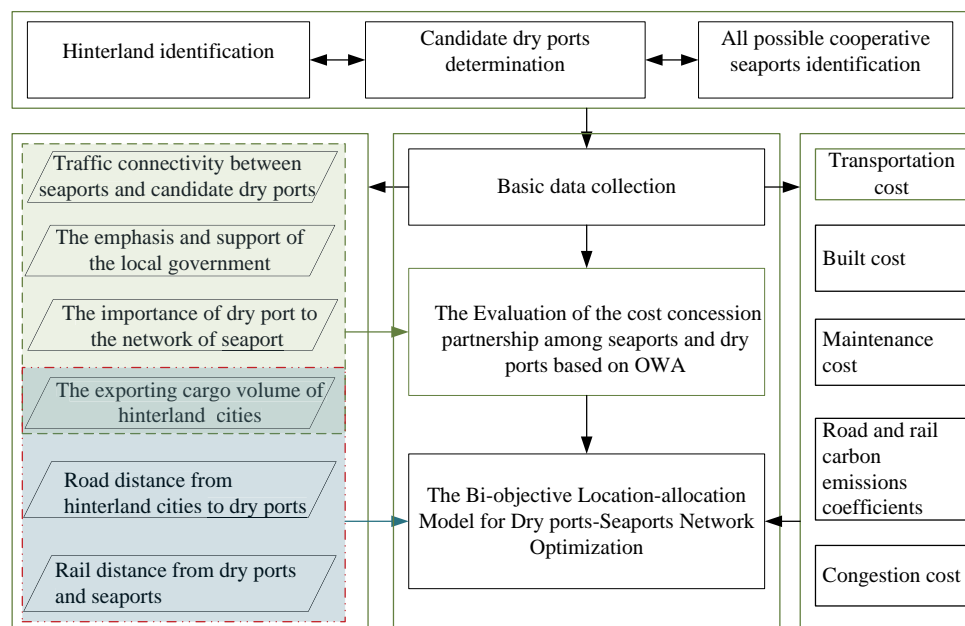


Fig. 2. The location-allocation decision-making framework for dry port-seaport network.

## RESULTS

### EXPERIMENTAL DATA

In this paper, dry ports in Henan province of China have been considered for the experimental study. Henan province is the core province of the Chinese Central Plains Economic Zone, who is far from the harbor. As the important region in “the Belt and Road initiative”(“B&R”) of China, Henan province is taking action to open to the outside world further and tring to play a more important role in”B&R”. Establishing the cooperation relationship among the dry ports within it and seaports in Chinese eastern coastal, is the important way for Henan province to participatate in “B&R”.

There are 18 cargoes origins in Henan, and 8 of them are chosen as the candidate dry port cities by the government (the green nodes in Figure3): Zhengzhou(ZZ), Shangqiu(SQ), Xinxiang(XX), Luoyang(LY), Hebi(HB), Nanyang(NY), Zhumadian(ZMD), Luohe(LH). And 7 seaports are considered: Tianjin(T), Qingdao(Q), Rizhao(R), Yantai(Y), Weihai(W), Lianyungang(L), Shanghai(S) (see Figure3). The basic data of hintland cities, candidate dry port cities and seaports from Chinese road and rail transport query tables and Henan statistical yearbook is shown in Table 1-2.



Fig. 3. The seaports, candidate dry port cities and hinterland cities of the case

Tab. 1. The basic data distance from the hinterland cities to candidate dry port cities and seaports

|              | distance to the candidate dry port cities (km) |     |     |     |     |     |     |     | distance to the seaports (km) |      |     |     |      |      |      | cargo supply (TEU) |
|--------------|--|-----|-----|-----|-----|-----|-----|-----|-------------------------------|------|-----|-----|------|------|------|--------------------|
|              | ZZ   | SQ  | XX  | LY  | HB  | NY  | ZMD | LH  | T                             | Q    | R   | L   | S    | Y    | W    |                    |
| Zhengzhou    | 0  | 202 | 70  | 144 | 160 | 262 | 213 | 161 | 708                           | 897  | 715 | 584 | 1046 | 962  | 1050 | 351718             |
| Sanmenxia    | 468  | 470 | 302 | 128 | 370 | 388 | 325 | 353 | 920                           | 1165 | 983 | 852 | 1314 | 1230 | 1138 | 5876               |
| Luoyang      | 144  | 346 | 178 | 0   | 246 | 293 | 237 | 220 | 840                           | 1026 | 844 | 713 | 1175 | 1097 | 1179 | 53790              |
| Jiaozuo      | 83   | 292 | 64  | 117 | 132 | 352 | 258 | 236 | 706                           | 987  | 805 | 674 | 1136 | 1052 | 1140 | 56884              |
| Xinxiang     | 70   | 225 | 0   | 178 | 90  | 332 | 278 | 211 | 630                           | 758  | 735 | 596 | 1068 | 886  | 974  | 33000              |
| Anyang       | 174  | 282 | 174 | 288 | 42  | 555 | 380 | 313 | 541                           | 648  | 583 | 706 | 1168 | 776  | 864  | 20870              |
| Shangqiu     | 202  | 0   | 225 | 346 | 253 | 392 | 334 | 200 | 635                           | 683  | 501 | 371 | 833  | 707  | 895  | 6038               |
| Nanyang      | 262  | 392 | 332 | 293 | 394 | 0   | 173 | 190 | 930                           | 1032 | 850 | 709 | 1064 | 1157 | 1245 | 34507              |
| Kaifeng      | 67   | 135 | 137 | 211 | 227 | 297 | 253 | 186 | 780                           | 824  | 642 | 512 | 974  | 889  | 974  | 8289               |
| Luohe        | 161  | 200 | 211 | 220 | 278 | 200 | 67  | 0   | 799                           | 914  | 732 | 545 | 1020 | 1039 | 1127 | 6502               |
| Xinyang      | 318  | 339 | 296 | 399 | 486 | 230 | 106 | 189 | 984                           | 1100 | 918 | 660 | 834  | 1225 | 1313 | 6465               |
| Pingdingshan | 142  | 273 | 213 | 163 | 275 | 242 | 149 | 94  | 813                           | 813  | 716 | 613 | 906  | 985  | 1046 | 11836              |
| Hebi         | 160  | 253 | 90  | 246 | 0   | 394 | 338 | 278 | 562                           | 705  | 669 | 646 | 1026 | 790  | 851  | 4533               |
| Puyang       | 187  | 246 | 123 | 301 | 102 | 449 | 405 | 302 | 511                           | 654  | 618 | 604 | 984  | 739  | 800  | 18883              |
| Xuchang      | 105  | 192 | 156 | 174 | 219 | 184 | 133 | 57  | 920                           | 743  | 660 | 561 | 866  | 915  | 976  | 48453              |
| Zhoukou      | 184  | 132 | 254 | 288 | 322 | 260 | 123 | 66  | 768                           | 730  | 596 | 496 | 761  | 916  | 977  | 9444               |
| Zhumadian    | 161  | 334 | 278 | 237 | 338 | 173 | 0   | 67  | 864                           | 842  | 708 | 608 | 871  | 1028 | 1089 | 6819               |
| Jiyuan       | 148  | 350 | 291 | 65  | 202 | 325 | 349 | 282 | 792                           | 812  | 710 | 704 | 1056 | 983  | 1070 | 16443              |

Tab. 2. The distance from Candidate dry port cities to Seaports (km)

| Distance  | Tianjin | Qingdao | Rizhao | Lianyungang | shanghai | Yantai | Weihai |
|-----------|---------|---------|--------|-------------|----------|--------|--------|
| Zhengzhou | 799     | 1061    | 710    | 559         | 998      | 969    | 1053   |
| Shangqiu  | 672     | 793     | 560    | 356         | 795      | 766    | 850    |
| Xinxiang  | 771     | 783     | 630    | 639         | 1078     | 929    | 937    |
| Luoyang   | 999     | 1185    | 833    | 683         | 1122     | 1316   | 1177   |
| Hebi      | 705     | 977     | 855    | 705         | 1144     | 1115   | 1192   |
| Nanyang   | 1220    | 1431    | 715    | 929         | 1004     | 1197   | 1505   |
| Zhumadian | 1081    | 1199    | 916    | 712         | 897      | 1175   | 1206   |
| Luohe     | 1015    | 1133    | 850    | 646         | 963      | 1109   | 1140   |

### DETERMINING THE MODEL PARAMETERS

Firstly, as the method in section 2, the cooperation cost concession coefficient matrix  $S = [s]_{8 \times 7}$  is obtained, see Table3. The values of other parameters in the objective function and the constrains used in this study are taken from combination of expert survey and the references [17]. For example, congestion cost  $c_d = 0.358 \text{ ¥/km-TEU}$ ,  $K_{rail} = 0.0007 \text{ ton/TEU-km}$ , and

$$K_{road} = 11.14272 \times \frac{l_{ik} e^{0.047772 v_{rd}}}{3280.8 v_{rd}} \quad (17)$$

### THE SOLUTION OF HINTERLAND-DRY PORT-SEAPORT SUSTAINABLE LOGISTICS NETWORK FOR THIS CASE

Based on the basic data and the model parameters determined in the above, we use Cplex to solve the MILP model in the section 3.1. Suppose decision makers are willing to use 3% of the higher logistics costs for carbon emissions reduction, according to the objectives trade-off strategy in the section 3.2, the relaxation coefficient should be chosen  $\varepsilon = 3\%$ . Then we can obtain the satisfactory solution shown in Table 4, 5, 6 and Figure 4.

Tab. 3. The cooperation cost concession coefficient matrix of dry ports and seaports.

| S         | Tianjin | Qingdao | Rizhao | Lianyungang | shanghai | Yantai | Weihai |
|-----------|---------|---------|--------|-------------|----------|--------|--------|
| Zhengzhou | 0.80    | 0.70    | 0.75   | 0.80        | 0.95     | 0.75   | 0.80   |
| Shangqiu  | 0.85    | 0.72    | 0.98   | 0.85        | 0.90     | 0.98   | 0.70   |
| Xinxiang  | 0.85    | 0.97    | 0.75   | 0.80        | 0.95     | 0.70   | 0.96   |
| Luoyang   | 0.80    | 0.90    | 0.80   | 0.80        | 0.95     | 0.92   | 0.97   |
| Hebi      | 0.79    | 0.99    | 0.98   | 0.93        | 0.93     | 0.97   | 0.99   |
| Nanyang   | 0.99    | 0.99    | 0.98   | 0.98        | 0.97     | 0.99   | 0.99   |
| Zhumadian | 0.95    | 0.95    | 0.85   | 0.98        | 0.90     | 0.93   | 0.99   |
| Luohe     | 0.94    | 0.95    | 0.76   | 0.98        | 0.92     | 0.90   | 0.90   |

Tab. 4. The candidate dry ports chosen for the satisfactory solution

| Candidate dry port cities | Zhengzhou | Shangqiu | Xinxiang | Luoyang | Hebi | Nanyang | Zhumadian | Luohe |
|---------------------------|-----------|----------|----------|---------|------|---------|-----------|-------|
| Chosen or not             | 1         | 0        | 1        | 1       | 1    | 0       | 1         | 0     |

Tab. 5. The hinterlands cargo allocation to dry ports (TEU)

| Hinterland cargo allocation | Zhengzhou | Shangqiu | Xinxiang | Luoyang | Hebi  | Nanyang | Zhumadian | Luohe |
|-----------------------------|-----------|----------|----------|---------|-------|---------|-----------|-------|
| Zhengzhou                   | 351720    | 0        | 0        | 0       | 0     | 0       | 0         | 0     |
| Sanmenxia                   | 0         | 0        | 0        | 5880    | 0     | 0       | 0         | 0     |
| Luoyang                     | 0         | 0        | 0        | 53790   | 0     | 0       | 0         | 0     |
| Jiaozuo                     | 0         | 0        | 56880    | 0       | 0     | 0       | 0         | 0     |
| Xinxiang                    | 0         | 0        | 33000    | 0       | 0     | 0       | 0         | 0     |
| Anyang                      | 0         | 0        | 0        | 0       | 20870 | 0       | 0         | 0     |
| Shangqiu                    | 6040      | 0        | 0        | 0       | 0     | 0       | 0         | 0     |
| Nanyang                     | 0         | 0        | 0        | 0       | 0     | 0       | 34510     | 0     |
| Kaifeng                     | 8290      | 0        | 0        | 0       | 0     | 0       | 0         | 0     |
| Luohe                       | 0         | 0        | 0        | 0       | 0     | 0       | 6500      | 0     |
| Xinyang                     | 0         | 0        | 0        | 0       | 0     | 0       | 6460      | 0     |
| Pingdingshan                | 11840     | 0        | 0        | 0       | 0     | 0       | 0         | 0     |
| Hebi                        | 0         | 0        | 0        | 0       | 4530  | 0       | 0         | 0     |
| Puyang                      | 0         | 0        | 0        | 0       | 18880 | 0       | 0         | 0     |
| Xuchang                     | 48450     | 0        | 0        | 0       | 0     | 0       | 0         | 0     |
| Zhoukou                     | 0         | 0        | 0        | 0       | 0     | 0       | 9440      | 0     |
| Zhumadian                   | 0         | 0        | 0        | 0       | 0     | 0       | 6820      | 0     |
| Jiyuan                      | 0         | 0        | 0        | 0       | 16440 | 0       | 0         | 0     |

Tab. 6. The dry ports cargo allocation to seaports (TEU)

| Dry Port cargo allocation | Tianjin | Qingdao | Rizhao | Lianyungang | Shanghai | Yantai | Weihai |
|---------------------------|---------|---------|--------|-------------|----------|--------|--------|
| Zhengzhou                 | 26330   | 0       | 200000 | 200000      | 0        | 0      | 0      |
| Shangqiu                  | 0       | 0       | 0      | 0           | 0        | 0      | 0      |
| Xinxiang                  | 0       | 0       | 89880  | 0           | 0        | 0      | 0      |
| Luoyang                   | 0       | 0       | 0      | 76110       | 0        | 0      | 0      |
| Hebi                      | 44290   | 0       | 0      | 0           | 0        | 0      | 0      |
| Nanyang                   | 0       | 0       | 0      | 0           | 0        | 0      | 0      |
| Zhumadian                 | 0       | 0       | 0      | 63740       | 0        | 0      | 0      |
| Luohe                     | 0       | 0       | 0      | 0           | 0        | 0      | 0      |

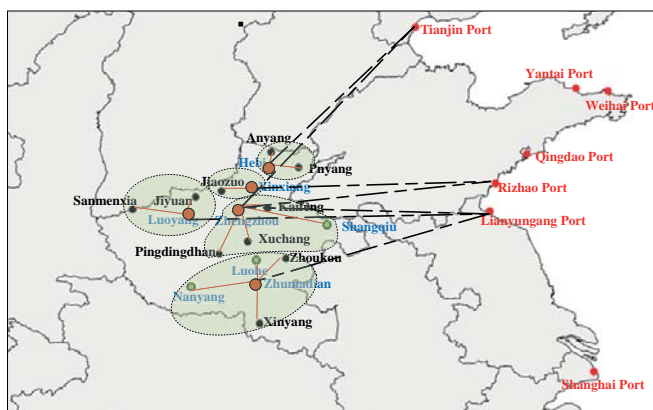


Fig. 4. The solution of hinterland-dry port-seaport sustainable logistics network

Table 4 shows the candidate dry ports location, in which “1” means the corresponding candidate dry port is chosen, and “0” is not chosen. In the satisfactory solution there are five dry ports has been chosen from the 8 candidate dry ports located in Zhengzhou, Xinxiang, Luoyang, Hebi, and Zhumadian.

Table 5 shows the the adjacency relations and cargo allocation among dry ports and 18 hinterland cities. For example, “6040” in Table 5 corresponds to Shangqiu (hinterland city) and Zhengzhou (dry port city), which means there is adjacency relation between Shangqiu and Zhengzhou dry port, and the 6040 TEU cargo supply by Shangqiu will served by Zhengzhou dry port to outside market.

Similarly, Table 6 shows the adjacency relations and cargo allocation among dry ports and 7 seaports. If the value is not “0”, there is a cooperation relationship between the corresponding dry port and seaport, and the value is the cargo

allocation quantity from the dry port to the corresponding seaport.

Figure 4 shows the whole Figure of the dry ports-seaports network considering the cost concession between 7 seaports and 8 candidate dry ports and the carbon emissions among 7 seaports, 8 candidate dry ports and 18 hinterland cities. And the total logistics cost of this satisfactory solution is  $\text{¥} 9.467966 \times 10^9$ , and the volume of carbon emissions is  $3.1138 \times 10^8$  tons.

## DISCUSSION

All the above results are based on the basic suppose that 3% logistics cost rising for the reduction of the carbon emissions, and also based on the evaluation of the cost concession partnership from seaports to dry ports. Then we will further analysis the impact of these two factors on the solution of location-allocation dry ports-seaports logistics network.

(1) Regardless of the environmental constraints, if we don't consider the cost concession agreement among seaports and dry ports, the optimization solution for the dry port-seaport logistics network is obtain in Figure 5(a).

In contrast, the solution considering the cost concession agreement is shown in Figure 5(b). And the cargo allocation from dry ports to seaports under the conditions considering the cost concession agreement or not is shown in Table 7.

Tab. 7. The dry ports cargo allocation to seaports considering the cost concession or not(TEU).

| consider cost concession or not | No      |        |             | Yes     |        |             |
|---------------------------------|---------|--------|-------------|---------|--------|-------------|
|                                 | Tianjin | Rizhao | Lianyungang | Tianjin | Rizhao | Lianyungang |
| Dry Port cargo allocation       |         |        |             |         |        |             |
| Zhengzhou                       | 8460    | 200000 | 200000      | 26330   | 200000 | 200000      |
| Shangqiu                        | 0       | 0      | 0           | 0       | 0      | 0           |
| Xinxiang                        | 0       | 140210 | 0           | 0       | 89880  | 0           |
| Luoyang                         | 0       | 0      | 76110       | 0       | 0      | 76110       |
| Hebi                            | 0       | 0      | 0           | 44290   | 0      | 0           |
| Nanyang                         | 0       | 0      | 0           | 0       | 0      | 0           |
| Zhumadian                       | 0       | 0      | 75570       | 0       | 0      | 63740       |
| Luohe                           | 0       | 0      | 0           | 0       | 0      | 0           |
| Total                           | 8460    | 340210 | 351680      | 70620   | 289880 | 339850      |

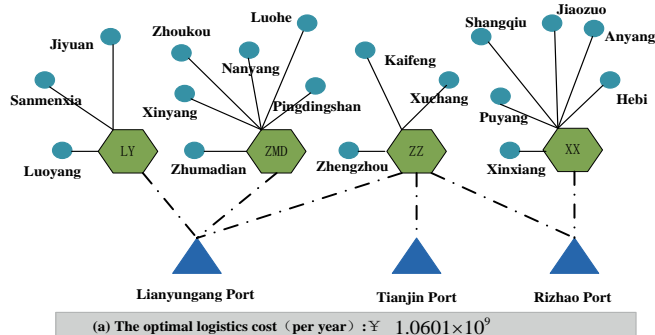


Fig. 5. (a) The optimization solution with no cooperation relationships between seaports and dry ports

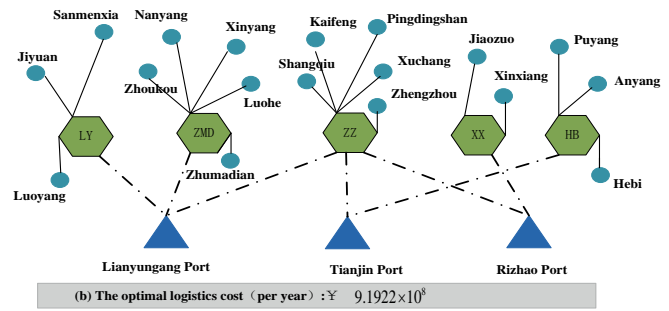


Fig. 5. (b) The optimization solution with cooperation relationships (without environmental constraints).

In Figure 5, there are four dry ports chosen by the optimization solution without considering the cost concession from the seaport to dry port, however five dry ports chosen with considering the cost concession, which means that the cost concession agreement plays an important role in the expansion and development of dry ports, and obviously it also helps to reduce hinterland logistics cost. It is consistent with the fact that most dry ports in China are growing under the support of the cooperation seaports [3].

From Table 7, we can see that the total quantity of the cargo allocation for different seaports are very different under this two conditions. Especially for the Tianjin port, the cost concession with dry ports made its cargo allocation increase from 8460 TEU to 70620 TEU, for example both Zhengzhou and Hebi dry ports have established cooperation relationship with the Tianjin port, even Tianjin port is not the nearest seaport for them, which illustrates that establishing cooperation relationship with dry ports has played a significant role in attracting hinterland cargo resources, which is consistent with the fact that Tianjin port is taking positive hinterland dry ports expansion strategy

to attracting hinterland cargo resources and improving competitiveness [18].

(2) Giving relaxation coefficient  $\varepsilon = 0:0.0001:0.15$ , the optimal values curves of  $f_1$  and  $f_2$  can be seen in the Figure 6. Figure 6 shows the optimal values of the two objectives variation with the variation of the level of the Logistics cost undertaker willing to compromise for the environmental cost. It shows that as the rise of the logistics optimal cost discount, the carbon emissions decrease gradually, and the two targets tend to a stable state when  $\varepsilon$  is about 0.12. What level logistics cost discount decision makers chosen for the reduction of emissions pollution, depends on the intensity of environmental consciousness of the decision-making group.

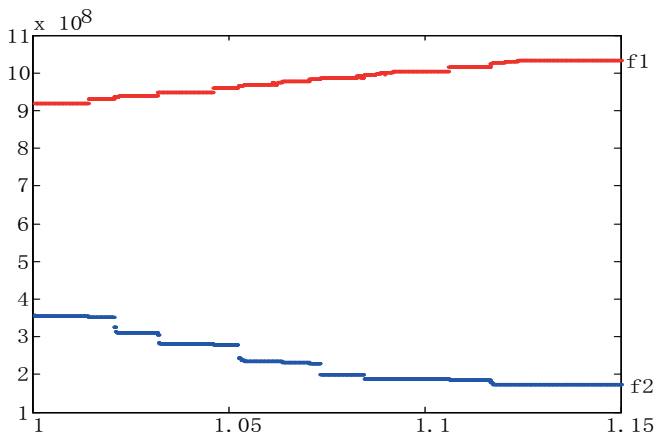


Fig. 6. Variation curves of the  $f_1$  and  $f_2$  with  $\epsilon = 0:0.0001:0.15$

## CONCLUSIONS

In this paper, we attend to proposed a sustainable hinterland-dry ports-seaports logistics network in a new perspective of the concession cooperation mechanism of seaports and dry ports and the environmental constraints. Firstly a new multi-criteria evaluation method based on the OWA operator is proposed to evaluate the cost concession partnership among seaports and dry ports. Then a bi-objective MILP model for hinterland -dry ports-seaports sustainable logistics network optimization has been developed, and a proper trade-off strategy proposed according the characters of this model. And then the location-allocation decision-making framework for hinterland-dry port-seaport network is shown in this paper. Finally a case involving configuration of dry ports in Henan Province is studied according to this method.

This study shows that the cooperation agreement among seaports and dry ports plays a significant role in the development of dry ports, and attracting hinterland cargo resources to enhance the competitiveness for seaports. It also shows that dry ports can be a key node to establish sustainable multimodal transport network oriented cargo export/import.

In conclusion, this paper provides decision-making basis for developing a effective and environment friendly hintland cities-dry ports-seaports network, gives insights in improving opening level for the inland regions, enhancing the competitiveness for seaports, and at the same time depressing environmental influence, which are all focuses in China now. In an on-going research, we will focus on the dry ports as the key core nodes to establish and optimization the land and sea integration logistics networks, under the background of rapid development of the “B&R” In China.

## ACKNOWLEDGMENTS

The paper is funded by the National Natural Science Foundation of China (71390520,71471109), the National Natural Science Foundation of Shanghai (15ZR1420200), the research project of Shanghai science and technology

committee (14DZ2280200; 14170501500), and Shanghai education development foundation (13SG48).

## REFERENCES

1. V. Roso, 2007. Evaluation of the dry port concept from an environmental perspective: A note. *Transportation Research Part D: Transport and Environment*, 12(7), 523-527.
2. A. K. Ng, F. Padilha, A. A. Pallis, 2013. Institutions, bureaucratic and logistical roles of dry ports: the Brazilian experiences. *Journal of Transport Geography*, 27, 46-55.
3. Y. H. Li, Q. L. Dong, S. W. Sun, 2015. Dry Port Development in China: Current Stm, M< m'm /atus and Future Strategic Directions. *Journal of Coastal Research*, 73, 641-646.
4. A. Beresford, S. Pettit, Q. Xu, 2012. Williams, S. A study of dry port development in China. *Maritime Economics & Logistics*, 14, 73-98.
5. V. Roso, J. Woxenius, K. Lumsden, 2009. The dry port concept: Connecting container seaports with the hinterland. *Journal of Transport Geography*, 17(5), 381-398.
6. T. Heaver, H. Meersman, E. Voorde, 2001. Co-operation and competition in international container transport: strategies for ports. *Maritime Policy and Management*, 28(3), 293-305.
7. T.E. Notteboom, 2002. Consolidation and contestability in the European container handling industry. *Maritime Policy and Management*, 29( 3), 257-269.
8. R. Robinson, 2002. Ports as elements in value-driven chain systems: the new paradigm. *Maritime Policy and Management*, 29( 3), 241-255.
9. R. Mansour, A.V. Ardavan, 2008. An Inland Port Location-Allocation Model for a Regional Intermodal Goods Movement System. *Maritime Economics & Logistics*, 10, 362-379.
10. X. J. Feng, Y. Zhang, Y. W. Li, W. Wang, 2013, A Location-Allocation Model for Seaport-Dry Port System Optimization. *Discrete Dynamics in Nature and Society* 1:1-8.
11. D. Ambrosino, A. Sciomachen, 2014. Location of mid-range dry ports in multimodal logistic networks. *Procedia-Social and Behavioral Sciences*, 108:118-128.
12. A. N. Samir, G. C. Nicoletta, and C. O. Alberto, 2014. Application of a Model based on the Use of DELPHI Methodology and Multicriteria Analysis for the Assessment of the Quality of the Spanish Dry Ports Location. *Procedia-Social and Behavioral Sciences* 162: 42-50.

13. A. N. Samir, G. C. Nicoletta, S. F. Francisco, 2015. How should the sustainability of the location of dry ports be measured? A proposed methodology using Bayesian networks and multi-criteria decision analysis. *Transport* 30(3):312-319.
14. R. R. Yager, 1988. On ordered weighted averaging aggregation operators in multi-criteria decision making. *IEEE Trans Syst Man Cybernet*, 18: 183-190.
15. H. R. Wei, M. Dong, S. Y. Sun, 2010. Inoperability Input-Output Modeling (IIM) of Disruptions to Supply Chain Networks. *INCOSE International Journal of Systems Engineering*, 13(4): 324-339.
16. Z. H. Hu, 2015. Heuristics for solving continuous berth allocation problem considering periodic balancing utilization of cranes. *Computers & Industrial Engineering*, 85:216-226.
17. Z. Chang, T. Notteboom, J. Lu, 2015. A two-phase model for dry port location with an application to the port of Dalian in China. *Transportation Planning and Technology*, 38(4): 442-464.
18. J. Wang, J.H. Ma, 2011. Applied research on the coexistence relationship between Tianjin Port and inland transportation system based on population ecology model. *Wseas Transactions on Mathematics*, 10(11):377-386.

## CONTACT WITH THE AUTHOR

**Hairui Wei**

Logistics Research Center  
Shanghai Maritime University  
Shanghai 201306  
**CHINA**

## WATER-EXIT PROCESS MODELING AND ADDED-MASS CALCULATION OF THE SUBMARINE-LAUNCHED MISSILE

Jian Yang<sup>1</sup>  
Jinfu Feng<sup>1</sup>  
Yongli Li<sup>2\*</sup>  
An Liu<sup>1</sup>  
Junhua Hu<sup>1</sup>  
Zongcheng Ma<sup>1</sup>

<sup>1</sup> Aeronautics and Astronautics Engineering College, Air Force Engineering University, China

<sup>2</sup> Engineering University of CAPF, Xi'an 710038, China

\* corresponding author

### ABSTRACT

*In the process that the submarine-launched missile exits the water, there is the complex fluid solid coupling phenomenon. Therefore, it is difficult to establish the accurate water-exit dynamic model. In the paper, according to the characteristics of the water-exit motion, based on the traditional method of added mass, considering the added mass changing rate, the water-exit dynamic model is established. And with help of the CFX fluid simulation software, a new calculation method of the added mass that is suit for submarine-launched missile is proposed, which can effectively solve the problem of fluid solid coupling in modeling process. Then by the new calculation method, the change law of the added mass in water-exit process of the missile is obtained. In simulated analysis, for the water-exit process of the missile, by comparing the results of the numerical simulation and the calculation of theoretical model, the effectiveness of the new added mass calculation method and the accuracy of the water-exit dynamic model that considers the added mass changing rate are verified.*

**Keywords:** Submarine-launched missile; Fluid-structure interaction; Water-exit dynamic model; Time-varying added-mass; Numerical simulation

### INTRODUCTION

With the development of modern military equipment, depending on the features such as good concealment and strong survivability, at present the submarine-launched missile has become an indispensable part of the national strategy and tactics forces [1]. Different from other types of missiles, the whole course of the submarine-launched missile is divided into three parts: underwater stages, water-exit stages and aerial stages. The water-exit stage is the special stage of the missile, in which the missile depends on the inertia or makes use of the thrust of the underwater engine to rise until its body is completely out of water. In the stage, the attitude and trajectory of the missile is affected by the wave,

which makes the missile deviate from the designed motion state and results in the unstable flight or even unsuccessful launch after the missile exits from water. Therefore, in order to provide the necessary initial conditions for the air trajectory of the missile, it is required to accurately predict and calculate the motion law of the missile in water-exit process [2]. As the basis of the research on the motion law of missile in water-exit process, the accuracy of the dynamic model determines the effect of the research.

In the whole course of the missile, the water-exit stage is the stage that the external conditions change the most severely and the load conditions are the most complex [3]. In the stage, on the one hand, the missile causes a series of complex changes in the flow field, such as the development and collapse

of vacuole; on the other hand, the flow field evolution process adversely acts on the missile by pressure or even the impact load generated by cavity collapse, which constantly changes the strained state of the missile, thus forming a complex fluid solid coupling process [4]. In order to establish an accurate dynamic model, the fluid solid coupling problem must be studied in depth, and the change law of the external flow field in the water-exit process must be accurately mastered.

At present, there are mainly two methods to study the fluid solid coupling problem [5]. One is the strong coupling method, which is mainly to establish the motion equations for the fluid and the structure and then to use the numerical method to solve the equations. The other method is the weak coupling method, which is also the added mass method. In the method, the fluid is simplified. And the load generated by the fluid at a certain point on the structural interface is equivalent to an inertial force produced by the movement of the structure and the fluid with a certain mass that is assumed to attach on the structure, which is so-called the added mass force. The method is simple in form and less in computation. At present, it has become the most mature method to solve this kind of problems and is widely used in engineering [6-8]. Therefore, as one of the important parameters of the hydrodynamic and dynamic load characteristics in the weak coupling method, the accuracy of the calculated results of the added mass will directly influence the effectiveness of the missile water-exit dynamic model.

For the calculation of the added mass, there are three main methods. 1. Theoretical calculation method. For the object with simple shape, the corresponding added mass theoretical solutions can be obtained by using the slender-body theory, slice theory and the engineering calculation method that uses the correction coefficient to consider the three-dimensional effect. 2. The method of pool experiment [9]. Weiqi Chen [10] designed the oblique water-exit experiment for the experimental model and carried out the parameter identification for the obtained experimental data. Then the added mass and drag coefficient of the model in axial direction are obtained. Gang Li [11] used the method of model constraint experiment to measure the added mass of the sphere, the ellipsoid and a type of submersible. The obtained conclusions were instructive for the hydrodynamic force design of the submersible. 3. Numerical calculation method of ideal fluid added mass based on potential flow theory. Huiping Fu [12] used the software Fluent as the platform and then applied the technology of dynamic mesh to carry out the research of the added mass calculation method on the basis of the RANS equation. Then the added mass of the underwater objects with two different shapes is obtained. On the basis of the CFD method, Uhlman [13] studied the added mass law of the super-cavity vehicle under the influence of the waves and compared the conclusion with the experimental result. For the swaying objects, Xuan Huang [14] used CFD technique to simulate the flow field of cavity and studied the added mass of the natural cavity disc and the axisymmetric slender body. In the three methods above, the theoretical calculation method can only be used for the objects with

simple shape, which has a strong limitation. The experiment method is complex and time-consuming, especially when the size of object is large or the linetype of object is complex, which may bring the great difficulty to the experiment. Therefore, for the submarine-launched missile which moves fast and has more complex linear shape, the above method cannot be applied. In contrast, the numerical simulation method can be used to calculate the added mass of objects with arbitrary shape and size. And the speed and accuracy are only limited to the hardware configuration and the turbulence model. Thus, the method can be used to calculate the added mass of the submarine-launched missile. However, at present, the numerical calculation method is mainly used to study the added mass of the underwater moving objects. The study of the added mass of the water-exit process is still in the initial stage, and the relevant references are also less. The mainly reason for this situation is that, the added mass is constant during underwater motion, but in water-exit stage, the added mass has a time-varying characteristics and is not constant. So there is a certain degree of difficulty in the research of the problem.

For the problems that contain the modeling and the time-varying added mass calculation of the submarine-launched missile in water-exit process, combining with features of the water-exit motion, introducing the added mass changing rate, the water-exit dynamic model is established in the paper. Then, from the model, by using the method of restraining numerical simulated conditions, a new fast effective calculation strategy for the time-varying added mass is proposed, which is later verified by the example of the sphere. On this basis, the added mass of a kind of submarine-launched missile in water-exit process is calculated under the different conditions. Then, by using the calculation results, the water-exit motion of the missile is simulated based on the water-exit dynamic model, and meanwhile the influence of the added mass changing rate on the water-exit process is investigated. The related conclusions have the reference meaning for the water-exit study and motion prediction of the submarine-launched missile.

## WATER-EXIT DYNAMIC MODEL

### FORCE ANALYSIS OF WATER-EXIT PROCESS

The force analysis of the submarine-launched missile in water-exit process is shown as Figure 1. The reference coordinate system  $O-xyz$  is the body coordinate system of the missile. The barycentre is set as the origin of the coordinate system. And the  $x$  axis coincides with the longitudinal axis of the missile and point to the head of the missile; the  $y$  axis is located in the longitudinal plane of the missile, and perpendicular to the  $x$ -axis and pointing upward. The  $z$  axis,  $x$  axis and  $y$  axis constitute the right hand system. The water-exit angle of the missile is  $\theta$ . The distance between the head of the missile and the surface of water is  $l_1$ . In water-exit

process, the missile is mainly affected by the interaction of gravity  $G$ , buoyancy  $B$ , fluid force  $F$  and derivative moment.

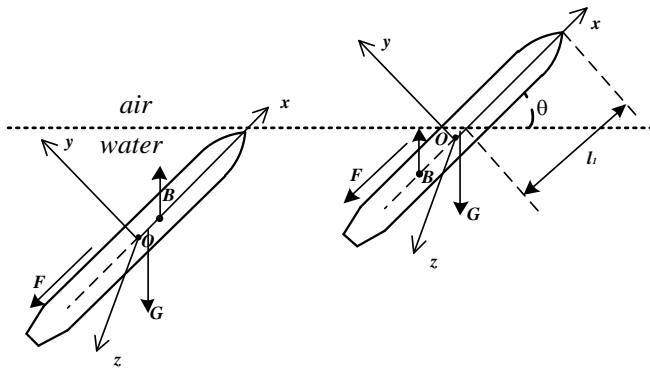


Fig. 1. Force analysis of water-exit process

## FLUID FORCE $F$

When the submarine-launched missile exits the water, the fluid force is continuously distributed on its surface in a regular rule. The distribution rule is determined by the shape of the missile, the characteristics of fluid properties, and the motion state of missile. At present, it is difficult to directly obtain the fluid force of the moving object in fluid. Considering that the actual fluid are viscous fluid, in order to simply the problem, under the reasonable assumptions [15], the fluid force is decomposed into fluid force with viscousness and ideal fluid force without viscousness to be calculated respectively in this paper.

### Effect of viscous fluid

Because the shape of the submarine-launched missile is symmetrical, there is almost no lift in the case of zero attack angle. Therefore, it is considered that the effect of the viscous fluid can be reflected in the resistance coefficient of the underwater moving missile. The effect mainly includes the drag generated by the motion of the missile and the force caused by the attack angle. Meanwhile, the velocity of the missile is at low speed and the speed changing range is small, so the influence of the Reynolds number changing on the drag coefficient is negligible [16]. In this paper, the product of the independent zero attack angle drag coefficient and the angle attack changing function is used to represent the resistance coefficient. So:

$$C_x = C_{x_0}(v) \cdot f_x(\alpha) \quad (1)$$

where,  $C_{x_0}(v)$  is the drag coefficient function in the state of zero attack angle,  $v$  is the velocity of the missile,  $f_x(\alpha)$  is the influence function of the attack angle  $\alpha$  on the drag coefficient. Then  $f_x(\alpha)$  is unfolded to the Taylor series expansion around  $\alpha=0$ .

$$f_x(\alpha) = f_x(0) + \sum_{n=1}^{\infty} \left( \frac{d^n f_x}{d\alpha^n} \right)_0 \frac{\alpha^n}{n!} \quad (2)$$

Because the magnitude of drag is independent with the positive and negative of  $\alpha$  and it is an even function. So Equation (2) can be converted to Equation (3).

$$f_x(\alpha) = f_x(0) + \left( \frac{d^2 f_x}{d\alpha^2} \right)_0 \frac{\alpha^2}{2!} \quad (3)$$

It is easy to obtain that  $f_x(0)=1$ , and let  $2k=(d^2 f_x/d\alpha^2)$ . Then, Equation (3) can be simplified as:

$$f_x(\alpha) = 1 + k\alpha^2 \quad (4)$$

The drag coefficient is calculated as:

$$C_x = C_{x_0}(v) \cdot (1 + k\alpha^2) \quad (5)$$

where, the zero attack angle drag coefficient  $C_{x_0}(v)$  and the coefficient  $k$  can be obtained by numerical calculation method. The speed range of the submarine-launched missile is small and the change of speed is not obvious. So  $C_{x_0}(v)$  can be considered as a constant  $C_{x_0}$ .

In summary, the calculation formula of drag is:

$$F_\mu = C_x \cdot \frac{1}{2} \rho S v^2 \quad (6)$$

where,  $S$  is the immersion area of the missile in the water-exit process;  $\rho$  is the density of fluid.

The effect of the viscous fluid can be expressed as:

$$\begin{cases} F_{\mu x} = F_\mu \cdot \cos \alpha \\ F_{\mu y} = -F_\mu \cdot \sin \alpha \\ M_{\mu z} = -F_{\mu y} \cdot \frac{1}{2} x_a \end{cases} \quad (7)$$

### Ideal fluid force

The ideal fluid is the incompressible, non-viscous fluid. The ideal fluid force can be obtained by the momentum and momentum moment theorem:

$$\begin{cases} -F_i = dQ_f / dt + \omega \times Q_f \\ -M_i = dK_f / dt + \omega \times K_f + v \times Q_f \end{cases} \quad (8)$$

where,  $F_i$  and  $M_i$  respectively represent main force and main moment of ideal fluid to the missile;  $Q_f$  and  $K_f$  respectively represent the momentum and momentum moment of ideal

fluid for the missile;  $\omega$  and  $v$  respectively represent the rotating angular velocity and velocity of the missile.

According to the theory of potential flow, introducing the added mass matrix, considering the axisymmetric characteristics of the missile, the force of ideal fluid is obtained as follows:

$$\begin{cases} F_{ix} = -\lambda_{11}\dot{v}_x + \omega_z (\lambda_{22}v_y + \lambda_{26}\omega_z) \\ F_{iy} = -\lambda_{22}\dot{v}_y - \lambda_{26}\dot{\omega}_z - \omega_z \lambda_{11}v_x \\ M_{iz} = -\lambda_{62}\dot{v}_y - \lambda_{66}\dot{\omega}_z + v_y \lambda_{11}v_x - v_x (\lambda_{22}v_y + \lambda_{26}\omega_z) \end{cases} \quad (9)$$

where,  $\lambda_{11}, \lambda_{22}, \lambda_{26} = \lambda_{62}, \lambda_{66}$  is added mass coefficients, which respectively represent vertical added mass, lateral added mass, added static moment, added inertia moment.

Unlike the traditional objects that only motion underwater, the added mass of submarine-launched missiles in water-exit process is time-varying. Therefore, on the basis of Equation (9), the influence factor of the added mass changing rate is introduced in the paper and the ideal fluid force for the missile in the water-exit process is obtained as follows:

$$\begin{cases} F_{ix} = -\lambda_{11}\dot{v}_x - \dot{\lambda}_{11}v_x + \omega_z (\lambda_{22}v_y + \lambda_{26}\omega_z) \\ F_{iy} = -\lambda_{22}\dot{v}_y - \dot{\lambda}_{22}v_y - \lambda_{26}\dot{\omega}_z - \dot{\lambda}_{26}\omega_z - \omega_z \lambda_{11}v_x \\ M_{iz} = -\lambda_{62}\dot{v}_y - \dot{\lambda}_{62}v_y - \lambda_{66}\dot{\omega}_z - \dot{\lambda}_{66}\omega_z + v_y \lambda_{11}v_x - v_x (\lambda_{22}v_y + \lambda_{26}\omega_z) \end{cases} \quad (10)$$

It can be inferred that the added mass is an important parameter to describe the effect of the ideal fluid. Its calculation result is related to the estimation of the effect of the fluid to the missile in the modeling process, which can directly affect the accuracy of the model. At present, the added mass of the objects with simple shape can be calculated by the slender body section theory. However, the object studied in this paper is the submarine-launched missile with a more complex linear shape. And there is greater error by using the slender body tangent theory to calculate the added mass of the missile in water-exit process. Therefore, in the following, the water dynamics model of the submarine-launched missile is combined with the software Fluent to study the added mass calculation strategy in water-exit process.

## OTHER PARAMETERS

Buoyancy  $B$  changes with the immersion depth of the missile. The influence of the surface heave is not considered and Buoyancy is obtained as follows:

$$B = \pi\rho g \int_0^{L-x_a} R^2(x)dx \quad (11)$$

In water-exit process, the location of buoyant centre of the missile changes constantly. And its location can be obtained as follows:

$$x_{b0} = \frac{\pi\rho g \int_0^{L-l} R^2(x)xdx}{B} \quad (12)$$

The location of barycentre is as follows:

$$x_0 = \frac{\int_0^L R^2(x)xdx}{\int_0^L R^2(x)dx} \quad (13)$$

And the immersion area of the missile in water-exit process is as follows:

$$S = 2\pi \int_0^{L-l} R(x)dx \quad (14)$$

The rotary inertia of the missile is as follows:

$$J = \pi\rho_0 \int_0^L R^2(x) \left[ 1/4 R^2(x) + (x - x_0)^2 \right] dx \quad (15)$$

In Equations (11) - (15),  $R(x)$  is the radius of the missile that changes with the  $x$  axis in body coordinate system.

## WATER-EXIT DYNAMIC MODEL

In summary, according to the relevant parameters and the force conditions of the submarine-launched missile, the dynamic model of the missile in water-exit process is established as follows:

$$\begin{cases} F_{ix} + F_{\mu x} + (B - G) \sin \theta + T = m(\dot{v}_x - v_y \omega_z - y_c \dot{\omega}_z) \\ F_{iy} + F_{\mu y} + (B - G) \cos \theta = m(\dot{v}_y + v_x \omega_z - y_c \omega_z^2) \\ F_{iz} + F_{\mu z} - Bx_b \cos \theta = J \cdot \dot{\omega}_z - my_c \dot{v}_y - my_c v_y \omega_z \end{cases} \quad (16)$$

where, the subscripts  $x$  and  $y$  respectively represent the corresponding components of the axis;  $x_c, y_c$  and  $z_c$  are barycentric coordinates.

## CALCULATION STRATEGY OF ADDED MASS

Considering that the added mass is only decided by the shape of the object and has nothing to do with the motion law of the missile, the study makes the following settings for Equation (9):

1) Let  $v_y = 0, \omega_z = 0$ . The direction of  $\dot{v}_x$  is along with the positive direction of  $x$  axis and the missile moves in the  $x$  axis direction with the increased speed at this moment. So  $F_{ix}$  in Equation (9) can be simplified into:

$$F_{ix+} = -\lambda_{11}\dot{v}_x - \dot{\lambda}_{11}v_x \quad (17)$$

The direction of  $\dot{v}_x$  is set along the negative direction of  $x$  axis, so there are:

$$F_{ix-} = \lambda_{11}\dot{v}_x - \dot{\lambda}_{11}v_x \quad (18)$$

From Equations (17) and (18), it is obtained as follows:

$$\begin{cases} \lambda_{11} = (F_{ix-} - F_{ix+}) / 2\dot{v}_x \\ \dot{\lambda}_{11} = -(F_{ix-} + F_{ix+}) / 2v_x \end{cases} \quad (19)$$

2) Let  $v_x = 0, \omega_z = 0$ . The direction of  $\dot{v}_y$  is along with the positive direction of  $y$  axis and the missile moves in the  $y$  axis direction with the increased speed at the moment. So  $F_{iy}$  and  $M_{iz}$  in Equation (9) can be simplified into:

$$\begin{cases} F_{iy+} = -\lambda_{22}\dot{v}_y - \dot{\lambda}_{22}v_y \\ M_{iy+} = -\lambda_{26}\dot{v}_y - \dot{\lambda}_{26}v_y \end{cases} \quad (20)$$

The direction of  $\dot{v}_y$  is set along the negative direction of  $y$  axis, so there are:

$$\begin{cases} F_{iy-} = \lambda_{22}\dot{v}_y - \dot{\lambda}_{22}v_y \\ M_{iy-} = \lambda_{26}\dot{v}_y - \dot{\lambda}_{26}v_y \end{cases} \quad (21)$$

From Equations (20) and (21), it is obtained as follows:

$$\begin{cases} \lambda_{22} = (F_{iy-} - F_{iy+}) / 2\dot{v}_y \\ \dot{\lambda}_{22} = -(F_{iy-} + F_{iy+}) / 2v_y \\ \lambda_{26} = (M_{iy-} - M_{iy+}) / 2\dot{v}_y \\ \dot{\lambda}_{26} = -(M_{iy-} + M_{iy+}) / 2v_y \end{cases} \quad (22)$$

3) Let  $v_x = 0, v_y = 0$ . The direction of  $\dot{\omega}_z$  is along with the counterclockwise direction of  $z$  axis and the missile rotates around the  $y$  axis direction at the moment. So  $M_{iz}$  in Equation (9) can be simplified into:

$$M_{iz+} = -\lambda_{66}\dot{\omega}_z - \dot{\lambda}_{66}\omega_z \quad (23)$$

The direction of  $\dot{\omega}_z$  is set along the clockwise direction of  $z$  axis, so there are:

$$M_{iz-} = \lambda_{66}\dot{\omega}_z - \dot{\lambda}_{66}\omega_z \quad (24)$$

From Equation (23) and (24), it is obtained as follows:

$$\begin{cases} \lambda_{66} = (M_{iz-} - M_{iz+}) / 2\dot{\omega}_z \\ \dot{\lambda}_{66} = -(M_{iz-} + M_{iz+}) / 2\omega_z \end{cases} \quad (25)$$

where,  $F_{x+}, F_{x-}, F_{y+}, F_{y-}$  respectively represent subjected fluid forces to the missile when the it move in positive direction of  $x$  axis, in negative direction of  $x$  axis, in positive direction of  $y$  axis and in negative direction of  $y$  axis.  $M_{y+}, M_{y-}, M_{z+}, M_{z-}$  respectively represent subjected fluid force moments to the missile when it move in positive direction and negative direction of  $y$  axis and rotate around clockwise direction and counter clockwise direction of  $z$  axis. So the calculation formulas of the added mass and the added mass changing rate of the submarine-launched missile in water-exit process are as follows:

$$\begin{cases} \lambda_{11} = (F_{ix-} - F_{ix+}) / 2\dot{v}_x \\ \lambda_{22} = (F_{iy-} - F_{iy+}) / 2\dot{v}_y \\ \lambda_{26} = (M_{iy-} - M_{iy+}) / 2\dot{v}_y \\ \lambda_{66} = (M_{iz-} - M_{iz+}) / 2\dot{\omega}_z \end{cases} \begin{cases} \dot{\lambda}_{11} = -(F_{ix-} + F_{ix+}) / 2v_x \\ \dot{\lambda}_{22} = -(F_{iy-} + F_{iy+}) / 2v_y \\ \dot{\lambda}_{26} = -(M_{iy-} + M_{iy+}) / 2v_y \\ \dot{\lambda}_{66} = -(M_{iz-} + M_{iz+}) / 2\omega_z \end{cases} \quad (26)$$

where, known from the related knowledge of fluid mechanics,  $F_{x+}, F_{x-}, F_{y+}, F_{y-}$  can be obtained by the surface integral of the intensity of pressure on surface of the missile and  $M_{y+}, M_{y-}, M_{z+}, M_{z-}$  can be obtained by the surface integral and distance integral of the intensity of pressure on surface of the missile.

In summary, the calculation strategy of the added mass can be described as follows: Firstly, through the CFD software, the flow field numerical model is established and the two groups of the motion law in same velocity and inverse acceleration is set, which is  $v, \dot{v}, \omega, \dot{\omega}$  with  $v, -\dot{v}, \omega, -\dot{\omega}$ . Then,  $F_{x+}, F_{x-}, F_{y+}, F_{y-}, M_{y+}, M_{y-}, M_{z+}, M_{z-}$  in the two conditions are calculated. Finally, the corresponding added mass is calculated by Equation (25). From the calculation process above, as long as the environment of flow field under different motion parameters is determined, by the proposed computation strategy in the paper, without solving the complex potential function and considering the influence of the free surface, the added mass of any shape at any time in water-exit process can be calculated by the fluid simulation software. Therefore, the calculation strategy can be used to calculate the added mass of the submarine-launched missile in water-exit process.

## NUMERICAL SIMULATION

The water-exit process involving two kinds of fluids is a complex non-linear unsteady multiphase coupling problem that contains free surface. As the interface between water and air, free surface is a special interface. On the hand, it is the boundary of the flow field and a necessary condition for solution of flow field. On other hand, its location is not predicted in advance, but as the part of the solution to the problem given by the solution process. Therefore, it is very difficult to use the numerical method to simulate the problem of two-phase flow with free surface. In order to simulate the two-phase flow with free surface in the paper, the VOF method is applied to capture the fluctuation of free surface [17]. In VOF method, different groups of fluid share a set of momentum

equations, the control domain is established both for water and air, and the free surface is captured by solving the added equations. In the calculation process, the volume fraction of each fluid component is recorded in every flow unit of the entire flow field. The method can make a better description for the phenomenon such as the fluctuation and roll of free surface and also has a great advantage in dealing with complex free surface flow problems. At the same time, the calculation cost of the method is relatively small, and the requirements for the hardware especially the memory size is relatively low. In addition, in order to adapt to the shape of fluid that changes with the motion of the missile in the water-exit process and obtain a good numerical solution, the dynamic mesh method is applied in the paper.

### CONTROL EQUATION

The following three-dimensional control equation is used:

$$\nabla \cdot \bar{U} = 0 \quad (27)$$

$$\frac{\partial(\rho\bar{U})}{\partial t} + \nabla \cdot (\rho\bar{U} \times \bar{U}) = -\nabla P + \nabla \times (\mu \nabla \times \bar{U}) + \rho g + F_{SV} \quad (28)$$

where,  $\bar{U} = (u, v, \omega)$  represent velocity vector of the fluid mass point in three directions of  $x, y, z$  axis;  $\rho$ ,  $\mu$  respectively represent the density of fluid and dynamic viscosity coefficient;  $g$  is the gravitational acceleration,  $F_{SV}$  is the equivalent volume force form of the surface tension, which obtained by the phase function.

VOF continuous equation

$$\frac{\partial F_q}{\partial t} + v_q \cdot \nabla F_q = \frac{S_{F_q}}{\rho_q} \quad (29)$$

The term at the right end of the equation is 0, and the solution equation can be written as:

$$\frac{\partial F}{\partial t} + \frac{\partial(uF)}{\partial x} + \frac{\partial(vF)}{\partial y} + \frac{\partial(\omega F)}{\partial z} = 0 \quad (30)$$

The constraint equation is:

$$\sum_{q=1}^2 F_q = 1 \quad (31)$$

Considering the viscosity of water, the control equation is closed by using the turbulence model 'standard  $k - \varepsilon$  model' which has a good stability.

Turbulence kinetic energy equation

$$\frac{\partial}{\partial t}(\rho k) + \frac{\partial}{\partial x_i}(\rho k u_i) = \frac{\partial}{\partial x_j} \left[ \left( \mu + \frac{\mu_t}{\sigma_k} \right) \frac{\partial k}{\partial x_j} \right] + G_k + G_b - \rho \varepsilon - Y_M + S_k \quad (32)$$

Diffusion equation  $\varepsilon$

$$\frac{\partial}{\partial t}(\rho \varepsilon) + \frac{\partial}{\partial x_i}(\rho \varepsilon u_i) = \frac{\partial}{\partial x_j} \left[ \left( \mu + \frac{\mu_t}{\sigma_\varepsilon} \right) \frac{\partial \varepsilon}{\partial x_j} \right] + C_{1\varepsilon} \frac{\varepsilon}{k} (G_k + C_{3\varepsilon} G_b) - C_{2\varepsilon} \rho \frac{\varepsilon^2}{k} + S_\varepsilon \quad (33)$$

### DYNAMIC MESH TECHNOLOGY

In the numerical calculation, the whole calculation domain is composed of meshes. The motion of the objects means the motion of the boundary in the object surface. That is to say, the motion conditions need to be defined on the boundary conditions. In the paper, UDF self-programming statement is introduced into the numerical calculation to define the motion speed of the meshes, and the water-exit motion of objects in specific direction is achieved. Where, the motion speed of the mesh for each current time step is the sums of the speed of the mesh for the last time step and the speed increment that caused by subjected two phase fluids pressure, viscous fluid force and own gravity for current time step. In the process of the water-exit motion, some of the meshes are constantly compressed and some of the meshes are constantly stretched. The distortion caused by deformation can affect the accuracy of the calculation. When the distortion reaches a certain extent, the negative volume meshes will be produced, which can lead to failure of the calculation. In this case, dynamic mesh technology need be used to define the motion and update of the mesh.

However, at present, in the main dynamic mesh update method, the local reconstruction method easily leads to non-converge of the calculation due to the poor quality of the rebuild meshes, and the dynamic stratification method is not suitable for the flow field area of the submarine-launched missile with a more complex shape in the paper<sup>[18]</sup>. Therefore, in order to obtain the good numerical solution and ensure the quality of dynamic mesh, especially in the case of simulating the completely non-linear free surface change caused by water-exit process, combining the two methods above, a new update method for the dynamic mesh is used.

In the water-exit process, the local flow field area around the water-exit object is set as the area subjected by new dynamic mesh update method and called the motion area, and other calculation area keep still. The speed of the object is assigned to the entire local dynamic meshes area and the front and back boundary of the area is restricted to keep still. The dynamic stratification update of the meshes in this area is carried out after the motion of this area. The meshes nearby the surface of the object only move as the moving area and the complex update operation for the meshes is not performed. The location of the mesh change is transferred to the plane boundary in the front and back of local dynamic mesh. This operation ensures that the mesh around the object

does not change and the mesh quality and quantity meet the requirement in the simulation of water-exit process. Besides, as same with the dynamic stratification method, the new updating method is also required to define an ideal height value for the adjacent mesh layer of the update boundary of the dynamic mesh. When the mesh in this layer is being stretched, the height of the mesh is allowed to increase until meeting the Equation (1), and its division form is the same as the dynamic stratification method [19].

$$h_{\min} > (1 + \alpha)h_{id} \quad (34)$$

where,  $h_{\min}$  is the minimum height of the nth layer mesh,  $h_{id}$  is the ideal height of the mesh, and  $\alpha$  is mesh cutting factor.

In this paper, the new method transfers the dynamic mesh problem at complex boundaries to a simple boundary. Therefore, for this method, on the one hand, the dynamic mesh technology that suit for the most fluid field calculation of the objects with complex shape such as the submarine-launched missile is achieved; on the other hand, the updating time of the meshes is effectively reduced. Meanwhile, for the calculation area in which the dynamic meshes continuously updates, the number of meshes is ensured to strictly keep constant so that the calculation speed cannot be reduce by the increase of the mesh.

## EXAMPLE VALIDATION

The added mass of the sphere has a theoretical analytical value and also has more reliable experimental data. Therefore, based on the proposed added mass calculation method in the paper, with the means of numerical simulation, the added mass of the sphere in water-exit process is calculated by simulation to verify the reliability of the added mass calculation method.

### Construct the calculation domain and divide the mesh

The overall calculation domain is a cuboid whose size is 20 \* 10 \* 10. Considering the curved face shape of the sphere (Diameter D = 1m) and that the unstructured meshes can better adapt to the change of the curved face, triangular meshes are used as the surface meshes of the model, and tetrahedron and hexahedron are used as the calculation domain. In order to ensure the speed and accuracy of calculation and reduce the number of dynamic meshes, the paper divided the whole calculation domain into the static and changing two areas. And when dividing meshes, under the criteria of quality priority, the tetrahedron meshes is used for the static area and the hexahedron meshes is used for the changing area. In the calculation process, the meshes in the static area remain unchanged and the meshes in the changing area are updated in real time according to the motion of the boundary.

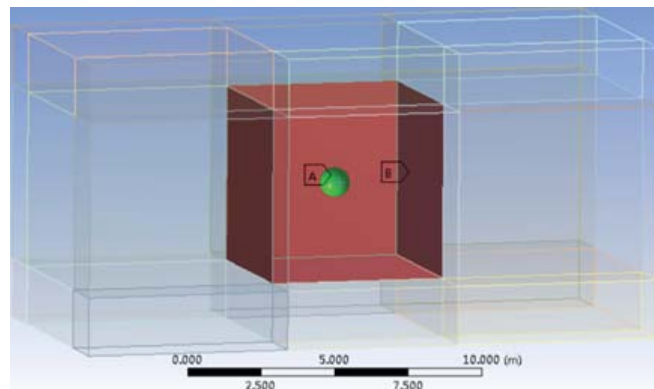


Fig. 2. Construction of the calculation domain

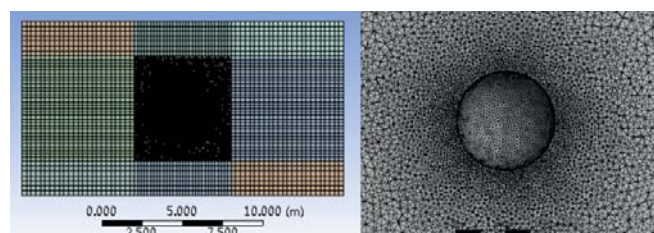


Fig. 3. Results of dividing the meshes

## Results of calculation

In the initial stage of the numerical calculation, the free surface is set at location that is 2m away from the centre of the sphere (coordinates Y = 2m), and the initial velocity  $V=[1,2]$  and acceleration  $a=\{[3,-3];[10,-10]\}$  is assembled into four group of motion laws to calculate. By the calculation strategy in the paper, vertical and horizontal added mass are obtained as shows in Table 1.

Tab. 1. Calculation results of added mass in one step

| Calculated conditon     | VA[1,3,-3] | VA[1,10,-10] | VA[2,3,-3] | VA[2,10,-10] |
|-------------------------|------------|--------------|------------|--------------|
| Theoretical value(kg)   | 261.79939  | 261.79939    | 261.79939  | 261.79939    |
| Vertical added mass(kg) | 259.97665  | 259.96674    | 260.03994  | 260.10492    |
| Relative error(%)       | 0.69624    | 0.70002      | 0.67206    | 0.64724      |
| Lateral added mass(kg)  | /          | 260.37681    | /          | 260.46103    |
| Relative error(%)       | /          | 0.54339      | /          | 0.51122      |

It is easy to see from Table 1 that the calculation results of vertical and lateral added mass in different combinations and the theoretical values are very close. The maximum relative error is 0.70002% and the minimum one is 0.51122%, which indicates that the calculation strategy is correct and effective. Meanwhile, the initial velocity and acceleration do not affect the calculation results, and the error is mainly from the mesh and turbulence model.

## CALCULATION OF ADDED MASS IN WATER-EXIT PROCESS

On the basis of the proposed added mass calculation method in the paper, the added mass of the submarine-launched missile in water-exit process is investigated. And in the study, the shape parameters of the missile are selected from [20]. The specific geometric model is shown in Figure 4.

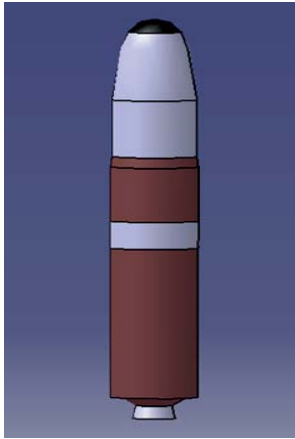


Fig. 4. Construction of submarine-launched missiles

The combinations  $[v, \dot{v}, \omega, \dot{\omega}] = [1, 5, 0.1, 1]$  and  $[v, \dot{v}, \omega, \dot{\omega}] = [1, 5, 0.1, 1]$  are selected. Then calculation is performed referring to the setting of the added mass in Section 3.3. In order to facilitate comparison, as shown in Equation (35), the immersion depth and added mass in water-exit process are dimensionless.

$$\bar{H} = H / L, \bar{\lambda} = \lambda / \rho V(L) \quad (35)$$

where,  $H$  is the length of the part of the missile that immersed underwater;  $L$  is the characteristic length of the missile;  $\lambda$  is the added mass;  $\rho$  is the density of water;  $V$  is the volume of the missile. Figure 5 is the calculation domain of numerical simulation for the missile.

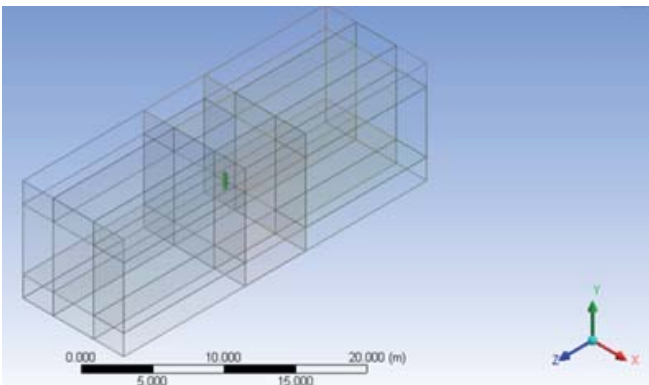


Fig. 5. Calculation domain

When the water-exit inclination angle of the missile is  $90^\circ$ ,  $60^\circ$  and  $45^\circ$ , the mesh is divided as Figures 6-8 shown, and the calculation results of the added mass in water-exit process are shown in Tables 2-4. It can be seen from the tables that although the set positions of the initial surface are same in calculation, non-dimensional immersion depths are different under the different inclination angle. In order to facilitate the comparative analysis of the added mass change law in water-exit process under the different angles, Figures 9-12 are drawn.

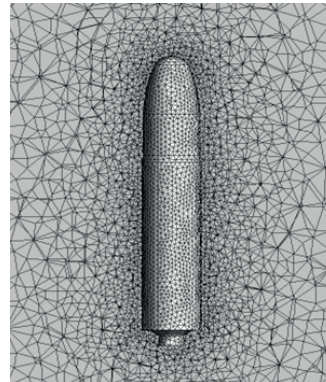


Figure 6. Inclination angle of  $90^\circ$

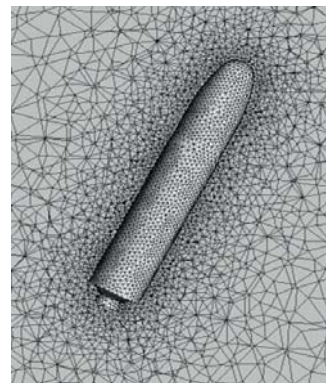


Figure 7. Inclination angle of  $60^\circ$

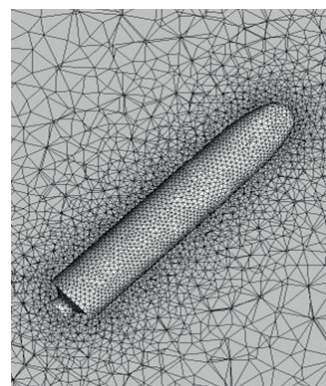


Figure 8. Inclination angle of  $45^\circ$

Tab. 2. The added mass at inclination angle of 90°

| non-dimensional immersion depth | $\lambda_{11}$ | $\lambda_{66}$ | $\lambda_{22}$ | $\lambda_{26}$ |
|---------------------------------|----------------|----------------|----------------|----------------|
| 0.06667                         | 0.01864        | 0.00696        | 0.01026        | 0.00427        |
| 0.2                             | 0.042          | 0.01637        | 0.07041        | 0.02728        |
| 0.4                             | 0.054          | 0.03517        | 0.23544        | 0.07206        |
| 0.53333                         | 0.05615        | 0.04015        | 0.3787         | 0.0924         |
| 0.66667                         | 0.0574         | 0.04127        | 0.53349        | 0.09616        |
| 0.86667                         | 0.05859        | 0.05014        | 0.7769         | 0.06462        |
| 0.93333                         | 0.06038        | 0.05565        | 0.85279        | 0.04632        |

Tab. 3. The added mass at inclination angle of 60°

| non-dimensional immersion depth | $\lambda_{11}$ | $\lambda_{66}$ | $\lambda_{22}$ | $\lambda_{26}$ |
|---------------------------------|----------------|----------------|----------------|----------------|
| 0.06376                         | 0.01844        | 0.00629        | 0.01563        | 0.00961        |
| 0.20232                         | 0.03879        | 0.02572        | 0.0805         | 0.04484        |
| 0.53333                         | 0.05513        | 0.05861        | 0.37927        | 0.13346        |
| 0.86435                         | 0.05827        | 0.07624        | 0.76438        | 0.0948         |
| 0.93363                         | 0.06258        | 0.08403        | 0.83012        | 0.07436        |
| 1.30313                         | 0.12307        | 0.10008        | 0.94742        | 0.03449        |
| 2.07293                         | 0.12796        | 0.10043        | 0.95595        | 0.03311        |

Tab. 4. The added mass at inclination angle of 45°

| non-dimensional immersion depth | $\lambda_{11}$ | $\lambda_{66}$ | $\lambda_{22}$ | $\lambda_{26}$ |
|---------------------------------|----------------|----------------|----------------|----------------|
| 0.07136                         | 0.02041        | 0.01123        | 0.03264        | 0.01888        |
| 0.20335                         | 0.03572        | 0.02736        | 0.0974         | 0.05066        |
| 0.53333                         | 0.05345        | 0.05587        | 0.3809         | 0.12454        |
| 0.86332                         | 0.05849        | 0.07691        | 0.74088        | 0.09224        |
| 0.92931                         | 0.06381        | 0.08178        | 0.79419        | 0.07955        |
| 1.47614                         | 0.12464        | 0.10015        | 0.9472         | 0.03415        |
| 2.41895                         | 0.12804        | 0.10043        | 0.95585        | 0.03306        |

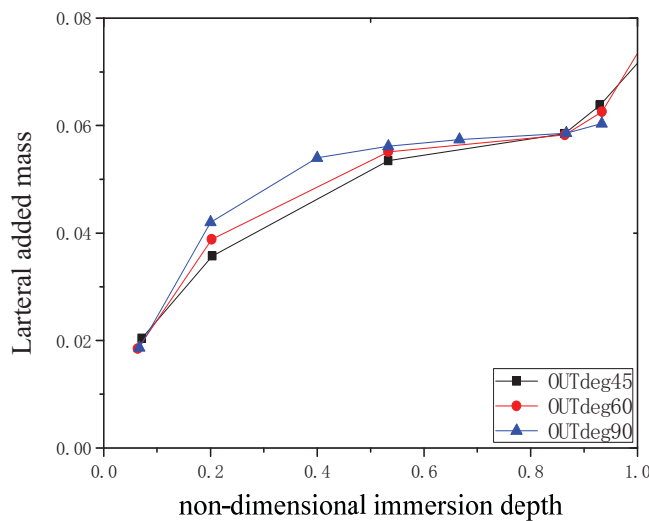


Fig. 9. Lateral added mass

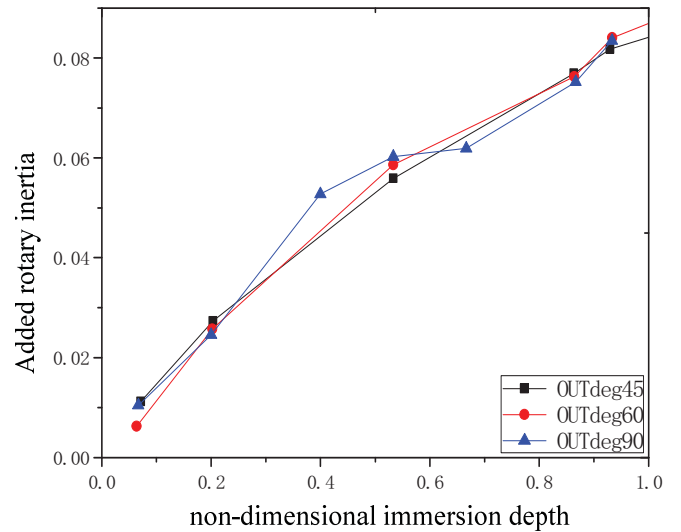


Fig. 10. Rotary inertia

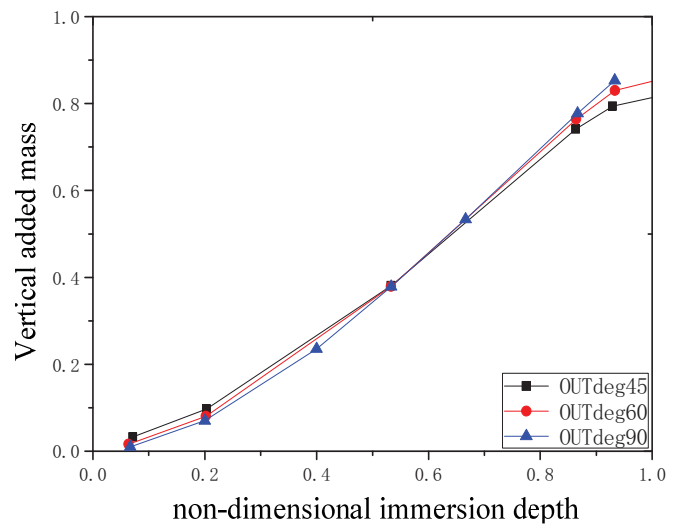


Fig. 11. Vertical added mass

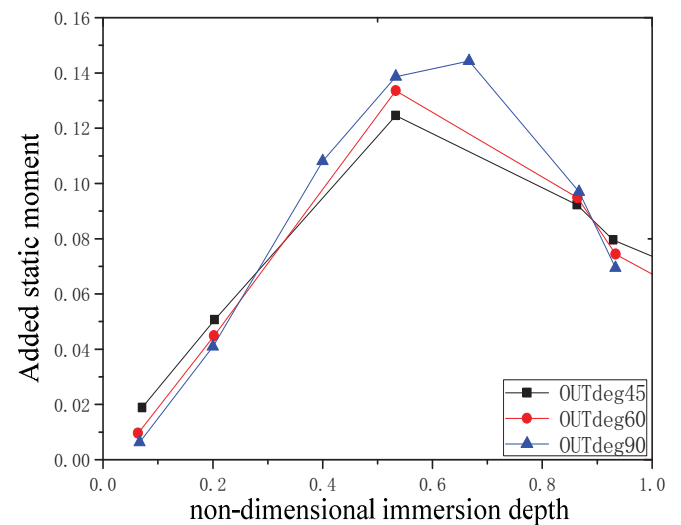


Fig. 12. Added static moment

The calculation results of lateral added mass are shown as Figure 9. It can be seen from the figure, in the water-exit process under the different inclination angles, with the non-dimensional immersion depth changing from 1 to 0, the lateral added mass firstly drops sharply and then its downward trend slows down, but the downward trend becomes bigger at the end of water-exit process. In water-exit process, with the same non-dimensional immersion depth, the lateral added mass of 90° is higher than the lateral added mass of 60° and 45°, and from the view of magnitude order, the maximum does not exceed 0.07.

The calculation results of added rotary inertia are shown as Figure 10. It can be seen from the figure, in the water-exit process under the different inclination angles, with the non-dimensional immersion depth changing from 1 to 0, the added rotary inertia decreases with an approximately linear trend. The downward trend of the results of 90° have a slow-down area around the immersion depth of 0.5, and from the view of magnitude order, the maximum does not exceed 0.09.

The calculation results of vertical added mass are shown as Figure 11. It can be seen from the figure, with the decrease of the immersion depth, the vertical added mass basically decreases with an approximately linear trend. The consistency of the data under three inclination angles is so good that the data can be approximately considered as the same one. From the view of magnitude order, the maximum does not exceed 0.9 which is about 10 times of the lateral added mass and added rotary inertia.

The calculation results of added static moment are shown as Figure 12. It can be seen from the figure, with the decrease of the immersion depth, the added static moment firstly increase and then decrease. And there is a maximum near the immersion depth of 0.6. From the view of magnitude order, the maximum does not exceed 0.15.

## SIMULATION OF WATER-EXIT PROCESS

The added mass is only related to the geometrical shape of the object. In water-exit process of the submarine launched missile, the added mass is only related to its immersion depth  $l$  and inclination angle  $\theta$ . Therefore, in order to obtain the ideal fluid force required in the simulation of water-exit process, the above added mass calculation method can be used to obtain a considerable amount of added mass of the missile under different immersion depth  $l$  and inclination angle  $\theta$ , and then a two-dimensional interpolation table of the water-exit whose row is immersion depth and column is inclination angle is established to express the added mass in water-exit process. Thus, according to the current immersion depth and inclination angle, the added mass of the missile in water-exit process can be obtained by interpolation. Then the ideal fluid force can be obtained by Equation (9). The added mass and the changing rate of the added mass in water-exit process are obtained by the equation below.

$$\begin{cases} \lambda_{11} = g_1(l, \theta) \\ \lambda_{22} = g_2(l, \theta) \\ \lambda_{26} = g_3(l, \theta) \\ \lambda_{66} = g_4(l, \theta) \end{cases} \begin{cases} \dot{\lambda}_{11} = g_5(l, \theta) \\ \dot{\lambda}_{22} = g_6(l, \theta) \\ \dot{\lambda}_{26} = g_7(l, \theta) \\ \dot{\lambda}_{66} = g_8(l, \theta) \end{cases} \quad (36)$$

Under the same condition, the methods of numerical simulation and theoretical calculation are both used to simulate the water-exit motion. In the two methods, the theoretical calculation is based on the established water-exit dynamic model of the submarine-launched missile. In addition, the required added mass parameters in the model are obtained by Equation (36). The set initial velocity  $v_{x0}$  is 10 m/s and  $v_{y0}$  is 0 m/s, the set initial water-exit inclination angle  $\theta_0$  is 45°, the set initial rotating angular velocity  $\omega_{z0}$  is 0, the set initial attack angle  $\alpha$  is 0°. In the whole process, the missile has no thrust, which means the thrust  $T=0$ . In order to eliminate the effects of free surface, the initial calculated position is set that the vertex of the head of the missile is at the location in the direction of the axis away from water surface in distance of two times of the missile diameter. Figure 13 shows the water-exit process that obtained by numerical simulation. And Figure 14 shows the water-exit process that obtained theoretical calculation.

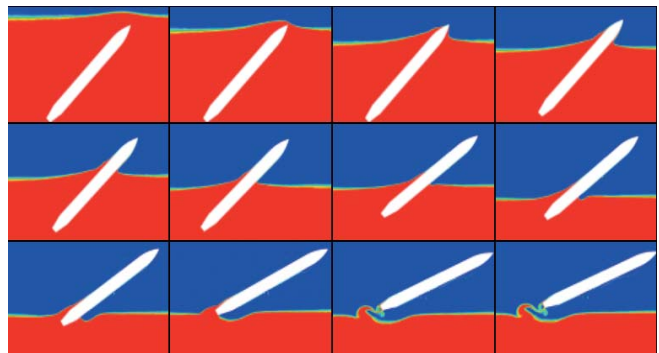


Fig. 13. Numerical simulated results of water-exit motion

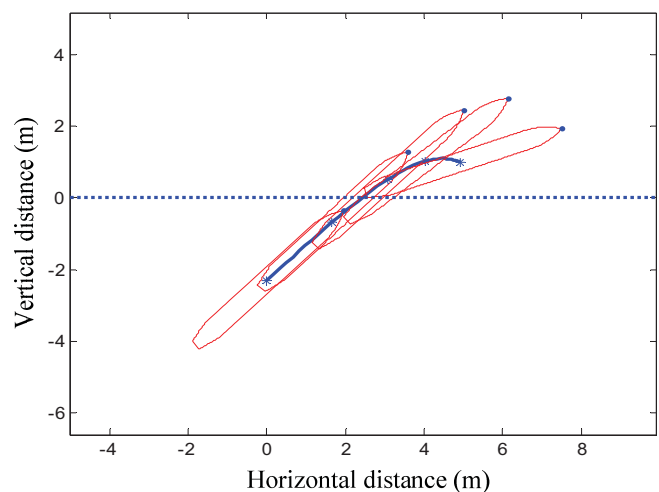


Fig. 14. Theoretical calculated results of water-exit motion

In Figure 14, the blue thick solid line is the trajectory of the barycentre motion of the missile, red fine solid line is the outline of the missile at all times, and the blue dotted line is the sea level.

It can be seen from Figure 13 and 14 that under the same working condition, the trajectory changing laws of the barycentre in water-exit process obtained by two methods are basically consistent. Therefore, on the one hand, the accuracy of the water-exit dynamics model of the submarine-launched missile established in the paper is verified. Thus, the established model can be used to predict and calculate the motion law of water-exit process in the future. On the other hand, the correctness of the proposed added mass calculation method in the paper is also verified.

In order to further investigate the validity of the added mass changing rate introduced in the modeling process of the submarine-launched missile, the influence of the added mass changing rate on the water-exit model of the missile is investigated by comparing the numerical simulated result with the simulated results obtained by solving the two theoretical models which respectively considers the added mass changing rate and don't consider the added mass changing rate. Figure 15 shows that the change of inclination angle of the missile in water-exit process under three different simulation conditions. In the figure, the red solid line represents the numerical simulation result, the blue solid line represents the simulation result obtained by solving the theoretical model that considers the added mass changing rate, and the blue dashed line represents the simulation result obtained by solving the theoretical model that don't consider the added mass changing rate. According to the comparison, before the missile touches the surface of water, the three simulation results are very similar, which indicates that the added mass changing rate has no effect on the accuracy of the model when the missile is completely immersed in water. As can be seen from Figure 15, in the water-exit process, after the head of the missile touching the surface of water, the decreasing trends of the inclination angles which reflected by the three simulated results are consistent. However, the simulation results of the theoretical model that considers the added mass changing rate are closer to the numerical simulation results. And by comparing, the simulation results of the theoretical model that don't considers the added mass changing rate is different from the other two simulation results for its smaller decreasing trend of the inclination angle. Therefore, it is inferred that the added mass changing rate can greatly affect the accuracy of the water-exit dynamics model so that it cannot be ignored in modeling process.

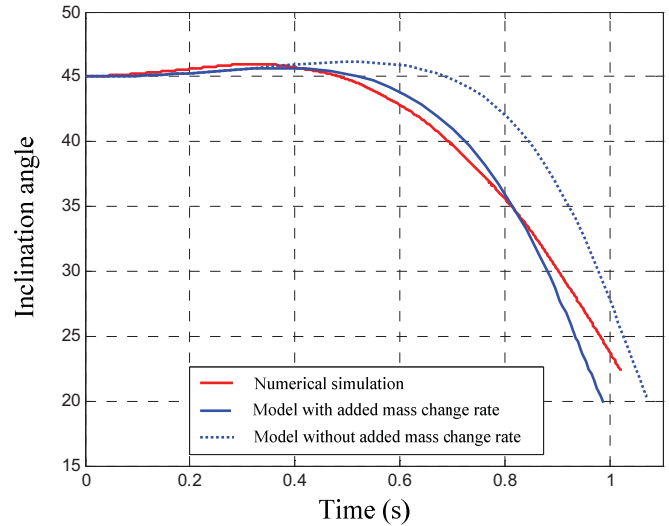


Fig. 15. Comparison of the water-exit inclination angle

Figure 16 is the comparison of the water-exit angular velocity of the missile under the three conditions. According to the comparison, in the process that the missile crosses the surface of water, the angular velocity of the model that don't consider the added mass changing rate is larger and the decrease of the inclination angle of the same model is relatively slow, which has a large deviation with the other two simulation results. In addition, it can be seen from the figure that there is still a little deviation between the numerical simulated result and theoretical result obtained by solving the water-exit model that don't consider the added mass changing rate.

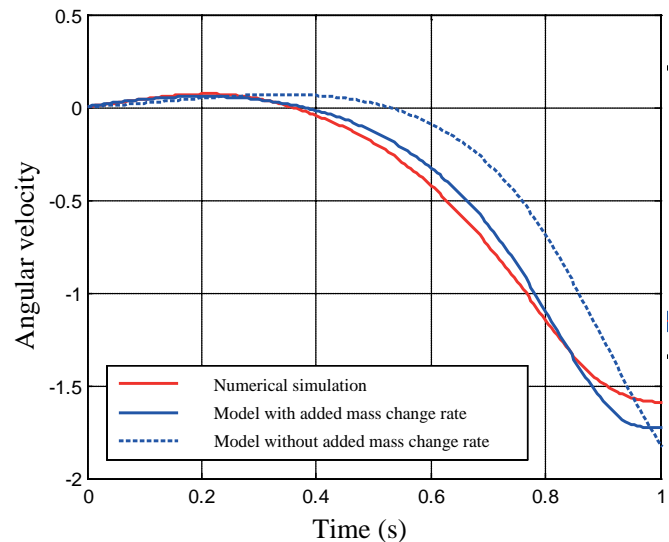


Fig. 16. Comparison of the water-exit angular velocity

Through analyzing, the reason of this phenomenon is that the calculation of the model ignores the disturbance on the surface of water such as cavity bubble and the surface heave in water-exit process. In addition, in the numerical

simulation, because of the choice of turbulence model, the setting of parameters and the partition of meshes, there is still some deviation between the numerical simulated result and the actual situation. In the future research work, the factors such as the disturbance on the surface of water will be considered to further improve the accuracy of the water-exit dynamic model.

In summary, the added mass change rating in water-exit process has a certain influence on water-exit motion. Therefore, the established theoretical model that considers the added mass changing rate in the paper can describe the water-exit process of the missile more accurately, which in the future will have a certain help for precisely studying the posture change of the submarine-launched missile in water-exit process and the flight trajectory of the missile after exiting from the water.

## CONCLUSION

The calculation problem of the time-varying added mass in the water-exit dynamic model of the submarine-launched missile is investigated in the paper. In this study, the water-exit dynamic model that contains the added mass changing rate is established and a new calculation strategy based on Fluent numerical simulation and aimed at obtaining time-varying added mass is proposed. On the basis of the new strategy, the added mass of the sphere and the submarine-launched missile in different immersion depth are calculated and the change laws of the time-varying added mass is obtained. Then the calculated results is introduced into the water-exit dynamic model for simulation. Thus, the water-exit motion trajectory under the given condition is also obtained and the influence of the added mass changing rate on the water-exit process is investigated. The corresponding conclusions are as follows:

(1) In the water-exit process, with the non-dimensional immersion depth changing from 1 to 0, the lateral added mass firstly drops sharply and then its downward trend slows down. At the end of water-exit process, the downward trend becomes sharp again and increases as the inclination angle increases. The added rotary inertia decreases with an approximately linear trend and have a slow-down area in the downward trend around the immersion depth of 0.5 when the missile vertically exits from water. The vertical added mass decreases in an approximately linear trend. The consistency of the data under different inclination angles is so good that the data is approximately considered to be the same. The added static moment firstly increases and then decreases. And its maximum value is near the immersion depth of 0.6. From the view of magnitude order, the maximum value does not exceed 0.15.

(2) Through the example of the sphere and the comparison of the missile water-exit trajectory in the same conditions between the numerical simulated result and the theoretical calculated simulated results that based on water-exit dynamic model, on the one hand, the feasibility of the new calculation strategy proposed in this paper for calculating the added

mass of the more complex linear shape is verified; on the other hand, the accuracy of the water-exit dynamics model established in this paper is also verified.

(3) The added mass changing rate has a certain influence. And in the water-exit dynamics model of the missile, the added mass changing rate need to be considered and cannot be ignored.

## ACKNOWLEDGEMENTS

This research was financially supported by the National Science Foundation of China (No.51541905)

## REFERENCE

1. C.X. Gong, W. Meng, 2009. The thunder in the depths of the ocean-the submarine-launched tactical missile. *Aerodynamic Missile Journal*, 5,11-14.
2. Z.X. Zhang, 2015. Dynamics modeling and simulation of water-exit course of small submarine-launched missile under wave disturbance. *Journal of National University of Defense Technology*, 37(6), 91-95.
3. X.Q. Xu, B. Tian, B.S. Li, 2010. The model and simulation of submarine to surface missile underwater trajectory. *Journal of Projectiles, Rockets, Missiles and Guidance*, 30(5), 149-152.
4. B.Y. Ni, S.L. Sun, L.Q. Sun, C. Zhang, 2012. Influence of additive mass variation of a missile during its entering into water. *Journal of Vibration and Shock*, 31(14), 171-176.
5. B Li, Habbal F, Ortiz M, 2010. Optimal transportation mesh free approximation schemes for fluid and plastic flows. *International Journal for Numerical Methods in Engineering*, 83(12), 1541-1579.
6. J. Li, C.J. Lu, X. Huang, 2010. Calculation of added mass of a vehicle running with cavity. *Journal of Hydrodynamics*, 22(2), 312-318.
7. X. Y. Huang, 2011. CFD modeling of liquid-solid fluidization: Effect of drag correlation and added mass force. *Particuology*, 9(4), 441-445.
8. EAD Barros, A Pascoal, ED Sa, 2008. Investigation of a method for predicting AUV derivatives. *Ocean Engineering*, 35(16), 1627-1636.
9. Kuwabara, S Someya, K Okamoto, 2008. Experimental investigation of added mass coefficient with a free oscillating circular cylinder. *Japan Society of Mechanical Engineering*, 74(6), 1396-1401.
10. W.Q.Chen, K. Yan, B.S. Wang, G.J. Shi, X.Y. Tang, Z.Y. Liu, 2007. Parameter identification of axial hydrodynamic forces

acting on axis-symmetric body exiting water obliquely. *Journal of Ship Mechanics*, 11(4):521-527.

11. G. Li, W.Y. Duan, Z.B. Guo, 2010. Added mass of submerged vehicles with complex shape. *Journal of Harbin Institute of Technology*, 42(7), 1145-1148.
12. H.P. Fu, J. Li, 2011. Numerical studies of added mass based on the CFD method. *Journal of Harbin Engineering University*, 32(2), 148-152.
13. Fine NE, Uhlman JS, Kring DC, 2001. Calculation of the added mass and damping forces on supercavitating bodies. In: Proceedings 4th International Symposium on Cavitation. Pasadena, CA, USA. pp. 1-8.
14. X. Huang, C.J. Lu, J. Li, 2009. Research on the added mass of a cavity running vehicle. *Chinese Journal of Hydrodynamics*, 24(6), 800-806.
15. W.S. Yan, 2005. The torpedo navigation mechanics. Northwestern polytechnical university press, Xi'an, Shaanxi Province, China.
16. Ye Chuan, Ma Dong-li, 2013. Dynamic modeling and stability analysis for underwater craft with wing. *Journal of Beijing University of Aeronautics and Astronautics*, 39(9), 1137-1143.
17. D.F.Che, H.X. Li, 2007. Multiphase flow and its application. Xi'an jiaotong university press, Xi'an, Shaanxi Province, China.
18. L.P. Zhang, X.G. Deng, H.X. Zhang, 2010. Reviews of moving grid generation techniques and numerical methods for unsteady flow. *Advances in Mechanics*, 40(4), 424-447.
19. X. Liu, N. Qin, H. Xia, 2006. Fast dynamic grid deformation based on Delaunay graph mapping. *Journal of Computational Physics*, 211, 405-423.
20. Y.L. Bai, 2013. Research on the dynamics and nonlinear control of the submarine-launched missile in multimedia environment. Harbin industrial university PhD thesis, Harbin, Heilongjiang, China.

## CONTACT WITH THE AUTHOR

**Yongli Li**

Engineering University of CAPF  
Xi'an 710038  
CHINA

## DYNAMIC CHARACTERISTICS OF MAGNETIC COUPLING IN HORIZONTAL AXIS WAVE ENERGY DEVICE

Jian Zhang<sup>1,2</sup>

YanJun Liu<sup>1,2,3</sup>

Jingwen Liu<sup>1,2</sup>

Tongtong He<sup>3</sup>

Yudong Xie<sup>1,2</sup>

<sup>1</sup>School of Mechanical Engineering, Shandong University, Jinan, Shandong 250061, China,

<sup>2</sup>Key Laboratory of High Efficiency and Clean Mechanical Manufacture, Ministry of Education

<sup>3</sup>Institute of Marine Science and Technology, Shandong University, Qingdao, Shandong 266237, China

### ABSTRACT

*To solve the dynamic response problems of magnetic coupling in the horizontal axis wave energy device, this has researched the dynamic characteristics of magnetic coupling. The fitting formula about torque and angle of the magnetic coupling is obtained through experiments. The mathematical models of the magnetic coupling torque transmission are established. The steady state error of the magnetic coupling and the transfer function of the output angle are obtained. The analytical solution of the step response of the output angle in time domain is derived. The influence of the torsional rigidity, the damping coefficient and the driven rotor's rotational inertia on dynamic characteristics of the magnetic coupling is analyzed. According to the analysis results, the design rules of magnetic coupling are proposed.*

**Keywords:** Wave energy; Magnetic coupling; Dynamic characteristics; Transfer function; Step response; Steady state error

### INTRODUCTION

Because of the global energy crisis, many countries are concentrating on developing renewable energy which has great benefits. Wave energy is an important renewable energy and it shows great development values because it is clean, pollution-free, abundant and widespread [1-6]. The wave energy utilization methods include mechanical, pneumatic and hydraulic forms, which are used in different situations accordingly [7-9], and whose service life, working performance and conversion efficiency are affected by various factors [10-12].

The horizontal axis wave energy device is a kind of mechanical utilization, in which wave energy captured by water turbine drives the generator. During the sea trials, the problems such as seal failure and excessive starting torque

of the mechanical drive device were found. In order to solve these problems, the magnetic coupling is applied, which is an isolated transmission and usually used in the situation where strict sealing property is required to achieve complete sealing [13-17].

If the transmission device is rigid, the unstable movements caused by random waves would directly affect the driven rotor [18]. However, the magnetic coupling is flexible and transmits torque through magnetic field. Therefore, it is meaningful to study the dynamic response characteristics of the magnetic coupling.

## MATERIAL AND METHODS

The magnetic coupling model is shown in Figure 1 to analyze its characteristics..

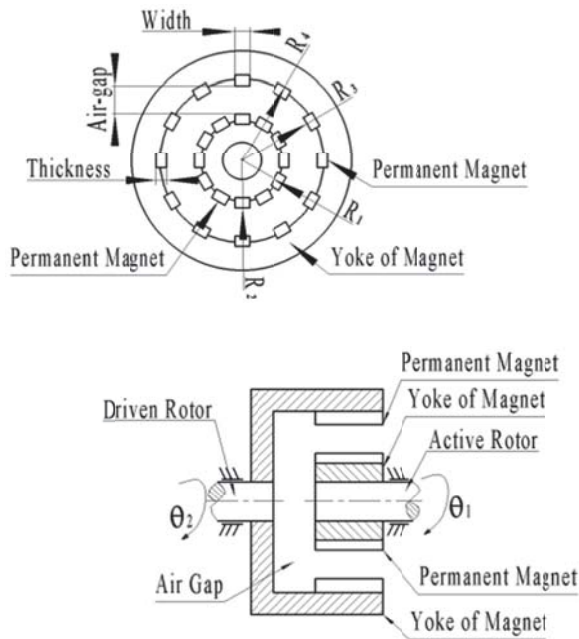


Fig. 1. Magnetic Coupling Model

The rotational inertias of the active rotor and driven rotor are  $J_1$  and  $J_2$ . The input torque and the output torque are  $T_1$  and  $T_2$ . The torsional rigidity is  $k(\theta)$ . The damping coefficients at the input and output sides are  $C_1$  and  $C_2$ . The force distribution of the magnetic coupling is shown in Figure 2. It is assumed that there is no leakage flux and the magnetic field is uniform.

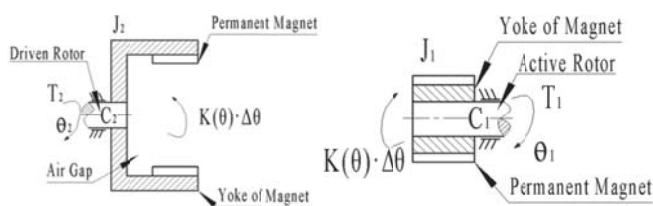


Fig. 2. Force Distribution.

According to Newton's Second Law, the following mathematical model is proposed.

$$T_1 = J_1 \ddot{\theta}_1 + C_1 \dot{\theta}_1 + k(\theta) \Delta\theta \quad (1)$$

$$k(\theta) \Delta\theta = J_2 \ddot{\theta}_2 + C_2 \dot{\theta}_2 + T_2 \quad (2)$$

$$\Delta\theta = \theta_1 - \theta_2 \quad (3)$$

When the magnetic coupling is working, the relationship between the load  $T_2$  and the angular velocity is linear, which can be treated as a damping effect. The damping coefficient is assumed as  $C_d$ , then the following formula is obtained.

$$T_2 = C_d \dot{\theta}_2 \quad (4)$$

The torsional  $k(\theta)$  rigidity changes with the angle difference  $\Delta\theta$ . In order to facilitate the analysis,  $k(\theta)$  is assumed as a constant  $k$ . The transfer function  $G_{12}(\theta)$  is defined as:

$$G_{12}(s) = \frac{\theta_2(s)}{\theta_1(s)} = \frac{k}{J_2 s^2 + C_s s + k} \quad (5)$$

where  $C_s = C_2 + C_d$ . From Equation (5), the driven rotor's rotating characteristic is influenced by not only the load and the torsional rigidity but also its own properties. Analyzing the influence of various parameters can help to improve the dynamic response characteristics of the driven rotor.

The synchronized characteristic between the active rotor and the driven rotor is directly affected by  $\Delta\theta$ . The smaller the  $\Delta\theta$ , the better the following performance is. Based on Equations (1)-(4), the error transfer function  $G_\Delta(s)$  can be expressed as

$$G_\Delta(s) = \frac{\Delta\theta(s)}{\theta_1(s)} = \frac{J_2 s^2 + C_s s}{J_2 s^2 + C_s s + k} \quad (6)$$

According to Equation (6),  $\Delta\theta$  is influenced by the rotational inertia  $J_2$ , the damping coefficient  $C_s$  of the driven rotor and the torsional rigidity. Assuming that the magnetic coupling rotates with a constant speed  $a$ , then  $\theta_1(s)$  is given by:

$$\theta_1(s) = \frac{s}{s^2} \quad (7)$$

The steady-state error  $e_{ss}$  of the magnetic coupling is described as

$$e_{ss} = \lim_{s \rightarrow 0} s E(s) = \lim_{s \rightarrow 0} s G_\Delta(s) \theta_1(s) \quad (8)$$

According to Equations (7)-(8),  $e_{ss}$  can be calculated as

$$e_{ss} = \lim_{s \rightarrow 0} s \frac{J_2 s^2 + C_s s}{J_2 s^2 + C_s s + k} \frac{s}{s^2} = \frac{a C_s}{k} \quad (9)$$

From Equation (9), the steady-state error is related to the magnetic coupling rotation speed  $a$ , the damping coefficient  $C_s$  of the driven rotor and the torsional rigidity  $k$ .

## RESULTS

### PROTOTYPE TEST

To choose proper parameters, prototyping experiment is taken to analyze the relationship between the torque  $T$  and the angle difference  $\Delta\theta$  of the magnetic coupling. The test-bed of prototype is shown as Figure 3. The collected data is shown as Table 1. The curves of the torque  $T$  and the angle difference  $\Delta\theta$  are demonstrated in Figure 4. The fourth-order equation is obtained by fitting curve, as shown in Equation (11).



Fig. 3. Test-Bed of Prototype.

Tab. 1. Collected Data between the Torque and the Angle Difference.

| Type                      | Values |       |       |       |       |       |       |       |       |       |
|---------------------------|--------|-------|-------|-------|-------|-------|-------|-------|-------|-------|
| $\Delta\theta/\text{rad}$ | 0      | 0.027 | 0.054 | 0.081 | 0.107 | 0.134 | 0.161 | 0.188 | 0.215 | 0.241 |
| T/Nm                      | 0      | 1.571 | 1.729 | 4.091 | 5.449 | 6.660 | 7.073 | 8.490 | 8.708 | 9.086 |
| $\Delta\theta/\text{rad}$ | 0.268  | 0.295 | 0.322 | 0.349 | 0.376 | 0.403 | 0.429 | 0.456 | 0.483 | 0.523 |
| T/Nm                      | 9.080  | 8.712 | 8.488 | 7.070 | 6.660 | 5.450 | 4.087 | 1.730 | 1.570 | 0.001 |

The quartic fitting formula between the torque  $T$  and the angle difference  $\Delta\theta$  is obtained by fitting curve as

$$T = 1052.9\Delta\theta^4 - 1056.9\Delta\theta^3 + 189.27\Delta\theta^2 + 39.312\Delta\theta - 0.06 \quad (10)$$

Hence, the torsional rigidity  $k$  is described as

$$k = 4217.6\Delta\theta^3 - 3170.7\Delta\theta^2 + 378.54\Delta\theta + 39.312 \quad (11)$$

The curve between  $k$  and  $\Delta\theta$  is shown as Figure 5. The maximum torsional rigidity  $k$  is 51.72 and the initial torsional rigidity  $k$  is approximately 40.

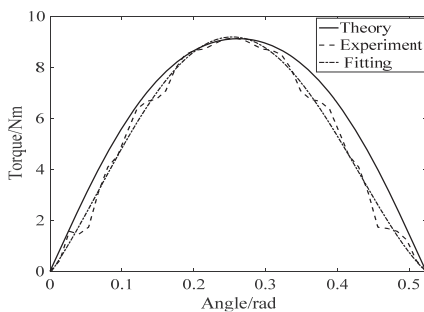


Fig. 4. Relation curve between  $M$  and  $\Delta\theta$

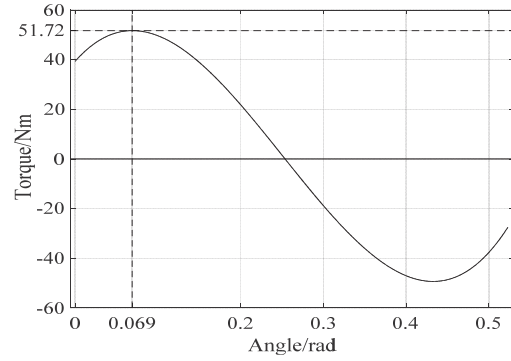


Fig. 5. Characteristic Curve between  $k$  and  $\Delta\theta$ .

### NUMERICAL ANALYSIS

In practice, input responses are usually similar to the unit step responses which are the most detrimental, that is why we choose to analyze the unit step response characteristics of the magnetic coupling.

The Laplace transform of the step input function is written as:

$$X_1(s) = L[\varepsilon(t)] = \frac{1}{s} \quad (12)$$

The magnetic coupling output function of the unit step response is

$$X_o(s) = G_{12}(s)X_1(s) = \frac{k}{J_2s^2 + C_s s + k} \frac{1}{s} \quad (13)$$

The magnetic coupling output function in time domain is obtained from inverse Laplace transform as

$$x_o(t) = L^{-1}\left[\frac{k}{J_2s^2 + C_s s + k} \frac{1}{s}\right] \quad (14)$$

In actual engineering, the magnetic coupling will be in an unstable state when it is in over-damping or critical-damping state, resulting in the system fail. It is common to consider the under-damping state only when the magnetic coupling is designed,

In under-damping state, the magnetic coupling output function in time domain is:

$$x_o(t) = 1 - e^{\frac{-C_s}{2J_2}t} \frac{2\sqrt{J_2k}}{\sqrt{4J_2k - C_s^2}} \sin\left(\frac{\sqrt{4J_2k - C_s^2}}{2J_2}t + \arctan\left(\frac{4J_2K}{C_s\sqrt{4J_2k - C_s^2}}\right)\right) \quad (15)$$

According to the measured parameters,  $C_s = 1.3716 \text{ N}\cdot\text{s} / \text{rad}$ ,  $J_2 = 0.17 \text{ Kg}\cdot\text{m}^2$  and it is necessary that  $k > 2.8 \text{ Nm} / \text{rad}$  in under-damping state. So the value of  $k$  is set as 5, 15, 30, 45, 60. The dynamic response of different torsional rigidity [19-22]. Table 2 shows the indexes of the dynamic characteristics. It can be found in Figure 6 and Table 2

that as the torsional rigidity rises, the overshoot increases, peak time and rise time decrease, however, the adjusting-time has little change. At the same time, the response oscillation becomes severe that is, the time, frequency and amplitude of oscillation increase gradually.

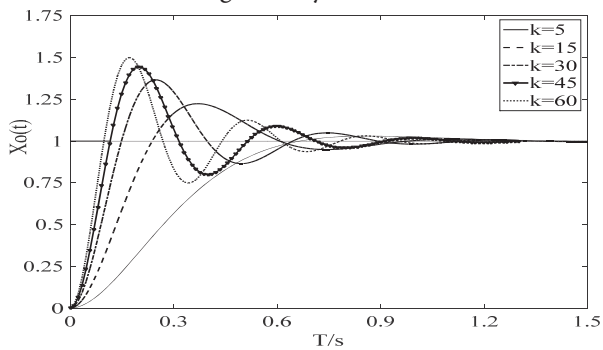


Fig. 6. The Dynamic Response Curve about  $k$ .

Tab. 2. Dynamic characteristic indexes.

| Performance Indexes        | Results |         |         |         |         |
|----------------------------|---------|---------|---------|---------|---------|
| Torsional Rigidity(Nm/rad) | 5       | 15      | 30      | 45      | 60      |
| Rise Time (s)              | 0.6649  | 0.2379  | 0.1488  | 0.1157  | 0.0975  |
| Peak Time (s)              | 0.8664  | 0.3705  | 0.2483  | 0.1995  | 0.1709  |
| Adjusting Time (s)         | 0.5791  | 0.7774  | 0.6045  | 0.6649  | 0.7215  |
| Maximum Overshoot(%)       | 2.4283  | 22.1618 | 36.0568 | 44.8918 | 50.1817 |

From Figure 5, the reasonable range of the torsional rigidity  $k$  is  $40 \sim 51.72 \text{ Nm/rad}$ . So  $k = 45 \text{ Nm/rad}$  is chosen. When  $J_2 = 0.17 \text{ Kg} \cdot \text{m}^2$ , the damping coefficient  $C_s$  should be less than  $5.5317 \text{ N} \cdot \text{s/rad}$ . Thus the value of  $C_s$  is set as 0.1, 1.5, 2.5, 3.5, 5. Figure 7 illustrates the curves of unit step dynamic response characteristics under different damping coefficients and Table 3 lists the indexes of dynamic characteristics. From Figure 7 and Table 3, with the increasing of damping coefficient  $C_s$ , the overshoot and peak time of magnetic coupling increases[23]. When the damping coefficient approaches 5.5, the magnetic coupling is closed to over-damping state, its influence on rise time is smaller and smaller with the increase of damping coefficient. when the damping coefficient is small enough, the magnetic coupling is closed to under-damping state, and the vibration tends to be persistent. Behinds, the amplitude increases with the decreasing of the damping coefficient. The smaller the damping coefficient is, the bigger the amplitude is[24].

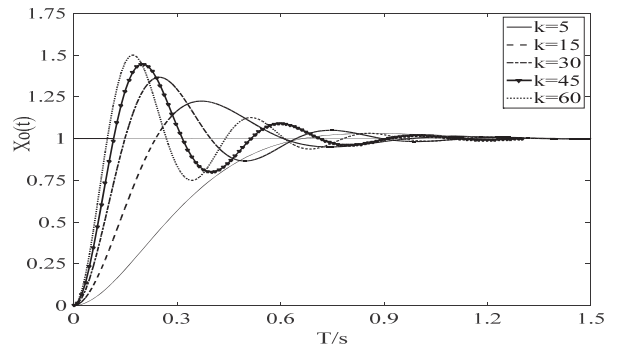


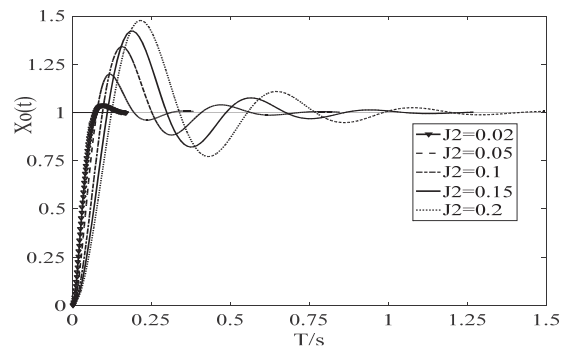
Fig. 7. Damping coefficient dynamic characteristic curves.

Tab. 3. Dynamic characteristics indexes.

| Performance Indexes  | Results |         |         |        |        |
|----------------------|---------|---------|---------|--------|--------|
| Damping Coefficient  | 0.1     | 1.5     | 2.5     | 3.5    | 5      |
| Rise Time (s)        | 0.104   | 0.1183  | 0.1410  | 0.1794 | 0.3881 |
| Peak Time (s)        | 0.195   | 0.2009  | 0.2165  | 0.2496 | 0.4511 |
| Adjusting Time(s)    | 10.842  | 0.6558  | 0.3231  | 0.3152 | 0.2489 |
| Maximum Overshoot(%) | 94.43   | 41.4261 | 20.3680 | 7.6775 | 0.131  |

According to part (1) and (2),  $k = 45 \text{ Nm/rad}$ ,  $C_s = 1.3716 \text{ N} \cdot \text{s/rad}$ . The rotational inertia of the driven rotor should satisfy  $J_2 > 0.0105 \text{ Kg} \cdot \text{m}^2$ . The value of  $J_2$  is set as 0.02, 0.05, 0.1, 0.15, 0.2. Figure 8 shows the curves of unit step dynamic response characteristics. Table 4 shows the indexes. From Figure 8 and Table 4, with the increase of rotational inertia, the rise time, the overshoot, the peak time and the adjusting time of the magnetic coupling rises, while the acceleration of the driven rotor reduces.

Fig. 8. The Curves of Dynamic Characteristics about Rotational Inertia.



Tab. 4. Dynamic characteristics index.

| Performance index      | Result |         |         |         |         |
|------------------------|--------|---------|---------|---------|---------|
|                        | 0.02   | 0.05    | 0.1     | 0.15    | 0.2     |
| Rotational inertia     | 0.02   | 0.05    | 0.1     | 0.15    | 0.2     |
| Rise time (s)          | 0.0728 | 0.0767  | 0.0949  | 0.1105  | 0.1235  |
| Peak time (s)          | 0.0955 | 0.1176  | 0.1566  | 0.1878  | 0.2151  |
| Accommodation time (s) | 0.0637 | 0.1755  | 0.375   | 0.6149  | 0.7364  |
| Maximum time (%)       | 3.7369 | 19.8887 | 34.2038 | 41.9949 | 49.5937 |

## DISCUSSION

Based on the analysis mentioned above, the dynamic characteristics of the magnetic coupling are impacted by the torsional rigidity  $k$ , the damping coefficient  $C_s$  and the rotational inertia  $J_2$  of the driven rotor. Once the magnetic coupling has been installed, the rotational inertia  $J_2$  and the damping coefficient  $C_s$  are fixed. However, the torsional rigidity  $k$  and the dynamic characteristics varies with the changes of angle difference  $\Delta\theta$ . To realize the required dynamic performance of the magnetic coupling, the reasonable range of the torsional rigidity  $k$  should be defined and the operating angle is supposed to ensure this range. If it is hard to meet the requirements in design, the external contributor can be applied to change the rotational inertia  $J_2$  and the damping coefficient  $C_s$ .

## CONCLUSIONS

It is obvious that the torsional rigidity  $k$ , the damping coefficient  $C_s$  and the rotational inertia  $J_2$  have different effects on the dynamic characteristics of the magnetic coupling.

According to the steady-state error, the steady performance is closely associated with the torsional rigidity  $k$  and the damping coefficient  $C_s$ . But it is not effected by the rotational inertia  $J_2$  which only has influence on the startup process of the magnetic coupling.

A large rotational rigidity  $k$  contributes to steady characteristics, startup characteristics and response characteristics, yet it leads to large overshoot and severe fluctuation. A small damping coefficient  $C_s$  will improve the steady performance of the magnetic coupling but it will result in serious oscillation. A large damping coefficient will cause the over-damping state and reduce the stability of magnetic coupling. The rotational inertia  $J_2$  has no effects on steady characteristics of the magnetic coupling. But it affects the startup stage. Though the small rotational inertia has benefit to the startup characteristic, it makes the magnetic coupling approach over-damping state. Therefore, the reasonable torsional rigidity and damping coefficient

should be chosen, and the rotational inertia should be neither too large nor too small.

## ACKNOWLEDGEMENTS

The research is supported by the Fundamental Research Funds of Shandong University (Project no.2016JC035) and the Natural Science Foundation of Shandong Province (Project no.ZR2016WH02), which are gratefully acknowledged.

## REFERENCES

1. Zheng, C.W. and C.Y. Li, "Variation of the wave energy and significant wave height in the China Sea and adjacent waters", *Renewable and Sustainable Energy Reviews*, 43, 381-387, 2015.
2. Wu, S., C. Liu, and X. Chen, "Offshore wave energy resource assessment in the East China Sea", *Renewable Energy*, 76, 628-636, 2015.
3. Rute Bento, A., P. Martinho, and C. Guedes Soares, "Numerical modelling of the wave energy in Galway Bay", *Renewable Energy*, 78: p. 457-466, 2015.
4. Parkinson, S.C., et al., "Integrating ocean wave energy at large-scales: A study of the US Pacific Northwest", *Renewable Energy*, 76: p. 551-559, 2015.
5. Behrens, S., et al., "Wave energy for Australia's National Electricity Market", *Renewable Energy*, 81: p. 685-693, 2015.
6. Astariz, S. and G. Iglesias, "The economics of wave energy: A review", *Renewable and Sustainable Energy Reviews*, 45: p. 397-408, 2015.
7. Wang, Y.-L., "A wave energy converter with magnetic gear", *Ocean Engineering*, 101: p. 101-108, 2015.
8. Siegel, S.G., 2015. Wave radiation of a cycloidal wave energy converter", *Applied Ocean Research*, 49: p. 9-19, 2015.
9. Cordonnier, J., et al., "SEAREV: Case study of the development of a wave energy converter", *Renewable Energy*, 80: p. 40-52, 2015.
10. Tiron, R., et al., "The challenging life of wave energy devices at sea: A few points to consider", *Renewable and Sustainable Energy Reviews*, 43: p. 1263-1272, 2015.
11. de Andres, A., et al., "Adaptability of a generic wave energy converter to different climate conditions", *Renewable Energy*, 78: p. 322-333, 2015.

12. Bacelli, G. and J.V. Ringwood, "Numerical Optimal Control of Wave Energy Converters", *Sustainable Energy*, 2(6): p. 294-302, 2015.
13. Krasilnikov, A.Y. and A.A. Krasilnikov, "Influence of type of high-coercivity permanent magnet on characteristics of end magnetic clutch", *Chemical and Petroleum Engineering*, 47(3): p. 186-192, 2011.
14. Staff, "Magnetic coupling protects machinery", UBM Canon LLC: Manhasset. p. 26, 1999,
15. Uno, "M., et al., Development of the Floating Centrifugal Pump by Use of Non Contact Magnetic Drive and Its Performance", *International Journal of Rotating Machinery*, 10(5): p. 337-344, 2004.
16. Krasilnikov, A.Y. and A.A. Krasilnikov, "Magnetic clutches and magnetic systems in sealed machines", *Chemical and Petroleum Engineering*, 48(5): p. 306-310, 2012.
17. Krasilnikov, A.Y., "Order of Selection and Design of Magnetic Clutches for Sealed Machines", *Chemical and Petroleum Engineering*, 49(7): p. 467-475, 2013.
18. Zhu, Z. and Z. Meng, "3D analysis of eddy current loss in the permanent magnet coupling", *Review of Scientific Instruments*, 87(7): p. 074701, 2016.
19. Isemael, Y.Y. "Molecular, Histological and biochemical effects of tea seed cake on hepatic and renal functions of *Oreochromis niloticus*", *Acta Scientifica Malaysia*, 1(1): p. 13-15, 2017.
20. Soehady, H.F. Asis, J. Tahir, S. Musta, B. Abdullah, M. Pungut, H. "Geosite Heritage and Formation Evolution of Maga Waterfall, Long Pasia, South of Sipitang, Sabah", *Geological Behavior*, 1(2): p. 34-38, 2017.
21. Ismail, I. Husain, M.L. Zakaria, R. "Attenuation of Waves From Boat Wakes In Mixed Mangrove Forest Of *Rhizophora* And *Bruguiera* Species In Matang, Perak", *Malaysian Journal Geosciences*, 1(2): p. 32-35, 2017.
22. Radmanfar, R.Rezayi, M. Salajegheh, S. Bafrani, V.A. "Determination the most important of hse climate assessment indicators case study: hse climate assessment of combined cycle power plant staffs", *Journal CleanWAS*, 1(2): p. 23-26, 2017.
23. Yasin, H. Usman, M. Rashid, H. Nasir, A. Sarwar, A. Randhawa, I.A. "Guidelines for Environmental Impact Assessment of JHAL flyover and underpass project in Faisalabad", *Geology, Ecology, and Landscapes*, 1(3): p. 205-212, 2017.
24. Hassan, M.A. Ismail, M.A.M. "Literature Review for The Development of Dikes's Breach Channel Mechanism Caused by Erosion Processes During Overtopping Failure", *Engineering Heritage Journal*, 1(2): p. 23-30, 2017.

#### CONTACT WITH THE AUTHOR

Yanjun Liu

*e-mail: lyj111ky@163.com*

School of Mechanical Engineering  
Shandong University  
Jinan, Shandong 250061  
**CHINA**

# APPLICATION OF COMPUTER IDENTIFICATION AND LOCATION ALGORITHM IN SMALL FAR INFRARED TARGET RECOGNITION OF SHIP UNDER SURGE INTERFERENCE

Renping Zhu

Department of Admission and Employment Office, Nanchang University, Nanchang 330031, China

## ABSTRACT

*The small far infrared target of ship in surge interference is easy to have visual deviation causing the low accuracy of target positioning and the bad target identification performance. In order to improve the accuracy of far small infrared targets recognition of ship under surge interference, this paper proposed far small infrared target recognition algorithm of ship based on distributed target position estimation and DOA location in computer vision model for constructing coherent distributed source array model of far small infrared target distribution of ship. This algorithm used MUSIC algorithm for the beamforming processing of far small infrared target echo model of ship. Combined with the adaptive filtering algorithm we carried out the surge interference suppression and the estimation of central direction of arrival and angle spread of far small infrared target of ship through multidimensional spectrum peak searching algorithm, realizing the joint estimation of distance of ship target, DOA and frequency parameters, so as to realize the accurate positioning and recognition of targets. Simulation results show that using this method for the far small infrared target recognition of ship under surge interference, the spectral peak sharpness of spectral peak search of target position is high, side-lobe suppression performance is good, which shows the high accuracy of target position estimation and location, the accuracy and anti-interference performance of far small infrared target recognition of ship is good, and has superior performance.*

**Keywords:** Computer identification; Target position estimation; Location; Ship; Infrared target; Surge interference

## INTRODUCTION

Modern war is a high-tech war. The development of ship target recognition technology is relatively slow. Besides the high degree of military secrecy, the background of the underwater environment is extremely complex. The impact of environmental interference on the working performance of underwater weapon systems and ship target recognition can not be ignored [1].

Ship target recognition is divided into active recognition and passive recognition according to the guidance performance of assault weapon. the ship far small infrared target recognition uses a variety of parameters of target information as feature vectors [2-4], such as in ship small far infrared target recognition, reflection echo of ship target

is the function of the target type, distance and direction, which includes the characteristics information such as echo broadening, amplitude, phase, reflection coefficient, target scale, energy spectrum [5]. Common signal features are: AR model parameters, Fourier power spectrum, wavelet transform parameters. Combined with DOA target location analysis and beamforming method [6-10], we achieve accurate positioning detection and identification of ship targets. For passive target recognition of ship radiated noise, the method includes LOFAR spectrum and the high order spectrum [11]. The feature extraction of nonlinear feature of ship radiated noise mainly uses the fractal, limit cycles, chaos and other new mathematical methods. For above methods under surge

interference, the identification accuracy is not high, the stability is not good [12].

Aiming at the above problems, this paper proposed far small infrared target recognition algorithm of ship based on distributed target position estimation and DOA location in computer vision model for constructing coherent distributed source array model of far small infrared target distribution of ship. This algorithm used MUSIC algorithm for the beamforming processing of far small infrared target echo model of ship. Then, combined with the adaptive filtering algorithm we carried out the surge interference suppression and the estimation of central direction of arrival and angle spread of far small infrared target of ship through multidimensional spectrum peak searching algorithm, realizing the joint estimation of distance of ship target, DOA and frequency parameters, so as to realize the accurate positioning and recognition of targets. Finally, we took the actual ship target information collected data as the test sample for identification performance test, which shows the superior performance of the proposed method in improving the accuracy of ship target recognition, and got the effectiveness conclusion.

## ARRAY MODEL OF SHIP FAR SMALL INFRARED TARGET DISTRIBUTION

### SHIP FAR SMALL INFRARED TARGET DISTRIBUTED MODELING

In the actual environment, the target will occupy a certain volume, so this does not idealize itself into a single point in the space. For such target, the received signal is no longer the echo of a single point source, but rather the superposition of multiple spatially similar point source echoes. Such target is called a distributed target [13-15]. We construct near field source model of ship target echo, assuming that equidistant line array which is composed of  $N = 2P$  array elements receives  $I$  near field sources, as shown in Fig. 1.

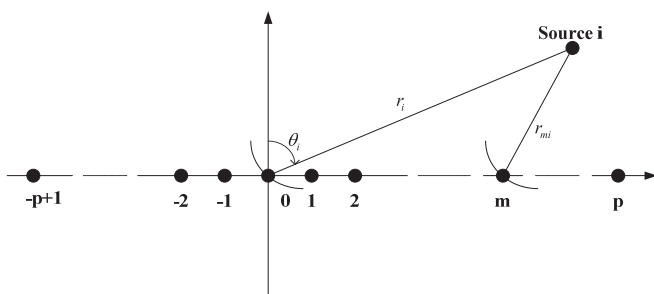


Fig. 1. Uniform linear array target distribution model of near infrared source of ship far small infrared target.

Let the array element coordinates of the ship far small infrared target at the center of the array be 0, taking it as the

phase reference point, then the echo signal of the receiving ship target of the  $m$ -th array element can be expressed as:

$$x_m(t) = \sum_{i=1}^I s_i(t) e^{j\varphi_{mi}} + n_m(t), -p+1 \leq m \leq p \quad (1)$$

Among them,  $s_i(t)$  is the complex envelope of the  $i$ th far small infrared target source of ship.  $x_m(t)$  is the observation signal received by the array element  $m$ .  $n_m(t)$  is the additive noise on the element  $m$ .  $\varphi_{mi}$  is the phase difference of the source  $i$  signal received by the element  $m$  relative to the reference element. The analytic expression of  $\varphi_{mi}$  is not difficult to get:

$$\varphi_{mi} = \frac{2\pi r_i}{\lambda} \left( \sqrt{1 + \frac{m^2 d^2}{r_i^2}} - \frac{2md \sin \theta_i}{r_i} - 1 \right) \quad (2)$$

Among them,  $r_i$ ,  $\theta_i$  is the distances of the  $i$ th near field source (relative to the reference element) and the DOA of the ship far small infrared target to be estimated, and  $\lambda$  is the wavelength of the source  $d$  is the array element interval.

$$\varphi_{mi} \approx \gamma_i m + \phi_i m^2 \quad (3)$$

$$\gamma_i = -2\pi \frac{d}{\lambda} \sin \theta_i, \quad \phi_i = \pi \frac{d^2}{\lambda r_i} \cos^2 \theta_i \quad (4)$$

Thus, the time delay phase difference is composed of two parts: the first is the linear term of array elements location, which is same as general far-field signal model; the second is the quadratic nonlinear term of array elements location, which is determined by DOA and distance parameters, this term increases with the decrease of near field sources [16], otherwise, when the distance tends to infinity, the nonlinear term is zero, the formula (3) degenerates into to far-field signal time delay difference model.

The  $N$ -dimension vector  $x(t)$  is used to represent the ship far small infrared target array output data vector, thus:

$$x(t) = As(t) + n(t) \quad (5)$$

Among them,

$$x(t) = [x_{-p+1}(t), x_{-p+2}(t), \dots, x_p(t)]_{N \times 1}^T \quad (6)$$

$$s(t) = [s_1(t), s_2(t), \dots, s_I(t)]_{I \times 1}^T \quad (7)$$

$$n(t) = [n_{-p+1}(t), n_{-p+2}(t), \dots, n_p(t)]_{N \times 1}^T \quad (8)$$

$$A = [a(\theta_1, r_1), a(\theta_2, r_2), \dots, a(\theta_I, r_I)]_{N \times I} \quad (9)$$

$$a(\theta_i, r_i) = [\exp(j[(-P+1)\gamma_i + (-P+1)^2\phi_i]), \exp(j[(-P+2)\gamma_i + (-P+2)^2\phi_i]), \dots, \exp(j[P\gamma_i + P^2\phi_i])]_{N \times 1}^T \quad (10)$$

Among them,  $1 \leq i \leq I$ , the  $i$ -th column vector  $a(\theta_i, r_i)$  of the matrix  $A$  is called the direction vector of the source  $i$  signal of the ship far small infrared target (also called rudder vector). The matrix  $A$  is called the direction matrix of the array (or response matrix). It can also be called the array manifold. The information of the ship far small infrared target can be used to determine the direction vector.

The distance  $r$  of the near field source of ship far small infrared target distribution relative to array center can be approximated:

$$r \leq 2D^2 / \lambda \quad (11)$$

Among them,  $D$  is the maximum aperture of the receiving array.  $\lambda = c / f$  indicates the operating wavelength corresponding to the central frequency  $f$  of the source.

## A COHERENT SOURCE OF TARGET LOCATION RECOGNITION

Its covariance matrix is:

$$R_z = E[z(t)z(t)^H] = R_s(\psi) + R_n \quad (12)$$

Among them,

$$R_s(\psi) = \sum_{i=1}^p \sum_{j=1}^p \int_{-\pi/2}^{\pi/2} \int_{-\pi/2}^{\pi/2} a(\theta) p_{ij}(\theta, \theta'; \psi_i, \psi_j) a^H(\theta') d\theta d\theta' \quad (13)$$

$$p_{ij}(\theta, \theta'; \psi_i, \psi_j) = E[s_i(\theta, \psi_i) s_j(\theta', \psi_j)] \quad (14)$$

is called the angle cross-correlation kernel, it reflects the degree of correlation between the echo signal in different angles. If the components of direction of arrival between different distribution source is irrelevant [19], the angle cross-correlation kernel can be simplified to  $p_{ij}(\theta, \theta'; \psi_i, \psi_j) = p_i(\theta, \theta'; \psi_i) \delta_{ij}$ , this shows that angle cross-correlation kernel is zero at  $i \neq j$ ,  $p_i(\theta, \theta'; \psi_i) \delta_{ij} = E[s_i(\theta, \psi_i) s_i^*(\theta', \psi_i)]$  is called angle cross-correlation kernel of the  $i$ th distribution source. At this time,

$$R_s(\psi) = \sum_{i=1}^p \int_{-\pi/2}^{\pi/2} \int_{-\pi/2}^{\pi/2} a(\theta) p_i(\theta, \theta'; \psi_i) a^H(\theta') d\theta d\theta'$$

In surge interference, for the coherent source in source,  $s(\theta; \psi_i) = \gamma_i g(\theta; \psi_i)$ ,  $\gamma_i$  is the random variable.  $g(\theta; \psi_i)$  is deterministic complex valued function. For coherent sources, the autocorrelation kernel of the angle is  $p(\theta, \theta'; \psi) = \eta g(\theta, \psi) g^*(\theta', \psi)$ , among them  $\eta = E[\gamma\gamma^*]$ . For the distribution source of signals incoherent from different angles in the same target, the autocorrelation kernel of the angle is  $p(\theta, \theta'; \psi) = p(\theta; \psi) \delta(\theta - \theta')$ ,  $p(\theta; \psi)$  is called the

angle power density of the distribution source. At this time, the covariance matrix of ship far small infrared target echo signal:  $R_s(\psi) = \sum_{i=1}^p \int_{-\pi/2}^{\pi/2} a(\theta) p(\theta; \psi_i) a^H(\theta) d\theta$ .

For modeling, the target model of related source is divided into coherent source model and partial correlation source model [20].

The so-called coherent source is that there is a strong correlation between the signals from different directions in the same target body. The angular density function  $s_i(\theta - \theta_i, t)$  can be expressed as:

$$s_i(\theta - \theta_i, t) = s_i(t) g_i(\theta - \theta_i) \quad (15)$$

$s_i(t)$  is the random signal, usually, the distribution of distributed targets is symmetrical. Then supposing that  $g_i(\theta - \theta_i)$  is the deterministic function taking  $\theta_i$  as the symmetry center with a single peak.  $g_i(\theta - \theta_i)$  which satisfies  $\int_{-\pi}^{\pi} g_i(\theta - \theta_i) d\theta = 1$  is called distribution function of the angular signal of the  $i$ -th distributed target signal source,  $\theta_i$  is the central direction of arrival of the distributed target, which is the parameter to be estimated. When the mathematical form of the angular signal distribution function  $g_i(\theta - \theta_i)$  (e.g., Gaussian distribution) is known, its shape is determined by unknown distributed parameters, and the observation data  $Z(t)$  of array at  $t$  time can be represented as:

$$z(t) = \sum_{i=1}^p s_i(t) b_i(\theta_i) + n(t) \quad (16)$$

Among them,  $b_i(\theta_i)$  is the direction vector of  $i$ th distributed target, which can be expressed as:

$$b_i(\theta_i) = \int_{-\pi}^{\pi} a(\theta) g_i(\theta - \theta_i) d\theta \quad (17)$$

Among them  $i = 1, 2, \dots, p$ ,  $p$  is the distributed target number.  $b_i(\theta_i)$  is determined by the mathematical form of angular signal distribution function of ship far small infrared target signal source and unknown distributed parameter, which is  $M$ -order direction vector.  $M$  is array element number of ship far small infrared targets in the array manifold vector. From  $\int_{-\pi}^{\pi} g_i(\theta - \theta_i) d\theta = 1$ , we can see the first element of the direction vector  $b_i(\theta_i)$  is 1. When  $g_i(\theta - \theta_i)$  is the  $\delta(\theta - \theta_i)$  function,  $b_i(\theta_i) = a(\theta)$ , the distributed ship far small infrared target is degraded into point target [21].

The direction vector of the distributed target is obtained, and  $b_i(\theta_i)$  can also be understood as a generalized array flow pattern.  $b_i(\theta_i)$  is known, we can construct the model of the array receiving data by following formulas:

$$a(\theta) = \left[ 1, e^{-j2\pi fd \sin(\theta)/c}, e^{-j2\pi fd \sin(\theta)/c}, \dots, \exp^{-j(M-1) \cdot 2\pi fd \sin(\theta)/c} \right] \quad (18)$$

$f$  is the center frequency of signal.  $c$  is the acoustic velocity.  $d$  is the array element spacing.

At this time, the generalized flow pattern vector of the distributed source model that the the angular signal distribution function is Gaussian distribution can be obtained by formula (17):

$$b_i(\theta_i) = \left[ 1, e^{-\sigma_{\theta_i}^2/2} e^{-j2\pi f d \sin(\theta)/c}, \dots, e^{-(M-1)\sigma_{\theta_i}^2/2} e^{-j(M-1)2\pi f d \sin(\theta)/c} \right] \quad (19)$$

Then the mathematical model of array reception can be obtained according to (16).

## BEAMFORMING OF MUSIC ALGORITHM AND TARGET ECHO

### IMPROVEMENT OF MUSIC ALGORITHM

Raich R proposed MUSIC (Multiple Signal Classification) algorithm, this algorithm is basic algorithm for target beamforming and orientation positioning recognition[22]. In this paper, the traditional one-dimensional MUSIC method is extended to two-dimensional MUSIC method, realizing the joint estimation of the near field source distance and azimuth angle two-dimensional parameters of the ship far small infrared targets [23]. According to above geometry model of coherent distribution of ship target and the basic assumption of parameter estimation, the covariance matrix  $R_x$  of observation signal is defined as:

$$R_x = E\{x(t)x^H(t)\} = AE\{s(t)s^H(t)\}A^H + E\{n(t)n^H(t)\} = AR_sA^H + R_n \quad (20)$$

Among them,  $R_x$  is the H matrix. The rank is  $N$ .  $R_s$  is the covariance matrix of signal. The rank is  $I$ .  $R_n = \sigma^2 I_N$  is the noise covariance matrix.  $I_N$  is the  $N \times N$  unit matrix. For finite length sample,  $t = 1, 2, \dots, K$ ,  $K$  is the number of snapshots (snapshots, i.e. a sampling point),  $R_x$  can be estimated following formula:

$$\hat{R}_x = \frac{1}{K} \sum_{t=1}^K x(t)x^H(t) \quad (21)$$

We carry out the eigendecomposition on the covariance matrix  $R_x$  of the observation signal:

$$R_x V = \Lambda V \quad (22)$$

Among them,  $\Lambda = \text{diag}[\rho_1, \rho_2, \dots, \rho_N]$  is the diagonal matrix consisting of the eigenvalues in descending order, that is:

$$\rho_1 \geq \rho_2 \geq \dots \geq \rho_I > \rho_{I+1} = \rho_{I+2} = \dots = \rho_M = \sigma^2 \quad (23)$$

$V = [v_1, v_2, \dots, v_I, v_{I+1}, v_{I+2}, \dots, v_N]$  is the eigenvector matrix corresponding to the eigenvalue  $\{\rho_i\}_{1 \leq i \leq N}$ , the signal subspace

and the noise subspace which are composed of eigenvectors are respectively defined as:

$$V_s = [v_1, v_2, \dots, v_I]_{N \times I}, \quad V_n = [v_{I+1}, v_{I+2}, \dots, v_N]_{N \times (N-I)} \quad (24)$$

Using the orthogonality of the signal subspace  $V_s$  and the noise subspace  $V_n$ , the formula (22) can be derived:

$$R_x V_n = \sigma^2 V_n \quad (25)$$

Formula (18) postmultiplies  $V_n$ , we get:

$$R_x V_n = (AR_sA^H + \sigma^2 I_N) V_n \quad (26)$$

Combining expressions (21) and formula (22), we can get:

$$A^H V_n V_n^H A = 0 \quad (27)$$

Therefore, the spectral function of the MUSIC method is:

$$P(\theta, r) = \left| a^H(\theta, r) V_n V_n^H a(\theta, r) \right|^{-1} \quad (28)$$

Among them,  $a(\theta, r)$  is all possible direction vector. Through two-dimensional spectral peak search of azimuth and distance for the spectral function  $P(\theta, r)$ , the peak value is the position information  $\{\theta_i, r_i\}_{1 \leq i \leq I}$  of the near field source.

Using the improved MUSIC algorithm for the beamforming processing of ship far small infrared target echo model [24], we get the echo vector  $b(k)$  of ship far small infrared target in surge interference, which can be expressed as the weighted combination of each point source on the continuous direction, that is:

$$b(k) = \int_{-\pi}^{\pi} f(\theta, k) a(\theta) d\theta \quad (29)$$

Among them,  $a(\theta) = [1, e^{-j\pi \sin \theta}, e^{-j2\pi \sin \theta}, \dots, e^{-j(M-1)\pi \sin \theta}]^T$  is the conventional  $M \times 1$ -order point source array flow pattern vector.  $f(\theta, k)$  is a random angle-time weighting function.

### BEAM FORMING ALGORITHM

Now, some parts of the relevant distribution source (PCD) can be defined as the point target in a relatively short period of observation interval, we use a weighted correlation function for the formation of the autocorrelation function, which only depends on the discrete time interval of  $l$ , and for the different angle, they all are zero.

$$E[f(\theta, k) f^*(\theta', k+l)] = \gamma_f(\theta, l) \delta(\theta - \theta'), \forall l \in Z \quad (30)$$

$\gamma_f(\theta, l)$  is the correlation function of  $f(\theta, k)$ , which is often called as the correlation kernel of the angle-time(ATCK). In the beamforming, zero-time related ICD type and full time related FCD type model can be regarded as the point target of PCD type of additional conditions [25-27]. The decision statistic of beam forming is obtained:

$$\begin{aligned}
ICD: \gamma_f(\theta, l) &= \gamma_f(\theta) \delta(l), \gamma_f(\theta) = \gamma_f(\theta, 0) \\
FCD: \gamma_f(\theta, l) &= \gamma_f(\theta), \forall l \in Z
\end{aligned}
\tag{31}$$

From above formulas, we can see that the statistical properties of the angular time weighting function  $f(\theta, k)$  can influence the statistical properties of the channel vectors of the PCD source. For  $b(k)$ , there is:

$$\begin{aligned}
b(k) &\in N(0_{M \times 1}, R_b), R_b = R_b(0) \\
R_b(l) &= E[b(k)b^H(k+l)] = \int_{-\pi}^{\pi} \gamma_f(\theta, l) a(\theta) a^H(\theta) d\theta
\end{aligned}
\tag{32}$$

For the ICD and FCD sources, the channel vector can also be described as the closed Gauss random vector of zero mean complex values, corresponding to the ICD and FCD distribution sources, and the correlation matrix of  $b(k)$  has the following properties:

$$\begin{aligned}
ICD: R_b(l) &= R_b \delta_l; (R_b(l) = E[b(k)b^H(k+l)]) \\
FCD: R_b(l) &= R_b, \forall l \in Z
\end{aligned}
\tag{33}$$

From the above analysis, we can see that ATCK contains the angular and temporal characteristics of the PCD source. From the previous analysis about the ICD and FCD sources, the focus of the study will be focused on how to determine the ATCK model by a limited number of parameters. Specially, ATCK can be written as:

$$\gamma_f(\theta, l) \Rightarrow \gamma_f(\theta, l | \xi), \xi = [\phi^T, \tau^T]^T
\tag{34}$$

In order to easily understand the concept of PCD model, a simple first-order autoregressive AR model is firstly proposed for the channel vector of surge interference.

$$b(k) = \alpha b(k-1) + \sqrt{1-\alpha^2} w(k)
\tag{35}$$

$\alpha$  represents the time correlation of two adjacent surge interference channel vector sampling values, and driven vector  $w(k)$  includes zero mean, independent identically distributed complex valued Gaussian random vector, these vectors are characterized by angular power density function of Gaussian shape.

$$\begin{aligned}
w(k) &\in N(0_{M \times 1}, R_w), R_w = R_w(0) \\
R_w(l) &= E[w(k)w^H(k+l)] \\
&= \int_{-\pi}^{\pi} \left[ \delta_l \cdot \frac{1}{\Delta\sqrt{2\pi}} e^{-\frac{(\theta-\theta_0)^2}{2\Delta^2}} \right] a(\theta) a^H(\theta) d\theta
\end{aligned}
\tag{36}$$

In formulas, two parameters  $\theta_0$  and  $\Delta$  represent the mean of angle and the angle standard deviation respectively.

## SURGE INTERFERENCE SUPPRESSION FILTER PROCESSING

On the basis of beamforming processing, the adaptive filtering algorithm is used to suppress the surge interference, and the filtering structure model of surge interference suppression is constructed, as shown in Fig. 2.

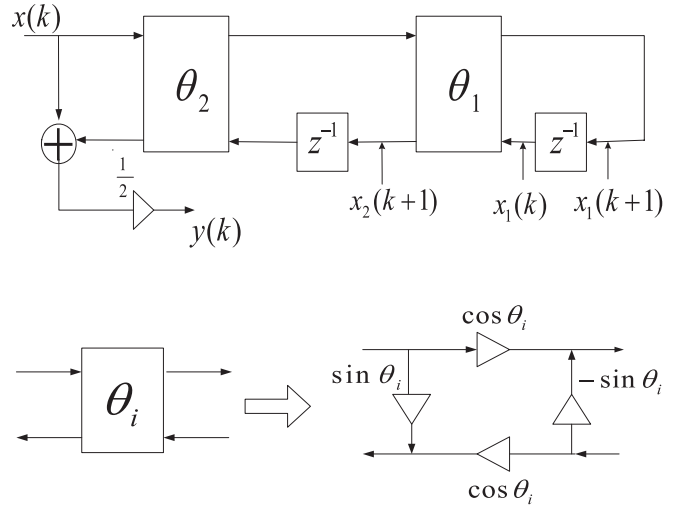


Fig. 2. Filtering structure of surge interference suppression.

The adaptive gradient algorithm is used for the adaptive iteration, and the selection of  $\theta_1(k)$  should minimize the energy of output signal of filter, so  $y(k)y^*(k)$  is the minimum. Here, “\*” represents complex conjugate. Thus, the iterative formula of the surge suppression filter of ship far small infrared target recognition is obtained:

$$\theta_1(k+1) = \theta_1(k) - \mu \text{Re}[y(k)x_1^*(k)]
\tag{37}$$

Among them,  $\mu$  is the parameter of the controllable convergence rate and accuracy, which is called step length.  $\varphi(k)$  is the difference of  $y(k)$  output to parameter  $\theta_1(k)$ , which is called the gradient signal, and it is generated by the input signal  $u(k)$  passing through the following transfer function:

$$H_B(z) = \frac{(1 + \sin \theta_2) \cos \theta_1(k) \cos \theta_2 z^{-1}}{\cos \theta_2 (1 + \sin \theta_1(k)(1 + \sin \theta_2) z^{-1} + \sin \theta_2 z^{-2})} G(z)
\tag{38}$$

Among them,

$$G(z) = \frac{1 - \sin \theta_2}{2} \frac{1 - z^{-2}}{1 + \sin \theta_1(k)(1 + \sin \theta_2) z^{-1} + \sin \theta_2 z^{-2}}
\tag{39}$$

For the convergence speed of acceleration algorithms, the corresponding complex number algorithm is proposed on the basis of this algorithm. The iterative formula of its parameter  $\theta_1$  is

$$\theta_1(k+1) = \theta_1(k) - \mu \text{Re}[y(k)x_1^*(k)]
\tag{40}$$

Among them,  $x_i(k)$  is called a reduced gradient signal, which is generated after the input signal  $u(k)$  passes through the following transfer function:

$$H'_B(z) = \frac{\cos \theta_1(k) \cos \theta_2 z^{-1}}{1 + \sin \theta_1(k)(1 + \sin \theta_2)z^{-1} + \sin \theta_2 z^{-2}} \quad (41)$$

The filter output  $y(k)$  and the gradient signal  $\varphi(k)$  can be represented as

$$y(k) = s_1(k) + n_1(k), \quad \varphi(k) = s_2(k) + n_2(k) \quad (42)$$

$$s_1(k) = AA_{H_H} e^{j(\Omega k + \theta_H)}, \quad s_2(k) = AA_{H_B} e^{j(\Omega k + \theta_{H_B})} \quad (43)$$

For gradient algorithms,  $A_H$ ,  $A_{H_B}$  and  $\theta_H$ ,  $\theta_{H_B}$  are the amplitude response and phase response of the transmission function of filter  $H(z)$  and  $H_B(z)$ , respectively. Through adaptive filtering, the suppression of surge interference in ship far small infrared target recognition has been realized.

## REALIZATION OF TARGET LOCATION ALGORITHM AND COMPUTER INTELLIGENT RECOGNITION OF SHIP TARGET

### MULTIDIMENSIONAL SPECTRAL PEAK SEARCH OF SHIP FAR SMALL INFRARED TARGET INFRARED TARGET

This paper proposed the ship far small infrared target recognition algorithm based on distributed target position estimation and DOA location [28,29]. Using the multidimensional spectrum peak search algorithm for central direction of arrival and extension angle estimation of far small infrared target of ship, we build the distributed target signal source model through a certain number of point target signal source, and construct the VEC-MUSIC multidimensional spectrum peak search algorithm. Supposing that there is a narrowband distributed source. It consists of a large number of scattering points around the source, the signal of receiving end can be expressed as the vector form:

$$x(t) = s(t) \sum_{n=1}^L \gamma_n(t) a(\theta + \tilde{\theta}_n(t)) + n(t) = s(t) v(t, \theta, \sigma_\theta) + n(t) \quad (44)$$

Among them,  $s(t)$  is the signal reflected from the ship far small infrared target distributed source.  $\gamma_n$  is the random gain of each signal, and  $\tilde{\theta}_n$  is the random angle offset relative to DOA. The probability density function of  $\tilde{\theta}_n$  is  $p(\tilde{\theta}; \sigma_\theta)$ , and  $\sigma_\theta$  is the standard deviation of the random angular offset  $\tilde{\theta}_n$ . Assuming that the gain factor  $\gamma_n$  is independent and zero mean, and  $E[|\gamma_n|^2] = 1/L$ . assuming

that the receiving array is the uniform linear array, then  $a(\theta) = [1, e^{-j2\pi\Delta \sin \theta}, \dots, e^{-j(M-1)2\pi\Delta \sin \theta}]^T$ .

In addition, the above model can be described as an integral form, and the array reception signal of the ship far small infrared target positioning recognition can be expressed as:

$$x(t) = s(t) \int_0^{2\pi} \gamma(\tilde{\theta}; t) a(\theta + \tilde{\theta}) d\tilde{\theta} + n(t) = s(t) v(t, \theta, \sigma_\theta) + n(t) \quad (45)$$

$\gamma(\tilde{\theta})$  is stochastic, and  $E[\gamma(\tilde{\theta}_1)\gamma(\tilde{\theta}_2)] = p(\tilde{\theta}; \sigma_\theta) \delta(\tilde{\theta}_1 - \tilde{\theta}_2)$ ,  $p(\tilde{\theta}; \sigma_\theta)$  can be understood as the spatial power distribution of the distribution source.

In fact, the distributed model established by (45) can be explained by the model (43) mentioned in the previous section, and taking  $b(k) = \int_{-\pi}^{\pi} f(\theta, k) a(\theta) d\theta$  in it, we can obtain:

$$z(k) = s(k) \int_{-\pi}^{\pi} f(\theta, k) a(\theta) d\theta + n(k), k \in Z \quad (46)$$

Compared with two formulas, it is not difficult to see that both of described model is consistent. The ship target echo signal vector  $s(t) = [s_1(t), s_2(t), \dots, s_q(t)]^T$  and noise vector  $n(t)$  are independent random vectors of zero-mean, and through the multi-dimensional spectrum peak search, their second moment are respectively:

$$E[s_r s_k^H] = P_s \delta(t, k), E[n_r n_k^H] = \sigma_n^2 I_M \delta(t, k) \quad (47)$$

Among them,  $\delta(t, k)$  is the kronnecker  $\delta$  function.  $P$  is the signal covariance matrix, and  $I_M$  is the M-order unit matrix.  $\sigma_n^2$  is the noise variance.

The covariance matrix of the observed data vector  $z(t)$  can be represented as:

$$R = E[z(t) z^H(t)] = B P_s B^H + \sigma_n^2 I_M \quad (48)$$

Among them,  $B = [b_1(\theta_1), b_2(\theta_2), \dots, b_q(\theta_q)]^T$ , the singular value of covariance matrix is decomposed into:

$$R = U_s \Lambda_s U_s^H + U_n \Lambda_n U_n^H \quad (49)$$

The column vectors of matrix  $U_s$  and  $U_n$  are respectively composed of singular values  $\sigma_1, \sigma_2, \dots, \sigma_q$  and corresponding singular vectors of  $\sigma_n$ . Moreover  $\sigma_1 \geq \sigma_2 \geq \dots \geq \sigma_q > \sigma_n$ , supposing that there is no correlation between the different distribution sources, namely  $U_n^H b_i(\theta_i) = 0$ , the orthogonality of the direction vector and the noise subspace. By using this method, we can obtain a multidimensional spectral peak search method of DOA estimation method of ship far small infrared targets:

$$f(\phi) = \frac{1}{b^H(\phi) \hat{U}_n U_n^H b(\phi)} \quad (50)$$

Supposing that the angular signal distribution function of the distributed target source is known, and the specific expression is determined by unknown parameter  $\phi_i$ .  $\phi_i$  is the vector of multiple parameters. According to the formula (50), the distributed target DOA and other unknown parameters can be obtained by multi-dimensional parameter spectral peak search.

### JOINT PARAMETER ESTIMATION ALGORITHM OF SHIP TARGET LOCATION

The multidimensional spectrum peak search algorithm is the extension of the MUSIC algorithm in the estimation of distributed target [30]. The theoretical basis is basically the same. According to the principle, we carry out the central direction of arrival and extended angle estimation of far small infrared targets of ship. If the unknown parameters of signal source only has two, namely the central direction of arrival  $\theta_i$  and expansion  $\sigma_i$ , the above method becomes the solution of the minimization problem:

$$(\theta_i, \sigma_i) = \arg \min b_i^H(\theta, \sigma) \hat{U}_n U_n^H b_i(\theta, \sigma) \quad (51)$$

For several common forms of distribution, they all satisfy:

$$b_i(\theta_i) = \Phi(\theta_i) h_i \quad (52)$$

Among them, the  $M$ -order diagonal matrix  $\Phi(\theta_i) = \text{diag}(a(\theta_i))$  and  $M$ -order vector  $h_i = \int_{-\pi}^{\pi} a(\theta) g_i(\theta) d\theta$  can prove that if the signal source angle signal distribution function  $g_i(\theta)$  is conjugate symmetric function, that is  $g_i(\theta) = g_i^*(-\theta)$ , the vector  $h_i$  is the real vector, that is  $h_i \in \mathbb{R}^M$ , the vector is the real vector. Combined (52) formulas with (3-8) formulas, the distributed target DOA becomes the solution of the minimization problem as follows:

$$(\theta_i, \sigma_i) = \arg \min h_i^H \Phi^H(\theta) \hat{U}_n U_n^H \Phi(\theta) h_i \quad (53)$$

Let  $Q_1(\theta) = \Phi^H(\theta) \hat{U}_n U_n^H \Phi(\theta)$ , we can see that the minimum eigenvalue of the matrix  $Q_1(\theta)$  takes the minimal value for the distributed target DOA.  $h(\sigma_i)$  is the corresponding eigenvector, and it is the real vector. The matrix  $Q_1(\theta)$  is non negative conjugate symmetric matrix, and the eigenvalues are non negative, so the distributed target DOA estimation corresponds to the spectral peak position of the following spatial spectrum.

$$f_1(\theta) = -\log_{10}(\lambda_{\min}[Q_1(\theta)]) \quad (54)$$

By searching the minimum eigenvalue, one-dimensional DOA estimation of the coherent distributed target is obtained. For the common form of distribution source position distribution,  $b_i(\theta_i) = G_i a(\theta_i)$ , among them,  $G_i$  is the  $M$ -order diagonal matrix and  $G_i = \text{diag}([h_{i1}, h_{i2}, \dots, h_{iM}])$  is only related to the distribution degree of the ship target, which

is not related to DOA of the target. When the distribution of  $\theta_{ik}$  is about the symmetrical distribution of  $\theta_i$ , all of  $h_{i1}, h_{i2}, \dots, h_{iM}$  are real numbers. The covariance matrix and singular value decomposition of the observed data vector can deduce  $BPB^H = U_s(\Lambda_s - \Lambda_s)U_s^H$ , and thus  $B$  can be transformed into  $B = U_s W$ , among them, is the  $q \times q$ -order nonsingular matrix.

From the above analysis, we can get the following equation:

$$\begin{bmatrix} h_{i1}^* h_{i2} e^{-j2\pi(d/\lambda)\sin\theta_i} \\ h_{i2}^* e^{j\theta_i} h_{i3} e^{-j2\pi(d/\lambda)\sin\theta_i} \\ \dots \\ h_{i(M-1)}^* e^{j(M-2)\times 2\pi(d/\lambda)\sin\theta_i} h_{iM} e^{-j(M-1)2\pi(d/\lambda)\sin\theta_i} \end{bmatrix} = \begin{bmatrix} (u_1^H w)^* u_2^H w \\ (u_2^H w)^* u_3^H w \\ \dots \\ (u_{M-1}^H w)^* u_M^H w \end{bmatrix} \quad (55)$$

$u_1, u_2, \dots, u_M$  is the row vector of  $U_s$ ,  $w$  is  $i$ -th column vector of  $W$ . Because  $h_{i1}, h_{i2}, \dots, h_{iM}$  are real numbers, from the above formula we can get:

$$\begin{bmatrix} (u_1^H w)^* u_2^H w \\ (u_2^H w)^* u_3^H w \\ \dots \\ (u_{M-1}^H w)^* u_M^H w \end{bmatrix} = e^{-j2\pi(d/\lambda)\sin\theta_i} \begin{bmatrix} (u_2^H w)^* u_1^H w \\ (u_3^H w)^* u_2^H w \\ \dots \\ (u_M^H w)^* u_{M-1}^H w \end{bmatrix} \quad (56)$$

Which can also be expressed as:

$$u_k^H w w^H u_{k-1} = e^{-j2\pi(d/\lambda)\sin\theta_i} u_{k-1}^H w w^H u_k \quad (57)$$

From above formulas, it only keeps the information which is related to distributed object DOA, and does not keep the information which is related to degree of distribution. Thus positioning estimation algorithm of the ship far small infrared targets based on the distributed target position estimation and DOA location:

1) estimate the covariance matrix of observed data  $\hat{R} = \frac{1}{N} \sum_{i=1}^N x_i x_i^H$ ,  $N$  is independent number of snapshots, perform the singular value decomposition on  $R$ , obtain the number of signal subspace  $U_s$  and number of distributed target  $q$ .

$$2) \text{ Let: } P_1 = \begin{bmatrix} u_1^T \otimes u_2^H \\ u_2^T \otimes u_1^H \\ \dots \\ u_{M-1}^T \otimes u_M^H \end{bmatrix}, P_2 = \begin{bmatrix} u_2^T \otimes u_1^H \\ u_3^T \otimes u_2^H \\ \dots \\ u_M^T \otimes u_{M-1}^H \end{bmatrix}, v = \text{vec}(w w^H) \quad (58)$$

The row vectors of  $U_s$  are plugged into (57), and  $P_2$  are computed, and then the generalized eigenvalue decomposition is computed:

$$P_1^H P_1 [v_1, v_2, \dots, v_{q \times q}] = \text{diag}(\alpha_1, \alpha_2, \dots, \alpha_{q \times q}) P_1^H P_2 [v_1, v_2, \dots, v_{q \times q}] \quad (59)$$

We use  $q$  phase angles of eigenvalues of model which is close to 1 to estimate DOA of distributed ship targets, so as to realize the joint estimation of the distance of ship target, DOA and frequency parameters, then realizing the classification recognition of ship target through computer recognition and machine learning classification algorithm.

## SIMULATION EXPERIMENT AND RESULT ANALYSIS

In order to test application performance of the proposed algorithm in realizing the positioning and recognition of ship far small infrared targets, we need a simulation experiment. The experiment uses Matlab 7 simulation design, supposing that the point distribution model of ship far small infrared targets is composed of the uniform line array which is composed of 14 array elements. The array element spacing is 0.25 times of minimum wavelength [31,32]. The signal source is two complex exponential signals with equal power. The signal frequencies are respectively 200Hz, 100Hz. The sampling frequency is 2000Hz. The signal-to-noise ratio is 10dB. Two far small infrared target signals of ship are  $10^\circ$  and  $30^\circ$ . The number of snapshots is 200. The replication number of experiment is 50 times. The distributed target signal source reach to the array respectively from the  $\theta_1 = 4^\circ, \theta_2 = 7^\circ$  direction of arrival. Expansion of two signal source respectively is  $\Delta_1 = 1^\circ, \Delta_2 = 2^\circ$ , and the signal to noise ratio of surge interference is 10. The number of snapshots of surge is 1000. The noises are white Gaussian noise and Gaussian colored noise [33]. Gaussian colored noise is formed

through a two order AR model of  $H(z) = \frac{z^{-2}}{1 - a_1 z^{-1} + a_2 z^{-2}}$ , among them,  $a_1 = 2\rho \cos(2\pi f_n / f_s), a_2 = \rho^2, 0 < \rho < 1, \rho$

is a coefficient responding spectrum width. According to the simulation environment and parameter settings, the searching results of the power spectrum of the ship's far small infrared target position estimation is obtained in surge interference are shown in Fig. 3. In this paper, the location search results after suppression of surge interference using the proposed method are shown in Fig. 4.

Compared with Figures 3-4, we can see that using this method for ship far small infrared target recognition, two spectrum peaks are respectively corresponding to 10 degrees and 30 degrees in horizontal ordinate, but they are different between them. The accuracy of target location is not good without surge interference suppression processing. From the average results of 50 experiments.

We can see that through the surge interference suppression, the spectral peak of target location estimation is much sharper, and the position estimation of ship target is more accurate which is easy to distinguish the signal which has a small difference in the two azimuth angles, so as to effectively achieve the accurate identification of ship far small infrared.

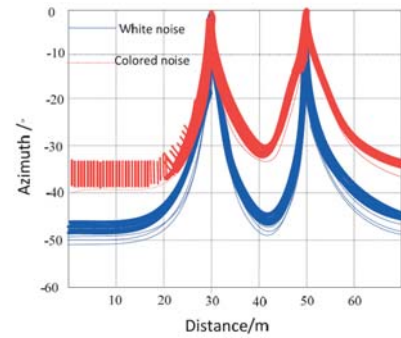


Fig. 3. Estimation result of locating and searching power spectrum intensity of ship target under surge interference.

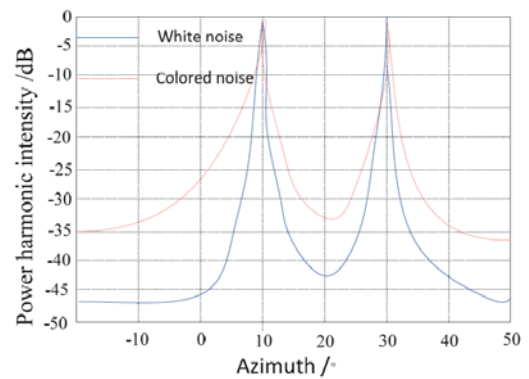


Fig. 4. Location search results after suppression of surge interference with using the proposed method.

In order to compare the performance of different methods, we further test the estimation results of azimuthal angle for ship far infrared target localization in this method and the traditional methods, and comparison results are shown in Fig. 5.

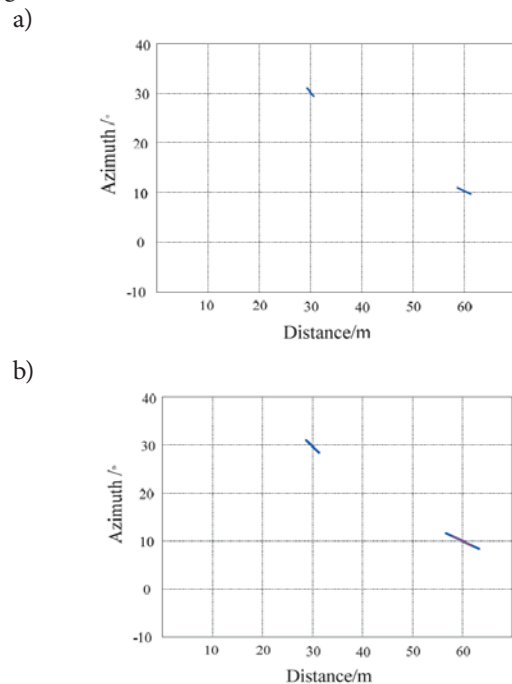


Fig. 5. Contrast results of azimuthal angle of ship far small infrared target localization. (a) Traditional two-dimensional MUSIC method (b) Proposed method in this paper

Simulation results show that the corresponding abscissas of the two spectrum peaks are 30 m and 60 m, and the corresponding ordinates are 30 degrees and 10 degrees in Fig. (a). The azimuth angle and distance of the two sources can be seen more directly from (b). But there is the difference between them. Compared with (a), we can see that the spectral peak of Gauss white noise is more sharp than the color noise environment. From (b) we can see that compared with the white noise with the color noise environment, the DOA estimation result of ship targets are more accurate, and the estimation error is low. Therefore, using the computer recognition method for target recognition of ship, the root-mean-square error  $\bar{E}$  comparison of the three kinds of ship far small infrared target recognition is shown in Table 1. The analysis of Table 1 shows that the error of proposed method for ship target recognition is low, and has better accuracy.

### CONCLUSIONS

The location recognition method of far small infrared target recognition algorithm of ship was studied in this paper. This paper proposed far small infrared target recognition algorithm of ship based on distributed target position estimation and DOA location in computer vision model for constructing coherent distributed source array model of far small infrared target distribution of ship. This algorithm used MUSIC algorithm for the beamforming processing of far small infrared target echo model of ship. Combined with the adaptive filtering algorithm we carried out the surge interference suppression and the estimation of central direction of arrival and angle spread of far small infrared target of ship through multidimensional spectrum peak searching algorithm, realizing the joint estimation of distance of ship target, DOA and frequency parameters, so as to realize the accurate positioning and recognition of targets. Simulation results show that using this method for the far small infrared target recognition of ship under surge interference, the spectral peak sharpness of spectral peak search of target position is high, side-lobe suppression performance is good, which shows the high accuracy of target position estimation and location, the accuracy and anti-interference performance of far small infrared target recognition of ship is good. Through the computer recognition method, we achieves smaller errors of far small infrared target recognition of ship, improving the accurate recognition ability

of ship target, and it has good application value of realizing the precision strike of ship target.

### REFERENCE

1. K. Zhong, H. Peng, L. D. Ge, 2015. Blind Equalization Based on FABA-SISO for Continuous Phase Modulation Signals over Time-varying Frequency-selective Fading Channels. JEIT, 37(11): 2672-2677.
2. Z. F. Shu, X. K. Dou, H. Y. Xia, et al. 2012. Low stratospheric wind measurement using mobile rayleigh doppler wind LIDAR. Journal of the Optical Society of Korea, 16(2): 141-144
3. R. Wang, Y. Ma, 2014. DOA Estimation of Wideband Linear Frequency Modulated Pulse Signals Based on Fractional Fourier Transform. Acta Armamentarii, 35(3): 421-427.
4. Y. Bengio, A. Courville, P. Vincent, 2013. Representation learning: a review and new perspectives. IEEE Transactions on Pattern Analysis and Machine Intelligence, 35(8): 1798-1828.
5. Z. Chen, J. Chen, 2014. The Design of Optimized Android Salvation Platform Based on Multi-State Visual Identity. Bulletin of Science and Technology, (4): 62-64.
6. J. L. Pan, Z. Xiong, L. N. Wang, 2015. Etal A Simplified UKF Algorithm for SINS/GPS/CNS Integrated Navigation System in Launch Inertial Coordinate System. Acta Armamentarii, 36(3): 484-491.
7. H. Y. Shi, N. Zhang, 2015. Moving Targets Indication Method in Single SAR Imagery Based on Sparse Representation and Road Information. Chinese Journal of Electronics, 43(3): 431-439.
8. Y. Y. Yao, L. Tang, 2016. Robot Visual Path Following Identification Optimization Simulation. Computer Simulation, 33(5):401-404.

Tab. 1. Comparison results of root mean square error of far and small infrared target recognition of ship.

| Target  | 1     | 2     | 3     | 4     | 5     | 6     | 7     | 8     | $\sigma$ | $\bar{E}$ |
|---|-------|-------|-------|-------|-------|-------|-------|-------|----------|-----------|
| Proposed method                               | 0.368 | 0.375 | 0.305 | 0.428 | 0.320 | 0.532 | 0.415 | 0.494 | 0.083    | 0.399     |
| Two-dimensional MUSIC method                  | 1.179 | 1.702 | 1.921 | 1.350 | 2.037 | 1.931 | 1.400 | 1.046 | 0.402    | 1.466     |
| High order spectrum feature extraction method | 0.870 | 0.755 | 0.799 | 0.861 | 0.884 | 0.614 | 0.635 | 0.639 | 0.133    | 0.716     |

9. Y. Ding, H. Dai, S. Wang, 2014. Image quality assessment scheme with topographic independent components analysis for sparse feature extraction. *Electronics Letters*, 50(7): 509-510.
10. L. C. Manikandan, R. K. Selvakumar, 2014. A new survey on block matching algorithms in video coding. *International Journal of Engineering Research*, 3(2): 121-125.
11. H. Bdi, L. J. Williams, 2010. Principal component analysis. *Wiley Interdisciplinary Reviews: Computational Statistics*, 2(4): 433-459.
12. J. Z. Jiang, X. L. Cheng, S. Ouyang, 2015. Fast Design of Double-prototype Discrete Fourier Transform Modulated Filter Banks. *JEIT*, 37(11): 2628-2633.
13. F. Ma, 2016. A license plate location algorithm based on wavelet transform and Tophat transform. *Electronic Design Engineering*, 24(22): 118-121.
14. N. Rajapaksha, A. Madanayake, L. T. Bruton, 2014. 2D space- time wave-digital multi-fan filter banks for signals consisting of multiple plane waves. *Multidimensional Systems and Signal Processing*, 25(1): 17-39.
15. X. Y. Jin, X. Y. Zhou, Zhang W. L. 2014. Modulation Recognition Using Adaptive MCMC in Multipath Fading Channel, Modulation Recognition Using Adaptive MCMC in Multipath Fading Channel. *Journal of Beijing University of Posts and Telecommunications*, 37(1): 31-34.
16. S. L. Xie, Y. Liu, J. M. Yang, et al. 2012. Time-Frequency Approach to Underdetermined Blind Source Separation. *IEEE Transactions on Neural Networks and Learning Systems*, 23(2): 306-315.
17. V. M. Alfaro, R. Vilanovab, 2013. Robust tuning of 2DoF five-parameter PID controllers for inverse response controlled processes. *Journal of Process Control*, 23(4): 453-462.
18. C. Y. Tuo, 2015. An Improved Localization Algorithm for Radio Frequency Identification Reader. *Computer Measurement & Control*, 23(3).
19. P. frihauf, M. Krstic, T. Basar, 2012. Nash equilibrium seeking in Noncooperative games. *IEEE Transaction on Automatic Control*, 57(5): 1192-1207.
20. M. R. Hesamzadeh, D. R. Biggar, 2012. Computation of extremal-Nash equilibria in a single-stage MILP. *IEEE Transaction on Power System*, 27(3): 1706-1707.
21. K. Oberleithner, M. Sieber, C. N. Nayeri, et al. 2011. Three-dimensional coherent structures in a swirling jet undergoing vortex breakdown: stability analysis and empirical mode construction. *Journal of Fluid Mechanics*, 679(1): 383-414.
22. T. Li, P. Gopalakrishnan, R. Garg, M. Shahnam, 2012. CFD-DEM study of effect of bed thickness for bubbling fluidized beds. *Particuology*, 10(5): 532-541
23. X. H. Lu, R. J. Chen, K. D. Chi, 2016. A Rescue Robot Perception System with Introduction of Infrared Heat Release Detection in Human Body. *Ship Electronic Engineering*, 36(3): 151-155.
24. K. Liu, J. H. Zhu, B. Yu, 2013. Longitudinal control of aircraft with thrust vectoring using robust dynamic inversion. *Control and Decision*, 28(7): 1113-1116.
25. Gao, W. and W. Wang, The fifth geometric-arithmetic index of bridge graph and carbon nanocones. *Journal of Difference Equations and Applications*, 2017. 23(1-2SI): p. 100-109.
26. Gao, W., et al., Distance learning techniques for ontology similarity measuring and ontology mapping. *Cluster Computing-The Journal of Networks Software Tools and Applications*, 2017. 20(2SI): p. 959-968.
27. Z. Zheng, L. Y. Wang, Y. Zhou, 2013. Chaos Theory and Its Application in Ships Target Recognition. *Ship Electronic Engineering*, 33(5): 48-50.
28. M.A. Hassan, M.A.M. Ismail, 2017. Literature Review for The Development of Dikes's Breach Channel Mechanism Caused by Erosion Processes During Overtopping Failure. *Engineering Heritage Journal*, 1(2): 23-30.
29. H. Yasin, M. Usman, H. Rashid, A. Nasir, A. Sarwar, I.A. Randhawa, 2017. Guidelines for Environmental Impact Assessment of JHAL flyover and underpass project in Faisalabad. *Geology, Ecology, and Landscapes*, 1(3): 205-212.
30. R. Radmanfar, M. Rezayi, S. Salajegheh, V.A. Bafrani, 2017. Determination the most important of hse climate assessment indicators case study: hse climate assessment of combined cycle power plant staffs. *Journal CleanWAS*, 1(2): 23-26.
31. I. Ismail, M.L. Husain, R. Zakaria, 2017. Attenuation of Waves from Boat Wakes in Mixed Mangrove Forest of Rhizophora And Bruguiera Species In Matang, Perak. *Malaysian Journal Geosciences*, 1(2):32-35.
32. H.F. Soehady, J. Asis, S. Tahir, B. Musta, M. Abdullah, H. Pungut, 2017. Geosite Heritage and Formation Evolution of Maga Waterfall, Long Pasia, South of Sipitang, Sabah. *Geological Behavior*, 1(2):34-38.

33. S.B. Shamsudin, A. Marzuki, M.S. Jeffree, K.A. Lukman, 2017. Blood lead concentration and working memory ability on malay primary school children in urban and rural area, Malacca. Acta Scientifica Malaysia, 1(1): 04-07.

#### **CONTACT WITH THE AUTHOR**

Renping Zhu

*e-mail: xgczrp@ncu.edu.cn*

Department of Admission and Employment Office  
Nanchang University  
Nanchang 330031  
**CHINA**

# BIG DATA ANALYSIS AND SIMULATION OF DISTRIBUTED MARINE GREEN ENERGY RESOURCES GRID-CONNECTED SYSTEM

Jun Tian

Lirong Huang

Foshan Polytechnic, Foshan 528137, China

## ABSTRACT

*In order to improve the working stability of distributed marine green energy resources grid-connected system, we need the big data information mining and fusion processing of grid-connected system and the information integration and recognition of distributed marine green energy grid-connected system based on big data analysis method, and improve the output performance of energy grid-connected system. This paper proposed a big data analysis method of distributed marine green energy resources grid-connected system based on closed-loop information fusion and auto correlation characteristic information mining. This method realized the big data closed-loop operation and maintenance management of grid-connected system, and built the big data information collection model of marine green energy resources grid-connected system, and reconstructs the feature space of the collected big data, and constructed the characteristic equation of fuzzy data closed-loop operation and maintenance management in convex spaces, and used the adaptive feature fusion method to achieve the auto correlation characteristics mining of big data operation and maintenance information, and improved the ability of information scheduling and information mining of distributed marine green energy resources grid-connected system. Simulation results show that using this method for the big data analysis of distributed marine green energy resources grid-connected system and using the multidimensional analysis technology of big data can improve the ability of information scheduling and information mining of distributed marine green energy resources grid-connected system, realizing the information optimization scheduling of grid-connected system. The output performance of grid connected system has been improved.*

**Keywords:** Distributed, Ocean, Green energy resources, Grid-connected system, Big data analysis

## INTRODUCTION

Green energy resources is also known as clean energy, which is the symbol and synonym of the environmental protection and the good ecosystem. Marine green energy resources are the renewable natural energy resources contained in the oceans, which is renewable and inexhaustible in the era of existence of solar system [1].

The marine green energy resources grid-connected system includes of ocean tidal power generating system, marine wind power generating system and ocean thermal energy conversion. The marine green energy resources is the current important resource. We carry out the effective integration scheduling and the operation and maintenance management on the distributed marine green energy grid-connected system

big data distributed marine green energy grid system, and provide accurate data basis for grid-connected generating system, so as to improve the ability of prediction and judgment of grid-connected generating system. The construction of distributed marine green energy resources grid-connected system and the parallel scheduling and the operation and maintenance management of the grid-connected system in the big data environment can improve the stability of the of green energy resources grid-connected system. The research of distributed marine green energy grid-connected system big data analysis method has important significance [2].

The data of marine green energy grid system big data analysis is mainly used for data fusion and scheduling. There are many big data analysis fusion scheduling and operation

and maintenance management algorithms, which can be divided into the fuzzy fusion scheduling and operation and maintenance management algorithm[3], the hierarchic fusion scheduling and operation and maintenance management algorithm, the mesh fusion scheduling and operation and maintenance management algorithm, the support vector machines fusion scheduling and operation and maintenance management algorithm and BP neural network fusion scheduling and operation and maintenance management algorithm[4-8]. Among them, the hierarchic fusion scheduling and operation and maintenance management algorithm takes the attributes category of distributed marine green energy grid-connected system according to the number of as hierarchic grid feature for the fusion scheduling and operation and maintenance management. In the hierarchic fusion scheduling and operation and maintenance management, with the change of category level, the object also changes [9]. Reference [10] proposes the data fusion scheduling and operation and maintenance management based on Naive Bayesian in cloud computing environment for the big data classification of distributed marine green energy grid-connected system. This method extracts semantic relevance and rule characteristics of big data of distributed marine green energy grid-connected system, and carries out the fusion scheduling and operation and maintenance management for the characteristics, and improves the precision of distributed marine green energy grid-connected system large database retrieval. But with the increase of distributed marine green energy grid-connected system large scale database, the accuracy of information fusion scheduling and operation and maintenance management is not good. Reference [11] proposes the method of big data fusion scheduling with operation and maintenance management of distributed marine green energy grid-connected system in cloud model combined fusion scheduling with operation and maintenance management. This method uses multi strategy similarity calculation for the substructure information feature modeling of big database in distributed marine green energy grid-connected system big data information, and realizes the collaborative recommendation fusion scheduling and operation and maintenance management of big data query and access in distributed marine green energy grid-connected system, but this method under similar information interference has low accuracy of big data information fusion of grid-connected system, and has no data dimension reduction, resulting in large computational overhead.

Aiming at the above problems, this paper proposed a big data analysis method of distributed marine green energy resources grid-connected system based on closed-loop information fusion and auto correlation characteristic information mining. This method realized the big data closed-loop operation and maintenance management of grid-connected system, and firstly built the big data information collection model of marine green energy resources grid-connected system, and reconstructs the feature space of the collected big data, and constructed the characteristic equation of fuzzy data closed-loop operation and maintenance management in convex

spaces, and then used the adaptive feature fusion method to achieve the auto correlation characteristics mining of big data operation and maintenance information, and improved the ability of information scheduling and information mining of distributed marine green energy resources grid-connected system, finally, we got valid conclusion from the simulation experiment analysis of big data analysis, which show the superior performance of this method in improving the big data analysis and operation and maintenance management ability of distributed marine green energy resources grid-connected system.

## BIG DATA STRUCTURE ANALYSIS AND FEATURE SELECTION OF MARINE GREEN ENERGY GRID-CONNECTED SYSTEM

### OVERALL FRAMEWORK OF LARGE DATA ANALYSIS OF MARINE GREEN ENERGY GRID-CONNECTED SYSTEM

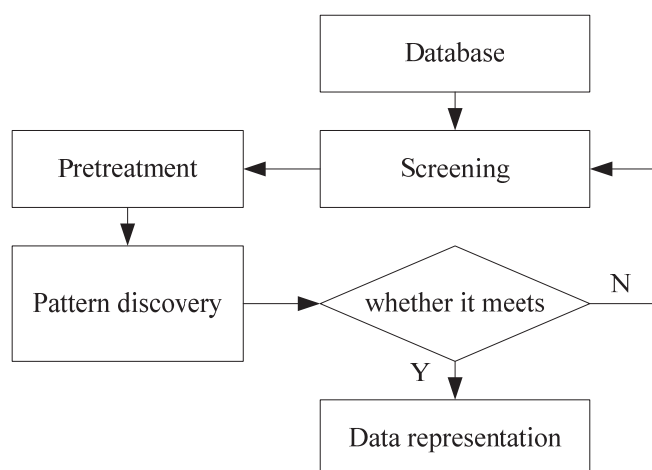


Fig. 1. Big data mining process of marine green energy resources grid-connected system.

In order to realize the integrated feature extraction and data fusion scheduling of big data of distributed marine green energy resources grid-connected system, we achieve the big data operation and maintenance management and pattern recognition of marine green energy resources grid-connected system through big data analysis method. Firstly, we build big data information acquisition model of marine green energy resources grid-connected system, and carry out the feature space reconstruction of collected big data, and combines with feature extraction methods for data mining, achieving the selective preference and data mining of big data feature in marine green energy resources grid-connected system. Data mining is used to analyze big data of grid-connected system. Data mining (DM) is the process of finding target data from massive data [12]. The massive data has a lot of interference options and the fuzziness and randomness. The location of target data is unknown, which is hidden in massive data, and

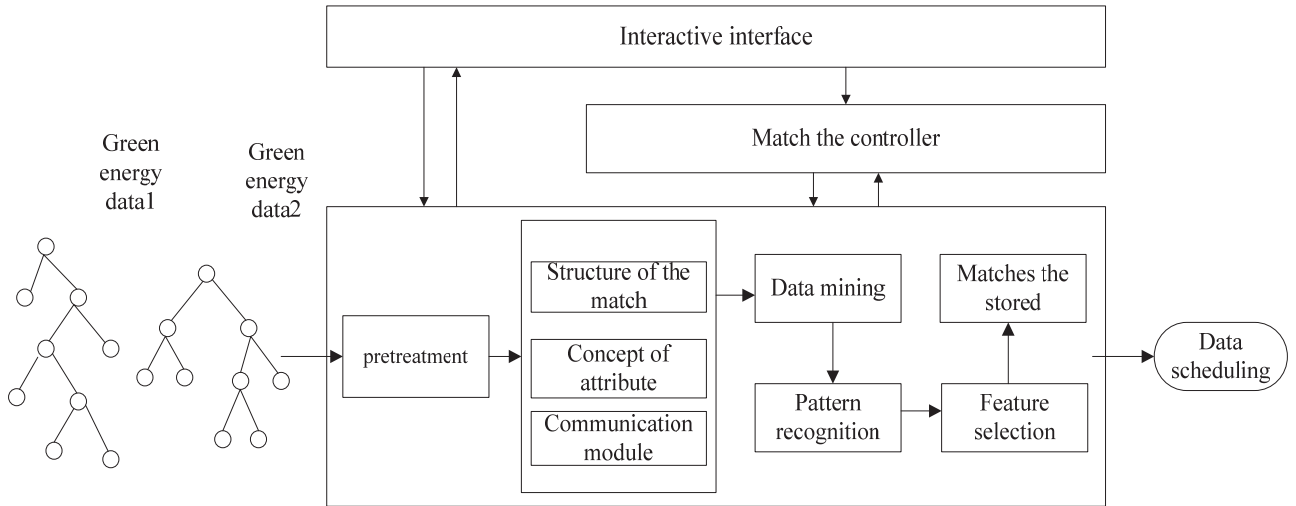


Fig. 2. Big data analysis model of marine green energy resources grid-connected system.

the class is unknown. In the big data analysis of green energy resources grid-connected system, we need to perform the data screening, the data preprocessing, the pattern extraction, the pattern analysis and the data application, to achieve the big data mining of marine green energy resources grid-connected system [13]. According to the above analysis, we build the big data analysis model of marine green energy resources grid-connected system, as shown in Fig. 2.

### BIG DATA INFORMATION COLLECTION MODEL

The Takens embedding theorem is used to reconstruct the phase space and the feature, and a clustering model of big data distribution of distributed marine green energy resources grid-connected system is obtained. [14-16].

Takens theorem: let  $M$  be the  $d$ -dimensional compact manifold.  $F$  is a smooth vector field.  $h$  is a smoothing function on  $M$ , and that is  $M \rightarrow R^{2d+1}$ , which shows that  $\Phi(z) = (h(z), h(\varphi_1(z)), \dots, h(\varphi_{2d}(z)))^T$  is an embedded vector.

For big data sampling time series  $\{x(t_0 + i\Delta t)\}$ ,  $i = 0, 1, \dots, N-1$  of distributed marine green energy resources grid-connected system, its phase space reconstruction trajectory is:

$$X = [x(t_0), x(t_0 + \Delta t), \dots, x(t_0 + (K-1)\Delta t)]$$

$$= \begin{bmatrix} x(t_0) & x(t_0 + \Delta t) & \dots & x(t_0 + (K-1)\Delta t) \\ x(t_0 + J\Delta t) & x(t_0 + (J+1)\Delta t) & \dots & x(t_0 + (K-1)\Delta t + J\Delta t) \\ \vdots & \dots & \ddots & \dots \\ x(t_0 + (m-1)J\Delta t) & x(t_0 + (1+(m-1)J)\Delta t) & \dots & x(t_0 + (N-1)\Delta t) \end{bmatrix}$$

(1)

Among them,  $x(t)$  represents the state vector of the embedding space.  $J$  is the reconstruction delay,  $m$  is the embedding dimension,  $\Delta t$  is the time interval of sampling,  $K = N - (m-1)J$ , and  $\tau$  represents the delay parameter,  $\tau = J\Delta t$ .  $\tau_w = (m-1)\tau = (m-1)J\Delta t$  is time window. We can see that in reconstructing phase space, we only select any

two parameters in  $m$ ,  $\tau$  and  $\tau_w$ , another parameter can be obtained directly by  $\tau_w = (m-1)\tau$ .

In the Laplace convex optimization space [17], we constructs the high-order linear differential equation combination model of fuzzy data closed loop operation and maintenance management:

$$B_l(A) = \min_{\beta \neq 0} \{w(\beta) + w(A^T \cdot \beta)\} \quad (2)$$

In formulas,  $A^T$  represents the transpose of matrix  $A$ . Simultaneous equation solving gets the solution of the equations:  $c_1 = -c_{-1} = 0.675$ ,  $c_2 = -c_{-2} = -2^{1/3} c_1 = -0.85$ , for  $s, \tilde{s} \geq 0$ , there is the mapping  $T: U \rightarrow U$ . The characteristic solution  $\forall u(t) \in U$  in variable kernel convex space solution obtains the objective function of big data clustering through constructing the expectation function of fuzzy data distributed distributed marine green energy resources grid-connected system closed loop operation and maintenance management in convex space:

$$\max_{x_{a,b,d,p}} \sum_{a \in A} \sum_{b \in B} \sum_{d \in D} \sum_{p \in P} x_{a,b,d,p} V_p \quad (3)$$

$$\text{s.t.} \quad \sum_{a \in A} \sum_{d \in D} \sum_{p \in P} x_{a,b,d,p} R_p^{bw} \leq K_b^{bw}(S), b \in B \quad (4)$$

$$\sum_{a \in A} \sum_{b \in B} \sum_{p \in P} x_{a,b,d,p} R_p^{cp} \leq K_d^{cp}(S), d \in D \quad (5)$$

$$\sum_{b \in B} \sum_{d \in D} x_{a,b,d,p} \leq \Delta_{a,p}, a \in A, p \in P \quad (6)$$

$$\sum_{d \in D} \sum_{p \in P} x_{a,b,d,p} \leq M \alpha_{a,b}, a \in A, b \in B \quad (7)$$

$$\sum_{b \in B} x_{a,b,d,p} \leq M \beta_{a,d,p}, a \in A, d \in D, p \in P \quad (8)$$

$$x_{a,b,d,p} \geq 0, a \in A, b \in B, d \in D, p \in P \quad (9)$$

According to the above data acquisition model, we carry out the big data analysis. The data analysis involves many techniques and methods, this paper uses fuzzy neural network classification decision method to classify the data, and builds the high dimensional feature space distribution structure model of distributed marine green energy resources grid-connected system big data.

## BIG DATA CLASSIFICATION AND HIGH DIMENSIONAL INFORMATION REORGANIZATION

We extract the feature vector of correlative dimension of distributed marine green energy resources grid-connected system big data in the phase space, and carry out the ensemble feature selection of data. In the reconstructed distributed marine green energy resources grid-connected system big data distribution phase space, and uses the nonlinear time series analysis method for the feature selection of correlative dimension [18]. For distributed marine green energy resources grid-connected system big data sequence  $x_1, x_2, \dots, x_n, \dots$ , we set the total number of points as  $N$ , the sampling time span of sequential  $\{x_i\}$  is  $j\tau$ , and its autocorrelation function is:

$$R_{xx}(j\tau) = \frac{1}{N} \sum_{i=0}^{N-1} x_i x_{i+j\tau} \quad (10)$$

Thus, we can fix  $j$  and make the correlation function about time  $\tau$  (taking  $\tau = 1, 2, \dots$ ), and the finite data set  $X$  is divided into  $c$  class according to the time delay of the big data embedding, among them  $1 < c < n$ , and the fuzzy clustering central matrix is defined as:

$$V = \{v_{ij} | i = 1, 2, \dots, c, j = 1, 2, \dots, s\} \quad (11)$$

$V_i$  is the  $i$ -th vector of the cluster center (the  $i$ -th cluster center vector). The fuzzy partition matrix is represented as:

$$U = \{\mu_{ik} | i = 1, 2, \dots, c, k = 1, 2, \dots, n\} \quad (12)$$

To construct the ontology model which reflects the associated feature of distributed marine green energy resources grid-connected system big data [19], the relative weight of distributed marine green energy resources grid-connected system big data is  $\omega = ((\omega_1, a_1), (\omega_2, a_2), \dots, (\omega_n, a_n))^T$ ,  $\omega_j \in [0, 1]$  and we use the average mutual information method to obtain the objective function that the data association is the features extraction:

$$J_m(U, V) = \sum_{k=1}^n \sum_{i=1}^c \mu_{ik}^m (d_{ik})^2 \quad (13)$$

In the formula,  $m$  is the weight index.  $(d_{ik})^2$  is the measuring distance between the sample  $x_k$  and  $V_i$ , which is expressed by Euclidean distance:

$$(d_{ik})^2 = \|x_k - V_i\|^2 \quad (14)$$

and

$$\sum_{i=1}^c \mu_{ik} = 1, k = 1, 2, \dots, n \quad (15)$$

Combining with the decision function of association mapping, the differential control coefficient of feature extraction of correlation dimension of distributed marine green energy resources grid-connected system big data is obtained by using Lagrange theorem:

$$\mu_{ik} = \frac{1}{\sum_{j=1}^c (d_{ik}/d_{jk})^{\frac{2}{m-1}}} \quad (16)$$

$$V_i = \frac{\sum_{k=1}^m (\mu_{ik})^m x_k}{\sum_{k=1}^n (\mu_{ik})^m} \quad (17)$$

The maximal linearly independent subset of distributed marine green energy resources grid-connected system big data closed loop operation and maintenance management is obtained, for an arbitrary set of data geometry  $i$ ,  $s_i^*$  is the least square fitting vector, the feature solution  $\forall u(t) \in U$  in kernel convex spaces satisfies the maximum Lyapunov functional, through construction of the fuzzy feature subset of the massive information, we get the iterative acceleration formula of big data classification of marine green energy resources grid-connected system:

$$(1 - \omega)x_i^{(k)} + \omega x_i^{-(k+1)} = x_i^{(k+1)}, i = 1, 2, \dots, n \quad (18)$$

In clustering sample sets, we add or delete sample  $A$  or  $B$ , and for fuzzy data sample set  $A, B$ , the convergence control function of fuzzy data closed loop operation and maintenance management in massive information is obtained under the control of attenuation constant  $T_1$  and  $T_2$ :

$$x_i^{(k+1)} = (1 - \omega)x_i^{(k)} + \frac{\omega}{a_{ni}} \left( b_i - \sum_{j=1}^{i-1} a_{ij} x_j^{(k+1)} - \sum_{j=i+1}^n a_{ij} x_j^{(k)} \right) \quad (19)$$

$$i = 1, 2, \dots, n$$

$$k = 1, 2, \dots, n$$

We use the support vector machine model to obtain the initial clustering center of big data clustering. The initial value the data fusion center has been given, we adjust the parameter  $c$  of clustering attributes classification and the fuzziness index  $m$ , and carry out the feature compression processing, reducing the dimension of feature selection, so as to reduce the computational overhead of data fusion scheduling and operation and maintenance management [20]. According to the data classification results, we use the following five steps for high dimensional information reorganization:

(1) we firstly select a  $k$  value to determine the total number of recombination clusters of high dimensional information. If the data set is  $m$ , order  $A_j(L)$  as the center of the cluster, among them,  $j = 1, 2, \dots, k$ . the distance to the cluster center is calculated;

- (2) select  $k$  examples in the data set, and initialise cluster centers  $F(x_i, A_j(L)), i = 1, 2, \dots, m, j = 1, 2, \dots, k$  ;  
 (3) use the simple Euler distance to assign the remaining clusters to the nearest cluster center, if satisfied:

$$D(x_i, A_j(L)) = \min\{D(x_i, A_j(L))\} \quad (20)$$

Thus  $x_i \in \omega_k$  ;

(4) in the massive information storage space, supposing a sample  $i \in S_s$ , let  $\beta_i^c \neq \pm\infty$ , when the stationary vector set  $\det(Q^i) = 0$  of the standard data set, through adaptive weighting of clustering center of massive data, when  $\forall i \in S_s$ , we can get  $\beta_i^c \neq \pm\infty$ . In convex optimization space, we carry out the self-adaptive adjustment of data clustering center, we can get:  $\forall i \in S - S_s, \gamma_i^c \neq \pm\infty$  in the sample updating process of set  $S_s$ , we use the example of each cluster to calculate the average value as the average value of new cluster:

$$C(l) = \sum_{j=1}^k \sum_{k=1}^{n_j} (\|x_k^j - A_j(L)\|)^2 \quad (21)$$

(5) if the average value is equal to the average value of the last iteration,  $\|C(l) - C(l-1)\| < \xi$ , the program is stopped, otherwise return to third step, let  $l=l+1$ , and the new cluster heart is calculated:

$$A_j(L+1) = \frac{1}{n_j} \sum_{i=1}^k X_i^j \quad (22)$$

## BIG DATA CLOSED LOOP OPERATION AND MAINTENANCE MANAGEMENT OF DISTRIBUTED MARINE GREEN ENERGY RESOURCES GRID-CONNECTED SYSTEM

### FUZZY DATA CLOSED-LOOP OPERATION AND MAINTENANCE INFORMATION FUSION

This paper proposes a big data analysis method of distributed marine green energy resources grid-connected system based on and closed loop information fusion and auto correlation feature information mining, realizing the big data closed-loop operation and maintenance management of grid-connected system [21]. In the convex space, we build the characteristic equation of fuzzy data closed loop operation and maintenance management, and the global fluctuation combination stable solution of high order linear differential equation of data closed loop operation and maintenance management of closed loop system satisfies  $\forall i \in S_s, \beta_i^c \neq \pm\infty$ , and  $\forall i \in S - S_s, \gamma_i^c \neq \pm\infty$ . For  $\forall i \in S_s$ , the the dual periodic solitary wave solution of data closed-loop operation and maintenance management is:

$$\beta_i^c = -\sum_{k \in S_s} R_{ik} Q_{kc} - R_{il} Y_c$$

$$= -\frac{1}{\det(Q^i)} \left( \sum_{k \in S_s} (-1)^{i+k} \det(Q_{\setminus ki}^i) Q_{kc} + Y_c (-1)^{i+1} \det(Q_{i1}^i) \right) \quad (23)$$

To build a set of homogeneous equations for  $\hat{H}_x^s$ -global strong stable functional, when the extremal functional formulas of polynomial kernel function and Gaussian kernel function satisfy  $d = 4, s_c = \frac{3}{2}$ , maximal linearly independent set expressions of fuzzy data closed-loop operation and maintenance management respectively are :

$$K(x_i, x_j) = \langle x_i, x_j \rangle \quad (24)$$

$$K(x_i, x_j) = (\langle x_i, x_j \rangle + 1)^d \quad (25)$$

$$K(x_i, x_j) = \exp(\|x_i - x_j\|^2 / 2\sigma^2) \quad (26)$$

For distributed marine green energy resources grid-connected system big data sequence  $\{x_n\}_{n=1}^N$  of single variable, in the reconstruction of the  $m$ -dimensional phase space dimension, the distance form phase point  $x_j$  to  $x_i$ , besides  $x_i$  itself is less than the  $x_j$  points of  $r$  which is expressed as:

$$Q = \sum_{j \neq i} H(r - \|x_i - x_j\|) \quad (27)$$

$H(\cdot)$  represents the Heavside function. That is:

$$H(x) = \begin{cases} 0, & x \leq 0 \\ 1, & x > 0 \end{cases} \quad (28)$$

We set the sampling point number of one-dimensional distributed marine green energy resources grid-connected system big data is  $n$ . The number of vector points in the reconstructed phase space is  $N = n - (m-1)\tau$ , and we calculate the number of related phase point pair in the phase points. The ratio of all possible pairs of  $N(N-1)/2$  matches is called association integral:

$$C_m(r) = \frac{2}{N(N-1)} \sum_{i=1}^N \sum_{j=i+1}^N H(r - \|x_i - x_j\|) \quad (29)$$

When the amount of data is  $N \rightarrow \infty$  and the distance  $r$  is small, that is  $r \rightarrow 0$ , if the correlation integral  $C_m(r)$  is obeyed by the exponential law, the correlation dimension features of the big data of distributed marine green energy resources grid-connected system is obtained as follows:

$$D = \frac{\ln C_m(r)}{\ln r} \quad (30)$$

In the calculation, the range  $r_{\min}$  and  $r_{\max}$  of  $r$  value is usually given, according to a certain growth rate to change

$r$ , and then start to increase from 1, increase 1 every time, gradually increase it to  $m_{\max}$ , we uses the adaptive feature fusion method to achieve the self correlation feature mining of big data operation and maintenance information. The MOLAP method can be used for data scheduling of distributed marine green energy resources grid-connected system, which is faster than other traditional analytical techniques and can be predicted [22].

In the closed-loop operation and maintenance management of fuzzy data, it is divided into data ETL layer, data storage layer, data analysis layer and application layer. [23]

### SELF CORRELATION FEATURES MINING OF BIG DATA OPERATION AND MAINTENANCE INFORMATION

We reduce the dimension for extracted integrated feature of correlation dimension of distributed marine green energy resources grid-connected system big data, and realize the autocorrelation feature mining of the big data operation and maintenance information, and use the K-L feature compression method for reducing the dimension [24-26], realizing the selective preference control of ensemble features of distributed marine green energy resources grid-connected system big data. The steps can be summarized as follows:

(1) calculate the intra-class dispersion matrix  $\hat{S}_w$  of  $l$ -dimensional feature vector  $\bar{X}(l, n_i)$  of distributed marine green energy resources grid-connected system big data, and find its  $l$  eigenvalues  $\lambda_1, \lambda_2, \dots, \lambda_l$  and eigenvectors matrix  $Y = [y_1, y_2, \dots, y_l]$ .  $\hat{S}_w$  is:

$$\hat{S}_w = \sum_{i=1}^c p_i \frac{1}{n_i} \sum_{k=1}^{n_i} \left[ \left( \bar{X}_k^{(i)} - \bar{m}_i \right) \left( \bar{X}_k^{(i)} - \bar{m}_i \right)^T \right] \quad (31)$$

Among them,  $p_i$  represents the prior probability of  $i$ -th categories of data fusion scheduling and operation and maintenance management attribute.  $n_i$  represents the number of samples of  $i$ -th categories of data fusion scheduling and operation and maintenance management attribute.  $\bar{m}_i$  represents the data represent the mean vector of  $n_i$ -th sample feature vector set  $\left\{ \bar{X}_k^{(i)}, k = 1, 2, \dots, n_i \right\}$  of  $i$ -th categories;

(2) compute the between-class scatter matrix of fusion scheduling and operation and maintenance management of distributed marine green energy resources grid-connected system :

$$S_b = \sum_{i=1}^c p_i \left( \bar{m}_i - \bar{m} \right) \left( \bar{m}_i - \bar{m} \right)^T \quad (32)$$

Among them,  $\bar{m} = \sum_{i=1}^c p_i \bar{m}_i$  is the ensemble average;

(3) calculate the average distance between classes:

$$J(\bar{X}_j) = \frac{y_j^T S_b y_j}{\lambda_j} \quad (33)$$

And put them in descending order:

$$J(\bar{X}_1) \geq J(\bar{X}_2) \geq \dots \geq J(\bar{X}_l);$$

(4) if it is reduced to  $d$  dimension, then we take top  $d$  larger eigenvectors  $y_j$  corresponding to  $J(\bar{X}_j)$ ,  $j = 1, 2, \dots, d$  and the transformation matrix is generated:

$$W = [y_1, y_2, \dots, y_d] \quad (34)$$

(5) considering the point which is satisfied  $|i - j| \geq \omega$ , the dimension reduction output results of the extracted feature vector of correlation dimension is obtained by K-L transform:

$$\bar{X}^* = W^T \bar{X} \quad (35)$$

Through the above processing, the correlation dimension feature vector of the big data of the distributed marine green energy resources grid-connected system is reduced to  $d$  dimension form  $l$  dimension, thus reducing the complexity and memory overhead of the fusion scheduling and the operation and maintenance management calculation.

Based on the principle of singular positive semidefinite, the quadratic programming model of support vector machines fuzzy data closed-loop operation and maintenance management is established. Suppose the matrix  $Q$  is positive semidefinite matrix:

$$\alpha = (\alpha_1, \alpha_2, \dots, \alpha_n) \neq 0 \quad (36)$$

The homogeneous solution of fuzzy data closed loop operation and maintenance management support vector machine model satisfies:

$$\alpha^T Q \alpha = \sum_{i=1}^n \sum_{j=1}^n \alpha_i \alpha_j Q_{ij} \geq 0 \quad (37)$$

Suppose there is  $n$  samples in the information data set  $S_s$ , then:

$$Q = \begin{bmatrix} 0 & y_1 & \dots & y_n \\ y_1 & Q_{11} & \dots & Q_{1n} \\ \vdots & \vdots & \ddots & \vdots \\ y_n & Q_{n1} & \dots & Q_{nn} \end{bmatrix} \stackrel{def}{=} \begin{bmatrix} 0 & y^T \\ y & Q \end{bmatrix} \quad (38)$$

According to the above hypothesis, we can see that the distribution matrix  $Q$  of periodic point is positive definite, and obtain the inverse matrix  $Q^{-1}$  of  $Q$ ,  $Q^{-1}$  is also the positive definite matrix at the same time. Because:

$$\begin{bmatrix} 0 & -y^T Q^{-1} \\ 0 & I_n \end{bmatrix} \begin{bmatrix} 0 & y^T \\ y & Q \end{bmatrix} = \begin{bmatrix} -y^T Q^{-1} & 0 \\ y & Q \end{bmatrix} \quad (39)$$

The fuzzy degree point set of massive fuzzy data, closed-loop operation and maintenance management satisfies:

$$\det(Q) = \det(Q) \cdot (-y^T Q^{-1}) \neq 0 \quad (40)$$

For the utility value of a single distributed marine green energy resources grid-connected system, the utility value model formula is:

$$Y(\text{Utility value}) = \sum f(x_i) \quad (i \text{ represents } 1, \dots, n\text{-th Electric energy meter after Notional Pooling})$$

$$f(x_i) = j(x_i) + s(x_i)$$

Among them, the solution result of cluster centers of closed loop operation and maintenance management is:

$$a_{ii}x_i^{(k+1)} = (1-\omega)a_{ii}x_i^{(k)} + \omega \left( b_i - \sum_{j=1}^{i-1} a_{ij}x_j^{(k+1)} - \sum_{j=i+1}^n a_{ij}x_j^{(k)} \right) \quad (41)$$

For selected feature vector, we use the random forest fusion scheduling and operation and maintenance management method for feature fusion scheduling and operation and maintenance management, to get a homogeneous vector group that the clustering center of distributed marine green energy resources grid-connected system big data is the quadratic programming [25].

$$(D - \omega L)x^{(k+1)} = [(1-\omega)D + \omega U]x^{(k)} + \omega b \quad (42)$$

$$x^{(k+1)} = (D - \omega L)^{-1} [(1-\omega)D + \omega U]x^{(k)} + \omega(D - \omega L)^{-1} b \quad (43)$$

Let:

$$\begin{cases} L_\omega = (D - \omega L)^{-1} [(1-\omega)D + \omega U] \\ f_\omega = (D - \omega L)^{-1} b \end{cases} \quad (44)$$

Thus, the convergence process of the fuzzy directional clustering of the test data satisfies:

$$x^{(k+1)} = L_\omega x^{(k)} + f \quad (45)$$

There is the Local optimal solution of big data fusion in grid connected system:

$$\begin{aligned} \frac{x_k - \alpha}{x_{k-1} - \alpha} &\approx \frac{x_{k+1} - \alpha}{x_k - \alpha} \\ (x_k - \alpha)^2 &\approx (x_{k+1} - \alpha)(x_{k-1} - \alpha) \\ x_k^2 - 2\alpha x_k - \alpha^2 &\approx x_{k+1}x_{k-1} - \alpha(x_{k-1} + x_{k+1}) + \alpha^2 \\ x_k^2 - x_{k+1}x_{k-1} &\approx \alpha(2x_{k-1} - x_{k+1} - x_{k-1}) \end{aligned} \quad (46)$$

We take the cluster centers obtained from the support vector machine model as the neighborhood data set, and the training template set is constructed. The quadratic programming of convex combination method is carried out for Lyapunov functional:

$$\alpha \approx \frac{x_{k+1}x_{k-1} - x_k^2}{x_{k-1} - 2x_k + x_{k+1}} = x_{k+1} - \frac{(x_{k+1} - x_k)^2}{x_{k-1} - 2x_k + x_{k+1}} \quad (47)$$

Among them:

$$\bar{x}_k = x_{k+1} - \frac{(x_{k+1} - x_k)^2}{x_{k-1} - 2x_k + x_{k+1}} \quad (48)$$

The expected output of fuzzy K means clustering is:

$$E_i((s_j^*, (s_i^*)_{i \in N \setminus \{j\}})) = \sum_{j=1}^m \sum_{k=1}^l p(x_{j_i}) \cdots p(x_{j_w}) u_{ki} \quad (49)$$

Through the above processing, we select a certain basic function to return the redundant data to the set, and fuzzy data closed-loop operation and maintenance management is realized. The method of adaptive feature fusion is used to realize the self correlation feature mining of big data operation and maintenance information.

#### 4. Simulation experiment and result analysis

In order to test the application performance of this method in the implementation of the information fusion and the data scheduling and other big data analysis of distributed marine green energy resources grid-connected system, we carry out the simulation experiment. The experimental hardware platform uses Intel i5-3230M 2.6GHz dual core CPU, RAM4GB DDR3, operating system is Windows 7, and editing software of algorithm is VC++ and Matlab. The experimental database of distributed marine green energy resources grid-connected system is CUP2016 grid-connected database of KDD. We carry out the big data feature information sampling of distributed marine green energy resources grid-connected system in the database. The normalized initial sampling frequency is  $f_1 = 0.8$  Hz. Termination frequency is  $f_2 = 0.15$  Hz. The training tree of random forest is 10, and the maximum step number of iterations is  $NP = 30$ . The embedding dimension of phase space reconstruction is  $m=4$ . Embedding time-delay parameter is  $\tau=11$ , sampling interval is 0.25 s. The sampling points are 1000 points. There is a 250Hz intra-class attribute difference unbalanced data data frequency component between the 400~600 sampling points. We take the frequency domain characteristic parameters of big data distribution  $\sigma = 10$ ,  $b = 8/3$ ,  $r = 28$ , and select the initial value  $[x_0, y_0, z_0] = [2, 2, 20]$ , integration step  $h = 0.01$ , and use four-order Rung-Kutta method to solve the characteristic equation of big data distribution for the optimum selection control of clustering information fusion center feature. When carrying out the recursive analysis, we take the parameters of phase space reconstruction  $m = 3$ ,  $\tau = 8$ , the threshold  $\varepsilon = 0.2\text{std}(x)$ , among them,  $\text{STD}(x)$  represents the standard deviation of the time series,  $l_{\min} = 3$ . According to the simulation environment and parameter settings, the big data raw data sampling of the distributed marine green energy resources grid-connected system is carried out, and the time domain waveform of data sampling is shown in Fig. 3.

Taking the above sampling data as the research object, we extract the correlation dimension integrated feature of data, and directly input the selected feature quantity to the big data information fusion scheduling and operation and maintenance manager for data fusion scheduling and operation and maintenance management, to achieve big data classification recognition of grid-connected system, and the data classification results are shown in Fig. 4.

The analysis results of Fig. 4 show that using this method for big data classification can realize data fusion scheduling and the operation and maintenance management, and can effectively realize the classification and recognition of big data, and improves the adaptive analysis and processing ability of big data of distributed marine green energy resources

grid-connected system. In order to quantitatively analyze the application performance of the proposed method for big data classification processing, Table 1 lists the performance comparison of distributed marine green energy resources grid-connected system big data analysis in different methods [27-30]. From the analysis, the proposed method classifies distributed marine green energy resources grid-connected system big data, which reduces the misclassification rate, and shortens the time of analysis processing of big data, and improves the ability of parallel scheduling of big data, and ameliorates the output performance of the grid-connected system [31,32].

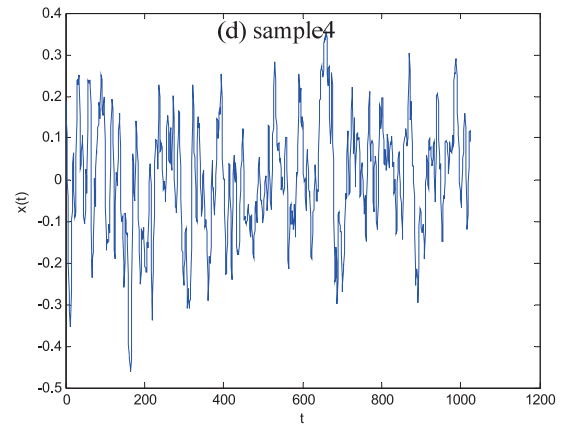
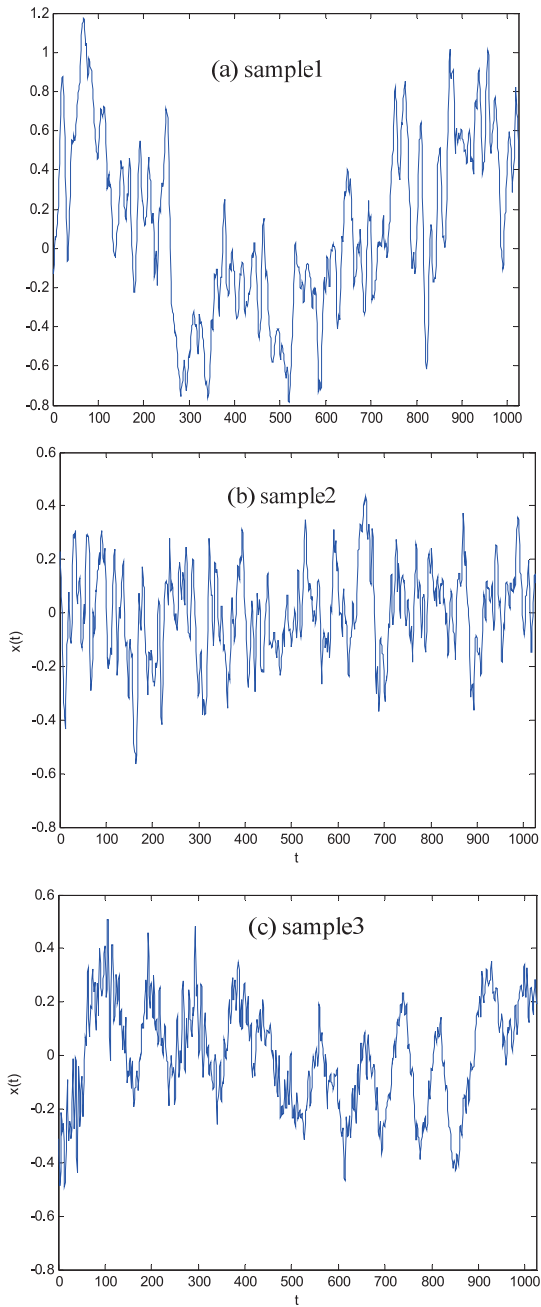
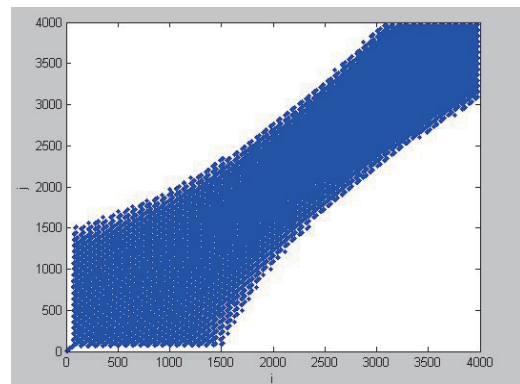
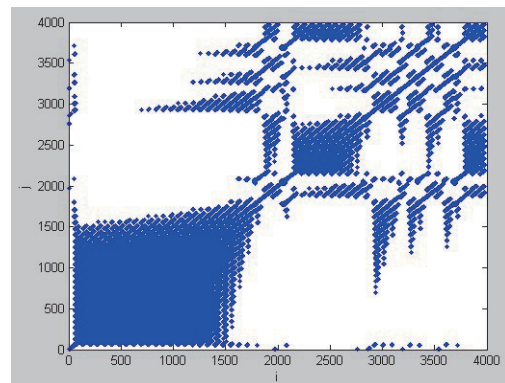


Fig. 3. Time domain waveform of big data sampling of distributed marine green energy resources grid-connected system.

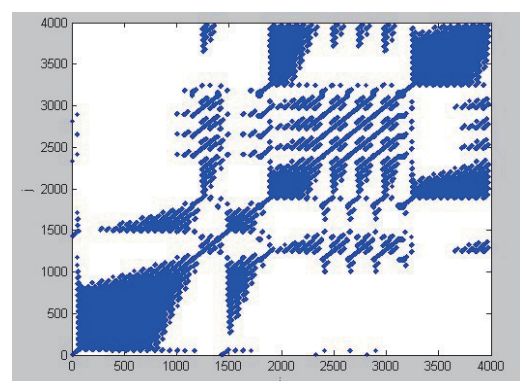
(a)sample1



(b)sample2



(c) sample3



(d)sample4

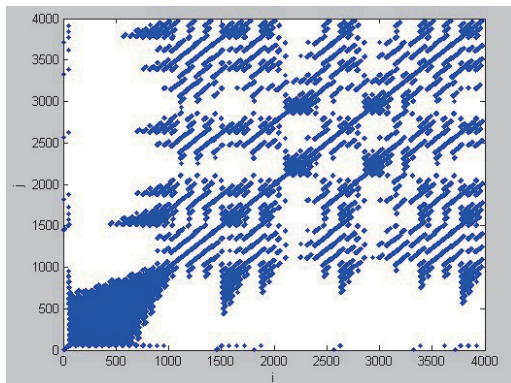


Fig. 4. Big data classification results of distributed marine green energy resources grid-connected system.

Table 1. Performance comparison of big data analysis and processing.

| Test sample | Proposed method           |                   | Traditional method        |                   |
|-------------|---------------------------|-------------------|---------------------------|-------------------|
|             | Misclassification rate /% | Computing time /s | Misclassification rate /% | Computing time /s |
| 1           | 0.14                      | 1.15              | 1.32                      | 16.32             |
| 2           | 0.11                      | 1.32              | 2.21                      | 10.21             |
| 3           | 0.02                      | 2.12              | 3.21                      | 12.33             |
| 4           | 0.03                      | 1.09              | 5.43                      | 9.09              |

## CONCLUSIONS

This paper studies the data mining, classification and identification in big data analysis of distributed marine green energy resources grid-connected system, and carries out the information integration and recognition of distributed marine green energy resources grid-connected system based on big data analysis method, improving the output performance of energy resources grid-connected system. This paper proposed a big data analysis method of distributed marine green energy resources grid-connected system based on closed-loop information fusion and auto correlation characteristic information mining. This method realized the big data closed-loop operation and maintenance management of grid-connected system, and built the big data information collection model of marine green energy resources grid-connected system, and reconstructs the feature space of the collected big data, and constructed the characteristic equation of fuzzy data closed-loop operation and maintenance management, and used the adaptive feature fusion method to achieve the auto correlation characteristics mining of big data operation and maintenance information, and improved the ability of information scheduling and information

mining of distributed marine green energy resources grid-connected system. The research results show that using this method for the big data analysis of distributed marine green energy resources grid-connected system and using the multidimensional analysis technology of big data can improve the ability of information scheduling and information mining of distributed marine green energy resources grid-connected system, realizing the information optimization scheduling of grid-connected system, and it has positive benefits on improving the output performance of grid-connected system.

## REFERENCES

1. M. Ceci, D. Malerba, 2007. Classifying Web documents in a hierarchy of categories: a comprehensive study. *Journal of Intelligent Information System*, 28(1): 37-78.
2. H. X. Wang, S. Y. Wang, X. Wang, et al. 2014. Analysis of LFM signals and improvement of IFM system. *Acta Armamentarii*, 35(8): 1193-1199.
3. M. A. Govoni, H. Li, J. A. Kosinski, 2013. Range-Doppler resolution of the linear-FM noise radar waveform. *IEEE Transactions on Aerospace and Electronic Systems*, 49(1): 658-664.
4. J. H. Lu, X. Han, J. X. Li, 2016. Consensus-based distributed fusion estimator with communication bandwidth constraints. *Control and Decision*, 31(12): 2155-2162.
5. M. Huang, L. T. Wang, H. C. Zhang, 2016. Face Recognition Based on Gabor Wavelet Transform and K-L Gaussian Riemannian Manifold Discriminant. *Computer Engineering*, 42(9): 208-213.
6. H. Hao, 2013. Multi component LFM signal detection and parameter estimation based on EEMD-FRFT. *Optik-International Journal for Light and Electron Optics*, 124(23): 6093-6096.
7. M. A. Govoni, H. Li, J. A. Kosinski, 2013. Range-Doppler resolution of the linear-FM noise radar waveform. *IEEE Transactions on Aerospace and Electronic Systems*, 49(1):658-664.
8. Y. Y. Fu, M. Zhang, D. G., Feng et al. 2014. Attribute privacy preservation in social networks based on node anatomy. *Journal of Software*, 25(4): 768-780.
9. D. G. Feng, M. Zhang, H. Li, 2014. Big data security and privacy protection. *Chinese Journal of Computers*, 37(1): 246-258.
10. J. Song, G. Y. Xu, R. P. Yao, 2016. Anonymized data privacy protection method based on differential privacy. *Journal of Computer Applications*, 36(10): 2753-2757.

11. C. Hazay, K. Nissim, 2012. Efficient set operations in the presence of malicious adversaries. *Journal of Cryptology*, 25(3):383-433.
12. Y. Pan, Y. Tang, H. Liu, 2012. Access control in very loosely structured data model using relational databases. *Acta Electronica Sinica*, 240(3): 600-606.
13. A. Rahman, H. Muhammah, L. Sungyoung, et al. 2015. Rough set-based approaches for discretization: a compact reviews. *Artificial Intelligence Review*, 44(2): 235-263.
14. Y. H. Qian, H. Zhang, Y. Sang, et al. 2014. Multigranulation decision-theoretic rough sets. *International Journal of Approximate Reasoning*, 55(1): 225-237.
15. F. Xu, J. J. Ma, 2015. Improvement of Threshold RSA Signature Scheme Based on Chinese Remainder Theorem. *JEIT*, 37(10): 2495-2500.
16. P. Curt, R. J. Thomas, S. Deming, 2012. A high-fidelity harmonic drive model. *ASME J of Dynamic Systems, Measurement, and Control*, 134(1): 457-461.
17. S. Ali, R. Ali, A. Iftikhar, 2017. Physico-chemical and microbiological assessment of some freshwater aquifers and associated diseases in district ghizer, gilgit-baltistan, Pakistan. *Acta Scientifica Malaysia*, 1(1): 08-12.
18. Y. Pan, C. A. Yuan, W. J. Li, M. H. Cheng, 2016. Access Control Method for Supporting Update Operations in Dataspace. *JEIT*, 38(8): 1935-1941.
19. M. J. Guo, Y. Huang, Z. Xie, 2013. A WebGIS Model Optimization Strategy under Multi-core Environment. *Computer Engineering*, 39(8): 15-19.
20. Y. Huang, J. Paisley, Q. Lin, et al. 2014. Bayesian nonparametric dictionary learning for compressed sensing MRI. *IEEE Transactions on Image Processing*, 23(12): 5007-5019.
21. L. Shen, G. Sun, Q. Huang, et al. 2015. Multi-level discriminative dictionary learning with application to large scale image classification. *IEEE Transactions on Image Processing*, 24(10): 3109-3123.
22. L. Shen, G. Sun, Q. Huang, et al. 2015. Multi-level discriminative dictionary learning with application to large scale image classification. *IEEE Transactions on Image Processing*, 24(10): 3109-3123.
23. J. J. Thiagarajan, K. N. Ramamurthy, A. Spanias, 2015. Learning stable multilevel dictionaries for space representations. *IEEE Transactions on Neural Networks & Learning Systems*, 26(9): 1913-1926.
24. J. Z. Jiang, F. Zhou, 2013. Iterative design of two-dimensional critically sampled MDFT modulated filter banks. *Signal Processing*, 93(11): 3124-3132.
25. N. Rajapakaha, A. Madanayake, Lt. 2014. Bruton, 2D space-time wave-digital multi-fan filter banks for sig[10]Gao, W. and W. Wang, The fifth geometric-arithmetic index of bridge graph and carbon nanocones. *Journal of Difference Equations and Applications*, 2017. 23(1-2SI): p. 100-109.
26. Gao, W., et al., Distance learning techniques for ontology similarity measuring and ontology mapping. *Cluster Computing-The Journal of Networks Software Tools and Applications*, 2017. 20(2SI): p. 959-968.nals consisting of multiple plane waves. *Multidimensional Systems and Signal Processing*, 25(1): 17-39.
27. H. Mahboubi, K. Moezzi, A. G. Aghdam, et al. 2014. Distributed deployment algorithms for improved coverage in a network of wireless mobile sensors. *IEEE Transactions on Industrial Informatics*, 10(1): 163-174.
28. N.S.A. Sukor, N. Jarani, S.F.M. Faisal, 2017. Analysis of Passengers' Access and Egress Characteristics to The Train Station. *Engineering Heritage Journal*, 1(2): 01-04.
29. S.C.A. Mana, M.M. Hanafiah, A.J.K. Chowdhury, 2017. Environmental characteristics of clay and clay-based minerals. *Geology, Ecology, and Landscapes*, 1(3): 155-161.
30. M. Bahmani, A. Noorzad, J. Hamed, F. Sali, 2017. The role of bacillus pasteurii on the change of parameters of sands according to temperatur compresion and wind erosion resistance. *Journal CleanWAS*, 1(2): 1-5.
31. N.A. Rahman, Z. Tarmudi, M. Rosssdy, F.A. Muhiddin, 2017. Flood Mitigation Measres Using Intuitionistic Fuzzy Dematel Method. *Malaysian Journal Geosciences*, 1(2):01-05.
32. R. Roslee, N. Simon, 2017. Rock Slopes Kinametic Analysis Along the Bundu Tuhan To Kundasang Highway, Sabah, Malaysia. *Geological Behavior*, 1(2):01-04.

#### CONTACT WITH THE AUTHOR

Jun Tian

*e-mail: 276154989@qq.com*

Foshan Polytechnic  
Foshan 528137  
CHINA

# MARINE SEARCH AND RESCUE OF UAV IN LONG-DISTANCE SECURITY MODELING SIMULATION

Lei Zheng <sup>1</sup>

Jianbo Hu <sup>1</sup>

Shukui Xu <sup>2</sup>

<sup>1</sup> College of Material Management and Safety Engineering, Air Force Engineering University, Xi'an 710051, China

<sup>2</sup> The 28th Research Institute of China Electronic Technology Group Corporation, Nanjing 210000, China

## ABSTRACT

*Long-distance safety of Marine search and rescue using drones can improve the searching speed. The current method is based on the long distance security classification of UAV. The degree of accuracy is low. A long-distance security modeling approach based on ArduinoMiniPro's Marine search-and-rescue applying UAV is proposed. The method puts the fault tree analysis and relevant calculation for risk identification into use. The main factors affecting the safety of unmanned aerial vehicle (UAV) are long-distance searching and rescuing. The experimental results show that the proposed method can effectively build modeling for the long-distance safety of the Marine search and rescue UAV.*

**Keywords:** Marine search and rescue, Unmanned aerial vehicle (UAV), Long distance security

## INTRODUCTION

As the integration of global economy, maritime transport, communication and tourism are booming, maritime search and rescue and related problems have become the focus of governments and economic entities [1]. Nowadays the rapid development of business, the terrestrial environment deteriorating, and the scarcity of resources are difficult problems. The vast ocean and its rich species have become the key to sustainable economic development. However, the frequent occurrence of marine disasters and a variety of marine disasters caused by inadequate management or training have become an urgent problem [3]. The high-occurrence shipwreck not only brings countless property loss and personal injury, but also causes serious pollution of the marine environment. In recent years, the global shipwrecks

are too numerous to mention. In 2000, there was a major shipwreck in Lusi fishery of Jiangsu province. When No. 03127 fishing boat was at berth, it was sunk in a fishing boat form Zhejiang, besides 3 rescued people, 9 people were missing in 12 people [4]. Accidents at sea can cause the immeasurable loss, which highlights the importance of maritime rescue [5]. The efficiency of maritime search and rescue has a very important role. The property and the life security are closely related to the benefits of the broad masses, every action of maritime search and rescue will affect the nerves of masses [6]. At present, what has the relatively high efficiency and accuracy of maritime search and rescue is the unmanned aerial vehicle search and rescue. It has less time-consuming and small deviation in marine search and rescue [7].

As a relatively emerging industry in recent years, the unmanned aerial vehicle has been applied to the fields of investigation, communications and surveillance. Now it has a very wide prospect in the civil fields about the marine applications, the forest fire prevention and the emergency rescue [8-9]. Compared with manned aircraft, the unmanned aerial vehicle has the advantages about the small size, the convenient operation, the low cost and the low requirement for using environment. It has new enlightenment to the development of maritime search and rescue technology [10-11]. The characteristics of rapid take-off and landing of the unmanned aerial vehicle makes it have no special requirements on the takeoff environment, so it can faster provide the surrounding environment of people in distress and geographical location information, thus narrowing the scope of the search and rescue and the scale of rescue, we don't need to spend a lot of time and resources to realize the search and rescue. But the safety of unmanned aerial vehicle in long distance has always been a problem that bothers people .

Reference proposes a long distance security modeling method of maritime search and rescue unmanned aerial vehicle based on visible spectrum. According to the long distance security model of current maritime search and rescue unmanned aerial vehicle, this method analyzes the related factors of long distance security of unmanned aerial vehicle. The Beidou system contains GPS satellite positioning, communication location system of Beidou satellite, Beidou unmanned aerial vehicles Server, Beidou integrated security controller. We research and analyze the safety of forced landing and the safety of aircraft failure in the process of the long distance search and rescue of unmanned aerial vehicles by using the above hardware. Thus the long distance security modeling of the maritime search and rescue unmanned aerial vehicle has been completed. The modeling method has the detailed hardware, but modeling speed is slow. Reference proposes a method of long distance security modeling method of maritime search and rescue unmanned aerial vehicle based on EKF. The establishment of dynamic networking of the maritime search and rescue unmanned aerial vehicle generates a dynamic multi-level security group management protocol according to the different levels of unmanned aerial vehicle long-distance security. The protocol designs the group key mechanism through the identity of each unmanned aerial vehicle, and divides the distance of unmanned aerial vehicle search and rescue at sea. The results are: the medium and long distance, the long distance and extra-long distance. The security is analyzed according to the grouping of the distance, and the modeling is realized by using the above protocol. The modeling method is simple, but there is a great deviation in the modeling of the long distance safety of unmanned aerial vehicle. Reference proposes a long distance security modeling method of maritime search and rescue unmanned aerial vehicle based on rules. According to the fuzziness of the unmanned aerial vehicle long distance safety index, we establish the fuzzy evaluation model of long distance security of unmanned aerial vehicle through the analytic hierarchy process and fuzzy evaluation method. For the characteristics

of long distance search, we research its potential safety hazard and classify it. This is convenient to classify and model the safety of unmanned aerial vehicle. Combined with examples, we carry out the experiments on this model. Experimental results show that the applicability of the modeling method is strong, but the correct rate of classification rate is low.

In view of above problems, this paper proposed a modeling method of the long distance security of maritime search and rescue unmanned aerial vehicle based on Arduino Mini Pro. Experimental results show that the proposed modeling method can efficiently model the long distance security of the marine search and rescue unmanned aerial vehicle, which has high practicability.

## **LONG DISTANCE SECURITY MODELING OF MARITIME SEARCH AND RESCUE UNMANNED AERIAL VEHICLE BASED ON ARDUINO MINI PRO**

In the process of maritime search and rescue, the environment of unmanned aerial vehicle is complex and diverse. Due to long flight, inevitably there will be security risks, so as to cause immeasurable loss [16-17]. Therefore, long distance security modeling of maritime search and rescue unmanned aerial vehicle is the priority among priorities in the development of unmanned aerial vehicle search and rescue. The basic for researching the long distance security is the identification of the security risk. We need to find the main factors influencing the long distance security of the unmanned aerial vehicle and the relatively weak link during the operation .

This paper uses the fault tree analysis method for the risk identification of the long distance security of the unmanned aerial vehicle, according to the importance of minimum cut sets and structure, we calculate and qualitatively analyze the main factors which are used to identify the long distance search and rescue security of the unmanned aerial vehicle, and build the safety evaluation system of long distance flight of the unmanned aerial vehicle [19-20].

### **THE SAFETY EVALUATION BASIS OF UAV LONG DISTANCE SEARCH AND RESCUE**

#### **The concept of the risk of long-distance search for UAV**

There is still no specific definition of risk in the world as so far. But as some researchers deepen their research, a rough definition of risk is appeared: risk is a comprehensive measure of the probability of an accident and the extent of the damage, the formula below is the risk function:

$$R = f(P, C) \quad (1)$$

In the formula,  $R$  is the risk value,  $P$  is the probability of an accident,  $C$  is the severity of the accident.

The function relationship of formula (1) usually takes the product of  $P$  and  $C$  as follow:

$$R = P \times C \quad (2)$$

The danger of long-distance search for drones is unavoidable because of objective existence, but the size of the risk is changed largely based on human's behaviors, that is people can adopt certain technical means and the prevention measures, descending failure rate and harm of UAV long distance accident to slow down the risk

### The ALARP principle of the risk of long-distance search for UAV

The ALARP principle is the two-flattening principle, The long-range risk of drones appears in all safety systems, and it may only be reduced by human safety measures, but the risk value is not zero, the cost is often reduced by risk while the exponential curve is going up, which need comprehensive analysis of risk and cost [21-23]. The UAV's long distance search and rescue risk ALARP principle is shown in Figure 1.

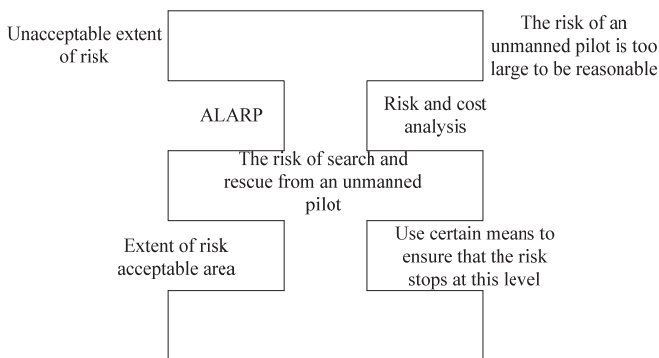


Fig. 1. UAV's long-range risk ALARP principle

Evaluate the safety of long-distance search for UAV, assuming that the risk value of the evaluation is not acceptable and in most cases, this risk is not allowed, it must be forced to reduce it and deal with special circumstances; assuming that the value of the risk is inacceptable area, the risk is allowed to exist, and periodic checks are only required. Assuming that the value of the evaluation is within the acceptable range, the long-range risk of UAV follows the ALARP principle and requires weigh and synthesize costs and risks by certain means: raise the maintenance costs do not significantly reduce risk, so the risk is tolerable and the cost is saved [24-27], on the contrary, investment must be increased to reduce risk. The extent of the UAV's long-distance search and rescue risk is reduced depends on the results of the analysis.

### The safety evaluation of UAV long distance search and rescue

The long-range safety evaluation of UAV is aimed at completing the long distance search and rescue, apply the basic theory and method of safety engineering to the marine search and rescue, make recognition and analysis of search and rescue the potential risk factors for long distances, to judge and predict UAV long search and rescue the accident possibility and its serious degree, and then to provide support the emergency response plan and maintenance management. The evaluation process of UAV long-distance marine search and rescue is as follows.

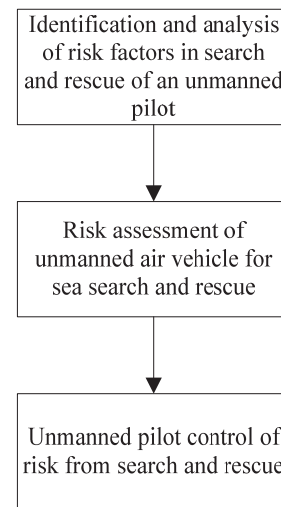


Fig. 2 UAV long distance search and rescue safety evaluation system

UAV ocean long distance search and rescue safety evaluation objectively reflect the extent of the risk of long-distance sea rescue accidents based on the analysis and risk assessment of the failure factors of long-distance search and rescue, guiding the drone search and rescue management to take effective remedial measures by this way and controlling the risk in the ALARP area, reducing the risk of long-distance search for UAV.

### UAV long-distance search and rescue risk identification

Long distance search and rescue risk discrimination for UAV, which is risk identification, it is the process of judging and identifying the historical accidents and accidents that have not occurred on the basis of researching and collecting of long distances search and rescue, which is the safety evaluation basis of UAV long distance search and rescue. The main task of UAV long-distance search and rescue risk identification are: finding out the factors of the long-distance search and rescue accident, and making qualitative analysis of the result. The long distance search and rescue risk is deduced by the failure tree which is used to identify and analyze its key factors. The specific steps for UAV long-distance search and rescue risk identification are:

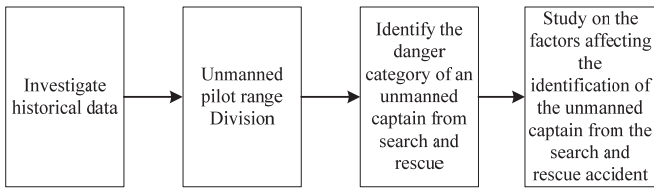


Fig. 3 UAV long distance search and rescue risk identification framework

The risk process changes with the changing conditions of the long distance search and rescue situation, the difference in the size of the entire UAV's long-distance search for different regional risks depends on the complexity of the environment and the changes in its conditions. So the research condition for the safety evaluation of UAV long distance search and rescue is to wait for the division of distance. It can also be used to evaluate the safety of a particular distance, and can consume less manpower, material and financial resources.

The minimum cut set mentioned above is the minimum set of accidents that will be analyzed which will harm to the safety and reliability of UAV. The cut sets can reflect the danger of long distance search and rescue. Every minimum cut set is a way to cause a crash, the more the number of minimum cut sets can reflect the more causes of the long search accident, the more easily lead to accidents, the safety and stability of long-distance search for UAV is poor.

The calculation of structural importance of the accident can help identify and analyze the relative importance of the minimum cut of an accident, which is conducive to long distance search and rescue security stability for UAV. The formula for calculating the importance of the structure based on the minimum cut set is:

$$I_{(i)} = 1 - \prod_{X_i \in K_j} \left(1 - \frac{1}{2^{n_j-1}}\right) \quad (3)$$

In this formula,  $X_i$  represents the  $i$  th basic accident,  $n_j$  is the total number of the  $i$  th accident in  $K_j$ ,  $K_j$  represents the  $j$  th minimum cut set in the fault tree,  $I_{(i)}$  represents the importance degree of the  $i$  th accident structure.

### The construction of UAV long distance search and rescue safety failure tree

To construct UAV long distance search and rescue safety failure tree, the minimum cutting set is determined by the operation of long distance search first, for the identification and analysis of long-distance search and rescue accident, the "long distance search and rescue safety" is considered as the minimum cut. The immediate factor that cause the UAV's long distance search and rescue safety declined are: from the failure of the drone's external structure, the failure of the drone's own structure and the overall structure of the drone, take it as an intermediate accident. At last analyze layer upon layer until all accidents are found.

Then calculate the minimum cutting and structural importance of failure tree. For a long distance search and

rescue safety failure tree, according to the top-down Boolean algebra, the minimum cut is obtained by the algorithm.

$$A = B1 + B2 + B3 = C1C2 + D1 + C3C4 + D2 + C17C18C19 = (D1 + D3 + C5 + C6 + C7)(C8 + C9 + C10) + D1 + C2 + (C11 + C12 + C13)(C14 + C15 + C16) + C17C18C19 = D1 + D2 + (D3 + C5 + C6 + C7)(C8 + C9 + C10) + (C11 + C12 + C13)(C14 + C15 + C16) + C17C18C19 = D1 + D2 + D3C8 + D3C9 + D3C10 + C5C8 + C5C9 + C5C10 + C6C8 + C6C9 + C6C10 + C7C8 + C7C9 + C7C10 + C11C14 + C11C15 + C11C16 + C12C14 + C12C15 + C12C16 + C13C14 + C13C15 + C13C16 + C17C18C19 \quad (4)$$

Formula (4) shows that the fault tree is made up of 2 first order minimum cut set, 21 second order minimum cut set, and 1 third order minimum cut set. It reflects 24 ways of reducing the safety of UAV over long distance search and rescue. It can be seen that the search for long distances is not that security.

To calculate the structural importance of the accident, according to the formula (3), the importance of every accident structure in this fault tree is:

$$I_{C5} = 1 - \left(1 - \frac{1}{2}\right) \left(1 - \frac{1}{2}\right) \left(1 - \frac{1}{2}\right) = 0.875 \quad (5)$$

$$I_{C6} = 1 - \left(1 - \frac{1}{2}\right) \left(1 - \frac{1}{2}\right) \left(1 - \frac{1}{2}\right) = 0.875 \quad (6)$$

$$I_{C7} = 1 - \left(1 - \frac{1}{2}\right) \left(1 - \frac{1}{2}\right) \left(1 - \frac{1}{2}\right) = 0.875 \quad (7)$$

$$I_{C8} = 1 - \left(1 - \frac{1}{2}\right) \left(1 - \frac{1}{2}\right) \left(1 - \frac{1}{2}\right) \left(1 - \frac{1}{2}\right) = 0.9375 \quad (8)$$

$$I_{C9} = 1 - \left(1 - \frac{1}{2}\right) \left(1 - \frac{1}{2}\right) \left(1 - \frac{1}{2}\right) \left(1 - \frac{1}{2}\right) = 0.9375 \quad (9)$$

$$I_{C10} = 1 - \left(1 - \frac{1}{2}\right) \left(1 - \frac{1}{2}\right) \left(1 - \frac{1}{2}\right) \left(1 - \frac{1}{2}\right) = 0.9375 \quad (10)$$

$$I_{C11} = 1 - \left(1 - \frac{1}{2}\right) \left(1 - \frac{1}{2}\right) \left(1 - \frac{1}{2}\right) = 0.875 \quad (11)$$

$$I_{C12} = 1 - \left(1 - \frac{1}{2}\right) \left(1 - \frac{1}{2}\right) \left(1 - \frac{1}{2}\right) = 0.875 \quad (12)$$

$$I_{C13} = 1 - \left(1 - \frac{1}{2}\right) \left(1 - \frac{1}{2}\right) \left(1 - \frac{1}{2}\right) = 0.875 \quad (13)$$

$$I_{C14} = 1 - \left(1 - \frac{1}{2}\right) \left(1 - \frac{1}{2}\right) \left(1 - \frac{1}{2}\right) = 0.875 \quad (14)$$

$$I_{C15} = 1 - \left(1 - \frac{1}{2}\right) \left(1 - \frac{1}{2}\right) \left(1 - \frac{1}{2}\right) = 0.875 \quad (15)$$

$$I_{C16} = 1 - \left(1 - \frac{1}{2}\right) \left(1 - \frac{1}{2}\right) \left(1 - \frac{1}{2}\right) = 0.875 \quad (16)$$

$$I_{C17} = 1 - \left(1 - \frac{1}{2^2}\right) = 0.250 \quad (17)$$

$$I_{C18} = 1 - \left(1 - \frac{1}{2^2}\right) = 0.250$$

$$I_{C19} = 1 - \left(1 - \frac{1}{2^2}\right) = 0.250$$

$$I_{D1} = 1; I_{D2} = 1$$

$$I_{D1} = 1 - \left(1 - \frac{1}{2}\right) \left(1 - \frac{1}{2}\right) \left(1 - \frac{1}{2}\right) = 0.875$$

The result of the formula above shows that the structure importance of basic accident  $C5 \sim C19$

$$\begin{aligned} I_{D1} = I_{D2} > I_{C8} = I_{C9} = I_{C10} > I_{C5} = I_{C6} = I_{C7} = I_{C11} = \dots = \\ = I_{C16} = I_{D3} > I_{C17} = I_{C18} = I_{C19} \end{aligned}$$

and  $D1 \sim D3$  are sorted by their size as:

(22)

## THE DIVISION OF UAV LONG-RANGE SEARCH SAFETY RATING SCALE

### Determine the relative risk value of the long distance search for UAV

Through the risk definition formula  $R = P \times C$ , combined with these studies, the risk value  $R$  for the long distance segment of the UAV are determined. Only in the condition that the failure rate  $P$  and the failure result  $C$  both represent the objective absolute value,  $R$  represents absolute risk value, in the rest of the situation  $R$  represents relative risk value. Through the above, and based on the limitation of the actual condition and the complexity of the long distance search and rescue condition, the value of  $R$  can only be set within the relative value category recently.

### The establishment of the scale model for the safety evaluation of UAV long distance search and rescue

It can be known by the nature of the relative value of UAV long distance search and rescue failure that it doesn't make sense to look at a single relative value, it is necessary to put the value in a real problem, and there is a certain standard that is relevant.

At present, there is no sound standard for the safety evaluation of UAV long distance search and rescues in China, it is needed to improve the support and verification of the failure database. It is very difficult to complete the safety evaluation criteria at the current stage. The rating of the long-range search and rescue safety is shown below:

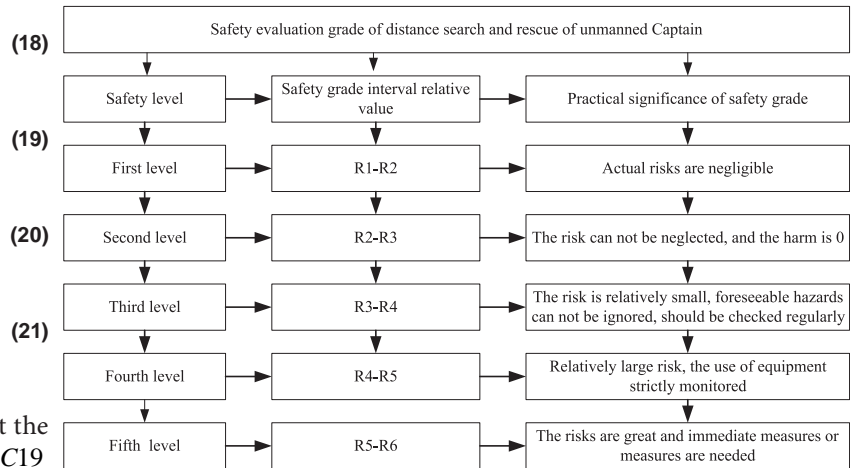


Fig. 4 Rating of the long-range search and rescue safety for UAV.

Assuming that the probability of failure and the range of consequences of failure is known, determine the value of  $R1 \sim R6$  in the figure above by this range. In the actual long-range search and rescue safety evaluation, calculate the relative value  $R$  of the risk then contrast with the figure above to determine the risk level of long-range search for UAV, then take appropriate measures to achieve the goal of the long distance safety evaluation and safety alert of the Marine search and rescue for UAV then complete the modeling.

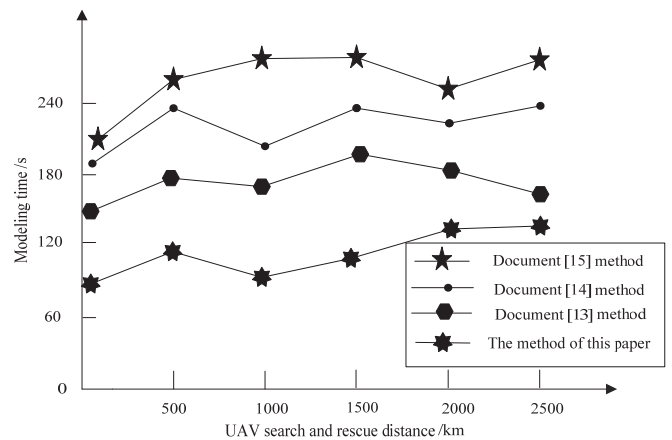


Fig. 5. Modeling time in different ways.

## EXPERIMENTAL RESULTS AND ANALYSIS

In order to prove the effectiveness of the long distance security modeling method of maritime search and rescue unmanned aerial vehicle based on ArduinoMiniPro, we need a simulation experiment. In Matlab environment, the long distance security modeling experimental platform of maritime search and rescue unmanned aerial vehicle is constructed. The experimental data are obtained from "eaglet3A" which was successful in flight test Dayi County of Chengdu in July

12, 2012. This unmanned aerial vehicle weighs 15 kg, and the wingspan is 2.6 meters, and the aircraft length is 2.1 meters. The search system of this unmanned aerial vehicle consists of the airborne detector, the ground station, the beacon, the unmanned aerial vehicle, the portable personnel positioning search and rescue device and the high resolution camera. The airborne equipment can activate the beacon in the range of 10 kilometers, so as to read the ID information of the person in distress at sea, and then locate the distress position quickly according to the GPS signal transmitted by the beacon. We use different methods to carry out the same experiment on the experimental subjects, so as to observe the practicality of the modeling method proposed in this paper. Figure 5 is the comparison of the modeling time (s) of different methods. Figure 6 is the comparison of modeling stability (%) of different methods. Figure 7 is the comparison of modeling errors (%) of different methods.

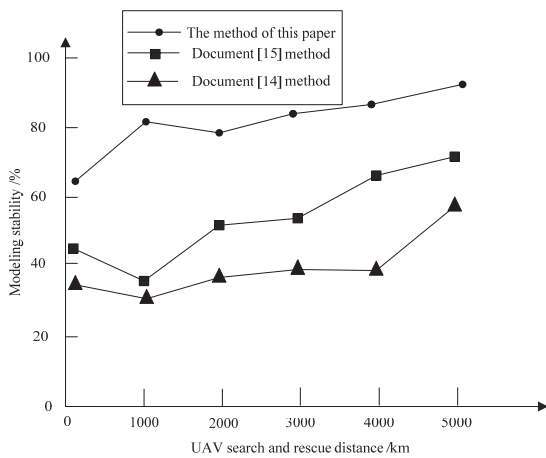


Fig. 6. Modeling stability contrasts in different ways

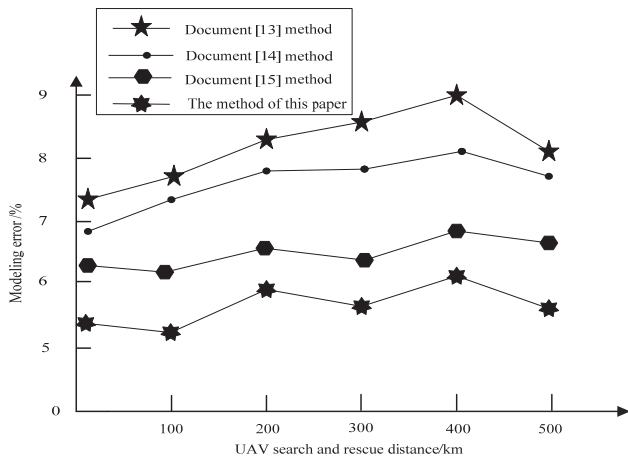


Fig. 7. Comparison of modeling errors of different methods

Analyzing three diagrams, we can see that the proposed modeling method in this paper is relatively good. The modeling method proposed in reference document studies and analyzes the safety of forced landing and the safety of the aircraft failure in the process of long distance search and rescue of unmanned aerial vehicle, but it ignores the

factors of external invasion. The method in reference divides the distance of unmanned aerial vehicle maritime search and rescue, and the results are as follows: the medium and long distance, the long distance and the extra-long distance, but there is no description of the risk in each group for the grouping result. The method in reference researches and classifies its security risks aiming at the characteristics of long distance search and rescue, and does not divide the existing accidents or the accident what is happening into the classification [28-30].

In this paper, the method use the fault tree analysis method and correlation calculations to realize the risk identification and the main factors affecting the safe of long distance search and rescue of the unmanned aerial vehicle, and obtains the safety evaluation grade model of long distance search and rescue of unmanned aerial vehicle, so that the modeling error is smaller, faster, and more stable.

Simulation results show that the proposed modeling method can efficiently model the long distance security of the marine search and rescue unmanned aerial vehicle and reduce the modeling time, and improve the safety of the long distance search and rescue of unmanned aerial vehicle, and provide support for the long distance marine search and rescue of unmanned aerial vehicle [31-33].

## CONCLUSION

Using the current method for modeling the long distance safety of marine search and rescue unmanned aerial vehicle, we can not model accurately and quickly, there is the large deviation problem about the modeling the long distance safety of marine search and rescue unmanned aerial vehicle. This paper proposed a modeling method of the long distance security of maritime search and rescue unmanned aerial vehicle based on Arduino Mini Pro. Simulation results show that the proposed method can effectively model the long distance security of the marine search and rescue unmanned aerial vehicle.

## REFERENCE

1. Liu Cuifang, Feng Xuexiao. Mining of Gas Path Fault Residuals Parameter Deviation for Small Uav Rotorcraft Engine. Report of science and technology, 2016,32(10):184-187.
2. LIU Yang, HAN Quan-quan, ZHAO Na. Design and realization of ground synthetic monitor and control system for UAV . Electronic Design Engineering, 2016,24(14):110-112.
3. Chen Shao-qian, WANG Xiang-xin, XING Xue-chu. The Egli Antenna System in the Application of the New Type of Unmanned Aerial Vehicle Development. Science Technology and Engineering, 2015,15(7):205-213.

4. He Hai-peng, YAN Yan, MA Liang, YANG Wan-kou. Iterated Extended Kalman Filters Applied to Attitude Measurement of Quadrotor. *Computer Simulation*, 2015,32(4):56-60.
5. Dong Bigui, Liu Shou, Liang Xu. Study on Design Evaluation Method of Advanced UAV Power System. *Computer Measurement & Control*, 2015,23(4):1242-1245.
6. Chen Z, Li Y, Sun M, et al. ADRC-GPC control of a quadrotor unmanned aerial vehicle. *Journal of Harbin institute of technology*, 2016, 48(9):176-180.
7. Liu wen-chan, qiuxiaofeng, Chen pengcheng, et al. SDN Oriented Software-Defined Security Architecture. *Computer science and exploration*, 2015, 9(1):63-70.
8. Xia J, Shi W. Perspective on water security issue of changing environment in China. *Journal of water conservancy*, 2016, 47(3):292-301.
9. Zhang S, Shi R, Zhao Y. Visual fusion and analysis for multivariate heterogeneous network security data. *Computer application*, 2015, 35(5):1379-1384.
10. Huang Z, Wang H, Wang Q, et al. Micromechanical Modeling of Elastic-Viscoplastic Behavior of Armco-Fe at High Strain Rate. *Journal of solid mechanics (English)*, 2016, 29(6):655-662.
11. Keke X U, Jicang W U, Zheng E. Real-time Dynamic Monitoring and Modeling for Large Building Based on GNSS. *Geodetic and geodynamics*, 2015, 35(2):214-218.
12. Liu N. Water security situation in China and the supporting role of science and technology innovation. *Hydroelectricity journal*, 2015, 34(5):1-3.
13. Wang Xiaoqin, Wang Miaomiao, Wang Shaoqiang, Wu Yundong. Extraction of vegetation information from visible unmanned aerial vehicle images. *Transactions of the Chinese Society of Agricultural Engineering*, 2015, 31(5):152-159.
14. LIU Xiaodong, ZHONG Maiying, LIU Hai. EKF-Based Fault Detection of Unmanned Aerial Vehicle Flight Control System. *Journal of Shanghai Jiaotong University*, 2015, 49(6):884-888.
15. ZHOU Huan, ZHAO Hui, HAN Tong, HUANG Han-qiao. Cooperative flight and evasion control of UAV swarm based on rules. *Systems Engineering and Electronics*, 2016, 38(6):1374-1382.
16. ZHANG Zhili. High Wind Power Stability of UAV Flight Control Simulation Model. *Computer Simulation*, 2017, 34(2):115-118.
17. LI Huaitao, TANG Daoguang, LIU Dawei, et al. Design and realization of UAV integrated management system based on Qt. *Electronic Design Engineering*, 2016, 24(8):75-79.
18. ZHENG Hui, LI Xiaohui, QU Yongping. Oblique Video Flow Mosaic Based on Unmanned Aerial Vehicle. *Science Technology and Engineering*, 2016, 16(32):263-268.
19. ZHAO Lifang, JING Lili. Large Uav Electronic Communication Signal Anti-jamming Method Study and Simulation. *Bulletin of Science and Technology*, 2015, 31(12):218-219.
20. WANG Tingting, QIAN Chengshan, ZHANG Yonghong, et al. Attitude Control System Design for Tilting Fixed-wing Unmanned Aerial Vehicle. *Computer Measurement & Control*, 2017, 25(2):64-66.
21. Almazyad A S, Seddiq Y M, Alotaibi A M, et al. A Proposed Scalable Design and Simulation of Wireless Sensor Network-Based Long-Distance Water Pipeline Leakage Monitoring System. *Sensors*, 2014, 14(2):3557-3577.
22. Guan Y L, Hou Y X, Jia H G, et al. Dynamic Modeling and Simulation of UAV Ground Maneuvers. *Bing Gong Xue Bao / Acta Armamentarii*, 2014, 35(7):1021-1026.
23. Isemael, Y.Y. Molecular, Histological and biochemical effects of tea seed cake on hepatic and renal functions of *Oreochromis niloticus*. *Acta Scientifica Malaysia*, 2017, 1(1): 13-15.
24. Lin W P, Chin C S, Mesbahi E. Remote robust control and simulation of robot for search and rescue mission in water// *Oceans*. IEEE, 2014:1-9.
25. Gao, W. and W. Wang. The fifth geometric-arithmetic index of bridge graph and carbon nanocones. *Journal of Difference Equations and Applications*, 2017. 23(1-2SI): p. 100-109.
26. Gao, W., et al., Distance learning techniques for ontology similarity measuring and ontology mapping. *Cluster Computing-The Journal of Networks Software Tools and Applications*, 2017. 20(2SI): p. 959-968.
27. De Araujo V, Almeida A P G S, Miranda C T, et al. A parallel hierarchical finite state machine approach to UAV control for search and rescue tasks// *International Conference on Informatics in Control, Automation and Robotics*. IEEE, 2014:410-415.
28. Hassan, S.R., Zaman, N.Q., Dahlan, I. Influence of Seed Loads on Start Up of Modified Anaerobic Hybrid Baffled (MAHB) Reactor Treating Recycled Paper Wastewater. *Engineering Heritage Journal*, 2017, 1(2):05-09.

29. Chelladurai, G. Influence of diets on growth and biochemical parameters of *Babylonia spirata*. *Geology, Ecology, and Landscapes*, 2017, 1(3): 162-166.
30. Wun, W.L., Chua, G.K., Chin, S.Y. Effect of Palm oil mill effluent (pome) treatment by activated sludge. *Journal CleanWAS*, 2017, 1(2): 6-9.
31. Harith, N.S.H., Adnan, A. Estimation of Peak Ground Acceleration of Ranau Based on Recent Earthquake Databases. *Malaysian Journal Geosciences*, 2014, 1(2): 06-09.
32. Lai, G.T., Razib, A.M.M., Mazlan, N.A., Rafek, A.G., Serasa, A.S., Simon, N., Surip, N., Ern, L.K., and Mohamed, T.R. Rock Slope Stability Assessment of Limestone Hills, Southern Kinta Valley, Ipoh, Perak, Malaysia. *Geological Behavior*, 2017, 1(2):05-09.
33. Lugo-Cárdenas I, Flores G, Lozano R. The MAV3DSim: A Simulation Platform for Research, Education and Validation of UAV Controllers. *IFAC Proceedings Volumes*, 2014, 47(3):713-717.

## CONTACT WITH THE AUTHOR

Lei Zheng

*e-mail: zhenglei78877@163.com*

College of Material Management  
and Safety Engineering  
Air Force Engineering University  
Xi'an710051  
CHINA

# RESEARCH ON INTELLIGENT DIAGNOSIS METHOD FOR LARGE-SCALE SHIP ENGINE FAULT IN NON-DETERMINISTIC ENVIRONMENT

Donghua Feng <sup>1,2</sup>

Yahong Li <sup>2</sup>

<sup>1</sup>School of Computer Science and Technology, Wuhan University of Technology, Wuhan, 430070, China

<sup>2</sup>College of Computer and Information Engineering, Nanyang Institute of Technology, Nanyang, 473004, China

## ABSTRACT

*Aiming at the problem of inaccurate and time-consuming of the fault diagnosis method for large-scale ship engine, an intelligent diagnosis method for large-scale ship engine fault in non-deterministic environment based on neural network is proposed. First, the possible fault of the engine was analyzed, and the downtime fault of large-scale ship engine and the main fault mode were identified. On this basis, the fault diagnosis model for large-scale ship engine based on neural network is established, and the intelligent diagnosis of engine fault is completed. The experiment proved that the proposed method has high diagnostic accuracy, engine fault diagnosis takes only about 3s, with a higher use value.*

**Keywords:** Non-determinism, Large-scale ship engine, Fault intelligent diagnosis

## INTRODUCTION

Large-scale ship is a transport with high cost, its safety has been a high degree of concern, large-scale ship engine fault intelligent diagnosis is an important method to ensure the safety of large-scale ship's navigation [1-2]. Through the intelligent diagnosis of faults, detect the large-scale ship engine problems timely, to ensure the safety of personnel on board [3-4]. As a typical reciprocating power machine [5], the complexity of the structure determines the efficiency of large-scale ship engine fault diagnosis [6-7]. the traditional intelligent diagnostic method based on the support vector machine, extracts the fault feature first and uses the principle of structural risk minimization to replace the principle of experience risk minimization in traditional machine learning method to identify the fault features of large-scale ship engine and realize the intelligent diagnosis of large-scale ship engine fault [8-9], but this method needs a long time to diagnose, cannot complete the fault diagnosis timely. To this end, an

intelligent diagnosis method for large-scale ship engine fault in non-deterministic environment based on neural network is proposed in this paper.

## ANALYSIS OF FAULT DIAGNOSIS PROCESS FOR LARGE-SCALE SHIP ENGINE IN NON- DETERMINISTIC ENVIRONMENT

There are a variety of complex factors in the whole process of design, manufacture, assembly, use and maintenance of the large-scale ship engine, the possible sources of fault are:

1) Design problems, large-scale ship engine design is a very complex work, small individual errors will inevitably appear in the design process.

2) Manufacturing problems, including defects in the entire manufacturing process, such as material defects, manufacturing errors;

3) Environment of the use, during the voyage process, some parts through the erosion of seawater, and bear long-term mechanical vibration, humidity, radiation and other harsh environments, resulting in large-scale ships fault;

4) Accidents, various papers reported large-scale ship engine faults occurred during the tsunami, storm and other accidents. In the above sources, due to the rapid development of modern industrial manufacturing level, the percentage of faults caused by manufacturing problems is declining in all sources of faults, while the proportion of environmental and human factors have increased.

The features of the ship engine fault are:

1) The faults of most ship engine parts are random. There is no inherent fault rate, since most of the fault comes from environmental and human factors, and these factors are random in their own, there is no definite intrinsic fault rate in the normal service life.

2) The overall fault rate of large-scale ship engines follows the “bathtub curve”. In the early stage of the use, the performance parameters of the various parts of the engine are in the stage of commissioning and process running. The performance parameters changed greatly and worked unstably that the total fault rate is relatively high. With the increase of the voyage time of the large-scale ships, engine parts complete the commissioning and process running, its performance is gradually stable, and the total fault rate has declined. When the use of time is more than 75% of economic life, the effects of engine wear, corrosion and fault caused by environmental factors are becoming more and more serious, and the total failure rate is increasing again.

3) Fault mechanism is complex. Modern large-scale ship engine integrated application of mechanical, electronic, computer, automatic control, detection technology and other multi-disciplinary advanced technology, is a large-scale complex mechanical and electrical equipment, the diversity of the working principle of the system led to the complexity of its fault mechanism.

4) The possibility of concurrent fault occurs. The complexity of the large-scale ship engine system determines the comprehensive fault features, any of the occurrence of a primary fault has a number of potential trigger fault, which is a multi-fault concurrent system.

In the large-scale ship fault detection, the engine fault detection is the most important content, once the engine is faulty, may lead to other system faults, so the ship engine fault detection is conducive to ensuring the normal operation of the ship. Large-scale ship engine fault mode varied, as shown in Table 1 is the downtime fault analysis of large-scale ship engine, Table 2 is the main fault mode of large-scale ship engine.

Tab. 1. Large-scale Ship Downtime Fault Analysis

| Fault classification  | Fault probability /% |
|---|----------------------|
| Fuel injection equipment and fuel supply system fault                       | 27.0                 |
| Valve and valve seat fault  | 11.9                 |
| Bearing fault   | 7.0                  |
| Leakage fault   | 17.3                 |
| Oil spill and lubrication system fault                                      | 5.2                  |
| Piston component fault  | 6.6                  |
| Turbocharging system fault (Including the fault caused by foreign invasion) | 4.4                  |
| Governor gear fault   | 3.9                  |
| Gear and drive fault  | 3.9                  |
| Leakage   | 3.2                  |
| Crankshaft fault  | 0.2                  |
| Fuel leakage  | 3.5                  |
| Other damage and rupture except special title                               | 2.5                  |
| Other faults  | 2.5                  |

Tab. 2. Main Fault Modes of the Large-scale Ship Engine

| Fault modes                    | Cause of fault   | Fault severity |
|--------------------------------|--|----------------|
| Machine abnormal sound         | Valve clearance or clear knock sound   | Severe         |
| Engine locking                 | Crankshaft locking   | Severe         |
| Engine stuck                   | The piston is stuck in the cylinder  | Severe         |
| Cylinder pressure improperly   | Piston ring leaks  | Severe         |
| Gas channeling, power improper | Increased fuel consumption (severe cylinder wear)  | Severe         |
| Gas channeling                 | Piston ring broken   | Severe         |
| Pistons dead                   | Inhalation of foreign matter caused by piston damage   | Severe         |
| Engine overheating             | Due to partial clogging of the watercourse or damage of the thermostat                             | General        |
| Engine block is damaged        | Piston broken or connecting rods broken, the cylinder broke by the connecting rod, engine scrapped | Fatal          |
| Piston ring leaking            | After leaking, the impact of oil low shell caused abnormal sound                                   | Severe         |

Through the analysis of Table 1 and Table 2, we can see that because of the interaction between the subsystems of the engine, the relationship is complicated, the engine fault presents a complex diversity, mainly reflected in the following aspects:

1) The complexity of the fault

Engine structure is complex, which has many fault excitation source and thermal parameters. As a reciprocating machine, in the same working condition, the characteristic parameters are different in the working cycle at different times, some faults showed the same fault features, which requires people to use multiple thermal parameters to multi-level comprehensive diagnosis.

2) The ambiguity of the fault

There is ambiguity between the cause of the engine fault and the fault symptom, such as the degree of influence of a fault symptom on the fault phenomenon and the possibility of a fault phenomenon.

3) Fault correlation and relativity

Under different conditions and circumstances, the performance of the engine fault features is sometimes not the same; engine fault of a subsystem may cause other related system fault.

4) The coexistence of multiple faults

Multiple engine faults may occur in the work at the same time, and there exists interference between the feature information of different parts.

## INTELLIGENT FAULT DIAGNOSIS METHOD FOR LARGE-SCALE SHIP ENGINE BASED ON NEURAL NETWORK IN NON- DETERMINISTIC ENVIRONMENT

Through the above discussion, the fault of large-scale ship engine is analyzed, and the main fault modes are expounded, which lays the foundation for the determination and implementation of intelligent fault diagnosis method for large-scale ship engine in non-deterministic environment.

The basic unit of artificial neural network is neuron, and the mathematical model of neuron corresponds to biological nerve cells. The classical neuron model is a non-linear structure with multiple input single output.

The mathematical description of the neural model to achieve large-scale ship engine fault diagnosis [10-12] can be expressed as:

$$u_k = \sum_{j=1}^n w_{kj} x_j \quad (1)$$

$$v_k = net_k = u_k - \theta_k \quad (2)$$

$$y_k = f(v_k) \quad (3)$$

In the above equation,  $x_j \in \{x_1, x_2, \dots, x_n\}$  represents the input signal of the large-scale ship engine fault diagnosis,  $w_{kj}$  and  $\theta_k$  represent the weight and thresholds of the neuron  $k$  respectively,  $f(\cdot)$  represents the fault transfer function, and  $y_k$  represents the output of the neuron  $k$ .

BP neural network is a multi-layer forward neural network, the network training uses the error back propagation algorithm, its feature is to use the error back propagation algorithm to adjust the weight of the neural network. BP network learning algorithm is through the reverse learning process so that the network output node error is minimal, the weight and threshold of the network correct along the negative gradient of error function. In the BP network, the nonlinear learning process is done by the interaction between the implicit layer and the output layer. When the output value does not match the expected value given in the sample, the error signal is returned from the output side, and the weight is continuously corrected until the desired output value is obtained at the output layer node as the training end of the samples. When the sample  $p$  completes the weight adjustment of the network, enter another batch of patterns to learn until  $N$  sample trainings are completed.

Set  $x_j$  as the input to the  $j$ th node of the large-scale ship engine in input layer based on the BP neural network.  $j = 1, 2, \dots, M$ ;  $w_{ij}$  represents the weight between the  $i$ th node of the input layer and the  $j$ th node of the implicit layer based on the BP neural network.  $\theta_i$  represents the threshold of the  $i$ th node of the BP neural network implicit layer;  $\phi(x)$  represents the implicit layer excitation function;  $w_{ki}$  represents the weight between the  $k$ th node of the output layer and the  $i$ th node of the implicit layer,  $i = 1, 2, \dots, q$ ;  $\psi(x)$  represents the output layer excitation function;  $a_k$  represents the  $k$ th node threshold of the output layer,  $k = 1, 2, \dots, L$ ;  $O_k$  represents the output of the  $k$ th node of the large-scale ship engine fault diagnosis output layer based on the BP neural network, the training step of the neural network can be expressed as: first input signal forward propagation process, then calculated the neuron output error from the output layer as the error gradient method to adjust the weight and thresholds of the basis, so that iterative adjustment of the network, the output error can eventually be close to the expected value. The specific process is described below.

Calculate the implicit Layer input of  $i$ th Node as  $net_i$ :

$$net_i = \sum_{j=1}^M w_{ij} x_j + \theta_i \quad (4)$$

Calculate the implicit layer output of the  $i$ th node as  $y_i$ :

$$y_i = \phi(net_i) = \phi\left(\sum_{j=1}^M w_{ij} x_j + \theta_i\right) \quad (5)$$

The input of the  $k$ th node in input layer as  $net_k$ :

$$net_k = \sum_{i=1}^q w_{ki} y_i + a_k = \sum_{i=1}^q w_{ki} \phi\left(\sum_{j=1}^M w_{ij} x_j + \theta_i\right) + a_k \quad (6)$$

The output of the  $k$ th node in input layer as  $O_k$ :

$$O_k = \psi(\text{net}_k) = \psi\left(\sum_{i=1}^q w_{ki} y_i + a_k\right) \quad (7)$$

$$= \psi\left(\sum_{i=1}^q w_{ki} \phi\left(\sum_{j=1}^M w_{ij} x_j + \theta_i\right) + a_k\right)$$

Set  $E_p$  as the quadratic error criterion function of each sample  $p$ , then:

$$E_p = \frac{1}{2} \sum_{k=1}^L (T_k - O_k)^2 \quad (8)$$

The total error criterion function of  $p$  training samples can be expressed as:

$$E = \frac{1}{2} \sum_{p=1}^p \sum_{k=1}^L (T_k^p - O_k^p)^2 \quad (9)$$

According to the error gradient descent method, the correction amount of the output layer weight  $\Delta w_{ki}$ , the correction amount of the output layer threshold  $\Delta a_k$ , the correction amount of the implicit layer weight  $\Delta w_{ij}$ , and the correction amount of implicit layer threshold  $\Delta \theta_i$  are corrected.

$$\begin{cases} \Delta w_{ki} = -\eta \frac{\partial E}{\partial w_{ki}} \\ \Delta a_k = -\eta \frac{\partial E}{\partial a_k} \\ \Delta w_{ij} = -\eta \frac{\partial E}{\partial w_{ij}} \\ \Delta \theta_i = -\eta \frac{\partial E}{\partial \theta_i} \end{cases} \quad (10)$$

Output layer weight adjustment formula:

$$\begin{aligned} \Delta w_{ki} &= -\eta \frac{\partial E}{\partial w_{ki}} = -\eta \frac{\partial E}{\partial \text{net}_k} \cdot \frac{\partial \text{net}_k}{\partial w_{ki}} \\ &= -\eta \frac{\partial E}{\partial O_k} \cdot \frac{\partial O_k}{\partial \text{net}_k} \cdot \frac{\partial \text{net}_k}{\partial w_{ki}} \end{aligned} \quad (11)$$

Output layer threshold adjustment formula:

$$\begin{aligned} \Delta a_k &= -\eta \frac{\partial E}{\partial a_k} = -\eta \frac{\partial E}{\partial \text{net}_k} \cdot \frac{\partial \text{net}_k}{\partial a_k} \\ &= -\eta \frac{\partial E}{\partial O_k} \cdot \frac{\partial O_k}{\partial \text{net}_k} \cdot \frac{\partial \text{net}_k}{\partial a_k} \end{aligned} \quad (12)$$

Implicit layer weight adjustment formula

$$\begin{aligned} \Delta w_{ij} &= -\eta \frac{\partial E}{\partial w_{ij}} = -\eta \frac{\partial E}{\partial \text{net}_i} \cdot \frac{\partial \text{net}_i}{\partial w_{ij}} \\ &= -\eta \frac{\partial E}{\partial y_i} \cdot \frac{\partial y_i}{\partial \text{net}_i} \cdot \frac{\partial \text{net}_i}{\partial w_{ij}} \end{aligned} \quad (13)$$

Implicit Layer Threshold Adjustment Formula:

$$\begin{aligned} \Delta \theta_i &= -\eta \frac{\partial E}{\partial \theta_i} = -\eta \frac{\partial E}{\partial \text{net}_i} \cdot \frac{\partial \text{net}_i}{\partial \theta_i} \\ &= -\eta \frac{\partial E}{\partial y_i} \cdot \frac{\partial y_i}{\partial \text{net}_i} \cdot \frac{\partial \text{net}_i}{\partial \theta_i} \end{aligned} \quad (14)$$

Because:

$$\frac{\partial E}{\partial O_k} = -\sum_{p=1}^p \sum_{k=1}^L (T_k^p - O_k^p) \quad (15)$$

$$\frac{\partial \text{net}_i}{\partial w_{ki}} = y_i, \quad \frac{\partial \text{net}_i}{\partial a_k} = 1 \quad (16)$$

$$\frac{\partial \text{net}_i}{\partial w_{ij}} = x_j, \quad \frac{\partial \text{net}_i}{\partial \theta_i} = 1$$

$$\frac{\partial y_i}{\partial \text{net}_i} = \phi'(\text{net}_i) \quad (17)$$

$$\frac{\partial O_k}{\partial \text{net}_k} = \psi'(\text{net}_k) \quad (18)$$

Get the formula:

$$\begin{cases} \Delta w_{ki} = \eta \sum_{p=1}^p \sum_{k=1}^L (T_k^p - O_k^p) \cdot \psi'(\text{net}_k) \cdot y_i \\ \Delta a_k = \eta \sum_{p=1}^p \sum_{k=1}^L (T_k^p - O_k^p) \cdot \psi'(\text{net}_k) \\ \Delta w_{ij} = \eta \sum_{p=1}^p \sum_{k=1}^L (T_k^p - O_k^p) \cdot \psi'(\text{net}_k) \cdot w_{ki} \cdot \phi'(\text{net}_i) \cdot x_j \\ \Delta \theta_i = \eta \sum_{p=1}^p \sum_{k=1}^L (T_k^p - O_k^p) \cdot \psi'(\text{net}_k) \cdot w_{ki} \cdot \phi'(\text{net}_i) \end{cases} \quad (19)$$

Through the above discussion, a large-scale ship engine fault diagnosis network model based on neural network is established. The process is divided into two steps. The first step is to acquire the appropriate number of training sample sets, and train the neural network to obtain the available fault diagnosis network model. The second step is to use the existing model to diagnose the unknown symptom data set, get the corresponding state and mode. The diagnosis process is the process of the neural network to compute the input vector and obtains the output. Before the learning and diagnosis of the network model, extract the original data and training sample data by summarizing the existing troubleshooting, diagnosis, maintenance experience and knowledge, and preprocessing the data smoothing, feature selection/extraction and so on. The purpose of building a sample space is to provide suitable training samples and diagnostic samples for the diagnostic network.

The purpose of the preliminary analysis of the fault model sample is to confirm whether the fault feature information contained in the fault sample space is sufficient, whether the fault features of the selected large-scale ship engine are reasonable, and evaluate whether the model can distinguish all large-scale ship engine fault modes. The space composition of large-scale ship engine fault samples is an important factor to determine the general performance of the established diagnostic system in practical diagnostic applications.

For the network fault diagnosis model, the correlation coefficient between the large-scale ship engine components can be expressed as:

$$\rho(f, x_j) = \frac{\sum_{i=1}^N (f_i - \bar{f})(x_{ij} - \bar{x}_j)}{\sqrt{\sum_{i=1}^N (f_i - \bar{f})^2 \sum_{i=1}^N (x_{ij} - \bar{x}_j)^2}} \quad (20)$$

Where  $f$  represents the target value and  $x_i$  represents the feature interval. Since the correlation coefficient  $\rho(f, x_j)$  is between  $(-1,1)$  and the absolute value is between  $(0,1)$ , the closer absolute value to 1, the similarity between the target and the feature is higher. In this way, the intelligent diagnosis method of large-scale ship engine fault based on neural network in non-deterministic environment is realized.

## EXPERIMENTAL RESULTS AND ANALYSIS

To prove the validity and feasibility of intelligent fault diagnosis method for large-scale ship engine in non-deterministic environment based on neural network, an experiment is carried out under the operating system of Windows 7 Ultimate. The CPU model is 3.2Ghz Intel Core I3, running platform is Microsoft Visual Studio. NET 2010. Through the construction of large-scale ship engine fault intelligent diagnostic platform, using the signal processing board shown in Figure 1 to deal with the engine data, the proposed method and the methods proposed in literature [8] and [9] are used, respectively, compare the results and complete the experiment.

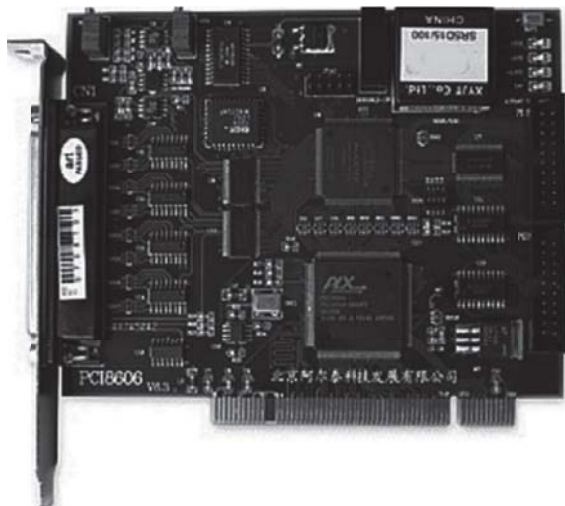


Fig. 1. Signal Processing Board

First, the experimental process of the proposed method is shown in Figure 2.

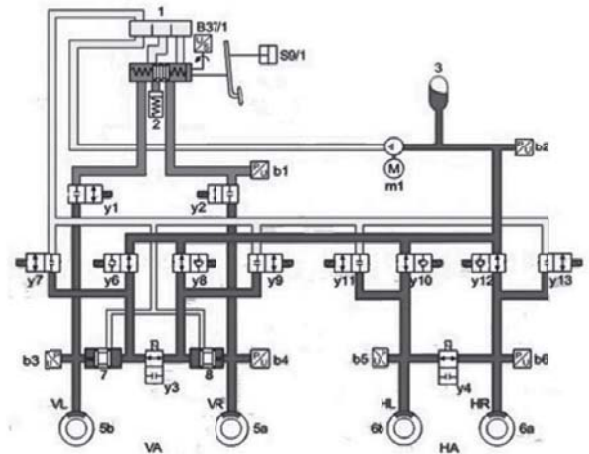


Fig. 2. Intelligent Diagnosis Process of Large-scale Ship Engine Fault Based on the Neural Network

Figure 2 showed that the proposed method can realize the intelligent diagnosis of large-scale ship engine fault, and effectively realize the real-time data monitoring and fault analysis, it can monitor the operating status of the components in the engine system which has a strong use value.

Then, the response time (s) and the time-consuming (s) of the proposed method are compared with that proposed in literature [8] and [9], which are shown in figure 3 and 4.

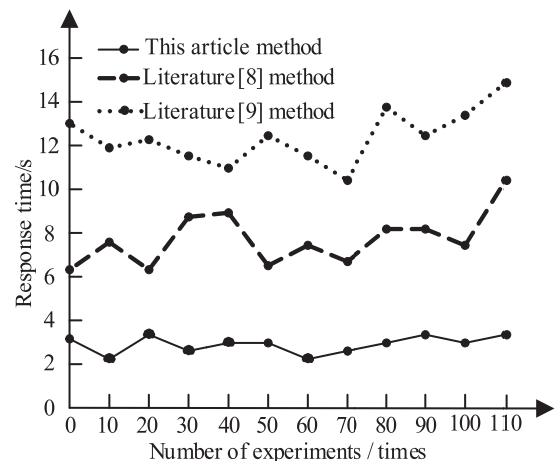


Fig. 3. Comparison of Response Time for Three Diagnosis Methods

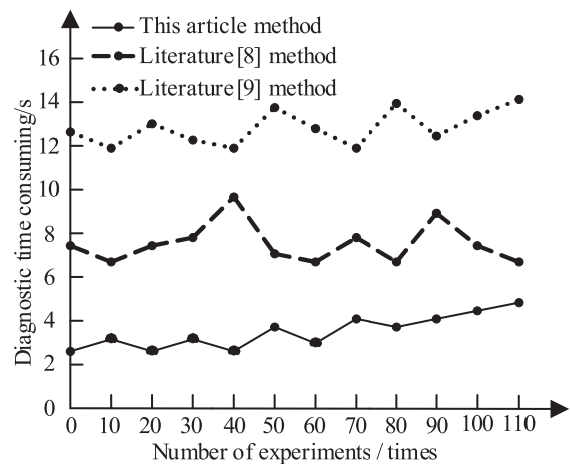


Fig. 4. Comparison of Time-consuming for Three Diagnosis Methods

The fault diagnosis delay is the time difference between the response time and the fault time of the ship engine fault. It can be seen from the above figure that the fault time of the proposed method is short, which can reflect the ship engine fault timely, reduce the engine fault caused by other ship system fault and reduce the difficulty of fault repair.

Finally, the efficiency of ship engine fault diagnosis is compared and the efficiency of ship engine fault diagnosis is set as (%). The calculation method is shown in equation (21). Through experiments, three methods are used to compare the efficiency of ship engine fault diagnosis. The comparison results shown in Figure 5.

$$\text{Diagnostic Efficiency} = \frac{\text{Diagnostic Accuracy} \times \text{Diagnostic Time Consuming}}{\text{Diagnostic Delay}} \quad (21)$$

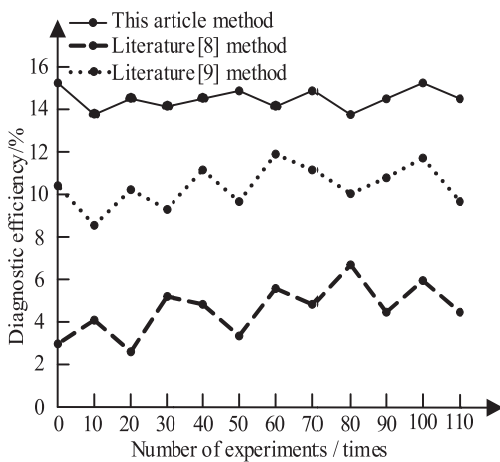


Fig. 5. Comparison of the Diagnostic Efficiency for Three Diagnosis Methods

Figure 5 showed that the diagnostic efficiency of the proposed method is higher which has a better diagnostic effect. Because of the fault diagnosis model is established before the fault diagnosis, the diagnostic accuracy is improved, which also improved the diagnostic efficiency [13-16].

In this paper, the proposed method is concerned with the fault diagnosis of ship engine, which has a less diagnostic response time, a faster diagnostic speed and a higher efficiency [17]. The diagnostic content of the proposed method is more comprehensive, which promote the research development in this field[18].

## CONCLUSION

1. In this paper, a fault diagnosis method for large-scale ship engine fault in non-deterministic environment based on neural network is proposed. Firstly, the fault source and fault features of large-scale ship engine are analyzed to determine the fault of large-scale ship engine and the main fault mode. Based on this, the neural network is used to construct the fault diagnosis model, and completed the intelligent diagnosis method

through the establishment of ship engine fault sample space and the selection of diagnosis model.

2. The experimental results showed that the proposed method has a higher reliability, and the real-time diagnosis is more real-time compared with the method proposed in literature [8] and [9], which can effectively diagnose the fault of large-scale ship engine in non-deterministic environment.

## REFERENCE

3. LI Suhua. Automobile Engine Fault Pattern Recognition Simulation under Variable Speed Conditions. Computer Simulation, 2016, 33(11):144-147.
4. Lei Y, Jia F, Lin J, et al. An Intelligent Fault Diagnosis Method Using Unsupervised Feature Learning Towards Mechanical Big Data. IEEE Transactions on Industrial Electronics, 2016, 63(5):3137-3147.
5. Cheng Y, Wang R, Xu M. A Combined Model-Based and Intelligent Method for Small Fault Detection and Isolation of Actuators. IEEE Transactions on Industrial Electronics, 2016, 63(4):2403-2413.
6. Chen M C, Hsu C C, Malhotra B, et al. An efficient ICA-DW-SVDD fault detection and diagnosis method for non-Gaussian processes. International Journal of Production Research, 2016, 54(17):1-11.
7. Wu F, Zhao J. A Real-Time Multiple Open-Circuit Fault Diagnosis Method in Voltage-Source-Inverter Fed Vector Controlled Drives. IEEE Transactions on Power Electronics, 2015, 31(2):1425-1437.
8. Moreira M V, Basilio J C, Cabral F G. Polynomial Time Verification of Decentralized Diagnosability of Discrete Event Systems" Versus "Decentralized Fault Diagnosis of Discrete Event Systems: A Critical Appraisal. IEEE Transactions on Automatic Control, 2015, 61(1):178-181.
9. Chao K H, Chen P Y. An Intelligent Fault Diagnosis Method Based on Extension Theory for DC-AC Converters. International Journal of Fuzzy Systems, 2015, 17(1):1-11.
10. ZENG Wentao, ZHANG Hua, YAN Wei. Application of Approximate Entropy and Support Vector Machine in Fault Diagnosis of Engine. Machinery Design & Manufacture, 2016, (11):46-49.
11. CUI Jianguo, LIU Baosheng, WANG Guihua, et al. Fault Diagnosis of Certain Key Components Based on Wavelet Packet and SVM Warship Engine. Fire Control & Command Control, 2016, 41(6):181-184.
12. Gao, W. and W. Wang, The fifth geometric-arithmetic

index of bridge graph and carbon nanocones. *Journal of Difference Equations and Applications*, 2017. 23(1-2SI): p. 100-109.

13. Gao, W., et al., Distance learning techniques for ontology similarity measuring and ontology mapping. *Cluster Computing-The Journal of Networks Software Tools and Applications*, 2017. 20(2SI): p. 959-968.
14. MI Weijian, SHEN Qing, LIU Yuan, et al. Engine fault diagnosis based on infrared thermal imaging technology. *Journal of Shanghai Maritime University*, 2016, 37(4): 65-69.
15. M.A. Hassan, M.A.M. Ismail. Literature Review for The Development of Dikes's Breach Channel Mechanism Caused by Erosion Processes During Overtopping Failure. *Engineering Heritage Journal*, 2017, 1(2): 23-30.
16. HUABIN Xiao, MENGYING Wang, SHUO Sheng. Spatial evolution of URNCL and response of ecological security: a case study on Foshan City. *Geology, Ecology, and Landscapes*, 2017, 1(3): 190-196.
17. R. Radmanfar, M. Rezayi, S. Salajegheh, V. A. Bafrani. Determination the most important of hse climate assessment indicators case study: hse climate assessment of combined cycle power plant staffs. *Journal CleanWAS*, 2017, 1(2): 23-26.
18. M.A.A. Maksou, K.M.A. Maksoud. Appraisalment of The Geologic Features as A Geo-Heritage in Abu-Roash Area, Cairo- Egypt. *Malaysian Journal Geosciences*, 2017, 1(2): 24-28.
19. T. Bata, N.K. Samaila, A.S. Maigari, M. B. Abubakar Simon Y. Ikyoive. Common Occurences Of Authentic Pyrite crystals in Cretaceous Oil Sands as Consequence of Biodegradation Processes. *Geological Behavior*, 2017, 1(2): 26-30.
20. S.B. Shamsudin, A.A. Majid. Association of blood lead levels and working memory ability of primary school children surrounding ex-copper mining area in Ranau, Sabah (Malaysia). *Acta Scientifica Malaysia*, 2017, 1(1): 01-03.

## CONTACT WITH THE AUTHOR

Donghua FENG

*e-mail: fengdonghua3fdh@163.com*

School of Computer Science and Technology  
Wuhan University of Technology  
Wuhan 430070  
**CHINA**

College of Computer and Information Engineering  
Nanyang Institute of Technology  
Nanyang 473004  
**CHINA**

# NUMERICAL SIMULATION STUDY ON EXPOSED REINFORCED ANTI-CORROSION LAYER DAMAGE OF THE CROSS-SEA BRIDGE UNDER THE MARINE ENVIRONMENT

Hao Qu <sup>1</sup>

Jufeng Su <sup>1</sup>

Pingming Huang <sup>2</sup>

Xiang Ren <sup>3</sup>

<sup>1</sup> School of Highway Engineering, Chang'an University, Xi'an, 710064, China

<sup>2</sup> Institute of Bridge Engineering, Chang'an University, Xi'an, 710064, China

<sup>3</sup> School of Architecture and Civil Engineering, Xi'an University of Science and Technology, Xi'an, 710054, China

## ABSTRACT

*To solve the problem of low precision of numerical simulation of the exposed reinforced anti-corrosion layer damage of the cross-sea bridge, we use the stress ratio between the double slash and the reinforced anti-corrosion layer to analyze the parameters and the damage rate in different qualities of reinforced anti-corrosion layers, use Ansys software to build reinforced finite element model, and analyze the damage degree when the inclination angle was 15 °, 45 ° and 60 °, respectively. The experimental results showed that the proposed method can improve the numerical simulation efficiency, the numerical simulation results, the experimental results, and the theoretical analysis results have good consistency and stability.*

**Keywords:** Cross-sea bridge, Reinforced, Anti-corrosion damage, Numerical simulation

## INTRODUCTION

The cross-sea bridge is currently a very important offshore project in China, and has an extraordinary influence on our national economy and transportation environment. But the exposed steel bars of the cross-sea bridge in the marine environment is susceptible to salt corrosion, steel corrosion [1], as well as erosion caused by wave erosion and so on. In the northern waters, it also caused by freezing and thawing cycle damage phenomenon. In order to have a better analysis, numerical simulation is needed [2]. In traditional methods, the stochastic aggregate model is used to analyze the constitutive relation of the damage interface and the mechanical properties of the concrete. Sometimes when the numerical simulation is carried out, the results are inconsistent with the actual results, and the efficiency is low [3]. It will increase the post-repair reinforcement work

[4], cost a lot of manpower and material resources [5], and with the emergence of structural failure [6]. In this paper, a numerical simulation method of the exposed reinforced anti-corrosion layer damage in the marine environment based on the double slash is proposed.

## DAMAGE ANALYSIS OF EXPOSED REINFORCED ANTI-CORROSION LAYER OF SEA-CROSSING BRIDGE

In the process of building a sea-crossing bridge, it is very important to select the reinforcement constitutive relationship for the exposed steel bars, here we use the double slash model which can reflect the reinforcement of the steel bars, to make

the constitutive relation simple and conform to the actual [7]. The formula is shown as follows:

$$\begin{cases} \sigma_s = E_s \varepsilon_s, E_s = f_y / \varepsilon_s \leq \varepsilon_y \\ \sigma_s = f_y + (\varepsilon_s - \varepsilon_y) \tan \theta', \tan \theta' = E'_s = \frac{f_u - f_y}{\varepsilon_u - \varepsilon_y}, \varepsilon_y \leq \varepsilon_s \leq \varepsilon_u \end{cases} \quad (1)$$

Where  $\sigma_s$  represents the steel bar stress,  $\varepsilon_s$  represents the steel strain,  $f_y$  represents the yield strength of the bar,  $E_s$  represents the modulus of the initial elasticity of the reinforcement,  $\varepsilon_y$  represents the yield strain of the reinforcement,  $\theta'$  represents the strengthening section stress in double slash model,  $E'_s$  represents reinforced section elastic modulus of the reinforcement in double slash model,  $f_u$  represents the behalf of the ultimate strength of steel,  $\varepsilon_u$  represents the behalf of the ultimate strain of steel.

Under the influence of the double damage factors of the reinforcement layer and the reciprocating load, the cross-section area, ultimate strength, yield strength and elastic modulus of the steel will change. To avoid the analysis is too complex, assuming that the elastic modulus is not affected by the steel damage and the impact of reciprocating loads. The cross-section area, the yield strength and the ultimate strength of the steel affected by the reciprocating load double damage factor is shown as:

$$f_y(n) = \sigma_{\max}(N_f) \left\{ 1 - \frac{\lg n}{\lg N_f} \left[ 1 - \frac{\sigma_{\max}(N_f)(1-\eta_m)}{(1-1.049\eta_m)f_y} \right] \right\} \quad (2)$$

When the damage rate of reinforced anti-corrosion layer is  $0 \leq \eta_m \leq 2\%$ :

$$A_s(n) = \left\{ 1 - \frac{n}{N_f} \left[ 1 - \frac{\sigma_{\max}(N_f)(1-\eta_m)}{(1-1.049\eta_m)f_y} \right] \right\} (1-\eta_m) A_s \quad (3)$$

When the damage rate of reinforced anti-corrosion layer is  $2\% \leq \eta_m \leq 10\%$ :

$$A_s(n) = \left\{ 1 - \frac{n}{N_f} \left[ 1 - \frac{\sigma_{\max}(N_f)(1-\eta_m)}{(1-1.049\eta_m)f_y} \right] \right\} (0.985 - 0.97\eta_m) A_s \quad (4)$$

When the damage rate of reinforced anti-corrosion layer is  $10\% < \eta_m \leq 20\%$ :

$$A_s(n) = \left\{ 1 - \frac{n}{N_f} \left[ 1 - \frac{\sigma_{\max}(N_f)(1-\eta_m)}{(1-1.049\eta_m)f_y} \right] \right\} (0.938 - 0.95\eta_m) A_s \quad (5)$$

$$\frac{f_u(n)}{f_y(n)} = 1.5 \quad (6)$$

Where  $f_y(n)$  represents the remaining yield strength of the steel bar,  $f_u(n)$  represents the ultimate strength of the steel bar,  $\sigma_{\max}(N_f)$  represents the maximum stress at the time of fatigue damage of the steel bar,  $n$  represents the number of cycles,  $\eta_m$  represents the mass breakage rate of the reinforced anti-corrosion layer,  $A_s(n)$  represents the remaining cross-sectional area of the steel bar, and  $A_s$  represents the area of the initial section of the steel bar.

The stress ratio [8] refers to the ratio of the minimum stress to the maximum stress under the reciprocating load. The magnitude of the stress refers to the difference between

the maximum stress and the minimum stress. In this paper, formula (7) is introduced to contact the stress ratio, the damage rate and the fatigue life under the premise of guaranteeing the same maximum stress, and then combined the formulas (2) to (6) to process the numerical simulation. The advantage of the formula (7) is: surface equation [9] is fitted according to the natural damage of reinforced components, so that the structure or components are as close as possible when meet the premise of safe operation. The fatigue life of the damaged steel structure or component is:

$$\log N_f = (15.138 + 0.086\eta_s) - (3.687 + 0.051\eta_s) \log S_{rc} - k\sigma_A \quad (7)$$

Where  $N_f$  represents the fatigue life or the number of cycles,  $\eta_s$  represents the average cross-sectional breakage of the steel,  $S_{rc}$  represents the nominal stress amplitude,  $k$  represents the influence factor of the guarantee rate, and  $\sigma_A$  represents the standard deviation of the naturally damaged steel bars obtained by statistical analysis of the test results.

Analysis of equations (2) to (7) can be found that when the maximum stress of the fatigue failure of the steel is kept constant, increased the stress ratio at the same damage rate, the stress amplitude of the steel is gradually reduced, resulting in the fatigue life of the steel increased which caused the strength and cross-sectional area of the steel bar decreased and gradually weakened. Finally, the bearing capacity of the damaged steel bar is affected by the reciprocating load, as shown in the following Figure 1.

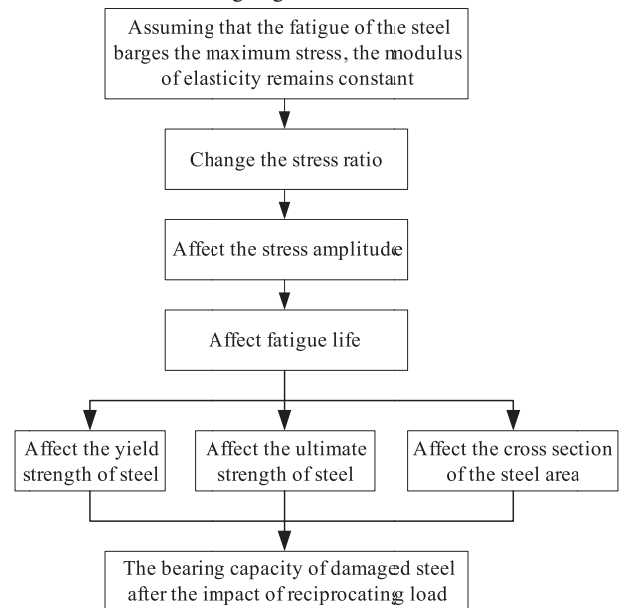


Fig. 1. Effect of Stress Ratio on the Bearing Capacity of Damaged Steel after the Reciprocating Load Is Applied

Using the above diagram, it is possible to better analyze the numerical simulation of the reinforced anti-corrosion layer damage.

## NUMERICAL ANALYSIS OF THE REINFORCED ANTI-CORROSION LAYER DAMAGE

The finite element model was established by using Ansys software [10-12]. The finite element parameters were set up: the thickness of the interface between reinforced concrete and concrete was 0.1mm, the elastic modulus was 15GPa, the Poisson's ratio was 0.25, the reinforced model was HRB335, and the density was 7800kg /m<sup>3</sup>. The finite element model established under the above parameters is shown in Figure 2 and Figure 3.

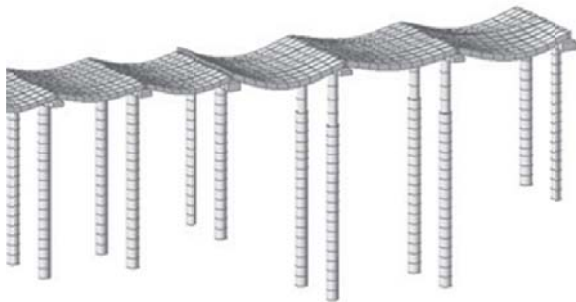
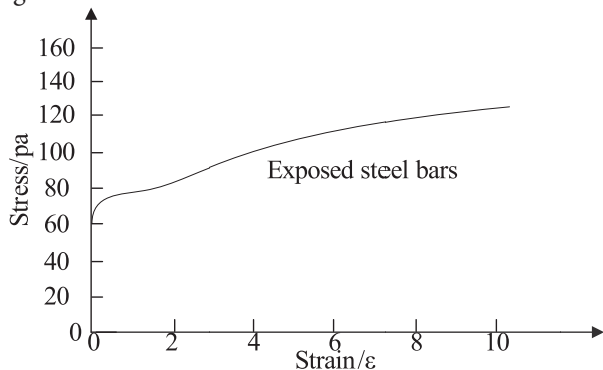
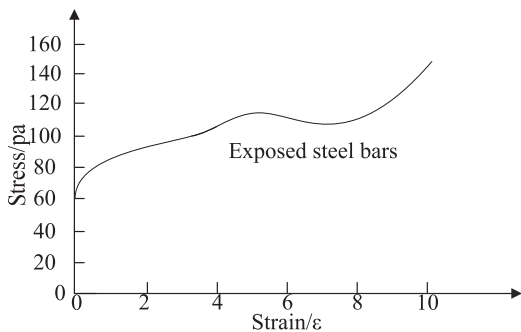


Fig. 2. Finite Element Model of the Steel Bars

(A) Damage Degree of the Steel Bar When the Inclination Angle Is 15 °



(B) Damage Degree of the Steel Bar When the Inclination Angle Is 45 °



(C) Damage degree of the Steel Bar When the Inclination Angle Is 60 °

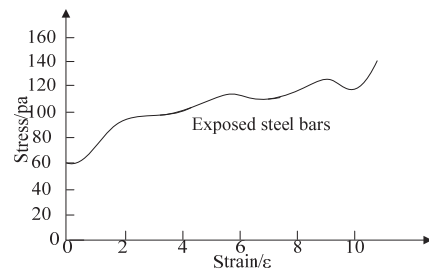


Fig. 3. The Damage Degree of the Steel Bars at Different Inclination Angles

When the inclination angle is 15 °, the stress distribution is uneven, and the crack is bent at the bottom of the steel specimen [13,14].

When the inclination angle is 45 °, the middle part of the stress is obviously uneven, the test process, when the bottom corner of the sample has not yet begun to break, the layers have been clearly dislocation.

When the inclination angle is 60 °, the numerical simulation is similar to the 45 ° model, but the 60 ° sample is damaged at the bottom corner and then damaged the layer.

## EXPERIMENTAL RESULTS AND ANALYSIS

To prove the reliability of the proposed method, an experiment is required. Experimental platform was established under SPSS20.0 environment, the experimental data were taken from a cross-sea bridge, the reinforced anti-corrosion layer was observed for 1 month, record the damage process.

### A. SIMULATION RESULTS OF STRESS CHANGES IN DIFFERENT METHODS

The Figure4 showed the numerical simulation results of the relationship between the stress and strain of the reinforced anti-corrosive layer damage caused by seawater. Figure 5 showed the numerical simulation results caused by other factors.

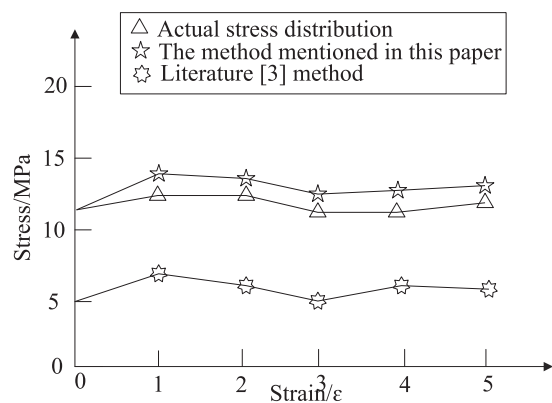


Fig. 4. Relationship between Stress and Strain in Different Methods under Seawater

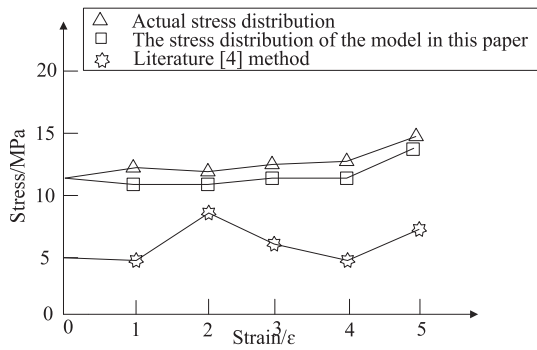
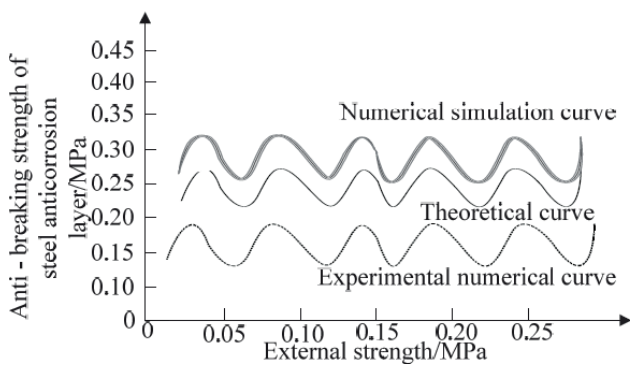


Fig. 5. Relationship between Stress and Strain in Different Methods under Other Factors

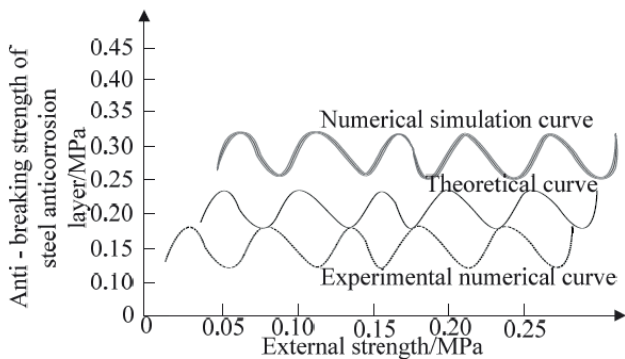
## B. COMPARISON OF NUMERICAL SIMULATIONS IN DIFFERENT METHODS

The Figure 6 showed the experimental results, theoretical analysis and numerical analysis of different methods. Figure 7 showed the comparison of the experimental and simulated load versus deflection curves for different methods.

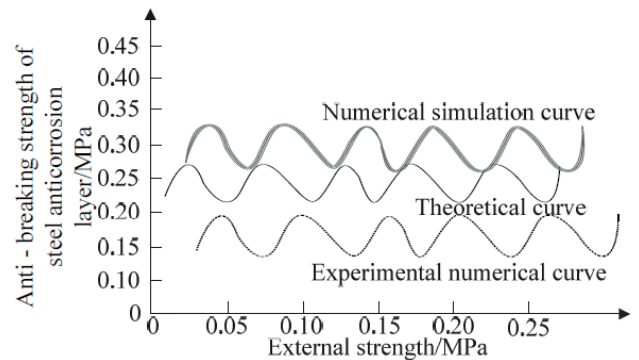
(A) Experimental Results of the Proposed Method and the Relationship between the Theoretical Analysis and Numerical Analysis



(B) Experimental Results of the Method Proposed in Literature [5] and the Relationship between the Theoretical Analysis and Numerical Analysis



(C) Experimental Results of the Method Proposed in Literature [4] and the Relationship between the Theoretical Analysis and Numerical Analysis



(D) Experimental Results of the Method Proposed in Literature [3] and the Relationship between the Theoretical Analysis and Numerical Analysis

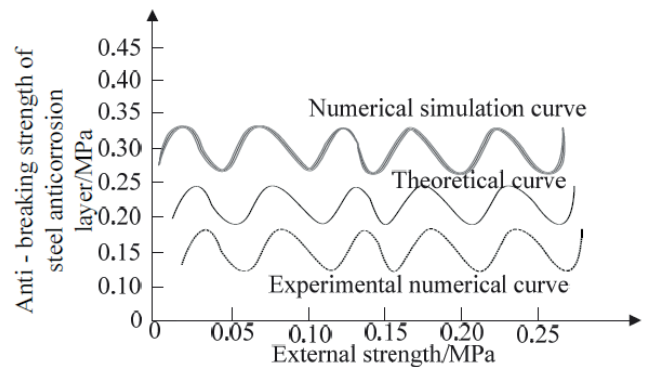
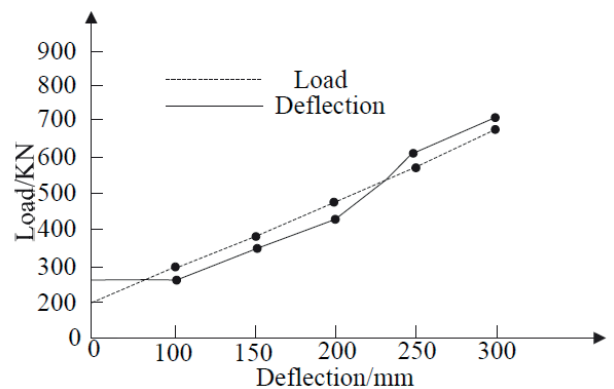
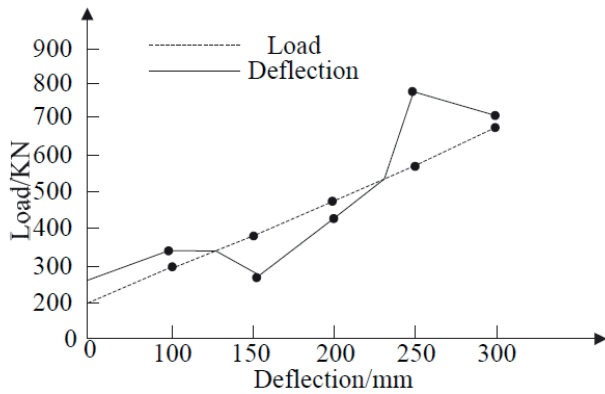


Fig. 6. Experimental Results Different of Methods and the Relationship between the Theoretical Analysis and Numerical Analysis

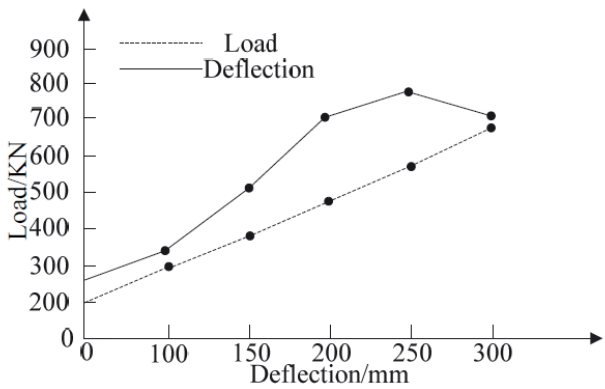
(A) Experimental and Simulated Load and Deflection Curves in the Proposed Method



(B) Experimental and Simulated Load and Deflection Curves in the Method Proposed in Literature [6]



(C) Experimental and Simulated Load and Deflection Curves in the Method Proposed in Literature [4]



(D) Experimental and Simulated Load and Deflection Curves in the Method Proposed in Literature [5]

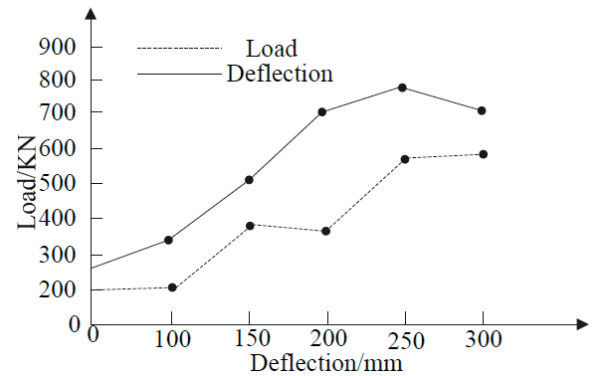


Fig. 7. Comparison of Experimental and Simulated Load and Deflection Curves in Different Methods

## DISCUSSION

Figure.4 and Figure.5 showed that the stress simulation results of the exposed reinforced anti-corrosive layer damage of the cross-sea bridge are consistent with the actual stress changes by using the proposed method [14]. The proposed method utilizes the double slash model which can reflect the reinforcement of the steel after the yield section and

make the constitutive relation simple and consistent with the actual, improve the distribution consistent of the simulation stress and the actual stress [15]. Compared with the experimental results, theoretical analysis and numerical analysis in other methods showed in Figure 6 and Figure 7, the results of the proposed method are in good agreement with the experimental and theoretical analysis. In the proposed method, the experimental data and the load values in the simulation results are almost linear, which further proved the proposed method has stability [16-18].

## CONCLUSION

The numerical simulation of the exposed reinforced anti-corrosion layer damage under the marine environment in the current method cannot achieve high-precision modeling and analysis. The proposed method analyzed the reinforced anti-corrosion layer damage with the stress ratio of the double slash model, established the finite element model by using Ansys software, and analyzed the damage degree of steel bar at 15, 45 and 60°, respectively, complete the numerical simulation and analysis of steel bar damage. The experimental results showed that the proposed method can provide a reference for the study of the exposed reinforced anti-corrosion layer damage for the cross-sea bridge.

## ACKNOWLEDGEMENT

Fund project:National Natural Science youth Foundation of China, project number: 51408484

## REFERENCES

1. LIU Jiawei, LIU Bing. Study of the Ramjet Cavity Shear Layer Characteristics with Numerical Simulation. *Computer Simulation*, 2017,34(3):82-87.
2. King J, Howell S, Derksen C, et al. Evaluation of Operation IceBridge quick-look snow depth estimates on sea ice. *Geophysical Research Letters*, 2016, 42(21):9302-9310.
3. HE Rui, JI Shao-hua, HUANG Ping-ming, et al. Numerical simulation of the effect of interface transition zone between mortar and aggregates on the mechanics properties of concrete. *Journal of Chang'an University(Natural Science Edition)*, 2015,35(2):31-37.
4. Lancioni G. Modeling the Response of Tensile Steel Bars by Means of Incremental Energy Minimization. *Journal of Elasticity*, 2015, 121(1):1-30.
5. Shan A. Analytical Research on Deformation Monitoring of Large Span Continuous Rigid Frame Bridge during Operation. *Engineering*, 2015, 07(8):477-487.

6. Sandhåland H, Oltedal H, Eid J. Situation awareness in bridge operations – A study of collisions between attendant vessels and offshore facilities in the North Sea. *Safety Science*, 2015, 79(4):277–285.
7. Armitage T W K, Ridout A L. Arctic sea ice freeboard from AltiKa and comparison with CryoSat-2 and Operation IceBridge. *Geophysical Research Letters*, 2015, 42(16):6724-6731.
8. DU Xiuli, ZHANG Renbo, JIN Liu. Meso-scale numerical investigation on the crack process of concrete cover induced by rebar non-uniform corrosion. *Journal of Chongqing Jianzhu University*, 2015,37(1):73-80.
9. YANG Lu, SHI Xu-wu. Numerical simulation of plastic damage model for reinforced concrete beam. *Journal of Shenyang University of Technology*, 2016,38(1):97-101.
10. 11.Gao, W. and W. Wang, The fifth geometric-arithmetic index of bridge graph and carbon nanocones. *Journal of Difference Equations and Applications*, 2017. 23(1-2SI): p. 100-109.
11. 12.Gao, W., et al., Distance learning techniques for ontology similarity measuring and ontology mapping. *Cluster Computing-The Journal of Networks Software Tools and Applications*, 2017. 20(2SI): p. 959-968.
12. TANG Guobin, XIANG Yiqiang. Mechanical properties and numerical simulation of crack interface in reinforced concrete. *Journal of Hydraulic Engineering*, 2015,46(1):42-57.
13. Sukor N S A, Jarani N, Faisal S F M, Analysis of Passengers' Access and Egress Characteristics to The Train Station. *Engineering Heritage Journal*, 2017, 1(2): 01-04.
14. Yang S, Li J, Song Y, Application of surfactant Tween 80 to enhance Fenton oxidation of polycyclic aromatic hydrocarbons (PAHs) in soil pre-treated with Fenton reagents. *Geology, Ecology, and Landscapes*, 2017, 1(3): 197-204.
15. Bahmani M, Noorzad A, Hamed J, Sali F, The role of bacillus pasteurii on the change of parameters of sands according to temperaturcompression and wind erosion resistance. *Journal CleanWAS*, 2017, 1(2): 1-5.
16. Tunggolou J, Payus C, Moringa Oleifera As Coagulant Used in Water Purification Process For Consumption. *Malaysian Journal Geosciences*, 2017, 1(2): 29-31.
17. Yew L K, Rahim I A, Prediction of Rock Mass Properties, Tunnel Stability and Support Pressure by Geological Strength Index (GSI) In Crocker Formation: A Case Study. *Geological Behavior*, 2017, 1(2): 31-33.
18. Shamsudin S B, Marzuki A, Jeffree M F, Lukman K A. Blood lead concentration and working memory ability on Malay primary school children in urban and rural area, Malacca. *Acta Scientifica Malaysia*, 2017, 1(1): 04-07.

## CONTACT WITH THE AUTHOR

Pingming Huang

*e-mail: quhao2166@163.com*

Institute of Bridge Engineering  
Chang'an University  
Xi'an, 710064  
**CHINA**

## RESEARCH ON INTELLIGENT AVOIDANCE METHOD OF SHIPWRECK BASED ON BIGDATA ANALYSIS

Wei Li <sup>1</sup>

Qian Huang <sup>2</sup>

<sup>1</sup> Information Center, Renmin Hospital of Wuhan University, Wuhan 430060, China

<sup>2</sup> Wuchang Polytechnic College, Wuhan 430060, China

### ABSTRACT

*In order to solve the problem that current avoidance method of shipwreck has the problem of low success rate of avoidance, this paper proposes a method of intelligent avoidance of shipwreck based on big data analysis. Firstly, our method used big data analysis to calculate the safe distance of approach of ship under the head-on situation, the crossing situation and the overtaking situation. On this basis, by calculating the risk-degree of collision of ships, our research determined the degree of immediate danger of ships. Finally, we calculated the three kinds of evaluation function of ship navigation, and used genetic algorithm to realize the intelligent avoidance of shipwreck. Experimental result shows that compared the proposed method with the traditional method in two in a recent meeting when the distance to closest point of approach between two ships is 0.13nmile, they can effectively evade. The success rate of avoidance is high.*

**Keywords:** Big data analysis, Shipwreck, Intelligent avoidance, Genetic algorithm

### INTRODUCTION

Ships at sea will encounter. Many factors such as the bad weather or the low visibility, the ship driver's dereliction of duty without using the safety speed, the risk judgment errors, or the improper avoidance operation[1-2] can cause the ship into the close quarters situation, even forming urgent danger[3-4]. More than 80% of the maritime accidents are owing to human factors[5-6]. Most of them are caused by violating International Regulations for Preventing Collisions at Sea and the driver's carelessness[7-8]. In order to alleviate the human error factors in the process of ship avoidance and fundamentally reduce the shipwreck caused by human decision-making errors, we need to research the intelligent avoidance methods for ship shipwreck[9]. The reference[10-12] proposes the method for avoiding maritime accidents based on big data for scientific decision. Through the cluster analysis

of sailing factors of ship accident and association rules mining for all kinds of accident factors, we can realize the intelligent avoidance of shipwreck, but this method has a series of problems that the recognition accuracy of ship collision avoidance is low, the probability of successful avoidance is low, and the feasibility of avoidance decision is poor. Therefore, a method of intelligent avoidance of ship collision based on big data analysis is proposed [13-17].

### CALCULATION OF DISTANCE TO SAFE POINT OF APPROACH OF SHIP BASED ON BIGDATA ANALYSIS

Using the big data analysis to calculate the ship safe distance of approach under the head-on situation, the crossing

situation, the overtaking situation. The specific process is as follows:

The ship safe distance of approach (SDA) is mainly determined by the radius of the collision region (SDA<sub>min</sub>), the room for manipulation of the ship and the encountering characteristics of ship. Because the radius of ship collision region (SDA<sub>min</sub>) is centered on this ship, the size of two ships, the circular area of the ship encountered situation will be considered, and the collision will occur when two ships enter the area. The radius of ship collision zone is calculated by big data analysis. Its formula is:

$$SDA \min = \frac{1}{2}L_0 + \frac{1}{2}L_t + 2P \quad (1)$$

Among them,  $L_0$  and  $L_t$  respectively indicate the length of our ship and the target ship;  $P$  indicates GPS positioning accuracy of the ship [18].

Considering the intersection relation between position of ship and our ship, different distance of the safe point of approach (SDA) models of ships are obtained, and the formula is as follows:

$$SDA = \begin{cases} R_f & (1) \\ R_f - Adm & (2) \\ R_f - v_t \cdot t & (3) \\ R_f - Trm & (4) \end{cases} \quad (2)$$

In the formula,  $Adm$  and  $Trm$  respectively represent the longitudinal distance of ship gyration and the horizontal distance of the ship gyration.  $t$  represents the time required that the small rudder angle of this ship changes to the new heading distance;  $v_t$  represents the real speed of the target ship sailing. According to the formula (2), when the target ship is overtaken by our ship, formula (3) holds; when the target ship is the overtaking ship or it is placed in (122.5°, 247.5°) relative to navigational position  $b$ , the formula (2) is workable. When the target ship relative to navigational position  $b$  satisfies:  $292.5^\circ \leq b \leq 150^\circ$  or  $0^\circ \leq b \leq 67.5^\circ$ , or  $67.5^\circ \leq b \leq 150^\circ$  and  $C_r \geq b + 180^\circ$ , or  $210^\circ \leq b \leq 292.5^\circ$  and  $C_r \leq b + 180^\circ$ , or  $v_r = 0$  and  $b \leq 90^\circ$ , or  $b \leq 270^\circ$ , thus, formula (1) is workable; otherwise, formula (4) is workable.

Among them, in formula (2):

$$R_f = SDA \min + v_t \cdot t + Adm \quad (3)$$

$$Adm = V \left( T + \frac{t_1}{2} + \frac{1}{K \delta_0} \tan \frac{\varphi_0}{2} \right) \quad (4)$$

$$+ R \tan \frac{\varphi_0}{2} \cos \varphi_0$$

$$Trm = \tan \frac{\varphi_0}{2} \cdot \frac{V}{K \delta_0} \sin \varphi_0 \quad (5)$$

$$\text{—} \quad (6)$$

In the formula,  $v_r$  represents the speed of relative motion of ship sailing;  $C_r$  represents course of relative motion of ship sailing;  $V$  represents speed of ship sailing;  $K$  represents turning index of ship sailing;  $T$  represents the turning lag index of ship;  $\delta_0$  represents the current rudder angle in ship sailing;  $\varphi_0$  represents the current redirection angle in the ship sailing;  $R$  represents turning radius of ship sailing;  $t_1$  represents the time required from the steering rudder angle to the current rudder angle  $\delta_0$  in the ship sailing.

Thus, when head-on situation and overtaking situation happen in ship channel, the calculation formulas of the ship safe distance of approach are as follows:

$$SDA \min = 1/2(L_1 \cdot \sin \beta + B_1 \cdot \cos \beta) + 1/2(L_2 \cdot \sin \theta + B_2 \cdot \cos \theta) + B_{\max} + 2P \quad (7)$$

$$SDA = 1/2(L_1 \cdot \sin \beta + B_1 \cdot \cos \beta) + 1/2(L_2 \cdot \sin \theta + B_2 \cdot \cos \theta) + B_{\max} + 2P + Trm \quad (8)$$

In the formula,  $B_1$  and  $B_2$  represent the ship beam of two ships respectively;  $\beta$  and  $\theta$  represent drift angles of two ships;  $B_{\max}$  represents the ship beam of the bigger one in two ships.

## CALCULATION OF RISK DEGREE OF SHIP COLLISION BASED ON BIGDATA ANALYSIS

According to the calculation results of safe distance of approach of ships, we use the big data analysis to judge the risk degree of collision of ships, and calculate the minimum value and maximum value of time of last minute action in dangerous situation of ships collision and the different value ranges of ship initial time of last minute action to judge the degree of risk degree ships collision and danger level. The detailed steps are described below:

According to the big data analysis, usually the small rudder angle of ship sailing is 10°. The maximum rudder angle is 30°. Generally, the redirection angle of ship is  $C_1$ , and the maximum redirection angle of ship is  $C_3$ . According to the geometrical analysis of relative motion in the ship sailing, the PIDVCA theory establishes the model for solving the target ship motion element and predicting movement element after our ship changes direction, and calculates the equations of the straight line  $RML$  and the straight line  $NRML$  respectively.

$$\begin{cases} y_{RML} = x \cdot \cot C_r + \frac{DCPA}{\sin C_r} \\ y_{NRML} = x \cdot \cot C_m + \frac{-SDA}{\sin C_m} \end{cases} \quad (9)$$

In the formula,  $C_r$  and  $C_m$  represent the course of our ship and the course of the target ship relative to our ship before and after the redirection. According to the formula (9), the coordinates of the intersection point  $b$  of two straight lines are calculated. Its expression is:

$$\begin{cases} x_b = \frac{\left[ \frac{-SDA \min}{\sin C_m} - \frac{DCPA}{\sin C_r} \right]}{\cot C_r - \cot C_m} \\ y_b = x_b \cdot \cot C_m + \frac{-SDA}{\sin C_m} \end{cases} \quad (10)$$

When our ship and target ship encounter, assuming that our ship turns right to  $C_m$ , and the sailing relative displacement generated by ships is expressed as  $SS$ . The components of the horizontal axis and the vertical axis are expressed as  $X_s$  and  $Y_s$ , and its calculation formula is as follows:

$$\begin{cases} x_s = v_t \cdot Tn \cdot \sin C_t + Dc \\ y_s = v_t \cdot Tn \cdot \cos C_t + Fd \end{cases} \quad (11)$$

Among them,  $Tn$  shows that the time required for cycle that our ship turns to  $90^\circ$  at full speed and full rudder;  $Dc$  represents the tactical diameter of ships;  $Fd$  represents the cyclic advance distance of ships. The formula of relative displacement  $SS$  of sailing generated by ships is as follows:

$$SS = \sqrt{x_s^2 + y_s^2} \quad (12)$$

The point  $a$  is taken from the straight line  $RML$ , which makes the length of  $ab$  equal to the relative displacement of the ship which is generated by the ship.  $a$  is used as the estimated helm point of our ship when it is sailing. We can derive the coordinate of estimated rudder point  $a$  of the ship at this time:

$$\begin{cases} x_a = x_b \cdot SS \cdot \sin C_r \\ y_a = y_b \cdot SS \cdot \cos C_r \end{cases} \quad (13)$$

Thus, the calculation formula of maximum critical distance  $Did_{\max}$  of the ship imminent danger is as follows:

$$Did_{\max} = \sqrt{x_a^2 + y_a^2} \quad (14)$$

The time from the current moment  $C(x, y)$  to estimated helm point  $a(x_a, y_a)$  is the helm time of ships. Its expression is:

$$T \ln = \sqrt{(x - x_a)^2 + (y - y_a)^2} / V \quad (15)$$

If  $a(x_a, y_a)$  is corresponding to the coordinate of initial rudder distance of ship, the calculation result in above formula (15) is the initial rudder time of ship  $T \ln(SDA, C_1)$  if  $a(x_a, y_a)$  is corresponding to the distance  $DE$  of close quarters situation of ship collision, the calculation result in above formula (15) is the last helm time  $T \ln(SDA, C_3)$  of close quarters situation of ship collision; if  $a(x_a, y_a)$  is corresponding to the distance  $DE_{\min}$  of close quarters situation of ship collision, the calculation result in above formula (15) is the last helm time  $T \ln(SDA_{\min}, C_3)$  in imminent danger situation of ship collision.

According to the minimum  $T \ln(SDA, C_3)$  and maximum  $T \ln(SDA_{\min}, C_3)$  of last helm time from above calculation of ship collision in imminent danger situation and the different

range of value of initial helm time  $T \ln(SDA, C_1)$  to determine the risk degree of ships collision and risk level.

(1) when  $T \ln(SDA, C_1) \geq 3 \text{ min}$ , if the sailing ship uses its minimum rudder angle and the minimum redirection angle to pass the safe distance of approach, the time is relatively abundant and it is a potential danger ( $ek = 1$ ) of ship collision;

(2) when  $T \ln(SDA, C_1) < 3 \text{ min}$  and  $T \ln(SDA, C_3) \geq 0$ , when the navigating ship uses its minimum rudder angle and the minimum redirection angle is close to the time of passing the safe distance of approach  $SDA$ , which is a common danger ( $ek = 2$ ) of ship collision;

(3) when  $T \ln(SDA, C_1) < 0$ , however  $T \ln(SDA_{\min}, C_3) \geq 0$ , the initial rudder time of ship sailing has been missed, and it is an imminent danger situation ( $ek = 3$ ) for the collision of ships;

(4) when  $T \ln(SDA_{\min}, C_3) < 0$ , the sailing ship is unable to travel from the minimum safe distance  $SDA_{\min}$  of approach, namely, it is unable to avoid the collision, which belongs to the imminent danger of ship collision ( $ek = 4$ ).

## INTELLIGENT AVOIDANCE OF SHIPWRECK BASED ON GENETIC ALGORITHM

On the basis of the judgment of risk degree of ship collision, three evaluation functions of ship sailing are calculated, and the intelligent avoidance of shipwreck is realized by genetic algorithm. Specific practices are as follows:

Firstly, we determine the target ship which has the maximum risk of collision with our ship on each ship route at sea, and calculate difference between the minimum distance and safe distance in the target ship and our ship to determine the security of our ship route. Thus, the computational expression of the safety evaluation function of navigation:

$$S(x') = \sum_{i=1}^{N-1} clear(x'_i) \quad (16)$$

Among them,  $x'$  is the chromosome, which represents a route of ship;  $i$  represents the node of a path on this route.  $i$  is from 1 to  $N-1$ .  $N$  represents the total number of genetic factors of a path on the route (i.e. the turning point or node), there are  $N-1$  short ship routes. Thus:

$$S(x) = \sum_{i=1}^{N-1} clear(x'_i) = \begin{cases} e^{k(g_i - \tau) - 1} & \text{if } g_i \geq \tau \\ h^*(\tau - g_i) & \text{others} \end{cases} \quad (17)$$

In the formula,  $\tau$  represents the safe distance of approach of ships;  $k$  and  $h$  represent the evaluation coefficient of security;  $g_i$  represents the minimum of distance between the target ship which has maximum risk degree of ship collision the during the sailing, when our ship route is between the  $i$ -th node and the  $i+1$ -th node in all target ships which are detected.

The economic evaluation function of ship sailing is calculated. The economic evaluation of ship sailing mainly includes the consumption of ship route in various aspects, such as the degree of smoothing of ship route, the voyage

consumption of ships, the time consumption, and other parameters. The calculation formula is as follows:

$$E(x') = w_d \sum_{i=1}^{N-1} dist(x'_i) + w_t \sum_{i=1}^{N-1} time(x'_i) + w_s \sum_{i=1}^{N-1} smooth(x'_i) \quad (18)$$

Among them,  $w_d$ ,  $w_t$  and  $w_s$  represent the coefficient factor of economic evaluation function of ship sailing;  $\sum_{i=1}^{N-1} dist(x'_i)$  represents the length of the whole course in the ship sailing, which satisfies  $dist(x'_i) = d(m_i, m_{i+1})$ . It shows the distance between two adjacent nodes on the ship route;  $smooth(x'_i) = s(m_i)$  represents the maximum curvature of  $i$  at nodes on the route;  $time(x'_i)$  represents the consumption time that ship pass two adjacent node on the route.

The evaluation function of traffic rules for ship sailing at sea is calculated. The formula is:

$$T(x') = \sum_{i=1}^{N-1} T\_Cost(x'_i) \quad (19)$$

In the formula,  $T\_Cost(x'_i)$  represents the degree that ships abide International Regulations for Preventing Collisions at Sea.

According to the three evaluation functions mentioned above, supposing that the course of our ship and the target ship  $j$  is expressed as  $\varphi_o$  and  $\varphi_{Tj}$ , and the steering avoidance of ship is analyzed. The specific process is as follows:

1. if board angle  $\theta_{Tj}$  of the target ship  $j$  which has the maximum risk degree of ship collision relative to this ship is:

- 1)  $000^\circ \leq \theta_{Tj} \leq 006^\circ$  and  $|180^\circ - |\varphi_{Tj} - \varphi_o|| \leq 6^\circ$ , or
- 2)  $354^\circ \leq \theta_{Tj} \leq 360^\circ$  and  $|180^\circ - |\varphi_{Tj} - \varphi_o|| \leq 6^\circ$ ,

It shows that when our ship and the target ship  $j$  form the head-on situation on the voyage, we can judge that our ship is the ship which avoids the pass-by ship or has the same circumvention responsibility, and we should take the action of turning right:

1. If our ship has  $dx'_i = (x'_{i+1} - x'_i) > 0$  at the next moment, and select  $T\_Cost(x'_j) = 0.01$ , which shows that our ship complies with the requirements of International Regulations for Preventing Collisions at Sea;
2. If  $dx'_i = (x'_{i+1} - x'_i) \leq 0$ , it shows that our ship has taken the wrong evasive action or has not taken the evasive action, which is regarded as breaking the requirements of International Regulations for Preventing Collisions at Sea, thus we should select  $T\_Cost(x'_j) = 1$  at this moment.

2. if board angle of the target ship  $i$  which has the maximum risk degree of ship collision relative to this ship is:

- 1)  $000^\circ \leq \theta_{Tj} \leq 006^\circ$  and  $|180^\circ - |\varphi_{Tj} - \varphi_o|| \leq 6^\circ$ , or
- 2)  $354^\circ \leq \theta_{Tj} \leq 360^\circ$  and  $|180^\circ - |\varphi_{Tj} - \varphi_o|| \leq 6^\circ$ , or

$$3) 006^\circ \leq \theta_{Tj} \leq 67.5^\circ \text{ and } |180^\circ - |\varphi_{Tj} - \varphi_o|| \leq 6^\circ,$$

It shows that our ship and the target ship  $j$  form the crossing situation on the voyage, we can judge that our ship has taken the action of turning to the right to avoid collision.

3. if board angle of the target ship  $j$  which has the maximum risk degree of ship collision relative to this ship is:

1)  $67.5^\circ \leq \theta_{Tj} \leq 112.5^\circ$  and  $|180^\circ - |\varphi_{Tj} - \varphi_o|| > 6^\circ$  show that our ship and the target ship form the crossing situation, and we can judge that the ship has taken evasive action of turning to the left;

2)  $112.5^\circ \leq \theta_{Tj} < 247.5^\circ$  indicates the target ship overtakes our ship, or

3)  $247.5^\circ \leq \theta_{Tj} < 354^\circ$  indicates that the ship is the crossing situation of larboard angle. According to International Regulations for Preventing Collisions at Sea, the ship can be judged as the direct route. The target ship which has maximum risk degree of collision gets out of the road. If our ship takes evasive action, which is inconsistent with the rules.

4) when our ship is overtaking the target ship, our ship is a given-way ship. because of the true bearing of our ship is  $a_o$  relative to the target ship, but our ship has not taken evasive action, which is inconsistent with the rules. Thus, the intelligent avoidance of shipwreck has been realized.

## EXPERIMENTAL RESULTS AND ANALYSIS

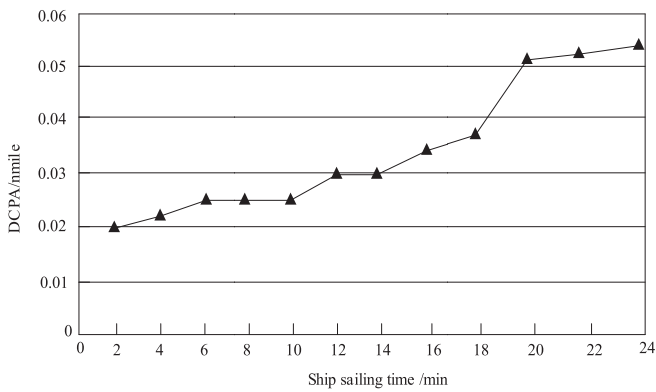
Experiment uses Visual Basic 8.0 as development platform, and uses the big data analysis software and genetic algorithm to simulate the intelligent avoidance process of shipwreck, in order to test the effectiveness and feasibility of the proposed method.

At the initial time, the sailing speed of the target ship 1 is 12 kn, and the sailing direction is  $302.8^\circ$ . The sailing speed of the target ship 2 is 15 Kn, and the sailing direction is  $152.7^\circ$ . The two ships in the voyage are 0.37nmile apart,  $DCPA = -0.04nmile$ ,  $TCPA = 1.23nmile$ ,  $SDA_{min} = 0.056nmile$ . According to the calculation of risk degree of ship collision, two ships have formed the immediate danger situation. We use the method proposed in this paper to carry out the intelligent evasive action of shipwreck. The experimental test result is shown in Figure 1. According to Figure 1 (a), we can see that the collision avoidance of two ships is successful. Evasive parameters in the whole process of ship collision avoidance are analyzed, as shown in Figure 1 (b) & (c).  $DCPA$  is increased from 0.02 nmile to 0.06, and the ship will pass through outside of  $SDZ_{min}$ . At this time, the ship  $TCPA$  will gradually change from 1.73 to -0.67, which shows that the ship has passed the distance to closest point of approach.

(a) Two Ships Run Safely Evading Each Other



(b) Data Analysis of Intelligent Avoidance of Shipwreck



(c) Data Analysis of Intelligent Avoidance of Shipwreck

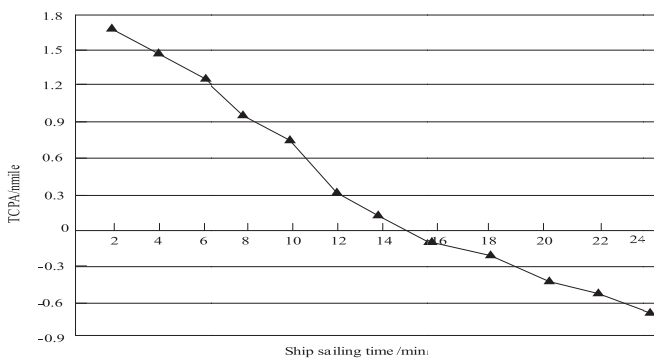


Fig. 1. Effect Diagram of Intelligent Avoidance Simulation of Shipwreck Based on Big Data Analysis

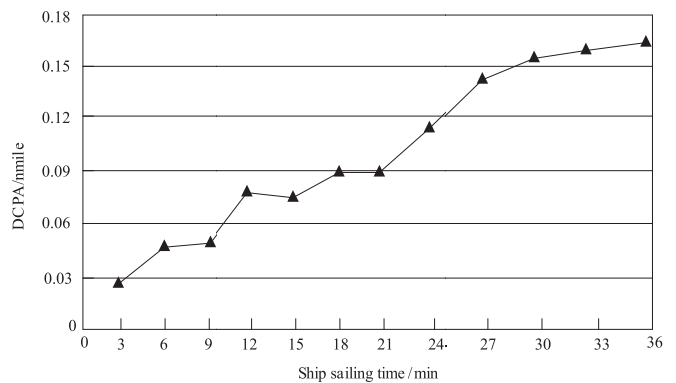
At the initial time, the sailing speed of the target ship 1 is 13 Kn, and the sailing direction is 308°. The sailing speed of the target ship 2 is 14 Kn, and the sailing direction is 199.2°. The two ships in the voyage are 0.46 nmile apart,  $DCPA = -0.04nmile$ ,  $TCPA = 2.05nmile$ ,  $SDA_{min} = 0.12nmile$ . According to the calculation of risk degree of ship collision, two ships have formed the immediate danger situation. We use the method proposed in this paper to carry out the intelligent

evasive action of shipwreck. According to Figure 2 (a), we can see that the collision avoidance of two ships is successful. Evasive parameters in the whole process of ship collision avoidance are analyzed, as shown in Figure 2 (b) &(c).  $DCPA$  is increased from  $-0.028nmile$  to  $-0.16$ , and the ship will pass through outside of  $SDZ_{min}$ . At this time, the ship  $TCPA$  will gradually change from 2.3 to  $-0.3$ , which shows that the ship has passed the distance to closest point of approach.

(a) Two Ships Run Safely Evading Each Other



(b) Data Analysis of Intelligent Avoidance of Shipwreck



(c) Data Analysis of Intelligent Avoidance of Shipwreck

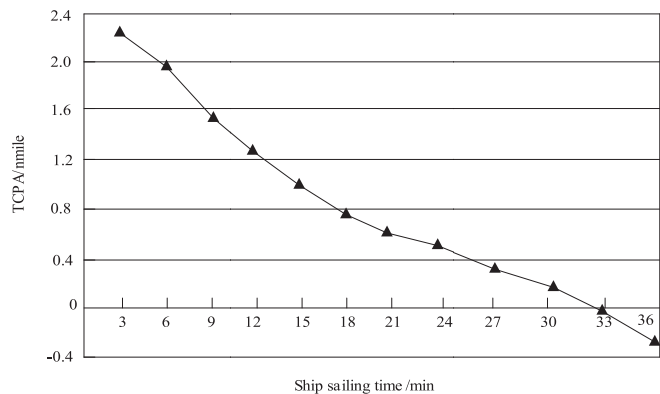


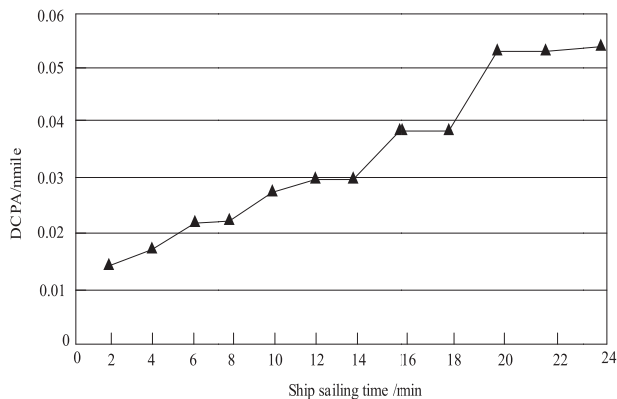
Fig. 2. Effect Diagram of Intelligent Avoidance Simulation of Shipwreck Based on Big Data Analysis

At the initial time, the sailing speed of the target ship 1 is 12 Kn, and the sailing direction is 305.2°. The sailing speed of the target ship 2 is 13 Kn, and the sailing direction is 195.1°. The two ships in the voyage are 0.44nmile apart,  $DCPA = -0.05nmile$ ,  $TCPA = 1.98nmile$ ,  $SDA_{min} = 0.12nmile$ . We judge that there is not enough room for ships handling in the left of target ship 1, and determine that the target ship 1 extends the encounter time by deceleration mode. The target ship 2 put full left rudder to 90°. According to Figure 3 (a), we can see that collision avoidance of two ships is successful. Evasive parameters in the whole process of ship collision avoidance are analyzed, as shown in Figure 3 (b) &(c).  $DCPA$  is increased from 0.0013nmile to 0.055, and the ship will pass through outside of  $SDZ_{min}$ . At this time, the ship  $TCPA$  will gradually change from 1.62 to -0.21, which shows that the ship has passed the distance to closest point of approach, and  $DCPA$  is nmile. At this time,  $|DCPA|$  is not more than  $SDZ_{min}$ , this is because two ships belong to the crossing encounter. According to the calculation of proposed method we can see that the two ships still can successfully realize collision avoidance.

(a)Two Ships Run Safely Evading Each Other



(b)Data Analysis of Intelligent Avoidance of Shipwreck



(c) Data Analysis of Intelligent Avoidance of Shipwreck

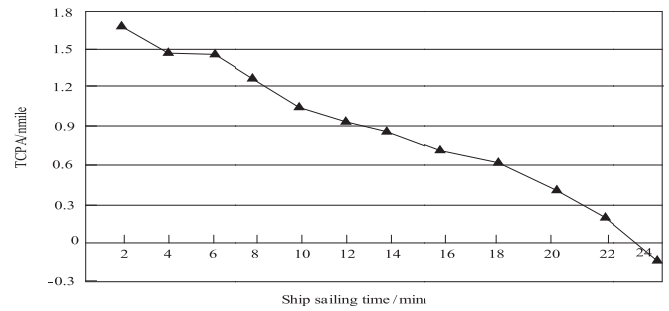


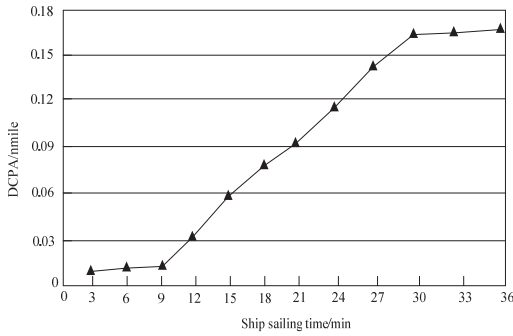
Fig. 3. Effect Diagram of Intelligent Avoidance Simulation of Shipwreck Based on Big Data Analysis

At the initial time, the sailing speed of the target ship 1 is 8 Kn, and the sailing direction is 304.9°. The sailing speed of the target ship 2 is 12 Kn, and the sailing direction is 185.3°. The two ships in the voyage are 0.62nmile apart,  $DCPA = -0.02nmile$ ,  $TCPA = 2.38nmile$ ,  $SDA_{min} = 0.062nmile$ . According to the calculation of risk degree of ship collision, two ships have formed the immediate danger situation. We use the method proposed in this paper to carry out the intelligent evasive action of shipwreck. According to Figure 4 (a), we can see that the collision avoidance of two ships is successful. Evasive parameters in the whole process of ship collision avoidance are analyzed, as shown in Figure 4 (b) &(c).  $DCPA$  is increased from 0.01nmile to 0.16, and the ship will pass through outside of  $SDZ_{min}$ . At this time, the ship  $TCPA$  will gradually change from 2.32 to -0.38, which shows that the ship has passed the distance to closest point of approach, and  $DCPA$  is nmile. This also shows that two ships in the closest point of approach are 0.13 nmile apart, which can achieve successful avoidance.

(a)Two Ships Run Safely Evading Each Other



(b) Data Analysis of Intelligent Avoidance of Shipwreck



(c) Data Analysis of Intelligent Avoidance of Shipwreck

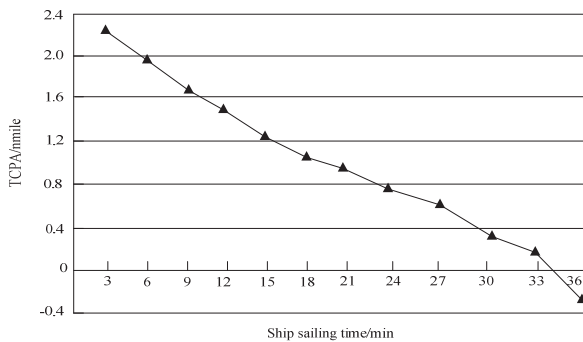


Fig. 4. Effect Diagram of Intelligent Avoidance Simulation of Shipwreck Based on Big Data Analysis

According to the analysis of above simulation test results, when the ship is sailing in the immediate and dangerous situation, the method proposed in this paper can realize the intelligent avoidance of shipwreck.

## CONCLUSION AND DISCUSSION

The method proposed in this paper analyzes the basic principle for avoiding shipwreck and the corresponding mathematical model of ship motion on the basis of previous research, and builds intelligent method for avoiding shipwreck based on big data analysis, combined with the mathematical model of ship motion, we carry out the simulation experiment based on the full analysis of genetic algorithm. The main research results are as follows:

(1) select a reasonable genetic code structure, and reasonably indicate the intelligent avoidance ship route of shipwreck.

(2) the method proposed in this paper considers the safety and economic performance of ships, and also takes into account the cases of observing International Regulations for Preventing Collisions at Sea.

(3) three operations such as the selection, crossover and mutation are used, and the way of parallel operation is used to realize the intelligent avoidance of shipwreck.

(4) this paper has fully analyzed the different situations that ship encounters, and makes a correct judgment according to

the dangerous degree of the close quarters situation of ship so as to realize the intelligent and safe avoidance of shipwreck.

(5) but the intelligent avoidance method of shipwreck realizes the avoidance only through the ship altering, which does not take into account the ship slowdown. Usually, in port water area, especially the junction of many sea-routes, more often, the ships achieve collision avoidance by the way of slowdown, which shows that the proposed method remains to be study on in depth.

## REFERENCES

1. Xiong Baoshun, Cui Haolin. Simulation Research on Target Path Obstacle Avoidance Planning for Express Robot. *Computer Simulation*, 2016, 33(9):369-374.
2. Vincent T L, Cliff E M, Grantham W J, et al. Some Aspects of Collision Avoidance. *Aiaa Journal*, 2015, 12(12):3-4.
3. Alonso-Mora J, Naegeli T, Siegwart R, et al. Collision avoidance for aerial vehicles in multi-agent scenarios. *Autonomous Robots*, 2015, 39(1):101-121.
4. Nilsson J, Ödblom A C E, Fredriksson J. Worst-Case Analysis of Automotive Collision Avoidance Systems. *IEEE Transactions on Vehicular Technology*, 2016, 65(4):1899-1911.
5. ZHOU Kai. Indoor Robot Obstacle Avoidance Algorithm Introduction of Pheromone Fuzzy Logic Guidance. *Bulletin of Science and Technology*, 2015, 31(12):220-222.
6. Rey D, Rapine C, Dixit V V, et al. Equity-Oriented Aircraft Collision Avoidance Model. *IEEE Transactions on Intelligent Transportation Systems*, 2015, 16(1):172-183.
7. YIN Xincheng, HU Yong, NIU Huimin. Path Planning Study for Robot Obstacle Avoidance in Unknown Environment. *Science Technology and Engineering*, 2016, 16(33):221-226.
8. Ho P F, Chen J C. WiSafe: Wi-Fi Pedestrian Collision Avoidance System. *IEEE Transactions on Vehicular Technology*, 2016, PP(99):1-1.
9. Chen Z, Fan M C, Zhang H T. How Much Control is Enough for Network Connectivity Preservation and Collision Avoidance?. *IEEE Transactions on Cybernetics*, 2015, 45(8):1647-1656.
10. 11. Gao, W. and W. Wang, The fifth geometric-arithmetic index of bridge graph and carbon nanocones. *Journal of Difference Equations and Applications*, 2017. 23(1-2SI): p. 100-109.
11. 12. Gao, W., et al., Distance learning techniques for ontology similarity measuring and ontology mapping. *Cluster*

Computing-The Journal of Networks Software Tools and Applications, 2017. 20(2SI): p. 959-968.

12. Lacharnay V, Lavernhe S, Tournier C, et al. A physically-based model for global collision avoidance in 5-axis point milling. *Computer-Aided Design*, 2015, 64(C):1-8.
13. Hassan, M.A., Ismail, M.A.M. Literature Review for The Development of Dikes's Breach Channel Mechanism Caused by Erosion Processes During Overtopping Failure. *Engineering Heritage Journal*, 2017, 1(2):23-30.
14. Yasin, H., Usman, M., Rashid, H., Nasir, A., Sarwar, A., Randhawa, I.A. Guidelines for Environmental Impact Assessment of JHAL flyover and underpass project in Faisalabad. *Geology, Ecology, and Landscapes*, 2017, 1(3): 205-212.
15. Radmanfar, R., Rezayi, M., Salajegheh, S., Bafrani, V.A. Determination the most important of hse climate assessment indicators case study: hse climate assessment of combined cycle power plant staffs. *Journal CleanWAS*, 2017, 1(2): 23-26.
16. Ismail, I., Husain, M.L., Zakaria, R. Attenuation of Waves from Boat Wakes In Mixed Mangrove Forest Of Rhizophora And Bruguiera Species In Matang, Perak. *Malaysian Journal Geosciences*, 2017, 1(2):32-35.
17. Soehady, H.F., Asis, J., Tahir, S., Musta, B., Abdullah, M., Pungut, H. Geosite Heritage and Formation Evolution of Maga Waterfall, Long Pasia, South of Sipitang, Sabah. *Geological Behavior*, 2017, 1(2):34-38.
18. Ali, S., Ali, R., Iftikhar, A. Physico-chemical and microbiological assessment of some freshwater aquifers and associated diseases in district ghizer, gilgit-baltistan, Pakistan. *Acta Scientifica Malaysia*, 2017, 1(1): 08-12.

## CONTACT WITH THE AUTHOR

Wei Li

*e-mail: maxx6317@163.com*

Information Center  
Renmin Hospital of Wuhan University  
Wuhan 430060  
**CHINA**

# RESEARCH ON BIG DATA ATTRIBUTE SELECTION METHOD IN SUBMARINE OPTICAL FIBER NETWORK FAULT DIAGNOSIS DATABASE

Ganlang Chen

School of Software, South China Normal University, Foshan, 528225, China

## ABSTRACT

*At present, in the fault diagnosis database of submarine optical fiber network, the attribute selection of large data is completed by detecting the attributes of the data, the accuracy of large data attribute selection cannot be guaranteed. In this paper, a large data attribute selection method based on support vector machines (SVM) for fault diagnosis database of submarine optical fiber network is proposed. Mining large data in the database of optical fiber network fault diagnosis, and calculate its attribute weight, attribute classification is completed according to attribute weight, so as to complete attribute selection of large data. Experimental results prove that ,the proposed method can improve the accuracy of large data attribute selection in fault diagnosis database of submarine optical fiber network, and has high use value.*

**Keywords:** submarine optical fiber network, fault diagnosis database; big data attribute selection

## INTRODUCTION

With the development of computer and Internet technology, the computer network is booming. It brings people convenience while also the network virus [1-2] affecting network security. According to the real-time performance of submarine optical fiber network fault diagnosis[3-5], a big data attribute selection method based on rough set of submarine optical fiber network fault diagnosis database is proposed[6].. The current candidate reduction is chosen to be the big data reduction in the submarine optical fiber network fault diagnosis database, so as to complete its attribute selection[7]. This method has become the focus of discussion of relevant experts and scholars, and its research has gradually entered the scope of experts and scholars. With the deepening of the research content, lots of research results have been produced .

In literature [8], a big data attribute selection method in submarine optical fiber network fault diagnosis database

based on decision tree local time scale feature extraction is proposed. The drawback of this method is that the selection of attributes is quit slow. Literature [9] proposed a big data attribute selection method for network fault diagnosis database. This method has a small range of applications, it may increase the load for big data attribute selection.

To solve above problems, this paper proposes a method of big data attribute selection based on support vector machine in submarine optical fiber network fault diagnosis database. First, the decision tree method is used to mine and calculate the big data in the submarine optical fiber network fault diagnosis database, and the attribute of the big data is obtained. Then, the big data attribute classification is completed through a subset of assessment, stop criteria and result validity verification generated by big data attribute subset in submarine optical fiber network fault diagnosis database. According to the similarity degree of data attribute

space, the calculation method of attribute similarity and weight is obtained. The loss function is analyzed to improve the feature selection algorithm of big data attribute and calculate the weight of big data attribute. The gradient rise method is used to solve the saddle point, and furthermore to realize the large data attribute selection in the submarine optical fiber network fault diagnosis database. Experiments show that the proposed method can effectively improve the accuracy of big data attribute selection in submarine optical fiber network fault diagnosis database, reduce the calculation process, energy and time consumption, and has good practical value.

## RESEARCH ON BIG DATA ATTRIBUTE SELECTION METHOD IN SUBMARINE OPTICAL FIBER NETWORK FAULT DIAGNOSIS DATABASE

### A. COLLECTION AND ANALYSIS OF BIG DATA ATTRIBUTE SELECTION METHOD

#### (a) Collection of big data attribute selection method

It is necessary to mine data in the submarine optical fiber network fault diagnosis database and then calculate its attributes to realize big data attribute analysis[10-12].By using the tree structure to show the result of data mining, the method is simple and intuitive[13-14], and therefore it is suitable for this paper. The specific process is shown in Figure 1.

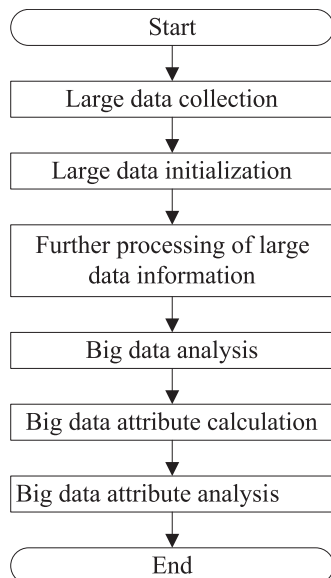


Fig. 1. Dig data attribute analysis process in submarine optical fiber network fault diagnosis database

$U$  is the big data set in submarine optical fiber network fault diagnosis database,  $F_1$  and  $F_2$  are two big data attributes

on node  $N$  of the decision tree. The information gain of  $F_1$  is greater than that of  $F_2$ , so the big data attribute  $F_1$  on node  $N$  is selected as a classification attribute.

Assume  $E_1$  and  $E_2$  are the information entropy of  $F_1$  and  $F_2$  respectively, we get

$$\begin{aligned} gain(F_1) \geq gain(F_2) &\Leftrightarrow I(p, n) - E(F_1) \geq \\ I(p, n) - E(F_2) &\Leftrightarrow E(F_1) \leq E(F_2) \Leftrightarrow E_1 \leq E_2 \end{aligned} \quad (1)$$

wherein,  $gain(F_1)$ ,  $gain(F_2)$  are the increased coefficients of  $F_1$  and  $F_2$ ,  $p$  and  $n$  are information entropy coefficient of  $F_1$  and  $F_2$ .

Let  $M$  be a line recording the reduction of big data in submarine optical fiber network fault diagnosis database, which belongs to the range of attribute  $j$  on node  $N$ . When the record is not reduced, the information entropy of the node attribute can be described as

$$E = \sum_{i=1}^m \frac{p_i + n_i}{p+n} \left( -\frac{p_i}{p+n_i} \log \left( \frac{p_i}{p+n_i} \right) - \frac{n_i}{p+n_i} \log \left( \frac{n_i}{p+n_i} \right) \right) = \frac{\varepsilon}{p+n} \quad (2)$$

In equation (2),  $m$  represents the range count of big data attribute in given submarine optical fiber network fault diagnosis database,  $n_i$  and  $p_i$  are the information entropy of big data attribute  $i$  value segment in the database, and  $\varepsilon$  represents the value segment of a big data attribute in a given database.

Reduce the centralized record of the dig data in submarine optical fiber network fault diagnosis database[15-16], we get attribute information entropy of the big data attribute node in new database as following:

$$\varepsilon = - \sum_{i=1}^m \left( p_i \log \left( \frac{p_i}{p_i + n_i} \right) + n_i \log \left( \frac{n_i}{p_i + n_i} \right) \right), \text{且 } \varepsilon \geq 0 \quad (3)$$

$$A = p_j \log \left( \frac{p_j}{p_j + n_j} \right) + n_j \log \left( \frac{n_j}{p_j + n_j} \right) - (p_j - 1) \log \left( \frac{p_j - 1}{p_j + n_j - 1} \right) - n_j \log \left( \frac{n_j}{p_j + n_j - 1} \right) \quad (4)$$

Let  $x = p_j$ ,  $y = n_j$ , we get equation (5)

$$\begin{aligned} \Delta E = E' - E &= \frac{\varepsilon + A}{p+n-1} - \frac{\varepsilon}{p+n} = \frac{A}{p+n-1} + \left( \frac{\varepsilon}{p+n-1} - \frac{\varepsilon}{p+n} \right) \\ &= \frac{A}{p+n-1} + \frac{\varepsilon}{(p+n-1)(p+n)} \end{aligned} \quad (5)$$

Wherein,  $A(x, y)$  represents a function of  $x, y$ , the big data attribute variables, in the database.

#### (b) Analysis of big data attribute selection method in submarine optical fiber network fault diagnosis database

The big data attribute selection error cloud formula is expressed as:

$$E = \sum_{i=1}^k \sum_{p \in C_i} |p - o_i|^2 \quad (6)$$

In the above function,  $E$  represents the sum of squared errors for all big data attributes,  $p$  represents an object of the

dataset,  $o_i$  is mean of class  $C_i$ ,  $C_i$  is the submarine optical fiber network fault diagnosis database, and  $n_i$  indicates the number of data object in class  $C_i$ . Use formula (7) to calculate the distance from each  $p$  in the data set to  $k$  cluster center:

$$dist(x, y) = \sqrt{\sum_{i=1}^d (x_i - y_i)^2} \quad (7)$$

And then the property extraction is completed through the attribute similarity.  $H_i, H_j \in R^D$  are two object spaces, where  $R^D$  represents a submarine optical fiber network fault diagnosis database,  $d(H_i, H_j)$  represents the distance between two object spaces, and  $d(H_{ik}, H_{jk})$  represents the spatial distance of the  $k$ -th dimension of the two object spaces.

$$d(H_i, H_j) = \max_{k=1,2,\dots,D} \{d(H_{ik}, H_{jk})\} \quad (8)$$

### B. SELECTION BIG DATA ATTRIBUTE IN SUBMARINE OPTICAL FIBER NETWORK FAULT DIAGNOSIS DATABASE BASED ON SUPPORT VECTOR MACHINE

According to the above discussion, the loss function of the big data attribute in the submarine optical fiber network fault diagnosis database is:

$$V(y_i, f(x_i)) = L(y_i) \cdot (f(x_i) - y_i)_+ \quad (9)$$

In the above equation:

$(f(x_i) - y_i)_+ = ((f_1(x_i) - y_{i1})_+, \dots, (f_m(x_i) - y_{im})_+)$ . Class mark  $y_i$  is encoded to  $y_i = (y_{i1}, \dots, y_{im})$ , an  $m$ -dimensional vector. Assume that the corresponding large data attribute diagnostic type is  $j$ , the  $j$ -th component of  $y_i$  is 1, and the remaining components are denoted by  $-1/(m-1)$ .  $L(y_i)$  is also an  $m$ -dimensional vector, with 0 as its  $j$ -th component and 1 as its remaining components.

In order to ensure that each attribute belongs to only a certain category,  $f_c(x)$  need to meet the conditions:

$$\sum_{c=1}^m f_c(x) = 0 \quad (10)$$

Since the above condition is satisfied for any of the data attributes  $x$ , it can be converted into

$$\sum_{c=1}^m \beta_c = 0, \sum_{c=1}^m \beta_{0c} = 0 \quad (11)$$

we get that SVM-based supervised big data attribute feature selection algorithm is equivalent to optimization problem:

$$\min_{\beta_c, \beta_{0c}, c=1, \dots, m} C \sum_{c=1}^m \sum_{i=1, y_i \neq c}^{n_c} \left( \beta_{0c} + x_i \beta_c + \frac{1}{m-1} \right) + \lambda_1 \sum_{c=1}^m \|\beta_c\|_1 + \frac{\lambda_2}{2} \sum_{c=1}^m \|\beta_c\|_2^2 \quad (12)$$

$$s.t. \begin{cases} \sum_{c=1}^m \beta_c = 0 \\ \sum_{c=1}^m \beta_{0c} = 0 \end{cases}$$

Wherein,  $C$  is the penalty parameter of the big data attribute in the submarine optical fiber network fault diagnosis database,  $\lambda_1$  and  $\lambda_2$  are adjustment parameters [17, 18].  $n_c$  indicates the number of data that does not belong to the  $c$ -th big data attribute. By solving the above equation, we get the weight  $\beta_{ci}$  of each attribute in the  $c$ -th big data,  $i = 1, 2, \dots, p$  which is also an important measure of the  $i$ -th characteristic of the data attribute, so as to complete the determination of the big data attribute in the submarine optical fiber network fault diagnosis database.

The normalization of big data attribute eigen values is:

$$\sum_{c=1}^m |\hat{\beta}_{cj} - \beta_{ck}|^2 \leq \frac{2M}{\lambda_2} \sum_{c=1}^m |\beta_{cj} - \beta_{ck}| \sqrt{2n_c(1-\rho_c)} \quad (13)$$

$\rho_c$  represents the correlation coefficient between feature  $j$  and feature  $k$  that does not belong to the big data attribute in the  $c$ -th submarine optical fiber network fault diagnosis database.

In order to solve the problem of the saddle point, the gradient rise method is used to solve the dual problem:

$$\max_{u_c, v_c, p, q} \min_{\beta_c, \beta_{0c}, a_c, t_c, u_c, v_c, p, q} L(\beta_c, \beta_{0c}, a_c, t_c, u_c, v_c, p, q) \quad (14)$$

In the above discussion, the big data attribute selection algorithm is improved by calculating the loss function, the weight of the big data attribute is calculated, and the saddle point is solved by the gradient rising method, so as to realize the selection process of big data attribute in submarine optical fiber network fault diagnosis database based on support vector machine. The process is shown in Figure 2.

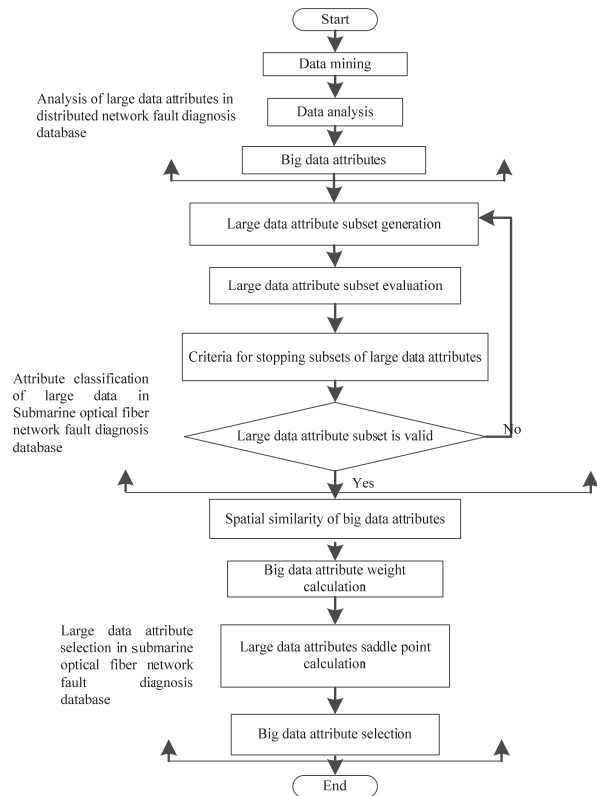


Fig. 2. Big data attribute selection process in submarine optical fiber network fault diagnosis database

## EXPERIMENTAL RESULTS AND ANALYSIS

In order to prove the validity of the big data attribute selection method in the submarine optical fiber network fault diagnosis database based on support vector machine, we use MATLAB 2008a as the platform and Intel P4 2G processor to perform the simulation experiment[19-23].

In this paper, we use three data sets in the network database to experiment, analyze the data attributes of three different experimental data sets, and compare the time consuming of three data sets.

In the first data set, the method proposed in this paper is compared with the data attribute selection method proposed in [8] and [9], and the comparison result is shown below.

First, the time consumed (min), calculated through formula (15), in the three methods for big data attribute selection is compared[24].

$$T = \frac{E \log L(\gamma)}{\sum_{i=1}^m f(x)} \cdot \sigma \quad (15)$$

$\sigma$  represents the response time parameter when the big data attribute is selected, and the average response time of the big data attribute selection is obtained according to the above three methods. The comparison results are shown in Table 1.

Tab. 1. Time-consuming comparison of three methods

| Numbers of experiments / times | The proposed method/min | The method proposed in literature [8]/ min | The method proposed in literature [9]/ min |
|--------------------------------|-------------------------|--|--|
| 50                             | 18                      | 25   | 23   |
| 100                            | 35                      | 47   | 44   |
| 150                            | 50                      | 71   | 66   |
| 200                            | 67                      | 89   | 85   |
| 250                            | 83                      | 112  | 109  |
| 350                            | 115                     | 159  | 148  |
| 500                            | 129                     | 218  | 213  |

According to the formula (16), the average time-consuming comparison of the three methods in the second data set is calculated. In order to ensure the accuracy of the experiment, 500 experiments were carried out, with 50 experimental data as a set of data, so as to complete the average time calculation, the time unit is seconds (s), the formula is:

$$T_0 = \frac{T - T'}{50} \quad (16)$$

In the above formula,  $T'$  represents the time spent in other work in the experiment. Through the calculation, we get the average time comparison of the three methods for big data attribute selection. The comparison results are shown in Table 2.

Tab. 2. Average time-consuming comparison of three methods for large data attribute selection

| Numbers of experiments / times | The proposed method/min | The method proposed in literature [8]/ min | The method proposed in literature [9]/ min |
|--------------------------------|-------------------------|--|--|
| 50                             | 14.8                    | 22.8                                       | 19.1                                       |
| 100                            | 14.4                    | 22.1                                       | 17.8                                       |
| 150                            | 14.1                    | 21.9                                       | 21.6                                       |
| 200                            | 15.1                    | 22.0                                       | 17.9                                       |
| 250                            | 15.2                    | 22.5                                       | 17.6                                       |
| 300                            | 15.1                    | 22.9                                       | 20.9                                       |
| 350                            | 15.5                    | 22.6                                       | 19.5                                       |
| 400                            | 15.2                    | 21.8                                       | 19.7                                       |
| 450                            | 15.3                    | 22.3                                       | 20.2                                       |
| 500                            | 15.0                    | 22.1                                       | 20.8                                       |

Then, we compared the average time-consuming of three method in the third data set, and got the results shown in Figure 3.

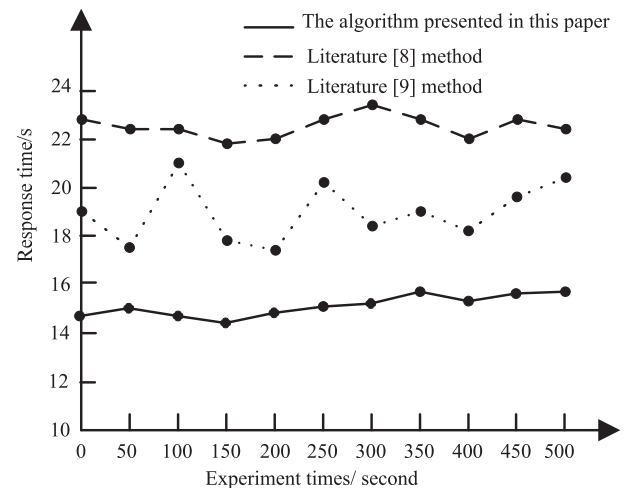


Fig. 3. The average time-consuming comparison of the three methods

In the figure above, the starting point of the line indicating the theoretically time consuming of the three methods. It can be seen that difference between actual and theoretical time-consuming of the proposed method is less than that of the literature [8] and the literature [9]. The average time-consuming polyline of the proposed method is close to a straight line and the fluctuation is small, which indicates that the proposed method is stable in the big data attribute selection.

Then compare the energy consumption of three methods, we assume  $N$  as the energy consumption unit,

$$N = \sum_{i=1}^m \beta_c \cdot \varepsilon \quad (17)$$

According to the above formula, the energy consumption of the three methods for big data attribute selection is compared. The results are shown in Table 3.

Tab. 3. Energy consumption comparison of the three methods for big data attribute selection

| Time/h | The proposed method /N | The method proposed in literature [8]/N | The method proposed in literature [9]/N |
|--------|------------------------|---|---|
| 5      | 31                     | 47                                      | 61                                      |
| 10     | 58                     | 92                                      | 117                                     |
| 15     | 86                     | 126                                     | 179                                     |
| 20     | 113                    | 174                                     | 236                                     |
| 25     | 139                    | 226                                     | 292                                     |
| 30     | 167                    | 268                                     | 348                                     |
| 40     | 194                    | 313                                     | 463                                     |
| 50     | 227                    | 359                                     | 562                                     |

In order to better display the results, we converted Table 3 into the following line chart. The energy consumption comparison results of the three methods are shown in Figure 4.

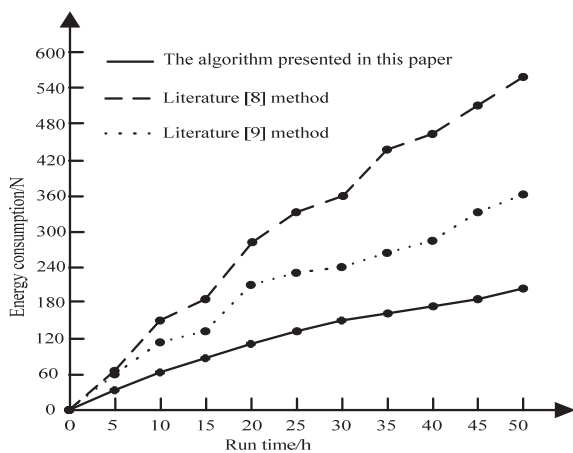


Fig. 4 The energy consumption comparison results of the three methods

It can be seen that the proposed method can effectively reduce the energy consumption in big data attribute selection process. The energy consumption fluctuation of the proposed method in big data attribute selection is smaller than that of literature [8] and the literature [9], which indicates that the proposed method is stable in the big data attribute selection.

At last, we compared the accuracy of three methods in big data attribute selection process. The experiment used three methods to select the data attributes of any seven databases in the network. Since the number of attributes in the database is large, accuracy indicates that the number of big data attributes can be selected correctly, and error indicates that the number of big data attributes can not be selected accurately. The results are shown in Table 4.

Tab. 4. The accuracy of three method for big data attribute selection

| Number of attributes | The proposed method |       | The method proposed in literature [8] |       | The method proposed in literature [9] |       |
|----------------------|---------------------|-------|---------------------------------------|-------|---------------------------------------|-------|
|                      | Accuracy            | Error | Accuracy                              | Error | Accuracy                              | Error |
| 132                  | 123                 | 9     | 109                                   | 23    | 113                                   | 19    |
| 210                  | 203                 | 7     | 187                                   | 23    | 196                                   | 14    |
| 218                  | 207                 | 11    | 201                                   | 17    | 289                                   | 29    |
| 345                  | 339                 | 6     | 319                                   | 26    | 327                                   | 18    |
| 426                  | 413                 | 13    | 401                                   | 25    | 407                                   | 19    |
| 457                  | 443                 | 14    | 426                                   | 31    | 431                                   | 26    |
| 543                  | 522                 | 21    | 507                                   | 36    | 516                                   | 27    |

The accuracy ratio is the ratio of the exact quantity to the total quantity. The error rate is the ratio of the number of errors to the total quantity. The formula is as follows (18).

$$\begin{cases} \eta = \frac{\text{Exact number}}{\text{Total quantity}} \times 100\% \\ \lambda = \frac{\text{Error number}}{\text{Total quantity}} \times 100\% \end{cases} \quad (18)$$

In the formula,  $\eta$  and  $\lambda$  indicate the accuracy and error rate. Using the above table information, the accuracy of the three methods for big data attribute selection are compared, the results are shown in Figure 5, Figure 6.

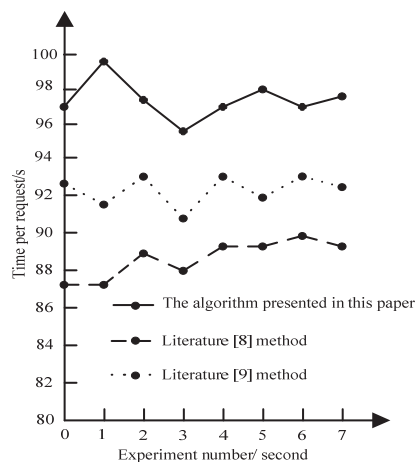


Fig. 5 Comparison of accuracy of three methods

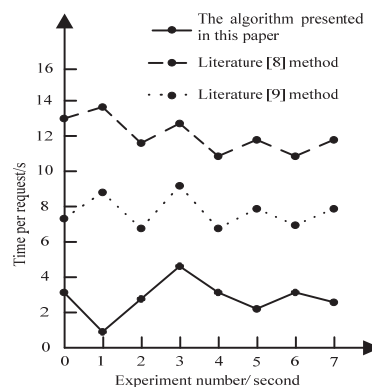


Fig. 6. Comparison of error rate of three methods

Through the above figure we can see that the method proposed in this article has the highest accuracy and the lowest error rate.

In summary, the method proposed in this paper can effectively reduce the energy consumption and cost of big data attribute selection in the submarine optical fiber network fault diagnosis database, improve the efficiency of big data attribute selection in the submarine optical fiber network fault diagnosis database, ensure the real-time of network fault diagnosis, and has great practical value.

## CONCLUSION

The choice of big data attribute in submarine optical fiber network fault diagnosis database is the basis of data mining and processing of submarine optical fiber network fault diagnosis database. Improve the time consumption of big data attribute selection is conducive to ensure the real-time fault diagnosis, thus improving the capability of submarine optical fiber network fault diagnosis. In this paper, the big data attribute method based on SVM in submarine optical fiber network fault diagnosis database can effectively reduce the time taken for fault diagnosis and improve the efficiency of fault diagnosis, and has good practical value.

## REFERENCES

1. Karabadjji N E I, Seridi H, Khelf I, et al. Improved decision tree construction based on attribute selection and data sampling for fault diagnosis in rotating machines. *Engineering Applications of Artificial Intelligence*, 2014, 35(35):71-83.
2. Zhang Q H, Qin A, Shu L, et al. Vibration sensor based intelligent fault diagnosis system for large machine unit in petrochemical industry. *International Journal of Distributed Sensor Networks*, 2015, 2015(3):1376-1381.
3. Jin S, Cui W, Jin Z, et al. AF-DHNN: Fuzzy Clustering and Inference-Based Node Fault Diagnosis Method for Fire Detection.. *Sensors*, 2015, 15(7):17366-17396.
4. Panda M, Khilar P M. Distributed self fault diagnosis algorithm for large scale wireless sensor networks using modified three sigma edit test. *Ad Hoc Networks*, 2015, 25(PA):170-184.
5. Zhang Q H, Hu Q, Sun G, et al. Concurrent Fault Diagnosis for Rotating Machinery Based on Vibration Sensors. *International Journal of Distributed Sensor Networks*, 2015, 2013(1):59-72.
6. Reppa V, Polycarpou M M, Panayiotou C G. Distributed Sensor Fault Diagnosis for a Network of Interconnected Cyberphysical Systems. *IEEE Transactions on Control of Network Systems*, 2015, 2(1):11-23.
7. Islam R, Khan S A, Kim J M. Discriminant Feature Distribution Analysis-Based Hybrid Feature Selection for Online Bearing Fault Diagnosis in Induction Motors. *Journal of Sensors*, 2016, 2016(2):1-16.
8. LAn-qiang, Liu Z, Yin C Q, et al. A Fault Diagnosis Method Forwavelet Packet and Neural Network-Based Submarine Cables. *Study on Optical Communications*, 2016, 42(2):16-22..
9. Gao Y, Yang C, Tian S, et al. Entropy Based Test Point Evaluation and Selection Method for Analog Circuit Fault Diagnosis. *Mathematical Problems in Engineering*, 2014, 2014(6):1-16.
10. Lei Y, Jia F, Lin J, et al. An Intelligent Fault Diagnosis Method Using Unsupervised Feature Learning Towards Mechanical Big Data. *IEEE Transactions on Industrial Electronics*, 2016, 63(5):3137-3147.
11. Wang S, Sun X, Li C. Wind Turbine Gearbox Fault Diagnosis Method Based on Riemannian Manifold. *Mathematical Problems in Engineering*, 2015, 2014(4):1-10.
12. Jin X, Chow T W S, Sun Y, et al. Kuiper test and autoregressive model-based approach for wireless sensor network fault diagnosis. *Wireless Networks*, 2015, 21(3):829-839.
13. Kelkar S, Kamal R. Adaptive Fault Diagnosis Algorithm for Controller Area Network. *IEEE Transactions on Industrial Electronics*, 2014, 61(10):5527-5537.
14. Unal M, Onat M, Demetgul M, et al. Fault diagnosis of rolling bearings using a genetic algorithm optimized neural network. *Measurement*, 2014, 58:187-196.
15. Lu Chong, Xu Hui, Yang Yongchun. Research and application of . decision tree classification algorithm based on electronic design engineering, 2016, 24 (18): 1-3.
16. Gao, W. and W. Wang, The fifth geometric-arithmetic index of bridge graph and carbon nanocones. *Journal of Difference Equations and Applications*, 2017. 23(1-2SI): p. 100-109.
17. Gao, W., et al., Distance learning techniques for ontology similarity measuring and ontology mapping. *Cluster Computing-The Journal of Networks Software Tools and Applications*, 2017. 20(2SI): p. 959-968.
18. Xue C, Jing L I, Wang H, et al. Effects of Target and Distractor Saturations on the Cognitive Performance of an Integrated Display Interface. *Chinese Journal of Mechanical Engineering*, 2015, 28(1):208-216.

19. Halim H, Abdullah R, Nor M J M, Aziz H A, Rahman N A. Comparison Between Measured Traffic Noise in Klang Valley, Malaysia And Existing Prediction Models. *Engineering Heritage Journal*, 2017, 1(2):10–14.
20. Ebrahimi N, Gharibreza M, Hosseini M, Ashraf M A. Experimental study on the impact of vegetation coverage on flow roughness coefficient and trapping of sediment. *Geology, Ecology, and Landscapes*, 2017, 1(3): 167-172.
21. Adugna O, Alemu A. Evaluation of brush wood with stone check dam on gully rehabilitation. *Journal CleanWAS*, 2017, 1(2): 10-13.
22. Guoming L, Yanmin C, Guowe Y, Xiaoping Y. Research on Data Management Model of National Defense Mobilization Potential Based on Geo-Spatial Framework. *Malaysian Journal Geosciences*, 2017, 1(2): 10-12.
23. Simon N, Roslee R, Lai G T. Temporal Landslide Susceptibility Assessment Using Landslide Density Technique. *Geological Behavior*, 2017, 1(2):10–13.
24. Isemael Y Y. Molecular, Histological and biochemical effects of tea seed cake on hepatic and renal functions of *Oreochromis niloticus*. *Acta Scientifica Malaysia*, 2017, 1(1): 13-15.

## CONTACT WITH THE AUTHOR

Ganlang Chen

*e-mail: chenganlang629@163.com*

School of Software  
South China Normal University  
Foshan 528225

**CHINA**

# A COMPARATIVE STUDY ON THE METHOD OF EXTRACTING EDGE AND CONTOUR INFORMATION OF MULTIFUNCTIONAL DIGITAL SHIP IMAGE

Fangping Yin

Guangdong Mechanical and Electrical College, Guangzhou 510515, China

## ABSTRACT

*The result of the extraction of the edge and contour information of the multifunctional digital ship image directly affects the evaluation and recognition of the subsequent image quality. At present, the common method used to extract the edge contour information is based on the Canny operator, and there is a problem that the edge is not clear. In order to obtain more accurate edge information, a method of extracting edge and contour information of multimedia digital image based on multi-scale morphology is proposed. Firstly, the digital ship image is made double filter and the fuzzy threshold segmentation, and then the edge and contour information is extracted by multi-scale morphology. Experiments show that the proposed method can obtain more accurate edge information compared with the other methods.*

**Keywords:** multifunctional digital image, edge and contour information, extraction

## INTRODUCTION

Human vision is usually through the target object's edge and contour [1], to distinguish the target objects [2-3], whereas in the multifunctional digital ship image, the edge is an important feature that distinguishes different regions [4-5]. The edge and contour information of multifunctional digital ship image refers to the part of that the local brightness changes significantly [6], it exists between the target image and another target image [7], the target image and background image, the regional image and another regional image [8-9]. At present, the edge feature extraction technology of multifunctional digital ship image has been widely used in the field such as target tracking, fingerprint recognition, laser remote sensing image segmentation and many others. The edge and contour information extraction of multifunctional digital ship image, has become one of the hot research topics [10-12]. In reference [13], a method of extracting edge and contour information of multifunctional digital ship

image based on self-enhancement is proposed. Firstly, the multifunctional digital image is subjected to make smoothing denoising by small-scale Gaussian filtering, and then the Canny edge detection operator is used to obtain the feature guidance information of the multifunctional digital image. In addition, each search of the multifunctional digital image is made sub-edge accumulation, and the edge and contour information of multifunctional digital image is extracted according to the degree of self-enhancement accumulation. The method has serious noise effects, and the extracted image edge and contour information is not clear. In reference [14], a method for edge and contour information extraction of multifunctional digital image based on Sobel operator gradient multiplication is suggested. In this method, the features of the target to be identified is to be extracted for the multifunctional digital image firstly. Then, the Sobel operator and the Roberts operator are used to extract the edge of the multifunctional digital image respectively. The two gradient

amplitude images are calculated by gradient multiplication, to complete the edge and contour information extraction of the multifunctional digital image. The method does not make image denoising, and there are many small edge redundancy information. Aiming at the problems in the application of the above methods, this paper presents a method for extracting the edge and contour information of multifunctional digital ship image based on multi-scale morphology by comparing the edge and contour information extraction method of multifunctional digital ship image. Through the experimental comparison and verification, the proposed method can eliminate the noise interference in the image, extract the more accurate edge and contour information, and can keep the better edge detail. Experimental results show that the proposed method can eliminate the influence of noise and preserve the details of the edge contour information of the image, and has good practical value.

## A COMPARATIVE STUDY ON THE METHOD OF EXTRACTING EDGE AND CONTOUR INFORMATION OF MULTIFUNCTIONAL DIGITAL SHIP IMAGE

### A. COMPARISON OF SMOOTH DENOISING METHODS FOR MULTIFUNCTIONAL DIGITAL SHIP IMAGES

(a) Multifunctional digital ship image denoising based on wavelet adaptive threshold

According to the wavelet decomposition characteristics of multifunctional digital ship image, the optimal threshold for denoising of different layer coefficients of multifunctional digital ship image after wavelet decomposition is determined [15-17], and the effect of smooth denoising is achieved. The specific process is as follows:

Assuming that a  $M \times N$ -sized multifunctional digital ship image  $z(i, j)$  is expressed as:

$$z(i, j) = y(i, j) + n(i, j) \quad (1)$$

Where  $0 \leq j \leq N-1$ ,  $0 \leq i \leq M-1$ ;  $i, j \in Z$  stands for the pixel position of the multifunctional digital ship image;  $y(i, j)$  represents the noise-free multifunctional digital ship image;  $n(i, j)$  represents the Gaussian white noise of the multifunctional digital ship image  $N(0, \sigma^2)$ . The discrete wavelet transform can be performed on both sides of the equal sign on the above equation (1), it can be got

$$W_z = W_y + W_n \quad (2)$$

Where  $W_z$  represents the wavelet coefficients obtained after wavelet transform of the digital ship image with noise;  $W_y$  represents the wavelet coefficients obtained by wavelet transform of the original multifunctional digital ship image;  $W_n$  represents the wavelet coefficients obtained by wavelet

transform of Gaussian white noise. Since the characteristics of the wavelet transform are a linear transformation, then:

$$W_y = W_z - W_n \quad (3)$$

The threshold selection is the key step of wavelet denoising and contraction of multifunctional digital ship image. The threshold selection method of multifunctional digital ship image is:

(A) The calculated expression for the fixed threshold of the multifunctional digital ship image is:

$$T = \alpha \sqrt{2 \ln A} \quad (4)$$

Where  $A$  represents the length of the wavelet coefficient of the multifunctional digital ship image;  $\alpha$  represents the standard deviation of the multifunctional digital ship image noise;  $T$  represents the estimation threshold of image. In practice, the variance of the image noise is unknown, and the standard deviation of the noise is estimated from the noisy signal of the multifunctional digital ship image. The expression is:

$$\alpha = \text{Media}(|Y_{ij}|) / 0.6745 Y_{ij} \in \text{subbanda} \quad (5)$$

Where  $Y_{ij}$  represents the coefficient of standard deviation of the multifunctional digital ship image;  $HH_1$  represents the sub-band coefficient of the multifunctional digital ship image.

(B) Threshold of Stein unbiased likelihood estimation of multifunctional digital ship image: a threshold  $a$  for the multifunctional digital ship image is set, to calculate its likelihood estimation; then, the threshold  $a$  of the multifunctional digital ship image is made non-likelihood minimization, thereby obtaining a selected threshold.

(C) When the image signal to noise ratio is small, if there is a large error in the unbiased likelihood estimation threshold, the fixed threshold method of (a) is used; otherwise, the unbiased likelihood estimation threshold is used.

(b) Assuming that the clear original multifunctional digital ship image is expressed as  $u(x, y)$ ; the multifunctional digital ship image affected by noise is expressed as  $u_0(x, y)$ ; the image noise is expressed as  $n(x, y)$ , since the noise has zero mean characteristic, the variance of the multifunctional digital ship image is expressed as  $\sigma_1$ , then the energy function of the multifunctional digital ship image is expressed as:

$$TV_p [u(x, y)] = \iint_{\Omega} |\nabla^p u(x, y)| dx dy + \frac{\lambda}{2} \iint_{\Omega} (u(x, y) - u_0(x, y))^2 dx dy \quad (6)$$

According to formula (6), a denoising  $TV_p$  model of multifunctional digital ship image is established, and the functional formula of multifunctional digital ship image is:

$$TV_p [u(x, y)] = \iint_{\Omega} F \left( x, y, u, \frac{\partial^p u}{\partial x^p}, \frac{\partial^p u}{\partial y^p} \right) dx dy \quad (7)$$

Where,  $\partial$ ,  $x^p$  and  $y^p$  represent the noisy scale coefficient of the multifunctional digital ship image;  $\lambda$  represents the parameter value of the multifunctional digital ship image;  $F$  represents the noise difference value of the multifunctional digital ship image, and its formula is as follows:

$$F = \left| \nabla^p u(x, y) \right| + \frac{\lambda}{2} [u(x, y) - u_0(x, y)]^2 \quad (8)$$

$\nabla^p$  represents the substitution operator of the gradient operator  $\nabla$  of multifunctional digital ship image with the  $p$ -order differential. The necessary conditions for solving the extreme value of the functional of multifunctional digital ship image are:

$$\lambda(u - u_0) - \nabla^p \left( \frac{\nabla^p u}{|\nabla^p u|} \right) = 0 \quad (9)$$

$$\nabla^p = \left( \frac{\partial^p u}{\partial x^p}, \frac{\partial^p u}{\partial y^p} \right) \quad (10)$$

The Euler-Lagrangian equation of the denoising model  $TV_p$  of multifunctional digital ship image is:

$$\lambda = \frac{1}{|\Omega| \sigma_1} \iint_{\Omega} \left[ \nabla^p \left( \frac{\nabla^p u}{|\nabla^p u|} \right) \right] (u - u_0) dx dy \quad (11)$$

(c) The denoising method of multifunctional digital ship image based on double filtering

The filtering results of the four different directions of templates are carried out calculation, so as to obtain the filter value of the noise point in multifunctional digital ship image. The details of the process are as follows:

For the noise point at  $(i, j_1)$  in the multifunctional digital ship image, the neighborhood size is expressed as  $(2N_1 + 1) \times (2N_1 + 1)$ , where  $N_1$  is a positive integer. The process of filtering the multifunctional digital ship image by double discrete wavelet method is as follows:

$$\begin{cases} a_1(i, j_1) = Med[B(i + k, j_1), -N_1 \leq k \leq N_1] \\ a_2(i, j_1) = Med[B(i, j_1 + k), -N_1 \leq k \leq N_1] \\ a_3(i, j_1) = Med[B(i + k, j_1 + k), -N_1 \leq k \leq N_1] \\ a_4(i, j_1) = Med[B(i - k, j_1 - k), -N_1 \leq k \leq N_1] \end{cases} \quad (12)$$

Where  $a_x(i, j_1)$  represents the filtered values of the four different directions of the multifunctional digital ship image;  $Med[\bullet]$  represents the median filter of the multifunctional digital ship image; and  $B(i, j_1)$  represents the gray scale matrix within a certain region of the multimedia digital ship image. The following calculations are made for the set  $\{a_x(i, j_1)\}$ :

$$\begin{cases} Z_{\max}(i, j_1) = \max\{a_x(i, j_1)\} \\ Z_{\min}(i, j_1) = \min\{a_x(i, j_1)\} \end{cases} \quad (13)$$

Where  $Z_{\max}(i, j_1)$  represents the maximum filter coefficient of the multimedia digital ship image;  $Z_{\min}(i, j_1)$  represents the minimum filter coefficient of the multimedia digital ship

image. For the noise point at  $(i, j_1)$  in the multimedia digital ship image, the filter value is calculated as follows:

$$f''(i, j_1) = Med[Z_{\max}(i, j_1), Z_{\min}(i, j_1), f'(i, j_1)] \quad (14)$$

Where  $f'(i, j_1)$  represents the gray value of any one of the pixels in multifunctional digital ship images.

The final filtering result of multimedia digital ship image is:

$$f'''(i, j_1) = \frac{P_1 a_{\max}(i, j_1) + P_2 a_{\min}(i, j_1) + P_3 a_{med1}(i, j_1) + P_4 a_{med2}(i, j_1)}{P_1 + P_2 + P_3 + P_4} \quad (15)$$

## B. COMPARISON OF MULTIMEDIA DIGITAL SHIP IMAGE SEGMENTATION METHOD

(a) Multimedia digital ship image segmentation method based on kernel self-organizing map and graph theory

According to the theory of information, the kernel self-organizing map can be derived for multimedia digital ship image segmentation, and the specific process is as follows:

The statistical properties of the neuron output  $y'$  of multimedia digital ship image are expressed by the random variable  $Y_d$  and the probability density  $Y_d$ . The calculated expression of the deferential entropy of  $Y_d$  is:

$$H(Y_d) = - \int_{-\infty}^{\infty} P_{Y_d(y')} \log P_{Y_d(y')} e y_d \quad (16)$$

For any random variables  $\hat{Y}$  and  $\hat{Y}$  in a multimedia digital ship image, the relational expression between the combination entropy  $H(\hat{Y}, \hat{Y})$  and the mutual information  $I(\hat{Y}, \hat{Y})$  is:

$$H(\hat{Y}, \hat{Y}) = H(Y) + H(\hat{Y}) - I(Y, \hat{Y}) \quad (17)$$

(b) Multimedia digital ship image segmentation method based on fractal network evolution

The spectral heterogeneity calculation formula of multimedia digital ship image segmentation method based on fractal network evolution is:

$$h_{color} = \sum_c (n_{merge} \times \sigma_c^{merge} - (n_{obj1} \times \sigma_c^{obj1} + n_{obj2} \times \sigma_c^{obj2})) \quad (18)$$

In the formula,  $n_{obj1}$  and  $n_{obj2}$  represent the number of pixels of two pixels before the multimedia digital ship images are merged;  $\sigma_c^{obj1}$  and  $\sigma_c^{obj2}$  represent the variance of the two pixels of the multimedia digital ship image;  $n_{merge}$  represents the variance of the pixel after the multimedia digital ship images are merged.

The shape heterogeneity of multimedia digital ship image segmentation method based on fractal network evolution is calculated as:

$$h_{shape} = w_{cmpct} \times h_{cmpct} - (1 - w_{cmpct}) \times h_{smooth} \quad (19)$$

Among them,  $w_{cmpct}$  represents the compactness weight of multimedia digital ship image, the value interval is  $[0, 1]$ ;  $h_{cmpct}$  represents the compactness heterogeneity of

the multimedia digital ship image;  $(1-w_{mpcr})$  represents the shape heterogeneity weight of the media digital ship image;  $h_{smooth}$  represents the smoothing heterogeneity of the multimedia digital ship image.

The total heterogeneity calculation formula of the multimedia digital ship image segmentation method based on the analysis of network evolution is:

$$heterogeneity = \tilde{w} \times h_{color} + (1 - \tilde{w}) \times h_{shape} \quad (20)$$

(c) Multimedia digital ship image segmentation method based on improved fuzzy threshold

Assuming that the size of the multimedia digital ship image  $G$  is expressed as  $M' \times N'$ , there are  $L$  levels of gray scale, expressed as  $\{0, 1, \dots, L-1\}$ ; the membership function of the multimedia digital ship image in the  $L$ -level gray scale is expressed as  $v(\hat{x})$ ;  $h(i'')$  represents the number of pixels with the gray value of  $i''$  in the multimedia digital ship image. The fuzzy rate of the multimedia digital ship image is expressed as:

$$v(\hat{x}) = \frac{2}{M' \times N'} \sum_{i''=0}^{L-1} h(i'') \min[\mu(i''), 1 - \mu(i'')] \quad (21)$$

If the minimum gray scale value in the multimedia digital ship image indicates the gray scale range from the minimum value of the abscissa to the threshold  $T'$  in the gray scale histogram of multimedia digital ship image. The multimedia digital ship image is weighted and averaged, and the weight coefficient of the image is  $g(\tilde{x})$ . the weighted average value  $\bar{a}$  of the multimedia digital ship image is calculated as:

$$\bar{a} = \sum_{\tilde{x}=a'}^{T'} \tilde{x}g(\tilde{x}) \quad (22)$$

Wherein, the weight coefficient of the multimedia digital ship image is  $g(\tilde{x})$ , indicating the proportion of the number of pixels which gray value is  $\tilde{x}$  (i.e., the information represented by the ordinate in the gray scale histogram of the multimedia digital ship image) to the number of total pixels in the interval  $[a', T']$ . It can be seen,  $\bar{a}$  will be close toward the corresponding gray value of the left peak, and fall in the adjacent location of its corresponding gray value. Similarly, the weighted average value  $b'$  can be calculated in the interval range from the threshold  $T'$  to the maximum gray scale value  $b'$  in the multimedia digital ship image, and the expression is:

$$\bar{b} = \sum_{\tilde{x}=T'}^{b'} \tilde{x}g(\tilde{x}) \quad (23)$$

Similarly,  $\bar{b}$  will fall at the adjacent position of the gray value corresponding to the right peak. If  $[\bar{a}, \bar{b}]$  is directly used as the search interval of the multimedia digital ship image, there is no guarantee that the interval length will be smaller than the peak separation after multiplying the coefficient  $\beta(0.3 \sim 0.8)$  of multimedia digital ship image, and further improvement is required. Let  $\bar{a}' = (a' + T')/2$ ,  $\bar{b}' = (b' + T')/2$ , then the calculation formula of window width  $\hat{c}$  of multimedia digital ship image is:

$$\hat{c} = \beta \left[ (\bar{b} - \bar{a}) - |\bar{a} - \bar{a}'| - |\bar{b} - \bar{b}'| \right] \quad (24)$$

### C. COMPARISON OF EDGE AND CONTOUR INFORMATION EXTRACTION METHODS FOR MULTIMEDIA DIGITAL SHIP IMAGE

For multimedia digital ship images, the continuous function variables of the digital ship image are usually approximated by the gray values of two adjacent points:

$$\nabla_{u'} = u'(m+1, n) - u'(m, n) \quad (25)$$

$$\nabla_{u'} = u'(m, 1+n) - u'(m, n) \quad (26)$$

(b) Method of edge and contour information extraction for multimedia digital ship image based on mathematical morphology

Assuming that  $m$  structure elements of multimedia digital ship image are selected for mathematical morphology calculation, the multivariate element  $B_m$  of multimedia digital ship image is expressed as:

$$B_m = l_1 \oplus l_2 \oplus l_3 \oplus \dots \oplus l_m \quad (27)$$

Supposing that  $\phi(x'', y'')$  represents the input gray scale function of the multimedia digital ship image;  $\varphi(x'', y'')$  represents the structural element function of multimedia digital ship image. Taking the structural element of the multimedia digital ship image with  $n'$  elements, and is defined in the structural element set  $R^2$  or  $Z^2$  of multimedia digital ship image,  $D_\phi$  and  $D_\varphi$  respectively represent the definition field of gray function  $\phi(x'', y'')$  and  $\varphi(x'', y'')$  of multimedia digital ship image.

The weighted average of the structural element functions of the multimedia digital ship image with  $n'$  elements is calculated as:

$$\phi_{avr}(x'', y'') = \frac{1}{n'} \sum_{i=1}^{n'} (\lambda' \phi'(x'', y'')) \quad (28)$$

According to the importance difference of the structural elements in the multimedia digital ship image, the weight value is set, where  $\lambda' \in [0, 1]$ .

If the corrosive operation is used, the edge detection operator of multimedia digital ship image is calculated as:

$$E'(x'', y'') = (\phi(x'', y'') \bullet B'(x'', y'')) \ominus \phi_{avr}(x'', y'') - (\phi(x'', y'') \bullet B'(x'', y'')) \ominus \phi_{avr}(x'', y'')$$

If the expansion-corrosion operation is used, the edge detection operator of multimedia digital ship image is calculated as:

$$E'(x'', y'') = (\phi(x'', y'') \circ B'(x'', y'')) \oplus \phi_{avr}(x'', y'') - (\phi(x'', y'') \bullet B'(x'', y'')) \ominus \phi_{avr}(x'', y'') \quad (29)$$

Based on the above calculation, the  $n'$  edge detection operators of multimedia digital ship image can be obtained, and the appropriate weight is added to it, so as to obtain the multi-element edge detection operator of multimedia digital ship image. The formula is as follows:

$$E_{avr}(x'', y'') = \sum_{i=1}^{n'} a' E'(x'', y'') \quad (30)$$

Let the gray scale range of the multimedia digital ship image is  $[1, L']$ , the occurrence probability of image pixel in each gray scale is expressed as  $P'_0, P'_1, P'_2, \dots, P'_l$ ; the image processed by the edge detection operator  $E'(x'', y'')$  of multimedia digital ship image is denoted as  $I'$ , and the entropy of  $I'$  of multimedia digital ship image can be calculated as:

$$\begin{cases} eI' = -\sum_k^l \log_2 \\ \check{k} = 1, 2, \dots, l \end{cases} \quad (31)$$

The weight value  $a''$  of the extracted digital ship image entropy is:

$$a'' = eI' / \left[ \sum_k^{n'} eI' \right] \quad (32)$$

(c) Edge and contour information extraction of multimedia digital ship image based on multi-scale morphology

The edge and contour features of the image are extracted by using the structural elements with different sizes of multimedia digital ship images. In order to obtain more accurate edge detection information, it is necessary to adjust the size of the structural element scale reasonably. After comparative analysis, the multi-scale structural elements are used, and the expression is defined as:

$$\theta_\gamma = \theta \oplus \theta \oplus \theta \oplus \theta \dots \oplus \theta \quad (33)$$

Where,  $\gamma$  stands for the scale parameter of the multimedia digital ship image, it is a positive integer;  $\theta$  represents the finite structural element of the multimedia digital ship image, and  $\theta$  is a cross-shaped  $3 \times 3$  structural element. Equation (33) shows that the large-scale structural elements of a multimedia digital ship image are obtained by performing multiple expansion operations on the small-scale structural elements of the image. The expression of the multi-scale morphological edge detection operator of multimedia digital ship image is:

$$E_M(x'', y'') = \sum_{i=1}^{n'} a' E'(x'', y'') \quad (34)$$

Where,  $E_M(x'', y'')$  is the new synthesized multimedia digital ship image.

## SIMULATION RESULTS AND ANALYSIS

The experimental platform is MATLAB 7.0, and the computer installation with Microsoft Windows 7 Professional (SP2) operating system, Intel (R) Core (TM) CPU 2.6Hz, 4GB

memory, and 720GB hard disk. Two  $320 \times 240$  multifunctional digital ship images for experiment from google are randomly selected. The test images are shown in Figure 1(a1) and Figure 1(a2). The second picture is cabin picture.

In order to verify the effectiveness of the proposed method compared with other methods, 8 Gaussian filter in reference [13] and double filter proposed in this paper are compared, and the results of the experimental analysis are shown in Figure 1.



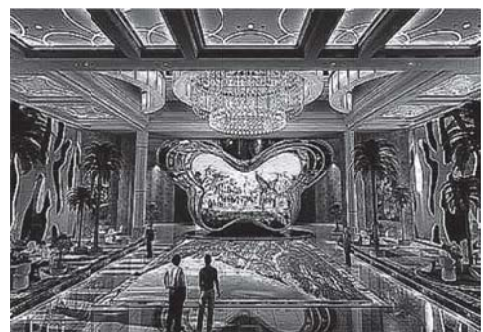
(a1) Original test Multimedia digital ship image



(a2) Original test Multimedia digital ship image



(b1) Denoising method based on Wavelet transform in section A



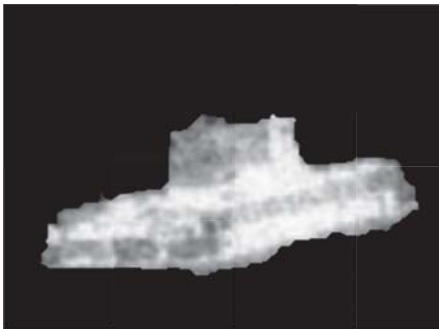
(b2) Denoising method based on Wavelet transform in section A



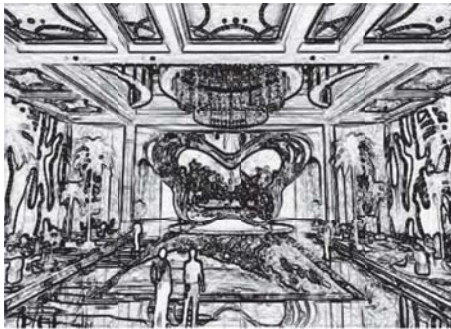
(c1) Denoising method in reference [13]



(c2) Denoising method in reference [13]



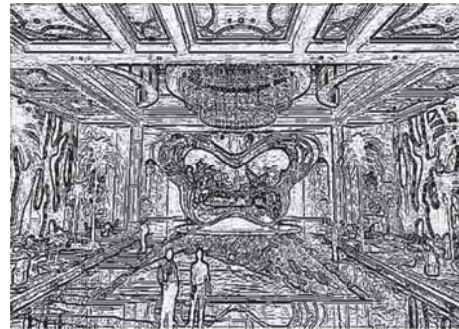
(d1) The results of edge extraction by the method in reference [13]



(d2) The results of edge extraction by the method in reference [13]



(e1) The results of edge extraction by the proposed method



(e2) The results of edge extraction by the proposed method

Figure 1 Multimedia digital ship image

The comprehensive comparative analysis of Figure 1 can be seen, the denoising effect of wavelet transform method used in section A and Gaussian filter method used in reference [13] for multimedia digital ship image denoising is not ideal, seriously affect the subsequent image processing. It can be seen from the edge extraction effect of Fig. 1(e1) and Fig. 1(e2) that it still contains a certain noise in the edge extraction by the method of section C and the method of reference [13], resulting in the incomplete extraction of edge and contour information, which cannot get more accurate edge information[18-22]. Compared with the other two methods, the proposed method has obvious advantages, and the noise in the original multimedia digital ship image is removed well, retaining better detail information for the subsequent image segmentation and edge and contour information extraction.

The simulation results show that the proposed method can obtain the ideal image edge and contour information, and realize the bidirectional balance between the denoising and the accurate extraction of edge and contour information of the target image. Compared with the traditional edge and contour information extraction method, the extraction effect is greatly improved[23].

## CONCLUSION

When the edge contour information of multimedia digital ship image is extracted by the current method, the image background cannot be better segmented with the image object because it contains a lot of noise, which can affect the quality of the subsequent image processing. This paper presents a method for edge contour information extraction of multimedia digital ship image based on multi-scale morphology. Experimental results show that the proposed method can eliminate the influence of noise and preserve the details of the edge contour information of the image, and has good practical value.

## REFERENCE

1. Tandon R, Simeone O. Harnessing cloud and edge synergies: toward an information theory of fog radio access networks . IEEE Communications Magazine, 2016, 54(8):44-50.

2. Kuo P C, Lu K H, Hsu Y N, et al. Fast three-dimensional video coding encoding algorithms based on edge information of depth map. *Iet Image Processing*, 2015, 9(7):587-595.
3. Cheng B N, Kuperman G, Deutsch P, et al. Group-centric networking: addressing information sharing requirements at the tactical edge. *IEEE Communications Magazine*, 2016, 54(10):145-151.
4. Wen S, Haghighi M S, Chen C, et al. A Sword with Two Edges: Propagation Studies on Both Positive and Negative Information in Online Social Networks. *IEEE Transactions on Computers*, 2015, 64(3):640-653.
5. Liu X F, Yao X R, Lan R M, et al. Edge detection based on gradient ghost imaging. *Optics Express*, 2015, 23(26):33802.
6. Tseng C S, Wang J H. Perceptual edge detection via entropy-driven gradient evaluation. *Iet Computer Vision*, 2016, 10(2):163-171.
7. Hidalgogato M C, Barbosa V C F. Edge detection of potential-field sources using scale-space monogenic signal: Fundamental principles. *Geophysics*, 2015, 80(5):J27-J36.
8. Hidalgogato M C, Barbosa V C F. Edge detection of potential-field sources using scale-space monogenic signal: Fundamental principles. *Geophysics*, 2015, 80(5):J27-J36.
9. Liu X, Fang S. A convenient and robust edge detection method based on ant colony optimization. *Optics Communications*, 2015, 353(8):147-157.
10. Gardiner B, Coleman S A, Scotney B W. Multiscale Edge Detection Using a Finite Element Framework for Hexagonal Pixel-Based Images. *IEEE Transactions on Image Processing*, 2016, 25(4):1-1.
11. Zheng Y, Zhou Y, Zhou H, et al. Ultrasound image edge detection based on a novel multiplicative gradient and Canny operator.. *Ultrasonic Imaging*, 2015, 37(3):238-50.
12. Sharma B, Mahajan P. Latest trend of variation of EDGE detection and object detection with pixel level variation and their comparison algorithms. *Genetic Epidemiology*, 2015, 35(7):606-19.
13. Tschirhart P, Morris B. Improved edge detection mapping through stacking and integration: a case study in the Bathurst Mining Camp. *Geophysical Prospecting*, 2015, 63(2):283-295.
14. Qu Z, Fang X, Su H, et al. Measurements for displacement and deformation at high temperature by using edge detection of digital image.. *Applied Optics*, 2015, 54(29):8731.
15. 11.Gao, W. and W. Wang, The fifth geometric-arithmetic index of bridge graph and carbon nanocones. *Journal of Difference Equations and Applications*, 2017. 23(1-2SI): p. 100-109.
16. 12.Gao, W., et al., Distance learning techniques for ontology similarity measuring and ontology mapping. *Cluster Computing-The Journal of Networks Software Tools and Applications*, 2017. 20(2SI): p. 959-968.
17. Any support wen-quan zeng, ai-min yu. An effective medical noisy image edge detection method . *Journal of electronic design engineering*, 2016, 24 (10) : 180-183.
18. Rahman N A, HalimH, Gotoh H, Harada E. Validation of Microscopic Dynamics of Grouping Pedestrians Behavior: From Observation to Modeling and Simulation. *Engineering Heritage Journal*, 2017, 1(2):15-18.
19. Gao W,Rajesh Kanna M R, Suresh E, Farahani M R. Calculating of degree-based topological indices of nanostructures. *Geology, Ecology, and Landscapes*, 2017, 1(3): 173-183.
20. Farajollahi G, Delavar M R. Assessing accident hotspots by using volunteered geographic information. *Journal CleanWAS*, 2017, 1(2): 14-17.
21. Roslee R,Mickey A C, Simon N, Norhisham M N. Landslide Susceptibility Analysis (Lsa) Using Weighted Overlay Method (Wom) Along the Genting Sempah To Bentong Highway, Pahang. *Malaysian Journal Geosciences*, 2017, 1(2): 13-19.
22. Ismail M N, Rahman A, Tahir S H. Wave-dominated shoreline deposits in the Late Miocene Sedimentary Sequence in the Miri Formation North Sarawak, Malaysia. *Geological Behavior*, 2017, 1(2):14-19.
23. TengY, Zhou Q. Environmental effect of Sudan I-IV: adsorption behaviors and potential risk on soil. *Acta Scientifica Malaysia*, 2017, 1(1): 16-17.

#### CONTACT WITH THE AUTHOR

Fangping Yin

*e-mail: styfp@tom.com*

Guangdong Mechanical and Electrical College  
Guangzhou 510515  
**CHINA**

# IDENTIFICATION ALGORITHM OF UNCERTAIN SONAR SIGNALS IN COMPLEX MARINE ENVIRONMENT

Xuefeng Zhang

School of Information and Communication Engineering, North University of China, Taiyuan 030051,  
China

## ABSTRACT

*The current identification algorithm using sonar signal parameters of bandwidth, frequency, duration and pulse waveform which are easy to detect and imitation, to identify the identity of sonar signal, resulting in part of the sonar signal identity is not easy to distinguish. Therefore, an algorithm based on signal feature extraction and digital watermarking is proposed to recognize the uncertain sonar signals. The algorithm embeds the digital watermark into the detection signal from the uncertain sonar. The identity of the signal is recognized by detecting whether the received signal contains watermarks. Experimental results showed that the proposed algorithm can effectively improve the recognition performance of sonar signal source.*

**Keywords:** Complex marine environment; Uncertain sonar signals; Identification algorithms

## INTRODUCTION

The ocean contains huge resources and benefits, making it gradually become a hot spot in the world. Therefore, understanding of underwater conditions becomes particularly important [1-2]. As an effective means of underwater detection and communication, underwater acoustic signals have been paid more and more attention by people [3]. With the development of underwater detection and communication technology, the marine environment is filled with many sound signals, the enemy often launch with highly similar signal which identity are not easy to distinguish to implement interference or trick [4]. Therefore, how to determine the identity of received underwater acoustic signals has become an urgent problem that needs to be solved [5]. The existing sonar signal identification algorithm uses sonar parameters such as bandwidth, frequency, duration and pulse waveform which are easy to detect and imitate, resulting in part of the sonar signal identity is not easy to distinguish [6]. Therefore, a new identification algorithm of uncertain sonar signals

in complex marine environment is proposed. In the sonar signal, digital watermark is embedded, the identity of the signal is recognized by detecting whether the received signal contains watermarks.

## IDENTIFICATION ALGORITHM OF UNCERTAIN SONAR SIGNALS IN COMPLEX MARINE ENVIRONMENT

### A. ANALYSIS OF UNCERTAIN SONAR SIGNALS IN COMPLEX MARINE ENVIRONMENT

In complex marine environment, different signal waveforms will produce different processing results and different detection performance. Wavelet analysis theory is used to extract the energy features of different sonar signals in complex marine environment. Hilbert spectrum features

of uncertain sonar signals are extracted by Hilbert Huang transform method [7]. Different types of sonar signal features are extracted by several algorithms. The specific process is as follows:

(1) energy extraction in different frequency bands based on wavelet packet decomposition

Taking the three-level wavelet packet decomposition as an example, the wavelet packet decomposition algorithm and the steps of extracting the energy features in each frequency band of the uncertain sonar signals in complex marine environment are given. The structure of the three-layer wavelet packet decomposition is shown in figure 1.

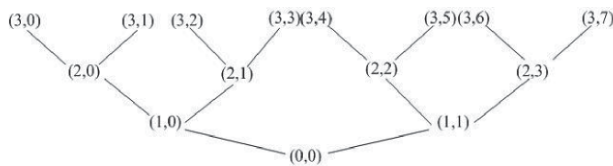


Fig. 1. Structure Diagram of Three-layer Wavelet Packet Decomposition

$(i, j)$  represents the  $j$  node in the  $i$  layer,  $i = 0, 1, 2, 3$ ,  $j = 0, 1, 2, 3, \dots, 7$ , each node represents a certain feature of sonar signal, where  $(0,0)$  represents the original signal  $S$ ;  $(1,0)$  represents the low frequency coefficient  $X_{10}$  of first layer in wavelet packet decomposition;  $(1,1)$  represents the high frequency coefficient  $X_{10}$  of first layer in wavelet packet decomposition, in order to push.

The first step: in the complex marine environment, the original sonar signal is carried out with three-layer wavelet packet decomposition;

The second step: the wavelet signal decomposition is used to reconstruct the sonar signal, and obtained the reconstructed signal in each frequency band of the sonar signal.

$$S = S_{30} + S_{31} + \dots + S_{37} \quad (1)$$

Where  $S_{ij}$  represents the reconstruction signal corresponding to  $X_{ij}$ .

Assumed that in a complex marine environment, the minimum frequency component of an uncertain sonar signal is 0, and the highest frequency component is 1. The frequency ranges they represent each are shown in Table 1.

Tab. 1. The Frequency Range Represented by the Reconstructed Signal

| Uncertain sonar signal | Frequency range /Hz | Uncertain sonar signal | Frequency range /Hz |
|------------------------|---------------------|------------------------|---------------------|
| S30                    | 0-0.125             | S34                    | 0.500-0.625         |
| S31                    | 0.125-0.250         | S35                    | 0.625-0.750         |
| S32                    | 0.250-0.375         | S36                    | 0.750-0.875         |
| S33                    | 0.375-0.500         | S37                    | 0.875-1.000         |

The third step: to find the energy  $E_j (j = 0, \dots, 7)$  of the reconstructed signals in the frequency bands of the uncertain

sonar signals,  $E_j = \sqrt{\sum_{k=1}^K |S_{3j}(k)|^2}$ ,  $S_{3j}(k)$  represents the magnitude of the discrete points of the reconstructed signal  $S_{3j}$ ,  $k = 1, 2, \dots, N$  and  $N$  are the points of the reconstructed signals.

The fourth step: construct the feature vector of uncertain sonar signals.  $E_j$  represents the energy of the reconstructed signal, with a total energy of  $E = \sqrt{\sum_{j=0}^7 E_j^2}$ . The feature quantity is  $F$ :

$$F = \left[ \frac{E_0}{E}, \dots, \frac{E_7}{E} \right] \quad (2)$$

According to the frequency range represented by the decomposed signal, the feature vectors extracted from the first class of sonar signals by wavelet packet decomposition can well represent the feature information of the target signals.

(2) Hilbert spectrum feature extraction based on Hilbert Huang Transform

To study the variation of frequency of uncertain sonar signals with time in complex marine environment, the instantaneous frequency is proposed. There has been a lot of controversies over the definition of instantaneous frequency, until the Hilbert transform and analytic signal method proposed. For any time series  $x(t)$  satisfying the requirement, the corresponding Hilbert transform  $y(t)$  can be expressed as a lower form:

$$y(t) = \frac{1}{\pi} \int_{-\infty}^{+\infty} \frac{x(\tau)}{t - \tau} d\tau = x(t) * \frac{1}{\pi t} \quad (3)$$

Then we can define the complex analytic signal  $x(t)$  of the uncertain sonar signal  $z(t)$ :

$$z(t) = x(t) + jy(t) = a(t)e^{-j\theta(t)} \quad (4)$$

The instantaneous amplitude and instantaneous phase of the sonar signal  $z(t)$  are analyzed:

$$a(t) = \sqrt{x^2(t) + y^2(t)} \quad (5)$$

$$\theta(t) = \arctan \frac{y(t)}{x(t)} \quad (6)$$

The instantaneous frequency of an uncertain sonar signal  $x(t)$  is defined as:

$$w(t) = \arctan \frac{d\theta(t)}{dt} \quad (7)$$

The instantaneous frequency of an uncertain sonar signal in a complex marine environment is the angular frequency of the signal at a moment, or it can be regarded as instantaneous phase change rate over time.

For stationary sonar signals, an analytic sonar signal with physical significance can be obtained by using the

instantaneous frequency defined above which solves the problem of negative frequency after Fourier transformation. But for non-stationary signals in the uncertain sonar signal, the frequency changes over time. The instantaneous frequency obtained after the direct Hilbert transform can also be negative which has no physical meaning. To solve this problem, empirical mode decomposition [8] is adopted to deal with the problem:

The first step: find out the extremum points of the original sonar signal  $x(t)$ , that is, the maximum and minimum points. The upper and lower envelopes of extreme points are obtained through the method of interpolation fitting;

The second step: calculate the mean value of the upper and lower envelope of the extremum point, denoted as  $m_{10}(t)$ .

The third step: calculate the difference between  $x(t)$  and  $m_{10}(t)$ , which is denoted as  $h_{10}(t)$ .

$$h_{11}(t) = h_{10}(t) - m_{11}(t) \quad (8)$$

The fourth step: verify that if  $h_{10}(t)$  meets the requirements of IMF. If satisfied, make  $imf_1 = h_{10}(t)$ ; otherwise, take  $h_{10}(t)$  as a new signal sequence, in accordance with step 1 to 3, get the upper and lower envelope mean  $m_{11}(t)$ , and calculate the difference between  $h_{10}(t)$  and  $m_{11}(t)$ , denoted as  $h_{11}(t)$ :

$$h_{11}(t) = h_{10}(t) - m_{11}(t) \quad (9)$$

The fifth step: verify that if  $h_{11}(t)$  meets the IMF requirement. Repeat the operation several times until  $h_{1i}(t)$  meets the IMF requirement. So far, the signal  $imf_i(t)$  has been received;

$$imf_1 = h_{1i}(t) \quad (10)$$

The sixth step: separate  $imf_1(t)$  from the original uncertainty sonar signal  $x(t)$  and get the signal  $r_1(t)$ :

$$r_1(t) = x(t) - imf_1(t) \quad (11)$$

The seventh step: take  $r_1(t)$  as a new signal sequence and repeat the above steps to find the other IMF components;

The eighth step: get a margin  $r_n(t)$  that hat can no longer be decomposed by EMD, which is called the residual component;

At this time, the original sonar signal  $x(t)$  can be expressed as a sum of finite intrinsic modes and functions after EMD decomposition.

$$x(t) = \sum_{i=1}^n imf_i(t) + r_n(t) \quad (12)$$

After EMD decomposition, in complex marine environment, the uncertainty sonar signals can be expressed as the sum of multiple IMF components and residuals. The residual of a sonar signal represents a long-period oscillation, either a constant or a monotonic function, which may contain great energy. Therefore, in practical applications, according to the needs of the study to decide whether to retain. The definition of the instantaneous frequency and

the instantaneous phase in front can be obtained, and each IMF can be expressed as:

$$imf_i(t) = \text{Re}((a_i(t)\exp(j\theta_i(t)))) = \text{Re}(a_i(t)\exp(j\int\omega_i(t)dt)) \quad (13)$$

Then the original uncertainty sonar signal  $x(t)$  can be represented as:

$$x(t) = \text{Re}(\sum_{i=1}^n a_i(t)\exp(j\int\omega_i(t)dt)) \quad (14)$$

Then we can do the Hilbert transform for each IMF component to obtain its instantaneous amplitude and instantaneous frequency, and summarize the instantaneous amplitude and instantaneous frequency of all IMF. Hilbert marginal spectrum is the total amplitude of instantaneous frequency of uncertain sonar signals in complex marine environment, which reflects the amplitude distribution at each frequency point.

Suppose there is a marine sonar signal with a sampling point of  $N$ , the sampling frequency is  $f_s$ , and the time length is  $T$ . According to Fourier analysis theory, the highest frequency component of the Fourier transform signal is  $f_s/2$ , and the frequency resolution of marine sonar signal is fixed  $f_s/N$ . By the theory of Hilbert transform [9], the frequency of the Hilbert marginal spectrum [10] is the instantaneous frequency, and is the derivative of the phase of its corresponding analytic signal. The highest instantaneous frequency of the Hilbert spectrum of marine sonar signals is the highest frequency inherent to the sampled signals. The frequency resolution in the Hilbert marginal spectrum is related to the sampling number  $N$  and the highest frequency inherent to the marine sonar signal:

$$\Delta f = f_{\max} / N \quad (15)$$

Due to the advantage of Hilbert marginal spectrum relative to Fourier amplitude spectrum and its higher frequency resolution, we use the HHT method to extract the marginal spectral features of the uncertain sonar signals in complex marine environment.

## B. DETECTION OF UNCERTAIN SONAR SIGNAL

The processing structure of the sonar signal receiver primarily depends on the form of the transmitted signal, the sonar signal processing has been smoothly smooth to obtain the smoothing weight coefficient and steady signal, the received signal is defined:

$$x(n)' = s(n)' + n(n)' \quad (16)$$

Where,  $s(n)'$  is the target echo signal,  $n(n)'$  and  $(0, \sigma^2)$  is the distributed Gauss white noise, and the signal is not correlated with noise.

In complex marine environment, the conditional probability density of the unknown sonar signal detection statistic  $M$  is:

$$p(M / H_1) = \frac{M}{\sigma^2} \exp\left(-\frac{M^2 + (aN / 2^2)}{2\sigma^2}\right) I_0\left(\frac{MaN}{2\sigma^2}\right) \quad (17)$$

$$p(M / H_0) = \frac{M}{\sigma^2} \exp\left(-\frac{M^2}{2\sigma^2}\right) \quad (18)$$

Formulae (17) and formulae (18) are Rician and Rayleigh distributions, where  $a$  is the amplitude of sonar signals. Thus, the false alarm probability is:

$$P_f = \exp\left(-\frac{\lambda^2}{2\sigma^2}\right) \quad (19)$$

The detection probability is:

$$P_D = \int_{\lambda}^{\infty} \frac{M}{\sigma^2} \exp\left(-\frac{M^2 + (aN / 2^2)}{2\sigma^2}\right) I_0\left(\frac{MaN}{2\sigma^2}\right) dM \quad (20)$$

Formulae (16) to (20) determines the detection performance of the receiver of uncertain sonar signals in complex marine environment.

### C. MATHEMATICAL WATERMARKING MODEL FOR UNDERWATER ACOUSTIC CHANNEL IN COMPLEX MARINE ENVIRONMENT

In the complex marine environment, if the velocity distribution function of underwater acoustic channel is  $c(z)$ , the position of the point source is  $(r_0, z_0)$ , and the initial sound velocity is  $c_0$ . Then, the sound propagation track  $r$  and propagation time  $t$  of any point source  $(r, z)$  with an initial grazing  $\theta_0$  at any point on the acoustic line of the initial grazing can be expressed in the lower form:

$$r = r_0 + \int_{z_0}^z \frac{\cos \theta_0}{\sqrt{n^2 - \cos^2 \theta_0}} dz \quad (21)$$

$$r = \frac{1}{c_0} \int_{z_0}^z \frac{n^2(z)}{\sqrt{n^2 - \cos^2 \theta_0}} dz \quad (22)$$

Where,  $n(z) = c_0 / c(z)$  represents refractive index.

In complex marine environment, the geometric propagation loss between the sound source and the receiving point can be calculated by the cross-sectional area of the acoustic beam tube between the two adjacent sound sources, as shown in figure 2.

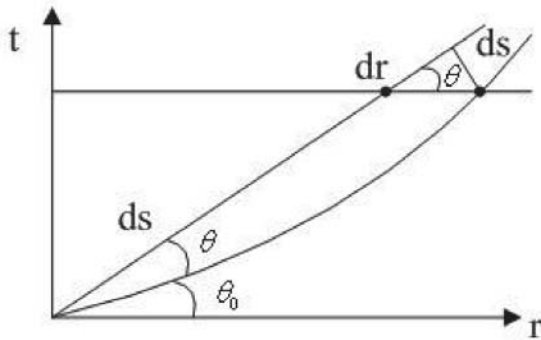


Fig. 2. The Propagation of Sound Energy Along the Ray Tube Bundle

Considering two acoustic lines emitted by the acoustic source at grazing angle  $\theta_0$  and  $\theta_0 + d\theta_0$ , they propagate along the acoustic track in the marine and arrive near the receiving point. The horizontal distance is  $dr$ . In  $d\theta_0$ , the sound power radiated from the sound source is  $\Delta P$ . According to the physical meaning of the sound intensity equation, the sound power between the sound lines is the same at the receiving point. In the sound beam tube, the sound intensity at the unit distance is  $I_0$ , the vertical area of the sound line is:

$$dS_0 = 2\pi \cos \theta_0 d\theta_0 \quad (23)$$

At the receiving point  $(r, z)$ , the vertical area of the sound line is:

$$dS = 2\pi r \sin \theta dr \quad (24)$$

At the receiving point  $(r, z)$ , the sound intensity  $I$  and the sound pressure  $A$  is:

$$I = \frac{I_0 \cdot dS_0}{dS} = \frac{I_0 \cos \theta d\theta_0}{r \cdot \cos \theta dr} \quad (25)$$

$$A = \sqrt{I} \quad (26)$$

The impulse response function  $h(t)$  of multipath channels can be determined by calculating the intrinsic sound line parameters:

$$h(t) = \sum_{i=1}^N A_i \delta(t - t_i) \quad (27)$$

$$A_i = (-1)^N \cdot \frac{\sqrt{I_i}}{\sqrt{I_{\max}}} \quad (28)$$

$$\tau_i = t_i - t_{\min} \quad (29)$$

Where  $N$  represents the total number of active channels in the sound field,  $A_i$  represents the normalized sound pressure amplitude value of a propagation path of the original sound,  $I_i$  represents the sound pressure amplitude value,  $I_{\max}$  represents the maximum amplitude of sound pressure,  $\tau_i$  represents relative delay,  $t_i$  represents the delay and  $t_{\min}$  represents the minimum delay.

If the transmit signal is  $s(t)$ , then the received signal is  $y(t)$ :

$$y(t) = s(t) * h(t) = s(t) * \left[ \sum_{i=1}^n A_i \delta(t - t_i) \right] \quad (30)$$

If the transmit signal 1 meter from the sound source is  $s(t)$ , then the received signal is  $y(t)$ , and the transmission loss is  $TL$ :

$$TL = 101g \frac{\frac{1}{T} \int_0^T s^2(t) dt}{\frac{1}{T} \int_0^T y^2(t) dt} = 101g \frac{\frac{1}{T} \int_0^T s^2(t) dt}{\frac{1}{T} \int_0^T \left[ \sum_{i=1}^N A_i s(t - \tau_i) \right]^2 dt} \quad (31)$$

The watermark  $W$  generated by the watermark generation algorithm is generally related to the key  $K$  and the secret information  $m$ , but in some applications, the watermark information is also related to the carrier content, the sonar signal  $S$ . Therefore,  $W = W(K, m)$ , after the watermark embedding algorithm, the watermark is embedded into the sonar signal  $S$  is the watermarked signal  $S_w$  can be expressed as  $S_w = T(W, S)$ . The received watermarked signal  $S'_w$  is transmitted via the underwater acoustic channel  $H$  from the watermarked signal  $S_w$  which can be expressed as  $S'_w = H(S_w)$ . Using the watermark extraction, detection algorithm  $D$  and watermark template  $W$  on the received watermark signal  $S'_w$ , considering the marine channel and additional noise in the channel, assuming the received signal can be expressed as  $r_{w0}$ :

$$r_{w0} = s_w * h + n_0 = s'_w + n_0 \quad (32)$$

Where  $h$  represents the impulse response of marine channel, and  $n_0$  represents an additive noise in the channel. Due to the influence of the ocean channel there will be a multi-way effect, the received signal will be extended in the time domain. In watermark detection, the same part of  $r_w$  as long as  $s$  is still taken from  $r_{w0}$ . On this basis, the received watermark signal  $r_w$  is performed three-layer DWT transform, and then the low frequency sub-band is transformed by DCT. Finally, according to the watermark length and the embedded position, it can be obtained:

$$R_w = dwt(r_w) = (R_1, \dots, R_4) \quad (33)$$

In the formula,  $R_w$  represents the wavelet coefficients of  $r_w$  after three-layer wavelet transform.

$$S'_{1Dw} = dwt(R_1) = (s'_{1Dw}, \dots, s'_{\frac{n}{8}Dw}) \quad (34)$$

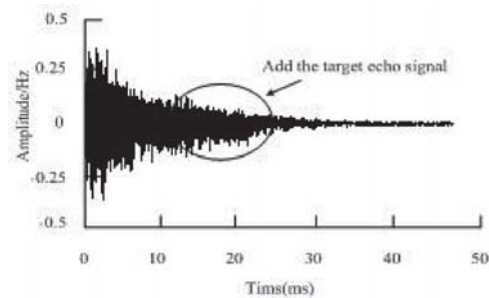
As shown in equation (34),  $S'_{1Dw}$  is the coefficient embedded in the watermark.

## EXPERIMENTAL RESULTS AND ANALYSIS

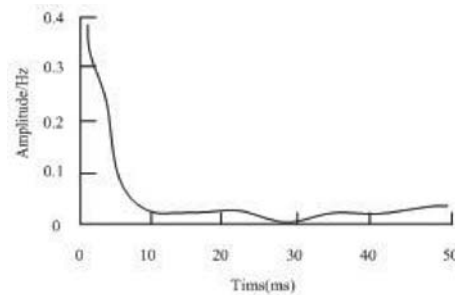
In this experiment, the actual marine test data of a kind of towed line array sonar is used as the verification of the identification algorithm of the sonar signal and each of the experimental tests obtained the sonar signal as a sample, a total of 50 sample data are obtained as a random signal of multiple different appearances. The experiment completed on the Matlab platform, compared the proposed algorithm with the matched filter detection algorithm, the validity of the proposed algorithm is verified by two aspects of the uncertain sonar signal detection result and the watermarked sonar signal detection result.

### A. DETECTION AND ANALYSIS OF UNCERTAIN SONAR SIGNALS

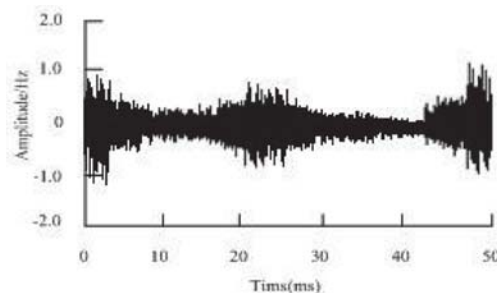
Figure 3 (a) showed the towed array sonar signal, the transmit signal bandwidth in the experiment is 30kHz, pulse width is 3.0ms, the center frequency is 30kHz; the sampling frequency is 100 kHz; the target echo located in 13.0 to 15.5ms, reverberation ratio is -1.0dB. The uncertain sonar signals are smoothed to obtain the weighting factor and the signal after the stabilization, as shown in Figure 3 (b) and figure 3 (c), respectively. To compare with the matched filtering method, the smoothing reverberation is first matched and filtered, and the result is shown in Figure 3 (d). Figure 3 (e) is the output of the signal detection in the proposed method.



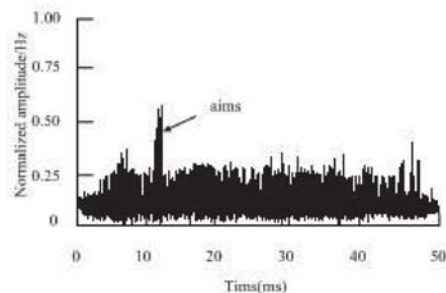
(a) Uncertain Signals in Simulation Marine Environment



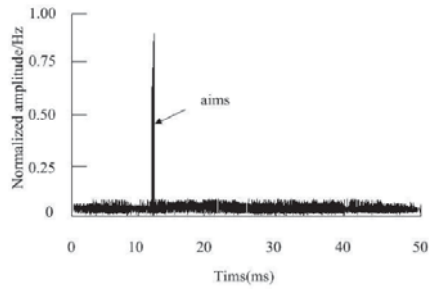
(b) Weight Coefficient



(c) Smooth Reverberation



(d) Matched Filtered Output



(e) Filter Output in This Paper

Fig. 3. Data Processing Results of Sea Trial Test

Figure 3 (e) showed that the proposed method can suppress the reverberation noise, detect the position of the target echo signal, and has a better ability to suppress the reverberation than the matched filtering method [11-12].

The Monte Carlo method was used to calculate the experimental results to obtain the Receiver operating characteristic(ROC) curve of the experimental receiver. The ROC curve showed that under the condition of a fixed signal mixing ratio, different threshold values correspond to different detection probability and false alarm probability [13-15]. By using the proposed algorithm and the matched filter detection algorithm on sea trial data processing, for the signal containing the target, in a fixed threshold, if the detection output is greater than the threshold, the target is detected, otherwise is not, which can estimate the detection probability of the threshold. Figure 4 showed the ROC curve at the signal mixing ratio of -2.0dB. The dotted line is the ROC curve of the matched filter detector, and the solid line is the ROC curve of the proposed algorithm. Figure 5 showed the ROC curve of the sea trial results, with a mixing ratio of 4.5dB. In the complex marine environment, the signal mixture ratio is not easy to measure [16]. The signal mixture ratio is obtained by formula (35):

$$SRR = 10 \log \left( \frac{P_{s+r} - P_r}{P_r} \right) \quad (35)$$

Where,  $SRR$  is the signal mixture ratio;  $P_{s+r}$  is the signal power of the target echo signal position which contains two parts of the target echo signal and the reverberation signal;  $P_r$  is the reverberation signal power near the target echo signal.  $P_r$  is used to approximate the reverberation signal power contained in the target echo signal location.

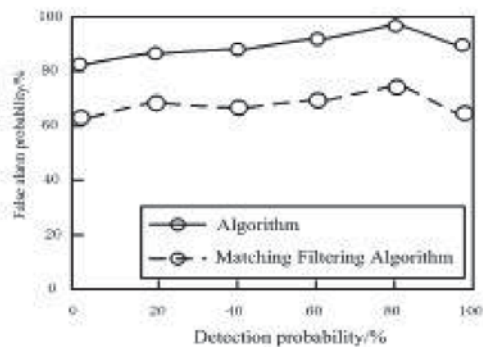


Fig. 4. ROC Curve under Simulated Signal SRR of -2.0dB

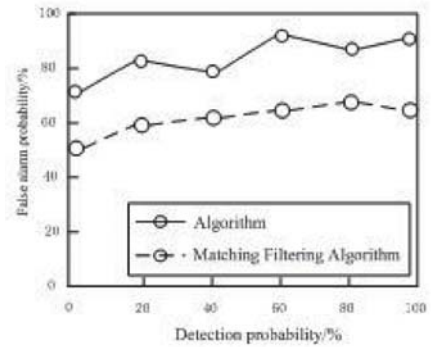
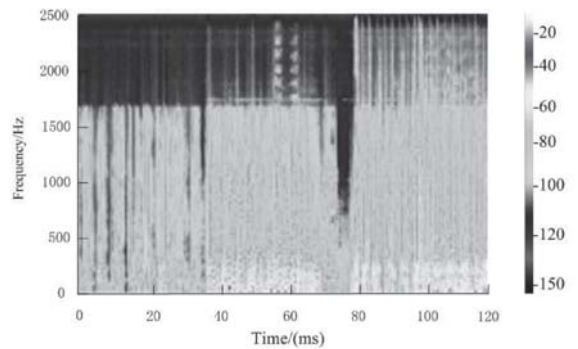


Fig. 5. ROC Curve under Sea Trial Signal SRR of 4.5dB

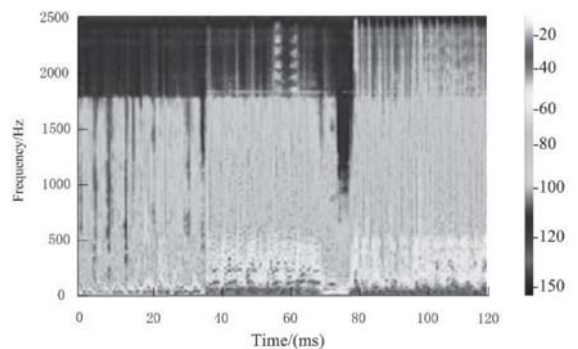
Figure 4 and figure 5 showed that the detection performance of the proposed method is superior to that of the matched filter. It is also found that the signal mixture ratio of simulation signal is less than the sea test signal, but the simulation signal performance is better, this is because the sea trial data contains strong interference signal, thus increasing the probability of false alarm. The stability of reverberation also affect the detection performance [17]. In the data processing, it is found that the unreasonable stabilization method can also reduce the detection performance [18].

## B. DETECTION AND ANALYSIS OF WATERMARKED SONAR SIGNALS

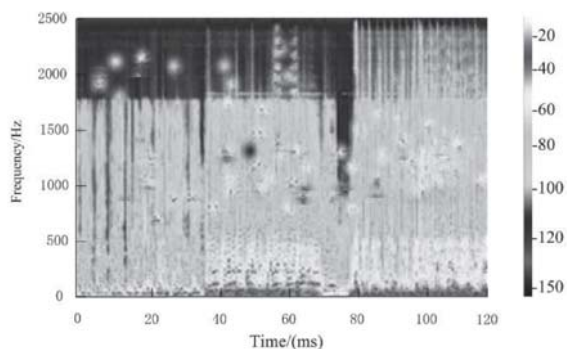
To verify the effectiveness and performance of the proposed algorithm, the detection performance of the watermarked sonar signal is analyzed.



(a) Original Carrier Signal



(b) Watermarked Signals (noiseless)



(c) Watermarked Signal (SNR=20dB)

Fig 6. Signal Analysis Spectrum

Figure 6 showed the spectrums of original signal, the watermarked signal (noiseless) and the watermarked signal (SNR=20dB), combined with the results shown in Figure 1, table 2 gives the specific performance of the watermark detection under different SWR conditions.

Tab. 2. Watermark Detection Results under Different SWR Conditions

| Watermark embedding ratio | The false alarm probability /% | The probability of missed/% |
|---------------------------|--------------------------------|-----------------------------|
| SWR=30dB                  | 1.09                           | 0.7                         |
| SWR=45dB                  | 4.9                            | 2.7                         |
| SWR=60dB                  | 7.0                            | 3.6                         |
| SWR=75dB                  | 9.4                            | 4.8                         |

Figure 6 and table 2 showed that with the increase of SWR, the probability of false alarm and the failure probability increases gradually, but the false alarm probability and failure probability of the proposed method are not high, which proved that this method has a better detection performance of watermarking.

## RESULTS AND DISCUSSION

For the difficulty to identify the identity of the received signal for the uncertainty in the complex marine environment, it is proposed to embed digital watermark in the active sonar transmit signal and detect whether the received signal contains the embedded watermark, and then realize the identity of uncertain sonar signals.

The main results of this paper are as follows:

1. The features of uncertain sonar signals and signal detection in complex marine environment are systematically studied and analyzed. A method of sonar identification using digital watermarking technology is proposed, and the feasibility and performance of this method are analyzed combined with sonar signal detection and detection resolution.

2. Underwater acoustic channel model is established based on the eigen ray model of, and digital watermarking model of underwater acoustic channel is established based on this model. Simulation results showed that the Influence of underwater acoustic channel on watermarking should be considered in the design of watermarking algorithm.
3. Considering the coherence of underwater acoustic channel, a block based DCT watermarking algorithm is designed and implemented. Firstly, the original carrier signal is partitioned according to the features of the underwater acoustic channel, and then the DCT transform is used for each sub-block. Finally, the watermark is embedded into each sub-block. The normalized correlation value is proposed at the end of the detection, so that the correlation value can be independent of the signal amplitude, which can improve the detection rate. Through simulation analysis, the feasibility and security of the algorithm are verified, and the shortcomings of this method are also proposed.

Through simulation analysis, it is proved that the proposed algorithm can improve watermark detection rate and signal resolution performance in the case of no significant impact on the detection performance of the sonar signal. Therefore, the research of this subject has great significance and practical value.

## REFERENCES

1. Ferguson B G, Lo K W. Passive and active sonar signal processing methods for port infrastructure protection and harbor security. *Journal of the Acoustical Society of America*, 2016, 140(4):3350-3350.
2. Wei C, Wwl A, Ketten D R, et al. Biosonar signal propagation in the harbor porpoise's (*Phocoena phocoena*) head: The role of various structures in the formation of the vertical beam.. *Journal of the Acoustical Society of America*, 2017, 141(6):4179.
3. Au W W, Copeland A, Martin S W, et al. Comparing the biosonar signals of free swimming dolphins with those of a stationary dolphin in a net pen. *Journal of the Acoustical Society of America*, 2015, 137(4):2335-2335.
4. Parks J K. Development of a Multichannel Optical Correlation Detector for Sonar Signals. *Journal of Aircraft*, 2015, 3(3):278-284.
5. Au W W L, Martin S W, Moore P W, et al. Dynamics of biosonar signals in free-swimming and stationary dolphins: The role of source levels on the characteristics of the signals. *Journal of the Acoustical Society of America*, 2016, 139(3):1381-1389.

6. De Maio A, Orlando D, Hao C, et al. Adaptive Detection of Point-Like Targets in Spectrally Symmetric Interference. *IEEE Transactions on Signal Processing*, 2016, 64(12):3207-3220.
7. Scandella B P, Pillsbury L, Weber T, et al. Ephemerality of discrete methane vents in lake sediments. *Geophysical Research Letters*, 2016, 43(9):n/a-n/a.
8. Wei C, Wwl A, Ketten D R, et al. Biosonar signal propagation in the harbor porpoise's (*Phocoena phocoena*) head: The role of various structures in the formation of the vertical beam.. *Journal of the Acoustical Society of America*, 2017, 141(6):4179.
9. Au W W, Copeland A, Martin S W, et al. Comparing the biosonar signals of free swimming dolphins with those of a stationary dolphin in a net pen. *Journal of the Acoustical Society of America*, 2015, 137(4):2335-2335.
10. LIANG Wei-xin, FENG Yong-xin, QIAN Bo, et al. An Optimization Recognition Algorithm of Amplitude-Frequency Modulation Signals. *Computer Simulation*, 2016, 33(8):415-420.
11. Gao, W. and W. Wang, The fifth geometric-arithmetic index of bridge graph and carbon nanocones. *Journal of Difference Equations and Applications*, 2017. 23(1-2SI): p. 100-109.
12. Gao, W., et al., Distance learning techniques for ontology similarity measuring and ontology mapping. *Cluster Computing-The Journal of Networks Software Tools and Applications*, 2017. 20(2SI): p. 959-968.
13. De'nan F, Nazri F M, Hashim N S. Finite Element Analysis on Lateral Torsional Buckling Behaviour Of I-Beam with Web Opening. *Engineering Heritage Journal*, 2017, 1(2):19-22.
14. Sarkar M I, Islam M N, Jahan A, Islam A, Biswas J C. Rice straw as a source of potassium for wetland rice cultivation. *Geology, Ecology, and Landscapes*, 2017, 1(3): 184-189.
15. Foroozanfar M. Environmental control in petroleum operations. *Journal CleanWAS*, 2017, 1(2): 18-22.
16. Wang J, Xu H. The Crust and Uppermost Mantle S-Wave Velocity Structure Beneath Japan Islands Revealed by Joint Analysis of P - And S Wave Receiver Functions. *Malaysian Journal Geosciences*, 2017, 1(2): 20-23.
17. Tahir S, Siong K Y, Musta B, Asis J. Facies and Sandstone Characteristics of The Kudat Formation, Sabah, Malaysia. *Geological Behavior*, 2017, 1(2):20-25.
18. Shamsudin S B, Majid A A. Association of blood lead levels

and working memory ability of primary school children surrounding ex-copper mining area in Ranau, Sabah (Malaysia). *Acta Scientifica Malaysia*, 2017, 1(1): 01-03.

#### CONTACT WITH THE AUTHOR

Xuefeng Zhang

*e-mail: wmsgczyz@163.com*

School of Information and Communication Engineering  
North University of China  
Taiyuan 030051  
**CHINA**